

Green Energy and Technology



Ali M. Eltamaly
Almoataz Y. Abdelaziz *Editors*

Modern Maximum Power Point Tracking Techniques for Photovoltaic Energy Systems

Green Energy and Technology

Climate change, environmental impact and the limited natural resources urge scientific research and novel technical solutions. The monograph series Green Energy and Technology serves as a publishing platform for scientific and technological approaches to “green”—i.e. environmentally friendly and sustainable—technologies. While a focus lies on energy and power supply, it also covers “green” solutions in industrial engineering and engineering design. Green Energy and Technology addresses researchers, advanced students, technical consultants as well as decision makers in industries and politics. Hence, the level of presentation spans from instructional to highly technical. ****Indexed in Scopus****.

More information about this series at <http://www.springer.com/series/8059>

Ali M. Eltamaly · Almoataz Y. Abdelaziz
Editors

Modern Maximum Power Point Tracking Techniques for Photovoltaic Energy Systems



 Springer

Editors

Ali M. Eltamaly
Sustainable Energy Technologies Center
King Saud University
Riyadh, Saudi Arabia

Almoataz Y. Abdelaziz
Electrical Power and Machines Department
Ain Shams University
Abbassia, Egypt

ISSN 1865-3529

Green Energy and Technology

ISBN 978-3-030-05577-6

<https://doi.org/10.1007/978-3-030-05578-3>

ISSN 1865-3537 (electronic)

ISBN 978-3-030-05578-3 (eBook)

© Springer Nature Switzerland AG 2020

This work is subject to copyright. All rights are reserved by the Publisher, whether the whole or part of the material is concerned, specifically the rights of translation, reprinting, reuse of illustrations, recitation, broadcasting, reproduction on microfilms or in any other physical way, and transmission or information storage and retrieval, electronic adaptation, computer software, or by similar or dissimilar methodology now known or hereafter developed.

The use of general descriptive names, registered names, trademarks, service marks, etc. in this publication does not imply, even in the absence of a specific statement, that such names are exempt from the relevant protective laws and regulations and therefore free for general use.

The publisher, the authors and the editors are safe to assume that the advice and information in this book are believed to be true and accurate at the date of publication. Neither the publisher nor the authors or the editors give a warranty, expressed or implied, with respect to the material contained herein or for any errors or omissions that may have been made. The publisher remains neutral with regard to jurisdictional claims in published maps and institutional affiliations.

This Springer imprint is published by the registered company Springer Nature Switzerland AG
The registered company address is: Gewerbestrasse 11, 6330 Cham, Switzerland

Preface

Solar photovoltaic energy systems (PVES) have been used to feed loads in remote areas as well as in central power plants connected to the electric utility. Many research works have been done to reduce the cost of the generated energy from the PVES. One of the most important factors of research work is to reduce the cost of generated energy by increasing the generated energy from the PVES by modifying its performance operations. This can be achieved by tracking the maximum power available from the PV systems which can increase the generated energy from PVES considerably and reduce its cost. The device used to track the maximum power available from the PVES is called maximum power point tracker (MPPT). MPPT uses a controlled technique to control the power electronics converters to be sure it extracts the maximum power available from the PVES. Conventional MPPT techniques like perturb and observe, hill climbing, incremental conductance, etc., have been introduced a long time ago, and they were working for unshaded PVES very well. But, in case of partial shading conditions, multi-peaks in the P-V curve of the PV array are generated, and these peaks may trap the conventional techniques to fall within one of the local peaks. With the advances of artificial intelligence, soft computing, and metaheuristic techniques, this limitation can be overcome, whereas metaheuristic techniques can track the global peaks in shaded or unshaded PVES which became a new trend in the tracking of the maximum power of the PVES. Many metaheuristic techniques are introduced and discussed in this book like particle swarm optimization (PSO), gray wolf optimization (GWO), genetic algorithm (GA), ant colony optimization (ACO), whale optimization (WO), simulated annealing (SA), etc. Also, hybrid techniques between the metaheuristic and conventional techniques or two hybrid metaheuristic techniques are introduced in many chapters of this book.

This book introduces many chapters to deal with the maximum power tracking of the PVES using modern MPPT techniques. This book introduces an overview of the modeling of PVES and its performance characteristics in different operating conditions. Also, a detailed description of the maximum power point variations in case of shaded and unshaded conditions is presented. A detailed historical review of the conventional and modern MPPT technique is also introduced to shed a light

on the development in this field. The most advanced techniques used as an MPPT are introduced and discussed in this book. Many techniques to deal with the effects of the partial shading on the PVES are also introduced and discussed. Many practical projects in this field are introduced and discussed in detail. Also, detailed power electronics circuits used as DC-DC converters have been introduced and discussed in detail in many chapters of this book.

This book will be very interesting for the readers who are looking for using PVES to feed loads in isolated areas as well as in the utility scale. It will also help them to know the PVES characteristics, modeling, operation, challenges, maximum power tracking, and practical implementation. This book will help the researchers, designers, and operators, as well as undergraduate/postgraduate students, to be familiar with the new trends of the field of PVES in general and MPPT in specific.

Mansoura, Egypt
Cairo, Egypt

Ali M. Eltamaly
Almoataz Y. Abdelaziz

Contents

History of Maximum Power Point Tracking	1
Mazen Abdel-Salam, Mohamed-Tharwat EL-Mohandes and Mohamed Goda	
PV Characteristics, Performance and Modelling	31
Ali M. Eltamaly and Hassan M. H. Farh	
Power Electronics for Practical Implementation of PV MPPT	65
Mohamed Abouelela	
Maximum Power Extraction from the Photovoltaic System Under Partial Shading Conditions	107
Hassan M. H. Farh and Ali M. Eltamaly	
Global Maximum Power Point Tracking-Based Computational Intelligence Techniques	131
Doaa Mohamed Atia	
On the Improvements of Perturb-and-Observe-Based MPPT in PV Systems	165
Mazen Abdel-Salam, Mohamed-Tharwat EL-Mohandes and Mohamed Goda	
Performance Analysis of Maximum Power Point Tracking (MPPT) for PV Systems Under Real Meteorological Conditions	199
K. M. Abo-Al-Ez, S. S. Kaddah, S. Diab and El-H. Abdraboh	
ANN and Multiple Linear Regression Based Modelling for Experimental Investigation of Photovoltaic Module Maximum Power Production Under Outdoor Condition of Mountainous Region	229
Amit Kumar Yadav and Hasmat Malik	

Adaptive Fuzzy Logic Controller as MPPT Optimization Technique Applied to Grid-Connected PV Systems	247
Mohamed M. Refaat, Yousry Atia, M. M. Sayed and Hossam Abdel Fattah	
Performance Improvement of Perturb and Observe Maximum Power Point Tracking Technique for Solar PV Applications	283
Ihechiluru Fortune Anya, Chitta Saha, Hafiz Ahmed, M. N. Huda and Sujan Rajbhandari	
An Efficient MPPT and Reliable Protection Scheme for PV-Integrated Microgrid Under Partial Shading and Array Faults	303
Murli Manohar, Ebha Koley and Subhojit Ghosh	
Artificial Bee Colony-Based GMPPT for Non-homogeneous Operating Conditions in a Bifacial CPVT System	331
Cihan Demircan, Ali Keçebaş and Hilmi Cenk Bayrakçı	
MPPT of PV System Under Partial Shading Conditions Based on Hybrid Whale Optimization-Simulated Annealing Algorithm (WOSA)	355
Ahmed A. Zaki Diab	
MPPT-Based Particle Swarm and Cuckoo Search Algorithms for PV Systems	379
Farag K. Abo-Elyousr, Alaaeldin M. Abdelshafy and Almoataz Y. Abdelaziz	
A New Hybrid Moth Flame Optimizer-Perturb and Observe Method for Maximum Power Point Tracking in Photovoltaic Energy System	401
Saber Arabi Nowdeh, Mohammad Jafar Hadidian Moghaddam, Shohreh Nasri, Almoataz Y. Abdelaziz, Mahmood Ghanbari and Iraj Faraji	
A New Hybrid Method Based on Gray Wolf Optimizer-Crow Search Algorithm for Maximum Power Point Tracking of Photovoltaic Energy System	421
Faraji Davoodkhani, S. Arabi Nowdeh, Almoataz Y. Abdelaziz, Saeedeh Mansoori, Sh. Nasri and Mohammad Alijani	
Dynamic Modeling Analysis of Direct-Coupled Photovoltaic Power Systems	439
Ahmed A. S. Mohamed	
Status Monitoring and Performance Investigation of a 5.1 kW Rooftop Grid-Tie Photovoltaic Energy System in Egypt	463
Ahmad H. Besheer, Mohamed A. Eldreny, Hassan Rashad and Ahmed Bahgat	

About the Editors



Dr. Ali M. Eltamaly (S'92–M'96–Ph.D.'2000) received his B.Sc. and M.Sc. in electrical engineering from Al-Minia University, Egypt, in 1992 and 1996, respectively. He received his Ph.D. in electrical engineering from Texas A&M University in 2000. He is currently a professor at Mansoura University, Egypt, and King Saud University, Riyadh, Saudi Arabia. His current research interests include renewable energy, smart grid, power electronics, motor drives, power quality, artificial intelligence, evolutionary and heuristic optimization techniques, and distributed generations. He published more than 20 books and chapters, and he has authored or coauthored more than 150 refereed journal and conference papers. He published a number of patents in the US patent office. He has supervised a number of M.S. and Ph.D. theses, and worked on a number of international technical projects. He got Professor Award for Scientific Excellence, Egyptian supreme council of Universities, Egypt, June 2017, and he has been awarded many prizes in different universities in Egypt and Saudi Arabia. He is participating as an editor and associate editor in many international journals and chaired many international conferences' sessions.



Almoataz Y. Abdelaziz (SMIEEE'2015) has received his B.Sc. and M.Sc. in electrical engineering from Ain Shams University, Cairo, Egypt, in 1985 and 1990, respectively, and the Ph.D. in electrical engineering according to the channel system between Ain Shams University, Egypt, and Brunel University, UK, in 1996.

He is currently a professor of electrical power engineering at Ain Shams University. He has authored or coauthored more than 350 refereed journal and conference papers and 20 chapters. He has supervised more than 70 M.Sc. and 15 Ph.D. theses in his research areas which include the applications of artificial intelligence, and evolutionary and heuristic optimization techniques to power systems, power system operation, planning, and control.

He is the chairman of IEEE Education Society Chapter in Egypt, a senior editor of *Ain Shams Engineering Journal*, editor of *Electric Power Components and Systems* journal, Editorial Board member, editor, associate editor, and Editorial Advisory Board member for many international journals.

He is also a senior member in IEEE, a member in IET and the Egyptian Sub-Committees of IEC and Cigré. He has been awarded many prizes for distinct researches and for international publishing from Ain Shams University, Egypt.

History of Maximum Power Point Tracking



Mazen Abdel-Salam, Mohamed-Tharwat EL-Mohandes
and Mohamed Goda

Abstract With time, the conventional fossil fuels for generating electric loads are depleted, so efforts are made to harness PV solar energy to serve the continuously increasing electric loads. The energy conversion efficiency of PV modules is very low, while they are expensive in price. This calls for operating the module at the maximum power point at all operating conditions. There exist numerous maximum power point tracking techniques in today's market to maintain the operation of PV module at maximum power such as off-line techniques, on-line or hill-climbing (HC) techniques and artificial intelligence (AI) techniques. Numerous approaches for improving, adapting, and optimizing these techniques have been published. However, they differ in many aspects such as tracking speed, tracking accuracy, steady-state efficiency and dynamic efficiency, number of sensors used, complexity, and cost. These MPPT techniques fail or deviate from tracking the correct maximum power point (MPP) under sudden or ramp variations of solar irradiation and ambient temperature as well as under partial shading with oscillations around MPP. From 1954 to 2018, all the researchers focused on MPPT, which is the main target of this chapter to follow up the history of development maximum power point tracking in PV systems as well as exploring the advantages and disadvantages of the many proposed MPPT methods in the literature. The history includes the off-line and on-line MPPT techniques along with their improvements as documented in the literature over the period 1954–2018. This chapter is framed as a review chapter.

M. Abdel-Salam · M.-T. EL-Mohandes
Electrical Engineering Department, Assiut University, Assiut, Egypt

M. Goda (✉)
Electrical Engineering Department, Ahram Canadian University, Giza, Egypt
e-mail: goda.masr@hotmail.com

1 Introduction

In 1954, Fuller et al. had received a patent-pending prize in physics for their first practical photovoltaic cell.

When the PV module is directly coupled to a resistive load, “e.g., DC lamp” as shown in Fig. 1, or to a dynamic load, “e.g., DC motor” as shown in Fig. 2, the module output current (I) and voltage (V) depend on the module’s operating point. The module’s operating point is located at the intersection of module and load I - V curves as shown in Fig. 3. Unfortunately, the module I - V curve is non-linear with only one maximum power point (MPP) at which the intersection rarely occurs. Also, the module I - V and P - V curves change under varying irradiation and ambient temperature conditions making the new location of the MPP as shown in Fig. 4. When the module/array is partially shaded, the P - V curve has multi-peaks as shown in Fig. 5.

Starting in “1954,” the maximum power point tracking (MPPT) is the aim of researchers to enhance efficiency and improve the performance of the PV systems.

MPP trackers are divided into two types: mechanical single- and dual-axis trackers and electrical trackers. The mechanical tracker “sun tracker” is a way to direct the PV module to follow the sun. However, this type is complex and costly in implementation and has low efficiency. Therefore, all attempts by scientists have been directed toward electrical tracking.

Electrical MPPT techniques are classified into three families: (i) off-line techniques such as fractional open-circuit voltage (FOCV) and fractional short-circuit

Fig. 1 PV panel connected to a resistive load (R)

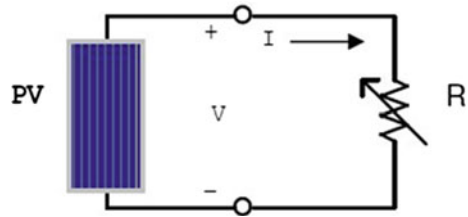
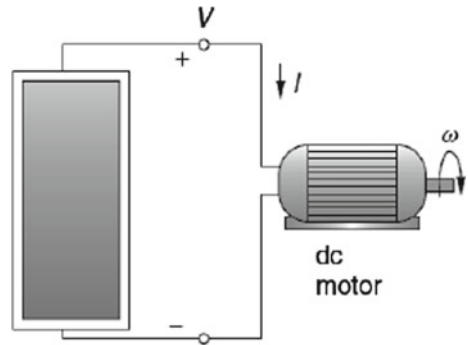


Fig. 2 PV panel connected to a dynamic load



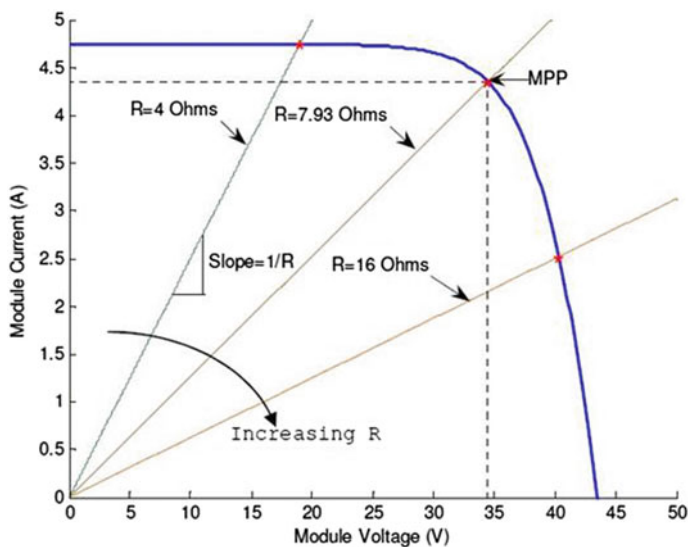


Fig. 3 Location of operating point as influenced by load resistance (R)

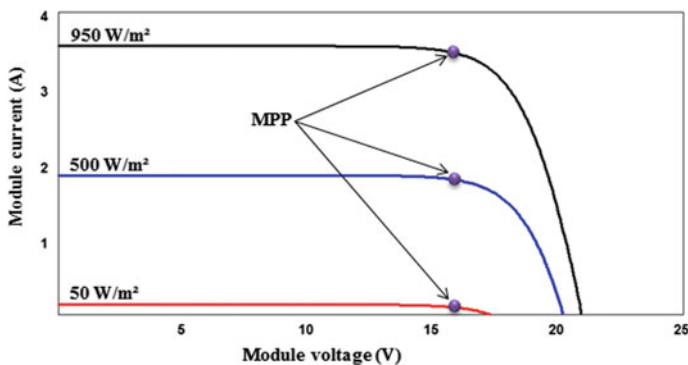


Fig. 4 Location of MPP as influenced by irradiation level

current (FSCC) techniques; (ii) on-line or hill-climbing (HC) techniques such as perturb-and-observe (P&O) and incremental conductance (InCond) techniques; (iii) artificial intelligence (AI) techniques including fuzzy logic control (FLC) technique, artificial neural network (ANN) technique, particle swarm optimization (PSO) technique, and genetic algorithm (GA), Fig. 6.

These MPPT techniques fail or deviate from tracking the correct maximum power point (MPP) under sudden or ramp variations of solar irradiation and ambient temperature as well as under partial shading with oscillations around MPP as shown in Fig. 7. This chapter is aimed at reporting on the history of the off- and on-line MPPT

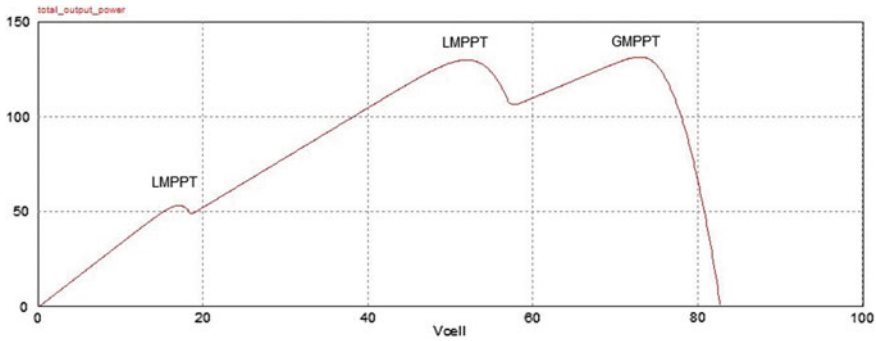


Fig. 5 Multi-MPP under partial shading conditions

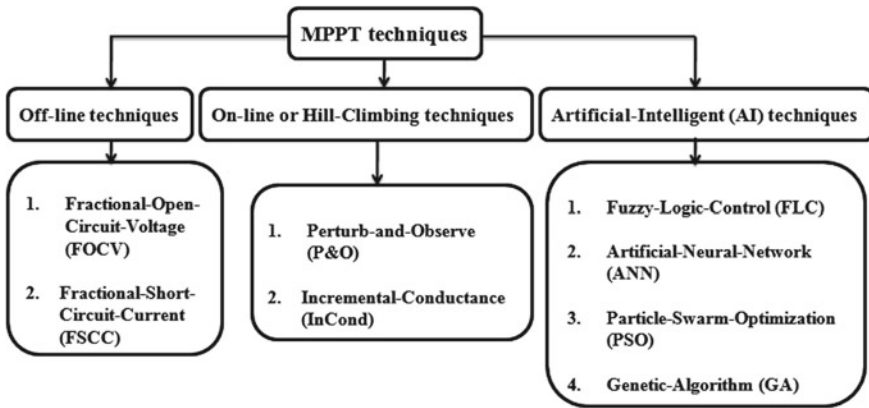


Fig. 6 MPPT techniques

techniques along with their improvements as documented in the literature over the period 1954–2018.

From 1954 to 1988, all the researchers focused on MPPT by selecting the module and/or load to ensure that the intersection point of the module and load current–voltage characteristic curves lies near to the MPP. Because this matching is not always satisfied under varying irradiation level and ambient temperature, some researchers over this period tried to find proper parameters of a battery to be connected to the PV system in order to improve the matching between module and load characteristics.

In 1961, Hooke et al. made a design study on a resistive load to ensure that the intersection point of the I – V curves of the module and a resistive load is the MPP. In 1976, Biran et al. made a design study on a dynamic load to ensure that the intersection point of the I – V curves of the module and a dynamic load is the MPP. In 1977, Braunstein made a design study on a battery load to ensure that the intersection point of the I – V curves of the module and a battery load is the MPP. In 1977, Appelbaum focused in his design study on both resistive load and storage

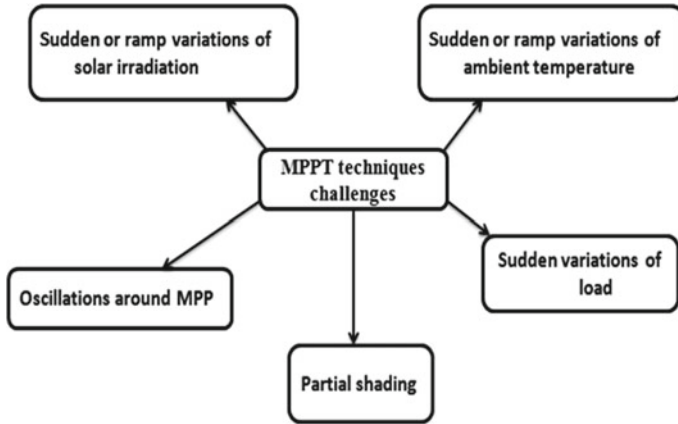


Fig. 7 Challenges facing MPPT techniques

battery fed from a PV system. In 1985, Anis et al. focused in their design study on a volumetric pump driven by a PV system. In 1988, Saied et al. focused in their design study on DC motor supplied by a PV system. In 1989, Khouzam et al. focused in their design study on centrifugal pumps driven by a PV system.

2 On-line Techniques

The name of “on-line” refers to operation of the MPP tracker with no need to switch the PV system off. The on-line or hill-climbing (HC) techniques were introduced before the off-line techniques. The on-line techniques include perturb-and-observe (P&O) and incremental conductance (InCond) techniques. The classical P&O technique had preceded the classical InCond technique in PV applications.

2.1 Classical Perturb-and-Observe (P&O) Technique

In this technique, the tracker of the classical P&O technique is based on perturbing the module operating voltage in any direction whatever increase or decrease of its value and observing the polarity of output power which detects the direction of the coming perturbation. The steady-state efficiency of the classical P&O technique is equal to 96.98%, and its dynamic efficiency is equal to 91.9% [1].

2.1.1 History of the Classical Perturb-and-Observe (P&O) Technique

In 1979, Fox et al. had the primacy in underlining the principle of P&O by using the fundamentals of hill-climbing technique which is a mathematical optimization technique that belongs to the family of local search. Schoeman et al. [2] presented the final version of the computational flowchart of the classical P&O technique. Since then, the researchers have been pursuing the development of this classical P&O technique based on the following directions:

Hint: All the modified P&O techniques proposed by Refs. [1, 3–18] are explained in detail in Chapter I through step-by-step flowcharts with particular emphasis on their advantages and drawbacks.

(i) Using variable step size to improve performance [7, 10, 16–27], Fig. 8.

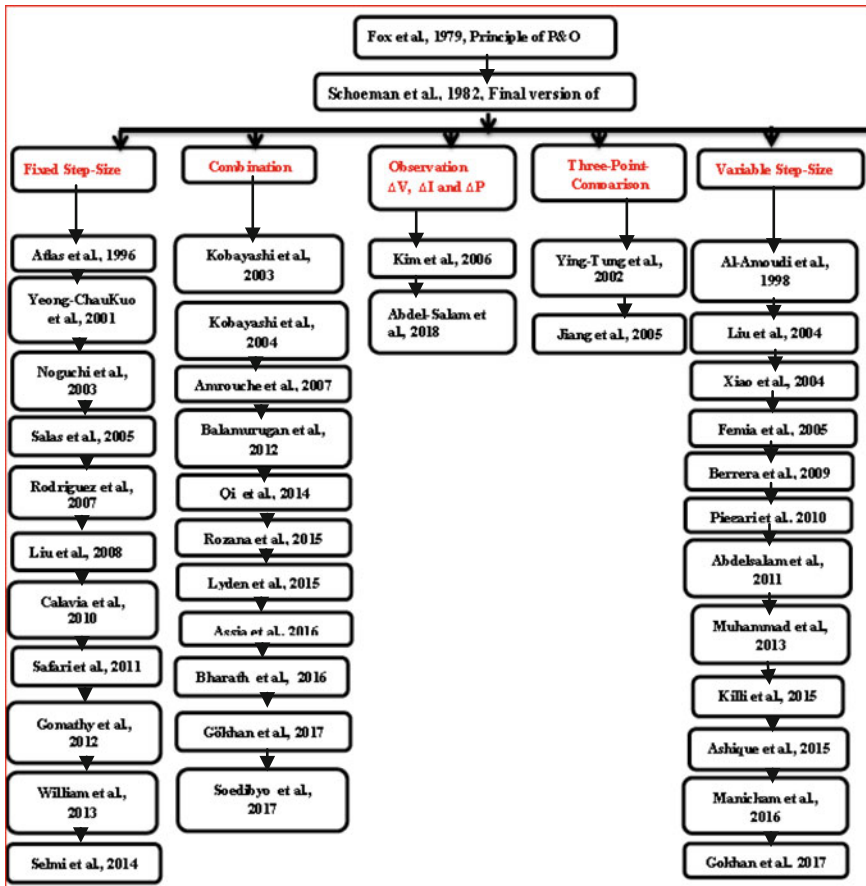


Fig. 8 History of P&O technique as regards fixed step size, combination, observation (ΔI , ΔV , ΔP), three-point comparison, and variable step size

In 2004, Xiao et al. proposed a modified adaptive hill-climbing (MAHC) technique based on variable step size. The voltage step size is updated on-line to be suitable for the sudden changes in irradiation level. The steady-state efficiency of the MAHC technique is equal to 97.3%, and its dynamic efficiency is equal to 96.3%.

In 2015, Ahmed et al. proposed a technique based on an adaptive step size (ΔV) in the range 0.5–2% of the open-circuit voltage. The ratio $\Delta P/P$ is considered to prevent the tracker from failing in tracking the correct MPP under sudden variation of solar irradiation. Moreover, the dynamic efficiency is improved by 2% in comparison with the classical P&O technique. The steady-state efficiency of the proposed technique is equal to 96%, and its dynamic efficiency is equal to 93.9%.

In 2013, Bennett et al. proposed a modified P&O technique based on solving two problems facing the classical one: (i) trade-off problem between its tracking speed and oscillation amplitude at uniform irradiation level and (ii) Its failure under increasing/decreasing irradiation with slopes. The proposed technique starts at 0.85% V_{oc} and then uses small voltage step. The step size is decremented by 50% when the voltage becomes close to V_{mpp} , the voltage corresponding to the maximum power point. The steady-state efficiency of the proposed technique is equal to 97.1%, and its dynamic efficiency is equal to 96.33%.

(ii) Using threshold module current-based parameter to improve its dynamic efficiency [28], Fig. 9.

In 2001, Chih-Chiang et al. proposed a technique based on an extra loop to be combined with the classical technique to solve the problem of sudden variation of solar irradiation. This loop includes a threshold current parameter to detect if there is a variation in irradiation level. The steady-state and dynamic efficiencies of the proposed technique are equal to 83.6%.

(iii) Using fixed perturbation step size to improve performance [29–39], Fig. 8.

In 1996, Atlas et al. touched the trade-off problem between the tracking speed and oscillation amplitude for the classical P&O technique. The authors used a suitable fixed step size to increase the tracking speed and decrease the oscillation amplitude too. However, the results showed that the oscillations were not damped completely but the tracking speed was increased.

In 2001, Yeong-Chau et al. tried to solve the problem of sudden variation of solar irradiation by using fixed step size and irradiation sensor. The dynamic efficiency is improved, but the dependency of the system on the irradiation sensor increases its cost and complexity.

In 2003, Noguchi et al. proposed a modified P&O technique with PI controller to solve the trade-off problem between the tracking speed and steady-state oscillations. The results showed better performance as regards damping the oscillations, but the tracking speed remained the same as the classical one.

In 2004, Liu et al. proposed a new scheme to implement the classical P&O technique for a DC–DC boost converter. It employs peak current control and instantaneous values to calculate the direction of the next perturbation.

In 2005, Salas et al. captured the correct MPP under sudden variation of solar irradiation with satisfactory efficiency that reached 97%. The proposed technique

includes a fixed step size under steady-state and dynamic conditions. However, the slope variations of solar irradiation are not considered.

In 2012, Gomathy et al. simulated a different MPPT technique in MATLAB/Simulink which was used for controlling the duty cycle of DC–DC boost converter. A modified P&O technique with fixed step size was considered and showed better performance as regards tracking speed.

In 2013, William et al. presented a modification on the tracker of the classical P&O technique and applied it on street lighting systems. The validation of the proposed design has been carried out by simulations and experimental results. The results showed better performance as regards the tracking speed and steady-state efficiency. The dynamic efficiency did not exceed 84% according to the results.

In 2014, Selmi et al. presented an implementation for the classical P&O technique and improvement for its performance under sudden variation of solar irradiation. However, this implementation was not tested under ramp variations of irradiation level or ambient temperature.

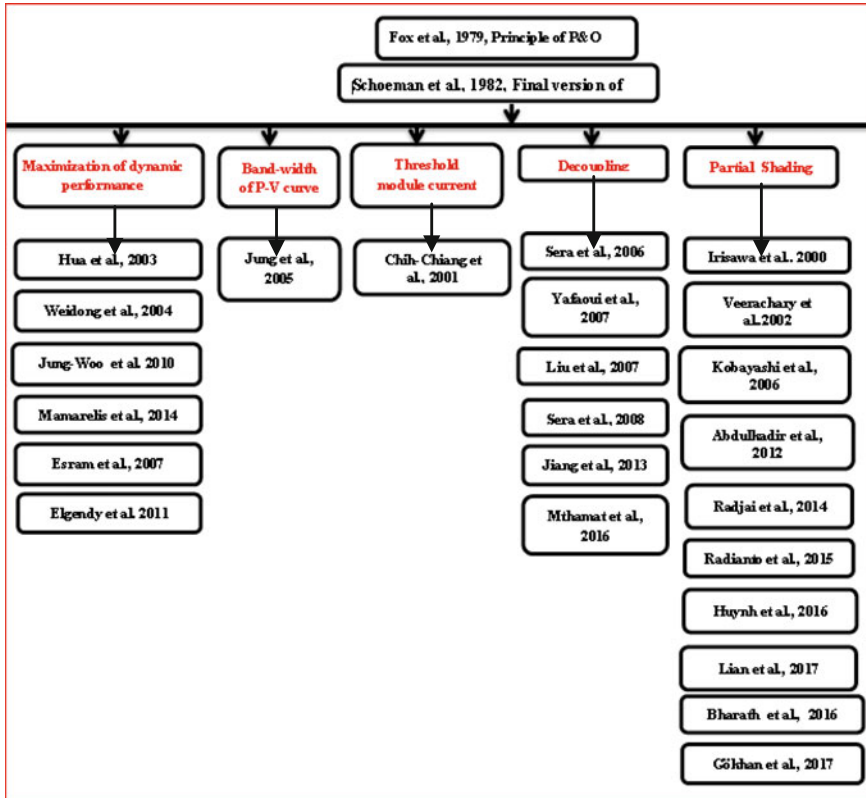


Fig. 9 History of P&O technique as regards maximization of dynamic performance, bandwidth, threshold module current, decoupling, and partial shading

In 2015 Kill et al. proposed an enhanced technique called “Drift-free modified P&O technique.” This technique is based on perturbing the operating voltage (ΔV) and observing the output current (ΔI) and power (ΔP). This technique focuses only on capturing the correct MPP under increasing irradiation level only. This technique is not able to track the correct MPP when the irradiation is suddenly decreased. The steady-state efficiency of the proposed technique is equal to 98.15%, and its dynamic efficiency is equal to 96%.

(iv) Three-point comparison instead of two-point comparison as in the classical P&O technique [11, 40] Fig. 8.

In 2005, Jiang et al. proposed a technique in an attempt to avoid the oscillation problem of the voltage perturbation and the problem of sudden variation of solar irradiation. In comparison with the classical one, the technique of the three-point weight comparison perturbs the module operating voltage and compares the module output power at three points of the P - V curve. The steady-state efficiency of the proposed technique is equal to 97%, and its dynamic efficiency is equal to 92%.

(v) Bandwidth of the P - V curve of the module [15], Fig. 9.

In 2005, Jung et al. proposed an improved perturb-and-observe (IP&O) technique based on the bandwidth of the module P - V curve. This technique presents better tracking speed without a satisfactory increase in dynamic efficiency. In addition to that, the tracker is complex.

(vi) Combination of the classical P&O technique with other tracking techniques to improve its performance [6, 41–52], Fig. 8.

In 2005, Dorofte et al. proposed a technique based on combining the classical P&O technique with the fractional open-circuit voltage (FOCV) technique to increase the steady-state accuracy and the tracking speed of the classical P&O method. The steady-state efficiency of the proposed technique is equal to 97%, and its dynamic efficiency is equal to 95%.

In 2010, Jung-woo et al. combined perturb-and-observe technique with the fractional open-circuit voltage technique (FOCV) technique. The authors used the FOCV technique only at tracker start-up. The FOCV interrupts the output current to let the tracker record the open-circuit voltage with a subsequent power loss in the PV systems. In 2011, Mei et al. combined a modified P&O technique with fuzzy logic technique to improve the dynamic efficiency. The authors compared the results with the classical P&O technique by using PV module (MSX60), DC–DC buck converter, and resistive load. The results showed that the combined technique has better performance when compared with the classical one.

In 2016, Mohapatra et al. presented a combination between the classical P&O method and the NN method where the irradiation level and ambient temperature are input variables. The current (IMPP) and voltage (VMPP) values corresponding to the MPP were collected at different irradiation levels and ambient temperature values. This NN-based MPPT tracker showed a better performance when compared with the classical one. The steady-state and dynamic efficiency values of the proposed technique are equal to 96%.

(vii) Decoupling of voltage perturbation from that due to sudden variation of irradiation level and ambient temperature [3–5, 13, 53], Fig. 9.

In 2006, Sera et al. presented dP-P&O technique to modify the dynamic performance of the classical perturb-and-observe technique by decoupling the change in module output power due to weather changes and the change in module output power due to voltage perturbation by recording an additional measurement in the middle of perturbation step. The steady-state and dynamic efficiency values of the dP-P&O technique are 99.6%.

In 2007, Yafaoui et al. tried to separate the change in module output power due to weather changes from the change in module output power due to voltage perturbation by proposing a modified perturb-and-observe technique (MP&O). The MP&O technique depends on using an estimate process in every perturbation step. The steady-state efficiency of the dP-P&O technique is 97.5%. The dynamic efficiency of the dP-P&O technique is 95%. The tracking speed of the classical P&O technique is doubled that of the MP&O technique because of the delay time due to the estimate process.

In 2016, Mamatha presented a modified technique based on decoupling the change in module output power due to voltage perturbation and irradiation level change. The proposed technique is almost similar to the technique by [3] but with low tracking efficiency. The steady-state and dynamic efficiency values of the proposed technique are equal to 94.8%.

(vii) Using datasheet parameters [14], Fig. 10.

In 2007, Azab proposed an enhanced perturb-and-observe technique. This enhanced technique is based on defining the MPP value according to the datasheet of the PV module, which is the drawback of the technique. The steady-state efficiency

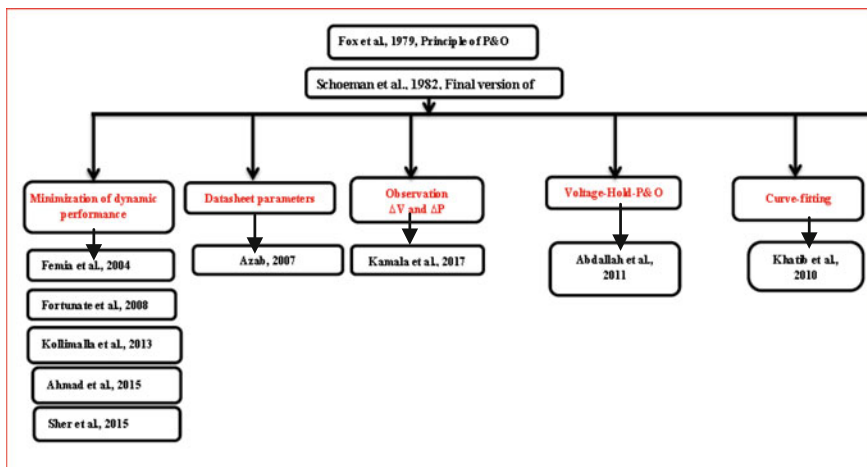


Fig. 10 History of P&O technique as regards minimization of dynamic performance, datasheet parameters, observation (ΔV , ΔP), voltage-hold P&O, and curve-fitting

of the proposed technique is equal to 95%, and its dynamic efficiency is equal to 95%.

(viii) Doing curve-fitting to improve dynamic efficiency under sudden variation of irradiation level or ambient temperature [12], Fig. 9.

In 2010, Khatib proposed a curve-fitting-based technique to improve the performance of the classical P&O by determining an optimum module voltage close to that corresponding to the max power (V_{mpp}) as determined from the datasheet of the PV module. Then, the classical P&O technique was applied with a small step size until reaching the real MPP. This attempt to improve the performance of the classical P&O technique did not provide satisfactory results where the average efficiency did not exceed 89.2%.

(ix) Voltage-hold perturbation and observation [9], Fig. 10.

In 2011, Abdallah et al. proposed a modified technique based on the voltage-hold perturbation and observation “VH-P&O” to track correctly the MPP under irradiation changes. The voltage across a capacitor is related to the increment/decrement of the module output current being dependent on the irradiation level. The VH-P&O technique does not perturb the operating voltage under suddenly changed irradiation but before exceeding the MPP voltage and directly forces the voltage to the capacitor, which is the important tracking parameter in this technique. The steady-state and dynamic efficiency values of the proposed technique are equal to 91%.

(x) Observation of the changes in module output voltage and power [8], Fig. 10.

In 2017, Kamal et al. proposed an improved P&O technique to solve the problem of the classical technique under sudden variation of solar irradiance. In this technique, the polarity of the voltage perturbation (ΔV) and power change (ΔP) was taken into account and multiplied together to decide where the next perturbation will be directed. The tracking efficiency showed overshoot values that can reach unjustified hypothetical values up to 400%.

(xi) Solving the problem of partial shading [27, 54–61], Fig. 9.

In 2003, Kobayashi et al. applied a two-stage MPPT control technique to realize a relatively simple control system which can track the real maximum power point even under non-uniform irradiation levels. The feasibility of this control concept is confirmed for steady irradiation as well as for rapidly changing irradiation by simulation study using software PSIM and LabView.

In 2007, Amrouche et al. proposed a modified technique to solve the problem of partial shading. This technique was based on combination of P&O and artificial neural network technique.

In 2015, Bharath et al. used an enhanced version of perturb-and-observe maximum power point tracking technique considering local maxima and minima caused by shading to select where to track the global maximum power and to make the solar panel to work at the global maximum power. This helps in improving the overall efficiency of the system. The technique was implemented on a 50-W solar panel using microcontroller and a boost converter.

In 2016, Zengrui et al. proposed a novel maximum power point tracking (MPPT) control technique for PV system based on an improved particle swarm optimization (PSO) technique and variable step perturb-and-observe (P&O) technique. Firstly, the PSO is to search for the global maximum power point. Then, the variable step P&O technique is used to track the global maximum power point (GMPP) accurately which changes according to the environmental conditions.

In 2017, Soedibyo et al. combined the P&O technique with the InCond technique to track the MPP under partial shading conditions. The results of the simulation indicated that the power output of the module covers 99.4% of the load demand in the investigated system.

(xii) Maximization of dynamic performance [48, 62–68], Fig. 9.

In 2003, Hua et al. proposed a modified P&O technique to capture the correct MPP under sudden variation of solar irradiation. The results showed that the tracker of the proposed technique had high tracking speed in response to the sudden changes of irradiation level.

In 2015, Jiang et al. proposed a modified P&O technique based on its combination with InCond technique. The results showed better performance under sudden variation of solar irradiation. However, the performance of the tracker under ramp variation of irradiation level was not discussed.

(xiii) Minimization of oscillation amplitude [10, 69–72], Fig. 10.

In 2005, Femia et al. proposed an optimized perturb-and-observe (OP&O) technique based on an adaptive step size to solve the problem of oscillation around the MPP which faces the classical one. The steady-state accuracy of this technique is better than that of the classical one. However, the trade-off problem between tracking speed and tracking accuracy remains unsolved.

In 2015, Zakzouk et al. proposed a modified P&O technique depending on a variable perturbation step during sudden variation of ambient temperature. The technique depends on voltage perturbation ΔV , corresponding power change ΔP , and $\Delta P/\Delta V$. The steady-state and dynamic efficiency values of the proposed technique are equal to 99.8%.

(xiv) Observation of the change of module output current, voltage, and power [73, 1], Fig. 8.

In 2006, Kim et al. proposed a modified P&O technique based on sensing current along with the voltage as well as observing polarity of current change and the corresponding power change. The proposed technique is based on the use of expensive current sensor. However, it presents better performance than the classical P&O technique.

In 2018, Abdel-Salam et al. proposed a modified P&O technique. The authors used the polarity of the module current change ΔI corresponding to voltage change ΔV and $\Delta I/\Delta V$ to direct the tracker to the correct MPP whatever the value of the change in irradiation level. The steady-state efficiency of the proposed technique is equal to 99.48%, and its dynamic efficiency is equal to 98.03%.

2.2 Incremental Conductance (InCond) Technique

The mechanism of the incremental conductance technique is that the slope of the module P – V curve is equal to zero at the MPP (e.g., $dP/dV = 0$ or $dP/dI = 0$ at MPP). For operating point located to the right of the MPP, the tracker moves the operating point toward the MPP by decreasing the operating voltage with a subsequent increase in the output power; i.e., the slope dP/dV is negative ($dP/dV < 0$ to the right of the MPP). On the other hand, when the operating point is located to the left of the MPP, the tracker moves the operating point toward the MPP by increasing the operating voltage with a subsequent increase in the output power; i.e., the slope dP/dV is positive ($dP/dV > 0$ to the left of the MPP). The incremental-conductance-technique-based tracker compares the operating conductance (I/V) with the incremental conductance ($\Delta I/\Delta V$). The correct MPP is captured when $(\Delta I/\Delta V)$ is equal to $(-I/V)$.

2.2.1 History of Incremental Conductance (InCond) Technique

The first researcher who discovered the classical incremental conductance technique is “Waszynezuk” in 1983, Fig. 10. “Phang et al. [74], Won et al. [75]” followed “Waszynezuk” in improving his version, Fig. 10. In 1995, Hussein et al. presented the final version of the computational flowchart of the classical incremental conductance technique with a “patent pending,” Fig. 10. There are many attempts to improve its performance in the literature based on the following directions:

(i) Using fixed perturbation step size [12, 24, 76–86], Fig. 11.

In 1997, Sugimoto et al. suggested a modified InCond technique to track correctly the MPP under sudden variation of solar irradiation. The module current is the main parameter to detect the occurrence of sudden variation of solar irradiation. The tracking speed was increased. However, the dynamic efficiency did not exceed 83%.

In 1999, Brambilla et al. proposed a modified InCond technique based on fixed step size to overcome the trade-off problem between the tracking speed and oscillations around the MPP. The steady-state error did not exceed 2.5%.

In 2013, Mahamudul et al. proposed a modified InCond technique to maximize the tracking efficiency. The steady-state efficiency of the modified technique was 98 against 97% for the dynamic efficiency. However, this technique was not tested under ramp variation of solar irradiation or ambient temperature.

(ii) Combination with other tracking techniques to improve its performance of the classical InCond technique [43, 87–96], Fig. 11.

In 2000, Irisawa et al. proposed a novel MPPT technique, based on combining the incremental conductance and the classical P&O techniques to solve the problem of oscillation facing the classical InCond method and the problem of sudden variation of irradiation level. The performance of this technique is better than the classical one as documented in their results. However, this method was not tested under ramp variations of irradiation level or ambient temperature.

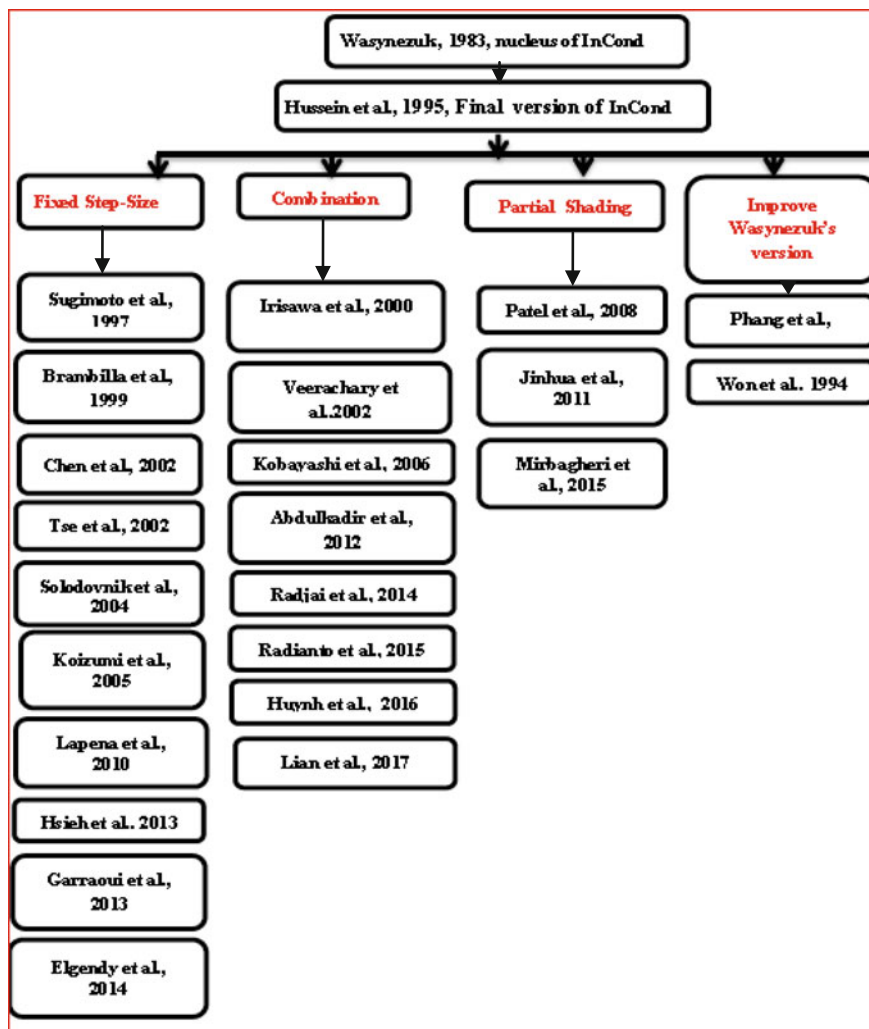


Fig. 11 History of InCond technique as regards fixed step size, combination, partial shading, and improved Wasynezuk's version

In 2012, Abdulkadir et al. combined a modified InCond technique with artificial neural network (ANN) technique. The MPPT system has been tested using a 100-W module under various operating conditions. The obtained results have proven that the MPP is tracked even under a sudden change in irradiation level. However, the oscillation amplitude around the MPP is high when compared with the classical InCond technique.

In 2014, Radjai et al. combined the classical InCond technique with fuzzy logic technique to overcome the problem of varying irradiation level. The dynamic effi-

ciency of this technique is 96%. However, the tracking speed is similar to that of the classical InCond technique.

In 2017, Lian et al. tried to solve the problem of partial shading by combining a modified INC technique and simulated annealing (SA) techniques. The modified INC technique employs an adaptive step size to increase the tracking speed and accuracy of the conventional INC. On average, the tracking time of the proposed technique is two times shorter than the SA technique when used alone for MPPT.

In 2015, Radianto et al. presented a hybrid MPPT composed of two techniques: incremental conductance (INC) and fuzzy logic (FL) control. This technique was found able to track maximum power point (MPP) under variable solar irradiance. The results showed that the proposed technique can track MPP under different irradiation levels. However, this method was not tested under ramp variations of solar irradiation.

(iii) Solving the trade-off problem between tracking speed and oscillation amplitude [45, 97–105], Fig. 12.

In 2008, Cha et al. tried to use the InCond technique to solve the trade-off problem between the tracking speed and oscillation amplitude. The tracking accuracy of this technique is better than the classical InCond technique. However, the tracking speed is similar to that of the classical InCond technique.

(iv) Solving the problem of partial shading [106–110], Fig. 11.

In 2008, Patel et al. proposed a modified InCond technique to solve the problem of partial shading. The tracker of this technique showed better performance in capturing the global maximum power point. However, oscillations remained around the MPP the same as the classical InCond technique.

In 2009, Ji et al. proposed a modified technique to capture the correct MPP under partial shading conditions. This modified technique was based on the InCond technique with a variable step size. This tracker based on this technique tries to scan all P – V curves and record the current and voltage for all local and global multi-peaks points. Then, it forces the operating point to stick at the highest peak.

(v) MPPT-based incremental resistance [45], Fig. 12.

In 2011, Mei et al. proposed a current-controlled variable-step-size incremental resistance MPPT technique to solve the problem of slow tracking speed under dynamic conditions and the problem of oscillations under steady-state conditions. The dynamic efficiency of this technique lies in the range 96–97.5%. However, its tracking accuracy is low when compared with the classical InCond technique.

(vi) MPPT-based power increment [82, 111], Fig. 12.

In 2012 and 2013, Hsieh et al. proposed a modified InCond technique based on power increment to solve the problem of low tracking speed of the tracker when the operation point is located to the left of the MPP on the I – V curve. The low tracking speed is attributed to the insignificant change of module output current which is the main parameter of the InCond technique. This is why the tracker cannot detect if there is a change in irradiation or no.

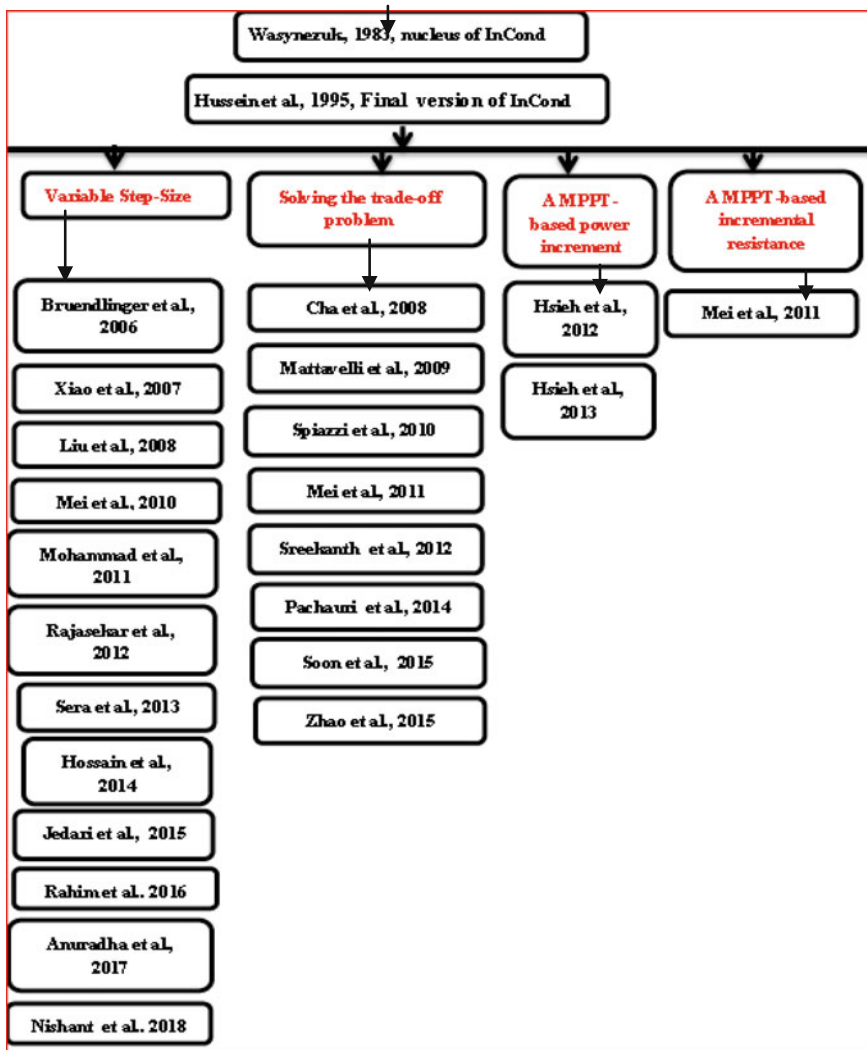


Fig. 12 History of InCond technique as regards variable step size, solving the trade-off problem, MPPT-based power increment, and MPPT-based incremental resistance

(vi) Using variable step size [27, 95, 98, 112–122], Fig. 12.

In 2006, Bruendlinger et al. proposed a variable-step-size incremental conductance technique to solve the problem of varying irradiation level. This technique applied large step size when the operating point is far from the MPP and small step size when the operating point is close to the MPP. The tracking efficiency is 2.4% superior to the classical InCond technique.

In 2007, Xiao et al. proposed an adaptive InCond technique to track correctly the MPP under sudden variation of solar irradiation and ambient temperature. The step size is varying on-line after the tracker senses the module output current. This technique showed better performance as regards the dynamic efficiency. The steady-state error did not exceed 1%. However, the tracking speed is similar to that of the classical InCond technique. Moreover, this technique was not tested under ramp variations of solar irradiation or ambient temperature.

In 2017, Anuradha et al. proposed a modified InCond technique with a variable step size. This technique was tested under sudden and ramp variations of solar irradiation and ambient temperature. The dynamic efficiency did not exceed 98%.

3 Off-line Techniques

The name of “off-line” refers to switching off the PV system, so the tracker can state its operation following one of these techniques. Off-line techniques include fractional open-circuit voltage (FOCV) and fractional short-circuit current (FSCC) techniques.

3.1 Fractional Open-Circuit Voltage (FOCV) Technique

This technique is also named constant-voltage technique. The tracker based on this technique selects the operating voltage equal to (70–85%) V_{oc} where V_{oc} is the open-circuit voltage of the module. This is the main drawback of this technique as it depends on the value of the open-circuit voltage. This calls for interrupting the module output current in order to measure the value of the open-circuit voltage making with a subsequent significant power loss in large PV systems. As the open-circuit voltage varies with weather condition, “e.g., ambient temperature or/and irradiation level,” the researchers always support this technique by combination with other MPPT techniques, so the tracker can work satisfactorily under all operating conditions.

3.1.1 History of Fractional Open-Circuit Voltage (FOCV) Technique

Fractional open-circuit voltage (FOCV) or constant-voltage (CV) technique does not address high tracking efficiency unless it is combined with other MPPT techniques [10, 22, 51, 56, 102, 123–156], Fig. 13.

In 2005, Dorofte et al. proposed a modified MPPT method based on combining the classical P&O technique with the fractional open-circuit voltage (FOCV) technique. This modified method aims at overcoming the trade-off problem between tracking speed and tracking accuracy as mentioned in Chapter I. The steady-state efficiency

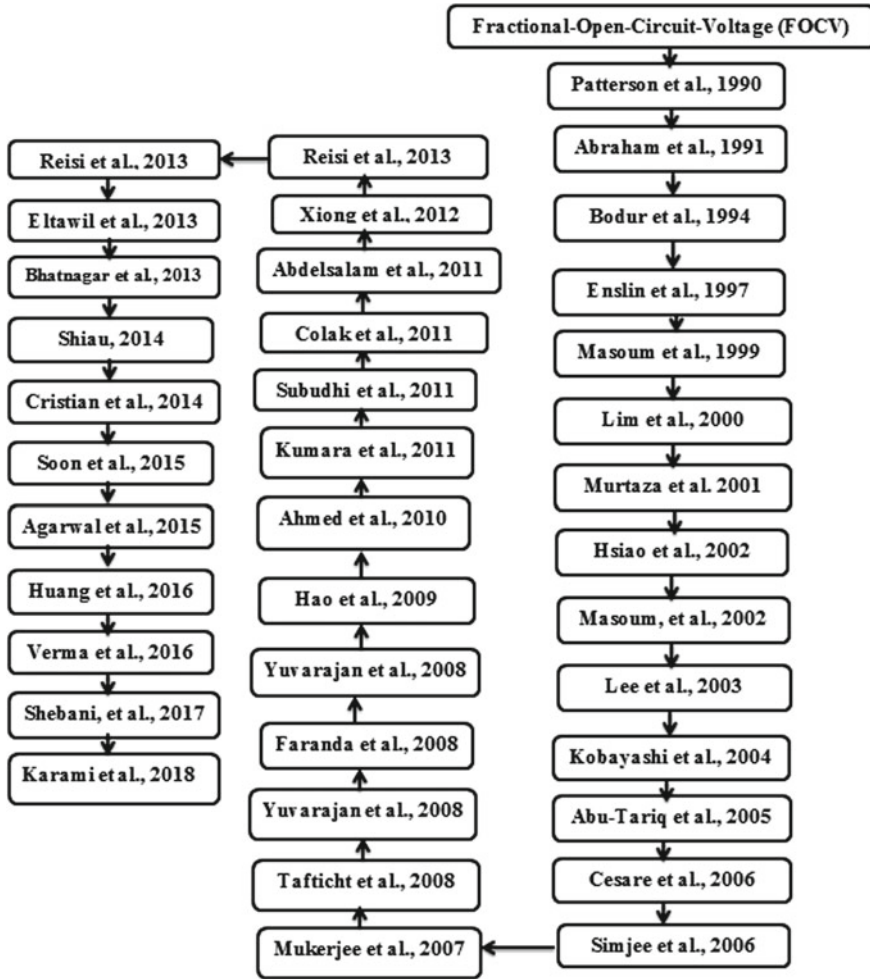


Fig. 13 History of FOCV technique

of the proposed technique is equal to 97%, and its dynamic efficiency is equal to 95%.

In 2008, Yuvarajan et al. proposed a modified P&O technique depending on fractional open-circuit voltage (FOCV) technique. The dynamic efficiency of the proposed technique is equal to 98.5%. The proposed technique is more accurate when compared with the classical P&O.

In 2016, Shebani et al. proposed a bisection numerical technique (BNA) based on FOCV technique. The BNA technique showed more accuracy when compared with FOCV technique under different irradiation levels. The proposed method has

dynamic efficiency equal to 96.7%. The implementation of this technique is very complex when compared with the FOCV technique.

In 2006, Cesare et al. tried to increase the efficiency of the classical P&O technique by using FOCV technique and adaptive P&O method. The model consists of PV array, DC–DC converter, and a resistive load. The results showed better performance when compared with the classical one. The steady-state accuracy and tracking speed are improved when compared with the classical P&O technique.

In 2007, Mukerjee et al. combined the P&O technique with FOCV. This technique addressed two issues. A variable-step-length technique was proposed to eliminate the trade-off problem between accuracy and tracking speed. The deviation from tracking the MPP is minimized.

In 2008, Yuvarajan et al. proposed a modified InCond technique depending on the open-circuit voltage and the short-circuit current techniques. The MPPT technique was validated under different values of irradiation level. The tracking speed and the steady-state efficiency are improved.

In 2009, Hu et al. proposed a technique to combine FOCV and a numerical analysis based on “quadratic interpolation.” An additional loop was proposed to include constant-voltage technique. This loop is used next to the classical InCond technique to enhance the dynamic efficiency under varying irradiation level. This technique captured the MPP with dynamic efficiency reached to 98%.

In 2012, Xiong et al. combined InCond and FOCV techniques to overcome the trade-off problem between the tracking speed and oscillation amplitude. The tracking speed of this modified technique is superior to that of the classical InCond technique.

In 2013, Eltawil et al. used FOCV technique in controlling three-phase grid-connected PV system. The tracking speed of the proposed tracker is high when compared with other modified techniques.

In 2014, Cristian et al. proposed a new MPPT scheme based on FOCV to solve the problem of sudden variation of solar irradiation. The steady-state and dynamic efficiency values are 95 and 94%, respectively.

3.2 Fractional Short-Circuit Current (FSCC) Technique

This technique is also named constant-current technique. The tracker based on this technique selects the operating current equal to (78–90%) I_{sc} where I_{sc} is the short-circuit current of the module. This is the main drawback of this technique as it depends on evaluating the value of the short-circuit current. This calls for disconnecting and short-circuiting the module to measure the value of the short-circuit current. The disconnection of the PV module results in a power loss. As the short-circuit current varies with weather condition, “e.g., irradiation level,” the researchers always support this technique by combination with other MPPT techniques, so the tracker can work satisfactorily under all operating conditions.

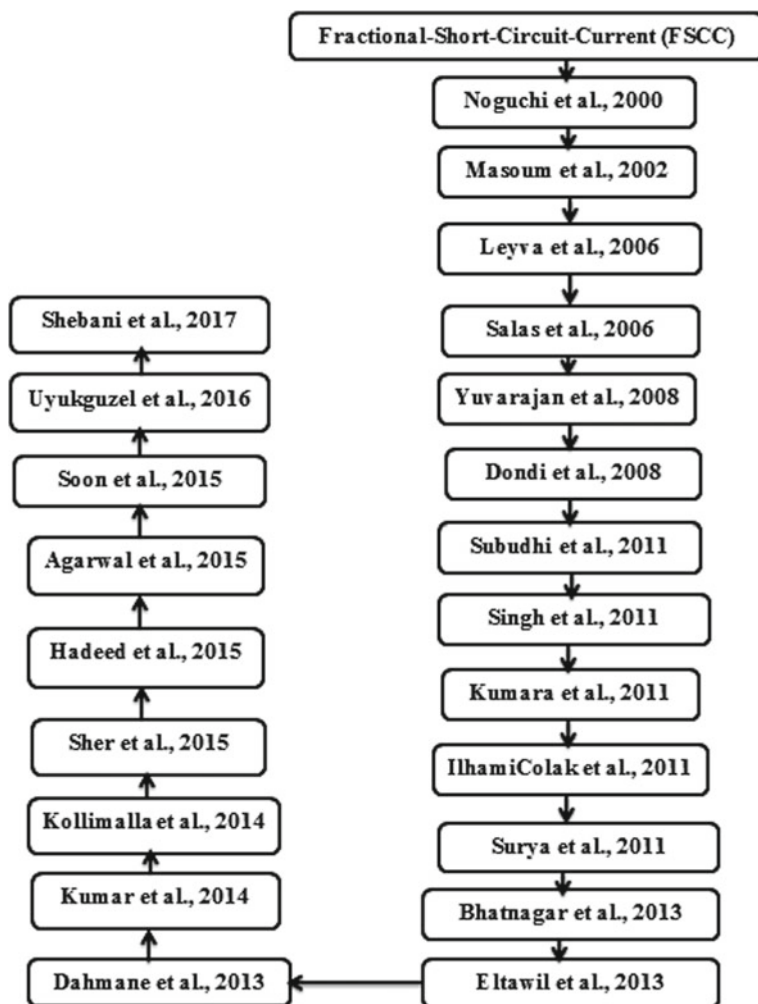


Fig. 14 History of FSC technique

3.2.1 History of Fractional Short-Circuit Current (FSCC) Technique

Many authors tried to support fractional short-circuit current (FSCC) technique to make it applicable to work under all operating conditions by combination with other MPPT techniques [49, 51, 72, 102, 131, 138, 142, 143, 146, 147, 157–170], Fig. 14.

In 2000, Noguchi et al. proposed a novel MPPT technique based on fractional short-circuit current to find an optimum operating current under different operating conditions for MPP tracking. The performance of the technique is different from the classical hill-climbing techniques. Its steady-state and dynamic efficiency values are 93 and 92%, respectively.

In 2007, Yuvarajan et al. proposed a modified P&O technique depending on fractional short-circuit current (FSCC) technique. The dynamic efficiency of the proposed technique was found equal to 98.5%. The proposed technique is more accurate when compared with the classical P&O.

In 2011, Kumara et al. proposed a modified technique to solve the problem of oscillations and sudden variation of solar irradiation. This modified technique is based on a combination of the classical perturb-and-observe (P&O) technique and FSCC technique. The proposed technique showed better performance as regards the reduction in the oscillation amplitude, but tracking the MPP under varying irradiation level was not efficient.

In 2012, Pardhan et al. proposed a new digital double-integral sliding-mode controller based on fractional short-circuit current (FSCC) technique to improve the dynamic efficiency of the MPP tracker. The dynamic efficiency of the proposed controller reached 99.5%. However, the oscillations around the MPP were not damped completely.

In 2013, Dahmane et al. used the fractional short-circuit current (FSCC) with a genetic algorithm (GA) to track the correct MPP under partial shading conditions. This modified technique captured the global maximum power point (GMPP) with dynamic efficiency that reached 97.5%

In 2014, Kumar et al. used the fractional short-circuit current (FSCC) combined with variable step size P&O technique to track the correct MPP under sudden and ramp variations of solar irradiation. This technique showed better performance when compared with the classical P&O method.

In 2015, Sher et al. proposed a hybrid MPPT method based on combining the fractional short-circuit current (FSCC) and hill-climbing (perturb-and-observe—P&O) method. The proposed MPPT uses a current threshold parameter to determine the change in irradiation level. This method was tested under sudden variation of irradiation level and achieved steady-state efficiency equal to 98.51 against 97.77% for the dynamic efficiency. Moreover, this method is better in performance when compared with the classical P&O method. However, this method is not tested under ramp variation of solar irradiation. Moreover, the authors did not compare this method with other modified P&O method proposed in the literature.

4 Conclusions

This chapter is aimed at reporting on the history of two families of maximum power point tracking techniques: (i) off-line techniques such as fractional open-circuit voltage (FOCV) and fractional short-circuit current (FSCC) techniques and (ii) on-line or hill-climbing (HC) techniques such as perturb-and-observe (P&O) and incremental conductance (InCond) techniques along with their improvements as documented in the literature over the period 1954–2018. The perturb-and-observe (P&O) method is the most popular and common one because of its easy implementation. These MPPT techniques fail or deviate from tracking the correct maximum power point

(MPP) under sudden or ramp variations of solar irradiation and ambient temperature as well as under partial shading with oscillations around MPP. The challenge among the authors is directed toward a MPPT method capable to overcome all of these drawbacks.

References

1. Abdel-Salam M, EL-Mohandes M, Goda M (2018) An improved perturb-and-observe based MPPT method for PV systems under varying irradiation level. *Sol Energy* 171:547–561
2. Schoeman JJ, VanWyk JD (1982) A simplified maximal power controller for terrestrial photovoltaic panel arrays. In: *Proceeding 13th annual IEEE power electronics specialists conference*, pp 361–367
3. Sera D, Teodorescu R, Kerekes T, Blaabjerg F (2006) Improve MPPT method for rapidly changing environmental conditions. In: *Proceeding 12th conference electronics and motion control*, Montreal, Quebec, Canada, pp 1614–1619
4. Yafaoui A, Wu B, Cheung R (2007) Implementation of maximum power point tracking algorithm for industrial photovoltaic systems. In: *Proceeding 2nd Conference Canadian Solar Buildings*. Calgary, Canada, 10–14 June 2007, pp 1–6
5. Liu Y, Xia D, He Z (2011) MPPT of a PV system based on the particle swarm optimization. In: *Electric utility deregulation and restructuring and power technologies (DRPT)*, pp 1094–1096
6. Dorofte C, Borup U, Blaabjerg F (2005) A combined two-method MPPT control scheme for grid-connected photovoltaic systems. In: *Proceeding of European conference on power electronics and applications*. Dresden, Germany, Sept 2005, pp 11–14
7. Killi M, Samanta S (2015) Modified perturb and observe MPPT algorithm for drift avoidance in photovoltaic systems. *IEEE Trans Ind Electron* 3(2):1–10
8. Kamala V, Premkumar K, Bisharathu A, Ramaiyer S (2017) A modified perturb and observe MPPT technique to tackle steady state and rapidly varying atmospheric conditions. *Sol Energy* 157:419–426
9. Abdalla I, Zhang L, Corda J (2011) Voltage-hold perturbation and observation maximum power point tracking algorithm (VH-P&O MPPT) for improved tracking over the transient atmospheric changes. In: *Proceeding of conference power electronics and applications*, Birmingham, United Kingdom, 30 Aug 2011, pp 1–10
10. Ahmed J, Salam Z (2015) An improved perturb and observe (P&O) maximum power point tracking (MPPT) algorithm for higher efficiency. *Elsevier Appl Energy* 150:97–108
11. Jiang J, Huang T, Hsiao Y, Chen Ch (2005) Maximum power tracking for photovoltaic power systems. *Tamkang J Sci Eng* 8(2):147–153
12. Khatib T, Mohamed A, Amim N (2010) An improved indirect maximum power point tracking method for standalone photovoltaic systems. In: *Proceeding conference applications of electrical engineering*. Selangor, Malaysia, 23–25 Mar 2010, pp 56–62
13. Sera D, Teodorescu R, Hantschel J, Knoll M (2008) Optimized maximum power point tracker for fast-changing environmental conditions. *IEEE Trans Ind Electron* 55(7):2629–2637
14. Azab M (2007) A new maximum power point tracking for photovoltaic systems. *World Acad Sci Eng Technol* 44:571–574
15. Jung Y, So J, Yu G, Choi J (2005) Improved perturbation and observation method (IP&O) of MPPT control for photovoltaic power systems. In: *Conference record of the thirty-first proceeding of IEEE conference photovoltaic specialists*. Daejeon, South Korea, 15–17 Feb 2005, pp 1788–1791
16. Xiao W, Dunford W (2004) A modified adaptive hill climbing MPPT method for photovoltaic power systems. In: *Proceeding 35th Annual IEEE Power Electronics Specialists Conference*. Aachen, Germany, 20–25 June 2004, pp 1957–1963

17. Femia N, Petrone G, Spagnuolo G, Vitelli M (2005) Optimization of perturb and observe maximum power point tracking method. *IEEE Trans Power Electron* 20(4):963–973
18. Zakzouk N, Elsharty M, Abdelsalam A et al (2015) Improved performance low-cost incremental conductance PV MPPT technique. *IET Renew Power Gener* 10(4):561–574
19. Al-Amoudi A, Zhang L (1998) Optimal control of a grid-connected PV system for maximum power point tracking and unity power factor. In: Seventh international conference on Power electro-nics and variable speed drives (Conf. Publ. No. 456), pp 80–85
20. Berrera M, Dolara A, Faranda R, Leva S (2009) Experimental test of seven widely adopted MPPT algorithm. In: Proceedings of the IEEE Bucharest power tech conference, pp 1–8
21. Piegari L, Rizzo R (2010) Adaptive perturb and observe algorithm for photovoltaic maximum power point tracking. *IET Renew Power Gener* 4:317–328
22. Abdelsalam A, Massoud A, Ahmed S, Enjeti P (2011) High-performance adaptive perturb and observe MPPT technique for photovoltaic-based microgrids. *IEEE Trans Power Electron* 26(4):1010–1021
23. Jiang Y, Qahouq J, Haskew T (2013) Adaptive step size with adaptive-perturbation-frequency digital MPPT controller for a single-sensor photovoltaic solar system. *IEEE Trans Power Electron* 28(7):3195–3205
24. Mahamudul H, Islam M, Shameem A, Rana J, Metselaar H (2013) Modeling of PV module with incremental conductance MPPT controlled buck-boost converter. In: Proceeding IEEE conference on advances in electrical engineering. Dhaka, 19–21 Dec, pp 197–202
25. Ashique RH, Salam Z, Aziz MJBA, Bhatti AR (2017) Integrated photovoltaic-grid dc fast charging system for electric vehicle: a review of the architecture and control. *Renew Sustain Energ Rev* 69:1243–1257
26. Mohapatra A, Nayak B, Mohanty K (2016) Performance improvement in MPPT of SPV system using NN controller under fast changing environmental condition. In: IEEE 6th international conference on power systems (ICPS), New Delhi, India, 4–6 Mar 2016, pp 1–5
27. Gokhan S, Botella JCH, Albert MDCM, Thomsen OC, Andersen MA (2017) Isolated boost converter with bidirectional operation for super capacitor applications. *J Power Electron* 13(4):507–515
28. Chih-Chiang H, Jong-Rong L (2001) Fully digital control of distributed photovoltaic power systems. In: Proceeding of conference IEEE international symposium on industrial electronics. Pusan, Korea, 1, pp 1–6
29. Atlas IH, Sharaf AM (1996) A novel on line MPP search algorithm for PV arrays. *IEEE Trans Energy Convers* 11:748–754
30. Yeong-Chau K, Tsong-Juu L, Jiann-Fuh C (2001) Novel maximum-power-point-tracking controller for photovoltaic energy conversion system. *IEEE Trans Ind Electron* 48:594–601
31. Liu C, Wu B, Cheung R (2004) Advanced algorithm for MPPT control of photovoltaic systems. In: Proceeding Conference Canadian solar buildings. Montreal, Canada, 20–24 Aug 2004, pp 20–24
32. Noguchi T, Matsumoto H (2003) Maximum power point tracking method of photovoltaic using only single current sensor. In: Proceeding 10th European Conference on Power Electronics and Applications. Toulouse, France, 2–4 Sept 2003
33. Salas V, Olias E, Lazaro A, Barrado A (2005) New algorithm using only one variable measurement applied to a MPPT. *Solar Energy Mater Solar Cells* 87:675–684
34. Calavia M, Perié JM, Sanz JF, Sallan J (2010) Comparison of MPPT strategies for solar modules. In: Proceeding international conference on renewable energies power quality. Granada, Spain, 22–25 Mar 2010, pp 11–17
35. Rodriguez C, Amaratunga G (2007) Analytic solution to the photovoltaic maximum power point problem. *IEEE Trans Circuits Syst* 54:2054–2060
36. Safari A, Mekhilef S (2011) Implementation of incremental conductance method with direct control. In: Proceeding IEEE conference on trends and developments in converging technology, Bali, 21–24 Nov 2011, pp 944–948
37. Gomathy S, Thangavel S (2012) Design and implementation of maximum power point tracking (MPPT) algorithm for a stand-alone PV system. *Int J Sci Eng Res* 3(3):2229–5518

38. William LE, Moore M, Jackson E, Nelson EN (2013) Networked multi-inverter maximum power-point tracking. U.S. Patent 8, 401, 706, issued March 19, 2013
39. Selmi T, Niby A, Devis L, Davis A (2014) P&O MPPT implementation using MATLAB/simulink. In: Proceeding IEEE conference on ecological vehicles and renewable energies, Monte-Corlo, 25–27 Mar 2014, pp 1–4
40. Ying-Tung H, China-Hong C (2002) Maximum power tracking for photovoltaic power system. In: Industry applications conference, pp 1035–1040
41. Bratcu A, Munteanu I, Bacha S, Raison B (2008) Maximum power point tracking of grid-connected photovoltaic arrays by using extremum seeking control. CEAI Conf 10:3–12
42. Kimball J, Krein P (2008) Discrete-time ripple correlation control for maximum power point tracking. IEEE Trans Power Electron 23(23):53–62
43. Liu F, Duan S, Liu B, Kang Y (2008) A Variable Step Size INC MPPT. IEEE Trans Ind Electron 55(7):1–10
44. Leyva R, Olalla C, Zazo H, Cabal C, Cid-Pastor A, Queinnec I, Alonso C (2011) MPPT based on sinusoidal extremum-seeking control in PV generation. Int J Photoenergy
45. Shan M, Tan CW (2011) A study of maximum power point tracking algorithms for stand-alone photovoltaic systems. IEEE Appl Power Electron Colloquium 5(4):15–25
46. Teo HG, Lee PS, Hawlader MNA (2012) An active cooling system for photovoltaic modules. Appl Energ 90(1):309–315
47. Bennett T, Zilouchian A, Messenger R (2013) A proposed maximum power point tracking algorithm based on a new testing standard. Sol Energy 89:23–41
48. Jiang L, Nayanassiri D, Maske L, Vilathgamuwa D (2015) Ahybrid maximum power point tracking for partially shaded photovoltaic systems in the tropics. Renew Energy 76:53–65
49. Kollimalla S, Kumar K (2014) A novel adaptive P&O MPPT algorithm considering sudden changes in the irradiance. IEEE Trans Energy Convers 29(3):2–10
50. Sundareswaran K, Vigneshkumar V, Sankar P, Simon SP, Nayak PSR, Palani S (2016) Development of an improved P&O algorithm assisted through a colony of foraging ants for MPPT in PV system. IEEE Transact Indust Informat 12(1):187–200
51. Shebani MM, Iqbal T, Quaicoe JE (2016) Modified droop method based on master current control for parallel-connected DC-DC boost converters. J Electr Comput Eng
52. Sebtahmadi SS, Sajadi A, Koniaka M, Biczal P, Mekhilef S (2018) Distributed control scheme for voltage regulation in smart grids. Int J Smart Grid and Clean Energ 1(2):18–25
53. Mamatha G (2016) Assessment of different MPPTS techniques for PV system. J Electr Eng 2(1):1–8
54. Kobayashi K, Takano I, Sawada Y (2003) A study on a two stage maximum power point tracking control of a photovoltaic system under partially shaded insolation conditions. In: IEEE power engineering society general meeting, pp 2612–2617
55. Amrouche B, Belhamel M, Guessoum A (2007) Artificial intelligence based P&O MPPT method for photovoltaic systems. In: Proceeding Rev Energies Renouvelables. Tlemcen, Algeria, 5–7 Sept 2007, pp 11–16
56. Kobayashi K, Matsuo H, Sekine Y (2004) A novel optimum operating point tracker of the solar cell power supply system. In: Proceeding 35th annual IEEE power electronics specialists conference, pp 2147–2151
57. Balamurugan M, Sahoo SK, Sukchai S (2017) Application of soft computing methods for grid connected PV system: a technological and status review. Renew Sustain Energ Rev 75:1493–1508
58. Qi J, Zhang Y, Chen Y (2014) Modeling and maximum power point tracking (MPPT) method for PV array under partial shade conditions. Renew Energy 66:337–345
59. Rozana R, Jusoh A (2017) Modified perturb and observe (P&O) with checking algorithm under various solar irradiation. Solar Energ 148:128–139
60. Lyden S, Haque ME (2015) A simulated annealing global maximum power point tracking approach for PV modules under partial shading conditions. IEEE Transact Power Electron 31(6):4171–4181

61. Soedibyo S, Irawan D (2017) Desain optimum proportional-integral-derivative pada maximum power point tracking Sistem fotovoltaic. *Jurnal Teknik Elektro dan Informatika* 6(2):10–18
62. Hua C, Lin J (2003) An online MPPT algorithm for rapidly changing illuminations of solar arrays. *Renew Energy* 28:1129–1142
63. Weidong X, Dunford WG (2004) A modified adaptive hill climbing MPPT method for photovoltaic power systems. In: *Inics specialists conference*, pp 1957–1963
64. Jung-Woo B, et al (2010) Maximum power point tracking control of photovoltaic system using neural network. In: *IEEE international conference on electrical machines and systems*, 2010
65. Mamarelis E, Petrone G, Spagnuolo G (2014) A two-step algorithm improving the P&O steady state MPPT efficiency. *Appl Energy* 113:414–421
66. ESRAM T, Kimball J, Krein P, Chapman P, Midya P (2006) Dynamic maximum power point tracking of photovoltaic arrays using ripple correlation control. *IEEE Trans Power Electron* 21(12):82–91
67. Elgendy M, Zahawi B (2012) Assessment of perturb and observe MPPT algorithm implementation techniques for PV pumping applications. *IEEE Trans Sustain Energy* 3(1):21–33
68. Alik R, Jusoh A (2017) Modified Perturb and Observe (P&O) with checking algorithm under various solar irradiation. *Sol Energy* 148:128–139
69. Femia N, Granozia D, Petrone G, Spagnuolo G, Vitelli M (2007) Predictive and adaptive MPPT perturb and observe method. *IEEE Trans Power Electron* 43:934–950
70. Fortunato M, Giustiniani A, Petrone G, Spagnuolo G, Vitelli M (2008) Maximum power point tracking in a one-cyclecontrolled single-stage photovoltaic inverter. *IEEE Trans Ind Electron* 55(7):2684–2693
71. Kollimalla S, Mishra K (2013) A new adaptive P&O MPPT algorithm based on FSCC method for photovoltaic system. In: *International conference on circuits, power and computing technologies, ICCPCT. Nagercoil, India, 21–23 Mar 2013*, pp 406–411
72. Sher HA, Murtaza AF, Al-Haddad K (2015) A hybrid maximum power point tracking method for photovoltaic applications with reduced offline measurements. In: *IEEE*, pp 1482–1485
73. Kim IS, Kim MB, Youn MJ (2006) New maximum power point tracker using sliding-mode observer for estimation of solar array current in the grid-connected photovoltaic system. *IEEE Transact Indust Electron* 53(4):1027–1035
74. Phang JCH, Chan DSH, Phillips JR (1984) Accurate analytical method for the extraction of solar cell model parameters. *Electron Lett* 20(10):406
75. Won CY, Kim DH, Kim SC, Kim WS, Kim HS (1994) A new maximum power point tracker of photovoltaic arrays using fuzzy controller. *Power Electronics Specialists Conference*, pp 396–403
76. Brambilla A, Gambarara M, Garutti A, Ronchi F (1999) New approach to photovoltaic arrays maximum power point tracking. In: *Proceeding 30th annual IEEE power electronics specialists conference*, pp 632–637
77. Sugimoto H, Dong H (1997) A new scheme for maximum photovoltaic power tracking control. In: *Proceeding of the power conversion conference*, pp 691–696
78. Chen Y, Smedley K (2002) A cost-effective single-stage inverter with maximum power point tracking. *IEEE Trans Power Electron* 17:1289–1294
79. Tse KK, Ho MT, Chung HH, Hui SY (2002) A novel maximum power point tracker for PV panels using switching frequency modulation. *IEEE Transact Power Electron* 17(6):980–989
80. Solodovnik E, Liu S, Dougal RA (2004) Power controller design for maximum power tracking in solar installations. *IEEE Trans Power Electron* 5:1–13
81. Enrique J, Andujar M, Bohorquez A (2010) A reliable, fast, and low cost maximum power point tracker for photovoltaic applications. *Sol Energy* 84:79–89
82. Hsieh G, Hsieh I, Tsai Y, Wang C (2013) Photovoltaic power-increment aided incremental-conductance MPPT with two-phased tracking. *IEEE Trans Power Electron* 28(6):2895–2911
83. Lapena O, Penella MT, Gasulla M (2010) A new MPPT method for low-power solar energy harvesting. *IEEE Trans Ind Electron* 57:3129–3138

84. Garraoui R, Hamed MB, Sbita L (2017) MPPT controllers based on sliding-mode control theory and fuzzy logic in photovoltaic power systems: a comparative study. In: Applications of sliding mode control, pp 215–231
85. Elgendy M, Zahawi B (2015) Operating characteristics of the P&O algorithm at high perturbation frequencies for standalone PV systems. *IEEE Trans Energy Convers* 30(1):89–98
86. Hussein KH, Mota I (1995) Maximum photovoltaic power tracking: an algorithm for rapidly changing atmospheric conditions. In: *IEE Proceedings—Generation, Transmission Distribution*, pp 59–64
87. Irisawa K, et al (2000) Maximum power point tracking control of photovoltaic generation system under non-uniform insolation by means of monitoring cells. In: *IEEE Photovoltaic Specialists Conference* pp 1707–1710
88. Veerachary M, Senjyu T, Uezato K (2002) Maximum power point tracking control of IDB converter supplied PV system. *IEE Proc Electric Power Appl* 148(6): 494–502
89. Kobayashi K, et al (2004) A novel optimum operating point tracker of the solar cell power supply system. In: 35th Annual IEEE Power Electronics Specialists Conference, pp 2147–2151
90. Abdulkadir M, Yatim AHM (2014) Hybrid maximum power point tracking method based on PSO and incremental conductance. In: *Proceeding IEEE conference on energy conversion (CENCON)*. Johor Bahru, 13–14 Oct 2014, pp 271–276
91. Radjai T, Rahmani L (2014) Implementation of a modified incremental conductance MPPT algorithm with direct control based on a fuzzy duty cycle change estimate or using dSPACE. *Sol Energy* 110(3):25–37
92. Zhao G, Harada K (1993) Controlled power interface between solar cells and AC source. *IEEE Trans Power Electron* 8:654–662
93. Ishaque K, Salam Z, Syafaruddin S (2011) A comprehensive MATLAB simulink PV system simulator with partial shading capability based on two-diode model. *Sol Energy* 85:2217–2227
94. Ishaque K, Salam Z, Taheri H (2011) Simple, fast and accurate two diode model for photovoltaic modules. *Sol Energy Mater Sol Cells* 95:586–594
95. Liu F, Kang Y, Zhang Y, Duan S (2008) Comparison of P&O and hill climbing MPPT methods for grid connected PV converter. In: *Proceeding IEEE conference on industrial electronics and applications*. Singapore 3–5 June 2008, pp 804–807
96. Peter P, Sharma P, Agarwal V (2012) Switched capacitor dc-dc converter based current equalization scheme for maximum power extraction from partially shaded PV modules without by pass diodes. In: *Proceedings of the IEEE photovoltaic specialists conference*, pp 1422–1427
97. Cha WJ, Kwon JM, Kwon BH (2008) Highly efficient step-up dc-dc converter for photovoltaic micro-inverter. *Solar Energ* 135:14–21
98. Mei Q, Shan M, Liu L, Guerrero JM (2010) A novel improved variable step-size incremental-resistance (INR) MPPT method for PV systems. *IEEE Trans Ind Electron* 58(6):242–247
99. Zhang M, Wu J, Zhao H (2004) The application of slide technology in PV maximum power point tracking system. In: *Proceedings of the 5th world conference*, pp 5591–94
100. Pandey A, Ashish K, Dasgupta H (2008) High performance algorithms for drift avoid an ce and fast tracking in solar MPPT system. *IEEE Trans Energy Convers* 23:1–9
101. Pachauri RK, Chauhan YK (2014) Fuzzy logic controlled MPPT assisted PV-FC power generation for water pumping system. In: *Proceeding IEEE conference on electrical, electronics and computer science*. Manit, Bhopal, 2–3 Mar 2014, pp 1–6
102. Soon T, Mekhilef S (2014) Modified incremental conductance MPPT algorithm to mitigate in accurate responses under fast-changing solar irradiation level. *Sol Energy* 101(3):33–42
103. Zhao Z, Eltawil M (2013) MPPT techniques for photovoltaic applications. *Renew Sustain Energy Rev* 25:793–813
104. Liu X, Lopes L (2004) An improved perturbation and observation maximum power point tracking algorithm for PV arrays. In: *Proceedings of the IEEE power electronics specialists conference (PESC)*, pp 201–205
105. Ishaque K, Salam Z, Amjad M, Mekhilef S (2012) An improved particle swarm optimization (PSO)-based MPPT for PV with reduced steady-state oscillation. *IEEE Trans Power Electron* 27:3627–3638

106. Patel H, Agarwal V (2008) Maximum power point tracking scheme for PV systems operating under partially shaded conditions. *IEEE Trans Ind Electron* 55(16):89–98
107. Alajmi B, Ahmed K, Finney S, Williams B (2011) Fuzzy-logic-control approach of a modified hill-climbing method for maximum power point in microgrid standalone photovoltaic system. *IEEE Trans Power Electron* 26(11):22–30
108. Alajmi B, Ahmed K, Finney S, Williams B (2011) A maximum power point tracking technique for partially shaded photovoltaic systems in microgrids. *IEEE Trans Industr Electron* 3(2):22–27
109. Patel H, Agarwal V (2009) MPPT scheme for a PV-fed single-phase single-stage grid-connected inverter operating in CCM with only one current sensor. *IEEE Trans Energy Convers* 24(2):56–63
110. Patel H, Agarwal V (2011) MATLAB-based modeling to study the effects of partial shading on PV array characteristics. *IEEE Trans Energy Convers* 23(30):2–10
111. Hsieh GC, Hsieh HI, Tsai CY, Wang CH (2012) Photovoltaic power-increment-aided incremental-conductance MPPT with two-phased tracking. *IEEE Transact Power Electron* 28(6):2895–2911
112. Bruendlinger R, Bletterie B, Milde M, Oldenkamp H (2006) Maximum power point tracking performance under partially shaded PV array conditions. *Proceedings 21st EUPVSEC*, pp 2157–2160
113. Xiao W, Dunford W (2007) A modified adaptive hill climbing MPPT method for photovoltaic power systems. In: *Proceedings conference 35th Annual, IEEE. Power electronics specialists, Aachen, Germany, June 20–25, 2007*, pp 1957–1963
114. Mohamed AE, Zhao Z (2011) MPPT techniques for photovoltaic applications. *Renew Sustain Energ Rev* 25:793–813
115. Lee CY, Chen PH, Shen YX (2012) Maximum power point tracking (MPPT) system of small wind power generator using RBFNN approach. *Expert Sys Appl* 38(10):12058–12065
116. Rajasekar S, Gupta R (2012, March) Solar photovoltaic power conversion using modular multilevel converter. In: *2012 Students conference on engineering and systems, IEEE*, pp 1–6
117. Sera D, Mathe L, Kerekes T, Spataru SB, Teodorescu R (2013) On the perturb-and-observe and incremental conductance MPPT methods for PV systems. *IEEE J Photovolt* 3:1070–1078
118. Hossain E, Bayindir R, Kabalci E, Perez R (2014) A comprehensive study on microgrid technology. *Int J Renew Energ Res (IJRER)* 4(4):1094–1107
119. Zadeh MJZ, Fathi SH (2017) A New approach for photovoltaic arrays modeling and maximum power point estimation in real operating conditions. *IEEE Transact Indust Electron* 64(12):9334–9343
120. Rahim NA, Amir A, Selvaraj J (2016) Study of the MPP tracking algorithms: focusing the numerical method techniques. *Renew Sustain Energ Rev* 62:350–371
121. Thangavelu A, Vairakannu S, Parvathyshankar D (2017) Linear open circuit voltage-variable step-size-incremental conductance strategy-based hybrid MPPT controller for remote power applications. *IET Power Electron* 10(11):1363–1376
122. Kumar N, Hussain I, Singh B, Panigrahi BK (2018) Normal harmonic search algorithm-based MPPT for solar PV system and integrated with grid using reduced sensor approach and PNKLM algorithm. *IEEE Transact Indust Appl* 54(6):6343–6352
123. Jiang S, Member S, Cao D, Li Y (2012) Grid-connected boost-half-bridge photo-voltaic micro inverter system using repetitive current control and maximum power point tracking. *IEEE Trans Power Electron* 27(11):11–22
124. Dandoussou A, Kamta M, Bitjoka L, Wira P, Kuitché A (2017) Comparative study of the reliability of MPPT algorithms for the crystalline silicon photovoltaic modules in variable weather conditions. *J Electric Sys Inform Tech* 4(1):213–224
125. Bodur M, Ermis M (1994) Maximum power point tracking for low power photo-voltaic solar panels. *Electro Tech Conf* 752:758–761
126. Enslin J, Snyman D (1997) Integrated photovoltaic maximum power point tracking converter. *IEEE Trans Electron* 44:769–773

127. Masoum M et al (1998) Optimal power point tracking of photovoltaic system under all operating conditions. In: 17th congress of the world energy council, Houston, pp 33–45
128. Lim Y, Hamill D (2000) Simple maximum power point tracker for photovoltaic arrays. *Electron Lett* 36:997–999
129. Farsadi M, Kalashani MB (2014) New structure for photovoltaic systems with maximum power point tracking ability. *Int J Power Electron Drive Sys (IJPEDS)* 4(4)
130. Hsiao Y, Chen C (2002) Maximum power tracking for photovoltaic power system. In: 37th IAS annual meeting industry applications conference, pp 1035–1040
131. Masoum M, Dehbonei A, Fuchs H (2002) Theoretical and experimental analyses of photovoltaic systems with voltage and current-based maximum power point tracking. *IEEE Power Eng* 22:62–72
132. Lee CY, Chen PH, Shen YX (2011) Maximum power point tracking (MPPT) system of small wind power generator using RBFNN approach. *Expert Sys Appl* 38(10):12058–12065
133. Abu-Tariq A, Asghar MJ (2005, November) Development of an analog maximum power point tracker for photovoltaic panel. In: 2005 international conference on power electronics and drives systems, vol 1, IEEE, pp 251–255
134. Cesare G, Caputo D, Nascetti A (2006) Maximum power point tracker for photovoltaic systems with resistive like load. *Sol Energy* 80:982–988
135. Simjee FI, Chou PH (2006) Efficient charging of supercapacitors for extended lifetime of wireless sensor nodes. *IEEE Trans Power Electron* 23(3):1526–1536
136. Pandey A, Dasgupta N, Mukerjee AK (2007) A Simple Single-Sensor MPPT Solution. *IEEE Transact Power Electron* 22(2):698–700
137. Tafticht T, Agbossou K, Doumbia ML, Cherita A (2008) An improved maximum power point tracking method for photovoltaic system. *Renew Energy* 33:1508–1516
138. Yuvarajan S, Xu S (2003) Photo-voltaic power converter with a simple maximum-power-point-tracker. *Int Symp Circuits Syst*, pp 399–402
139. Faranda R, Leva S, Maugeri V (2008) “MPPT techniques for PV Systems”, energetic and cost comparison. In: Power and energy society general meeting—conversion and delivery of electrical energy in the 21st century, pp 1–6
140. Hao Y, Xiaobo W (2009) Compensation loop design of a photovoltaic system based on constant voltage MPPT. In: Proceeding IEEE conference on power and energy engineering. Wuhan, 27–31 Mar 2009, pp 1–4
141. Kumar K, Ark S (2014) Performance study on a grid connected 20 Kw solar photovoltaic installation in an industry in Tiruchirappalli (India). *Energy Sustain Dev* 23(1):294–304
142. Subudhi B, Mohanty S, Ray PK (2016) A grey wolf-assisted perturb & observe MPPT algorithm for a PV system. *IEEE Transact Energ Convers* 32(1):340–347
143. Colak I, Belkaid A, Kayisli K (2017) Implementation of a modified P&O-MPPT algorithm adapted for varying solar radiation conditions. *Electric Eng* 99(3): 839–846
144. Xiong Y, Qian S, Xu J (2012) Research on constant voltage with incremental conductance MPPT method. In: Proceeding IEEE conference on power and energy engineering. Shanghai, China, 27–29 Mar 2012, pp 1–4
145. Reisi AR, Moradi MH, Jamasb S (2013) Classification and comparison of maximum power point tracking techniques for photovoltaic system: a review. *Renew Sustain Energy Rev* 19:433–443
146. Eltawil M, Zhao Z (2013) MPPT techniques for photovoltaic applications. *Renew Sustain Energy Rev* 25:793–813
147. Bhatnagar A, Nema B (2013) Conventional and global maximum power point tracking techniques in photovoltaic applications: a review. *J Renew Sustain Energy* 5:1–23
148. Shiau JK, Lee MY, Wei YC, Chen BC (2014) Circuit simulation for solar power maximum power point tracking with different buck-boost converter topologies. *Energy* 7(8):5027–5046
149. Hoarcă C, Răducu M (2014) Performance comparison of three MPPT algorithms: aESC, mESC and P&O. In: 2015 7th international conference on electronics, computers and artificial intelligence (ECAI), 25–27 June 2014, pp 35–42

150. Agarwal V (2013) Flyback configuration based micro-inverter with distributed MPPT partially shaded PV module and energy recovery scheme. In: Proceedings of the IEEE 39th photovoltaic specialists conference, pp 2927–2931
151. Huang L, Liu X, Ravichandran K, Sánchez-Sinencio E (2016) A highly efficient reconfigurable charge pump energy harvester with wide harvesting range and two-dimensional MPPT for internet of things. *IEEE J Solid-State Circuits* 51(5):1302–1312
152. Verma O, Prakash A, Aggarwal A (2016) Opposition and dimensional based modified firefly algorithm. *Exp Syst Appl* 44(1):68–76
153. Karami N, Moubayed N, Outbib R (2017) General review and classification of different MPPT techniques. *Renew Sustain Energy Rev* 68:1–18
154. Enslin J, Snyman D (1992) Simplified feed-forward control of the maximum power point in PV installations. In: *Industrial electronics, control, instrumentation, and automation*, vol 541, pp 548–553
155. Enslin J, Beukes H (1993) Analysis of a new compound converter as MPPT, battery regulator and bus regulator for satellite power systems. In: *Power electronics specialists conference*, pp 846–852
156. Masoum M, Sarvi M (2005) Design, simulation and implementation of a fuzzy- based maximum power point tracker under variable insolation and temperature conditions. *Iran J Sci Technol* 29(6):1–12
157. Noguchi T, Togashi S, Nakamoto R (2000) Short-current pulse based adaptive maximum-power-point tracking for photovoltaic power generation system. *IEEE Trans Ind Electron* 151:157–162
158. Leyva R, Alonso C (2006) MPPT of photovoltaic systems using extreme seeking control. *IEEE Trans Aerosp Electron Syst* 42(1):249–258
159. Salas V, Olias E, Lazaro A, Barrado A (2005) Evaluation of a new maximum power point tracker (MPPT) applied to the photovoltaic stand-alone systems. *Solar Energy Mater Solar Cells* 87(1):807–815
160. Dondi D, Bertacchini A, Brunelli D, Larcher L, Benini L (2008) Modeling and optimization of a solar energy harvester system for self-powered wireless sensor networks. *IEEE Transact Indust Electron* 55(7):2759–2766
161. Thongam SJ, Ouhrrouche M (2011) MPPT control methods in wind energy conversion systems. Fundamental and advanced topics in wind power. *IntechOpen* 3(2):340–347
162. Kumara B, Chauhan YK, Shrivastava V (2011) A comparative study of maximum power point tracking methods for a photovoltaic-based water pumping system. *Int J Sustain Energy* 33(4):797–810
163. Kumari JS, Saibabu TCC (2011) Modeling and simulation of pv array and its performance enhancement using MPPT (P&O) technique. *Int J Comput Sci Commun Netw* 1(1): 9–16
164. Kumar R, Shimi S, Chatterji S, Ansari F (2014) Modeling of solar PV module and maximum power point tracking using ANFIS. *Renew Sustain Energy Rev* 33(60):2–12
165. Hadeed K, Sher HA, Murtaza AF, Noman A, Addoweesh KE, Chiaberge M (2015) A new sensorless hybrid MPPT algorithm based on fractional short-circuit current measurement and P&O MPPT. *IEEE Transact Sustain Energy* 6(4):1426–1434
166. Agarwal S (2004) A new algorithm for rapid tracking of approximate maximum power point in photovoltaic systems. *IEEE Power Electron Lett* 2(1):1–9
167. Agarwal N, Rai A, Kaushika N, Singh B (2010) Simulation model of ANN based maximum power point tracking controller for solar PV system. *Sol Energy Mater SolCells* 95(77):3–8
168. Uuyukguzel B, Aksoy M (2016) A current-based simple analog MPPT circuit for PV systems. *Turkish J Electric Eng Comput Sci* 24:3621–3637
169. Sharma P, Agarwal V (2014) Exact maximum power point tracking of grid connected partially shaded PV source. *IEEE Trans Power Electron* 29(9):84–92
170. Wu L, Zhao Z, Liu J (2007) A. single-stage three-phase grid-connected photovoltaic system with modified MPPT method and reactive power compensation. *IEEE Trans Energy Convers* 22(88):1–6

PV Characteristics, Performance and Modelling



Ali M. Eltamaly and Hassan M. H. Farh

Abstract This chapter discusses the photovoltaic (PV) characteristics, performance, modelling, maximum power point tracker techniques and grid interconnection. It covers four different PV generator models with their characteristics and their performance analysis. In addition, the four most famous conventional MPPT techniques with some of the soft computing MPPT techniques have been discussed including detailed comparison, assessment, and discussion with the limitations, merits and demerits of these MPPT techniques. Interconnection of the PV energy system with electric utility has been discussed at the end of this chapter.

1 Introduction

Among all the renewable energy sources, photovoltaic (PV) represents a very important and promising energy source where it provides very clean energy without any environmental effect. Solar energy supply, the sunlight, is free and abundant source of energy. However, currently solar PV modules have a relatively low efficiency level compared not only to the efficiency of conventional fossil fuel but also to the efficiency of other renewable energy sources such as wind or hydro [1–4]. Improving the efficiency of PV system through tracking the global maximum power from the PV system with and without partial shading conditions is considered as a very hot development area.

PV module consists of series and parallel PV cells to achieve high-voltage and current output. The common PV cell technologies can be classified into multi-crystalline,

A. M. Eltamaly (✉)

Electrical Engineering Department, Mansoura University, Mansoura, Egypt

e-mail: eltamaly@mans.edu.eg

Sustainable Energy Technologies Center, King Saud University, Riyadh 11421, Saudi Arabia

H. M. H. Farh

Electrical Engineering Department, College of Engineering, King Saud University, Riyadh 11421, Saudi Arabia

e-mail: hfarh1@ksu.edu.sa

© Springer Nature Switzerland AG 2020

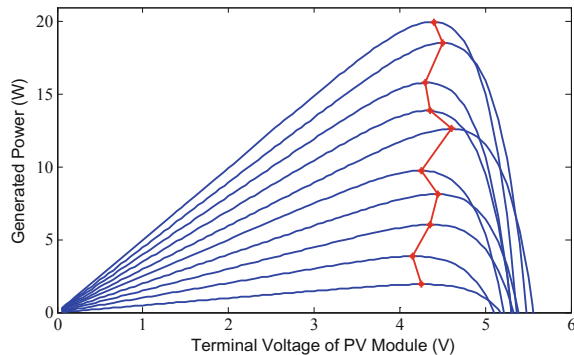
A. M. Eltamaly and A. Y. Abdelaziz (eds.), *Modern Maximum Power Point Tracking Techniques for Photovoltaic Energy Systems*, Green Energy and Technology, https://doi.org/10.1007/978-3-030-05578-3_2

mono-crystalline, thin-film and multi-junction PV cells. Each PV cell technology has its own manufacturing process and characteristics. To investigate and study the performance of the PV system, PV models are used to conclude the output PV characteristics under different irradiance and temperature conditions. The PV model generally consists of a photocurrent source, diodes and resistors. The most common PV models are the single- and double-diode models [5]. The single-diode model consists of five parameters, which are the PV current, diode saturation current, ideality factor, series resistance and parallel resistance. This PV model has acceptable accurate PV model estimation and low computation cost, whereas the two-diode PV model has an additional parallel diode that is used to compensate the recombination losses in the depletion region [6]. This increased the unknown parameters to become seven parameters. The additional unknown parameters are the diode saturation current and ideality factor. On the other hand, a three-diode PV model is proposed to address the leakage current issue due to the periphery connected to the PV cell during measurement [7].

The relation between the output power generated and output PV voltage for different radiations and temperatures is shown in Fig. 1, where each curve represents certain radiation and temperature. A unique peak is generated under uniform radiation as shown in this figure. In addition, the maximum power points (MPPs) are located at different output voltages. For this reason, numerous MPP trackers (MPPT) have been developed and discussed in many literatures such as [8–11]. On the other hand, P–V characteristics contain multiple peaks (one global peak—GP and many local peaks—LPs) under non-uniform or partial shading conditions (PSCs) and most conventional MPPT techniques fail to track the GP [12, 13], whereas soft-computing-based bio-inspired techniques such as flower pollination [14], ant bee colony [15, 16], firefly [17, 18], ant colony [19], cuckoo search [20], particle swarm optimization (PSO) [10, 20–25], improved bat [26] and S-Jaya [27] algorithms can follow the GP under partial shading condition.

This chapter discusses the PV characteristics, performance, modelling, MPPT and grid interconnection. It covers four different PV generator models with their characteristics and performance analysis. Also, the four most famous conventional MPPT

Fig. 1 P–V curves of PV cell under different environmental conditions



techniques with some of the soft computing MPPT techniques are discussed including detailed comparisons and discussion with the limitations, merits and demerits of these MPPT techniques.

2 Photovoltaic Generator Models



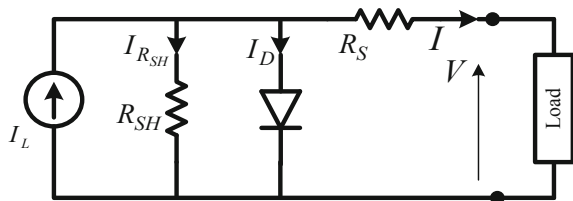
2.1 Single-Diode Model

The single-diode model of a PV cell/module is shown in Fig. 2. It represents the most common PV model due to the lowest number of physical parameters-based model used. The model is typically used to determine I–V curves using either four or five parameters: I_L is the internal generated current of PV cell (light current), I_o is the diode reverse saturation current, R_S is the series resistance, a is the modified ideality factor, and R_{SH} is the shunt resistance, which is assumed to be infinite in the four-parameter version. The four-parameter simplified model is less computationally intensive, and its accuracy for different technologies is debatable: Cristea et al. [28] have revealed that it matches module I–V curves over a wide range of irradiance, and Celik et al. [29] discovered that it overpredicts energy capture around solar noon under high irradiance conditions [30]. The five-parameter version requires numerical methods to be solved. Also, it can be developed using only manufacturers' data provided at standard test condition (STC—1000 W/m² and 25 °C). The main equation that describes the single-diode model is introduced as follows:

$$I = I_L - I_o \left[\exp \left(\frac{V + IR_S}{a V_t} \right) - 1 \right] - \frac{V + IR_S}{R_{SH}} \quad (1)$$

where I_o is the diode saturation current, a is the diode ideality factor, and $V_t = kT/q$, represents the thermal voltage. The parameter k is the Boltzmann constant ($1.3806503 \times 10^{-23}$ J/K), q is the electron charge ($1.60217646 \times 10^{-19}$ C), and T is the temperature of the PV module in Kelvin.

Fig. 2 Equivalent circuit of single PV diode model



2.2 Two-Diode Model

The single-diode equation assumes a constant value for the ideality factor (a). In practical, the ideality factor is a function of voltage across the device. At high voltage, when the recombination in the device is dominated by the surfaces and the bulk regions, the ideality factor is close to one. However, at lower voltages, recombination in the junction dominates and the ideality factor approaches two. The junction recombination is modified by adding a second diode in parallel with the first one and setting the ideality factor typically to two. Two-diode model is a modified version of single-diode PV model which takes into account the effect of recombination by introducing another diode in parallel as shown in Fig. 3. In the two-diode model, the first diode is representative of the diffusion and surface recombination, and the second diode accounts for recombination in the depletion region, which is most common at higher irradiances. At low irradiance and temperatures, two-diode PV model gives more accurate curve characteristics compared to single-diode model. The two-diode model is especially suggested for accurate modelling of low irradiance conditions [30]. A wide variety of research works have been done to implement a mathematical model for PV cell. Two-diode model has been used in many literatures [31–33]. The main expression that describes the two-diode model is introduced as follows:

$$I = I_L - I_{o1} \left[\exp \left(\frac{V + IR_S}{aV_t} \right) - 1 \right] - I_{o2} \left[\exp \left(\frac{V + IR_S}{aV_t} \right) - 1 \right] - \frac{V + IR_S}{R_{SH}} \quad (2)$$

One downside to the two-diode model is the difficulty to determine its parameters accurately. Ishaque et al. [6] solved the two-diode model as the single-diode model is solved, and they discovered that it gives closer results between simulations and measured data for a variety of panel types than the single-diode model. Given its added complexity, unless the two-diode model allows for a significant increase in accuracy, it likely makes more sense to continue to use and attempt to improve the single-diode model [30].

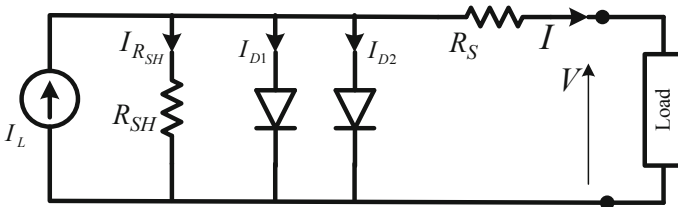


Fig. 3 Equivalent circuit of two-diode model

2.3 Multi-diode PV Model

Figure 4 shows the equivalent circuit of multi-diode PV model. It includes the photocurrent source (I_L), series and parallel diodes (D_{nm}) with n -by- m dimension, series resistance (R_S), and parallel resistance (R_{SH}). R_s is the sum of structure resistance, and R_p represents the leakage current. By adding more diodes, the multi-diode PV model has more degree of freedom to adjust itself to model the output characteristics of different PV cells [5].

From Fig. 4, the output current I of the generalized multi-diode PV model is introduced as follows:

$$I = I_L - \sum_{i=1}^n I_{o,i} \left[\exp \left(\sum_{j=1}^m \frac{V + IR_S}{a_{ij} N_s V_t} \right) - 1 \right] - \frac{V + IR_S}{R_{SH}} \quad (3)$$

where I_o is the diode saturation current, a is the diode ideality factor, $V_t = kT/q$, represents the thermal voltage, and N_s is the number of cells connected in series per string. The parameter k is the Boltzmann constant ($1.3806503 \times 10^{-23}$ J/K), q is the electron charge ($1.60217646 \times 10^{-19}$ C), and T is the temperature of the PV module in Kelvin.

2.4 Empirical PV Models

The most empirical PV model used in the USA is the King/Sandia Model [34], which contains many detailed empirical factors proved from linear fits of I–V hundreds' curves at different irradiance and temperatures. Although the K/S model has the most accurate modelling across a wide range of operating conditions and technologies,

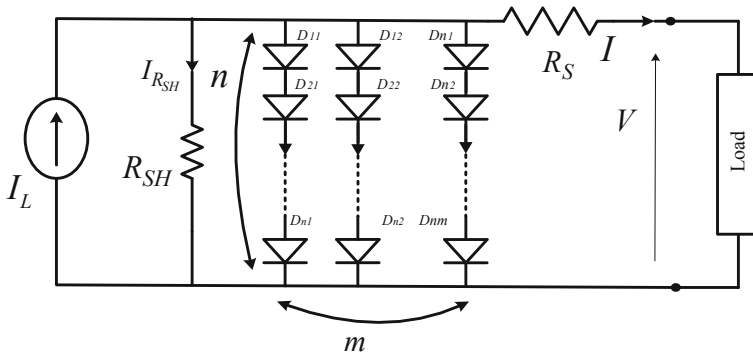


Fig. 4 Equivalent circuit of multi-diode PV model

particularly non-crystalline-silicon technologies, the empirical coefficients have only been determined for limited PV modules because I–V curve collection to generate the coefficients is very time consuming. A recent NIST study [35] compared K/S model to measured data over a year for four different technologies mounted vertically, and they matched within 5–6% on both a monthly and annual basis. Matching was worst during the summer when the sun's angle of incidence was highest, suggesting reflective or other spectral light losses that may not have been accounted for in the model.

A comparison between the models available in NREL's System Advisor Model (SAM), including both the K/S and the CEC single-diode models, is achieved in [36], comparing them to measured data from a crystalline silicon array in Albuquerque, NM. In this sunny climate, the two PV models has similar performance in terms of accuracy, suggesting that there may be little benefit to using such a detailed model, at least for crystalline silicon technologies. Although the comparison revealed the relatively good agreement and the lack of availability of K/S model coefficients for many modules, the two models used different methods to determine radiation and temperature. So, it is not obvious that the PV models agree to what extent. Recent work at Sandia National Laboratories [37] used the I–V curve data that are available from the IEC 61853 (IEC, 2011) to empirically determine the single-diode model parameters. Although this technique is successful for many modules, the implementation generates unlogic coefficients for some that need improvements. Most importantly though, it is only calculating the single-diode parameters under STC and uses published modelling relations [38] to translate the parameters to other radiations and temperatures. These parameter translations should be further studied and modified as necessary as more data for each PV module will become available [30].

3 Maximum Power Point Tracking Techniques

The maximum power point (MPP) and its corresponding voltage change based on the change of the temperature or irradiation. Thus, it is compulsory to track the MPP of the PV array to maximize the efficiency of PV system. All in all, the MPPT process participates mainly in reducing the PV system cost and improving the overall efficiency [39]. This part covers the four most common and efficient conventional MPPT techniques. In addition, some soft computing MPPT techniques will be covered in brief as follows.

3.1 Conventional MPPT Techniques

Numerous conventional MPPT techniques have been used to track the unique MPP under uniform condition (without PSC). The most famous conventional techniques

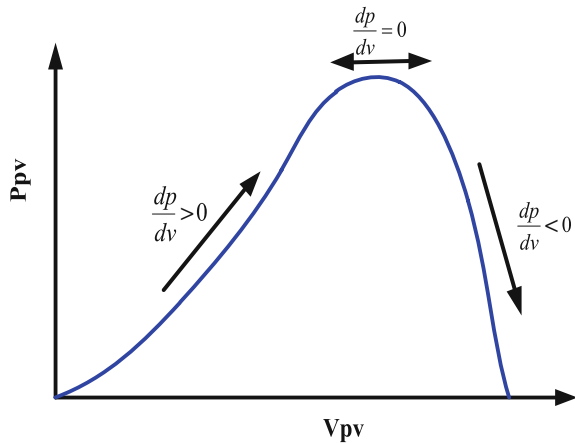
are perturb and observe (P&O), incremental conductance (IncCond), hill climbing (HC) and constant voltage (CV). The basic idea of operation, literature review, merits and demerits in addition to comparisons of these conventional techniques have been introduced in the following subsections.

3.1.1 Perturb-and-Observe Technique

Perturb-and-observe (P&O) technique uses the measured PV voltage, current, and the output power and then takes the decision to increase or decrease the voltage using the duty ratio of the DC–DC converter until the MPP is tracked. Figure 5 shows the idea behind this technique on the P–V characteristic. Figure 6 shows the flowchart of P&O technique. The logic of the P&O is to perturb the PV output voltage and observe the power change. If the PV power captured increased, the perturbation decision should be kept in the same direction regardless of whether the PV voltage increases or decreases until MPP is tracked, whereas if the output power decreased, the voltage increment (ΔV) should be reversed. The maximum power is extracted when $dP/dV = 0$ [26, 28–31].

Finally, the advantages and disadvantages of P&O MPPT technique are presented in Table 1. The results in [40–45] revealed that P&O has less performance than IncCond but outperformed the other conventional MPPT techniques. In addition, some authors discovered that some improvements on P&O put it in the same rank with IncCond [46–48].

Fig. 5 P–V characteristic of the PV array explaining the P&O concept



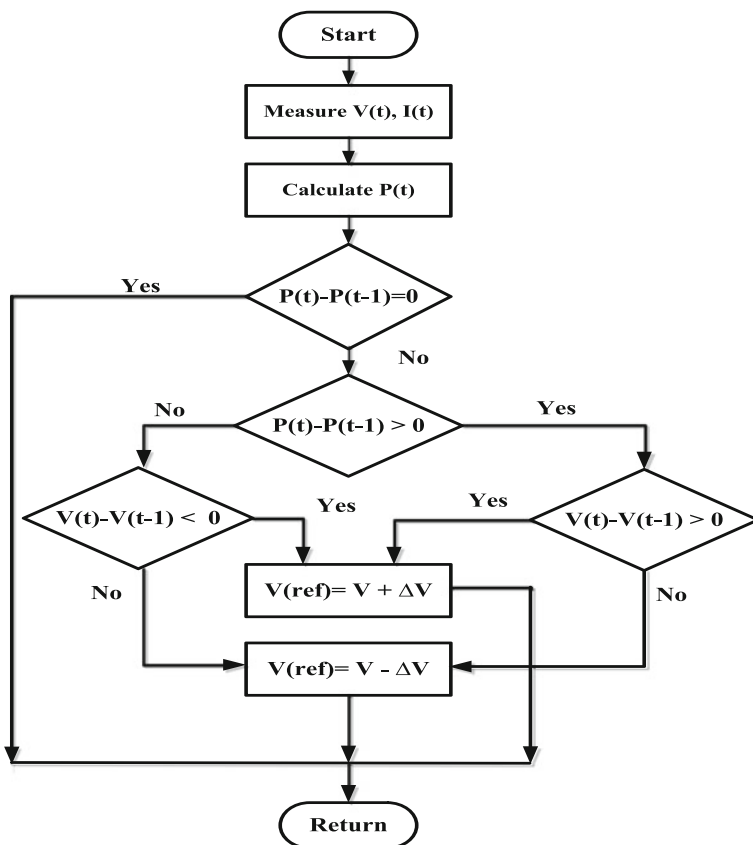


Fig. 6 Flowchart of P&O technique concepts

Table 1 Advantages and disadvantages of P&O MPPT technique

References	Advantages	Disadvantages
[41, 42, 44, 49]	<ul style="list-style-type: none"> • Easy to implement • Upright, accurate and good performance under uniform radiation • Online and does not depend on PV array 	<ul style="list-style-type: none"> • Oscillations around steady state occur during fast-varying environmental conditions • Difficulty of the step size control

3.1.2 Incremental Conductance MPPT Technique

Incremental conductance (IncCond) MPPT technique is one of the most widely used MPPT strategies which has the advantage of fast tracking of the MPP. Compared to P&O MPPT strategy, IncCond combines and utilizes the unique characteristics of both the output P–V curve and I–V curve of the PV array and thus tracks the MPP faster and more accurately. IncCond MPPT technique relies on the P–V characteristic slope where the MPP is tracked when $dP/dV = 0$ as follows [39, 40]:

$$\frac{d(V_{PV}, I_{PV})}{dV_{PV}} = I_{PV} + V_{PV} * \frac{dI_{PV}}{dV_{PV}} = 0 \quad (4)$$

$$\frac{dI_{PV}}{dV_{PV}} = -\frac{I_{PV}}{V_{PV}} \quad (5)$$

$$dV_{PV} \cong \Delta V_{PV} = V_{PV}(t_2) - V_{PV}(t_1) \quad (6)$$

The current change dI_{PV} and the voltage change dV_{PV} are approximately equal to ΔV_{PV} ΔI_{PV} as the following:

$$dV_{PV} \cong \Delta V_{PV} = V_{PV}(t_2) - V_{PV}(t_1) \quad (7)$$

$$dI_{PV} \cong \Delta I_{PV} = I_{PV}(t_2) - I_{PV}(t_1) \quad (8)$$

As shown in Fig. 7 [50], the MPP is tracked and caught when $\frac{dI_{PV}}{dV_{PV}} = -\frac{I_{PV}}{V_{PV}}$ is satisfied, and the MPP is achieved. If $\left(\frac{dI_{PV}}{dV_{PV}} > -\frac{I_{PV}}{V_{PV}}\right)$, the operating point will be left to the MPP on the P–V curve. If $\left(\frac{dI_{PV}}{dV_{PV}} < -\frac{I_{PV}}{V_{PV}}\right)$, the operating point will be right to the MPP as shown in Fig. 7.

Numerous comparative researches revealed that IncCond is the most efficient conventional MPPT technique compared to other conventional techniques (P&O, HC, CV, OV, SC, TP, PC, TPE, TS and Fixed duty cycle) in terms of steady-state

Fig. 7 P–V characteristic explaining the IncCond concept

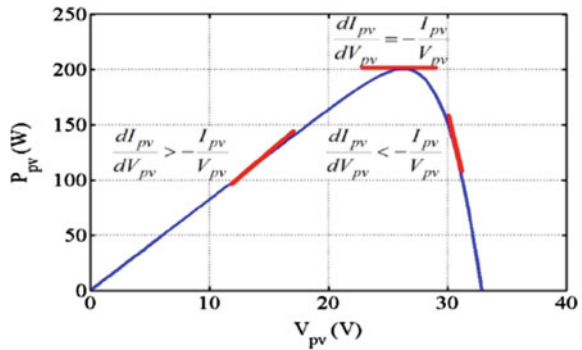


Table 2 Advantages and disadvantages of IncCond technique

References	Advantages	Disadvantages
[41, 44, 49, 51, 52]	<ul style="list-style-type: none">• Online, accurate, reliable and efficient• Variable step size makes it more adequate to fast-varying environmental conditions• Oscillation around steady state is less	<ul style="list-style-type: none">• Response time is longer when environmental conditions change• Highly expensive• Speed and accuracy depend on step size, so oscillations might happen

error, dynamic response and efficiency followed by P&O technique [41–43, 45]. The finding agreed with the finding discovered by Gupta et al. [44] which revealed that IncCond has superior performance as compared to P&O and CV in terms of tracking efficiency, rise time, fall time and dynamic response [44]. In similar, Ishaque et al. revealed that IncCond performance is slightly better than P&O and very sensitive to its perturbation size, especially at low irradiance levels [40]. On the other hand, both Faranda and Hohm discovered that P&O and IncCond have superior and similar performance in addition to higher efficiency compared to other conventional techniques [47, 48]. Advantages and disadvantages of IncCond MPPT technique are given in Table 2.

Comparing to P&O MPPT strategy, IncCond MPPT strategy is more complex. IncCond MPPT strategy could make a flexible decision of the next step size based on current judge—a large step size promises fast responding speed, while small step size satisfies accurate tracking result. For this reason, it usually leads to a higher cost. The complexity of IncCond MPPT strategy is caused by the design of a reference value ε which determines both the tracking speed and the accuracy of the tracking result.

Usually, it would take a long time to select a suitable ε ; for example, in my research ε is between 0.005000000000000000400750099999999999999 and 0.0050000000000000004007501. If ε equals the previous value, the step size is not large enough to distinguish the tracking speed of IncCond MPPT strategy from the one of P&O MPPT strategies. However, if ε equals the later value, the tracking result turns to unstable and misses the goal in several seconds [39].

3.1.3 Hill-Climbing MPPT Technique

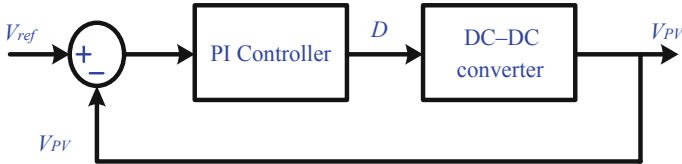
The hill-climbing (HC) technique is very easy in implementation where no priori data are needed. It relies on the DC–DC converter duty cycle change in order to determine the change of the power until the power change reaches zero (MPP). Rapid change of solar irradiance may cause the HC algorithm to lose MPP fast tracking completely due to lack of fast response. Also, oscillations around MPP during fast-varying environmental conditions are happened [8, 53–56]. Advantages and disadvantages of HC MPPT technique are given in Table 3.

Table 3 Advantages and disadvantages of HC-based MPPT technique

References	Advantages	Disadvantages
[49, 51, 57, 58]	<ul style="list-style-type: none"> • No priori data is needed • Easy in idea and implementation 	<ul style="list-style-type: none"> • Oscillations around steady state occur during fast-varying environmental conditions • Suitable step size is important • Less efficient under dynamic state

3.1.4 Constant-Voltage MPPT Technique

Constant-voltage (CV) technique forces the PV array's voltage to a fixed value where the MPP voltage (V_{MPP}) is approximated to 76% of the PV array's open-circuit voltage (V_{OC}) [43]. The shortcomings of this technique are that the V_{MPP} is not always at 76% of the V_{OC} ; therefore, it increases the steady-state error and reduces the efficiency. The CV controller has some merits such as only one voltage sensor is needed and the current sensor is not required [48]. Also, it is the easiest technique to be implemented and has low installation cost, but its efficiency is poor with respect to other active MPPT techniques. The block diagram of a CV controller is shown in Fig. 8 where V_{PV} is only measured in order to provide the duty cycle of the DC–DC converter by PI regulator to track the MPP [44]. Advantages and disadvantages of CV-based MPPT technique are introduced in Table 4.

**Fig. 8** Block diagram of CV controller**Table 4** Advantages and disadvantages of CV technique

References	Advantages	Disadvantages
[42, 44, 49, 58]	<ul style="list-style-type: none"> • Easy to implement • CV uses one voltage sensor; hence, the cost will be reduced • Economical and more efficient during low radiation 	<ul style="list-style-type: none"> • Priori data is needed • Less accuracy and efficiency due to approximation ($V_{MPP} = 0.76V_{OC}$), which is not right in some cases

3.2 Soft Computing MPPT Techniques

3.2.1 Fuzzy Logic Control MPPT

Fuzzy logic is a form of many-valued logic which deals with reasoning that is approximate rather than fixed and exact. In contrast with traditional logic which usually sets two-value logic as true or false, fuzzy logic can have varying values. Fuzzy logic variables may have a truth or false value that ranges in different degrees and be expressed by linguistic variables. In these cases, fuzzy logic control could provide both fast process speed and the needed accuracy to some extent [39, 59].

The objective of FLC is to track and extract the maximum power from the PV system for a given irradiance (W/m^2) and temperature ($^{\circ}\text{C}$). It does not require any technical knowledge of the PV system, while its simplicity gives it an advantage in tracking its MPP under fast-varying atmospheric conditions [60, 61]. The FLC has two inputs which are $\frac{dP_{PV}}{dV_{PV}}$ and $\Delta\left(\frac{dP_{PV}}{dV_{PV}}\right)$, i.e., (E_{rr}) and (ΔE_{rr}) which are determined from the PV output power and voltage (fuzzification) as follows:

$$E_{rr} = \frac{P_{PV}(k) - P_{PV}(k-1)}{V_{PV}(k) - V_{PV}(k-1)} \quad (9)$$

$$\Delta E_{rr} = E_{rr}(k) - E_{rr}(k-1) \quad (10)$$

The output from FLC is the required change in the duty cycle of the DC–DC converter (de-fuzzification). The FLC block diagram is shown in Fig. 9. The advantages of using FLC are in it being a universal control algorithm, very simple, adaptive, fast tracking response, parameter insensitivity and can work properly even with an imprecise input data. Also, FLC has better and efficient response in tracking the MPP, especially in the case of rapidly changing atmospheric conditions [62–65]. One of its drawbacks occurs in PSC where it may stick around LP.

Figure 10 shows the input and output membership functions, and Table 5 introduces the input and output fuzzy rules [8]. The variation step of E_{rr} and ΔE_{rr} may vary according to the system. Once E_{rr} and ΔE_{rr} are calculated and transferred to the logic variables based on the membership functions, the FLC output, which is typically duty ratio change, ΔD of the DC–DC boost converter is estimated in rules as given in Table 5.

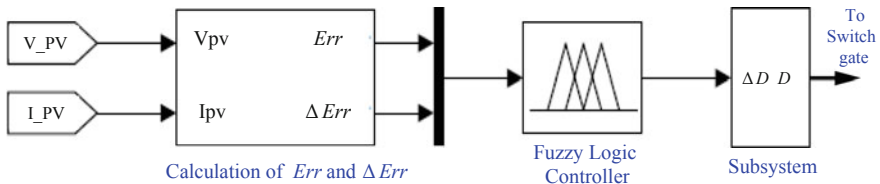


Fig. 9 FLC block diagram in MATLAB/Simulink

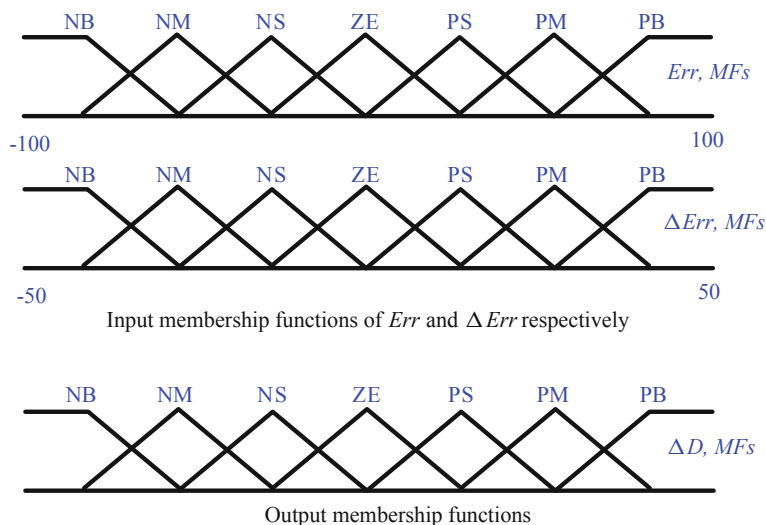


Fig. 10 Membership functions of FLC

Table 5 Fuzzy rules for the input and output variables

E_{rr}	ΔE_{rr}						
	NB	NM	NS	ZE	PS	PM	PB
NB	NB	NB	NB	NB	NM	NS	ZE
NM	NB	NB	NB	NM	NS	ZE	PS
NS	NB	NB	NM	NS	ZE	PS	PM
ZE	NB	NM	NS	ZE	PS	PM	PB
PS	NM	NS	ZE	PS	PM	PB	PB
PM	NS	ZE	PS	PM	PB	PB	PB
PB	ZE	PS	PM	PB	PB	PB	PB

Based on recent comparative studies of FLC-based MPPT given in Table 6, it is concluded that FLC has faster convergence speed in tracking the unique peak under uniform conditions compared to the conventional techniques [8, 66, 67]. Also, adaptive FLC performs well compared to the direct and indirect FLC-based MPPT during dynamic and steady-state conditions regardless of the converter type [51, 68, 69]. In conclusion, FLC should be combined with a scanning and storing algorithm or other AI techniques to track the GP under PSC to achieve fast and accurate convergence, high tracking efficiency and drift avoidance [70]. The advantages and disadvantages of FLC-based MPPT are given in Table 7.

Table 6 Recent comparative studies of FLC with other MPPT techniques

References	Variable control	DC–DC converter	Findings
[8]	Duty cycle	Boost	FLC has better performance in terms of tracking speed and drift avoidance followed by P&O, INC and HC MPPT techniques in both dynamic response and steady state
[71]	Duty cycle	Boost	FLC-based auto-scaling variable step size is proposed to achieve the merits of fast tracking and convergence speed during transient and steady state (no oscillations) compared to fixed step IncCond in both simulation and experimental works
[70]	Duty cycle	Boost	The proposed FLC with a scanning and storing algorithm has better performance compared to variable-step-size IncCond, conventional PSO and FLC-based HC in both simulation and experimental works. Many merits are achieved such as fast and accurate convergence to the GP, high tracking efficiency and no oscillations during transient and steady-state conditions
[51, 68]	Duty cycle	Boost–SEPIC	Adaptive FLC performs well compared to the direct and indirect FLC-based MPPT in terms of the active power and current oscillations, rising time, settling time and over/undershoots during dynamic and steady-state conditions. The antecedent and consequent membership functions of the proposed adaptive FLC are tuned synchronously
[69]	Duty cycle	Boost	Adaptive gain FLC outperforms the conventional FLC where it integrates two different rules. The first rule is used to adjust the duty cycle of the boost converter, while the second one is used for online adjusting of the controller's gain
[66]	Duty cycle	Buck	FLC has good performance compared to P&O during dynamic and steady-state conditions in terms of tracking efficiency and response time
[72]	Duty cycle	Buck–boost	The three best MPPT techniques are FLC, GA and PSO in terms of the performance (tracking speed, the average tracking error, the variance and the efficiency) and the implementation cost (sensors type, circuit type and software complexity). PID and ANN show less performance
[67]	Duty cycle	SEPIC	FLC-based MPPT performs better than P&O in terms of accuracy, tracking speed and convergence speed during dynamic and steady-state conditions in both simulation and experimental works

Table 7 Advantages and disadvantages of FLC-based MPPT technique

References	Advantages	Disadvantages
[49, 73–78]	<ul style="list-style-type: none"> • Highly robust, fast response, better performance and adjustable accuracy • Less oscillation during conditions variation • Able to work with imprecise inputs and good efficiency • More effective when combined with other EA techniques • Does not require accurate mathematical model and detailed information of the system 	<ul style="list-style-type: none"> • High complexity and expensive • Offline (priori information is required) • Efficiency of the whole system is dependent on the designer's performance and precision of the rules • Fails to converge under dynamic states • Rules cannot be changed, once defined

3.2.2 Artificial Neural Network Technique

Artificial neural network (ANN) represents one of the artificial intelligent MPPT techniques that has the ability to solve nonlinear problems. Therefore, it can be applied to track the GP over the LPs. ANN consists of three layers: input, hidden and output layers. The input layer is defined from the PV array such as temperature, irradiance and I_{sc} or V_{oc} [64, 79, 80]. ANN adjusts and controls the duty cycle of the DC–DC converter (ANN output) to track the GP.

Based on recent comparative studies of ANN-based MPPT given in Table 8, it can be observed that ANN is efficient and accurate in tracking the unique peak under uniform conditions compared to conventional techniques and mitigates their shortcomings related to tracking speed and oscillations around MPP at steady state [80–83]. On the other hand, ANN is more preferable if combined with other conventional or AI MPPT techniques to extract the GP instead of LP from the PV array, where ANN is used to predict the GP region whereas conventional or AI technique is used to track the GP. The reasons behind these are irradiance sensors are relatively expensive or may not be available, in addition to sufficient training it needs a huge number of data points that increases network complexity, and it is time consuming especially for partial shading condition (PSC). Also, enlarged optimization scope for the size and hidden number of layers and retraining due to system ageing is required as a result of PV characteristics change. For example, Punitha et al. combined ANN with IncCond to track the GP efficiently compared to P&O and FLC-based HC [84], while Jiang et al. combined ANN with P&O where ANN is used to predict GP searching area and P&O to track the GP. The findings revealed that the proposed hybrid MPPT can track the GP more efficiently and accurately compared to P&O, Fibonacci search, conventional PSO and DE [85]. Also, Loubna et al. proved that ANN with a scanning and storing algorithm has better performance than variable P&O with global scanning and IncCond based on FLC [86]. Finally, Karatepe et al. proposed ANN-integrated FLC with polar information controller to track the unique peak under uniform condition and the GP under PSCs. The ANN is trained once for several PSCs to determine the global voltage (VGP). The FLC uses VGP as a

Table 8 Recent comparative studies of ANN with other MPPT techniques

References	Variable control	DC–DC converter	Findings
[81]	Duty cycle	Flyback converter	Simulation and experimental findings reveal that variable-step-size ANN performed well in terms of tracking accuracy, response time, overshoot and ripple compared to the fixed-step-size ANN that has the same disadvantages of P&O technique related to tracking speed and oscillations around steady state
[88]	Duty cycle	Boost	ANN is used directly to track the GP, while the P&O technique is used only to refine the result. The prediction accuracy depends on the preselected number of power measurements, the ANN size and prior information
[86]	Duty cycle	Boost	ANN with a scanning and storing algorithm has good performance in terms of tracking speed, response time and efficiency compared to variable P&O with global scanning and IncCond based on FLC
[85]	Duty cycle	Buck–boost	Two implementations of ANN are combined with P&O where ANN is used to predict the GP search area and P&O is used to track the GP. The proposed hybrid MPPT can track the GP efficiently and accurately in terms of tracking speed and convergence speed compared to P&O, Fibonacci search, conventional PSO and DE
[84]	V_{MPP}	Buck	The proposed ANN combined with IncCond can track the GP efficiently compared to P&O and FLC-based HC in terms of tracking speed and convergence speed. An ANN is used to provide V_{ref} to the modified IncCond
[87]	Duty cycle	Boost	ANN is combined with FLC where the former is used to track the GP under several PSCs with SP, BL and TCT configurations

reference voltage to adjust the duty cycle of the boost converter [87]. The advantages and disadvantages of ANN-based MPPT are listed in Table 9.

Table 9 Advantages and disadvantages of ANN-based MPPT technique

References	Advantages	Disadvantages
[49, 51, 76–78, 89]	<ul style="list-style-type: none"> • Fast tracking speed, acceptable accurateness • Effective, less oscillations in conditions variation and good efficiency • Can be trained offline and used in the online environment 	<ul style="list-style-type: none"> • High complexity and expensive • Requires extensive information about the PV parameters • Additional cost of temperature and irradiance sensors

3.2.3 Adaptive Neuro-Fuzzy Inference System Technique

Adaptive neuro-fuzzy inference system (ANFIS) is one of the most efficient AI-based MPPT that uses ANN for internal data training and FLC for external data. Hence, it has the advantages of both techniques. The inputs of ANN are error (E_{rr}) and error change (ΔE_{rr}), and the ANN output will be the input to FLC. The FLC provides the optimal duty cycle of the DC–DC converter to track the GP [90]. It is difficult to obtain the membership functions and fuzzy rules using trial and error, so the ANN part in ANFIS reduces the error and optimizes the parameters, whereas FLC has the ability to work with imprecise inputs and good efficiency in addition to accurate mathematical model and detailed information of the system are not required [44, 91].

Based on recent comparative studies of ANFIS-based MPPT given in Table 10, it can be observed that ANFIS can extract the maximum power efficiently and accurately regardless of whether PSC occurs or not. Radianto et al. proved that ANFIS can extract the GP of the TCT configuration through adjusting the duty cycle of the boost converter [92]. This is supported by Faiza et al. which revealed that ANFIS can track the GP efficiently and accurately under various configurations such as HC, BL, TCT and SP. In addition, the highest maximum power has been achieved with TCT configuration [91]. The advantages and disadvantages of ANFIS MPPT technique are given in Table 11.

3.2.4 Differential Evolution and Genetic Algorithm

Differential evolution (DE) is one of the most powerful stochastic, optimization-based evolutionary algorithms (EA) which is similar to GA. However, unlike GA which relies on crossover, DE on the other hand relies on mutation (difference vector) to convert the operating point towards the best solution in a search area [95]. It also depends on the generation of initial random population similar to the other EA where it refines and improves the further candidate solutions using selection, mutation and crossover. On the other hand, GA depends on the survival of the fittest through the first generation of initial random population. Then, an objective function is defined to determine the fitness of each solution, followed by evaluating the fitness of each

Table 10 Recent comparative studies of ANFIS with other MPPT techniques

References	Variable control	DC–DC converter	Findings
[44]	Duty cycle	Boost	Firstly, ANFIS has better tracking efficiency than FLC and ANN techniques. Secondly, IncCond has superior performance compared to P&O and CV in terms of tracking efficiency, rise time, fall time and dynamic response. Finally, Neural FL has better efficiency than other conventional and hybrid MPPT techniques
[93]	Duty cycle	Buck	Design and implementation of the proposed ANFIS, CV and IncCond using Altera EP4CE6E22C8N FPGA card. The findings reveal that ANFIS is more efficient and has better dynamic response followed by IncCond and finally CV
[91]	Duty cycle	Boost	ANFIS can track the GP efficiently and accurately under various PSCs and different configurations such as HC, BL, TCT and SP. TCT has the best performance with the highest maximum power
[94]	Duty cycle	Boost	ANFIS can track the unique MPP quickly and efficiently under dynamic and steady-state conditions
[92]	Duty cycle	Boost	ANFIS is used to extract the GP of the TCT configuration through adjusting the duty cycle of the boost converter

Table 11 Advantages and disadvantages of ANFIS-based MPPT techniques

References	Advantages	Disadvantages
[44, 91]	<ul style="list-style-type: none"> • Higher efficiency under PSCs, faster tracking speed and robustness • Collective advantages of both FL and ANN • Simple and does not require too much computing or mathematical equations • The ANN part in ANFIS reduces the error and optimizes the parameters 	<ul style="list-style-type: none"> • High complexity and expensive • Difficult to obtain membership functions and rules • More sensors are required • Insufficient training on the PV array leads to less accuracy

Table 12 Recent comparative studies of DE and GA with other MPPT techniques

References	Variable control	DC–DC converter	Application	Findings
[96]	Duty cycle	Buck–boost	Stand-alone PV	Modified DE outperforms classic PSO in tracking the GP under PSC in terms of accuracy, tracking speed, convergence speed and efficiency. Classic PSO may trap at LP for some PSCs
[97]	Duty cycle	Buck–boost	Grid-connected	DE is proposed to study its effectiveness in handling PSCs (variable GP). It outperforms the HC in terms of convergence speed, tracking speed and accuracy. Also, no oscillation around MPP occurs during dynamic and steady states
[98]	Duty cycle	Boost	Stand-alone PV	Jaya DE can track the GP accurately and quickly where it outperforms the state-of-the-art improved P&O with ACO (ACOPPO), PSO and FPA techniques in terms of tracking speed, convergence speed and accuracy under dynamic and steady states
[72]	Duty cycle	Buck–boost	Stand-alone	GA and PSO outperform PID, FLC and ANN, in terms of performance and implementation cost (sensors type, circuit type and software complexity). Both GA and PSO provide a good GP tracking and show very good performance, but design and hardware implementation of GA is more difficult and complex than PSO
[99]	Duty cycle	Boost	Stand-alone PV	GA succeeds in tracking the GP under PSCs compared to P&O and IncCond which fail to detect GP and track the first MPP whether it is GP or LP
[100]	Duty cycle	Boost	Stand-alone PV	Both GA and the binary search method can track the GP in all PSCs efficiently and accurately with error percentage less than 2%

(continued)

Table 12 (continued)

References	Variable control	DC–DC converter	Application	Findings
[101]	Duty cycle	Buck	Grid-connected	GA is integrated with P&O. The GA parameters (population size and number of iterations) are decreased, thus catching the GP in a shorter time
[102]	Duty cycle	Boost	Stand-alone PV	GA combined with FLC improves the performance and efficiency of FLC where GA can optimize the FLC membership functions and rules. It has better performance in terms of tracking speed, response time, efficiency and robustness

individual and finally creating a new population using genetic operators (selection, crossover and mutation) [72].

Based on recent comparative studies of DE and GA with other MPPT techniques introduced in Table 12, although DE already has acceptable performance to track GP under PSCs, further modifications and improvements on DE have been done by Ramli et al. [96] which shows that DE is more efficient in tracking the GP under PSC compared to classic PSO in terms of accuracy, tracking speed, convergence speed and efficiency where classic PSO may trap at LP for some PSCs. The proposed MPPT technique given in [96] has three main merits that are (1) no random numbers are used, (2) only one tuning parameter is required (mutation factor) and (3) implementation simplicity [96]. In addition, a modified DE proposed by Tajuddin et al. outperformed the HC when tracking the GP in terms of convergence speed, tracking speed and accuracy. In addition, oscillation around MPP did not occur during dynamic and steady-state conditions [97]. Finally, Kumar et al. proposed that Jaya DE that can track the GP more accurately and quickly compared to the state-of-the-art improved P&O with ACO (ACOPO), PSO and FPA techniques in terms of tracking speed, convergence speed and accuracy under dynamic and steady-state conditions [98].

On the other hand, GA also has the ability to track the GP under PSC where the comparative study achieved by Yousra et al. revealed that GA can track the GP under PSC compared to conventional techniques (P&O and IncCond) which fail to detect GP and track the first MPP notwithstanding whether it is GP or LP [99]. In addition, Ramaprabha et al. proved that both GA and the binary search method can track the GP for all PSCs efficiently and accurately [100]. Also, a comparative study done by Kermadi et al. revealed that both GA and PSO track the GP with good performance and less implementation cost, whereas design and implementation of GA is more difficult and complex than PSO [72]. On the other hand, many researchers proposed that GA should be combined and optimized with other MPPT techniques because GA may fall in one of the LPs in some cases of PSCs. For example, GA is optimized

Table 13 Advantages and disadvantages of DE- and GA-based MPPT techniques

References	Tech.	Advantages	Disadvantages
[76, 96]	DE	<ul style="list-style-type: none"> • Simple and straightforward • Rapid convergence • Capable of tracking the GP regardless of the initial parameter values • Few control parameters required 	<ul style="list-style-type: none"> • Slow convergence to the GP • Limited local search ability
[49, 51, 77, 103]	GA	<ul style="list-style-type: none"> • High speed, accuracy and good efficiency • Possible wide search • Applicable to fast change in atmospheric conditions 	<ul style="list-style-type: none"> • High complexity and expensive • Much computation process • High memory needed • More time consumed

and combined with P&O to improve the performance and efficiency of the former in handling and catching the GP under PSC, where GA parameters are decreased and the GP tracked in a shorter time [101]. Also, GA combined with FLC can improve the performance and efficiency of FLC where GA can obtain the best subsets of the membership functions. Optimized FLC has better performance in terms of tracking speed, response time and efficiency in addition to robustness than FLC alone [102]. Finally, the advantages and disadvantages of DE- and GA-based MPPT techniques are given in Table 13.

4 Grid-Connected PV Energy System (Case Study)

Photovoltaic (PV) or solar cell systems were initially fabricated for use in the 1950s and were used primarily to power satellites in space from solar power. In the 1970s, PV systems began to be used for terrestrial applications to provide power for remote and grid-connected applications. Today, the use of grid-connected PV systems is becoming increasingly popular, particularly as the USA and countries around the world push for higher utilization of renewable energy sources. However, the grid can become more unpredictable as the penetration of variable power sources, like solar, increases. In order to overcome potential instability issues, recent research has begun to focus on making the grid a more intelligent system, where power sources and loads can communicate and adaptively react to needs of the surrounding system. One important aspect of enabling a more intelligent grid is the ability for renewable energy sources to monitor their own condition so that they can provide diagnostic information to the rest of the grid [104].

The PV energy system is interconnected to the utility grid through DC–DC boost converter and PWM converter as shown in Fig. 11. The boost converter is used to track the MPP available from PV system, and the PWM converter is used to convert DC voltage to AC voltage to be connected with electric utility. The control system

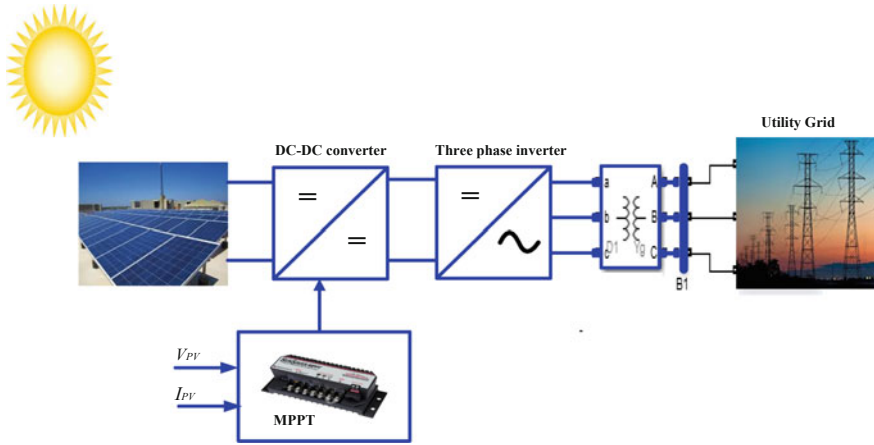


Fig. 11 PV energy system interconnected to the utility grid

has two controllers: the first one is used for PV MPPT through controlling the duty ratio of the boost converter using FLC and P&O techniques for comparison validity. On the other hand, the other one (grid-side controller) is used to control active and reactive power output from the system through controlling d -axis and q -axis current components, respectively. For the purpose of achieving the accurate comparisons and the performance assessment purposes of MPPT techniques, the same PV energy system and same environmental conditions are used for the two MPPT techniques. The main objective of this work is to introduce the FLC as MPPT for utility-grid-integrated PV energy systems and compare its performance with P&O technique in same operating conditions.

The whole PV energy system is simulated in Simulink. The simulation model consists of PV array with a peak power of 100 kW connected through boost converter to a three-phase inverter that is connected to an ideal 380-V utility grid through a filter, as shown in Fig. 11. The PV array consists of strings of PV modules connected in parallel, N_p . Each string consists of modules connected in series, N_s . The PV array consists of 66 parallel strings and 5 series-connected modules per string. The inputs to the PV array are sun irradiance (W/m^2) and cell temperature ($^{\circ}\text{C}$). The main characteristic of the module used (SunPower SPR-305E-WHT-D) is given in Table 14, and the P–V characteristics of the PV array are shown in Fig. 12. The maximum power is extracted using two efficient techniques which are P&O and FLC. The explanation of the operation idea and how each technique modelled in Simulink are introduced in the previous sections.

The boost converter (shown in Fig. 11) is controlled to track the MPP by controlling the output voltage of PV array, $V_{d,\text{in}}$ by varying the duty ratio D in response to variations in $V_{d,\text{in}}$. The relation between the boost converter input and output voltage is shown as follows [10, 105]:

Table 14 Characteristics of SunPower SPR-305E-WHT-DPV module

Maximum power (P_{\max})	305.2 W
Cells per module	96
Open-circuit voltage (V_{OC})	64.2 V
Short-circuit current (I_{sc})	5.96 A
Voltage at maximum power point (V_{MPP})	54.7 V
Current at maximum power point (I_{MPP})	5.58 A

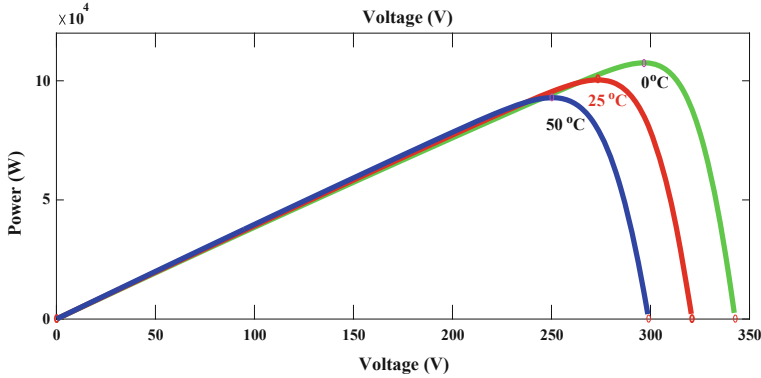


Fig. 12 P–V characteristics of PV array under study

$$\frac{V_{d,out}}{V_{d,in}} = \frac{1}{(1 - D)} \quad (11)$$

where $V_{d,out}$ is the output DC voltage and D is the duty ratio of boost converter. The previous equation shows that the duty ratio D is inversely proportional to $V_{d,in}$ at constant $V_{d,out}$ and directly proportional $V_{d,out}$ at constant $V_{d,in}$.

The three-phase PWM converter circuit consists of three legs, one for each phase, as shown in Fig. 11. The objective of the three-phase PWM converter is to shape and control the three-phase output voltages in magnitude and frequency (Fixed Voltage Fixed Frequency, FVFF) with an essentially constant input voltage for utility-grid-connected availability. Also, PWM inverter is used to help MPPT technique by ensuring the DC voltage will remain constant in all operating conditions. The modulation index m_a of the three-phase PWM converter is obtained as follows [106, 107]:

$$m_a = \frac{\hat{V}_{control}}{\hat{V}_{tri}} = \frac{\hat{V}_{LLC}}{V_{d,out}} \quad (12)$$

where $\hat{V}_{control}$ is peak value of the control signal and \hat{V}_{tri} is peak value of the triangular signal.

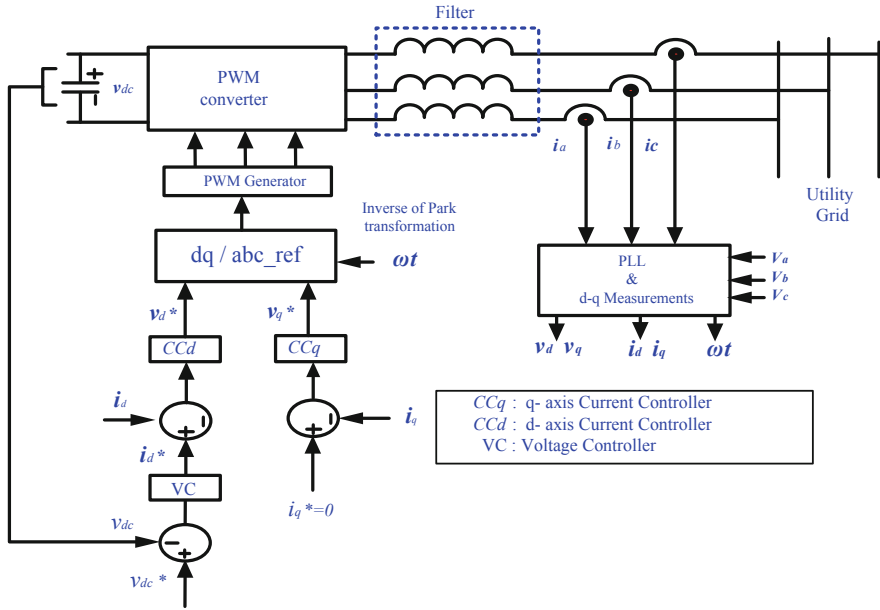


Fig. 13 Control scheme of the three-phase grid-side converter

4.1 Active and Reactive Output Power Control

The control of the grid-side inverter contains two control loops for controlling the active and reactive output power. The two control loops are the inner and outer control loops. The dc-link voltage is controlled to become constant using the outer loop. The reactive power is controlled by setting the q -axis current reference to zero value for unity power factor using the inner loop. As shown in Fig. 13, there are two current controllers for direct, I_d , and quadrature, I_q , components of inverter output current. Also, phase-locked loop (PLL) as grid synchronization technique is used to synchronize the control system with the phase angle of the grid utility.

The active and reactive power, P_s and Q_s , respectively, can be defined as follows [3, 108–110]:

$$P_s = \frac{3}{2} v_d i_d \quad (13)$$

$$Q_s = \frac{3}{2} v_d i_q \quad (14)$$

So, active and reactive power control is achieved through controlling the q -axis and d -axis grid current components, respectively.

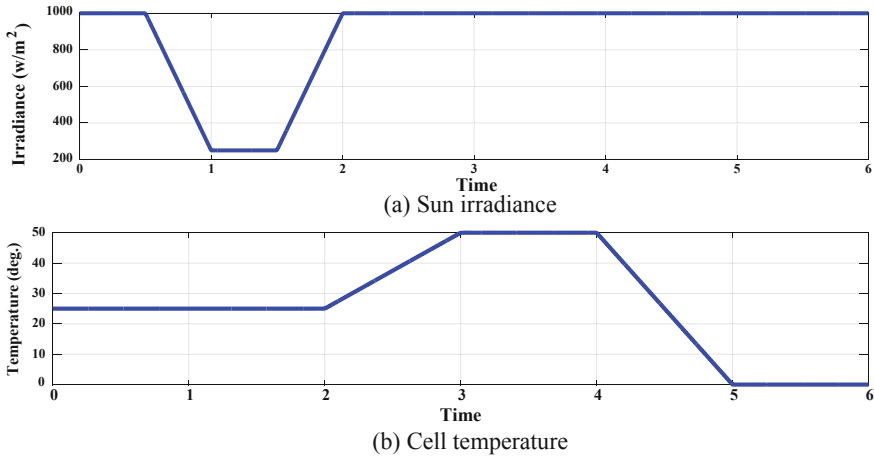


Fig. 14 Sun irradiance and cell temperature change

4.2 Simulation Results and Discussions

The whole PV energy system shown previously in Fig. 11 is simulated using Simulink. It consists of a 100-kW solar PV array, a DC–DC boost converter operating at switching frequency of 20 kHz, an input inductance of 5 mH, output capacitor of 24 mF and three-phase voltage source PWM converter connected to 380-V utility grid. Figure 14 shows the solar irradiance and cell temperature used in simulation as inputs to the PV array. The maximum power, solar irradiance and cell temperature are taken from the characteristics of the installed PV array provided by the manufacturer (SunPower SPR-305E-WHT-D).

The whole PV energy system control in Simulink includes the MPPT controller and the grid-side controller. The PV is directly controlled by the P&O or FLC to track the maximum power available by controlling duty ratio of the DC–DC boost converter. Figure 15 shows the output power available and the PV voltage for both the two proposed efficient P&O and FLC techniques. At certain irradiance and temperature, the PV output power and voltage are estimated and these values agree with the P–V curve shown previously in Fig. 12. Also, it introduces the controlled duty ratio of the DC–DC boost converter provided by the two efficient techniques to track the MPP. The P&O and FLC are used to control the duty ratio which tracks the maximum power point at variable irradiance and temperature. It is clear from Fig. 15 that the FLC has better performance, accuracy and flexibility compared to P&O in both dynamic and steady-state response. Also, the FLC has better performance for the maximum power compared to P&O based on efficiency and tracking speed. Also, it can be observed that oscillation around maximum power is limited with FLC compared to other state-of-the-art technique.

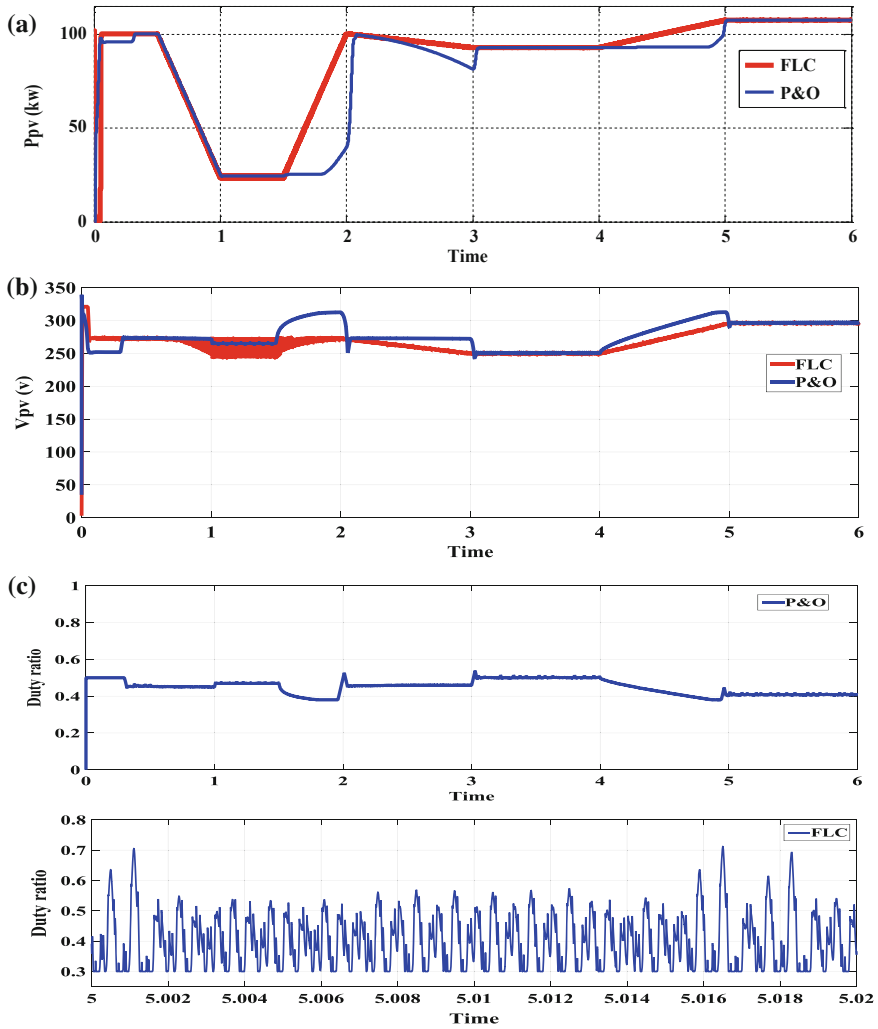


Fig. 15 PV array: **a** output power, **b** output voltage and **c** duty ratio

It can be noticed from Fig. 16 that the grid-side controller is responsible for maintaining the dc-link voltage constant at 500 V. The dc-link voltage is controlled by exporting active power to the grid as shown in Fig. 16c. The reactive power of the grid has been controlled to be zero as shown in Fig. 16d. The results obtained from Fig. 16 show that the control system especially FLC is working effectively and quickly in tracking the maximum power and the grid-side controller accurately controls the active and reactive power through the i_d and i_q , respectively.

The output power is regulated in order to keep dc-link voltage constant approximately. By applying the inverse Park transformation to d - q voltage vector compo-

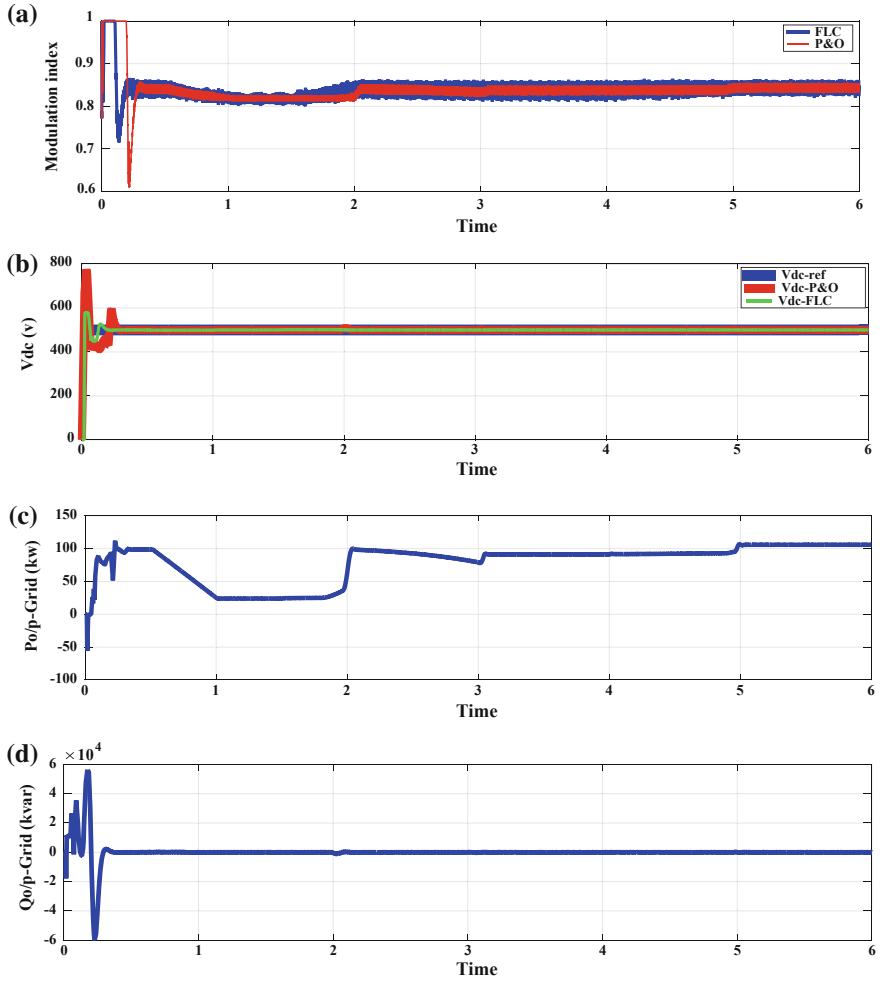


Fig. 16 Different simulation waveforms: **a** m_a , **b** dc-link voltage using P&O and FLC, **c** active power (kw) and **d** reactive power (kVar)

nents, the desired U_{abc}^* voltage references are obtained. These are passed to a PWM generator for generating the pulses to drive the inverter switches. The output voltage of the inverter and grid is shown in Fig. 17.

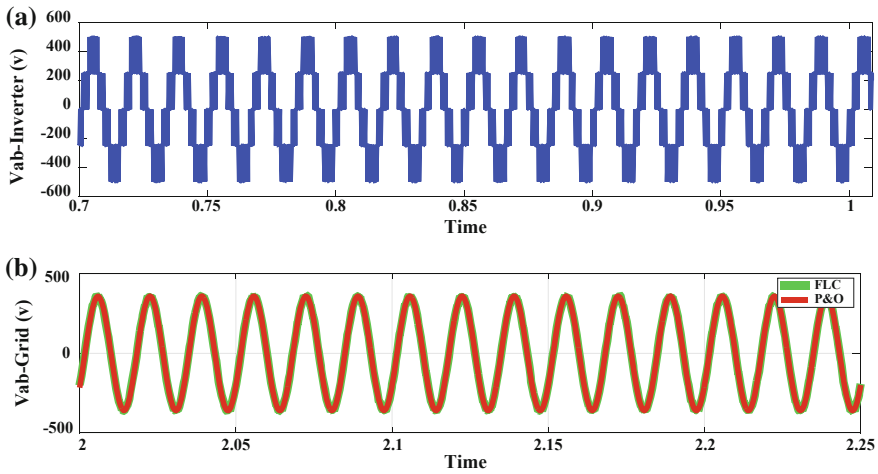


Fig. 17 Output voltage: **a** V_{ab} —Inverter, **b** V_{ab} —Grid

5 Conclusions

This chapter discusses the PV characteristics, performance, modelling and grid inter-connection. It covers four different PV generator models with their characteristics and performance analysis. Also, the four most famous conventional MPPT techniques with some of the soft computing MPPT techniques are discussed including detailed comparisons and discussion with the limitations, merits and demerits of these MPPT techniques. A grid-connected PV energy system is proposed in this chapter as a case study where the whole system is simulated in Simulink. The PV array is connected to the grid through the DC–DC boost converter and three-phase converter. The maximum power extracted from the PV is achieved using FLC technique and compared to P&O technique. The FLC is more efficient and quick in response for the MPPT than P&O. Also, the oscillation around maximum power is limited with FLC. On the other hand, the main function of the grid-side controller is to separately control the active and reactive power via two control loops which are the inner current control loop and the outer dc-link voltage control loop. The outer dc-link voltage control loop maintains a constant voltage on the dc-link capacitor for active power control, while the inner control loop is used to control the reactive power by setting the q -axis current reference to zero value for unity power factor. The simulation results prove the superiority of FLC compared to the other state-of-the-art technique. Also, the simulation results prove the robust control of dc-link voltage, active power and reactive power transmitted to the utility grid.

References

1. Wang F (2014) Photovoltaic system deployment optimization. University of Delaware
2. Eltamaly AM (2015) Performance of smart maximum power point tracker under partial shading conditions of PV systems. In: 2015 IEEE international conference on smart energy grid engineering (SEGE). IEEE, pp 1–8
3. Farh HM, Eltamaly AM (2013) Fuzzy logic control of wind energy conversion system. *J Renew Sustain Energy* 5(2):023125
4. Mohamed MA, Eltamaly AM, Farh HM, Alolah AI (2015) Energy management and renewable energy integration in smart grid system. In: 2015 IEEE international conference on Smart energy grid engineering (SEGE). IEEE, pp 1–6
5. Soon JJ, Low K-S, Goh ST (2014) Multi-dimension diode photovoltaic (PV) model for different PV cell technologies. In: 2014 IEEE 23rd international symposium on Industrial electronics (ISIE). IEEE, pp 2496–2501
6. Ishaque K, Salam Z, Taheri H (2011) Simple, fast and accurate two-diode model for photovoltaic modules. *Sol Energy Mater Sol Cells* 95(2):586–594
7. Nishioka K, Sakitani N, Uraoka Y, Fuyuki T (2007) Analysis of multicrystalline silicon solar cells by modified 3-diode equivalent circuit model taking leakage current through periphery into consideration. *Sol Energy Mater Sol Cells* 91(13):1222–1227
8. Rezk H, Eltamaly AM (2015) A comprehensive comparison of different MPPT techniques for photovoltaic systems. *Solar energy* 112:1–11
9. Eltamaly AM, Farh HM, Othman MF (2018) A novel evaluation index for the photovoltaic maximum power point tracker techniques. *Solar Energy* 174:940–956
10. Eltamaly AM (2015) Performance of smart maximum power point tracker under partial shading conditions of photovoltaic systems. *J Renew Sustain Energy* 7(4):043141
11. Eltamaly AM (2018) Performance of MPPT techniques of photovoltaic systems under normal and partial shading conditions. In: *Advances in renewable energies and power technologies*, Elsevier, pp 115–161
12. Farh H, Othman M, Eltamaly AM, Al-Saud M (2018) Maximum power extraction from a partially shaded PV system using an interleaved boost converter. *Energies* 11(10):2543
13. Eltamaly AM, Hassan MHF (2019) Dynamic global maximum power point tracking of the PV systems under variant partial shading using hybrid GWO-FLC. *Solar Energy* 177:306–316
14. Farh HM, Eltamaly A, Al-Saud M (2019) Interleaved boost converter for global maximum power extraction from the photovoltaic system under partial shading. *IET Renew Power Gener*
15. soufyane Benyoucef A, Chouder A, Kara K, Silvestre S (2015) Artificial bee colony based algorithm for maximum power point tracking (MPPT) for PV systems operating under partial shaded conditions. *Appl Soft Comput* 32:38–48
16. Sundareswaran K, Sankar P, Nayak P, Simon SP, Palani S (2015) Enhanced energy output from a PV system under partial shaded conditions through artificial bee colony. *IEEE Trans Sustain Energy* 6(1):198–209
17. Sundareswaran K, Peddapati S, Palani S (2014) MPPT of PV systems under partial shaded conditions through a colony of flashing fireflies. *IEEE Trans Energy Convers* 29(2):463–472
18. Teshome D, Lee C, Lin Y, Lian K (2017) A modified firefly algorithm for photovoltaic maximum power point tracking control under partial shading. *IEEE J Emerg Sel Top Power Electron* 5(2):661–671
19. Jiang LL, Maskell DL, Patra JC (2013) A novel ant colony optimization-based maximum power point tracking for photovoltaic systems under partially shaded conditions. *Energy Build* 58:227–236
20. Farh HM, Eltamaly A, Al-Saud M (2019) A novel GPA assessment for meta-heuristic global maximum power tracker techniques of partial shaded photovoltaic systems. *IET Renew Power Gener*
21. Chao K-H, Lin Y-S, Lai U-D (2015) Improved particle swarm optimization for maximum power point tracking in photovoltaic module arrays. *Appl Energy* 158:609–618

22. Ishaque K, Salam Z, Shamsudin A, Amjad M (2012) A direct control based maximum power point tracking method for photovoltaic system under partial shading conditions using particle swarm optimization algorithm. *Appl Energy* 99(Suppl C):414–422
23. Rajasekar N et al (2014) Application of modified particle swarm optimization for maximum power point tracking under partial shading condition. *Energy Procedia* 61:2633–2639
24. Babu TS, Rajasekar N, Sangeetha K (2015) Modified particle swarm optimization technique based maximum power point tracking for uniform and under partial shading condition. *Appl Soft Comput* 34:613–624
25. Dileep G, Singh S (2017) An improved particle swarm optimization based maximum power point tracking algorithm for PV system operating under partial shading conditions. *Sol Energy* 158:1006–1015
26. Wu Z, Yu D (2018) Application of improved bat algorithm for solar PV maximum power point tracking under partially shaded condition. *Appl Soft Comput* 62:101–109
27. Huang C, Wang L, Yeung RS-C, Zhang Z, Chung HS-H, Bensoussan A (2018) A prediction model-guided Jaya algorithm for the PV system maximum power point tracking. *IEEE Trans Sustain Energy* 9(1):45–55
28. Cristea M, Chiritoiu V, Costache M, Zaharie I, Luminosu I (2010) On a model of the typical cell from a solar panel. In: *AIP Conference Proceedings*, vol 1203, no 1. AIP, pp 433–438
29. Celik AN, Acikgoz N (2007) Modelling and experimental verification of the operating current of mono-crystalline photovoltaic modules using four-and five-parameter models. *Appl Energy* 84(1):1–15
30. MacAlpine SM (2014) Characterization and capture of photovoltaic system losses due to nonuniform conditions. University of Colorado at Boulder
31. Hejri M, Mokhtari H, Azizian MR, Ghandhari M, Soder L (2014) On the parameter extraction of a five-parameter double-diode model of photovoltaic cells and modules. *IEEE J Photovolt* 4(3):915–923
32. Bikaneria J, Joshi SP (2014) Modelling and simulation of PV cell based on two-diode model. *Int J Recent Trends Eng Technol* 11(1):589
33. Shannan NM, Yahaya NZ, Singh B (2014) Two diode model for parameters extraction of PV module. In: *2014 IEEE conference on energy conversion (CENCON)*. IEEE, pp 260–264
34. Kratochvil JA, Boyson WE, King DL (2004) Photovoltaic array performance model. Sandia National Laboratories
35. Fanney AH, Dougherty BP, Davis MW (2009) Comparison of predicted to measured photovoltaic module performance. *J Sol Energy Eng* 131(2):021011
36. Cameron CP, Boyson WE, Riley DM (2008) Comparison of PV system performance-model predictions with measured PV system performance. In: *33rd IEEE photovoltaic specialists conference, PVSC'08*. IEEE, pp 1–6
37. Hansen C (2013) Estimation of parameters for single diode models from measured IV curves. Sandia National Laboratories
38. De Soto W, Klein S, Beckman W (2006) Improvement and validation of a model for photovoltaic array performance. *Sol Energy* 80(1):78–88
39. Xia Q (2012) Solar photovoltaic system modeling and control
40. Ishaque K, Salam Z, Lauss G (2014) The performance of perturb and observe and incremental conductance maximum power point tracking method under dynamic weather conditions. *Appl Energy* 119:228–236
41. Jeddi N, Ouni LEA (2014) Comparative study of MPPT techniques for PV control systems. In: *2014 international conference on electrical sciences and technologies in Maghreb (CISTEM)*. IEEE, pp 1–7
42. Tofoli FL, de Castro Pereira D, de Paula WJ (2015) Comparative study of maximum power point tracking techniques for photovoltaic systems. *Int J Photoenergy* 2015
43. Cavalcanti M, Oliveira K, Azevedo G, Neves F (2007) Comparative study of maximum power point tracking techniques for photovoltaic systems. *Eletrônica de Potência* 12(2):163–171
44. Gupta A, Chauhan YK, Pachauri RK (2016) A comparative investigation of maximum power point tracking methods for solar PV system. *Sol Energy* 136:236–253

45. Zainudin HN, Mekhilef S (2010) Comparison study of maximum power point tracker techniques for PV systems
46. Houssamo I, Locment F, Sechilariu M (2010) Maximum power tracking for photovoltaic power system: development and experimental comparison of two algorithms. *Renew Energy* 35(10):2381–2387
47. Hohm D, Ropp ME (2003) Comparative study of maximum power point tracking algorithms. *Prog Photovoltaics Res Appl* 11(1):47–62
48. Faranda R, Leva S (2008) A comparative study of MPPT techniques for PV Systems. In: 7th WSEAS international conference on application of electrical engineering (AEE'08), Trondheim, Norway
49. Danandeh M, Mousavi GS (2017) Comparative and comprehensive review of maximum power point tracking methods for PV cells. *Renew Sustain Energy Rev*
50. Kalashani MB, Farsadi M (2014) New structure for photovoltaic systems with maximum power point tracking ability. *Int J Power Electron Drive Syst (IJPEDS)* 4(4):489–498
51. Nabipour M, Razaz M, Seifossadat SG, Mortazavi S (2017) A new MPPT scheme based on a novel fuzzy approach. *Renew Sustain Energy Rev* 74:1147–1169
52. Bendib B, Belmili H, Krim F (2015) A survey of the most used MPPT methods: conventional and advanced algorithms applied for photovoltaic systems. *Renew Sustain Energy Rev* 45:637–648
53. Shimizu T, Hashimoto O, Kimura G (2003) A novel high-performance utility-interactive photovoltaic inverter system. *IEEE Trans Power Electron* 18(2):704–711
54. Koutroulis E, Kalaitzakis K, Voulgaris NC (2001) Development of a microcontroller-based, photovoltaic maximum power point tracking control system. *IEEE Trans Power Electron* 16(1):46–54
55. Xiao W, Dunford WG (2004) A modified adaptive hill climbing MPPT method for photovoltaic power systems. In: 2004 IEEE 35th annual power electronics specialists conference, PESC 04, vol 3. IEEE, pp 1957–1963
56. Veerachary M, Senjyu T, Uezato K (2001) Maximum power point tracking control of IDB converter supplied PV system. *IEE Proc-Electr Power Appl* 148(6):494–502
57. Verma D, Nema S, Shandilya A, Dash SK (2016) Maximum power point tracking (MPPT) techniques: recapitulation in solar photovoltaic systems. *Renew Sustain Energy Rev* 54:1018–1034
58. Eltawil MA, Zhao Z (2013) MPPT techniques for photovoltaic applications. *Renew Sustain Energy Rev* 25:793–813
59. Farh HM, Eltamaly AM, Othman MF (2018) Hybrid PSO-FLC for dynamic global peak extraction of the partially shaded photovoltaic system. *PLoS one* 13(11):e0206171
60. Ansari MF, Chatterji S, Iqbal A (2010) A fuzzy logic control scheme for a solar photovoltaic system for a maximum power point tracker. *Int J Sustain Energ* 29(4):245–255
61. Azzouzi M (2012) Comparaison between MPPT P&O and MPPT fuzzy controls in optimizing the photovoltaic generator. *Int J Adv Comput Sci Appl* 3(12):57–62
62. Chekired F, Mellit A, Kalogirou S, Larbes C (2014) Intelligent maximum power point trackers for photovoltaic applications using FPGA chip: a comparative study. *Sol Energy* 101:83–99
63. Mahamudul H, Saad M, Ibrahim Henk M (2013) Photovoltaic system modeling with fuzzy logic based maximum power point tracking algorithm. *Int J Photoenergy* 2013
64. Kamarzaman NA, Tan CW (2014) A comprehensive review of maximum power point tracking algorithms for photovoltaic systems. *Renew Sustain Energy Rev* 37:585–598
65. Messai A, Mellit A, Guessoum A, Kalogirou S (2011) Maximum power point tracking using a GA optimized fuzzy logic controller and its FPGA implementation. *Sol Energy* 85(2):265–277
66. Bendib B, Krim F, Belmili H, Almi M, Boulouma S (2014) Advanced fuzzy MPPT controller for a stand-alone PV system. *Energy Procedia* 50:383–392
67. El Khateb AH, Rahim NA, Selvaraj J (2013) Fuzzy logic control approach of a maximum power point employing SEPIC converter for standalone photovoltaic system. *Procedia Environ Sci* 17:529–536

68. Kwan TH, Wu X (2016) Maximum power point tracking using a variable antecedent fuzzy logic controller. *Sol Energy* 137:189–200
69. Guenounou O, Dahhou B, Chabour F (2014) Adaptive fuzzy controller based MPPT for photovoltaic systems. *Energy Convers Manag* 78:843–850
70. Boukenoui R, Salhi H, Bradai R, Mellit A (2016) A new intelligent MPPT method for stand-alone photovoltaic systems operating under fast transient variations of shading patterns. *Sol Energy* 124:124–142
71. Chen Y-T, Jhang Y-C, Liang R-H (2016) A fuzzy-logic based auto-scaling variable step-size MPPT method for PV systems. *Sol Energy* 126:53–63
72. Kermadi M, Berkouk EM (2017) Artificial intelligence-based maximum power point tracking controllers for Photovoltaic systems: comparative study. *Renew Sustain Energy Rev* 69:369–386
73. Gounden NA, Peter SA, Nallandula H, Krithiga S (2009) Fuzzy logic controller with MPPT using line-commutated inverter for three-phase grid-connected photovoltaic systems. *Renew Energy* 34(3):909–915
74. Bounechba H, Bouzid A, Nabti K, Benalla H (2014) Comparison of perturb & observe and fuzzy logic in maximum power point tracker for PV systems. *Energy Procedia* 50:677–684
75. Chiu C-S (2010) TS fuzzy maximum power point tracking control of solar power generation systems. *IEEE Trans Energy Convers* 25(4):1123–1132
76. Seyedmahmoudian M et al (2016) State of the art artificial intelligence-based MPPT techniques for mitigating partial shading effects on PV systems—a review. *Renew Sustain Energy Rev* 64:435–455
77. Ram JP, Babu TS, Rajasekar N (2017) A comprehensive review on solar PV maximum power point tracking techniques. *Renew Sustain Energy Rev* 67:826–847
78. Kandemir E, Cetin NS, Borekci S (2017) A comprehensive overview of maximum power extraction methods for PV systems. *Renew Sustain Energy Rev* 78:93–112
79. Ishaque K, Salam Z (2013) A review of maximum power point tracking techniques of PV system for uniform insolation and partial shading condition. *Renew Sustain Energy Rev* 19:475–488
80. Rai AK, Kaushika N, Singh B, Agarwal N (2011) Simulation model of ANN based maximum power point tracking controller for solar PV system. *Sol Energy Mater Sol Cells* 95(2):773–778
81. Messalti S, Harrag A, Loukriz A (2017) A new variable step size neural networks MPPT controller: review, simulation and hardware implementation. *Renew Sustain Energy Rev* 68:221–233
82. Laudani A, Fulginei FR, Salvini A, Lozito G, Mancilla-David F (2014) Implementation of a neural MPPT algorithm on a low-cost 8-bit microcontroller. In: 2014 international symposium on power electronics, electrical drives, automation and motion (SPEEDAM). IEEE, pp 977–981
83. Mancilla-David F, Riganti-Fulginei F, Laudani A, Salvini A (2014) A neural network-based low-cost solar irradiance sensor. *IEEE Trans Instrum Meas* 63(3):583–591
84. Punitha K, Devaraj D, Sakthivel S (2013) Artificial neural network based modified incremental conductance algorithm for maximum power point tracking in photovoltaic system under partial shading conditions. *Energy* 62:330–340
85. Jiang LL, Nayanassiri D, Maskell DL, Vilathgamuwa D (2015) A hybrid maximum power point tracking for partially shaded photovoltaic systems in the tropics. *Renew Energy* 76:53–65
86. Bouselham L, Hajji M, Hajji B, Bouali H (2017) A New MPPT-based ANN for photovoltaic system under partial shading conditions. *Energy Procedia* 111:924–933
87. Karatepe E, Hiyama T (2009) Artificial neural network-polar coordinated fuzzy controller based maximum power point tracking control under partially shaded conditions. *IET Renew Power Gener* 3(2):239–253
88. Rizzo SA, Scelba G (2015) ANN based MPPT method for rapidly variable shading conditions. *Appl Energy* 145:124–132

89. Anh HPH (2014) Implementation of supervisory controller for solar PV microgrid system using adaptive neural model. *Int J Electr Power Energy Syst* 63:1023–1029
90. Saravanan S, Babu NR (2016) Maximum power point tracking algorithms for photovoltaic system—a review. *Renew Sustain Energy Rev* 57:192–204
91. Belhachat F, Larbes C (2017) Global maximum power point tracking based on ANFIS approach for PV array configurations under partial shading conditions. *Renew Sustain Energy Rev* 77:875–889
92. Radianto D, Asfani DA, Hiyama T (2012) Partial shading detection and MPPT controller for total cross tied photovoltaic using ANFIS. *ACEEE Int J Electr Power Eng* 3(2)
93. Aldair AA, Obed AA, Halihal AF (2017) Design and implementation of ANFIS-reference model controller based MPPT using FPGA for photovoltaic system. *Renew Sustain Energy Rev*
94. Kharb RK, Shimi S, Chatterji S, Ansari MF (2014) Modeling of solar PV module and maximum power point tracking using ANFIS. *Renew Sustain Energy Rev* 33:602–612
95. Salam Z, Ahmed J, Merugu BS (2013) The application of soft computing methods for MPPT of PV system: a technological and status review. *Appl Energy* 107:135–148
96. Ramli MA, Ishaque K, Jawaid F, Al-Turki YA, Salam Z (2015) A modified differential evolution based maximum power point tracker for photovoltaic system under partial shading condition. *Energy Build* 103:175–184
97. Tajuddin MFN, Ayob SM, Salam Z, Saad MS (2013) Evolutionary based maximum power point tracking technique using differential evolution algorithm. *Energy Build* 67:245–252
98. Kumar N, Hussain I, Singh B, Panigrahi B (2017) Rapid MPPT for uniformly and partial shaded PV system by using JayaDE algorithm in highly fluctuating atmospheric conditions. *IEEE Trans Ind Inform*
99. Shaiek Y, Smida MB, Sakly A, Mimouni MF (2013) Comparison between conventional methods and GA approach for maximum power point tracking of shaded solar PV generators. *Sol Energy* 90:107–122
100. Ramaprabha R, Mathur B (2012) Genetic algorithm based maximum power point tracking for partially shaded solar photovoltaic array. *Int J Res Rev Inf Sci (IJRRIS)* 2
101. Daraban S, Petreus D, Morel C (2014) A novel MPPT (maximum power point tracking) algorithm based on a modified genetic algorithm specialized on tracking the global maximum power point in photovoltaic systems affected by partial shading. *Energy* 74:374–388
102. Larbes C, Cheikh SA, Obeidi T, Zerguerras A (2009) Genetic algorithms optimized fuzzy logic control for the maximum power point tracking in photovoltaic system. *Renew Energy* 34(10):2093–2100
103. Fathy A (2015) Reliable and efficient approach for mitigating the shading effect on photovoltaic module based on Modified Artificial Bee Colony algorithm. *Renewable Energy* 81:78–88
104. Kim K (2014) Hot spot detection and protection methods for photovoltaic systems. University of Illinois at Urbana-Champaign
105. Farh HM, Othman MF, Eltamaly AM (2017) Maximum power extraction from grid-connected PV system. In: 2017 Saudi Arabia smart grid (SASG). IEEE, pp 1–6
106. Eltamaly AM, Farh HM (2013) Maximum power extraction from wind energy system based on fuzzy logic control. *Electr Power Syst Res* 97:144–150
107. Eltamaly AM, Alolah A, Farh HM (2013) Maximum power extraction from utility-interfaced wind turbines. In: New developments in renewable energy. InTech
108. Zhang J, Wang T, Ran H (2009) A maximum power point tracking algorithm based on gradient descent method. In: IEEE power & energy society general meeting, PES'09. IEEE, pp 1–5
109. Chinchilla M, Arnaltes S, Burgos JC (2006) Control of permanent-magnet generators applied to variable-speed wind-energy systems connected to the grid. *IEEE Trans Energy Convers* 21(1):130–135
110. Eltamaly AM, Farh HM (2015) Smart maximum power extraction for wind energy systems. In: 2015 IEEE international conference on smart energy grid engineering (SEGE). IEEE, pp 1–6

Power Electronics for Practical Implementation of PV MPPT



Mohamed Abouelela

Abstract Using MPPT with solar panel (PV) installations has clear advantages. Several techniques are available for building PV MPPT using analog or digital and microcontroller-based control algorithms. MPPT algorithms are simple enough, but implementing a working MPPT controller is not a simple task, because it is required to know the particularities of the underlying switching converter. Many of the so-called scientific papers published on this topic simply use computer simulations instead of real hardware, and the readers find themselves lacking vital information. In this chapter, we will consider the following topics in detail:

1. The basic theory of operation of the switched-mode power supply.
2. DC/DC converters and how it can be used for maximum power tracking.
3. The concept of MPPT for PV arrays.
4. Power electronics and fundamentals of power switches.
5. Practical implementation of power modules used in DC/DC converters.
6. Driver circuits.
7. Software and control algorithms needed for DC/DC converters.
8. Practical DC/DC converters for MPPT of PV systems.
9. Design procedure of PV MPPT for different types of loads.
10. Battery charger circuits with MPPT.
11. Grid-connected inverters with MPPT for PV systems.

Although the above topics will be covered theoretically and analytically, more attention to practical implementation will be considered. By the end of this chapter, the reader will be able to design, implement and test an MPPT circuit for a given load profile.

M. Abouelela (✉)

Electrical Engineering Department, Faculty of Engineering,, King Saud University, Riyadh, Kingdom of Saudi Arabia

e-mail: mabouelela@ksu.edu.sa

© Springer Nature Switzerland AG 2020

A. M. Eltamaly and A. Y. Abdelaziz (eds.), *Modern Maximum Power Point Tracking Techniques for Photovoltaic Energy Systems*, Green Energy and Technology, https://doi.org/10.1007/978-3-030-05578-3_3

1 Introduction: Switched-Mode Power Supply (SMPS)

A switched-mode power supply is an electronic circuit that regulates the output from a given unregulated DC source. The main advantages of SMPS over the traditional linear regulator are its high efficiency and its high-power capabilities. The main concept depends on using switching element (power transistor) while controlling the on/off ratio (duty cycle) of this switch. Figure 1 demonstrates the basic idea of an SMPS. Define the duty cycle D as: $D = t_{on}/T_s$, and hence,

$$V_O = DV_d. \quad (1)$$

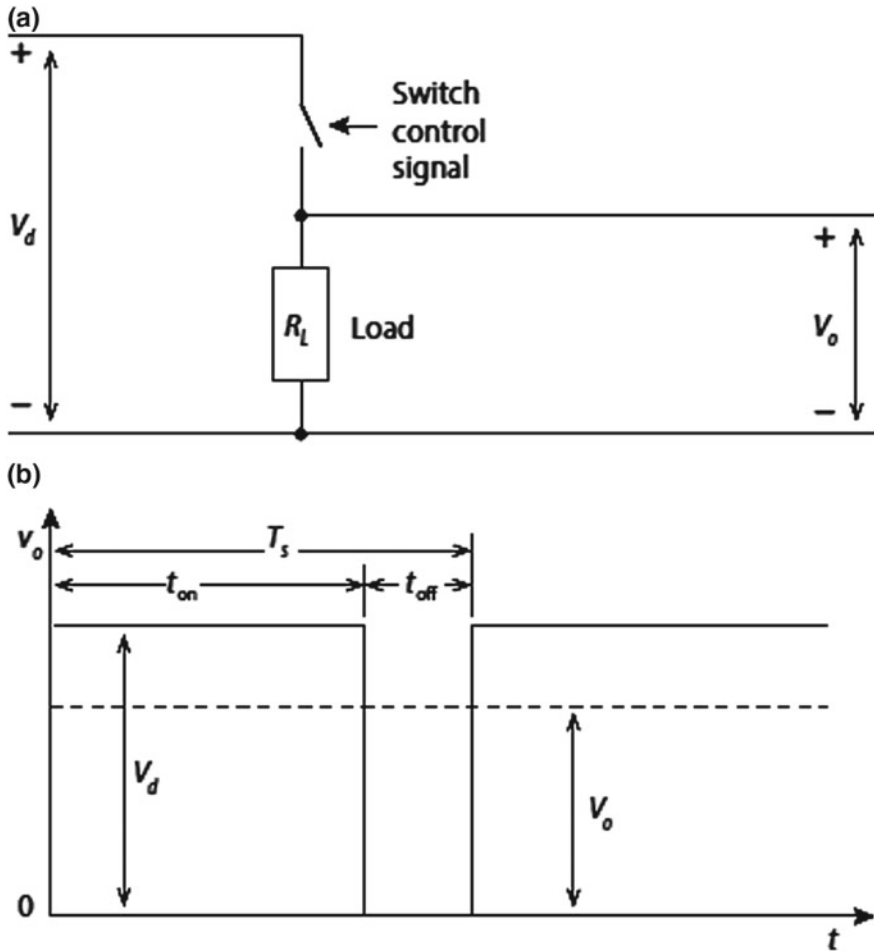


Fig. 1 Basic circuit for SMPS

where V_d is the input voltage available from a given DC source like batteries or rectifier circuit. Since the relation in Eq. (1) is linear, the output can be changed linearly by controlling the duty cycle D . A smoothing circuit (low-pass filter) may be added at the output to obtain DC waveform instead of the rectangular waveform shown in Fig. 1b. Typical applications of SMPS are in DC/DC converters and MPPT for PV systems.

1.1 Switched-Mode Power Supply Modeling and Topologies

Different SMPS topologies or techniques are available in the literatures and publications. Each topology aims at achieving certain performance objectives while considering:

- The series switch, on/off resistance.
- The low-pass filter components used to smooth the DC output voltage.
- The losses in switches at high frequencies, a high switching frequency results in smaller sizes for inductors and capacitors. On the other hand, high-frequency switching may add power losses and electrical noise inside the SMPS circuit.

1.2 Selection of SMPS Topologies

There are several topologies commonly used to implement SMPS. Each topology has its own unique features, which makes it best suited for a certain application. To select the best topology for a given specification, it is essential to know the basic operation, advantages, drawbacks, complexity and the area of usage of a particular topology. The following factors help while selecting an appropriate topology:

- (a) Is the output voltage higher or lower than the whole range of the input voltage?
- (b) How many outputs are required?
- (c) Is input to output dielectric isolation required?
- (d) Is the input–output voltage very high?
- (e) Is the input–output current very high?
- (f) What is the maximum voltage applied across the transformer primary and what is the maximum duty cycle?

Factor (a) determines whether the power supply topology should be a buck or buck–boost type. Factors (b) and (c) determine whether or not the power supply topology should have a transformer. Reliability of the power supply depends on the selection of a proper topology on the basis of factors (d), (e) and (f).

2 Buck Converter

The buck converter topology produces output voltage less than the input voltage ($V_{OUT} < V_{IN}$). The basic circuit and its switching waveforms are shown in Fig. 2. A power switch Q_1 (MOSFET) is used. The output is obtained through the switch and a low-pass filter, built using a simple inductor and a capacitor. In a steady state, with the switch ON, the input provides energy to the output and to the inductor (L). During the time interval T_{OFF} , the switch is OFF, and the inductor current continues to flow in the same direction, as the stored energy within the inductor continues to supply the load current. The diode D_1 completes the inductor current path, while Q_1 is OFF; thus, it is called a freewheeling diode. The DC load voltage V_{out} as shown in Fig. 2c can be found simply from the relation:

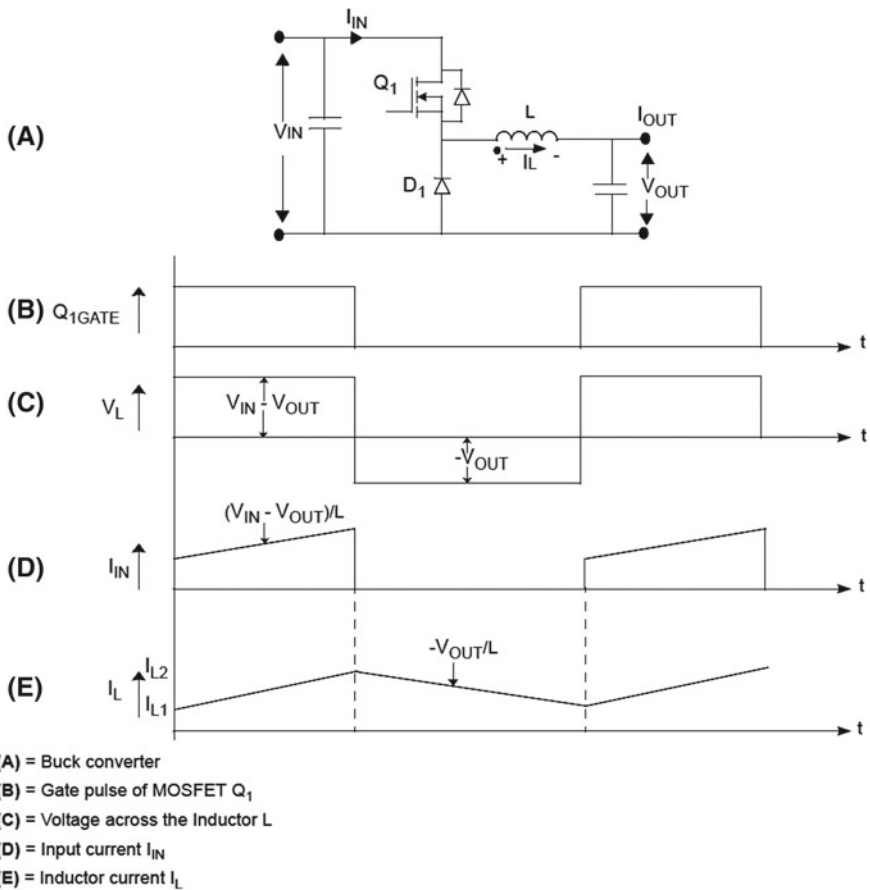


Fig. 2 Buck converter circuit and waveforms [1]

$$V_{\text{out}} = D V_{\text{IN}} \quad (2)$$

Since $D < 1$, then V_{out} is always less than V_{IN} .

The corresponding input and inductor current are given in Fig. 2d and e, respectively. If the desired ratio $V_{\text{OUT}}/V_{\text{IN}}$ is less than 0.1, it is strongly recommended to use a two-stage buck converter, to avoid power losses in the power switch when operated with narrow switching on period. The resultant reduction ratio in this case will be equal to the multiplication of the two cascaded converter reduction ratios as given by the equation:

$$D_{\text{total}} = D_1 \cdot D_2 \quad (3)$$

Although the buck converter can be either continuous or discontinuous, its input current is always discontinuous, as shown in Fig. 2d. This results in a larger electromagnetic interference (EMI) filter than the other topologies. The design of the filter components will highly affect the ripple factor of the output DC voltage. For higher load current, the synchronous buck converter is used where a MOSFET with a very low ON-state resistance $R_{\text{DS(on)}}$ is used instead of the freewheel diode, to avoid the excessive power loss inside this diode (D_1). This MOSFET is turned on and off synchronously with the buck MOSFET. Therefore, this topology is known as a synchronous buck converter. The drive signal for this MOSFET is the complement of the main switching signal used for buck switch. Because a MOSFET can conduct in either direction, we should turn off the MOSFET immediately if the current in the inductor reaches zero; otherwise, the direction of the inductor current will reverse (after reaching zero) because of the output LC resonance. In such a scenario, the synchronous MOSFET acts as a load to the output capacitor and dissipates energy in the $R_{\text{DS(on)}}$ of the MOSFET, resulting in an increase in power loss during discontinuous mode of operation, and the output voltage may fall below the regulation limit. To deliver higher load current at a low output voltage, the multiphase synchronous buck converter may be used. In this topology as shown in Fig. 3, more than one converter is connected in parallel to deliver current to the load. To optimize the input and output capacitors, all the parallel converters operate on the same time base and each converter starts switching after a fixed time/phase from the previous one. The design of input and output capacitors is based on the switching frequency of each converter multiplied by the number of parallel converters. As shown in Fig. 4e, the input current drawn by a multiphase synchronous buck converter is continuous with less ripple current as compared to a single converter shown in Fig. 3d. Therefore, a smaller input capacitor meets the design requirement in case of a multiphase synchronous buck converter.

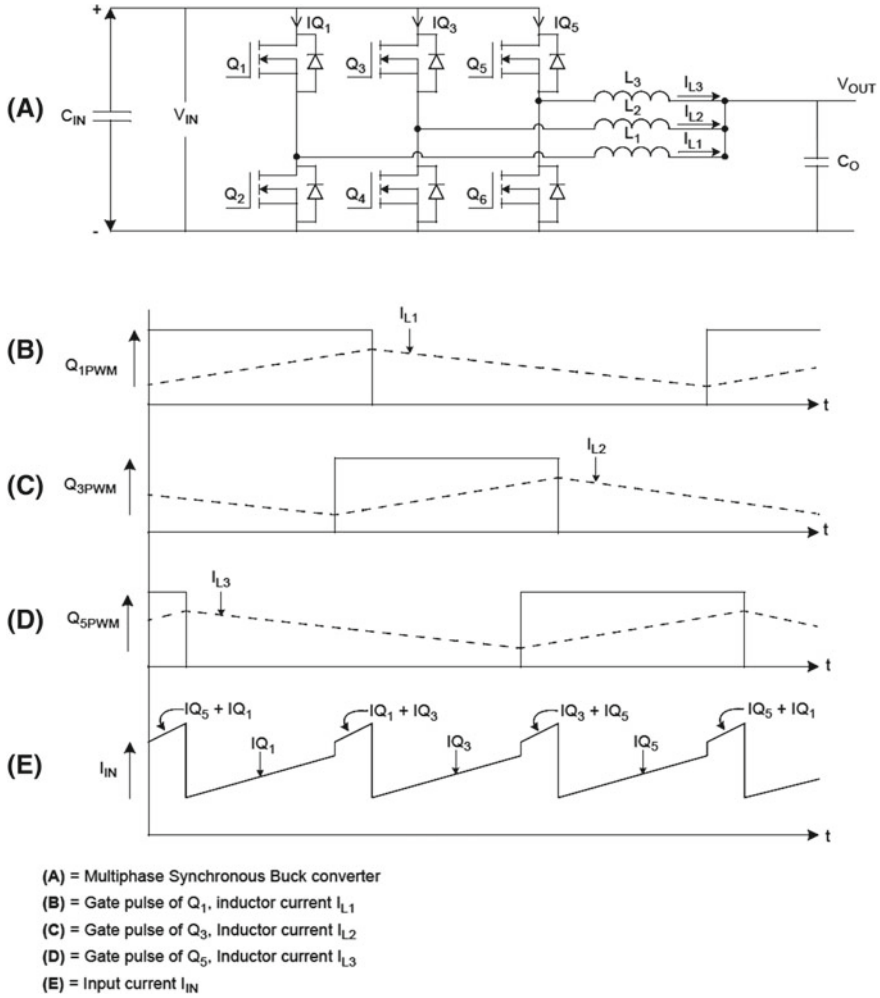


Fig. 3 Multiphase synchronous buck converter [1]

3 The Boost Converter

A boost converter is a DC/DC converter that can produce V_{OUT} greater than V_{IN} . The basic circuit used for a boost converter and its waveforms are given in Fig. 4. In the boost converter, an inductor (L) is used to store energy from the input source when the MOSFET (Q_1) is ON. With Q_1 closed for a period of T_{ON} , the input voltage energizes the inductor (L); therefore, the inductor current rises linearly from its present value I_{L1} to I_{L2} , as given in Fig. 4d, and the output load current I_{OUT} is provided from the discharge of the output capacitor C_O . The value of C_O must be as high as needed to

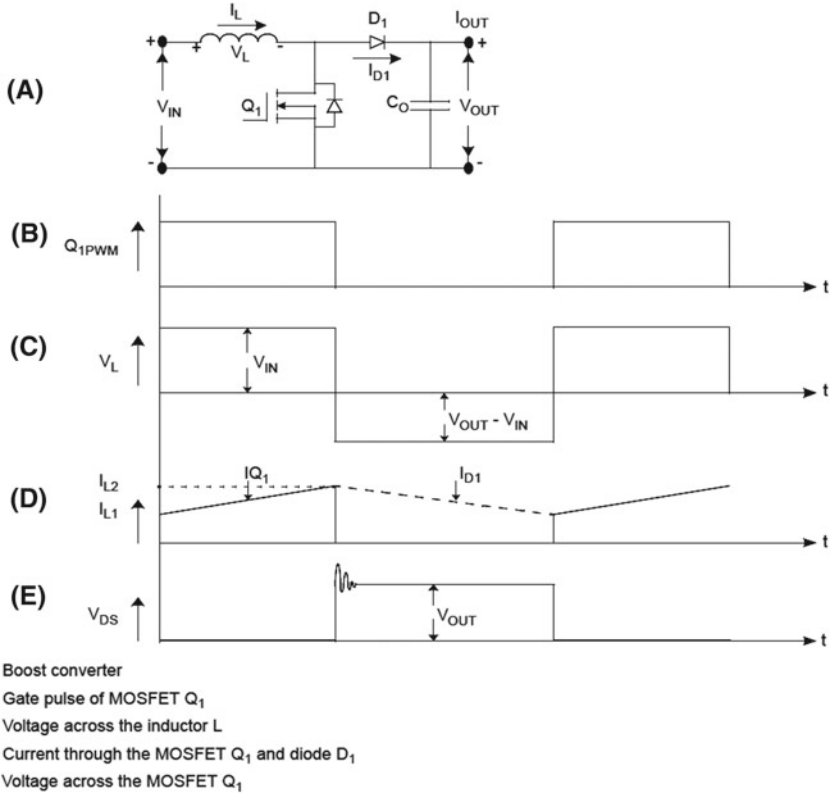


Fig. 4 Boost converter [1]

supply the load current during the ON period T_{ON} while keeping the output voltage as constant as possible (with minimum ripple factor) [2].

During the OFF period T_{OFF} , the inductor delivers the stored energy to the load, and the load voltage in this case will be equal to V_{IN} plus V_L . The diode D_1 completes the inductor current path through the output capacitor during the Q_1 OFF period (T_{OFF}).

$$\begin{aligned} V_{OUT} &= V_{IN} + V_L && \text{OFF period, } V_L \text{ is the inductor voltage} \\ V_{OUT} &= V_C && \text{ON period, } V_C \text{ is the capacitor voltage.} \end{aligned}$$

By controlling the ON/OFF ratio (duty cycle), we can obtain $V_{OUT} > V_{IN}$, which is given by:

$$V_{OUT} = V_{IN}/(1 - D) \quad (4)$$

Since the inductor current is continuous as shown in Fig. 4d, and never becomes zero during one whole cycle (T_S); therefore, this boost converter is working in continuous conduction mode. The diode D_1 ensures the load current flowing in the same direction all the time.

The root-mean-square (RMS) ripple current in the output capacitor is given by Eq. 5 calculated using the waveform given by Fig. 4d.

$$I_{\text{RIPPLERMS}} = (I_{D1})^2 - (I_{\text{OUT}})^2 \quad (5)$$

where

$I_{D1\text{RMS}}$	RMS value of I_{D1}
$I_{\text{RIPPLERMS}}$	Ripple RMS current of capacitor
I_{OUT}	Output DC

A plot for the ratio $V_{\text{OUT}}/V_{\text{IN}}$ as a function of the duty cycle is shown in Fig. 5 based on Eq. 5 (ideal curve). A practical curve that includes the non-ideal behavior of the circuit component is also shown. Working at D higher than 0.75 is impractical because of the losses in the inductor, capacitor and the semiconductor switch, while working at OFF periods.

If both buck and boost are combined together, buck–boost converter is obtained. In a buck–boost converter, the output voltage can be both higher and lower than the input voltage. The simplified schematic of a buck–boost converter is depicted in Fig. 6, while the input–output relation is given by:

$$V_{\text{OUT}} = DV_{\text{IN}}/(1 - D) \quad (6)$$

Note that for $V_{\text{OUT}} < V_{\text{IN}}$ $D < 0$ while for $V_{\text{OUT}} > V_{\text{IN}}$ $D > 0.5$.

Fig. 5 Dependence of $V_{\text{OUT}}/V_{\text{IN}}$ on D

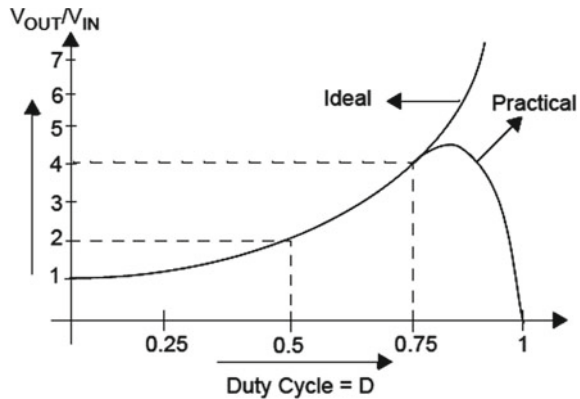
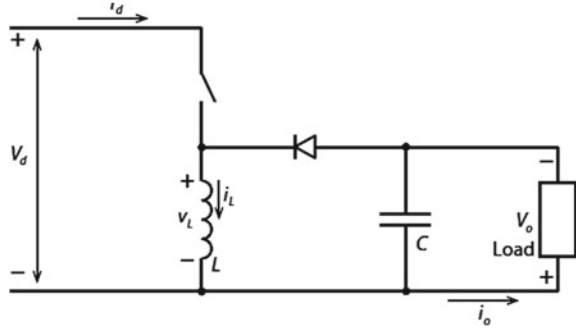


Fig. 6 Buck–boost converter



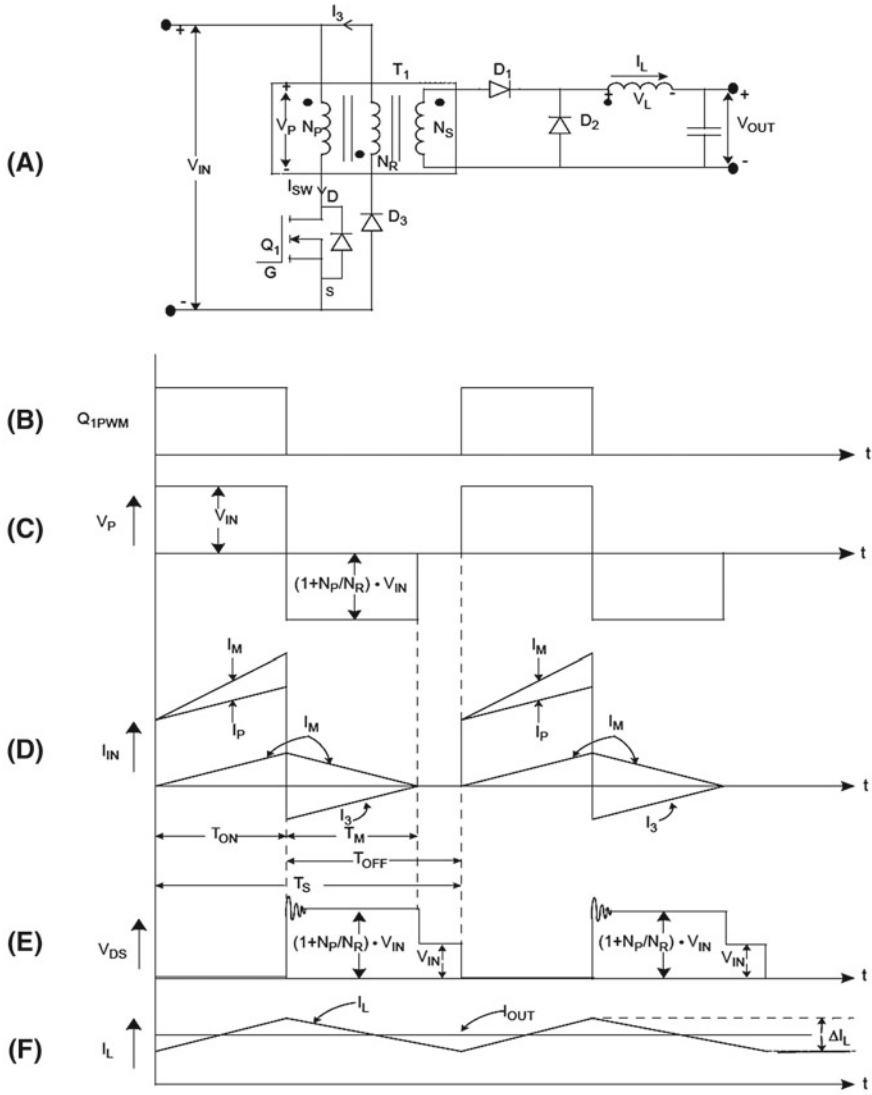
4 Forward Converter

This topology uses a transformer to isolate the load from the input source. It is based on the basic buck converter topology and adds more flexibility for the controlling output voltage to input voltage ratio. The basic circuit and switching waveforms are given in Fig. 7, where a switch (Q_1) is connected in series with the transformer (T_1) primary. The transformer is used to step down the primary voltage and provides isolation between the input voltage source V_{IN} and the output voltage V_{OUT} . In the steady state of operation, when the switch is ON for a period of T_{ON} , the dot end of the winding becomes positive with respect to the non-dot end. Therefore, the diode D_1 becomes forward-biased and the diodes D_2 and D_3 become reverse-biased.

Equation 7 gives the output voltage as a function of input voltage, transformer ratio and the duty cycle.

$$V_{OUT} = V_{IN} \cdot (N_S/N_P) \cdot D \quad (7)$$

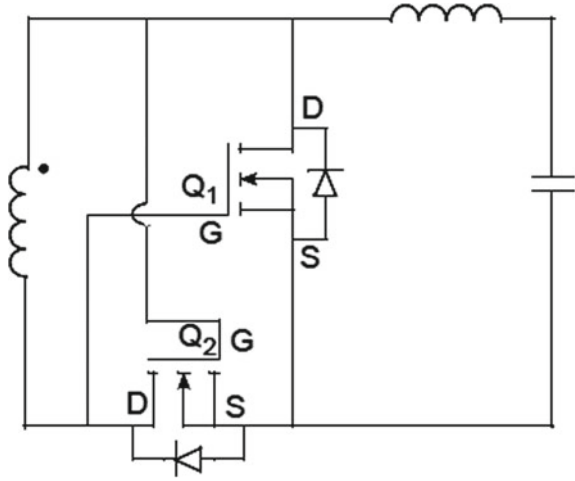
When Q_1 is OFF, there the stored energy in the magnetic core has to dissipate. One such method is shown in Fig. 7. The N_R winding is used for this purpose where the flux stored inside the magnetic core induces a negative voltage at the dot end of the N_R winding, which forward-biases the diode D_3 and resets the magnetizing energy stored in the core. Resetting the magnetizing current during the OFF period is important to avoid saturation. The diode D_2 completes the inductor current path during the Q_1 OFF period (T_{OFF}). To reduce losses in output diode rectifiers (D_1 , D_2 in Fig. 7), a synchronous MOSFET can be used instead of diodes. The MOSFETs Q_1 and Q_2 are complementary and self-driven from the transformer secondary, as shown in Fig. 8. Improving the load transient response and implementing current mode control require reducing the output inductor value and the use of a better output capacitor to meet the output voltage ripple requirement, as discussed in the “buck converter.” Multiple output, forward converter coupled inductor can be also used to get better cross-load regulation requirements as explained for buck converter in Fig. 3.



- (A) = Forward Converter power circuit diagram.
 (B) = Gate pulse of MOSFET Q_1
 (C) = Voltage across the transformer primary winding N_P
 (D) = Current through N_P and N_R
 (E) = Voltage across the MOSFET Q_1
 (F) = Output Inductor current I_L

Fig. 7 Forward converter [1]

Fig. 8 Synchronous buck converter [3]



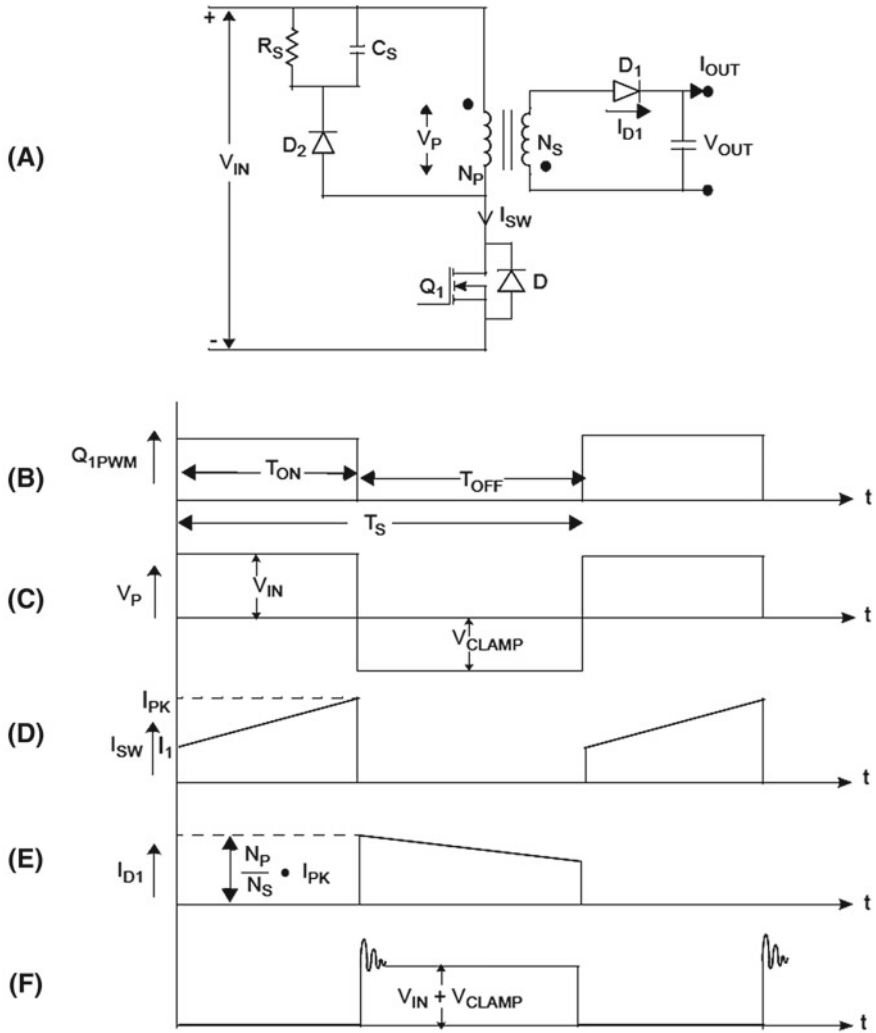
5 Flyback Converter (FBT)

The basic circuit and switching waveforms for flyback converter (FBT) are shown in Fig. 9. The difference between the flyback and forward converters is:

- The secondary output is out of phase for flyback.
- No need to reset winding N_R .
- A snubber circuit (R_S and C_S in Fig. 9) is used for the reset function.
- There is no inductor to store energy in the output circuit as the transformer secondary does the same function.

As the diode D_1 becomes reverse-biased, the load current (I_{OUT}) is supplied from the output capacitor (C_O). The output capacitor value should be large enough to supply the load current for the time period T_{ON} , with the maximum specified droop in the output voltage. At the end of the T_{ON} period, when the switch is turned OFF, the transformer magnetizing current continues to flow in the same direction. The magnetizing current induces a negative voltage in the dot end of the transformer winding with respect to non-dot end. The diode D_1 becomes forward-biased and clamps the transformer secondary voltage equal to the output voltage. The energy stored in the primary of the flyback transformer transfers to secondary through the flyback action. This stored energy provides energy to the load and charges the output capacitor. Since the magnetizing current in the transformer cannot change instantaneously at the instant, the switch is turned OFF, the primary current transfers to the secondary, the amplitude of the secondary current will be the product of the primary current, and the transformer turns ratio, N_S/N_P . Equation 8 gives the transfer relation for the flyback converter:

$$V_{OUT} = V_{IN} \cdot (N_S/N_P) \cdot (D/1 - D) \quad (8)$$



- (A) = Flyback converter power circuit
 (B) = Gate pulse for the MOSFET Q_1
 (C) = Voltage across the primary winding
 (D) = Current through MOSFET Q_1
 (E) = Current through the diode D_1
 (F) = Voltage across the MOSFET Q_1

Fig. 9 Flyback converter, [1]

To dissipate the stored leakage energy in the magnetic core of the flyback transformer, as shown in Fig. 9 a snubber circuit consisting of D_2 , R_S and C_S is used. In this method, the leakage flux stored inside the magnetic core induces a positive voltage at the non-dot end primary winding, which forward-biases the diode D_2 and provides the path to the leakage energy stored in the core, and clamps the primary winding voltage to a safe value. During this process, C_S is charged to a voltage slightly more than the reflected secondary flyback voltage, which is known as flyback overshoot. The spare flyback energy is dissipated in resistor R_S . This clamp voltage is directly proportional to R_S . The flyback overshoot provides additional forcing volts to drive current into the secondary leakage inductance during the flyback action. This results in a faster increase in the transformer secondary current and improves the efficiency of the flyback transformer. Flyback topology is recommended for output power ranged from 5 to 150 W low-cost power supply. Because it does not use an output inductor, cost and volume as well as losses inside the flyback converter can be optimized.

6 Push–Pull Converter

A push–pull converter is a transformer-isolated converter built on the basic forward topology. The circuit and switching waveforms are given in Fig. 10. Q_1 and Q_2 are complementary switches to low energy storage in the primary of center-tapped transformer, during alternate half cycles. The transformer steps down the primary voltage and provides isolation between the input and the output terminals. The transformer used is a center-tapped primary and a center-tapped secondary type. The switches Q_1 and Q_2 are driven by control signals, such that both switches should create equal and opposite flux in the transformer core. As given in Fig. 10b, this may be achieved by choosing equal ON periods for Q_1 and Q_2 .

The OFF time of Q_2 is equal to $T_S/2$, while the ON time is chosen to keep equal and opposite flux in the transformer core. After the time period $T_S/2$, while Q_2 turns ON, the diode D_6 is reverse-biased, and the complete inductor current starts flowing through the diode D_5 and transformer secondary N_{S1} . As the input voltage V_{IN} is applied to the transformer primary N_{P2} in the reverse direction, the dot end becomes negative with respect to the non-dot end. As the input voltage applies across the transformer primary N_{P2} , the value of the magnetic flux density in the core is changed from its initial value of B_2 to B_1 , as shown in Fig. 11. Assuming the number of primary turns N_{P1} is equal to N_{P2} , the number of secondary winding turns N_{S1} is equal to N_{S2} , the ON period of both switches is equal, the magnetic saturation in the transformer core can be avoided, and the condition of equal and opposite flux in the transformer core is achieved. After the T_{ON} period, Q_2 turns OFF and remains off for the rest of the period T_S , as shown in Fig. 10. Note that T_{ON} must be less than $T_S/2$. The input–output relation for the push–pull converter is given in Eq. 9.

$$V_{OUT} = V_{IN} \cdot (N_S/N_P) \cdot 2 \cdot D \quad (9)$$

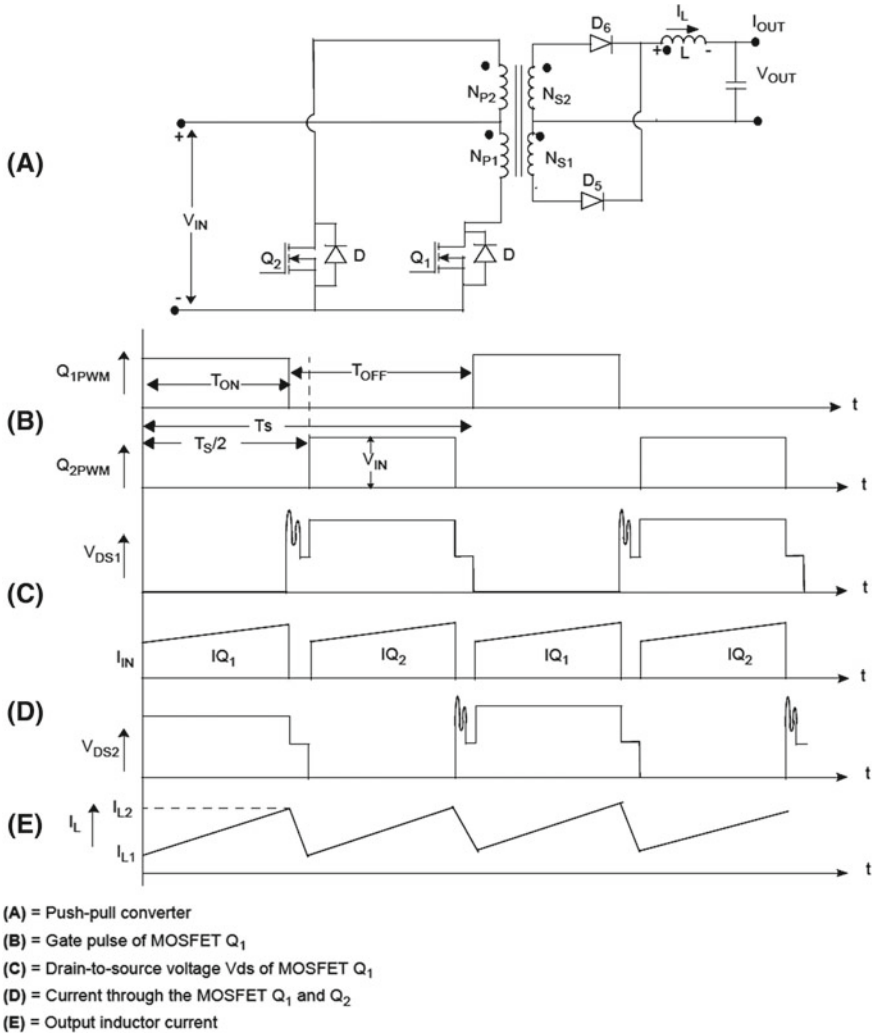
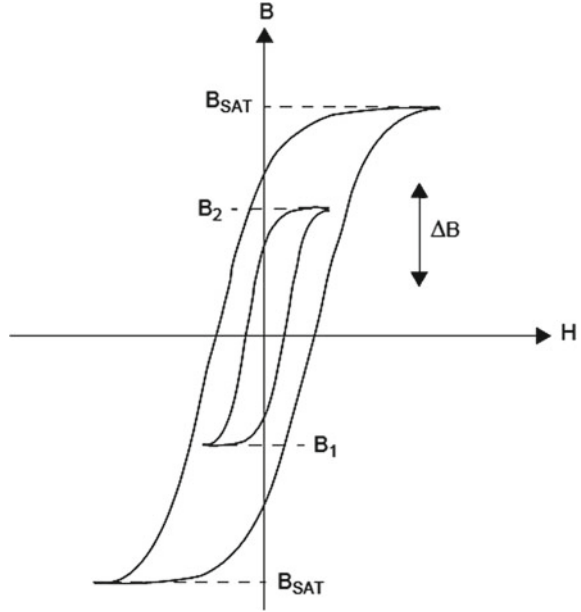


Fig. 10 Push-pull converter [3]

One basic principle of the push-pull configuration is that it requires a center-tapped transformer. In this case, each winding is active only during one half of the switching cycle, which means only 50% utilization of primary copper. The unused copper occupies space in the bobbin and increases the primary leakage inductance. The high voltage ($2 \cdot V_{IN}$) stress on the switch, and 50% utilization of the transformer primary makes the push-pull topology undesirable when the input voltage is high. The push-pull topology is most favorable for low-voltage applications such as 110

Fig. 11 BH curve for push-pull transformer voltage [1]



V_{AC} input direct off-line SMPS or low input voltage DC/DC isolated converter for the power rating of up to 500 W.

7 Half-Bridge Converter

The basic circuit and associated half-bridge converter waveforms are given in Fig. 12. It uses a center-tapped transformer only at the secondary winding. The input voltage V_{IN} is applied to the input bridge formed by two capacitors C_3 and C_4 and two MOSFET switches Q_1 and Q_2 ; therefore, it is called a half-bridge converter. The bridge output is applied to the transformer primary N_P . Since the capacitors C_3 and C_4 are equal, they will be charged at DC voltage, equal to half the input voltage. When the switch Q_1 is ON, D_3 is forward and the output capacitor is charged through the output inductor L , while when Q_2 is ON D_4 is forward and supply current is in the same direction to keep the output voltage as constant as possible. The control of the output voltage is accomplished through the modulation of the ON period for both Q_1 and Q_2 as given in Fig. 12b. In case when both switches are OFF, V_{OUT} is applied to the inductor L in the reverse direction; therefore, the inductor current I_L decreases linearly from its initial value of I_{L2} to I_{L1} , as shown in Fig. 12e. To avoid magnetic saturation in the transformer core, two conditions must be fulfilled:

- The number of N_{S1} is equal to N_{S2} .
- The ON period of both switches should be equal.

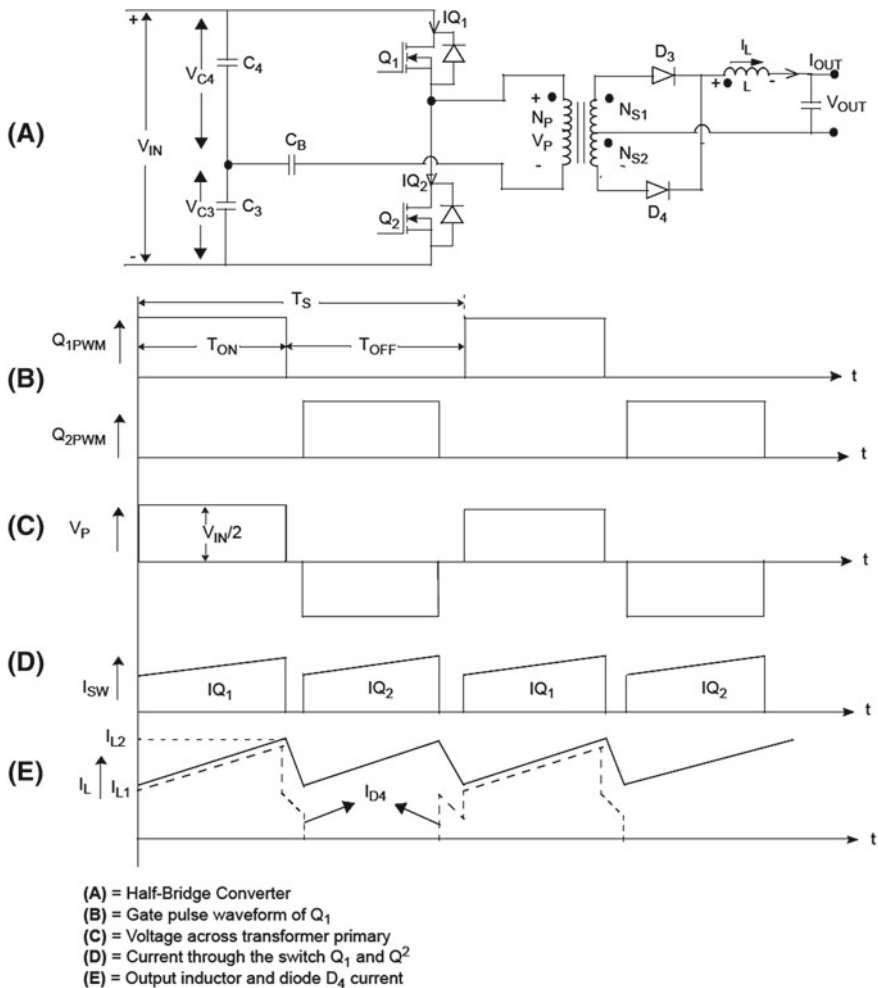


Fig. 12 Half-bridge converter [1]

Note that when either of the switches turns ON for the T_{ON} period, it affects the entire input voltage V_{IN} of the other switch. The input–output relation for half-bridge rectifier is given by:

$$V_{OUT} = V_{IN}(N_S/N_P).D \quad (10)$$

where $N_S = N_{S1} = N_{S2}$.

A small DC blocking capacitor is placed in series with the transformer primary, to block the DC flux in the transformer core. The value of the DC blocking capacitor is given by Eq. 11.

$$C_B = I_{\text{PRIM}} \cdot T_{\text{ONMAX}} / \Delta V \quad (11)$$

where

- I_{PRIM} maximum primary current
 T_{ONMAX} maximum ON time of either MOSFET
 ΔV permissible droop in primary voltage because of the DC blocking capacitor

The half-bridge topology is best suited for applications up to 500 W and favorable for high-voltage applications such as 220 V_{AC} input direct off-line SMPS.

8 Half-Bridge Resonant Converter

High switching frequency (more than 100 kHz) is needed to reduce the volume of the passive components and the overall converter size. However, increasing the switching frequency decreases the efficiency due to losses in the power switches at high switching speed. Resonant technique is used to achieve the above requirement. There are three main resonant topologies available:

- 1—Series resonant converter.
- 2—Parallel resonant converter.
- 3—LLC (inductor–inductor–capacitor) resonant converter.

9 Series Resonant Converter (SRC)

As shown in Fig. 13, series resonant circuit (L_R and C_R) is connected with transformer primary. As a result, primary current is approximately sinusoidal, and the current through the switch at its transition period is minimized, hence reducing the switching losses. It is preferred to operate at switching frequency, a little bit greater than the resonance frequency as shown in Fig. 14 which plots of the normalized primary current versus the relative operating switching frequency (f_s/f_{res}) for different values of the circuit quality factor (Q), while achieving zero voltage switching (ZVS). The major disadvantages of series resonant converter are:

- Light load regulation.
- High circulating energy.
- High turn-off current at high input voltage.

Fig. 13 Series resonance converter [1]

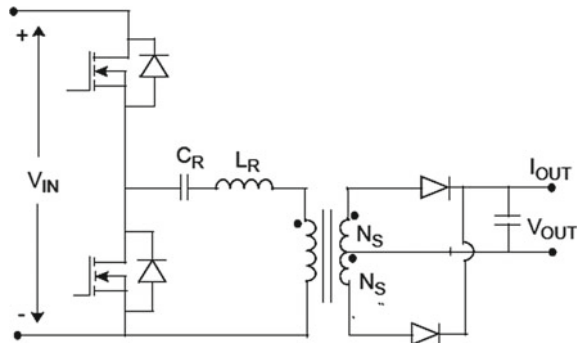
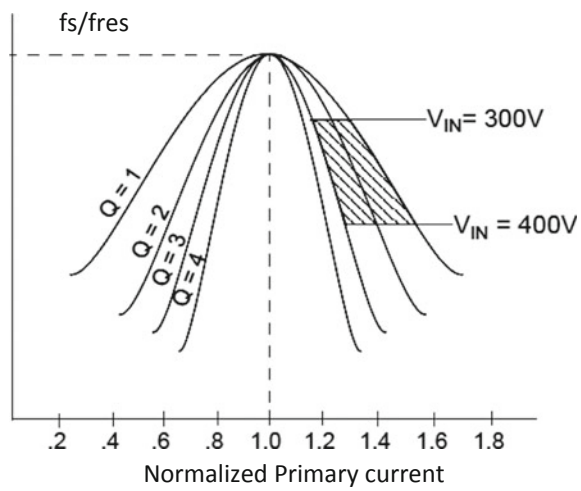


Fig. 14 Frequency response of primary current [1]



10 Parallel Resonant Converter (PRC)

As shown in Fig. 15, a resonance circuit L_R and C_R is connected in parallel with the transformer primary. The operation switching frequency is also more than the resonant frequency. The operating region is much smaller at low loads (Q is very high), as given in Fig. 16. Given the same analysis as the series resonance converter, we can conclude that a parallel resonant converter is not a good choice for a front-end DC/DC converter. The major problems are: high circulating energy and high turn-off current at high input voltage conditions.

Figure 17 gives parallel resonance converter waveforms where we can observe that losses increase as V_{IN} increases at the same switching frequency.

Fig. 15 Parallel resonance converter

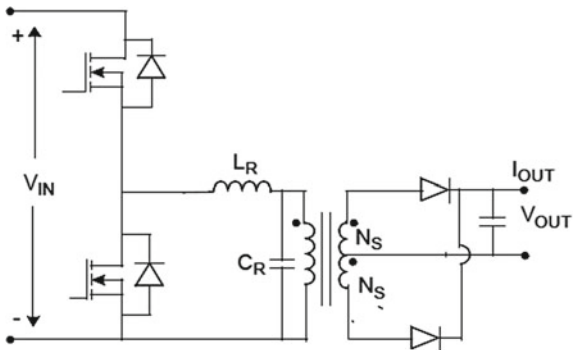


Fig. 16 Frequency response of primary current [3]

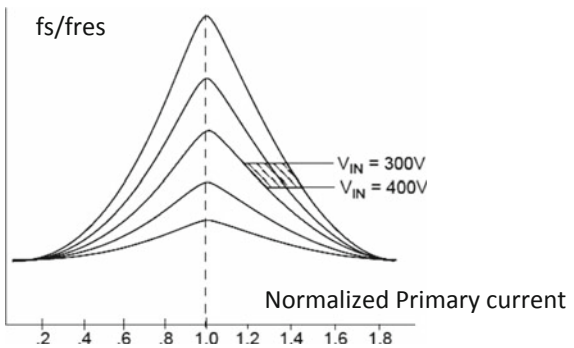
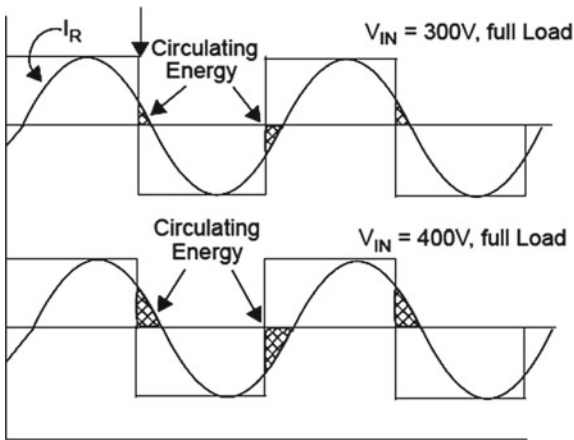


Fig. 17 Parallel resonance converter waveforms [3]



11 LLC Resonant Converter

The LLC resonant converter uses an inductor L_R and a capacitor C_R , connected in series with the transformer primary. Another resonant inductor L_M is connected in parallel with the transformer primary, as given in Fig. 18. The presence of L_M results in double-tuned resonance as shown in Fig. 19. The LLC resonant converter is designed to operate at a switching frequency higher than the resonant frequency set by L_R and C_R . The benefit of using LLC resonant converter is the possibility of using narrow switching frequency range with light load and zero voltage switching (ZVS) capability even at no load. In addition, its special DC gain characteristic, as shown in Fig. 19, makes the LLC resonant converter an excellent choice for the front-end DC/DC application. The first resonant frequency is determined by L_R and C_R , while the other resonant frequency is determined by L_M , L_R , C_R as given by Eq. (12).

Fig. 18 LLC resonant converter

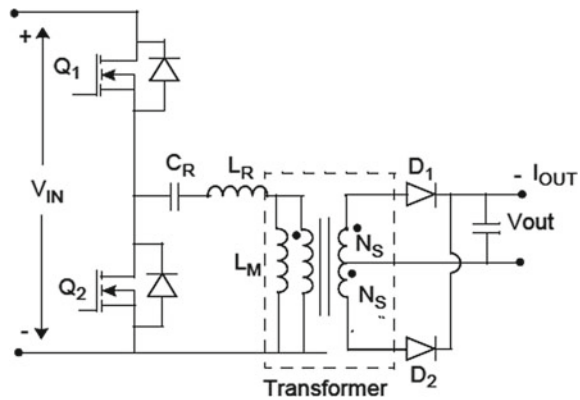
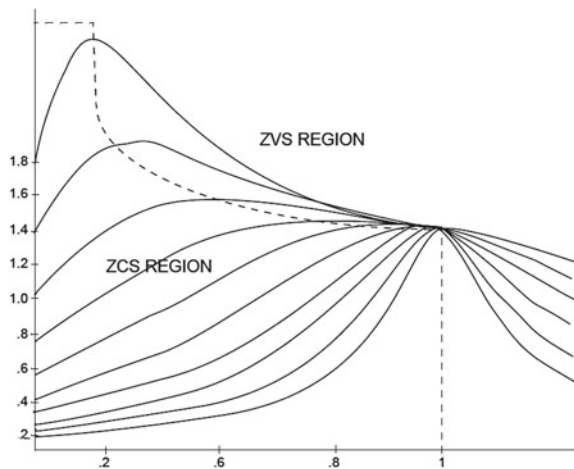


Fig. 19 Frequency response



$$\begin{aligned}
 F_{R1} &= \frac{1}{(2 \cdot \pi \cdot \sqrt{(L_R \cdot C_R)})} \\
 F_{R2} &= \frac{1}{(2 \cdot \pi \cdot \sqrt{((L_M + L_R) \cdot C_R)})}
 \end{aligned} \tag{12}$$

12 Full-Bridge Converter

A full-bridge or H-bridge converter is a transformer-isolated buck converter. The basic circuit and waveforms are given in Fig. 20. The four switches Q_1 Q_2 and Q_3 Q_4 are used to generate pulsating AC voltage at the transformer primary. The transformer is used to step down the primary voltage and also to provide isolation between the input source and the output voltage V_{OUT} . The voltage applied in the primary when either of the switches is ON is half of the input voltage, thereby doubling the switch current. In a push–pull topology, voltage applied in the transformer primary when either of the switches is ON is full input voltage; however, the voltage stress of the switch is twice the input voltage. This condition makes both half-bridge and push–pull topologies unsuitable for applications require high power (>500 W).

A full-bridge converter adds the voltage properties of the half-bridge converter, to the current properties of push–pull converter. The switch pair arms Q_1 Q_2 and Q_3 Q_4 are switched alternately at the selected switching period. In steady-state operation, the arm Q_1 Q_2 is ON, the diode D_4 becomes OFF, and diode D_3 becomes ON. The diode D_3 carries the full load current through the secondary winding N_{S1} . The difference between the primary reflected voltage to the secondary and the output voltage is applied across the inductor L in the forward direction to charge the output capacitor and maintain the output voltage. The switch pair Q_3 Q_4 will be turned ON after half of the switching period $T_S/2$, as shown in Fig. 20c. Therefore, during the T_{OFF} period, there is a situation where all the four switches are OFF.

After the time period $T_S/2$, when the arm switch Q_3 Q_4 is turned ON for a period of T_{ON} , the diode D_4 carries the full load current through the secondary winding N_{S2} . As the input voltage is applied across the transformer primary, the switch carries the reflected load current plus the transformer primary magnetizing current. The difference of the primary reflected voltage to the secondary and the output voltage is applied across the inductor L in the forward direction.

Assuming the number of secondary winding turns N_{S1} is equal to N_{S2} , and to avoid magnetic saturation in the transformer core, the T_{ON} period of both switch pairs Q_1 Q_2 and Q_3 Q_4 should be equal. After the T_{ON} period of the switch pair Q_3 Q_4 , it turns OFF and remains OFF for the rest of the period T_S , as shown in Fig. 20b.

Note that when either of the diagonal switch pairs turns ON for a period of T_{ON} , it applies the entire input voltage V_{IN} to the other switch. The relation between the input voltage and the output voltage is given by Eq. 13.

$$V_{OUT} = 2 \cdot V_{IN} \cdot (N_S/N_P) \cdot D \tag{13}$$

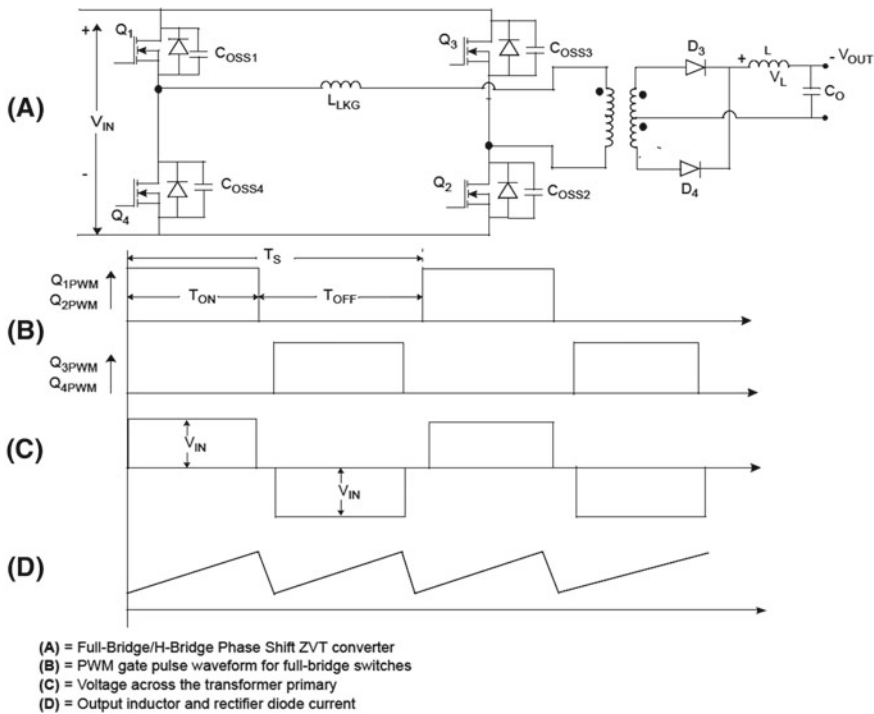


Fig. 20 Full-bridge/H-bridge phase-shift ZVT converter. Ref. [2]

13 Application Considerations

Since the maximum voltage stress across any switch is V_{IN} , and with the complete utilization of magnetic core and copper, this combination makes the full-bridge converter an ideal choice for high input voltage and high-power range SMPS (<1000 W) applications. Since in the full-bridge converter, four switches have been used, the switching device loss is increased. For applications requiring output power of more than 1000 W, the loss in the switching device becomes impractical to handle in a full-bridge converter. The conduction loss of a MOSFET can be reduced by using a good MOSFET, and switching losses can be reduced by using either a zero voltage switching (ZVS during turn-ON transition), a zero current switching (ZCS during turn-OFF transition), or both techniques. If the input current is shaped to be sinusoidal to achieve ZCS, increases the peak and the RMS current through the MOSFET in the high-power application, is also increased. This leads to the increase of the conduction losses, so at high input voltage, the ZVS technique is preferred for the MOSFET.

14 Full-Bridge/H-Bridge Phase-Shift Zero Voltage Transition (ZVT) Topology

A full-bridge converter (Fig. 20) using the phase-shift ZVT technique is known as an H-bridge phase-shift ZVT topology. The parasitic output capacitor of the MOSFETs and the leakage inductance of the switching transformer are used as a resonant tank circuit to achieve zero voltage across the MOSFET at the turn-on transition. There are two major differences in the operation of a phase-shift ZVT and simple full-bridge topology:

In a phase-shift ZVT converter, the gate drive of both of the diagonal switches is phase shifted.

Both halves of the bridge switch network are driven through the complementary gate pulse with a fixed 50% duty cycle.

The phase difference between the two half-bridge switching network gate drives controls the power flow from primary to secondary, which results in the effective duty cycle. Power is transferred to the secondary only when the diagonal switches are ON. If either the top or bottom switches of both legs are ON simultaneously, zero voltage is applied across the primary. Therefore, no power is transferred to the secondary during this period. When the appropriate diagonal switch is turned OFF, primary current flows through the output capacitor of the respective MOSFETs causing switch drain voltage to move toward to the opposite input voltage rail. This causes zero voltage across the MOSFET to be turned ON next, thus creating zero voltage switching when it turns ON. This is possible when enough circulating current is provided by the inductive storage energy to charge and discharge the output capacitor, the respective MOSFETs. Figure 21 shows the gate pulse required, and the voltage and current waveform across the switch and transformer.

A comparison table for the most commonly used DC/DC converters is given in [4].

15 The DC/DC Converter as an MPPT

One of the important applications of SMPS as a DC/DC converter is in maximum power tracing, especially when PV arrays are used as a power source. The MPPT circuit used may be one of the topologies described above. A feedback loop is employed with the DC/DC converter circuit to keep maximum power point tracking [5]. The feedback action if correctly tuned will keep maximum power transfer against climatic and load variations for different types or technologies of solar cells. The operation of the DC/DC converter for MPPT can be easily understood with the help of example 1.

Example 1 A PV module has its MPP at $V_{MPP} = 17$ V and $I_{MPP} = 6$ A at a given level of solar irradiance. The module has to power a load with a resistance $R_L = 10\Omega$. Calculate the duty cycle of the DC/DC converter if a buck–boost converter is used.

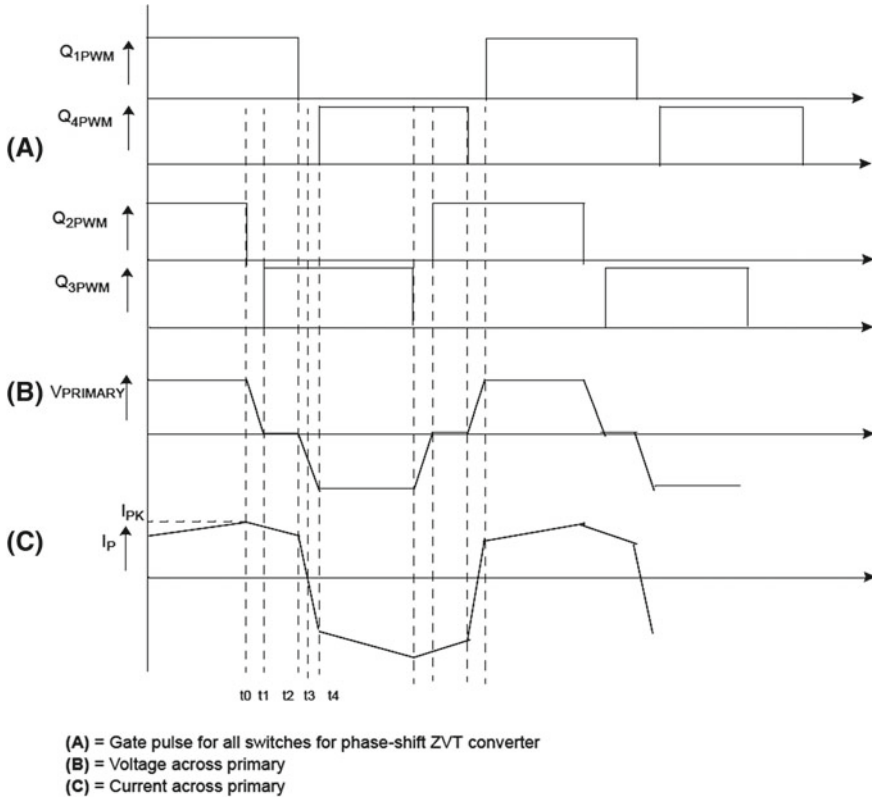


Fig. 21 Full-bridge/H-bridge phase-shift ZVT waveforms. Ref. [2]

Solution

The maximum power from the module is $P_{MPP} = V_{MPP} \cdot I_{MPP} = 102 \text{ W}$.

If this power should be dissipated at the resistor, we have to use the relation

$P_L = V_L^2 / R_L$ and hence the voltage at the resistor $V_L = 31.94 \text{ V}$

Using Eq. (1.6) to find D ; with $V_{OUT} = V_L = 31.94 \text{ V}$ and $V_{IN} = V_{PV} = 17 \text{ V}$

We find $D = 0.65$.

16 Power Electronics and Fundamentals of Power Switches

16.1 Definition and History

Power electronics devices are applied when control and conversion of electrical power are needed, and usually they operate as switches. The introduction of silicon

controlled rectifiers (SCRs) led to the development of a new area of application called the power electronics. The first known electronic switch was the mercury arc rectifier (1900). The first semiconductor device working as a voltage-controlled power switch was the silicon controlled rectifier (SCR) and was available by 1957 where four layers' silicon structure was used to achieve switching characteristics at high power. Although the power bipolar junction transistor (BJT) was already available, its power capabilities were limited to a few tens of watts. In general, the SCRs have higher power range and its application area is spread to many fields such as drives, power supplies, aviation electronics and high-frequency inverters. Starting from this date, we can say that a technology related to power electronics had been originated. The employment of power electronics in renewable energy field is indispensable as we need to convert and control the available energy from the renewable sources such as solar and wind energy into electrical energy suitable to be used by our domestic applications. Circuits like inverters, converters and mechanical drives are typical applications of power electronics used with renewable energy sources.

16.2 Classification of Power Semiconductors

The power semiconductors may be classified according to fabrication materials and applications [6].

a. Power Diodes

A power diode used a polarity switch for high-power applications like rectification of high-voltage and high-current rectifying circuits. It requires a finite time for switching. High switching speed is necessary for most of power converter applications to avoid using large component (inductors and capacitors) in the filtering circuit. We have two general classifications for power diodes:

- General purpose: Rating up to 6000 V, 4500 A.
- High speed (or fast recovery): Rating up to 6000 V, 1100 A, reverse recovery time 0.1–5 μ s; it is essentially assigned for high-frequency switching.

Figure 22 shows the switching characteristics of the diode during turn-off time. If the diode is suddenly reversed, it keeps conducting resulting in current flowing in the opposite direction. This is because of a capacitive effect due to stored charges in its depletion layer. The diode current flows for a reverse recovery time t_{RR} . From Fig. 22, we can define the following time intervals:

Time T_a : Charges stored in the depletion layer are removed.

Time T_b : Charges from the semiconductor layer are removed.

Total reverse recovery time is $T_{RR} = T_a + T_b$

So, working at high switching speed needs a diode with a relatively low reverse recovery time to avoid excess power loss during transition from ON to Off states.

Schottky diode utilizes a Schottky barrier consisting of a metal–semiconductor junction unlike conventional diodes that provide diode characteristics through a PN

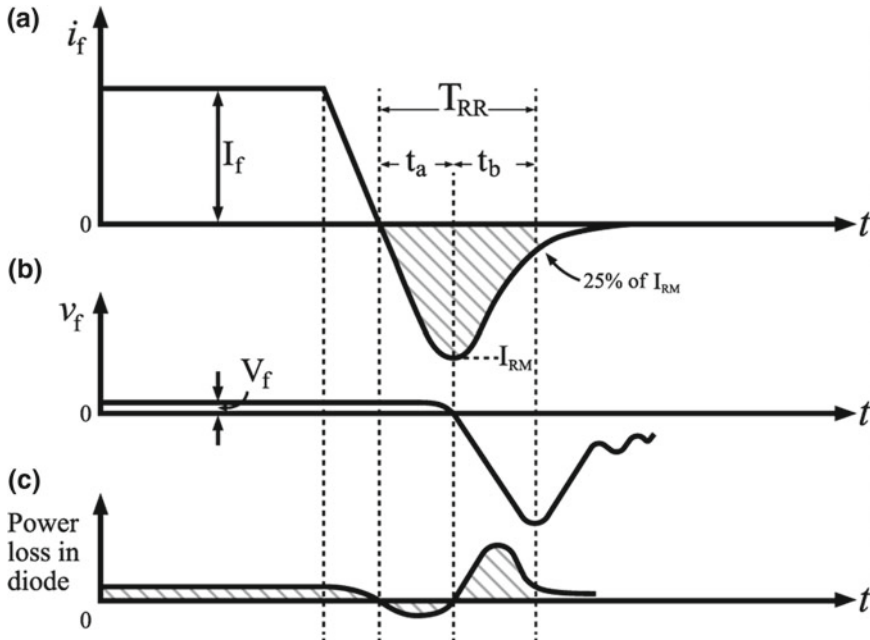


Fig. 22 Turn-off characteristics of power diode: **a** Variation of the current I_f ; **b** variation of the voltage drop V_f ; and **c** variation of the power loss [1]

(semiconductor–semiconductor) junction. The structure of Schottky diode is given in Fig. 23a, while its IV characteristic compared to the conventional PN junction diode is given in Fig. 23b. This results in much lower V_F characteristics while enabling faster switching speeds.

Typical high-power Schottky diode available in the market is the APT100S20B from Microsemi [7] and has maximum rates of: 200 V reverse voltage, 120 A forward and 70 ns reverse recovery time.

b. Thyristors

A thyristor is a three-terminal solid-state device with a four-layer structure as given in Fig. 24a with the IV characteristics given in Fig. 24b. Its basic function is to work as a voltage-controlled switch that may support high-power capabilities. It conducts when the gate receives a current trigger, continuing to conduct until the voltage between the anode and the cathode is reversed, or until the voltage is removed (by some other means).

Once a thyristor is in a conduction mode, the gate circuit has no control and the thyristor continues to conduct. In conduction mode, forward voltage is very small (0.5–2 V). Thyristor can be turned off by making the voltage between anode and cathode ≤ 0 V. Line-commutated thyristors are turned off due to the sinusoidal nature of their input voltage. Forced-commutated thyristors are turned off by an extra circuit

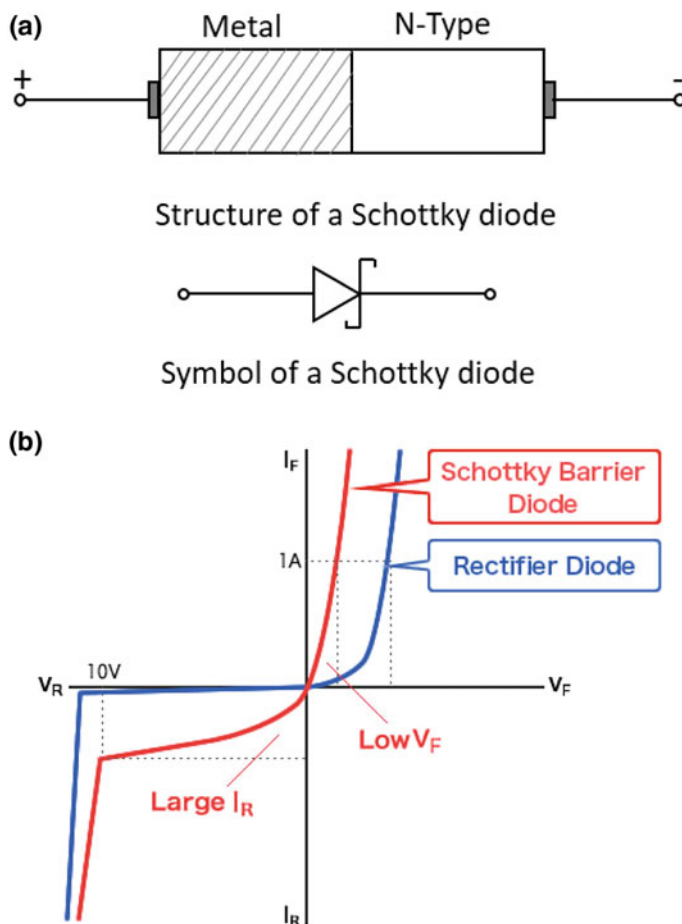


Fig. 23 a Schottky diode structure and symbol. b IV characteristics

called commutation circuitry. Natural or line-commutated thyristors are available with rating up to 6000 V, 4500 A. Turn-off time became very small (10–20 μ s in 3000 V, 3600 A). The thyristors are mostly suitable for controlling AC power and rarely used in DC/DC converters and MPPT as well. To obtain power control at both half cycles, two thyristors may be connected back to back, and such device structure is called TRIAC and widely used in AC power controllers like heaters, light systems and speed control.

c. Power Transistor

There are several types of transistors that can be used as power devices. The types of power transistors are:

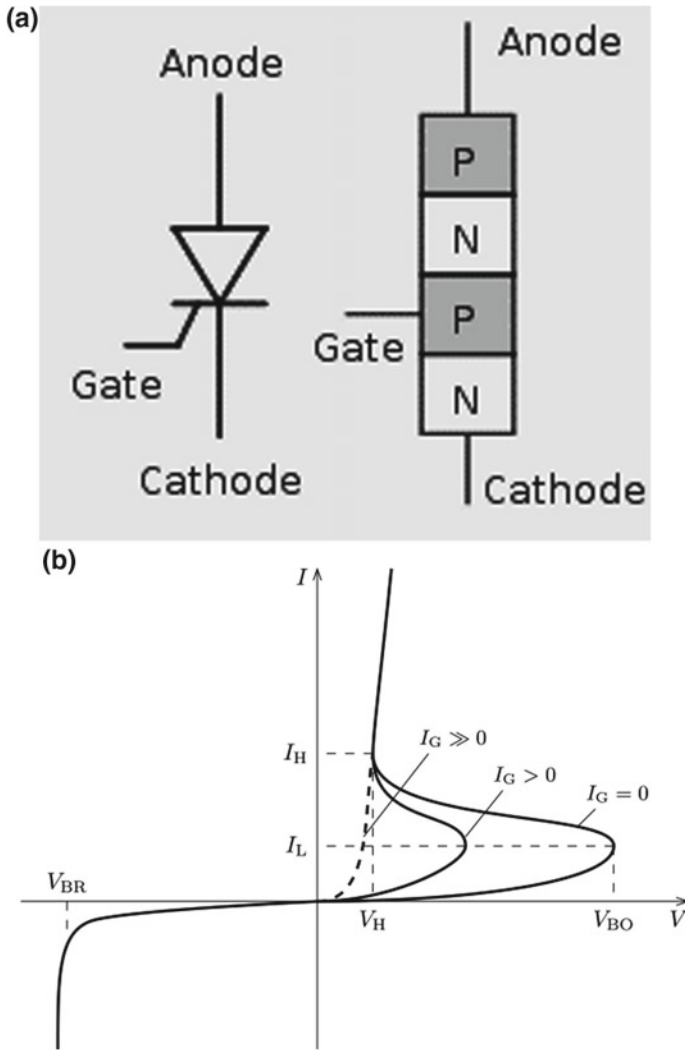


Fig. 24 a Thyristor structure. b IV characteristics

- Bipolar junction transistors (BJTs).
- Power MOSFETs.
- Insulated-gate bipolar transistors (IGBTs).

d. Bipolar Junction Transistors (BJTs)

Power bipolar junction transistor (BJT) is the first semiconductor device that allows full power control through its turn-on and turn-off operations. The BJT behavior is a current-controlled device with typical IV characteristics as shown in Fig. 25. It is

used in power converters at frequency below 10 kHz and power ratings up to 1200 V, 400 A.

When $V_{BE} > 0$, $I_B > I_{TH}$ conduction (on) mode.

When $V_{BE} < 0$, $I_B < I_{TH}$ no conduction (off) mode.

As that of a power diode, BJT has large off-state blocking voltage and large on-state current density which makes the BJT losses relatively high.

BJT has low DC gain (β) and large saturation voltage V_{CEsat} . The NPN structure is mostly preferred than PNP in power control due to its higher switching speed. Typical absolute maximum rating for a high-power BJT **BUV48A from STMicroelectronics** is given in [8], where we can deduce that BJT power transistor consumes excess power loss in both input and output circuits due to the values of V_{BE} , I_B and V_{CE} at saturation. Other electrical parameters for the BJT **BUV48A** with test conditions—pulse test: pulse duration $\leq 300 \mu s$ and duty cycle $\leq 2\%$ —are also available in [8].

e. Power Metal–Oxide–Semiconductor Field-Effect Transistors (MOSFETs)

The MOSFET is a three-terminal device that works as voltage-controlled current source. The MOSFET behavior is a voltage-controlled device with typical IV characteristics as shown in Fig. 26 where we can deduce that the MOSFET can be used as a switch between drain D and source S under the control of voltage between gate and source V_{GS} .

The ON-state resistance of a MOSFET has no theoretical limit, so the ON-state loss can be far lower than a BJT. The ON and OFF switching time of a MOSFET depends on the presence or absence of a key charge quantity in the device and is equal to the time required to insert or remove this controlling charge quantity. It is

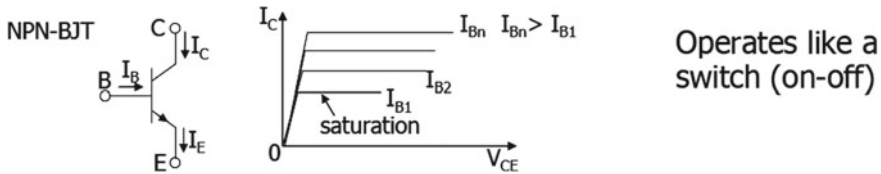


Fig. 25 NPN BJT symbol and typical IV characteristics

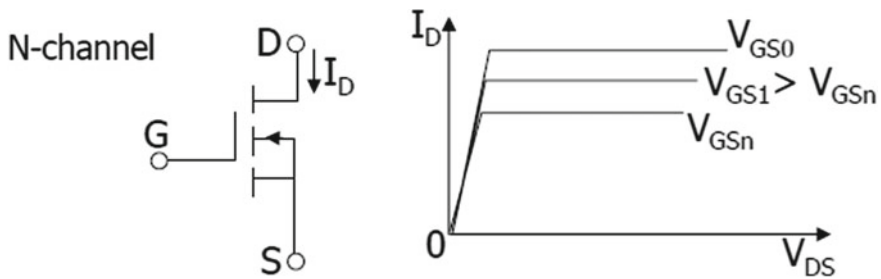


Fig. 26 MOSFET symbol and typical IV characteristics

used in high-speed power converters at frequency range of several tens of kHz and power ratings up to 1000 V, 100 A (relatively low power ratings).

When $V_{GS} > V_{GTH}$, conduction (on) mode $I_D > 0$.

When $V_{GS} < V_{GTH}$, no conduction (off) mode. $I_D = 0$.

V_{GTH} is the threshold voltage of the MOSFET defined as the voltage between gate and source at which the device starts conducting.

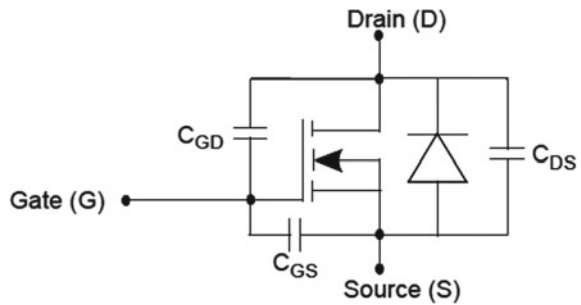
The input circuit consumes almost no power; hence, there is no need to drive current from the control circuit like μ -controllers or CMOS logic gates which in most cases have low drive current capabilities. A MOSFET has positive temperature coefficient for the ON-state resistance, which makes it easy to parallel many small devices to deliver higher current. Figure 27 gives the equivalent circuit of a MOSFET with a parasitic capacitor and body diode. When applying high input to the gate, the capacitor C_{GS} starts charging. As soon as V_{GS} reaches V_{GTH} , I_D starts increasing from zero to its steady-state value. During this period, the gate current charges also both capacitors, C_{GS} and C_{GD} . The drain-to-source voltage remains at V_{DS} so long as the drain current (I_D) reaches the steady-state value (I_D). The time required for drain current to reach its steady-state value " I_D ", as shown in Fig. 28, is known as the current rise time T_{RI} . When drain current reaches I_D , V_{GS} is clamped to V_{GSID} , and the entire gate current starts flowing through C_{GD} to charge it. This causes the drain-to-source voltage V_{DS} to drop. The rate of change of V_{DS} is given by Eq. 14.

$$I_{GATE} = \frac{(V_G - V_{GSID})}{R_G}$$

$$\frac{\Delta V_{DS}}{\Delta t} = \frac{I_G}{C_{GD}} \quad (14)$$

The sequence is reversed when the MOSFET is turned OFF. The gate-to-source voltage first decays to V_{GSID} , and then the drain-to-source voltage starts rising toward V_{DS} . As shown in Fig. 29, when the drain-to-source voltage reaches its steady-state value (V_{DS}), I_D starts decaying toward zero, and also V_{GS} and I_G decay to zero. The time required for I_D to reach zero is known as turn-off delay T_{FI} . There are three types of losses in a MOSFET:

Fig. 27 MOSFET equivalent circuit



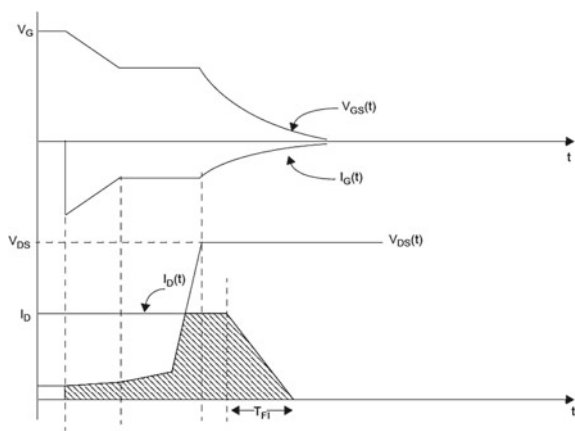


Fig. 28 MOSFET turn-on characteristics

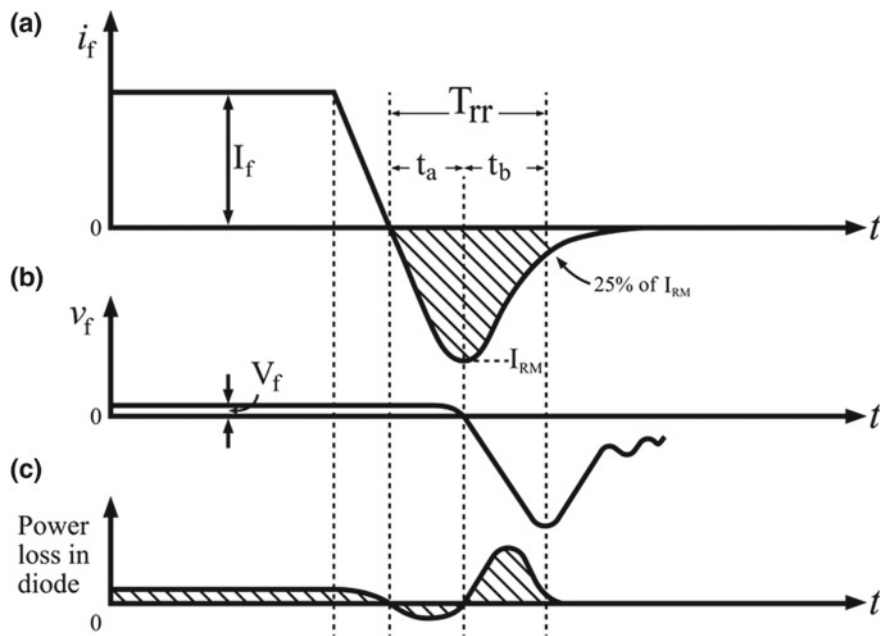


Fig. 29 MOSFET turn-off characteristics

1 – Conduction loss, 2 – Switching loss and 3 – Gate charge loss.

At low frequencies, conduction loss is dominant, but as we begin switching at frequencies between 100 and 150 kHz, switching and gate charge losses start contributing a significant amount of power dissipation. Conduction loss depends on the ON-state resistance of MOSFET ($R_{\text{DS(on)}}$), which can be reduced by selecting a low $R_{\text{DS(on)}}$ MOSFET.

The switching losses of the MOSFET are given by the area under the waveforms of V_{DS} and I_{D} , shown shaded in Figs. 28 and 29. The switching losses of the MOSFET can be reduced by selecting a MOSFET with lower C_{DS} capacitance and shifting the current I_{D} and the voltage V_{DS} waveform to reduce the overlap period during transition. Loss due to gate charge is caused by charging the gate capacitance and then dumping the charge to ground in every switching cycle. For practical considerations, a lower $R_{\text{DS(on)}}$ device comes with high gate capacitance which limits the switching speed (longer turn-on and turn-off time) and increases switching losses. While selecting a MOSFET driver, care must be taken to ensure that the driver can source and sink the maximum peak current required by a MOSFET gate to turn ON and OFF in a given specified time. A MOSFET gate needs large current as the device turns ON and, for the rest of the period, a high gate-to-source voltage at low current level. The general rule of faster switching time to reduce the switching loss will cause high-frequency noise because of high $\Delta V/\Delta t$ and high $\Delta I/\Delta t$, which may cause an increase of the EMI filter size. The safe operating area (SOA) of a MOSFET is decided by maximum drain current $I_{\text{D(MAX)}}$, internal junction temperature T_{J} and the breakdown voltage BV_{DS} rating. There are two basic ways to avoid the MOSFET over stressing: using device with a higher rate or using snubber circuit [3].

f. Insulated-Gate Bipolar Transistor (IGBT)

The IGBT is a power switching transistor which combines the advantages of MOSFETs and BJTs for use in power supply and motor control circuits, which makes it ideal as a semiconductor power solid-state switch. The result of this hybrid combination is that the “IGBT” has the output switching and conduction characteristics of a bipolar transistor but is voltage-controlled like a MOSFET. High-current and high-voltage BJTs are available, but their switching speeds are slow, while power MOSFETs may have higher switching speeds, but high-voltage and high-current devices are expensive and hard to achieve. The advantage gained by the insulated-gate bipolar transistor device over a BJT or MOSFET is that it offers greater power gain than the standard bipolar-type transistor combined with the higher voltage operation and lower input losses of the MOSFET. In effect, it is a FET integrated with a bipolar transistor in the form of Darlington-type configuration as given in Fig. 30 which gives the IGBT structure, symbol and IV curve.

Also, the IGBT has a much lower “on-state” resistance, R_{ON} , than an equivalent MOSFET. This means that the I^2R drop across the bipolar output structure for a given switching current is much lower. The forward blocking operation of the IGBT is identical to a power MOSFET.

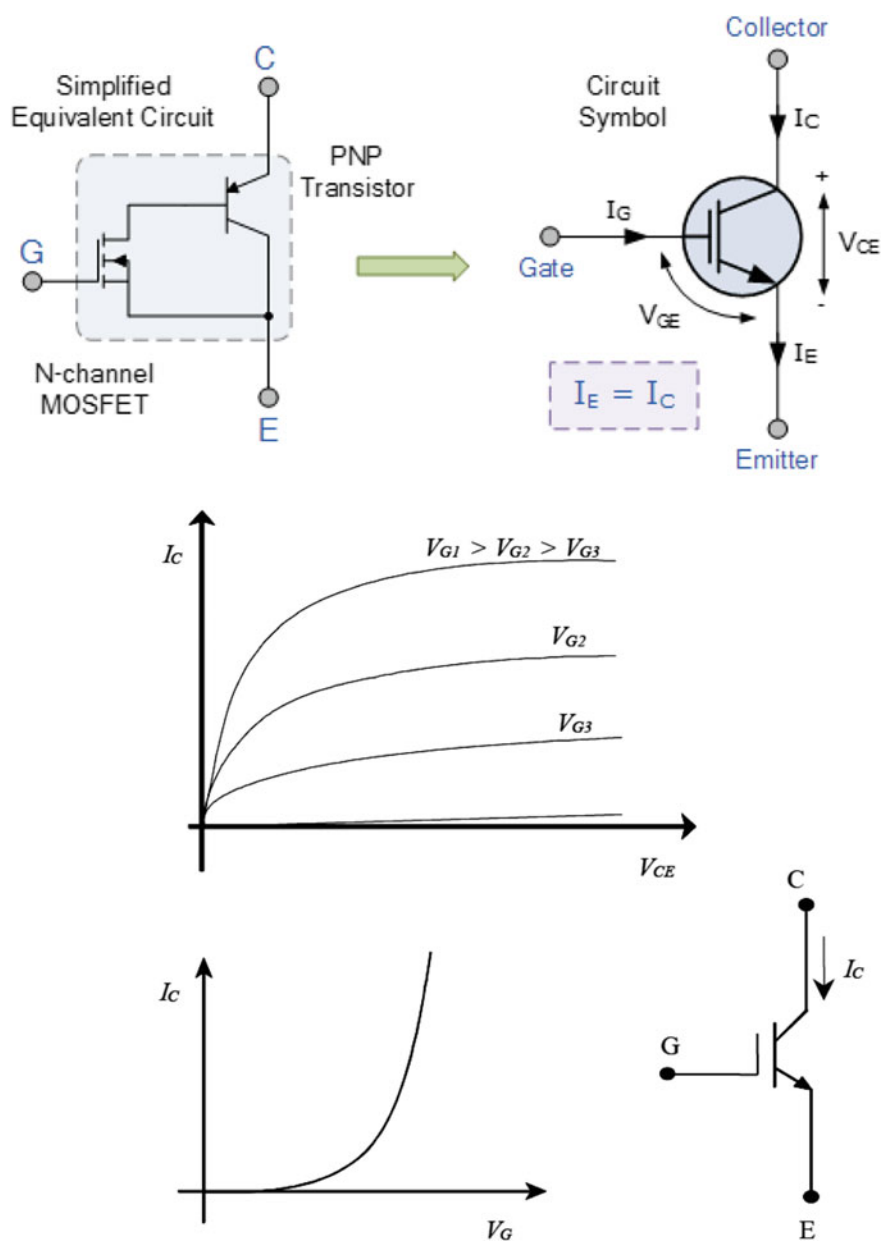


Fig. 30 IGBT structure and IV characteristics [9]

When used as static controlled switch, the insulated-gate bipolar transistor has voltage and current ratings similar to that of the bipolar transistor. However, the presence of an isolated gate in an IGBT makes it a lot simpler to drive than the BJT as much less drive power is needed.

An insulated gate bipolar transistor is simply turned “ON” or “OFF” by activating and deactivating its Gate terminal. Applying a positive input voltage signal across the gate and the emitter will keep the device in its “ON” state, while making the input gate signal.

The main advantages of using the insulated-gate bipolar transistor over other types of transistor devices are its high-voltage capability, low ON-state resistance, ease of drive, relatively fast switching speeds and combined with zero gate drive current makes it a good choice for moderate speed, high-voltage applications. Different applications of power semiconductor devices are shown in Fig. 31. Recently, Toshiba introduced a modified structure of the IGBT named as the injection-enhanced gate transistor (IEGT). It is a voltage-driven device for switching large current. IEGTs are fabricated using a unique emitter structure. The outstanding turn-off performance and the wide safe operating area of IEGTs make it possible to reduce the power consumption, shrink the size and improve the efficiency of equipment. Figure 32 gives the market share between several suppliers.

The design of the passive components of a given DC/DC converter is beyond the scope of this chapter; the reader may find more details about the design of the coupling transformer and smoothing filter in the literatures. The appropriate SMPS topology can be selected based on input voltage, output power and output current

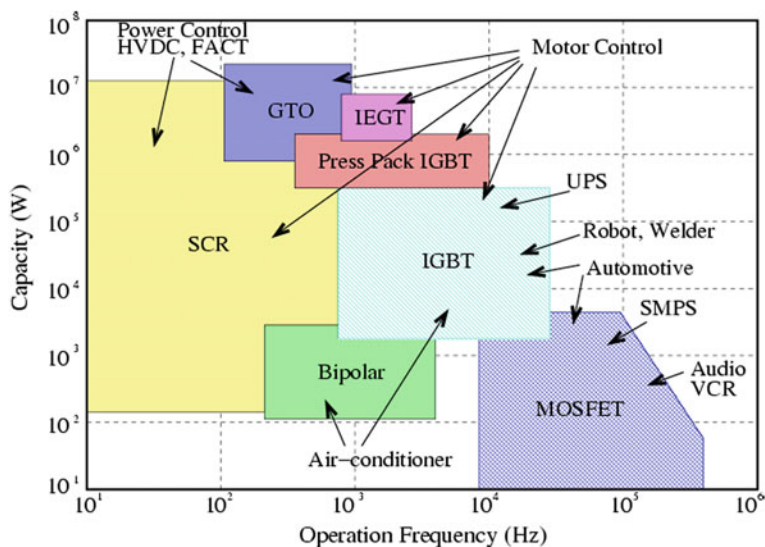


Fig. 31 Power versus switching frequency

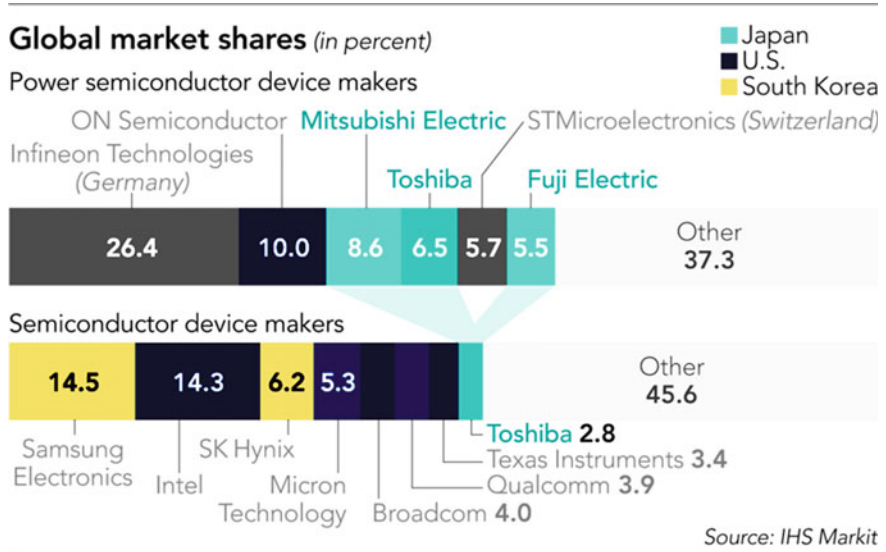


Fig. 32 Power semiconductor market [10]

Table 1 SMPS selection guide [1]

Input voltage	Output power	Preferred topology
Universal input (90–264) V_{AC}	$P_o < 150\text{ W}$. Load current $< 10\text{ A}$	Flyback, forward
Universal input (90–264) V_{AC}	$P_o < 150\text{ W}$. Load current $> 10\text{ A}$	Forward
Universal input (90–264) V_{AC}	$150\text{ W} < P_o < 350$	Two-switch forward, half-bridge, push–pull
Universal input (90–264) V_{AC}	$P_o < 500\text{ W}$	Half-bridge, push–pull
$V_{in} > 350\text{ V}_{DC}$	$P_o < 750\text{ W}$	Half-bridge
$V_{in} < 200\text{ V}_{DC}$	$P_o < 500\text{ W}$	Push–pull
$V_{in} > 350\text{ V}_{DC}$	$500 < P_o < 1000\text{ W}$	Full-bridge
$V_{in} > 350\text{ V}_{DC}$	$P_o > 1000\text{ W}$	ZVT full-bridge
$V_{in} > 350\text{ V}_{DC}$	$P_o > 2000\text{ W}$	More than one ZVT full-bridge in parallel, interleaved with more than one ZVT full-bridge

(see Table 1). The selection of topology may differ to meet some of the specific requirements of the power supply including cost, size and personal experience of the designer.

g. The Power Module

The power modules can be built either using discrete devices available from several suppliers [7] or using complete power modules like that shown available from CREE [11].

h. The Control Module

The control function can be implemented using analog or digital techniques to produce pulse-width modulation (PWM) signal that drives the power devices [5]. The digital control can be accomplished using programmable digital circuits mainly μ -controller-based or field-programmable gate array (FPGA) where any of them may be programmed to implement the perturb and observe (P&O) algorithm or the incremental conductance method.

i. The Driver Circuit

Driver circuits are most commonly used to amplify signals from controllers or micro-controllers in order to control power switches in semiconductor devices. Driver circuits often take on additional functions which include isolating the control circuit and the power circuit, detecting malfunctions, storing and reporting failures to the control system, serving as a precaution against failure, analyzing sensor signals and creating auxiliary voltages. Transformers or optocouplers (OCs) are often used for isolation. Figure 33 shows typical driver circuit for power MOSFET where the 4N25 OC is used for isolation.

j. Integrated Circuit Driver

The driver circuits for both MOSFET and IGBT are available in single IC chip from different manufacturers. Fig. 34 examples of integrated driver: TLP 5214 driver

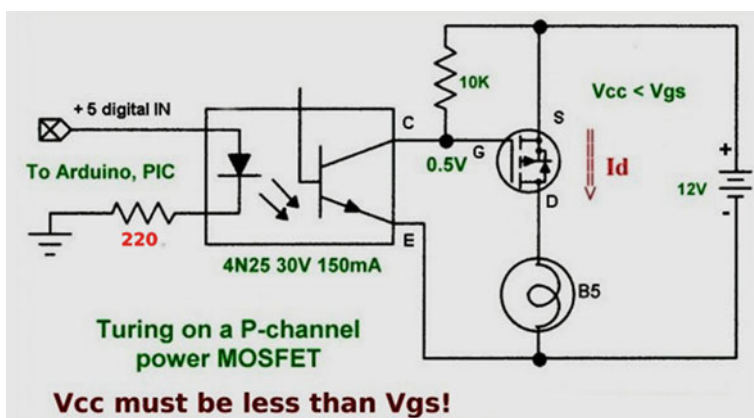
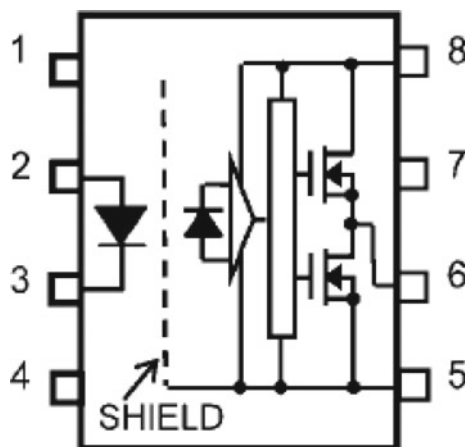
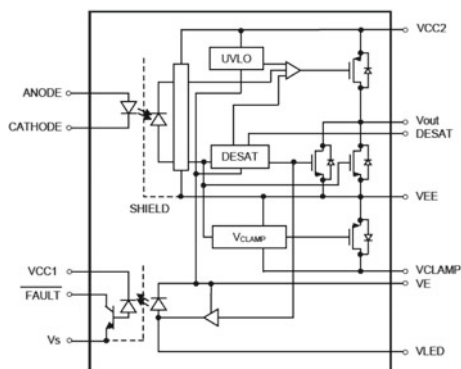


Fig. 33 Typical driver circuit for power MOSFET

Fig. 34 TLP 5214 internal circuit [12], an example of integrated driver circuits.
TLP 352 internal circuit [13]



TLP 352 internal circuit [15].



[12], TLP 352 driver [13]. The TLP 352 is a DIP8 package that contains optocoupler and two MOSFET driver circuits in totem pole output that can both sink and source current. The TLP 352 is ideal for IGBT and power MOSFET gate drive.

17 Design of MPPT

In order to optimally design MPPT module for a given PV array, several parameters must be considered. These parameters are related to different constraints needed to be defined before starting the design and define the needed components. We can summarize these design parameters as:

- The input voltage range.
- The output voltage range.

- The input–output voltage relation.
- The power available from the source and that needed by the load.
- The load profile: constant voltage, constant current and constant power.
- The load type: resistive, reactive, electric load only or electromechanical (e.g., DC motor drive water pump in irrigation system).
- The load dynamic behavior: static (e.g., battery charger, low-speed (motors + mechanical load) and high-speed time variation (e.g., digital electronic circuits or computer board).
- After defining the above parameter which may impose some constraint on the design, we have to decide about the suitable component to be used for implementing the basic building blocks described in Sect. 4. With the help of information provided above in this chapter, we can decide about:
 - The topology of the DC/DC converter that will act as a MPPT.
 - The power switch type needed to meet the power input–output ranges (MOSFET BJT or IGBT).
 - The load directly coupled or need some galvanic (transformer) isolation.
 - The control type: analog or digital.
 - The sensor needed to complete the closed-loop function of the controller.
 - The control algorithm.
 - The type of the μ -controller: P&O or incremental conductance.
 - The capabilities of the μ -controller as regarding: processing speed, resolution of analog-to-digital converter and mathematical efficiency (support floating point or some digital signal processing algorithms).
- Power consumption of the control circuit and switch losses.

The scope of this book cannot cover the consideration of the above constraints when designing an MPPT, but we can consider a design example to demonstrate how we can make use of the information given in this chapter.

Design Example:

Example 2 Design an MPPT used in PV solar streetlamp with lamp power = 24 W at 12 V.

Solution

The system under consideration is an off-grid solar streetlamp. The solar streetlamp consists of high-power LEDs, a lead-acid battery, a solar controller and a solar panel. Assuming the streetlamp is to be illuminated for 12 h/day in the evening, and then the total energy needed by the load will be:

$$\text{The Lamp Energy Consumption/day} = 24 \times 12 = 288 \text{ Wh.}$$

Assuming 15% losses in MPPT and the battery charger circuit, then the needed energy to be supplied from the PV source will be:

$$\text{PV energy} = 288 \times 1.15 = 331.2 \text{ Wh}$$

Excess solar capacity needs to be considered for charge recovery from a cloudy day giving the designer a fixed number of days from which to recover from a series of cloudy days (recharge time). Assuming 20% cloudy days/year, then about 20% PV excess energy is needed. Assuming on the average 5 h insulation/day, then the power of the PV panels needed is:

$$\text{PV panel power} = 331.2 \times 1.2/5 = 80 \text{ W}$$

From the available panel in the market, we can select 80 W module ready for 12 V battery charging with

$$V_{OC} = 19.8 \text{ V} \quad \text{and} \quad I_{SC} = 5.95 \text{ A} \quad \text{and} \\ V_{MPP} = 14.95 \text{ V} \quad \text{and} \quad I_{MPP} = 5.35 \text{ A}$$

At STC (1000 W/M², 25 °C)

From the above data, we can decide about the following constraints about the MPPT:

$$V_{IN} 12 \text{ V} < V_{IN} < 21 \text{ V}$$

$$V_{OUT} 11.8 \text{ V} < V_{OUT} < 13.8 \text{ V}$$

This output voltage limit is imposed by the 12 V battery charging states.

$$I_{IN} 0.6 \text{ A} < I_{IN} < 6.5 \text{ A}$$

The suitable topology for implementing an MPPT for the above requirements is the flyback converter given in Fig. 9. The following components can meet the design constraints:

Q1 is a power N-MOSFET 60 V 30 A (with built-in flywheel diode) from ON semiconductor ref. NTD5414NT4G.

D1 is a Schottky power rectifier from On semiconductor ref. MBR3100RLG.

D2 is a 100 V Schottky diode from ON semiconductor ref. MBR1100RL.

C is a cap. 16 V 220 μF ± 20% from United Chemi-Con ref. ESMG160ELL221MF11D.

The transformer is 28.6 μH 10% from ICE ref. TO08029.

The snubber circuit parameters are:

C ceramic chip capacitor 560pF from Vishay ref VJ1206Y561KBBAT4X.

R 10 KΩ resistor ± 1.0% from Vishay/Dale ref CRCW120610R0FKEA.

Using the output–input relation for the flyback converter (Eq. 8) and with $N_S/N_P = 1$ and using the minimum and maximum values for V_{OUT} and V_{IN} , we can find the duty cycle range as: $0.512 < D < 0.559$. The driver circuit for the power MOSFET may be the TLP 352 given above. The pulse-width modulator can be implemented using any general purposes μ-controller board, for example Arduino

Uno with built-in PWM and 10-bit analog-to-digital converter. The panel current and voltage are measured using current and voltage sensors and used in the P&O algorithm to control the duty cycle of the PWM in the above range of the duty cycle D .

18 Conclusions

This chapter deals with power electronics and design aspects related to MPPT for PV systems. The basics of switched-mode power supplies are covered in detail where attention is focused on hardware and circuit design. An MPPT for PV panels is simply a DC to DC converter based on the SMPS principle of operation while considering the nonlinear IV characteristics of the PV panel as a power source. The different topologies for the MPPT are given in detail with some comparative analysis which may help the reader to choose the topology which matches the requirements of the considered PV installation. The specification of the electronic components used for circuit building is given in detail with some practical examples. Several techniques for building PV MPPT using analog or digital and microcontroller-based control algorithms are also presented without going into the details of the algorithms. MPPT algorithms are simple enough, but implementing a working MPPT controller is not a simple task, because it is required to know the particularities of the underlying switching converter and the load profile and type. Using computer simulation methodologies available in most of scientific papers published on MPPT is helpful, but for real hardware, the readers find themselves lacking vital information. Through this chapter, the needed HW information is covered with specifications, circuit analysis and design examples. The reader will be then able to design, implement and test an MPPT circuit for a given load profile.

References

1. Switched mode power supply reference manual (2014) ON Semiconductor, www.onsemi.com
2. Eltalmaly AM (2015) Performance of smart maximum power point tracker under partial shading conditions of photovoltaic systems. *J Renew Sustain Energy* 7(4): 043141
3. Solar Energy Fundamentals, Technology, and Systems, Klaus Jäger, Olindo Isabella, Arno H.M. Smets, René A.C.M.M. van Swaaij, Miro Zeman, Copyright Delft University of Technology, 2014
4. Switch Mode Power Supply Topologies Compared, www.we-online.com/midcom
5. Abou El- Ela M, Roger JA (1984) Optimization of the function of a photovoltaic array using feedback control system. *Solar Cells*, 13:107–119
6. Power semiconductor applications philips semiconductors, https://threeurons.files.wordpress.com/2011/08/pwrfet_use.pdf
7. <https://www.microsemi.com>
8. BUT70 W data sheets, <https://www.st.com/resource/en/datasheet/but70w.pdf>
9. Fundamentals of MOSFET and IGBT Gate Driver Circuits, Laszlo Balogh, Texas Instrument Application Report SLUA618—March 2017—Revised SLUP169—April 2002

10. Evolution of Power Semiconductor Devices, <http://www.iue.tuwien.ac.at/phd/park/node14.html>
11. <https://www.wolfspeed.com/power>
12. TLP 5214 data sheets, <https://toshiba.semicon-storage.com/info/docget.jsp?did...TLP5214>
13. TLP 352 data sheets, <https://toshiba.semicon-storage.com/info/docget.jsp?did...TLP352>

Maximum Power Extraction from the Photovoltaic System Under Partial Shading Conditions



Hassan M. H. Farh and Ali M. Eltamaly

Abstract Partial shading condition (PSC) has a bad effect not only on the shaded PV modules/arrays itself but also on the output power generated from the partially shaded photovoltaic (PSPV) system. It reduces the output power generated from the photovoltaic (PV) system and contributes in hot spot problem that may lead to thermal breakdown of shaded PV modules. Under PSC, multiple peaks, one global peak (GP) and many other local peaks (LPs) are generated in the P – V curve. This chapter concentrates on alleviating the partial shading effects and extracting the global maximum power available from the PSPV system. This has been achieved using the suitable and the best PV system design topologies and the efficient maximum power point tracker (MPPT) techniques in tracking the GP under PSC. Therefore, it is concluded that the partial shading (PS) mitigation techniques can be classified into PV system design topologies and MPPT techniques to not only alleviate the PS effects of the PSPV system but also to extract the GP. The PV system design topologies consist of the bypass and blocking diodes, PV system architectures, PV array configuration and PV array reconfiguration, whereas the MPPT techniques concentrate the most efficient heuristic MPPT in tracking the GP under PSC.

1 Introduction

Renewable energy systems are considered as the power of the future. Solar photovoltaic (PV) energy systems represent the most promising option of the renewable generation systems (RGSs) which are clean, abundant, noise-free and friendly to

H. M. H. Farh

Electrical Engineering Department, College of Engineering, King Saud University, Riyadh 11421, Saudi Arabia

e-mail: hfarh1@ksu.edu.sa

A. M. Eltamaly (✉)

Electrical Engineering Department, Mansoura University, Mansoura, Egypt

e-mail: eltamaly@mans.edu.eg

Sustainable Energy Technologies Center, King Saud University, Riyadh 11421, Saudi Arabia

© Springer Nature Switzerland AG 2020

A. M. Eltamaly and A. Y. Abdelaziz (eds.), *Modern Maximum Power Point Tracking Techniques for Photovoltaic Energy Systems*, Green Energy and Technology, https://doi.org/10.1007/978-3-030-05578-3_4

107

the environment compared to the conventional energy resources such as natural gas, fossil fuel, coal, etc. For these reasons, RGSs, especially solar and wind, are attracting interest all over the world. In addition, tracking the maximum power from these RGSs and choosing a suitable power electronics converter that matches the utility grid requirements are considered to be a hot development area as it can improve the system's efficiency, reliability, power quality and flexibility [1–9].

Partial shading problem occurs when some PV cells and/or modules are shaded due to different reasons. It may occur due to reasons related to the site itself, which can be overcome at the beginning during the PV system installation. For example, choosing the suitable and best sites for the PV system installation in terms of site characteristics (temperature and irradiance) and no nearby buildings and towers may play a significant improvement in the output power generated and overall efficiency of the PV system. On the other hand, it may occur due to inevitable reasons such as neighbouring buildings, towers, trees, dust, degradation due to ageing and moving clouds or some other objects. The shaded PV cells/modules are forced to carry the high current of the other unshaded cells/modules and consume power—act as a load—instead of generating power. As the percentage of the shading area increases, the power losses also increase and the output power decreases. The partially shaded photovoltaic (PSPV) condition reduces the generated power and contributes to hot spot problems that may lead to thermal breakdown of shaded PV modules. Therefore, the shaded PV cells/modules/arrays have a negative effect on the output power captured and overall efficiency of the PSPV system. The power losses of the PV system due to partial shading or inaccurate global maximum power tracking is extraordinarily high and may exceed 70% of the total power generated. Consequently, tracking the global maximum power is of interest in order to achieve high power efficiency, less power losses and high output power [10–13].

Under the uniform condition, a unique peak will be generated as shown in Fig. 1a. On the other hand, under partial shading conditions (PSCs), different radiation on each PV array generates different power from one PV module/array to another. In addition, multiple peaks, one global peak (GP) and many local peaks (LPs) will be generated due to using bypass diodes for protecting the shaded PV modules/arrays from the hot spot points and thermal breakdown as shown in the P – V characteristic of Fig. 1b.

Conventional MPPT techniques especially incremental conductance (IncCond) and perturb and observe (P&O) followed by hill climbing (HC) and constant voltage (CV) are efficient, accurate and reliable in tracking the unique peak under uniform conditions (unshaded) but they fail to track the GP and stick at the first peak regardless of whether it is GP or LP under PSCs [5, 14, 15]. Whereas, heuristic MPPT techniques-based bio-inspired such as flower pollination [16], ant bee colony [17, 18], firefly [19, 20], ant colony [21], cuckoo Search [22], particle swarm optimization (PSO) [12, 22–25] and grey wolf optimizer (GWO) [26] algorithms can follow the GP under PSCs.

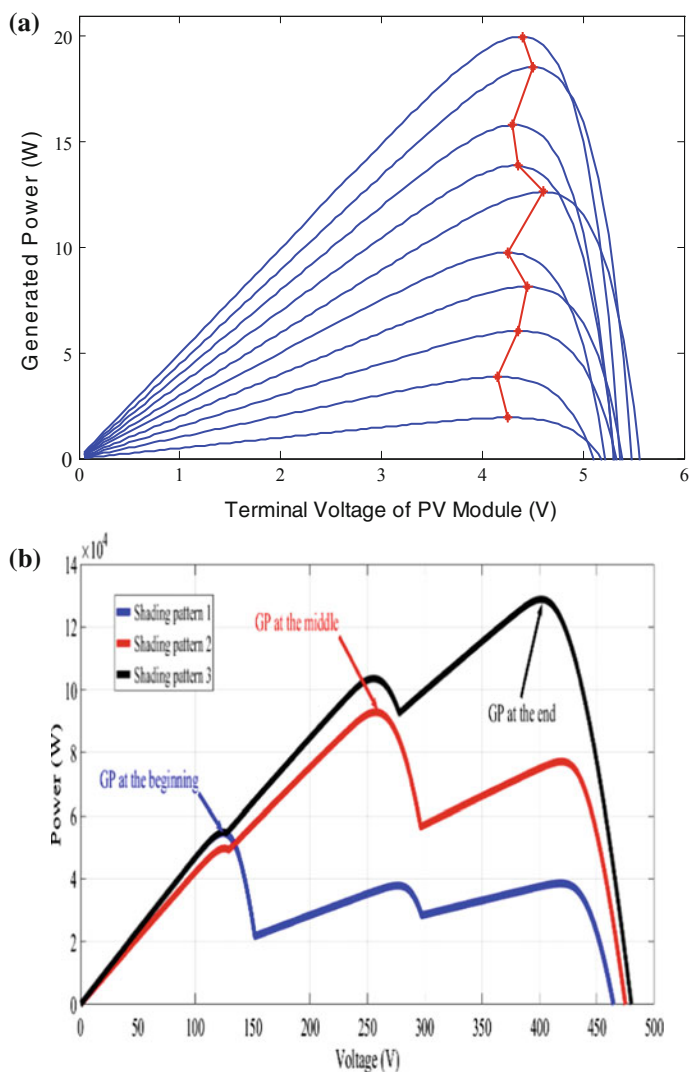


Fig. 1 P - V characteristic of the PV array: **a** uniform condition and **b** partial shading conditions

2 Partial Shading Mitigation Techniques

PS mitigation techniques have been classified into two major categories which are PV system design topologies and MPPT techniques as shown in Fig. 2. This chapter will concentrate on the PV system design topologies to maximize the output power generated and alleviate the PS effects. The PV system design topologies include the bypass and blocking diodes, PV system architectures, PV array configuration and PV

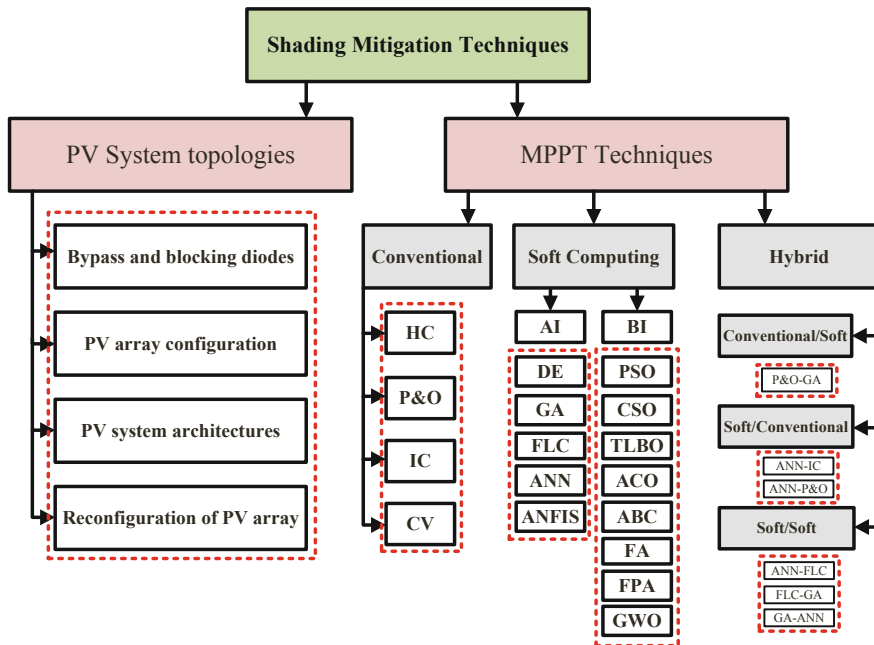


Fig. 2 Classification of PSPV mitigation techniques

array reconfiguration. Also, it will concentrate on the most efficient heuristic MPPT techniques such as PSO, GWO and FPA that can track the GP under PSC.

2.1 PV System Topologies

2.1.1 Bypass and Blocking Diodes

Bypass diodes are connected across one or more PV modules while the blocking diode is connected in series with the PV array to prevent the reverse current from flowing through shading modules. Under uniform conditions, the bypass diode will be in reverse bias but it will be in conduction mode under non-uniform or PSCs as shown in Fig. 3. The bypass diode has two basic important functions [13, 27–29] which are as follows:

- (1) Protection of the PV module against hot spot problem and thermal breakdown that may be occurred. High reverse voltage will be generated across the shaded cells or modules that are not protected using bypass diodes. Therefore, it consumes instead of generating power [12, 13]. Therefore, the power losses

Fig. 3 PV array with the bypass and blocking diodes

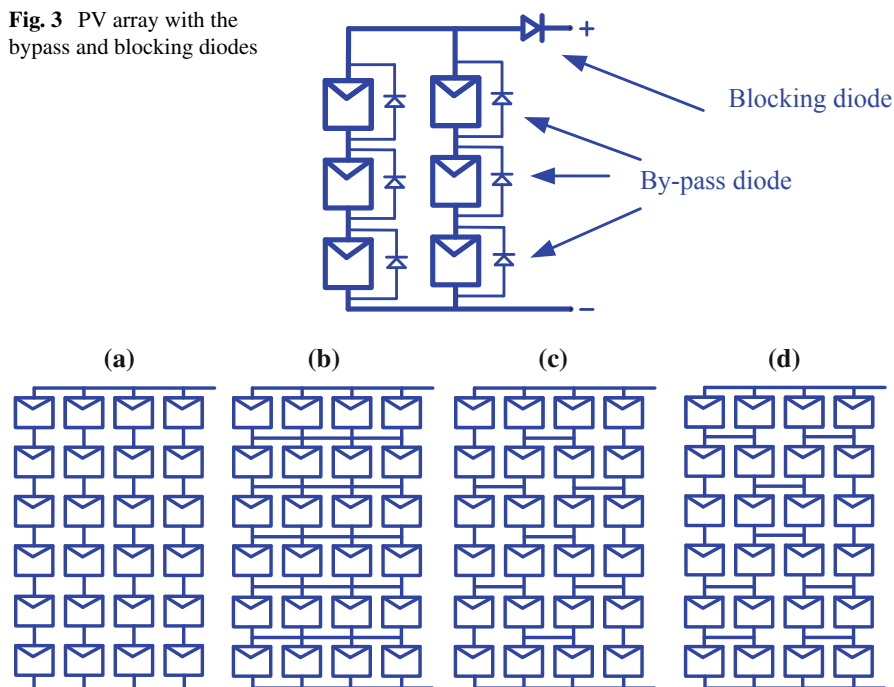


Fig. 4 PV array configurations: **a** SP, **b** TCT, **c** BL and **d** HC

increase and the total output power generated and the PV system's efficiency both decrease.

- (2) Reduces the reverse voltage drop across the shaded cells in the modules, thus limiting the shading voltage drop to the diode reverse voltage (0.4–0.7 V). The diode reverse voltage improves the overall output voltage of the module. In addition, the consumed power of the shaded cells will be reduced. This power consumption reduction leads to a reduction in the local heating at the shaded area and extends the lifetime of the modules [30]. As a result, it alleviates the PS effects considerably [13].

2.1.2 PV Array Configuration

Partial shading effects can be alleviated using different configurations for the PV modules. In recent advances, several PV array configurations have been presented in many literatures [31–34] such as series, parallel, series–parallel (SP), total-cross-tied (TCT), bridge-linked (BL) and honeycomb (HC) configurations. The most famous PV array configurations are SP, TCT, BL and HC configurations which are shown in Fig. 4.

Table 1 Merits and demerits of different PV array configurations

Configuration	Merits	Demerits
SP	<ul style="list-style-type: none"> • Efficient under uniform conditions • Good cost efficiency • Low complexity 	<ul style="list-style-type: none"> • SP is more sensitive to different radiation levels than others, and the power decreases sharply during PS • Not applicable with PS
BL	<ul style="list-style-type: none"> • Applicable with PS • BL has higher peak power by 2.5% than SP • Continue to feed the grid during PS 	<ul style="list-style-type: none"> • Medium complexity • Moderate efficiency
TCT	<ul style="list-style-type: none"> • Applicable with PS • TCT has better performance, less susceptible to PS, more reliable, higher peak power values and efficiency • Continue to feed the grid during PS 	TCT has maximum wiring connection and the complexity is higher than other configurations
HC	<ul style="list-style-type: none"> • Applicable with PS • Medium MPP improvement • Continue to feed the grid during PS 	<ul style="list-style-type: none"> • Medium complexity • Moderate efficiency

Kaushika et al. [35] investigated the performance of the three different configurations (SP, TCT and BL) in PV arrays to find which configuration was less susceptible to the PS problem and electrical mismatch. The results proved the superiority of TCT and BL in terms of maximum power and fill factor for all cases of fresh cells, soiled cells and even shaded ones [35]. This is supported by the studies of Karatepe et al. [36] and Wang et al. [37] which revealed that TCT performs better compared to other configurations in terms of maximum power, fill factor and normalized array efficiency using two different methods, the analytical method and piecewise linear parallel branches model [36, 37]. On the other hand, SP is more sensitive to different radiation levels than others, and the power decreases sharply during PSCs. Also, the grid power decreases rapidly for the SP, whereas TCT and BL continue to feed the grid even after the occurrence of PSCs. In addition, TCT and BL configurations increase the maximum power by 2.3 and 3.8%, respectively, compared with the SP configuration [31, 38]. In conclusion, TCT has better performance, less susceptible to PS effects, more reliable, higher maximum power and efficiency. Table 1 shows the merits and demerits of different PV array configurations.

2.1.3 PV System Architectures

PV system architectures refer to the art of designing and constructing PV modules. Different PV architectures can track the GP of individual PV modules. Hence, the PV architectures which enable MPPT for each module will be more suitable for partial shading, but this will increase the overall cost of the system. The PV system architectures can be classified into centralized architecture, series-connected

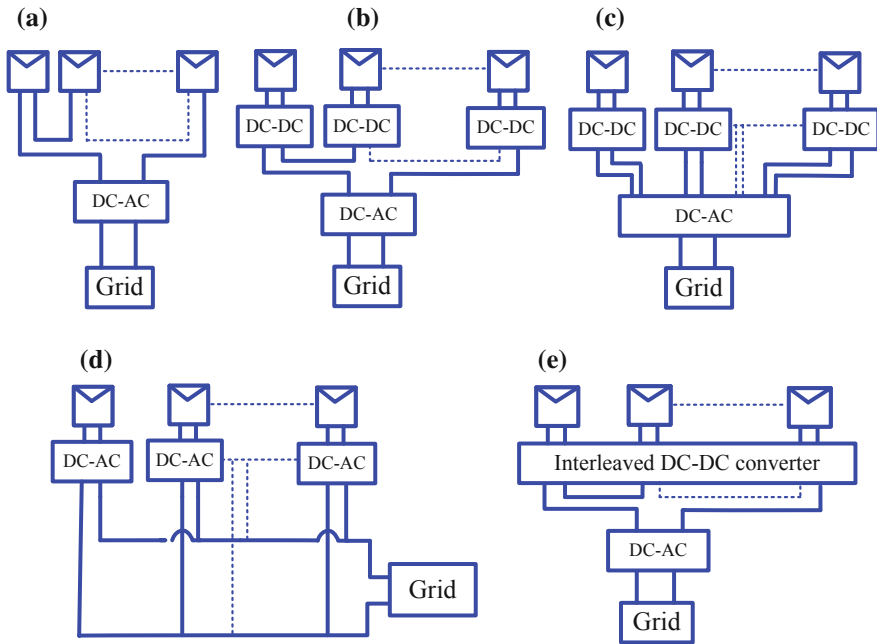


Fig. 5 PV system architectures: **a** centralized, **b** series-connected MIC, **c** parallel-connected MIC, **d** micro-inverters and **e** interleaved DC–DC converter

micro-converters, parallel-connected micro-converters, micro-inverters and interleaved DC–DC converter which are shown in Fig. 5 [5, 31, 39]. Centralized architecture is the most conventional architecture and tracking of the GP of individual PV modules is not available. Therefore, this architecture is more susceptible to PSC and electrical mismatch loss (MML). However, it is suitable to low-cost and low-power PV systems [40]. This type of architecture also cannot achieve GP tracking for each individual module; therefore, it will cause lower MML while tracking the MPP of individual PV modules. To avoid this shortage, both the series-connected and parallel-connected MICs apply a DC–DC converter to track the GP of each MIC and then feed the resulting power to a central inverter. These two methods increase the cost to some extent due to the cost brought by the application of a large amount of power electronics [31, 41]. MIC topology is adequate to PSC to extract the maximum power available from the whole PV system where each PV array extracts its own MPP through its own MPPT controller [40, 42]. Hence, both series-connected and parallel-connected MICs can track the GP where series-connected MIC can be used in high-voltage applications while parallel-connected MIC can be used in low-voltage applications and enhance the DC-link voltage regulation.

One of the earliest works on interleaved DC–DC converter, dated back to over 40 years ago where it was used to design a power supply for the Jet Propulsion Laboratory [43]. Benyahia et al. [44] investigated the P&O MPPT performance with

IBC for fuel cell generators supplying electricity to power trains. In another study, Arango et al. [45] proposed an asymmetrical interleaved DC–DC converter and a voltage multiplier cells combined together (boost, buck-boost and flyback-based) for PV and fuel cell applications to achieve high output voltage and ripple reduction in the generator and load. However, variable DC-link voltage was generated and two DC–DC converters had to be used for each PV array that resulted in total cost increase. A study by Deihimi et al. [46] also investigated the performance of variable IBC (series-connected) but it interfaced with multi-energy sources of different outputs. Although variable IBC provides higher voltage gains in addition to a wide range of applications from low to high voltage/power, the DC-link voltage is unstable (variable) [47]. Hence, the whole system will operate in asymmetric condition and the maximum power generated from PSPV cannot be captured. Therefore, variable IBC is not able to mitigate and fix the DC-link voltage variations. As a result, it is not preferred to be applied with the PSPV system where the irradiance of all PV modules/strings/arrays is different, and the output voltage/current of each DC–DC converter is not the same. Hence, fixed IBC is the best choice to enhance the stability of DC-link voltage. Recently, many literature studies [48–58] have been done to prove the superiority of the interleaved DC–DC converters compared to the CBC with constant input power in terms of ripples, energy savings, efficiency, steady state, electromagnetic emission and reliability. For example, the researchers in [50, 53, 55] have shown the possibility of using IBC with PV in terms of reliability evaluation, ripple reduction and faster transient response. However, they performed their studies on standalone PV without PS in order to highlight the IBC performance where the input power is constant, which is different under PSCs. On the other hand, the researchers in [46, 51, 56, 59, 60] demonstrated the possibility of using IBC for high-voltage applications compared to the CBC, whereas Rehman et al. [61] introduced a detailed comparisons of interleaved DC–DC converter topologies in terms of cost, reliability, flexibility and efficiency that can be used in renewable energy applications. The latter proved that buck and boost are more reliable, less cost and more efficient while Cuk and single-ended primary-inductor converters (SEPICs) are more flexible than others as they are ripple-free and able to increase or decrease the output voltage. Finally, Ngai-Man et al. [58] proved the better performance of a two-phase IBC using the SiC diodes compared to IBC using the Si diodes in terms of higher efficiency and power density. Based on the comparisons of all PV system architectures in terms of applicability with PS, the merits and demerits are shown in Table 2, whereas the previous studies on IBC for different applications is listed in Table 3.

2.1.4 PV Array Reconfiguration

Once PS is detected, reconfiguration of PV array between fixed and adaptive arrays will be activated via a controllable switching matrix as shown in Fig. 6. The basic function of the reconfiguration process is to provide the best connection to alleviate the PS effects and increase the power extracted from the PV array [31]. Determination

Table 2 Comparisons of the PV system architectures

Topology	Applicable to PS	Merits	Demerits
Centralized [39]	NA	<ul style="list-style-type: none"> • Suitable under the uniform condition • Less cost 	<ul style="list-style-type: none"> • Conventional • GP tracking is not available • More susceptible to PS and mismatch power loss
Series/parallel MIC [31]	Yes	<ul style="list-style-type: none"> • Series and parallel MIC are applicable with PS • Series MIC are suitable with HV applications • Parallel MIC are suitable with LV applications • Large scale preferred 	<ul style="list-style-type: none"> • The total cost increased
Micro-inverter	NA	<ul style="list-style-type: none"> • Allows the monitor of the power production of each individual panel 	<ul style="list-style-type: none"> • Not applicable with PS • DC-link voltage un-controllable • More expensive
Multi-input dc–dc converter [42]	Yes	<ul style="list-style-type: none"> • Applicable with PS • Maximum power available is achieved • DC-link voltage is regulated • Conventional MPPT techniques are available 	<ul style="list-style-type: none"> • Larger number of inductor and semiconductor devices are required which increase both cost and size

of the most appropriate points for the switching matrix is very important in terms of cost and energy efficiency in addition to the TCT configuration in adaptive array facilitates the interconnection with fixed array and maximizes the power captured from the PV system. However, more switching elements and more complex connection structure need to be used. On the other hand, high cost occurs in SP connection structure adaptive panels where the PV modules are connected in series to fixed part [62–65]. Mathematical formula for reconfiguration of PV array grid-connected was proposed by the researchers in [65–67]. However, it is limited to a fully reconfigurable array and does not indicate the global optimal reconfiguration directly. Also, it is more suitable for a small number of PV modules. El-Dein et al. [68] covered the limitations and shortcomings of the previous studies through the mathematical formula for PV array reconfiguration as a mixed integer quadratic programming problem. The optimal reconfiguration can be found directly using a branch and bound algorithm. This formula is suitable with fully or partially reconfigurable array and can be used for a large number of PV modules. Also, Karakose et al. proposed an

Table 3 Previous studies on IBC for different applications till 2017

References	Converter used	Control variable	Application	Advantages	Disadvantages
[44]	IBC	P&O MPPT	Fuel cell electric vehicle	<ul style="list-style-type: none"> Improves Power quality Low-cost, low power consumption 	<ul style="list-style-type: none"> Rapid changes in $P_{o/p}$ Severe cell degradation Decreases efficiency
[45]	Asymmetrical interleaved dual boost and buck-boost and flyback converter	Duty cycle	PV and fuel cell	High-voltage conversion ratio and ripple reduction	<ul style="list-style-type: none"> $P_{i/p}$ is constant; not similar to PSC Variable dc-link voltage Two DC-DC converters for each array that increase the total cost
[46]	Variable IBC	Duty cycle	Hybrid energy system	<ul style="list-style-type: none"> Wide range of applications from low to high voltage/power (different output characteristics) 	<ul style="list-style-type: none"> Variable DC-link voltage
[42]	Variable IBC	Duty cycle	Standalone PV system	<ul style="list-style-type: none"> The efficiency is almost 99% Increases the energy harvested by distributed MPPT 	<ul style="list-style-type: none"> Power generated by each PV module and the output DC voltage becomes unbalanced

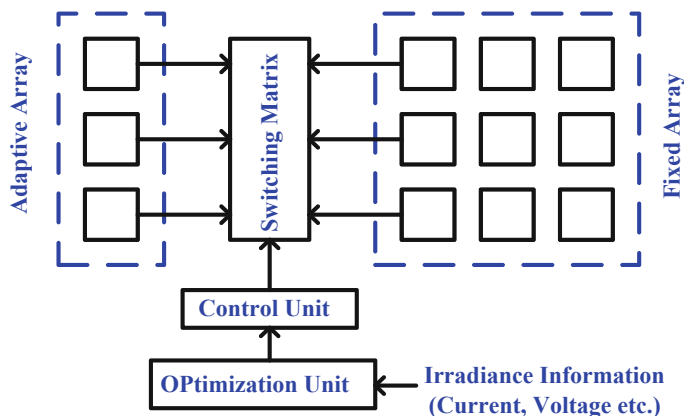


Fig. 6 Reconfiguration process

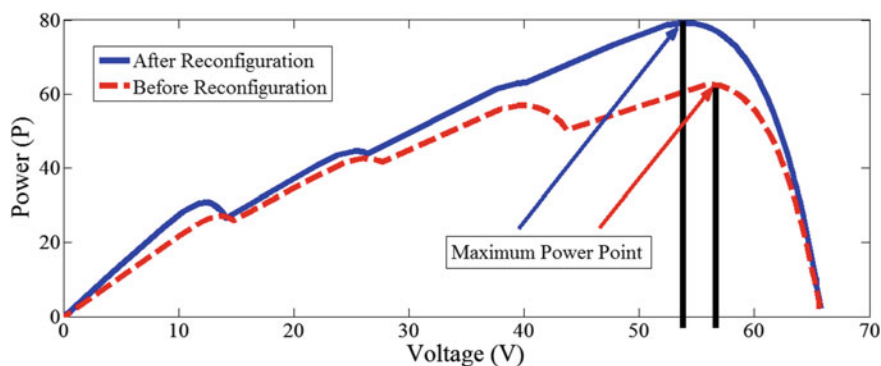


Fig. 7 MPP variation for reconfiguration

efficient algorithm based on GA used for PV array reconfiguration. This algorithm is suitable for a great number of panels and it provides efficient results in terms of operating speed [69]. On the other hand, the simulation results proved that the output power can be increased between 10 and 30% using the reconfiguration process as shown in Fig. 7 [31, 62, 63], whereas the experimental prototype in [39] improved the output power by 45% under certain PSC compared to the system without reconfiguration. Hence, the array output power and efficiency will be increased. Also, the reconfiguration will reduce the effect of bypass diodes through disappearing multiple MPPs and hot spot points. Merits and demerits of the PV array reconfigurations are introduced in Table 4.

Table 4 Merits and demerits of the PV array reconfiguration

Topology	Merits	Demerits
Reconfiguration of PV array	<ul style="list-style-type: none"> • Mitigates the PS effects • Significant increase in the output power to 45% under PSCs • High efficiency • Shaded PV modules are reconnected in the best possible position 	<ul style="list-style-type: none"> • More complex due to more switching elements are needed • High cost • Unsuitable to some PSCs

3 MPPT of Partial Shading PV Arrays

As discussed in the introduction section, conventional MPPT techniques are not accurate and efficient to deal with the PS problem where it cannot track the GP under PSC, whereas heuristic or soft computing techniques can track the GP and deal with the PS problem efficiently. They can track the GP without falling or trapping in LPs with high tracking speed, high convergence speed, less response time and high efficiency [4]. Therefore, this chapter concentrates on the modern and efficient MPPT techniques that can track the GP instead of LP and handle the PS problem. These modern and efficient MPPT techniques are classified into heuristic and hybrid MPPT techniques as follow:

3.1 Heuristic MPPT Techniques

3.1.1 Particle Swarm Optimization Technique

The particle swarm optimization (PSO) technique is considered as one of the most efficient heuristic techniques. It can track the GP accurately with low oscillation around the steady state. The GP tracking depends on the particle's velocity and position, which are updated to track the GP instead of LPs by sending the duty cycle one by one to the DC–DC boost converter [70, 71]. Each particle in the swarm has mainly two variable parameters, which are the position vector x_i^k and the velocity vector v_i^k . The new position can be estimated as follows [71]:

$$x_i^{k+1} = x_i^k + v_i^{k+1} \quad (1)$$

The new position of the particle is determined through calculating the velocity using current position x_i^k , particle velocity v_i^k and global best position G_{best} as follows:

$$v_i^{k+1} = \omega v_i^k + c_1 r_1 (P_{\text{best } i}^k - x_i^k) + c_2 r_2 (G_{\text{best}}^k - x_i^k) \quad (2)$$

where ω is the inertia weight that determines the research area. It can be set to constant value (0.5) or variable to accelerate the GP tracking [72]. c_1 and c_2 are the acceleration coefficients, where c_1 is self-confidence and c_2 is swarm-confidence. The range of c_1 varies from 1.5 to 2 while the range of c_2 varies from 2 to 2.5 [73].

Some authors [74–77] used the conventional PSO which is able to handle PSCs and track the GP accurately, but they discovered that it is low during the steady-state oscillations [72]. As a result, others [78, 79] have added some modifications to it. Later, an improved or a deterministic PSO (DPSO) was proposed to improve the tracking capability of the conventional PSO, where the random number in the velocity equation is removed as follows [79]:

$$v_i^{k+1} = \omega v_i^k + c_1 * P_{\text{best } i} + c_2 * G_{\text{best}} - (c_1 + c_2)x_i^k \quad (3)$$

$$v_i^{k+1} = \omega v_i^k + c_1 * P_{\text{best } i} + c_2 * G_{\text{best}} - c_3 x_i^k \quad (4)$$

The PSO algorithm begins the search by sending initial duty cycles to the DC–DC converter and the obtained PV voltage and current are used to compute the P_{best} and G_{best} values as shown in the PSO flow chart in Fig. 8. The new duty cycles are computed using the velocity and position equations, based on Eqs. (1) and (4).

3.1.2 Grey Wolf Optimization Technique

Grey wolf optimizer (GWO) is counted as one of the most modern heuristic optimization technique that first introduced by [80] in 2014. This technique is inspired from the lifestyle of the grey wolves in a purse, chasing, attacking, and hunting prey in wildlife. Mostly, grey wolves like to live in a pack 5–10 on average. They have a very strict social dominant hierarchy [80], where it has four levels of leadership. Leaders which we call it alpha (α), and subleaders called beta (β) and so on which it called leadership pyramids as shown in Fig. 9 [26, 80], where the dominance of wolves increase from top to bottom [81]. The behaviour of grey wolves has been mimicked in the optimization field with GWO. The leadership hierarchy of the grey wolves is done by assuming the leaders; wolves called alpha (α), and subleaders called beta (β), the lower rank called delta (δ) and lowest rank wolves called omega (ω).

As mentioned above, grey wolves encircle prey during the hunt. In order to mathematically model encircling behaviour, the following equations are proposed [80]:

$$\vec{E} = \left| \vec{C} \cdot \vec{D}_p(t) - \vec{D}(t) \right| \quad (5)$$

$$\vec{D}(t+1) = \vec{D}_p(t) - \vec{A} \cdot \vec{E} \quad (6)$$

where t is the current iteration, A and C are coefficient vectors where their values have the ability to save balance between the exploration and exploitation in the searching

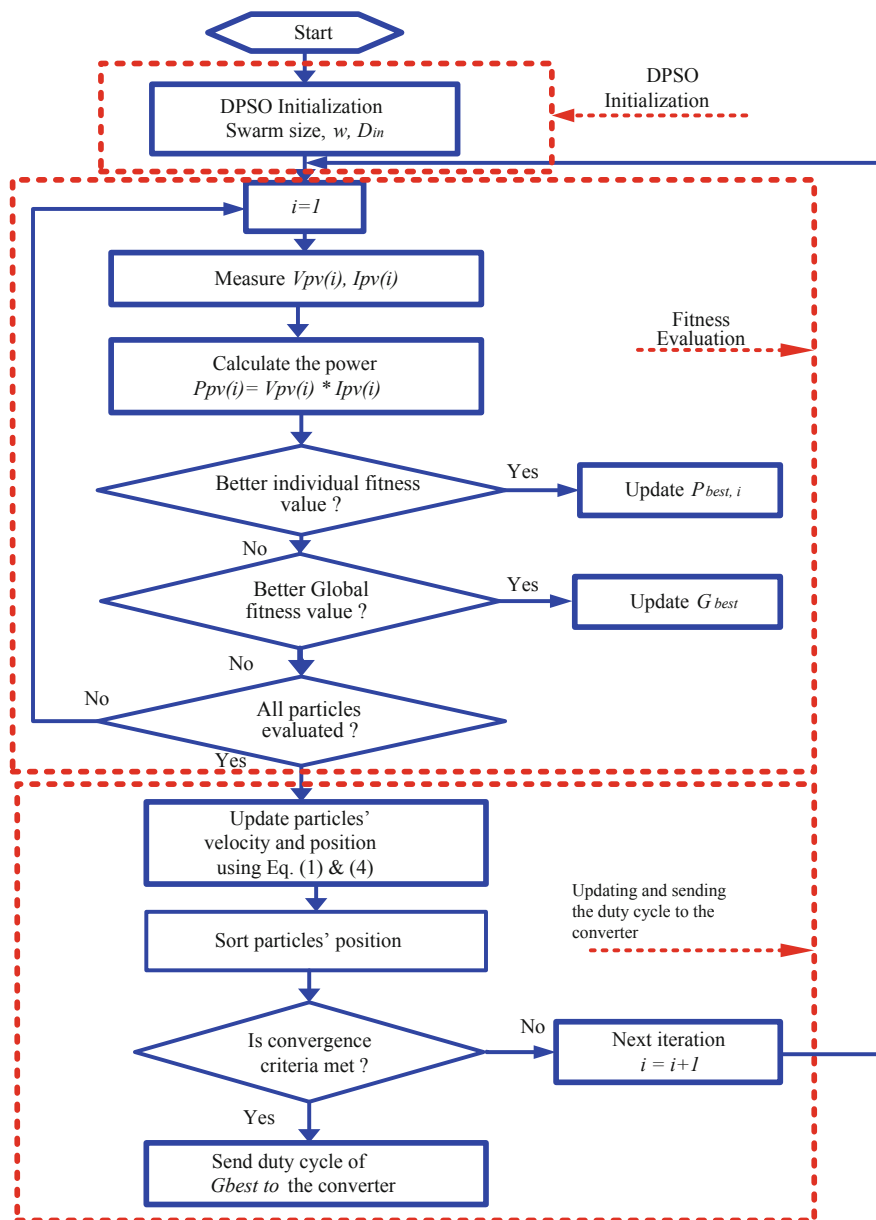
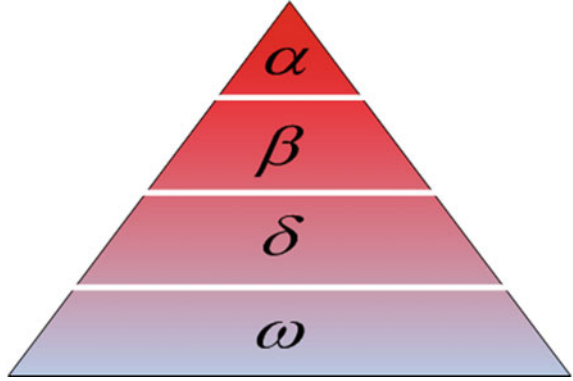


Fig. 8 Flow chart of deterministic particle swarm optimization (DPSO)-based maximum power point tracker (MPPT)

Fig. 9 Leadership pyramids with four levels of leadership (α , β , δ and ω)



area, D_p is the position vector of the prey and D indicates the position vector of a grey wolf. The two coefficient vectors A and C can be calculated as follow:

$$\vec{A} = 2\vec{a} \cdot \vec{r}_1 - \vec{a} \quad (7)$$

$$C = 2 \cdot \vec{r}_2 \quad (8)$$

where the coefficient a is decreasing linearly from 2 to 0 and r_1 and r_2 are random vectors with value between 1 and 0.

The hunting technique of the grey wolves is done by circling the prey and the pack should obey the orders of the alpha wolf (D_α) as a high priority and the beta wolves (D_β) and delta wolves (D_δ) as a lower priority orders. This leadership hierarchy can be mimicked mathematically using the following equations:

$$\vec{E}_\alpha = \left| \vec{C}_1 \cdot \vec{D}_\alpha - \vec{D} \right|, \vec{E}_\beta = \left| \vec{C}_2 \cdot \vec{D}_\beta - \vec{D} \right|, \text{ and } \vec{E}_\delta = \left| \vec{C}_3 \cdot \vec{D}_\delta - \vec{D} \right| \quad (9)$$

$$\vec{D}_1 = \vec{D}_\alpha - \vec{A}_1 \cdot \vec{E}_\alpha, \vec{D}_2 = \vec{D}_\beta - \vec{A}_2 \cdot \vec{E}_\beta, \text{ and } \vec{D}_3 = \vec{D}_\delta - \vec{A}_3 \cdot \vec{E}_\delta \quad (10)$$

$$\vec{D}(t+1) = \frac{\vec{D}_1 + \vec{D}_2 + \vec{D}_3}{3} \quad (11)$$

The exploration and the exploitation of the solution depend on the values of a and A values; when $|A| \leq 1$, the wolves tend to exploitation (converge to prey) and when $|A| \geq 1$, the wolves tend to exploration (diverge from the prey because it may be one of the LPs).

3.1.3 Flower Pollination Algorithm

Flower pollination algorithm (FPA) is a heuristic-based nature inspired that takes its idea from flowers pollination process in plants. Pollination may be self-pollination or cross-pollination. Self-pollination takes place when the same flower is pollinated internally, whereas cross-pollination occurs when pollen moves from one flower to another. The pollen may be transferred via wind and in this case, it is called abiotic pollination while it may via insects and in this case, it is called biotic pollination. The four steps to design FPA are as following [82, 83]:

Step 1: Global pollination appeared in biotic and cross-pollination, and pollen carrying pollinators fly and follow Lévy flights.

Step 2: Local pollination represented in a biotic and self-pollination.

Step 3: Flower constancy considers as an equivalent to a reproduction probability, which is proportional to the similarity of two flowers involved.

Step 4: The local pollination and global pollination have been controlled and switched via switch probability $P \in [0, 1]$.

The above steps have to be converted into proper mathematical equations. For example, at the global pollination step, the pollinators load the flower pollen gametes, so the pollen can fly a long distance. Therefore, global pollination (Step 1) and flower constancy (Step 3) can be mathematically modelled as [82, 83]:

$$x_i^{k+1} = x_i^k + \gamma L(\lambda)(g_* - x_i^k) \quad (12)$$

where x_i^t is the solution vector x_i at iteration t and g is the best solution (duty cycle) of boost converter duty cycle. c denotes a scaling factor that used for controlling the step size. $L(\lambda)$ represents the Lévy flights-based step size Γ that corresponds to the strength of the pollination. Insects can fly a long distance with different distance steps; this is drawn from a Lévy distribution [82, 83]:

$$L \approx \frac{\lambda \Gamma(\lambda) \sin\left(\frac{\pi\lambda}{2}\right)}{\Gamma} \frac{1}{S^{1+\lambda}} \quad (S \geq S_0 > 0) \quad (13)$$

where $\Gamma(\lambda)$ represents gamma function.

3.2 Hybrid MPPT Techniques

Hybrid MPPT techniques is a combination of conventional/soft computing [84] or soft computing/conventional [85, 86] or soft computing/soft computing [87–89] in order to handle the PSCs and track the GP accurately and efficiently. Some soft computing MPPT, especially those based on AI such as FLC [90, 91] and ANN cannot handle the PSCs where they may fail to track the GP. Therefore, they are

Table 5 Recent combined and hybrid MPPT techniques

References	Variable control	DC–DC converter	Application	Findings
[92]	Duty cycle	Boost	Standalone	FLC combined with scanning and storing algorithm has fast and accurate convergence to the GP, high efficiency, no oscillations during transient and steady-state conditions compared to variable step size IC, conventional PSO and FLC-based HC in both simulation and experimental works
[86]	V_{MPP}	Buck	Standalone PV	Hybrid ANN-IC can track the GP under PSC effectively and accurately compared to P&O and FLC-based HC where ANN provides V_{ref} to IC
[85]	Duty cycle	Buck-boost	Standalone PV	Hybrid ANN-P&O can track the GP efficiently and accurately compared to P&O, Fibonacci search, conventional PSO and DE. ANN is used to predict the GP region then P&O tracks the GP
[89]	Duty cycle	Boost	Standalone PV	ANN-FLC where ANN is trained once under several PSCs to determine the GP voltage with SP, BL and TCT configurations. FLC uses the GP voltage to send the duty cycle for the boost converter
[84]	Duty cycle	Buck	Grid-connected	Hybrid P&O-GA can catch the GP in a shorter time because the GA parameters (population size and number of iterations) are decreased

(continued)

Table 5 (continued)

References	Variable control	DC–DC converter	Application	Findings
[87]	Duty cycle	Boost	Standalone PV	Hybrid FLC-GA has better performance and efficiency compared to P&O where GA optimizes FLC membership functions and rules
[88]	–	Not used	Standalone PV	GA optimized ANN-based MPPT where GA is used to determine the number of neurons in multi-layer perceptron neural network. The PV system design eliminates the DC–DC converter and its losses

optimized and integrated with other techniques to improve the tracking efficiency and convergence speed.

Based on the recent combined and hybrid MPPT techniques introduced in Table 5, soft computing-based AI can be used to optimize another soft computing-based AI, for example, GA optimized FLC membership functions and rules as in [87], GA optimized ANN as in [88] and finally, ANN optimized FLC performance where ANN trained under several PSCs to determine the GP voltage and FLC using the GP voltage to send the duty cycle to the boost converter [89]. On the other hand, conventional P&O is embedded inside the soft computing GA to increase the GA's effectiveness in tracking the GP in a shorter time through reducing the GA parameters [84]. The conventional MPPT techniques are not accurate and stuck at the first peak regardless of whether it is LP or GP. Therefore, soft computing can be used to optimize a conventional one such as ANN-IC where ANN provide V_{ref} to IC [86] and ANN-P&O where ANN is used to predict the GP region while P&O tracks the GP [85].

4 Conclusions

Partial shading reduces the output power generated from the PV system. Also, thermal destruction of shaded PV modules may be occurred due to hot spot points. Under PSC, multiple peaks, one GP and many other LPs are generated in the P – V curve due to using bypass diodes for protecting the shaded PV modules. PV system design topologies participate mainly in alleviating the partial shading effects and so extracting the global maximum power available from the PSPV system with the helping of modern and efficient heuristic MPPT techniques such as PSO, GWO and FPA. The

PV system design topologies consist of the bypass and blocking diodes, PV system architectures, PV array configuration and PV array reconfiguration. Each kind of PV system design topologies has its own merits and demerits. For PV system configuration, TCT has the superior performance compared to other configurations in terms of maximum power, fill factor and efficiency. TCT and BL configurations increase the maximum power by 2.3 and 3.8%, respectively, compared with the SP configuration. For PV system architectures, interleaved DC–DC converter may represent the best solution not only in mitigating the partial shading effects but also in extracting the global maximum power available under PSC. On the other hand, heuristic MPPT techniques are the most efficient MPPT techniques in tracking the GP instead of LP under PSC. They can track the GP without trapping in LPs with high tracking and convergence speed and high efficiency.

References

1. Arunkumari T, Indragandhi V (2017) An overview of high voltage conversion ratio DC-DC converter configurations used in DC micro-grid architectures. *Renew Sustain Energy Rev* 77:670–687
2. Saharia BJ, Saharia KK (2015) Simulated study on nonisolated DC-DC converters for MPP tracking for photovoltaic power systems. *J Energy Eng* 142(1):04015001
3. Farh HM, Othman MF, Eltamaly AM (2017) Maximum power extraction from grid-connected PV system. In: 2017 Saudi Arabia smart grid (SASG). IEEE, pp 1–6
4. Eltamaly AM, Farh HM, Othman MF (2018) A novel evaluation index for the photovoltaic maximum power point tracker techniques. *Sol Energy* 174:940–956
5. Farh H, Othman M, Eltamaly A, Al-Saud M (2018) Maximum power extraction from a partially shaded PV system using an interleaved boost converter. *Energies* 11(10):2543
6. Eltamaly AM, Farh HM (2013) Maximum power extraction from wind energy system based on fuzzy logic control. *Electr Power Syst Res* 97:144–150
7. Eltamaly AM, Farh HM (2015) Smart maximum power extraction for wind energy systems. In: 2015 IEEE international conference on smart energy grid engineering (SEGE). IEEE, pp 1–6
8. Eltamaly AM, Alolah A, Farh HM (2013) Maximum power extraction from utility-interfaced wind turbines. In: *New developments in renewable energy*. InTech
9. Mohamed MA, Eltamaly AM, Farh HM, Alolah AI (2015) Energy management and renewable energy integration in smart grid system. In: 2015 IEEE international conference on smart energy grid engineering (SEGE). IEEE, pp 1–6
10. Ji Y-H, Jung D-Y, Kim J-G, Kim J-H, Lee T-W, Won C-Y (2011) A real maximum power point tracking method for mismatching compensation in PV array under partially shaded conditions. *IEEE Trans Power Electron* 26(4):1001–1009
11. Silvestre S, Chouder A (2008) Effects of shadowing on photovoltaic module performance. *Prog Photovoltaics Res Appl* 16(2):141–149
12. Eltamaly AM (2015) Performance of smart maximum power point tracker under partial shading conditions of photovoltaic systems. *J Renew Sustain Energy* 7(4):043141
13. Duong MQ, Sava GN, Ionescu G, Necula H, Leva S, Mussetta M (2017) Optimal bypass diode configuration for PV arrays under shading influence. In: 2017 IEEE international conference on environment and electrical engineering and 2017 IEEE industrial and commercial power systems Europe (EEEIC/I&CPS Europe). IEEE, pp 1–5
14. Teo J, Tan RH, Mok V, Ramachandaramurthy VK, Tan C (2018) Impact of partial shading on the PV characteristics and the maximum power of a photovoltaic string. *Energies* 11(7):1–22

15. Rezk H, Eltamaly AM (2015) A comprehensive comparison of different MPPT techniques for photovoltaic systems. *Sol Energy* 112:1–11
16. Ram JP, Rajasekar N (2017) A new global maximum power point tracking technique for solar photovoltaic (PV) system under partial shading conditions (PSC). *Energy* 118:512–525
17. soufyane Benyoucef A, Chouder A, Kara K, Silvestre S (2015) Artificial bee colony based algorithm for maximum power point tracking (MPPT) for PV systems operating under partial shaded conditions. *Appl Soft Comput* 32:38–48
18. Sundareswaran K, Sankar P, Nayak P, Simon SP, Palani S (2015) Enhanced energy output from a PV system under partial shaded conditions through artificial bee colony. *IEEE Trans Sustain Energy* 6(1):198–209
19. Sundareswaran K, Peddapati S, Palani S (2014) MPPT of PV systems under partial shaded conditions through a colony of flashing fireflies. *IEEE Trans Energy Convers* 29(2):463–472
20. Teshome D, Lee C, Lin Y, Lian K (2017) A modified firefly algorithm for photovoltaic maximum power point tracking control under partial shading. *IEEE J Emerg Sel Topics Power Electron* 5(2):661–671
21. Jiang LL, Maskell DL, Patra JC (2013) A novel ant colony optimization-based maximum power point tracking for photovoltaic systems under partially shaded conditions. *Energy Build* 58:227–236
22. Ahmed J, Salam Z (2014) A maximum power point tracking (MPPT) for PV system using Cuckoo Search with partial shading capability. *Appl Energy* 119(Supplement C):118–130
23. Chao K-H, Lin Y-S, Lai U-D (2015) Improved particle swarm optimization for maximum power point tracking in photovoltaic module arrays. *Appl Energy* 158:609–618
24. Rajasekar N et al (2014) Application of modified particle swarm optimization for maximum power point tracking under partial shading condition. *Energy Procedia* 61:2633–2639
25. Farh HM, Eltamaly AM, Othman MF (2018) Hybrid PSO-FLC for dynamic global peak extraction of the partially shaded photovoltaic system. *PLoS ONE* 13(11):e0206171
26. Eltamaly AM, Farh HM (2019) Dynamic global maximum power point tracking of the PV systems under variant partial shading using hybrid GWO-FLC. *Sol Energy* 177:306–316
27. Patel H, Agarwal V (2008) MATLAB-based modeling to study the effects of partial shading on PV array characteristics. *IEEE Trans Energy Convers* 23(1):302–310
28. Chin CS, Neelakantan P, Yang SS, Chua BL, Tze Kin Teo K (2011) Effect of partially shaded conditions on photovoltaic array's maximum power point tracking. *Int J Simul–Syst Sci Technol* 12(3)
29. Eltamaly AM (2018) Performance of MPPT techniques of photovoltaic systems under normal and partial shading conditions. In: *Advances in renewable energies and power technologies*. Elsevier, pp 115–161
30. Singh PO (2011) Modeling of photovoltaic arrays under shading patterns with reconfigurable switching and bypass diodes. *Theses and dissertations*
31. Bidram A, Davoudi A, Balog RS (2012) Control and circuit techniques to mitigate partial shading effects in photovoltaic arrays. *IEEE J Photovoltaics* 2(4):532–546
32. Ramaprabha R, Mathur B (2012) A comprehensive review and analysis of solar photovoltaic array configurations under partial shaded conditions. *Int J Photoenergy* 2012
33. Wang Y-J, Hsu P-C (2009) Analysis of partially shaded PV modules using piecewise linear parallel branches model. *World Acad Sci Eng Technol* 60(2):783–789
34. Wang Y-J, Hsu P-C (2011) An investigation on partial shading of PV modules with different connection configurations of PV cells. *Energy* 36(5):3069–3078
35. Kaushika ND, Gautam NK (2003) Energy yield simulations of interconnected solar PV arrays. *IEEE Trans Energy Convers* 18(1):127–134
36. Karatepe E, Boztepe M, Colak M (2007) Development of a suitable model for characterizing photovoltaic arrays with shaded solar cells. *Sol Energy* 81(8):977–992
37. Wang Y-J, Lin S-S (2011) Analysis of a partially shaded PV array considering different module connection schemes and effects of bypass diodes. In: *2011 international conference and utility exhibition on power and energy systems: issues & prospects for Asia (ICUE)*. IEEE, pp 1–7

38. Picault D, Raison B, Bacha S, Aguilera J, De La Casa J (2010) Changing photovoltaic array interconnections to reduce mismatch losses: a case study. In: 2010 9th international conference on environment and electrical engineering (EEEIC). IEEE, pp 37–40
39. Das SK, Verma D, Nema S, Nema R (2017) Shading mitigation techniques: state-of-the-art in photovoltaic applications. *Renew Sustain Energy Rev* 78:369–390
40. Kandemir E, Cetin NS, Borekci S (2017) A comprehensive overview of maximum power extraction methods for PV systems. *Renew Sustain Energy Rev* 78:93–112
41. Xia Q (2012) Solar photovoltaic system modeling and control. University of Denver
42. Dhople SV, Ehlmann JL, Davoudi A, Chapman PL (2010) Multiple-input boost converter to minimize power losses due to partial shading in photovoltaic modules. In: 2010 IEEE energy conversion congress and exposition (ECCE). IEEE, pp 2633–2636
43. Garth DR, Muldoon W, Benson G, Costague E (1971) Multi-phase, 2-kilowatt, high-voltage, regulated power supply. In: 1971 IEEE power electronics specialists conference. IEEE, pp 110–116
44. Benyahia N et al (2014) MPPT controller for an interleaved boost dc–dc converter used in fuel cell electric vehicles. *Int J Hydrogen Energy* 39(27):15196–15205
45. Arango E, Ramos-Paja CA, Calvente J, Giral R, Serna S (2012) Asymmetrical interleaved DC/DC switching converters for photovoltaic and fuel cell applications—part I: circuit generation, analysis and design. *Energies* 5(11):4590–4623
46. Deihimi A, Mahmoodieh MES, Irvani R (2017) A new multi-input step-up DC–DC converter for hybrid energy systems. *Electr Power Syst Res* 149:111–124
47. Mohapatra A, Nayak B, Das P, Mohanty KB (2017) A review on MPPT techniques of PV system under partial shading condition. *Renew Sustain Energy Rev* 80:854–867
48. Lakpathi G, Reddy SM, Ganesh KL, Satyanarayana G (2013) An effective high step-up interleaved DC–DC converter photovoltaic grid connection system
49. Khadmun W, Subsingha W (2013) High voltage gain interleaved DC boost converter application for photovoltaic generation system. *Energy Procedia* 34(Supplement C):390–398
50. Khosroshahi A, Abapour M, Sabahi M (2015) Reliability evaluation of conventional and interleaved DC–DC boost converters. *IEEE Trans Power Electron* 30(10):5821–5828
51. Henn GA, Silva R, Praca PP, Barreto LH, Oliveira DS (2010) Interleaved-boost converter with high voltage gain. *IEEE Trans Power Electron* 25(11):2753–2761
52. Yang B, Li W, Zhao Y, He X (2010) Design and analysis of a grid-connected photovoltaic power system. *IEEE Trans Power Electron* 25(4):992–1000
53. Ramaprabha R, Balaji K, Raj S, Logeshwaran V (2013) Comparison of interleaved boost converter configurations for solar photovoltaic system interface. *J Eng Res [TJER]* 10(2):87–98
54. Prasanth P, Seyezhai R (2016) Investigation of four phase interleaved boost converter under open loop and closed loop control schemes for battery charging applications. *Int J Adv Mater Sci Eng (IJAMSE)* 5(1)
55. Aghdam FH, Hagh MT, Abapour M (2016) Reliability evaluation of two-stage interleaved boost converter interfacing PV panels based on mode of use. In: 2016 7th Power electronics and drive systems technologies conference (PEDSTC). IEEE, pp 409–414
56. Lai C-M, Cheng Y-H, Teh J, Lin Y-C (2017) A new combined boost converter with improved voltage gain as a battery-powered front-end interface for automotive audio amplifiers. *Energies* 10(8):1128
57. Rehman Z, Al-Bahadly I, Mukhopadhyay S (2015) Multiinput DC–DC converters in renewable energy applications—an overview. *Renew Sustain Energy Rev* 41(Supplement C):521–539
58. Ho CN-M, Breuninger H, Pettersson S, Escobar G, Canales F (2013) A comparative performance study of an interleaved boost converter using commercial Si and SiC diodes for PV applications. *IEEE Trans Power Electron* 28(1):289–299
59. Lakpathi G, Reddy SM, Ganesh KL, Satyanarayana G (2013) An effective high step-up interleaved DC–DC converter photovoltaic grid connection system. *Int J Soft Comput Eng (IJSCE)* 3(4):2231–2307
60. Khadmun W, Subsingha W (2013) High voltage gain interleaved dc boost converter application for photovoltaic generation system. *Energy Procedia* 34:390–398

61. Rehman Z, Al-Bahadly I, Mukhopadhyay S (2015) Multiinput DC–DC converters in renewable energy applications—an overview. *Renew Sustain Energy Rev* 41:521–539
62. Nguyen D, Lehman B (2008) An adaptive solar photovoltaic array using model-based reconfiguration algorithm. *IEEE Trans Ind Electron* 55(7):2644–2654
63. Karakose M, Baygin M, Baygin N, Murat K, Akin E (2014) An intelligent reconfiguration approach based on fuzzy partitioning in PV arrays. In: 2014 IEEE international symposium on innovations in intelligent systems and applications (INISTA) proceedings. IEEE, pp 356–360
64. Karakose M, Baygin M, Baygin N (2014) An analysis approach for optimization based reconfiguration in photovoltaic arrays. In: 2014 IEEE 23rd international symposium on industrial electronics (ISIE). IEEE, pp 954–959
65. Velasco G, Negroni J, Guinjoan F, Piqué R (2005) Energy generation in PV grid-connected systems: a comparative study depending on the PV generator configuration. In: IEEE international symposium on industrial electronics, pp 1025–1030
66. Velasco G, Guinjoan F, Pique R (2008) Grid-connected PV systems energy extraction improvement by means of an electric array reconfiguration (EAR) strategy: operating principle and experimental results. In: 2008 IEEE power electronics specialists conference, PESC 2008. IEEE, pp 1983–1988
67. Velasco-Quesada G, Guinjoan-Gispert F, Piqué-López R, Román-Lumbreras M, Conesa-Roca A (2009) Electrical PV array reconfiguration strategy for energy extraction improvement in grid-connected PV systems. *IEEE Trans Ind Electron* 56(11):4319–4331
68. El-Dein MS, Kazerani M, Salama M (2013) Optimal photovoltaic array reconfiguration to reduce partial shading losses. *IEEE Trans Sustain Energy* 4(1):145–153
69. Karakose M, Murat K, Akin E, Parlak K (2014) A new efficient reconfiguration approach based on genetic algorithm in PV systems. In: 2014 IEEE 23rd international symposium on industrial electronics (ISIE). IEEE, pp 23–28
70. Titri S, Larbes C, Toumi KY, Benatchba K (2017) A new MPPT controller based on the Ant colony optimization algorithm for photovoltaic systems under partial shading conditions. *Appl Soft Comput* 58(Supplement C):465–479
71. Ishaque K, Salam Z, Amjad M, Mekhilef S (2012) An improved particle swarm optimization (PSO)-based MPPT for PV with reduced steady-state oscillation. *IEEE Trans Power Electron* 27(8):3627–3638
72. Ishaque K, Salam Z (2013) A review of maximum power point tracking techniques of PV system for uniform insolation and partial shading condition. *Renew Sustain Energy Rev* 19:475–488
73. Al-Obeidat F, Belacel N, Carretero JA, Mahanti P (2010) Automatic parameter settings for the PROAFTN classifier using hybrid particle swarm optimization. In: Canadian conference on AI, 2010. Springer, Berlin, pp 184–195
74. Ishaque K, Salam Z, Taheri H, Shamsudin A (2011) Maximum power point tracking for PV system under partial shading condition via particle swarm optimization. In: 2011 IEEE applied power electronics colloquium (IAPEC). IEEE, pp 5–9
75. Liu Y, Xia D, He Z (2011) MPPT of a PV system based on the particle swarm optimization. In: 2011 4th international conference on electric utility deregulation and restructuring and power technologies (DRPT). IEEE, pp 1094–1096
76. Miyatake M, Inada T, Hiratsuka I, Zhao H, Otsuka H, Nakano M (2004) Control characteristics of a fibonacci-search-based maximum power point tracker when a photovoltaic array is partially shaded. In: The 4th international power electronics and motion control conference, IPEMC 2004, vol 2. IEEE, pp 816–821
77. Eltamaly AM (2015) Performance of smart maximum power point tracker under partial shading conditions of PV systems. In: 2015 IEEE international conference on smart energy grid engineering (SEGE). IEEE, pp 1–8
78. Soltani I, Sarvi M, Marefatjou H (2013) An intelligent, fast and robust maximum power point tracking for proton exchange membrane fuel cell. *World Appl Program* 3(7):264–281
79. Ishaque K, Salam Z (2013) A deterministic particle swarm optimization maximum power point tracker for photovoltaic system under partial shading condition. *IEEE Trans Ind Electron* 60(8):3195–3206

80. Mirjalili S, Mirjalili SM, Lewis A (2014) Grey wolf optimizer. *Adv Eng Softw* 69:46–61
81. Cherukuri SK, Rayapudi SR (2017) Enhanced grey wolf optimizer based MPPT algorithm of PV system under partial shaded condition. *Int J Renew Energy Dev* 6(3):203
82. Abdelaziz A, Ali E, Elazim SA (2016) Optimal sizing and locations of capacitors in radial distribution systems via flower pollination optimization algorithm and power loss index. *Eng Sci Technol Int J* 19(1):610–618
83. Yang X-S (2012) Flower pollination algorithm for global optimization. In: *International conference on unconventional computing and natural computation*, 2012. Springer, Berlin, pp 240–249
84. Daraban S, Petreus D, Morel C (2014) A novel MPPT (maximum power point tracking) algorithm based on a modified genetic algorithm specialized on tracking the global maximum power point in photovoltaic systems affected by partial shading. *Energy* 74:374–388
85. Jiang LL, Nayanisiri D, Maskell DL, Vilathgamuwa D (2015) A hybrid maximum power point tracking for partially shaded photovoltaic systems in the tropics. *Renew Energy* 76:53–65
86. Punitha K, Devaraj D, Sakthivel S (2013) Artificial neural network based modified incremental conductance algorithm for maximum power point tracking in photovoltaic system under partial shading conditions. *Energy* 62:330–340
87. Larbes C, Cheikh SA, Obeidi T, Zerguerras A (2009) Genetic algorithms optimized fuzzy logic control for the maximum power point tracking in photovoltaic system. *Renew Energy* 34(10):2093–2100
88. Kulaksız AA, Akkaya R (2012) A genetic algorithm optimized ANN-based MPPT algorithm for a stand-alone PV system with induction motor drive. *Sol Energy* 86(9):2366–2375
89. Karatepe E, Hiyama T (2009) Artificial neural network-polar coordinated fuzzy controller based maximum power point tracking control under partially shaded conditions. *IET Renew Power Gener* 3(2):239–253
90. Farh HM, Eltamaly AM (2013) Fuzzy logic control of wind energy conversion system. *J Renew Sustain Energy* 5(2):023125
91. Eltamaly AM (2010) Modeling of fuzzy logic controller for photovoltaic maximum power point tracker. In: *Solar future 2010 conference*, Istanbul, Turkey
92. Boukenoui R, Salhi H, Bradai R, Mellit A (2016) A new intelligent MPPT method for stand-alone photovoltaic systems operating under fast transient variations of shading patterns. *Sol Energy* 124:124–142

Global Maximum Power Point Tracking-Based Computational Intelligence Techniques



Doaa Mohamed Atia

Abstract The photovoltaic (PV) systems are gaining popularity for both stand-alone and grid-connected applications. These systems offer benefits of being static, modular, environmental friendly, and converts light from the sun, which is a perennial source of clean and green energy. The energy conversion in the PV system is although instantaneous, yet less efficient because of optical and electrical losses. The optical loss caused by partial shading reduces PV system output greatly, if not properly mitigated. The reduced efficiency of shaded PV arrays is a significant obstacle in the rapid growth of solar power systems. The shading mitigation techniques ensure global peak operation of PV plant under undesirable shading condition. Multitudes of such mitigation techniques are available in the literature, though each one of them exhibits some vulnerability. The maximum power point tracking-based computational intelligence techniques that properly detect the global MPP are stated and discussed. Artificial neural networks (ANN), fuzzy logic control (FLC), and different types of meta-heuristic algorithm have been used such as particle swarm optimization (PSO), ant colony optimization (ACO), artificial bee colony optimization (ABC), genetic algorithm optimization (GA), differential evolution optimization (DE), cuckoo optimization (CS), firefly optimization (FA), grey wolf optimization (GWO), and bat optimization (BA). This chapter presents the proposed approaches in each method and provides a brief discussion of their characteristics. This comprehensive review of shading mitigation techniques would certainly help the researcher to select appropriate mitigation techniques for a given PV application.

1 Introduction

There are several drawbacks of the first three categories for shading mitigation techniques which are high cost, more passive components are used and complexity of control unit finally high switching loss compared to the fourth categories based on

D. M. Atia (✉)

Photovoltaic Cells Design Department, Electronics Research Institute, Cairo, Egypt
e-mail: doaa@eri.sci.eg

© Springer Nature Switzerland AG 2020

A. M. Eltamaly and A. Y. Abdelaziz (eds.), *Modern Maximum Power Point Tracking Techniques for Photovoltaic Energy Systems*, Green Energy and Technology, https://doi.org/10.1007/978-3-030-05578-3_5

131

global maximum power point tracking-based computational intelligence techniques. The PV system configuration is given in Fig. 1. Under uniform conditions, there is a single MPP in P–V characteristics, so it is simple to track the MPP. On the other hand, when some PV modules or cells receive different values of solar irradiance in the case of partial shading, P–V curve has multiple peaks. Thus, the MPPT algorithm should have the ability to find global MPP from the multiple localized maximum power peaks. There are several MPPT techniques which proved their efficiency in tracking global MPP and give the best performance for all operating conditions. Theoretically, the ideal MPPT technique for PV system should have:

1. The ability to accurately track the global MPP under partial shading conditions.
2. The ability to respond to rapid climatic condition changing.
3. The system independency and does not rely on the configuration of the PV arrays.
4. The system robustness under climatic disturbances and PV panel parameter variations.
5. The simplicity to implement with low computational complexity and low system cost.

Global optimization techniques such as computational intelligence (CI) algorithms are useful for solving real-life nonlinear problems, as compared to simple mathematical methods. Swarm algorithm (particle swarm optimization, ant colony algorithm, and artificial bee colony), differential evolution (genetic algorithm and differential evolution), and nature-inspired algorithm (firefly algorithm, cuckoo search, bat algorithm, and grey wolf algorithm) are given in Fig. 2, in addition to artificial intelligent techniques (neural networks, fuzzy logic). In the following sections, various CI-based MPPTs are discussed in details [1–5].

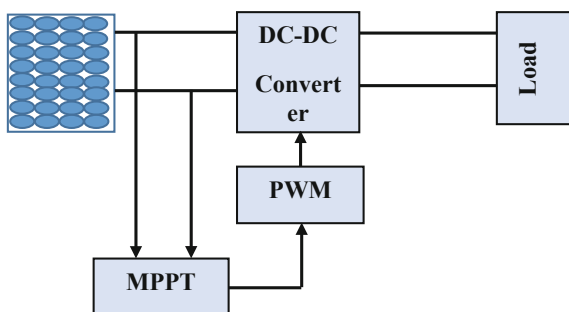


Fig. 1 MPPT control structure

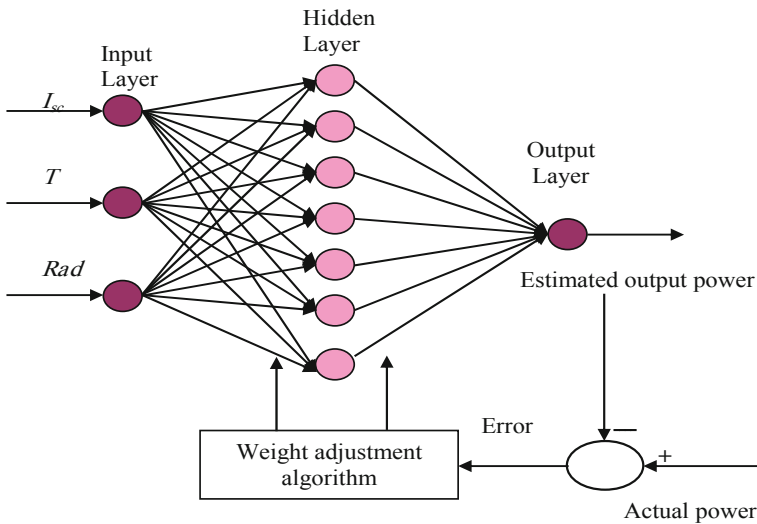


Fig. 2 ANN configuration to estimate the MPP of the shaded PV array [1]

2 Artificial Intelligent Techniques

2.1 Artificial Neural Networks

Artificial neural network (ANN) can be used to predict the MPP of PV panels under normal and up-normal operating conditions [6]. ANN consists of three layers which are an input layer, a hidden layer, and an output layer, shown in Fig. 2. Solar irradiance, air temperature, wind velocity, open-circuit voltage, terminal voltage of PV array, PV output current, voltage derivative, power derivative, and incremental conductance (dV/dI) may be taken as inputs. The sun's position is also used as another input to consider the shading effect. The system is first trained with a set of input and output data. During the training process, the weights are determined by training to correctly map input data to the desired output. Minimizing the error between the network output power and the desired output power level is the main object of the training process. Once the network is trained, then the network is expected to estimate the maximum output power of a PV array for any shading condition. It is assumed that shading due to moving objects such as clouds has a uniform effect on the PV array, and hence, it uses only the sun's position to consider the effect of partial shading [6].

Type of neural network, training parameters (it may be solar radiation, air temperature, wind speed, open-circuit voltage, short-circuit current, and maximum power point), number of training data, and model for simulating training dataset are the parameters that can affect neural network operation in MPPT. Neural network has

several advantages which are fast tracking speed, small/no oscillation at the stable state and fast for rapid irradiance change. While disadvantages of the neural network are tracking accuracy influenced by PV array model, training data required are generated from simulated models.

2.2 Fuzzy Logic Control

Fuzzy logic control (FLC) consists of three stages: fuzzification, inference mechanism, rule base, and defuzzification as presented in Fig. 3. Recently, several researchers have used the fuzzy logic control (FLC) approach to improve the performance of the MPPT controller under PSCs. Fuzzy logic is used to improve the performance of P&O technique and hill climbing method [7, 8]. Optimized FLC using the genetic algorithm (GA) approach, which has been successfully tested under PSCs, is done. Also, FLC with ANN is employed to track the GMPP in [9].

In this method, irradiance level and cell temperatures are the main inputs to train the ANN process to determine the MPP. However, this information cannot be acquired in some shading conditions. The fuzzy logic MPPT method produces faster tracking response than the conventional MPPT method to achieve the MPP under uniform solar irradiance. When the PV array experiences shaded condition, it fails to track the global peak (GP). MPPT based on FLC with initial voltage tracking function (IVTF) which is able to track GP under shaded condition. IVTF is used to estimate the new and resettable initial voltage. The PV array operates at the calculated initial voltage for tracking the GP. This technique is efficient for tracking the GP with increased efficiency [10].

Parameters affecting FLC performance are input/output scaling factors, membership functions: range/shape, and type of input/output. Advantages of fuzzy logic control are fast tracking speed, good dynamic performance and small oscillation at

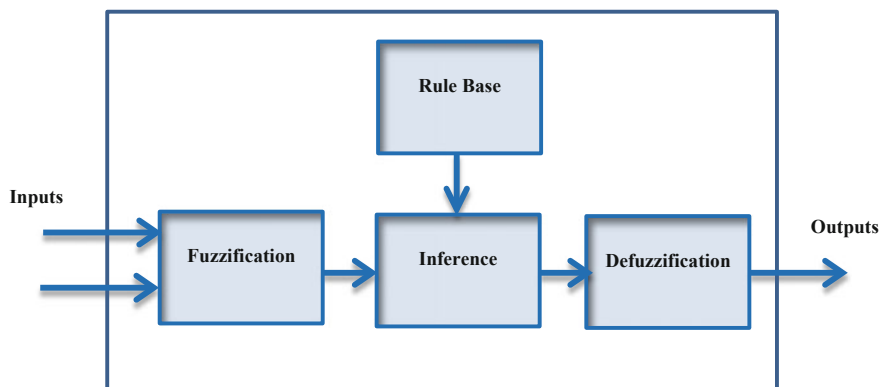


Fig. 3 Block diagram of FLC-based MPPT

stable state, and easy to combine with the advanced optimization algorithm. Disadvantages of fuzzy logic control are represented in fuzzy rules which affect the system performance, and the system performance depends on the selection of fuzzy parameters.

3 Meta-Heuristic Algorithms

Global optimization techniques such as computational intelligence (CI) algorithms are useful for solving real-life nonlinear problems, as compared to simple mathematical methods. Swarm algorithm (particle swarm optimization, ant colony algorithm, and artificial bee colony), differential evolution (genetic algorithm and differential evolution) and nature-inspired algorithm (firefly algorithm, cuckoo search, bat algorithm, and grey wolf algorithm) are given in Fig. 4.

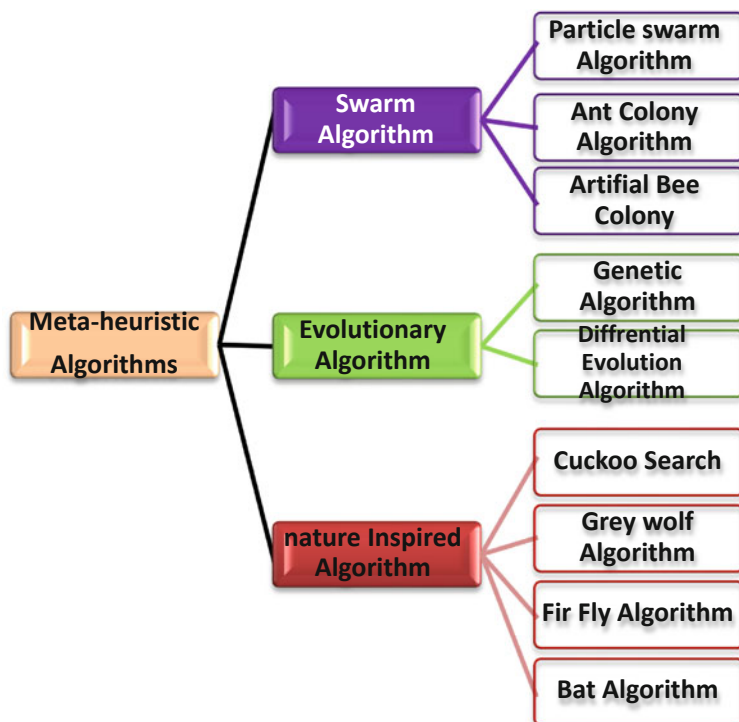


Fig. 4 Classification of meta-heuristic MPPT-based algorithms

3.1 Swarm Algorithm

3.1.1 Particle Swarm Optimization-Based MPPT

Particle swarm optimization (PSO) is one of the meta-heuristic search tools that receive considerable attention in engineering applications. PSO was first introduced in 1995 by Kennedy and Ebrahat; this method is inspired by the natural behavior of birds flocking [11–13]. This theory basically explores a specific area called the solution space, where each location has a possibility degree for the solution of problems. The PSO moves each particle throughout the solution space to determine the optimum solution according to the individual and neighboring particle experiences of the PSO during optimization. Therefore, particles involved in optimization use the memory of the particles to modify the particle fitness by following the behavior of the successful particles in the swarm. The PSO procedure starts with a random particle (initialization), continues by searching for optimal solutions within the past iterations (movement), and then evaluating the particle quality according to the fitness function (evaluation) [14]. Figure 5 shows the flowchart of PSO-based MPPT. At the beginning, the number of duty cycles has been randomly nominated. Then, each one is applied to the PV array. The system current and voltage are measured in order to estimate PV power. Such power represents the fitness function of particle i . In the next step, the comparison between new fitness value and power corresponding to p_{best} is stored in history. In case of the new estimated power is greater than the old one, it is selected as the best fitness value. After evaluating all particles, old velocity and position for each particle can be updated. When the stopping criterion is achieved, PSO-based tracker stopped and gives optimal duty cycle which corresponds to global power [15–20].

The basic PSO algorithm that defines the next position of the candidate solution is as follows [21]:

$$V_i^{k+1} = w \times V_i^k + r_1 \times c_1 \times (P_{bi} - X_i^k) + r_2 \times c_2 \times (G_b - X_i^k) \quad (1)$$

$$X_i^{k+1} = X_i^k + V_i^k \quad (2)$$

where i represents the optimization vector variable, k is the number of iterations, V_i^k and X_i^k are the respective velocity and position of the i th variable within k iterations, w is the inertia weight factor, c_1 is the cognitive coefficient of the individual particles, c_2 is the social coefficient of all the particles, and r_1 and r_2 are the random selected variables in the range $[0, 1]$. These random parameters mainly aim to maintain stochastic movement within the iterations. To maintain the search space in a certain area, the velocity values are set to the range of $[0, V_{\text{max}}]$. In PSO, the parameters w , c_1 , and c_2 are highly mutable.

The best self-experienced location (P_{bi}), which records the best position experienced by the i th particle up to the current iteration, is updated once Eq. 1 is satisfied. In addition, the variable (G_b) records the G_b experienced location met by all con-

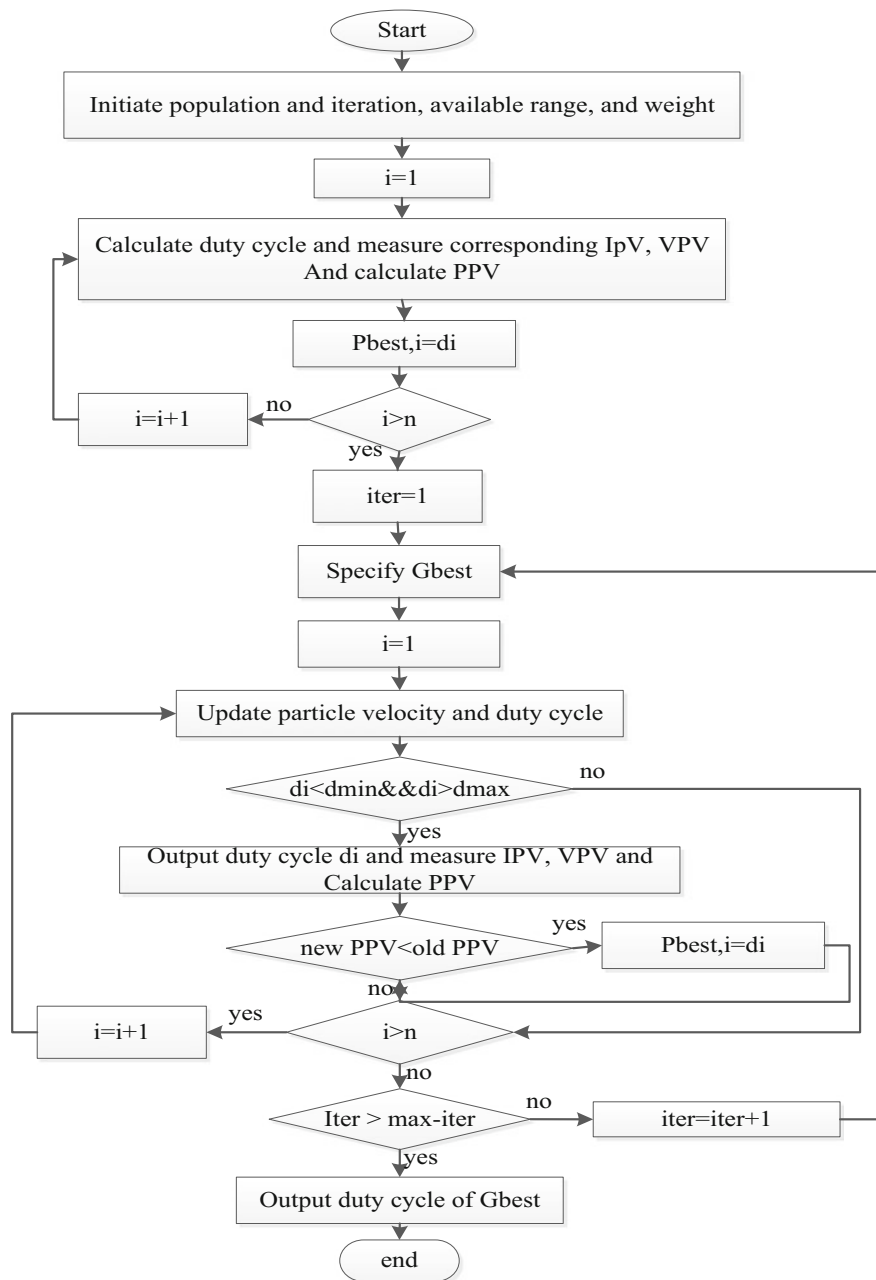


Fig. 5 Flowchart for searching mechanism by PSO-based tracker [20]

tributed particles throughout the past iterations and is compared with the P_{bi} in each iteration. The update condition of G_b and P_{bi} is presented in Eqs. 4 and 5. These equations indicate that G_b is only recorded as P_{bi} if the conditions below are satisfied [21].

$$P_{bi} = X_i^k \quad \text{if } F(X_i^k) \geq F(P_i) \quad (3)$$

$$G_b = P_{bi} \quad \text{if } F(P_M) \geq F(G_b) \quad (4)$$

Equation 5 shows the location matrix of the particles as a solution to the MPPT problem in the D dimensional search space [21].

$$X_i^k = [X_1^k \cdot X_2^k \cdot X_3^k, \dots, X_i^k, \dots, X_{(N-1)}^k \cdot X_N^k] \quad (5)$$

where X_i^k is the location of the i th particle at the k th iteration. Practically, the generated power fluctuates because of variations in the insolation levels and partial shading degrees. Therefore, the algorithm should be initialized when Eq. 6 is satisfied. If this step is neglected, the actual values of the acquired P_{bi} and G_b values should not be considered [21].

$$\left| \frac{F(X_{i+1}) - F(X_i)}{F(X_i)} \right| > \Delta P \quad (6)$$

Parameters affecting PSO performance are acceleration coefficients (the velocity and the position), inertia weight, population size, and maximum number of iterations. Advantages of PSO are global tracking technique, low computational complexity, and easy to combine with the basic algorithm. Disadvantages of PSO are standard PSO-based MPPTs have slow tracking speed when applying to large-scale PV arrays, sensitive to the control parameters.

3.1.2 Ant Colony Algorithm

Ant colony optimization (ACO) is a meta-heuristic algorithm used for global solution search in a stochastic problem. The algorithm was first introduced by Dorigo and Gambardella in 1997 based on the foraging behavior of actual ants to find the best path toward food [22]. Shen et al. [23] and Dorigo et al. [24] modified the algorithm and presented it in the form of an optimization method. Basically, ACO mimics the social behavior of ants searching for a food source. In general, the ACO trail will be selected and updated if it represents a good problem solution [25]. A brief and simplified description of ACO is presented step by step in Fig. 6. In the ACO-based MPPT technique, each location represents the voltage value of the PV array. The objective function is the output power of the PV array, and the fitness of each ant is evaluated according to its voltage value.

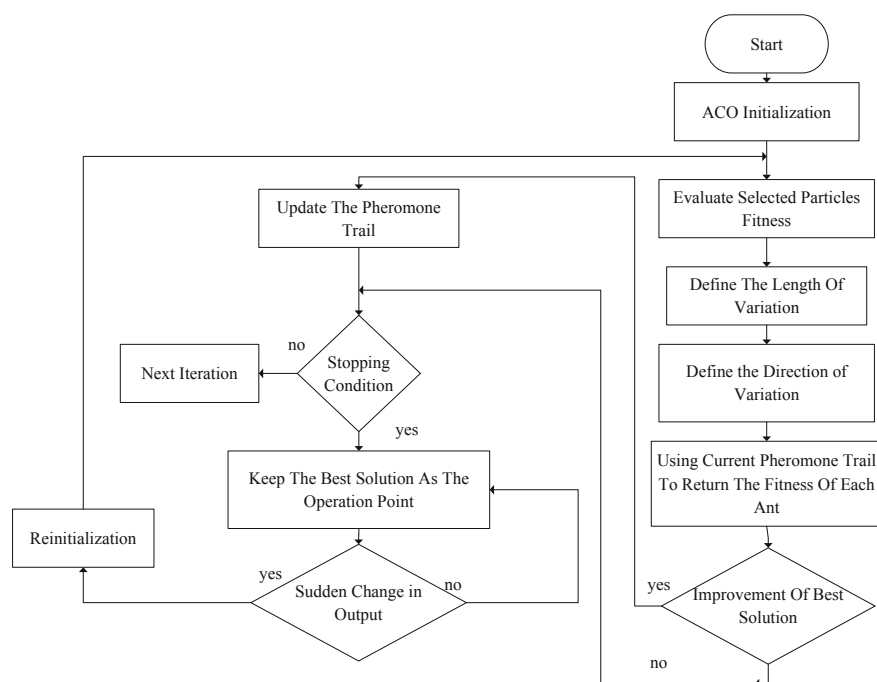


Fig. 6 Flowchart of ACO method

ACO has recently been used to solve problems in different renewable energy sectors [26–28]. ACO-based MPPT was tested at different four predefined shading conditions and showed satisfactory results under these conditions. The proposed method was fast and has a low system cost. It has the ability to track global MPP by using a single current sensor at the output of the PV system. The convergence speed of ACO is independent of the initial conditions. In addition to the sole application of ACO for the MPPT problem, some researchers used the advantages of the ACO approach to design hybridized methods in which ACO is employed to optimize the performance of other methods.

A new bio-inspired MPPT controller based on the ant colony optimization algorithm with a new pheromone updating strategy (ACO NPU MPPT) that saves the computation time and performs an excellent tracking capability with high accuracy, zero oscillations, and high robustness. First, the different steps of the design of the proposed ACO_{NPU} MPPT controller are developed. Then, several tests are performed under standard conditions for the selection of the appropriate ACO NPU parameters (number of ants, coefficients of evaporation, archive size, etc.). To evaluate the performances of the obtained ACO NPU MPPT, in terms of its tracking speed, accuracy, stability, and robustness, tests are carried out under slow and rapid variations of weather conditions (irradiance and temperature) and under different partial shading patterns. The solution archive stores a finite number of complete solutions to

the problem which serve as a reference to build new solutions. Accordingly, the following equations are used in ACO_R [21]:

$$G_i(x) = \sum_{l=1}^k w_l g_l^i(x) = \sum_{l=1}^k w_l \frac{1}{\sigma_l^i \sqrt{2\pi}} \exp\left(-\frac{(x - \mu_l^i)^2}{2\sigma_l^{i2}}\right) \quad (7)$$

where $G_i(x)$ is the Gaussian Kernel for the i th dimension of the solution; $g_l^i(x)$ is the l th sub-Gaussian function for the i th dimension of the solution; μ_l^i and σ_l^i are the i th dimensional mean value and the standard deviation for the i th solution, respectively. The pheromone equation τ_{li} given by [21]:

$$\tau_{li}(x) = \frac{1}{\sigma_l^i \sqrt{2\pi}} \exp\left(-\frac{(x - \mu_l^i)^2}{2\sigma_l^{i2}}\right) \quad (8)$$

The pheromone equation reflects the most relevant information for the construction of the objective function.

The ant colony optimization-based new pheromone update (ACO_{NPU}) is mainly based on a new process for updating the pheromone during execution which is performed by selecting the best solutions. A number of ants “ m ” of the best solutions in the archive are selected, where a pheromone initialization for each solution is performed as follows:

Calculate the distances D_i between each x_i solution among the selected solutions ($i = 1, \dots, m$) and the best solution x_{best} in the archive.

$$D_i = |x_i - x_{\text{best}}| \quad (9)$$

where D_i corresponds to the Euclidean distance, $1 < i < m$. Compute the Gaussian φ_i by the equation below:

$$\varphi_i = e^{\frac{-D_i^2}{2t}} \quad (10)$$

where t is the standard deviation of the Gaussian (usually $t = 0.05$). The pheromone's value τ_i is calculated as follows:

$$\tau_i = \frac{\varphi_i}{\sum_{j=1}^m \varphi_j} \quad (11)$$

The movement of ants is conditioned by pheromone values τ_i previously calculated for each solution of the archive. We must firstly select a reference point which is the solution to which an ant is attracted. The probability that an ant is attracted to the k th solution is τ_k . Once the reference point $x_k(t - 1)$ is selected, the position of the i th ant is obtained by the equation:

$$x_i = x_k(t - 1) + dx \quad (12)$$

where x_i is the solution vector of the k th ant at iteration t ; $x_k(t - 1)$ is the selected best solution in the solution archive (reference point); d_x is a variable generated randomly $[-\alpha, \alpha]$ to determine the length of the jump. For each value of x_i , the corresponding value d_i is calculated using the relationship:

$$d_i(t) = 1 - x_i(t)/x_{\text{ref}} \quad (13)$$

At the end of the second stage of the algorithm, m new solutions are generated, where only the K best solutions in the archive are selected among all $m + K$ solutions. Once the archive is reinitialized by the best solutions, we select the m best solutions and update their pheromones with Eqs. 9–11. Therefore, the functional objective function of the PV system is given by Eq. 14

$$\text{Objective function} = P = V_{\text{PV}} \times I_{\text{PV}}(G, T) \quad (14)$$

where V_{PV} represents the panel voltage; I_{PV} represents the panel current; T represents the panel temperature; and G represents the panel irradiation. Calculate the distances D_i between each V_i solution among the selected solutions ($i = 1, \dots, m$) and the best solution V_{best} in the archive.

$$D_i = |V_i - V_{\text{best}}| \quad (15)$$

Compute a Gaussian φ_i by the equation below:

$$\varphi_i = e^{\frac{-D_i^2}{2t}} \quad (16)$$

where t is the standard deviation of the Gaussian. The pheromone's value i is computed as follows:

$$\tau_i = \frac{\varphi_i}{\sum_{j=1}^m \varphi_j} \quad (17)$$

Then, a perturbation of the voltage is computed according to Eq. 10

$$V_i(t) = V_k(t - 1) + d_x \quad (18)$$

For each value of voltage V_i , the corresponding value of duty cycle d_i , which is used to control the system, is computed as follows:

$$d_i(t) = 1 - V_i(t)/V_{\text{ref}} \quad (19)$$

Parameters affecting ACO performance are the size of the archive, balance coefficient, convergence speed constant, population size, and maximum number of iterations. Advantages of ACO are high accuracy under partial shading, reduced cost with proposed application structure and faster tracking speed than conventional PSO, and DE MPPT. Disadvantages of ACO are one additional parameter to set compared to DE and PSO.

3.1.3 Artificial Bee Colony

A novel artificial bee colony algorithm (ABC) is developed to overcome the conventional methods' drawback with simple and robust MPPT scheme uses very few controlled parameters and the algorithm convergence criteria are not dependent on initial conditions of the system. It is a swarm-based meta-heuristic algorithm capable of solving multidimensional as well as multimodal optimization problems very easily. The artificial bees are divided into three classifications, i.e., employed, onlooker, and scout bees, as shown in Fig. 7 [29, 30]. The bee which currently searches the food or exploits the food production source is called as an employed bee, a bee that waits in the hive to make decisions to choose a food source is called as an onlooker, and the scout bee is used to carry the random search for a new food source. All three groups work together by communication and coordination to get the optimal solution in lesser time. Here, the duty cycle is the food position and maximum power as the food source of ABC algorithm. The ABC tracks MPP with good accuracy and efficiency under partial shading conditions. Parameters affecting ABC performance are a number of trials, population size, and maximum number of iterations. Advantages of ABC are high accuracy under various shadings, less parameters to set than PSO, DE and ACO, low complexity, easy to use tuning parameters, and independent of the initial conditions. Disadvantages of ABC are slow tracking speed.

3.2 Evolutionary Algorithm

3.2.1 Genetic Algorithm

Genetic algorithm (GA) is a meta-heuristic optimization method for finding solutions based on evolution of biological behavior. This method was introduced by Holland in 1975 through the principle of survival of the fittest [31]. In general, GA models the candidates' solutions, known as chromosomes, in the problem search space through fixed-length strings. The evolution process helps the best fitness chromosome to survive and mate from one generation to the next. In other words, the GA is an iterative method through which a population of chromosomes evolves and improves through generations affected by GA operators. In each generation, parents are selected from the existing population and used to generate children in the next generation. The objective function is the main evaluative factor for improving population fitness over

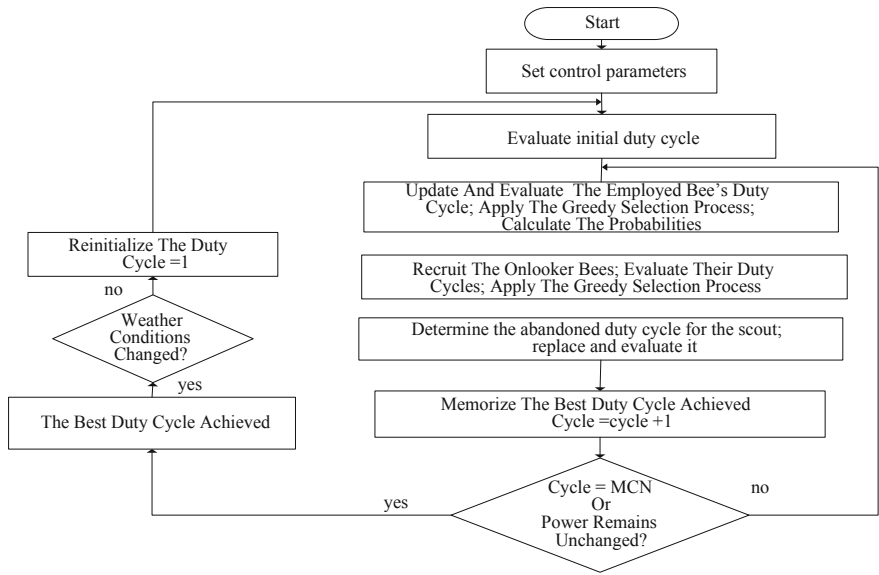


Fig. 7 Basic flowchart of artificial bee colony algorithm [30]

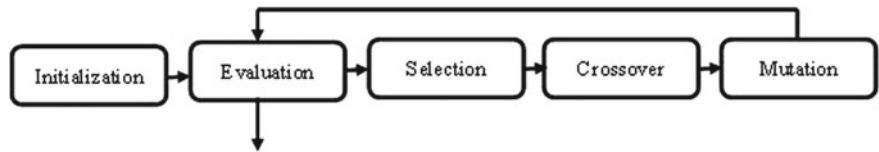


Fig. 8 Life cycle of population, recombination, and mutation

time. The procedure and life cycle of the population are shown in Fig. 8, and the GA steps are initialization, selection, crossover, and mutation. The flowchart of the GA algorithm is shown in Fig. 9.

GA was used to find the global maximum power point of the PV system under a certain simplified PSC. MPPT control was developed based on the GA approach, and the method was verified through two different cases of partial shading patterns. However, the verification part is limited to simulation validations, and the feasibility of the method under an actual practical environment has not been presented [32, 33].

GA method has been mostly used in hybrid methods to improve the performance of other MPPT techniques. Integration of P&O method and GA leads to reduce the population size and decrease the number of iterations. The hybrid method adopted a faster convergence, as well as a more accurate output for PV system under various partial shading patterns when comparing with a normal GA approach [34]. Another form of hybrid optimization method is carried out by applying GA to tune the parameters of a fuzzy logic controller used in MPP tracking under PSC. The performance of the fuzzy logic control improved as parameters, such as rule base and membership

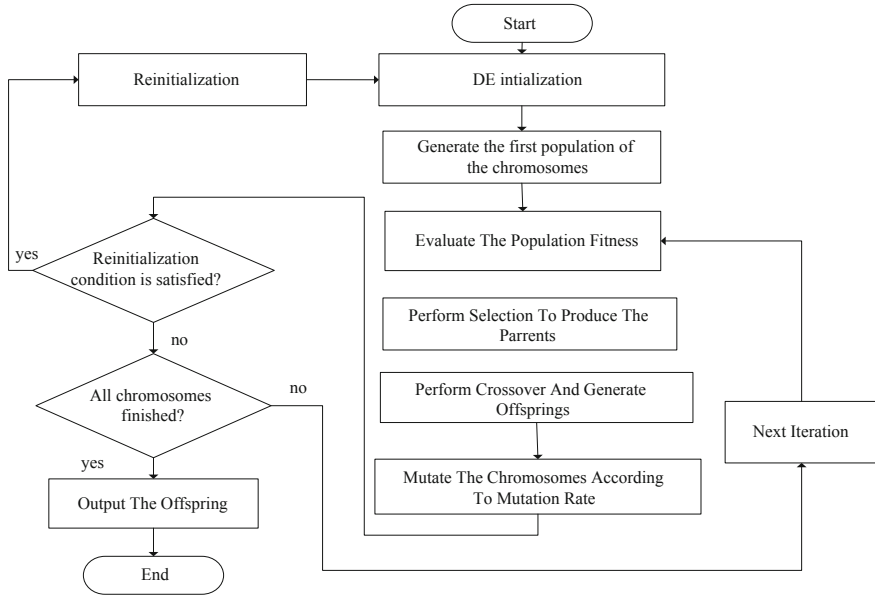


Fig. 9 GA flowchart

functions, are tuned to their optimized values by using GA techniques. GA method was finally used as a tool to train the ANN system. In this approach, GA is used to define the neuron numbers in a multilayer perceptron neural control [35]. If the chromosomes are coded in continuous numbers, and α is considered as crossover rate, the offspring will be crossed over as below [21]:

$$\text{offspring}_1 = \alpha \times \text{parents}_1 + (1 - \alpha) \times \text{parents}_2 \quad (20)$$

$$\text{offspring}_2 = (1 - \alpha) \times \text{parents}_1 + \alpha \times \text{parents}_2$$

This operator randomly manipulates the chromosome with a specific rate called mutation rate (β). For the continuous coded chromosomes, the mutation follows the statement below [21]:

$$\text{offspring} = \pm \beta \text{ offspring} + \text{offspring} \quad (21)$$

In the application of GA-based MPPT system, the initial parent population is shown as:

$$X = [\text{parent}^1, \text{parents}^2, \text{parents}^3, \dots, \text{parents}^N] \quad (22)$$

where n is the population size, and each parent represents initial voltage values in which the algorithm starts the evaluation process. The PV output power is the objective function $f(x_i)$. The fitness values of each position are estimated by the objective function and are used to evolve the population and improve the population fitness through the generations. In MPPT, GA should be reinitialized due to sudden changes in operating parameters such as load, solar radiation, or partial shading patterns. Therefore, the following conditions reinitialize GA-based MPPT once they have been satisfied [21]:

$$|V(k+1) - V| < \Delta V \quad (23)$$

$$\left| \frac{P(k+1) - P(k)}{P(k)} \right| > \Delta P \quad (24)$$

Parameters affecting performance are encoding format, crossover probability, mutation probability, population size, and maximum number of iterations. Advantages of GA are global tracking technique, uniform implementation scheme, and low computational complexity. Disadvantages of GA are slow tracking speed due to the series format for applying each particle in the population and initial conditions dependent.

3.2.2 Differential Evolution Algorithm

The differential evolutionary (DE) algorithm has the concept of GA, and Storn and Price were first introduced DE [36, 37]. Due to simplicity, DE is one of the most powerful population-based optimizations. In this algorithm, existing particles with the best fitness records remain in the population, while the others are replaced by new particles. DE is suitable for problems with many local optimum solutions [38–40]. The algorithm consists of four steps which are initialization, mutation, crossover, and selection. Renewable energy systems were recently used the DE algorithm to solve the global MPP tracing in PSC problem. In the DE-based MPP tracking method, the duty cycle of DC–DC converter is the target vector. However, the method is based on a static objective function in which the P–V curve must be predetermined, which makes the method impractical for real-time MPPT application [38]. The search time was decreased by avoiding the additional measurement from the output of the converter setup. Figure 10 gives the flowchart of DE algorithm [39–42].

The algorithm must be initialized by assigning the initial locations to the target vector. The parameters are randomly selected to be recombined to enhance the stochastic nature of the DE and cover the entire search space. Assuming the NP as the total population size, Eq. 25 describes $X_{i,G}$ as the target vector of the i th particle in the G th iteration [21].

$$x_{f,G}; \quad i \in (1, 2, 3, \dots, NP) \quad (25)$$

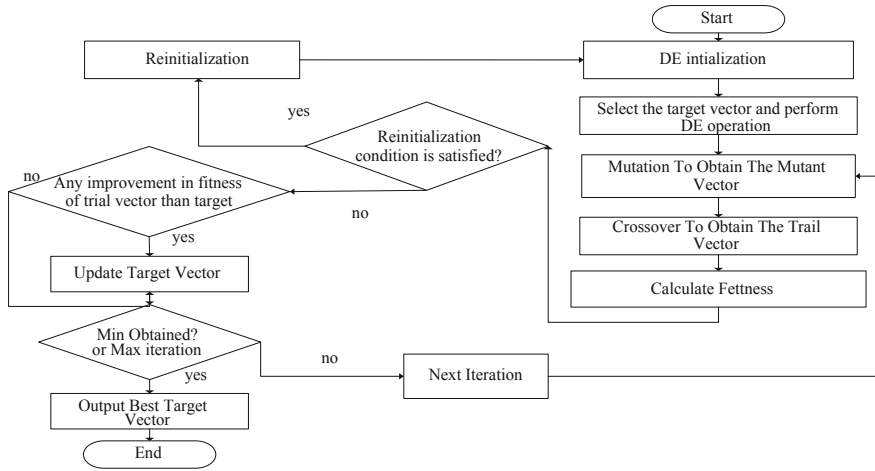


Fig. 10 Flowchart of DE method

The v_i, G which is the mutant vector of the i th particle in iteration G , is formed by mutating each particle of the target vector by using the equation below [21]:

$$v_{f,G+1} = x_{f,G} + k \cdot (x_{r1,G} - x_{f,G}) + F \cdot (x_{r2,G} - x_{r3,G}) \quad (26)$$

where r_1, r_2 , and r_3 are the random numbers in the range of $(1, 2, \dots, NP)$, and NP denotes the number of particles. K and F are the scaling and combination factors, respectively, which are ranged in $[0, 2]$. The DE parameters, like other meta-heuristic methods, affect the performance of the system significantly. Parameter selection is an important responsibility for a designer, especially when the engineering problem is significantly critical, such as MPP tracking from the nonlinear output of partially shaded PV system. The most common parameter selection method is the rule of thumb by Storn. In the DE-based MPPT, the output power will be evaluated when the crossover sections are completed and the trial components of trial vectors are generated [21].

$$u_{f,G+1} = \begin{cases} v_{f,G+1} & \text{if } (rnd_j \leq CR) \text{ or } j = rn_f \\ x_{f,G} & \text{if } (rnd_j > CR) \text{ or } j \neq rn_f \end{cases} \quad (27)$$

$$x_{f,G+1} = \begin{cases} u_{f,G} & \text{if } f(u_{f,G}) \geq f(x_{f,G}) \\ x_{f,G} & \text{if } f(u_{f,G}) < f(x_{f,G}) \end{cases} \quad (28)$$

Parameters affecting performance are scaling factor, crossover rate, population size, and maximum number of iterations. Advantages of DE are global tracking technique and simple implementation. Disadvantages of DE are sensitive to the control parameters of the algorithm.

3.3 Nature-Inspired Algorithm

3.3.1 Cuckoo Search

The cuckoo search (CS) method is based on the reproduction strategy of some species of cuckoo bird which are reported to lay their eggs in the nests of other birds. This parasitic reproduction approach is the basis of the CS optimization method. In this approach, seeking the right host nest is a key step. This is similar to searching for food, which is a random process and can be modeled using mathematical functions. One of the common methods for modeling animal's food-seeking trajectory is the Lévy flight model. The operational behavior of the CS technique is similar to the HC and P&O methods. Unlike these methods, however, the step size of the CS is based on Lévy flight and is a population-based algorithm. Due to Lévy flight, compared with standard PSO and DE techniques, the CS method has more efficient randomization and faster convergence [43, 44]. Figure 11 shows the flowchart for searching mechanism by CS-based tracker. At the beginning, the number of duty cycles is randomly nominated. Then, each one is applied to PV. The system current and voltage are measured in order to estimate PV power. Such power represents the fitness value. The duty cycle related to best fitness function has been selected as current best nest (d_{best}). Next, Lévy flight is applied in order to generate new nests. New fitnesses' values are tested through the PV system. Afterward, the worst nest is randomly destroyed, and this process simulates the behavior of the host bird discovering the cuckoo's eggs and destroying them.

The PV power is measured and the current best nest is selected. When the stopping criterion is achieved, CS-based tracker stopped and gives optimal duty cycle which corresponds to global power.

The Lévy flight model represents a random walk where step sizes are defined using Lévy distribution, which is determined by the following equation [21]:

$$\text{Lévy}(\lambda) \approx u = 1^{-\lambda} \quad \text{where } (1 < \lambda < 3) \quad (29)$$

For each iteration, the Lévy flight is performed to determine the new solution using the following expression [21]:

$$x_i^{t+1} = x_i^t + a \oplus \text{Lévy}(\lambda) \quad (30)$$

where i is the number of samples (or eggs), t is the iteration number, the product \oplus indicates entry-wise multiplication, and a is the step size which needs to be tuned properly according to the constraints of the optimization problem. The value of a is often defined using the initial step α_0 , and the difference between two samples (x_j^t and x_i^t), as shown by the following equation [21]:

$$a = \alpha_0 + (x_j^t - x_i^t) \quad (31)$$

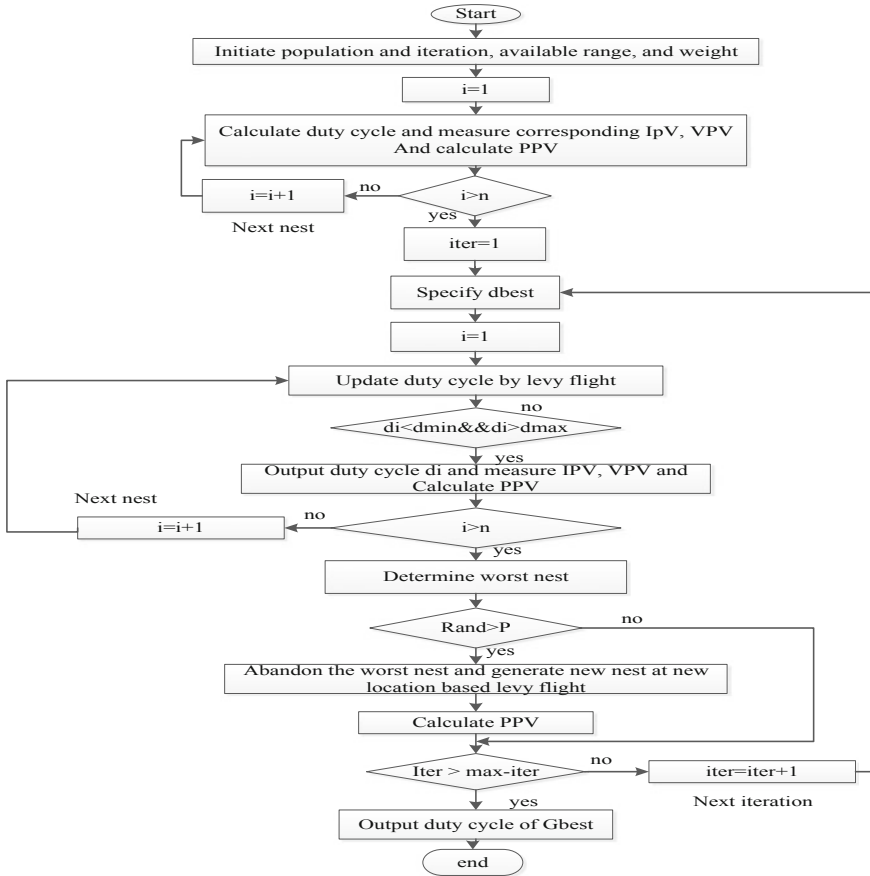


Fig. 11 Flowchart for searching mechanism by CS-based tracker

Parameters affecting performance are initial step change, fraction of worse nests, parameters for Lévy distribution, population size, and maximum number of iterations. Advantages of CS are easy to implement, fast tracking speed, and easy to combine with other swarm-based algorithms. Disadvantages of CS are easy to fall into local optima on the boundary when the parameters are inappropriately set low convergence rate.

3.3.2 Grey Wolf Algorithm

Grey wolf optimization (GWO) is another population-based optimization technique, based on the hierarchical leadership and the hunting behavior of the grey wolf and recently presented in [45]. When seeking prey, grey wolves can be classified into four

types based on the fitness evaluation of each type where the first type possesses the highest fitness and the fourth is the worst. Grey wolves have three main steps in their hunting behavior: (a) searching, tracking, and approaching prey; (b) pursuing and encircling prey; and (c) attacking prey. Circling behavior by the wolves is a key step in the hunting procedure and for the purpose of designing the GWO algorithm. The GWO method is applied to MPPT where the number of participating grey wolves represents the converter's duty cycles and the MPP is prey being hunted [46].

Circling behavior of the wolves is a key step in the hunting procedure and for the purpose of designing GWO algorithm is mathematically represented by Eq. 33 [21]:

$$\vec{D} = |\vec{c} \cdot \vec{x}_{p(t)} - \vec{x}_{(t)}| \quad (32)$$

$$\vec{x}_{(t+1)} = \vec{x}_{p(t)} \vec{A} \cdot \vec{D} \quad (33)$$

where t is the number of the iteration, X_p and X are the positions vectors of the prey and the grey wolf, respectively; and A , C and D are the coefficient vectors calculated by Eq. 32–35 [21]:

$$\vec{A} = 2 \cdot \vec{a} \cdot \vec{r}_1 - \vec{a} \quad (34)$$

$$\vec{c} = 2 \cdot \vec{r}_2 \quad (35)$$

where components of a are linearly decreased from 2 to 0 across iterations and r_1, r_2 are random vectors in $[0, 1]$. GWO optimization method is applied to MPPT where the number of participating grey wolves represents the converter's duty cycles and the MPP is prey being hunted. For number of grey wolves, i.e., duty ratios, the controller measures V_{pv} and I_{pv} through sensors and computes the output power. The flowchart of GWO-based MPPT algorithm is shown in Fig. 12 [47].

Parameters affecting performance are exploration and exploitation factor, population size, and maximum number of iterations. Advantages of GWO are easy to implement, few parameters to set, and good tracking accuracy. Disadvantages of GWO are low tracking speed.

3.3.3 Firefly Algorithm

The FA is a population-based optimization method and similar to PSO. The FA is inspired by illuminated bugs and is mathematically presented in [48, 49]. FA has less parameters to be tuned and the particles in FA aggregate more closely around each optimum, without rapid fluctuation. Flashing light is a key component of the population-based behavior of fireflies and is used to attract mating partners and potential prey, as well as a mechanism for protective warning. As such, brightness is important and used to determine the new position for particles in the search space (Fig. 13) [2, 21, 48–50].

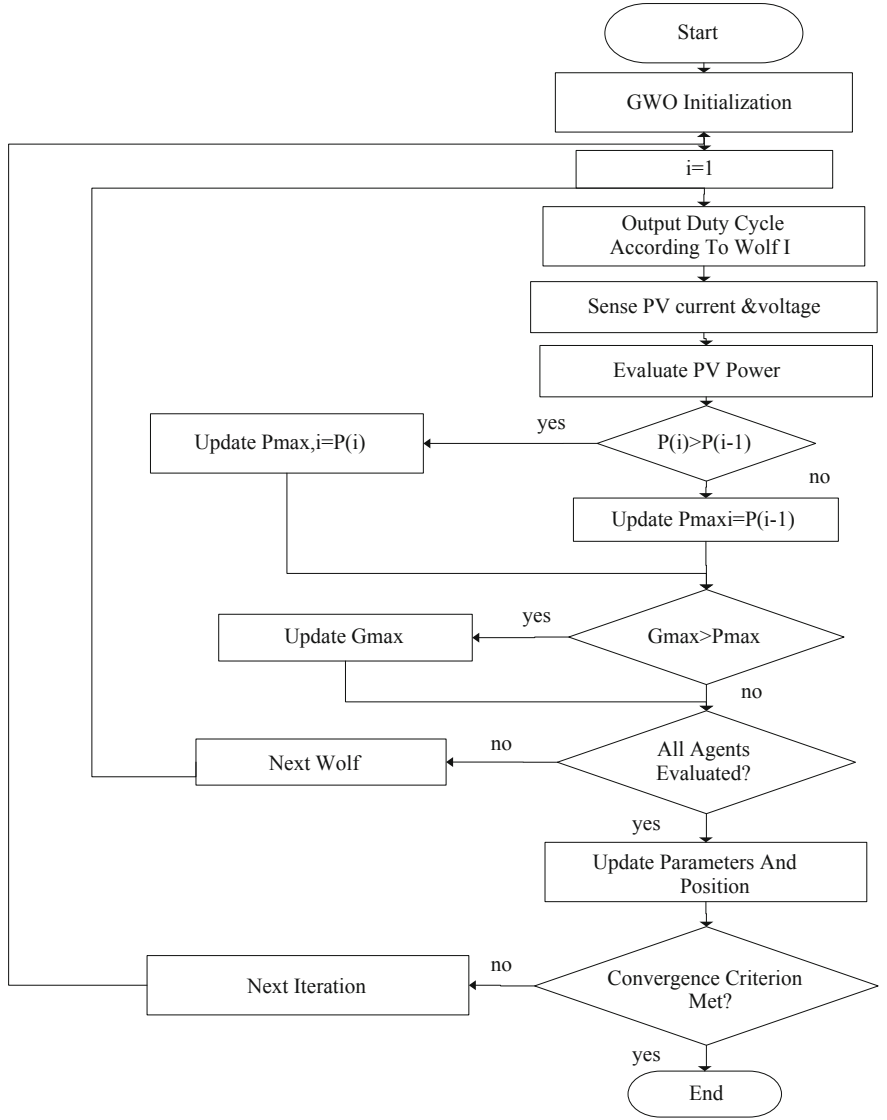


Fig. 12 Flowchart of the proposed GWO algorithm

For example, if the firefly p has lower brightness than firefly q , the new position for firefly p is determined by Seyedmahmoudiana et al. [21]:

$$X_p^{t+1} = X_p^t + \beta(r)(X_q - X_p) + (\text{rand} - 0.5) \quad (36)$$

where X_p and X_q represent the positions of two fireflies, r is the distance between these two fireflies, β is the level of attractiveness, and α is a random movement factor and is a constant value in the range of $[0, 1]$. It is important to mention that a large value of α makes it possible to search for the solution through a large search space, whereas a smaller value of α tends to facilitate local search. The degree of attractiveness (β) can be calculated using the following equation [21]:

$$\beta(r) = \beta_0 e^{-\gamma(X_{pq})^n}, \quad n \geq 1 \quad (37)$$

where γ is the absorption coefficient and controls the light intensity, and β_0 is initial attractiveness.

For a population of fireflies, i.e., duty ratios, the digital controller measures V_{pv} and I_{pv} and computes the output PV power. The steps of FA algorithm toward MPPT are described below [2]:

In the first step (parameter setting), fix the constants of the FA and the termination criterion. In this algorithm, the position of the firefly is taken as a duty cycled of the DC–DC converter. The brightness of each firefly is taken as generated power P_{pv} of the PV system, corresponding to the position of this firefly. In the second step (initialization of fireflies), the fireflies are positioned in the allowable solution space between d_{\min} and d_{\max} where d_{\min} and d_{\max} represent the minimum and maximum values of the duty ratio of the DC–DC converter. In the third step (brightness evaluation), the DC–DC converter is operated corresponding to the position of each firefly (i.e., duty ratio) sequentially. For each duty ratio, the corresponding PV output power, P_{pv} , is taken as the brightness or light intensity of the respective firefly. This step is repeated for the position of all fireflies in the population. The fourth step (update the position of fireflies), the firefly with maximum brightness remains in its position and the remaining fireflies update their position. In the fifth step (program termination), terminate the program if the termination criterion is reached; else go to step 3. The optimization algorithm is terminated once the displacement of all fireflies in consecutive steps reaches a set minimum value. Once the program is terminated, the DC–DC converter operates at the optimum duty cycle corresponding to GMPP. In the final step (reinitiate FA), if the solar insolation changes which is detected by the digital controller by sensing the change in the power output [2].

Parameters affecting performance are initial attractiveness, absorption coefficient, random movement factor, population size, and maximum number of iterations. Advantages of FA are better performance, fast tracking speed, and not sensitive to the initial conditions. Disadvantages of FA are easy to fall into local optima when the parameters are inappropriately set.

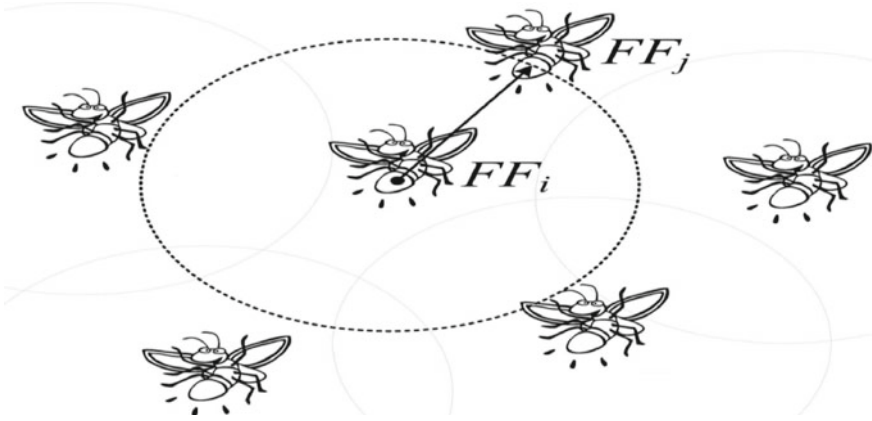


Fig. 13 Behavior of fireflies

3.3.4 Bat Algorithm

Bat algorithm (BA) is a population-based optimization algorithm inspired by the echolocation features of micro-bats in locating their foods. Small bats (micro-bats) feed primarily on insects which detect using echolocation. The direction and intensity of the return signal enable them to locate potential prey in direction and also in distance. At first, the bat overflies the search space, while emitting a set of ultrasonic pulses of certain amplitude (intensity) and a rate (density). Between the pulse trains, it receives the feedback signals (its own signal and eventually the signals from other bats in the swarm) by echolocation and interprets them. If the signals received in return have a low intensity and a strong rate, then it is very likely that prey is detected and the bat should head toward it. As the bat approaches the prey, it gradually intensifies the amount of pulses (the ultrasound rate) and, at the same time, progressively decreases the intensity of these pulses. Bat algorithm is developed then by idealizing some of the echolocation characteristics of micro-bats [51].

Bat algorithm maintains a swarm of N micro-bats, where each micro-bats flies randomly with a velocity v_i at position x_i , with a varying loudness A_i and pulse emission rate $r_i \in [0, 1]$ depending on the proximity of their target. During the optimization task, every bat is randomly assigned a frequency which is drawn uniformly from $[f_{\min}, f_{\max}]$. Then, the velocity v_i and the position x_i of each bat at time step t are defined and updated with:

$$f_i = f_{\min} + (f_{\max} - f_{\min})\beta \quad (38)$$

$$v_i^{t+1} = v_i^t + (x_i^t - x_0)f_i \quad (39)$$

$$x_i^{t+1} = x_i^t + v_i^{t+1} \quad (40)$$

where $\beta \in [0, 1]$ is a vector randomly drawn from a uniform distribution. x^t is the current global best location (solution) which is achieved after comparing all the solutions among all the N bats at each iteration t . If a random number is greater than the pulse emission r_i^t , then the exploitation stage is selected and the position is replaced by the solution generated by the local search. As a result, a new solution is drawn locally by using a random walk around the current best solution:

$$x_{\text{new}} = x_0 + \epsilon A^t \quad (41)$$

where ϵ is a random number which can be drawn from a uniform distribution in $[-1, 1]$ or Gaussian distribution, while $A \leq A_i^t$ is the average loudness of all the bats at this time step. If a random number is smaller than the loudness A_i^t and the new solution improve the fitness value, this means that the bat is moving toward the prey (the optimal solution). Then, the new solution is accepted and its loudness and emission rates are updated to control the exploration and exploitation. It is suggested that loudness decreases from positive value A_i^0 to $A_{\min} = 0$ whereas the pulse rate of pulse emission increases from 0 to R_i

$$A_i^{t+1} = \alpha A_i^t \quad (42)$$

$$r_i^{t+1} = R_i(1 - \exp(-\gamma t)) \quad (43)$$

$$|x_i^k - x_j^k| \leq \Delta x \quad i, j = 1, 2, 3 \dots, (i \neq j) \quad (44)$$

$$\frac{|P_{\text{PV new}} - P_{\text{PV last}}|}{P_{\text{PV last}}} > \Delta p \quad (45)$$

where α is a constant in the range of $[0,1]$, and γ is a positive constant. In this work, A_{i0} and R_i are set to 1.

The bat algorithm is applied to the tracking of GMPP by the direct duty cycle control method. Thus, the optimization variable is defined as the duty cycle of the PWM signal. The complete flowchart of the proposed bat algorithm-based MPPT is illustrated in Fig. 14.

Parameters affecting performance are movement of virtual bats, velocity, weights, loudness, and pulse emission. Advantages of BA are faster, more efficient, sustainable, and more reliable than conventional and other soft computing-based methods, give the best solution in quick time. Disadvantages of BA are bat algorithm converges very quickly at the early stage and then convergence rate slows down, there is no mathematical analysis to link the parameters with convergence rates, and accuracy may be limited if the number of function evaluations is not high.

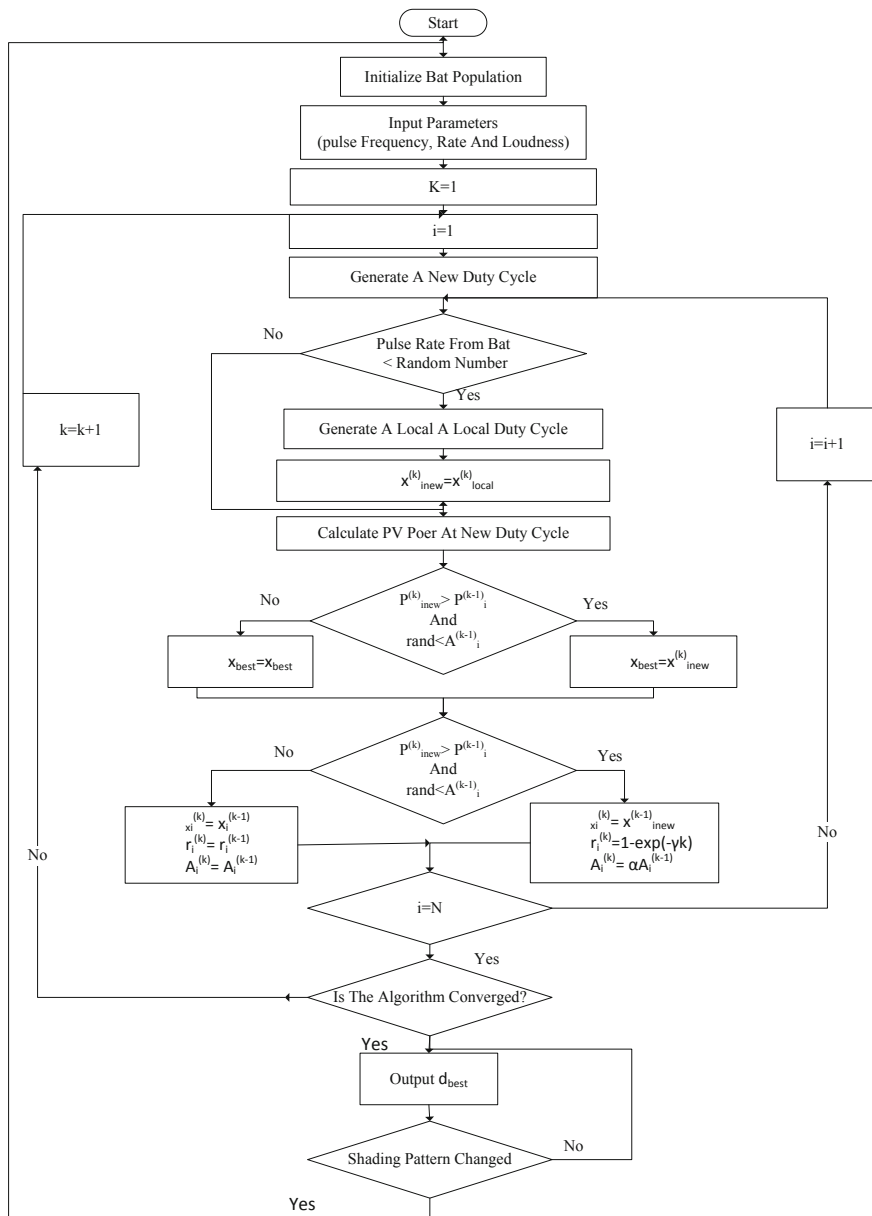


Fig. 14 Complete flowchart of the MPPT-based bat algorithm [51]

4 Hybrid Methods for MPPT

A simple and efficient hybrid MPPT technique for PV systems under PSC was developed with a combination of P&O or IC and artificial neural network [52]. This approach was noted to be less costly with simple structure and fast response. In a different work, an FL-based P&O MPPT was studied using peak current control with a variation of the reference current for better transient with the improved steady-state performance [53]. The analysis showed an improved transient response of 15% and the power loss reduction in the steady state. An ANN-Polar coordinated fuzzy controller-based MPPT control was applied for PV under PSC [54]. The FL with polar information controller utilizes the global MPP voltage as a reference voltage to produce the required control signal for the power converter, and the MPPT is estimated through the ANN algorithm. Meanwhile, an ANN-based modified IC algorithm for MPPT under PSC was simulated and implemented in hardware using FPGA [55]. The analysis revealed that the improved FL-P&O MPPT method is able to track the real absolute MPP for PSC. FL and P&O-based MPPT for PV array under PSCs were implemented in MATLAB/Simulink [56]. FL is adopted into the conventional MPPT to enhance the overall PV system performance and for the optimization of the solar PV array under PSC. This method has improved performance because it can facilitate the PV array to reach the MPP faster and achieve a stable output power. An MPPT algorithm based on a modified GA was also concentrated on tracking the GMPP in PV array with PSC [57]. A P&O algorithm was integrated into the GA function to create a single algorithm. The control part and the GMPPT algorithm were implemented on a digital signal processor and tested on an experimental small-scale PV system. The algorithm does not need some sort of preset up configuration and can be directly applied to any type of PV characteristic with an unknown number of local MPPs. The assessment of GA and conventional methods for MPPT of shaded solar PV generators is carried out [58]. They concluded that IC and P&O algorithms fail to achieve MPP of the PV if the PV panel is under PSC. To solve this problem, GA algorithm was used and it successfully enabled the system to reach the global MPP. Alternatively, an MPPT method for PV systems PSC was formulated where a global MPP searching technique is obtained by linking IC and scanning approach method which utilizes duty cycle sweep to track the global MPP when the PV array is under PSC [59]. A hybrid MPPT technique based on P&O and PSO is indicated to have excellent performance [60]. P&O was employed to assign the nearest local maximum, whereas the PSO technique was used to search for the GMPP. MPPT of PV systems under PSCs through a colony of flashing fireflies was verified to have faster convergence, simple computational steps and low-cost implementation on the microcontroller. The technique was studied for two dissimilar configurations of PV arrays under PSCs and the tracking performance compared with conventional P&O and PSO methods under identical conditions. PV system MPPT control based on PSO-DE hybrid algorithm was tested under PSC. Compared with the PSO algorithm and DE algorithm, the hybrid tracking algorithm requires a much shorter time to reach the GMPP [61]. In another work [62], an ANN-based hybrid MPPT algorithm

was proposed. The basic idea of the proposed MPPT method is to use the ANN classifier to recognize the region of the global peak voltage from the irradiance values when irradiance sensors are available. Alternatively, the peak voltage is recognized from the measured current values on each stair of the I–V curve. The obtained information through ANN could be used to locally track the MPP using any conventional tracking algorithm. The effectiveness of the proposed MPPT is well proved using both simulations and experimental setup. The results are shown to have more PV yield compared to other techniques and under various PSCs, and their method can track the global MPP with fast tracking speed [21]. FLC-based GWO and PSO are studied by Eltamaly et al. [63, 64].

5 Analytical Comparison

Published research in this field of MPPT indicates the difficulty of evaluating and comparing the best MPPT approaches and techniques. In general, the final MPPT technique is selected based on the application requirements and preferences. Therefore, the knowledge about the nature of the application and the limitations is an essential prerequisite. In addition, the test benches, applications, and environmental conditions used to verify the performance of the designed MPPT techniques are not similar. Therefore, a comparison among these methods should be fair. Compared with the conventional MPPT techniques, the intelligent approaches commonly have lower oscillation around MPPT and higher reliability for sudden changes in irradiance levels. In addition, they mostly show better performance in the most significant criteria. However, their behavior with regard to the main criteria, such as efficiency, reliability under PSCs, convergence speed, system independence, and steady-state oscillation, might be different. The performance of these techniques in accordance with the accredited literature is discussed and presented in Fig. 15 and Table 1. It is shown that the axis *A*, *B*, *C*, *D*, *E*, and *F* refer to periodic tuning and parameter dependency, simplicity, efficiency, reliability under PSCs, system independency, and convergence speed, respectively. According to the reviewed studies, the FLC and ANN methods in their original forms are incapable of tracking the global maximum points under PSCs. However, they obtain satisfactory results under normal conditions. The most significant advantage of the ANN method is its independence from detailed information of the PV system. However, its reliability is largely affected by the training process, which makes the system exclusive for each PV system. Therefore, the ANN method cannot operate for another PV system unless it undergoes a new training process. This problem may also occur when the characteristics of the array change due to aging or degradation.

The main advantages of FLC are its system independence and ease of implementation. However, the computational cost of the system for designing the fuzzification rule base and defuzzification process increases. Compared with other AI-based MPP techniques, the FLC requires more perception and comprehension of the PV system by the designer to design the different FLC parameters, such as rules and member-

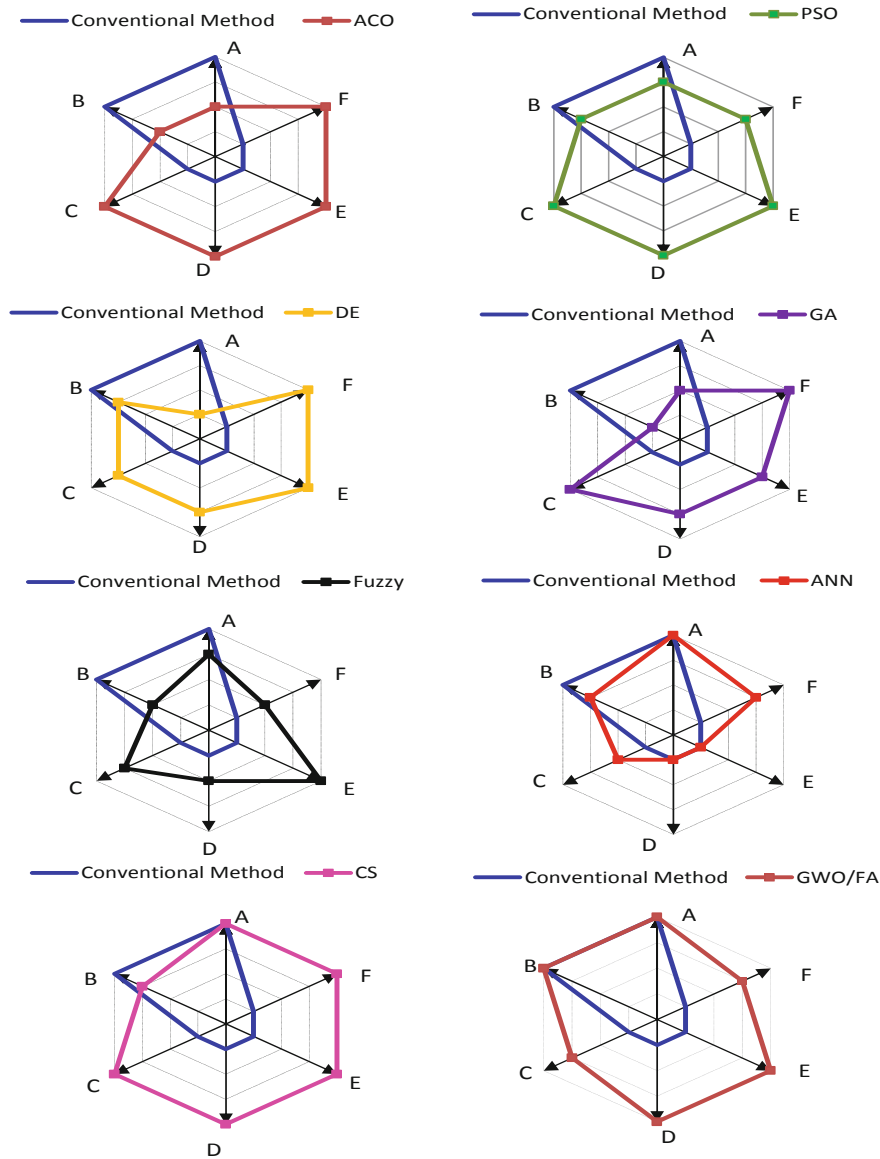


Fig. 15 Comparison of new and conventional MPPT methods to six main parameters [21]

Table 1 Comparison of different MPPT techniques [48]

Criteria	ANN	FLC	PSO	ACO	DE	GA	GWO/FA	CS
Convergence speed	Average	Average	Fast	Fast	Fast	Fast	Medium	Very fast
System independency	Poor	Poor	High	High	High	High	High	High
Ability to track under PSCs	Poor	Poor	High	High	Average high	Average high	High	High
Ability to track under normal condition	High	High	High	High	High	High	High	High
Efficiency in PSCs	Poor	Poor	High	High	High	High	High	Very high
Algorithm complexity	Simple	Medium	Simple	Simple	Simple	Complex	Medium	Medium
Implementation cost and complexity	High	High	Average low	Average low	Average low	Average low	Average low	Average low
Periodic tuning	Yes	Yes	No	No	No	No	No	No
Dependency of the initial design	High	High	Medium	Medium	Low	Medium	Medium	Medium
Oscillation around MPP	No	No	No	No	No	No	No	No

ship functions. Therefore, this method can be considered more system dependent than others. System independence speed and decision making based on approximate values make the fuzzy logic controller one of the most suitable techniques for complex engineering challenges. Thus, this method can be considered one of the more reliable options for finding the MPP in the nonlinear characteristics of PV systems under normal conditions and some PSC. However, this technique highly depends on designer knowledge in the different steps of the algorithms. In addition, the method needs extensive computation in the fuzzification, rule base, and defuzzification stages.

All the PSO-based methods are suitable to operate under PSC. The methods are mainly related to their heuristic behavior for exploring the search space that comprises multiple maximum power points. The main problems of the PSO method are implementation complexity, poor dynamic response due to the interruption for measurement process, long tracking process as a result of undefined initial points, and significant dependency on the coefficient designs and initial conditions. Overall, PSO has a fast convergence speed, high sensitivity atmospheric change, low hardware implementation cost, and high efficiency with no oscillation around MPP.

ACO can also track the MPP under both normal and PSC. Unlike PSO, ACO is not dependent on the design of the initial location of the particles. In addition, it is capable of tracking MPP in a system with minimized sensors, which results in a more cost-effective system. However, theoretically, this condition can be similar for all the meta-heuristic approaches, such as PSO, DE, and GA. In general, ACO comprises three factors: the positive feedback mechanism that increases the probability of detecting optimal solutions in initial iterations, the distributed computation to ensure that the algorithm is not involved in the local optimum, and the greedy search that helps the algorithm find the optimal solution with higher convergence speed [65]. Overall, the most significant advantages of the ACO over other AI-based methods are system independence, high convergence speed, and initial location independence of particles. However, these advantages might increase the computational burden because of complex calculations. In addition, due to the lack of research in this area, the reliability and robustness of the technique under different PSCs have not been experimentally verified.

The GA and DE techniques, which have almost similar concepts, can track the global MPP under PSCs because of their ability to solve multi-objective problems. Both algorithms are system independent, efficient, have no need for periodic tuning, and have no oscillation around MPP. Moreover, the advantages of the DE algorithm are simplicity because of the few required control parameters, fast convergence speed, and initial location independence. However, experimental verifications for purely using either of these methods under PSC conditions are lacking. Unlike the PSO and ACO theories, the methods do not remember previous movements and locations that the particles have experienced throughout the program. Therefore, the algorithm is more likely to be stuck in the local optimum. The CS MPPT technique also has a very fast convergence speed compared to other MPPT techniques, achieved using Lévy flight during its operation. CS technique requires only a few parameters to be tuned; however, it has fairly complex operation compared with other soft computing-based MPPT methods GWO and FA techniques. The convergence speed toward the GMPP

for both algorithms is an improvement upon common AI techniques, and they have less complex structure compared with CS algorithms. However, GWO or FA-based MPPT unit results in output oscillation during the tracking period compared with CS algorithms. Therefore, in the applications which are very sensitive to output power fluctuations, CS technique is preferred [65, 66].

6 Conclusion

Many shading mitigation techniques are developed over the years and gained momentum in last two decades due to the recent emphasis on green technology. A comprehensive review of important shading mitigation techniques as reported in the literature is categorically brought out in this chapter. The major hurdles in the rapid growth of the PV systems are the development of efficient power electronics topology to track global maximum power point. It is established that efficient tracking against partial shading condition enhances overall efficiency of the PV system. A wide range of MPPT literature emphasizing the suitability of global MPPT techniques to mitigate partial shading are therefore reviewed, categorized, and discussed. All important methods are broadly classified and found to have variations in either implied algorithm or in hardware architecture. Each method has its own merits and demerits, so it is difficult to determine which one is suitable for a specific application.

References

1. Bidram A, Davoudi A, Balog R, Balog S (2012) Control and circuit techniques to mitigate partial shading effects in photovoltaic array. *IEEE J Photovoltaics* 2(4):532–546
2. Sundareswaran K, Peddapati S, Palani S (2014) MPPT of PV systems under partial shaded conditions through a colony of flashing fireflies. *IEEE Trans Energy Convers* 29(2):463–472
3. Bouilouta A, Mellit A, Kalogirou S (2013) New MPPT method for stand-alone photovoltaic systems operating under partially shaded conditions. *Energy* 55:1172–1185
4. Danandeh M, Mousavi S (2018) Comparative and comprehensive review of maximum power point tracking methods for PV cells. *Renew Sustain Energy Rev* 82:2743–2767
5. Jiang L, Srivatsan R, Maskell D (2018) Computational intelligence techniques for maximum power point tracking in PV systems: a review. *Renew Sustain Energy Rev* 85:14–45
6. Hyok J, Yong J, Gu K, Hyung K, Won L, Yuen W (2011) A real maximum power point tracking method for mismatching compensation in PV array under partially shaded conditions. *IEEE Trans Power Electron* 26:1001–1009
7. Alajmi B, Ahmed KH, Finney S, Williams B (2013) A maximum power point tracking technique for partially shaded photovoltaic systems in microgrids. *IEEE Trans Ind Electron* 60:1596–1606
8. Ramaprabha R, Balaji M, Mathur B (2012) Maximum power point tracking of partially shaded solar PV system using modified Fibonacci search method with fuzzy controller. *Int J Electr Power Energy Syst* 43:754–765
9. Chen Y, Jhang Y, Liang R (2016) A fuzzy-logic based auto-scaling variable step-size MPPT method for PV systems. *Sol Energy* 126:53–63

10. Punitha K, Devaraj D, Sakthivel S (2013) Development and analysis of adaptive fuzzy controllers for photovoltaic system under varying atmospheric and partial shading condition. *Appl Soft Comput* 13:4320–4332
11. Eberhart R, Kennedy J (1995) A new optimizer using particle swarm theory. In: *Proceedings of the sixth international symposium on micro machine and human science*: New York, NY, pp 39–43
12. Eberhart R, Shi Y, Kennedy J (2001) *Swarm intelligence*. Elsevier
13. James K, Russell E (1995) Particle swarm optimization. In: *Proceedings of the 1995 IEEE International conference on neural networks*, pp 1942–1948
14. Seo J, Im CH, Heo C, Kim J, Jung H, Lee C (2006) Multimodal function optimization based on particle swarm optimization. *IEEE Trans Magn* 42:1095–1098
15. Liu Y, Huang Sh, Huang J, Liang W (2012) A particle swarm optimization-based maximum power point tracking algorithm for PV systems operating under partially shaded conditions. *IEEE Trans Energy Convers* 27(4):1027–1035
16. Kamarzaman N, Ta C (2014) A comprehensive review of maximum power point tracking algorithms for photovoltaic systems. *Renew Sustain Energy Rev* 37:585–598
17. Phimmason V, Endo T, Kondo Y, Miyatake M (2009) Improvement of the maximum power point tracker for photovoltaic generators with particle swarm optimization technique by adding repulsive force among agents. *Electr Mach Syst*, 1–6
18. Miyatake M, Veerachary M, Toriumi F, Fujii N, Ko H (2011) Maximum power point tracking of multiple photovoltaic arrays: a PSO approach. *IEEE Trans Aerosp Electron Syst* 47:367–380
19. Seyedmahmoudian M, Mekhilef S, Rahmani R, Yusof R, Shojaei A (2014) Maximum power point tracking of partial shaded photovoltaic array using an evolutionary algorithm: a particle swarm optimization technique. *J Renew Sustain Energy* 6(2):1–13
20. Rezk H, Fathy A, Abdelaziz AY (2017) A comparison of different global MPPT techniques based on meta-heuristic algorithms for photovoltaic system subjected to partial shading conditions. *Renew Sustain Energy Rev* 74:377–386
21. Seyedmahmoudiana M, Horan B, Soon T, Rahmani R, Oo A, Mekhilef S, Stojcevski A (2016) State of the art artificial intelligence-based MPPT techniques for mitigating partial shading effects on PV systems—a review. *Renew Sustain Energy Rev* 64:435–455
22. Dorigo M, Gambardella L (1997) Ant colony system: a cooperative learning approach to the traveling salesman problem. *IEEE Trans Evol Comput* 1:3–66
23. Shen Q, Jiang J, Tao J, Shen G, Yu R (2005) Modified ant colony optimization algorithm for variable selection in QSAR modeling: QSAR studies of cyclooxygenase inhibitors. *Chem Inf Model* 45:1024–1029
24. Dorigo M, Birattari M, Stutzle T (2006) Ant colony optimization. *IEEE Comput Intell Mag* 1:28–39
25. Dorigo M, Maniezzo V, Colnari A (1996) Ant system: optimization by a colony of cooperating agents. *IEEE Trans Syst Man Cybern Part B Cybern* 26:29–41
26. Rahmani R, Yusof R, Seyedmahmoudian M, Mekhilef S (2013) Hybrid technique of ant colony and particle swarm optimization for short term wind energy forecasting. *Wind Eng Ind Aerodyn* 123:163–170
27. Sabrina T, Larbes C, Toumi K, Benatchba K (2017) A new MPPT controller based on the ant colony optimization algorithm for photovoltaic systems under partial shading conditions. *Appl Soft Comput* 58:465–479
28. Yu L, Liu K, Li K (2007) Ant colony optimization in continuous problem. *Front Mech Eng China* 2:459–462
29. Benyoucef A, Chouder A, Kara K, Silvestre A, Sahed O (2015) Artificial bee colony based algorithm for maximum power point tracking (MPPT) for PV systems operating under partial shaded conditions. *Appl Soft Comput* 32:38–48
30. Ramli M, Twaha S, Ishaque K, Al-turki Y (2017) A review on maximum power point tracking for photovoltaic systems with and without shading conditions. *Renew Sustain Energy Rev* 67:144–159

31. Holland J (1975) *Adaptation in natural and artificial systems: an introductory analysis with applications to biology, control, and artificial intelligence*. UMichigan Press
32. Ramaprabha R, Mathur B (2012) Genetic algorithm based maximum power point tracking for partially shaded solar photovoltaic array. *Int J Res Rev Inf Sci (IJRRIS)* 2(1):161–163
33. Mohajeri H, Moghaddam M, Shahparasti M, Mohamadian M (2012) Development a new algorithm for maximum power point tracking of partially shaded photovoltaic arrays. In *Proceedings of the 2012, 20th Iranian conference on electrical engineering (ICEE)*, IEEE, pp. 489–494
34. Shaiek Y, Ben Smid M, Sakly A, Mimouni M (2013) Comparison between conventional methods and GA approach for maximum power point tracking of shaded solar PV generators. *Sol Energy* 90:107–122
35. Kulaksız A, Akkaya R (2012) A genetic algorithm optimized ANN-based MPPT algorithm for a stand-alone PV system with induction motor drive. *Sol Energy* 86:2366–2375
36. Storn R, Price K (1997) Differential evolution—a simple and efficient Heuristic for global optimization over continuous spaces. *J Global Optim* 11:341–359
37. Storn R, Price K (1995) Differential evolution—a simple and efficient adaptive scheme for global optimization over continuous spaces. ICSI, Berkeley
38. Tajuddin M, Ayobb Sh, Salamb Z, Saad M (2013) Evolutionary based maximum power point tracking technique using differential evolution algorithm. *Energy Build* 67:245–252
39. Tey K, Mekhilef S, Yang H, Chuang M (2014) A differential evolution based MPPT method for photovoltaic modules under partial shading conditions. *Int J Photoenergy* 2014:1–10
40. Karaboga D, Okdem S (2004) A simple and global optimization algorithm for engineering problems: differential evolution algorithm. *Turk J Electr Eng* 12(1):53–60
41. Taheri H, Salam Z, Ishaque K (2010) A novel maximum power point tracking control of photovoltaic system under partial and rapidly fluctuating shadow conditions using differential evolution. In: *Proceedings of the 2010 IEEE symposium on industrial electronics and applications (ISIEA)*, IEEE, pp 82–91
42. Tajuddin M, Ayob S, Salam Z (2012) Tracking of maximum power point in partial shading condition using differential evolution (DE). In: *Power energy (PECon)*, pp 384–393
43. Ahmed J, Salam Z (2014) A maximum power point tracking (MPPT) for PV system using Cuckoo search with partial shading capability. *Appl Energy* 119:118–130
44. Assis A, Mathew Sh (2016) Cuckoo search algorithm based maximum power point tracking for solar PV systems. *J Renew Sustain Energy* 2(1):20–38
45. Mirjalili S, Mirjalili SM, Lewis A (2014) Grey wolf optimizer. *Adv Eng Softw* 69:46–61
46. Mohanty S, Subudhi B, Ray PK (2016) A new MPPT design using grey wolf optimization technique for photovoltaic system under partial shading conditions. *IEEE Trans Sustain Energy* 7:181–188
47. Rocha M, Sampaio L, da Silva S (2018) Maximum power point extraction in PV array under partial shading conditions using GWO-assisted beta method. *Renew Energy Power Qual J* 1(16):450–455
48. Yang X (2009) Firefly algorithms for multimodal optimization. In: *Stochastic algorithms: foundations and applications SAGA 2009. Lecture notes in computer sciences*, vol 5792, pp 169–178
49. Yang X (2010) *Nature-inspired metaheuristic algorithms*. Luniver Press
50. Sundareswaran K, Peddapati S, Palani S (2014) MPPT of PV systems under partial shaded conditions through a colony of flashing fireflies. *IEEE Trans Energy Convers* 29:463–472
51. Kaced K, Larbes C, Ramzan N, Bounabi M (2017) Bat algorithm based maximum power point tracking for photovoltaic system under partial shading conditions. *Sol Energy* 158(September):490–503
52. Lian L, Nayanisiri D, Maskell D, Vilathgamuwa D (2013) A simple and efficient hybrid maximum power point tracking method for PV systems under partially shaded condition. In: *Proceedings of the annual conference on IEEE industrial electronics society*, pp 14–19, 2013
53. Souza N, Lopes L, Liu X (2005) An intelligent maximum power point tracker using peak current control. In: *Proceedings of the IEEE power electronics specialists conference*, pp 172–177

54. Syafaruddin, Karatepe E, Hiyama T (2009) Artificial neural network-polar coordinated fuzzy controller based maximum power point tracking control under partially shaded conditions. *IET Renew Power Gener* 3:239–253
55. Punitha K, Devaraj D, Sakthivel S (2013) Artificial neural network based modified incremental conductance algorithm for maximum power point tracking in photovoltaic system under partial shading conditions. *Energy* 62:330–340
56. Chin C, Chin Y, Chua B, Kiring A, Teo K (2012) Fuzzy logic based MPPT for PV array under partially shaded conditions. In: *Proceedings of the international conference on advanced computer science applications and technologies*, pp 133–138
57. Daraban S, Petreus D, Morel C (2014) A novel MPPT (maximum power point tracking) algorithm based on a modified genetic algorithm specialized on tracking the global maximum power point in photovoltaic systems affected by partial shading. *Energy* 74:374–388
58. Shaiek Y, Smida M, Sakly A, Mimouni M (2013) Comparison between conventional methods and GA approach for maximum power point tracking of shaded solar PV generators. *Sol Energy* 90:107–122
59. Unlu M, Camur S, Arifoglu B (2013) A new maximum power point tracking method for PV systems under partially shaded conditions. In: *Proceedings of the international conference on power engineering, energy and electrical drives*, pp 13–17
60. Lian K, Jhang J, Tian I (2014) A maximum power point tracking method based on perturb-and-observe combined with particle swarm optimization. *IEEE J Photovoltaics* 4:626–633
61. Li F, Deng F, Guo S, Fan X (2013) MPPT control of PV system under partially shaded conditions based on PSO-DE hybrid algorithm. In: *Proceedings of the Chinese control conference*, pp 7553–7557
62. Jiang L, Nayanisiri D, Maskell D, Vilathgamuwa D (2015) A hybrid maximum power point tracking for partially shaded photovoltaic systems in the tropics. *Renew Energy* 76:53–65
63. Eltamaly A, Farh H (2019) Dynamic global maximum power point tracking of the PV systems under variant partial shading using hybrid GWO-FLC, vol 177, pp 306–316
64. Eltamaly A, Farh H, Othman M (2018) A novel evaluation index for the photovoltaic maximum power point tracker techniques. *Sol Energy* 174:940–956
65. Jiang L, Maskell D, Patra J (2013) A novel ant colony optimization-based maximum power point tracking for photovoltaic systems under partially shaded conditions. *Energy Build* 58:227–236
66. Farh H, Eltamaly A, Othman M (2018) Hybrid PSO-FLC for dynamic global peak extraction of the partially shaded photovoltaic system. *PloS one* 13(11):e0206171

On the Improvements of Perturb-and-Observe-Based MPPT in PV Systems



Mazen Abdel-Salam, Mohamed-Tharwat EL-Mohandes
and Mohamed Goda

Abstract There exist numerous maximum power point tracking techniques in today's market to maintain the operation of PV module at maximum power irrespective of the solar irradiation level and ambient temperature such as perturb-and-observe (P&O) method, incremental conductance (InCond) method, fractional short-circuit current (FSCC) method, and fractional open-circuit voltage (FOCV) method. The perturb-and-observe (P&O) method is the most popular one because of its easy implementation. The classical perturb-and-observe method may fail or deviate from tracking the right direction to capture the correct maximum power point (MPP) of a PV module exposed to a suddenly changed solar irradiation or ambient temperature. The classical method fails to capture the MPP when the solar irradiation or ambient temperature follows a ramp with different slopes. This is because the method can't discriminate whether the change in module power is due to its own voltage perturbation or due to the change in the irradiation or ambient temperature level. Numerous approaches for improving, adapting, and optimizing the classical P&O method have been published. However, they differ in many aspects such as tracking speed, tracking accuracy, steady-state efficiency, and dynamic efficiency as well as the number of used sensors, complexity, and cost. This chapter is aimed at reporting on the improvements made on the classical perturb-and-observe method under sudden or ramp variations of irradiation level and/or ambient temperature with their advantages and disadvantages as documented in the literature. This chapter is framed as a review chapter.

M. Abdel-Salam · M.-T. EL-Mohandes
Electrical Engineering Department, Assiut University, Assiut, Egypt

M. Goda (✉)
Electrical Engineering Department, Ahram Canadian University, Giza, Egypt
e-mail: goda.masr@hotmail.com

© Springer Nature Switzerland AG 2020
A. M. Eltamaly and A. Y. Abdelaziz (eds.), *Modern Maximum Power Point Tracking Techniques for Photovoltaic Energy Systems*, Green Energy and Technology, https://doi.org/10.1007/978-3-030-05578-3_6

1 Introduction

In light of depletion with time the conventional fossil fuels for the generation of electric energy, efforts are made to harness PV solar energy to serve continuously increasing electric loads. The energy conversion efficiency of PV modules is very low, while they are expensive in price. This calls for operating the module at the maximum power point at all operating conditions, which is the main target of this chapter.

The resistance of load dictates the operating condition of the PV module because of the PV module's operating point will be located at the intersection of the module and the load I – V curves. There is only one operating point at which the PV module provides its maximum power point (MPP) whatever the value of the load. This occurs when the load resistance is equal to its optimal value. But it is very difficult and even if it is done, the operating point itself changes under varying irradiation and ambient temperature conditions [1].

The goal of the maximum power point tracking (MPPT) is to match the resistance of load to the optimal resistance of PV module. The MPPT uses a DC–DC converter between the PV module and load to acts as an interface to operate at the maximum power point (MPP) by changing the duty cycle of the converter as requested by the MPPT tracker [1].

There exist numerous maximum power point tracking techniques in today's market to maintain the operation of PV module at maximum power irrespective of the solar irradiation level and ambient temperature such as perturb-and-observe (P&O) method, constant voltage (CV) method, incremental conductance (InCond) method, and fractional open-circuit voltage method. The perturb-and-observe (P&O) method is the most popular and common one because of its easy implementation [2].

The classical P&O method depends on the perturbation of the operating voltage and observation of the polarity of the output power. The classical P&O method fails to capture the correct MPP under sudden or ramp variations of solar irradiation and ambient temperature. This is because the method can't discriminate whether the change in module power is due to its own voltage perturbation or due to the change in the irradiation and ambient temperature level [2].

Numerous approaches for improving, adapting, and optimizing the classical P&O method have been published. However, they differ in many aspects such as tracking speed, tracking accuracy, steady-state efficiency, and dynamic efficiency as well as the number of used sensors, complexity, and cost [2].

2 Classical Perturb-and-Observe (P&O) Method [3]

The mechanism of the classical P&O method is based on the perturbation of the module operating point and observation of the change in module output power. The polarity of the module output power defines the direction of the coming perturbation. For positive polarity, the next voltage perturbation can increase or decrease in the voltage, the same as that for the previous perturbation. For negative polarity, the

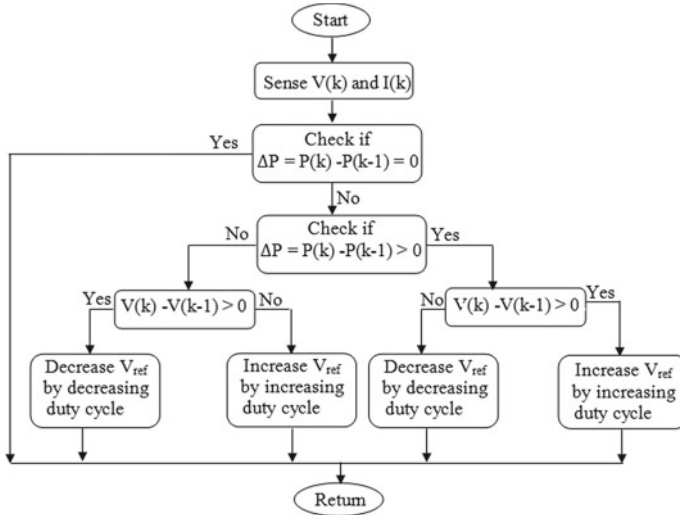


Fig. 1 Flowchart of the classical P&O method

next voltage perturbation will be in the opposite direction of the previous one. The flowchart of the classical P&O method is shown in Fig. 1.

- Step 1: The tracker senses the PV module/array output current $I(k - 1)$ and output voltage $V(k - 1)$ to calculate the tracker power $P(k - 1)$ ($= V(k - 1) * I(k - 1)$) at the $(k - 1)$ th sampling instance.
- Step 2: The tracker perturbs the voltage.
- Step 3: The tracker senses the module/array output current $I(k)$ and output voltage $V(k)$ to calculate the output power $P(k)$ [$= V(k) * I(k)$] at the (k) th sampling instant.
- Step 4: The tracker observes the polarity of the change of the output power (ΔP) which is equal to $[P(k) - P(k - 1)]$.
- Step 4.1: If $\Delta P > 0$, the next perturbation must be in the same direction of the previous one.
- Step 4.1.1: If the previous perturbation (ΔV) which is equal to $[V(k) - V(k - 1)]$ is positive, the next perturbation will be positive and the duty cycle is to be increased to increase the operating voltage (V_{ref}) as the type of the DC–DC converter is boost one.
- Step 4.1.1.1: The trackers go back to step #1.
- Step 4.1.2: If the previous perturbation (ΔV) which is equal to $[V(k) - V(k - 1)]$ is negative, the next perturbation will be negative and the duty cycle is to be decreased to decrease the operating voltage (V_{ref}).
- Step 4.1.2.1: The trackers go back to step #1.
- Step 4.2: If $\Delta P < 0$, the next perturbation must be in the opposite direction of the previous one.

- Step 4.2.1: If the previous perturbation (ΔV) which is equal to $[V(k) - V(k - 1)]$ is positive, the next perturbation will be negative and the duty cycle is to be decreased to decrease the operating voltage (V_{ref}).
- Step 4.2.1.1: The trackers go back to step #1.
- Step 4.2.2: If the previous perturbation (ΔV) which is equal to $[V(k + 1) - V(k)]$ is negative, the next perturbation will be positive and the duty cycle is to be increased to increase the operating voltage (V_{ref}).
- Step 4.2.2.1: The trackers go back to step #1.
- Step 4.3: If $\Delta P = 0$, the MPP is captured.
- Step 4.4: The tracker goes back to step #1.

Figure 2 shows that the classical P&O method proceeds in the correct direction under uniform irradiation level and constant ambient temperature. Figure 3 shows that the classical P&O method proceeds in the wrong direction under the sudden variation of solar irradiation.

3 Methodology

This chapter presents briefly the different methods proposed in the literature for maximum power point tracking in PV systems under varying irradiation level and ambient temperature. The problems facing these methods for MPPT under the sudden variation of solar irradiation and ambient temperature are explored.

The tracking speed is defined as how fast the tracker is to capture the MPP when the irradiation level and ambient temperature change. The time taken to reach the MPP must be short. The shorter the time taken to reach the MPP, the smaller is the power losses with the improvement of the efficiency [2].

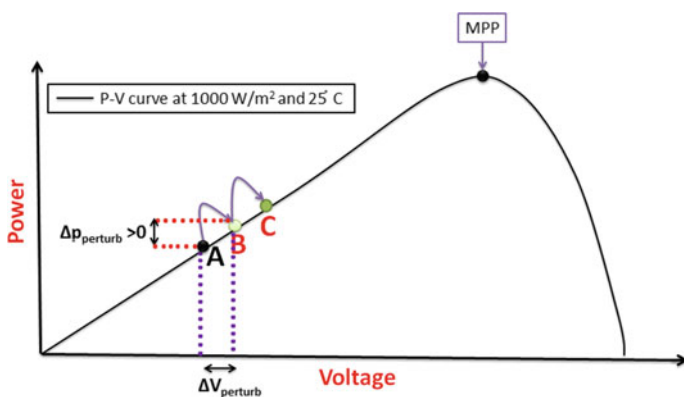


Fig. 2 MPP tracking by the classical P&O method under uniform irradiation level and constant ambient temperature for operating point lied to the left of the MPP with correct first voltage perturbation

The steady-state MPPT efficiency ($\eta_{\text{steady-state}}$) is the ratio of the captured power drawn by the tracker to the maximum power provided theoretically by the PV module (as determined from the module datasheet) under stable irradiation level and ambient temperature [2].

The dynamic MPPT efficiency (η_{dynamic}) refers to the ratio of the captured power drawn by the tracker to the maximum power provided theoretically by the PV module (as determined from the module datasheet) under non-uniform irradiation level and ambient temperature over the test time [2].

Most of the MPPT methods depend on sensing the module output voltage and current. The irradiance or temperature sensors are rarely used in MPPT [3].

4 Comparison Between Techniques

Some solutions have been recently reported to overcome two problems facing the classical P&O method under the sudden variation of irradiation level and ambient temperature.

The first problem is devoted to explore the possibility of the classical P&O method to predict false results due to the variation of irradiation level [2].

The second problem is focused on the deviation of the classical P&O method from the MPP due to the exposure to suddenly changed ambient temperature [2].

5 dP-P&O Method [4, 5]

Sera et al. [4, 5] proposed a modified perturb-and-observe algorithm based on decoupling the effect of ramp change of irradiation on the module output power from that

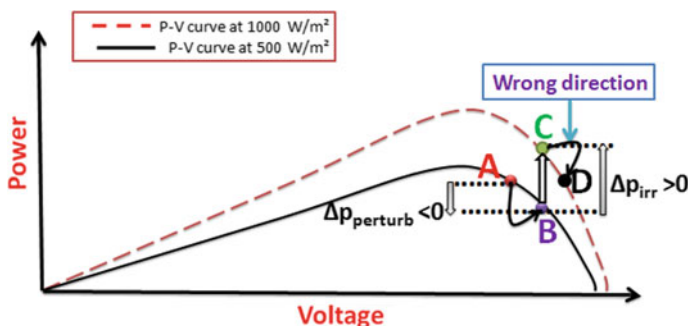


Fig. 3 MPP tracking by the classical P&O method with module exposed to a large increasing step of irradiation level with initial operating point lied to the right of MPP and incorrect first voltage perturbation $|\Delta P_{\text{irr}}| > |\Delta P_{\text{perturb}}|$

Fig. 4 Sequence of dP-P&O method [4, 5]

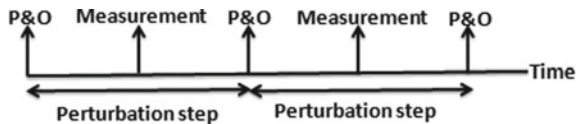
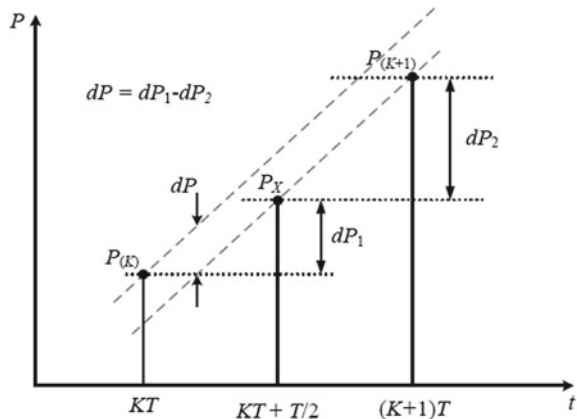


Fig. 5 Mechanism of dP-P&O method [4, 5]



due to the perturbation in the operating voltage. This algorithm is named dP-P&O. The decoupling mechanism is made by adding an extra measurement at the middle of the perturbation time ($T/2$). Thus, the tracker receives the change in the module output power caused by perturbation of the operating voltage only.

Figures 4 and 5 show the mechanism of dP-P&O algorithm:

$$dP = dP_1 - dP_2 = (P_x - P_k) - (P_{k+1} - P_x) = 2P_x - P_k - P_{k+1} \quad (1)$$

The dP-P&O algorithm method is not able to track the correct MPP under step sudden variation of irradiation level because the authors assumed the change in irradiation takes place at a constant rate, i.e., as a ramp change. The flowchart of the classical P&O method is shown in Fig. 6.

- Step 1: The tracker senses the module/array output current $I(k - 1)$ and output voltage $V(k - 1)$ to calculate the tracker power $P(k - 1) (= V(k - 1) * I(k - 1))$ at the $(k - 1)$ th sampling instance.
- Step 2: The tracker perturbs the voltage.
- Step 3: The tracker senses the module/array output current $I(k)$ and output voltage $V(k)$ to calculate the output power $P(k) [= V(k) * I(k)]$ at the (k) th sampling instant.
- Step 4: Decoupling process between the change in power caused by the voltage perturbation of the tracker and the change in power caused by irradiation change at the sampling instant ($T/2$) between the $(k - 1)$ th and (k) th sampling instants.

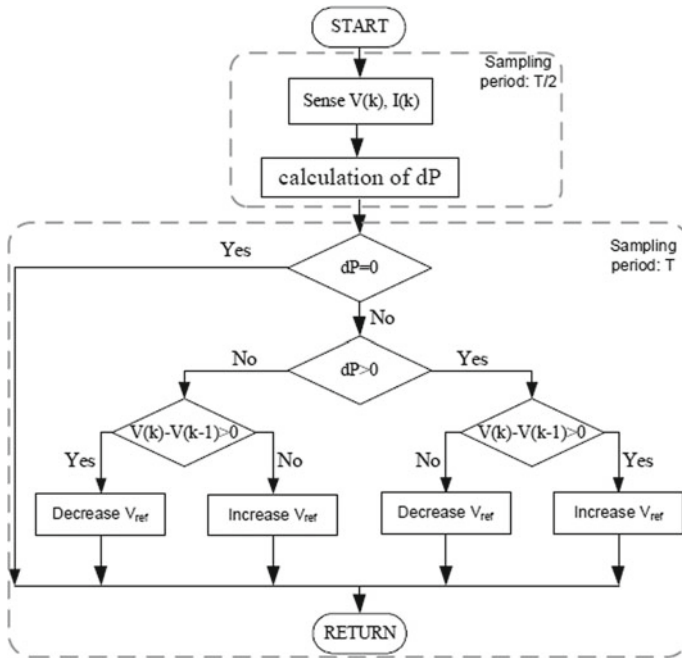


Fig. 6 Flowchart of the dP-P&O method [4, 5]

Step 5: Calculate the power change caused purely by the voltage perturbation of the tracker command by using Eq. (1).

Hint: In the dP-P&O method, the power change $P_{k+1} - P_k$, Fig. 5, is replaced by dP as calculated in Eq. (1) to avoid confusion of the tracker due to the rapidly changing irradiation.

Step 6: The tracker uses the classical P&O method after decoupling process.

Step 6-a: If dP is positive and the voltage perturbation is positive, the tracker decreases the duty cycle to increase the voltage because of the type of the DC–DC converter is buck one.

Step 6-b: If dP is positive and the voltage perturbation is negative, the tracker increases the duty cycle to decrease the voltage.

Step 6-c: If dP is negative and the voltage perturbation is positive, the tracker increases the duty cycle to decrease the voltage.

Step 6-d: If dP is negative and voltage perturbation is negative, the tracker decreases the duty cycle to increase the voltage.

Step 7: If $dP = 0$ (reaching MPP), the tracker will stop tracking process and if $dP \neq 0$, the tracker returns to step 1.

6 Modified Perturb-and-Observe (MP&O) Method [6]

Yafaoui et al. proposed [6] a modified P&O algorithm called (MP&O) which depends on separating two changes in module output power. (i) The change in module output power caused by (sudden) step change of irradiation level and (ii) the change in module output power caused by voltage perturbation. This algorithm adds every perturbation step an irradiation-changing estimate process to ensure that the tracker receives the change in module output power due to the change of irradiation level, Fig. 7.

Figure 8 shows the flowchart of the MP&O method. Because the estimate process stops tracking of the maximum power point by keeping the PV voltage constant, the tracking speed of MP&O method is only half of the classical P&O method. Figure 9 shows the flowchart of the MP&O method.

- Step 1: The tracker senses module/array output voltage $V(k - 2)$ and current $I(k - 2)$ at the $(k - 2)$ th step.
- Step 2: The tracker calculates the power at the $(k - 2)$ th step, which is equal to $P(k - 2) [= V(k - 2) * I(k - 2)]$.
- Step 3: The tracker perturbs the voltage to be at $(k - 1)$ th.
- Step 4: The tracker senses module/array output voltage $V(k - 1)$ and current $I(k - 1)$ at the $(k - 1)$ th step.

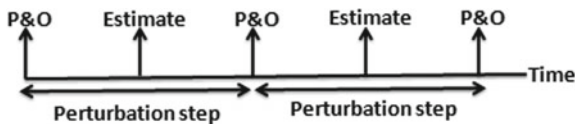


Fig. 7 Sequence of MP&O method [6]

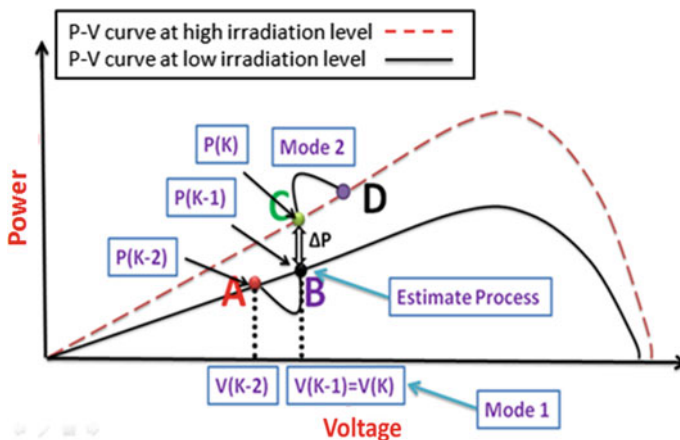


Fig. 8 Modes 1 mode 2 of MP&O method [6]

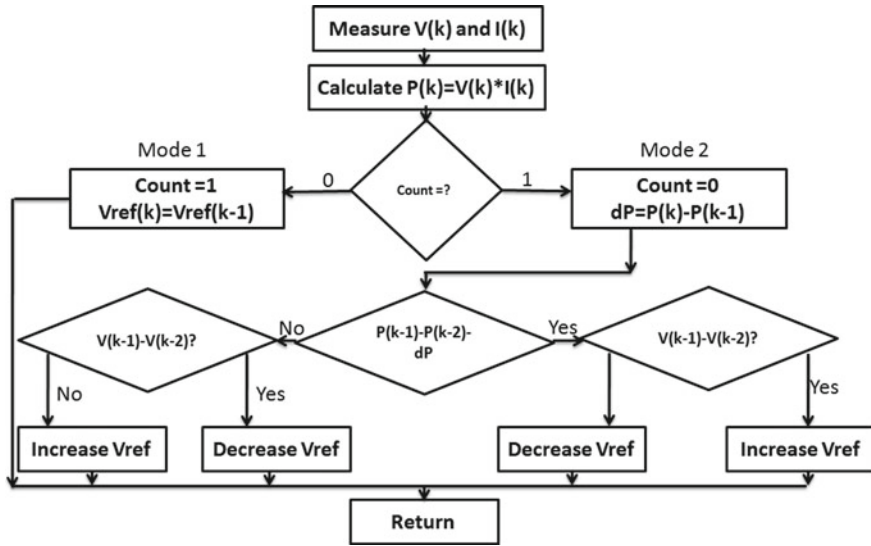


Fig. 9 Flowchart of MP&O algorithm [6]

- Step 5: The tracker calculates the power at $(k - 1)$ th which is equal to $P(k - 1)$ $[= V(k - 1) * I(k - 1)]$.
- Step 6: The tracker keeps the PV voltage constant for the next control period (estimate process with no voltage perturbation) according to mode 1 to be at k th step.
- Step 7: The tracker senses module/array output voltage $V(k)$ and current $I(k)$ at the (k) th step.
- Step 8: The tracker calculates the power at (k) th, which equal to $P(k) = V(k) * I(k)$.
- Step 9: The tracker calculates the power variation due to the voltage perturbation and irradiation change which is equal to $P(k) - P(k - 2)$ according to mode 1.
- Step 10: The tracker calculates the power variation due to the irradiation change only, which is equal to dP $[= P(k) - P(k - 1)]$ according to mode 2.
- Step 11: The tracker calculates the power variation due to the voltage perturbation only, which is equal to the difference between power variations in steps 9 and 10 $(= [P(k) - P(k - 2)] - dP)$ according to mode 2.
- Step 12: The tracker determines the new PV voltage based on the step 11 according to the classical P&O method as follows:
- Step 12-a: If the change in power is positive (increase of power) and the voltage perturbation is positive (increase of voltage), the tracker decreases the duty cycle to increase the voltage as the type of the DC-DC converter is buck one.

- Step 12-b: If the change in power is positive and the change in voltage perturbation is negative, the tracker increases the duty cycle to decrease the voltage.
- Step 12-c: If the change in power is negative and the change in voltage perturbation is positive, the tracker increases the duty cycle to decrease the voltage.
- Step 12-d: If the change in power is negative and the change in voltage perturbation is negative, the tracker decreases the duty cycle to increase the voltage.
- Step 13: If the change in power due to the voltage perturbation as calculated in step 11 is equal to zero (reaching MPP), the tracking process terminates; otherwise, the tracker returns to step 1.

7 Estimate-Perturb-Perturb (EPP) Method [7]

A new method was proposed [7] to enhance the dynamic efficiency of the classical P&O method and the speed of the tracker of the MP&O method. This method is named the Estimate-Perturb-Perturb (EPP) method. The tracker of the EPP method adds an irradiation-changing estimate process after every two consequent perturbations, Fig. 10. The EPP method is faster than the MP&O method with one and half times [6].

Figure 11 shows the flowchart for the proposed EPP method. Figure 10 shows the time sequences for the EPP method. Compared with the MP&O method, the EPP method has the same delay time between the estimate process and the perturb process. Therefore, the EPP method has obvious advantages over the MP&O method.

- Step 1: The tracker senses module/array output voltage $V(k - 3)$ and current $I(k - 3)$ at the $(k - 3)$ th step.
- Step 2: The tracker calculates the power at the $(k - 2)$ th, which is equal to $P(k - 3) [= V(k - 3) * I(k - 3)]$.
- Step 3: The tracker perturbs the voltage to be at the $(k - 2)$ th step.
- Step 4: The tracker senses module/array output voltage $V(k - 2)$ and current $I(k - 2)$ at the $(k - 2)$ th step.
- Step 5: The tracker calculates the power at the $(k - 2)$ th step, which is equal to $P(k - 2) [= V(k - 2) * I(k - 2)]$.
- Step 6: The tracker calculates the change in power $P(k - 3) - P(k - 2)$ and determines the second perturbation according to the classical P&O method.
- Step 7: The tracker perturbs the voltage (second perturbation) to be at the $(k - 1)$ th step.
- Step 8: The tracker senses module/array output voltage $V(k - 1)$ and current $I(k - 1)$ at the $(k - 1)$ th step.

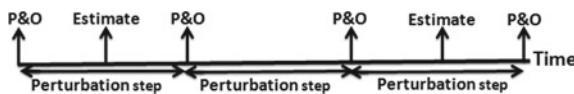


Fig. 10 Sequence of EPP method [7]

- Step 9: The tracker calculates the power at the $(k - 1)$ th step, which is equal to $P(k - 1) [= V(k - 1) * I(k - 1)]$.
- Step 10: The tracker keeps the PV voltage constant for the next control period (estimate process with no voltage perturbation) according to mode 1 to be at the k th step.
- Hint: The estimate process is made after two perturbation steps in voltage to increase the tracking speed when compared with the MP&O [6] as explained above.
- Step 11: The tracker senses module/array output voltage $V(k)$ and current $I(k)$ at the (k) th step.
- Step 12: The tracker calculates the power at the (k) th, which is equal to $P(k) [= V(k) * I(k)]$.
- Step 13: The tracker calculates the power variation due to the voltage perturbation and irradiation change, which is equal to $P(k) - P(k - 2)$ according to mode 1.
- Step 14: The tracker calculates the power variation due to the irradiation change only, which is equal to $dP [= P(k) - P(k - 1)]$ according to mode 2.
- Step 15: The tracker calculates the power variation due to the voltage perturbation only, which is equal to the difference between power variations in steps 9 and 10 $[= \{P(k) - P(k - 2)\} - dP]$ according to mode 2.
- Step 16: The tracker determines the new PV voltage based on step 15 according to the classical P&O method as follows:

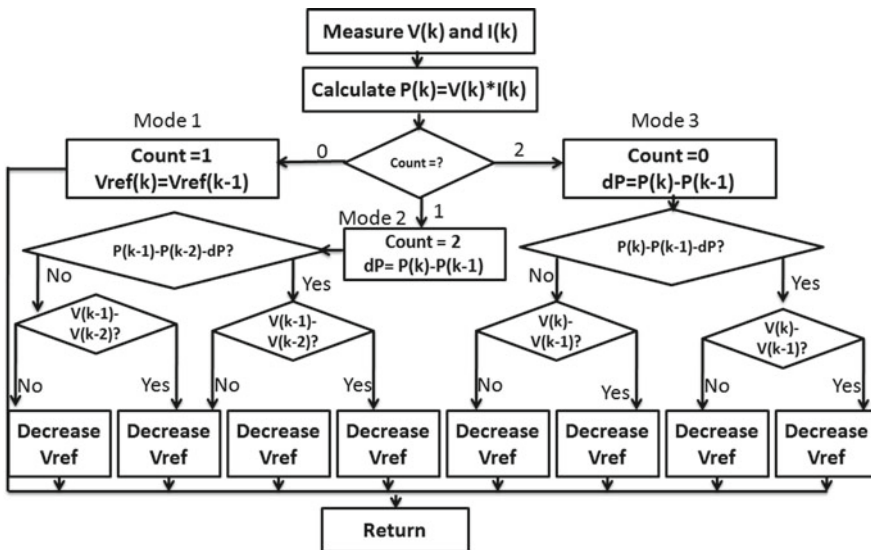
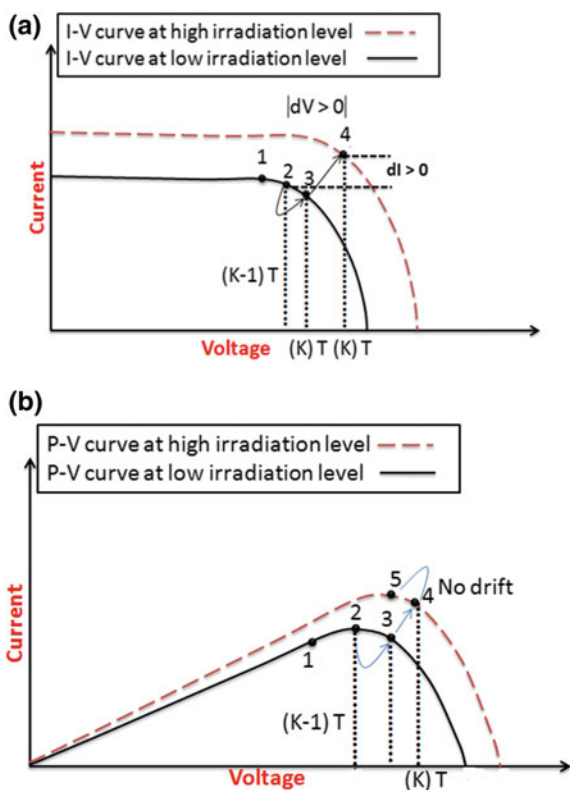


Fig. 11 Flowchart of EPP method [7]

- Step 16-a: If the change in power is positive and the voltage perturbation is positive, the tracker decreases the duty cycle to increase the voltage because of the type of the DC–DC converter is buck one.
- Step 16-b: If the change in power is positive and the change in voltage perturbation is negative, the tracker increases the duty cycle to decrease the voltage.
- Step 16-c: If the change in power is negative and the change in voltage perturbation is positive, the tracker increases the duty cycle to decrease the voltage.
- Step 16-d: If the change in power is negative and the change in voltage perturbation is negative, the tracker decreases the duty cycle to increase the voltage.
- Step 17: If the change in power due to voltage perturbation as calculated in step 15 is equal to zero (reaching MPP), the tracking process terminates; otherwise, the tracker returns to step 1.

Fig. 12 Performance of the drift-free modified P&O under sudden variation of solar irradiation on **a** the I – V curve **b** the P – V curve



8 Drift-Free Modified P&O Method [8]

Figure 12 shows the operating principle of the free-drift modified method [8]. As shown in Fig. 12a, the initial operating point is at point (2). The operating voltage is perturbed and point (2) moves to point (3). While the voltage is perturbed, the irradiation is suddenly increased making the operating point to move from point (3) to point (4). Now the tracker calculates the net change in module output current, which is equal to $\Delta I [= I_4(k) - I_2((k - 1))] > 0$. Also, the tracker calculates the change in module output power and voltage which is equal to $\Delta P [= P_4(k) - P_2(k - 1)] > 0$ and $\Delta V [= V_4(k) - V_2(k - 1)] > 0$, respectively, according to the P - V curve as shown in Fig. 12b. The three changes ΔP , ΔV , and ΔI are positive. One can observe that both ΔV and ΔI can never have the same sign for a unique irradiation level. Both ΔV and ΔI could be positive only for an increase in irradiation level shown in Fig. 12a. Thus, an increase in irradiation can be detected by using the additional current change ΔI and thereby the duty cycle is to be increased for decreasing the operating voltage to eliminate the drift problem resulting from moving the operating point closer to the MPP as shown in Fig. 12b. The flowchart of the drift-free modified P&O MPPT technique is shown in Fig. 13.

- Step 1: The tracker senses the module/array output current $I(k - 1)$ and output voltage $V(k - 1)$ at the $(k - 1)$ th step.
- Step 2: The tracker calculates the output power at the $(k - 1)$ th step, which equal to $P(k - 1) [= V(k - 1) * I(k - 1)]$.

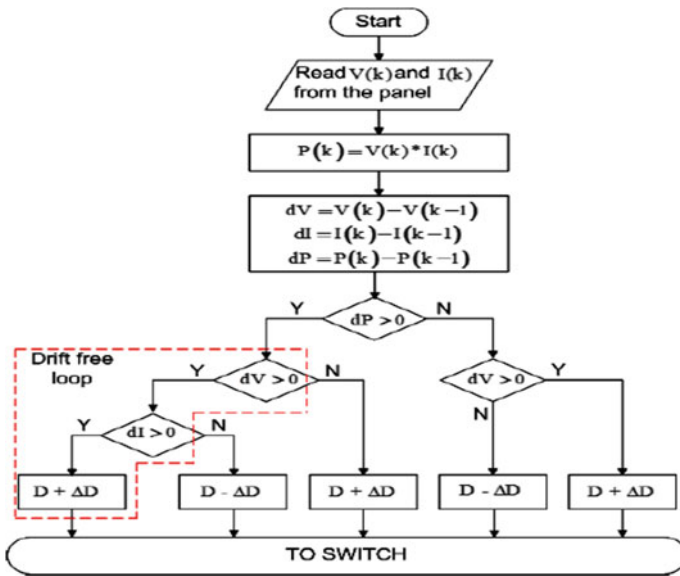


Fig. 13 Flowchart of drift-free modified P&O MPPT algorithm [8]

- Step 3: The tracker perturbs the voltage to be at the (k) th step.
- Step 4: The tracker senses module/array output voltage $V(k)$ and current $I(k)$ at the (k) th step.
- Step 5: The tracker calculates the power at the (k) th step, which is equal to $P(k)$ $[= I(k) * V(k)]$.
- Step 6: The tracker calculates the change in current $dI [= I(k) - I(k - 1)]$.
- Step 7: The tracker calculates the change in voltage $dV [= V(k) - V(k - 1)]$.
- Step 8: The tracker calculates the change in power $dP [= P(k) - P(k - 1)]$.
- Step 8-a: If $dP > 0$ and $dV < 0$, the tracker increases the duty cycle to decrease the voltage because of the type of the DC–DC converter is buck one.
- Step 8-b: If $dP > 0$, $dV > 0$, and $dI > 0$, the tracker increases the duty cycle to decrease the voltage.
- Step 8-c: If $dP > 0$, $dV > 0$, and $dI < 0$, the tracker decreases the duty cycle to increase the voltage.
- Step 8-d: If $dP < 0$ and $dV > 0$, the tracker increases the duty cycle to decrease the voltage.
- Step 8-e: If $dP > 0$ and $dV < 0$, the tracker decreases the duty cycle to increase the voltage.

9 Combined Two-Method MPPT Tracker [9]

Dorofte et al. proposed [9] a combined two-algorithm MPPT control scheme to overcome the trade-off problem between tracking speed and tracking accuracy and to increase the dynamic efficiency of the classical perturb-and-observe method when the irradiation level is suddenly varied. This proposed algorithm is based on combining the classical P&O method with the fractional open-circuit voltage (FOCV) method. Figure 14 shows the flowchart for the combined two-algorithm MPPT scheme.

- Step 1: The tracker senses module output current I .
- Step 2: If $I < 0.7$ A, the tracker follows the FOCV method.
- Step 2-a: The tracker measures the module open-circuit voltage $V_{o,c}$ corresponding to a duty cycle D of zero value.
- Step 2-b: The tracker sets the operating point voltage at $0.75 V_{o,c}$.
- Step 2-c: The tracker waits for 40 s and back to measure again the module open-circuit voltage $V_{o,c}$ at zero value of the duty cycle D .
- Step 2-d: The tracker sets the operating point voltage again at $0.75 V_{o,c}$.
- Step 2-e: The tracker moves back to step 1 to sense module output current I again.
- Step 3: If $I > 0.7$ A, the tracker follows the classical P&O method.
- Step 3-a: The tracker senses the module output current $I(k - 1)$ and voltage $V(k - 1)$ at the $(k - 1)$ th step.
- Step 3-b: The tracker calculates the module power at the $(k - 1)$ th step, which is equal to $P(k - 1) [= V(k - 1) * I(k - 1)]$.
- Step 3-c: The tracker perturbs the voltage to be at the k th step.

- Step 3-d: The tracker senses the module output current $I(k)$ and voltage $V(k)$ at the (k) th step.
- Step 3-e: The tracker calculates the module power at the (k) th step, which is equal to $P(k) [= V(k) * I(k)]$.
- Step 3-f: The tracker calculates the change in module output voltage $\Delta V [= V(k) - V(k - 1)]$.
- Step 3-g: The tracker calculates the change in module output voltage $\Delta P [= P(k) - P(k - 1)]$.
- Step 3-h: The tracker calculates the slope $\Delta P / \Delta V$.
- Step 3-i: If the slope is positive, the tracker increases the voltage by increasing the duty cycle because the type of the DC–DC converter is boost one.
- Step 3-j: If the slope is negative, the tracker decreases the voltage by decreasing the duty cycle.
- Step 4: The tracker moves back to step 1 to sense module output current (I) again.

10 Method Proposed Based on Product Sign of Voltage and Power Changes [10]

Kamal et al. proposed [10] an improved P&O technique to solve the problem of the classical method under sudden variation of solar irradiance. In this technique,

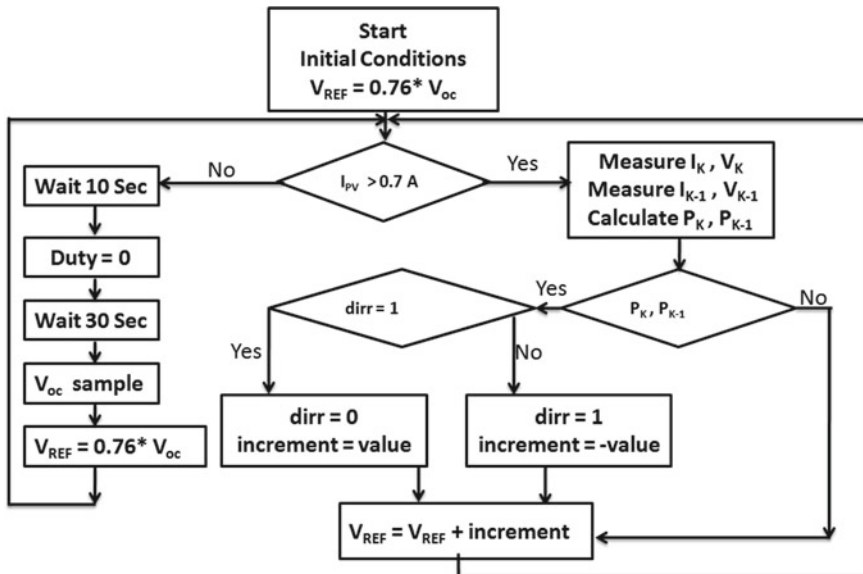


Fig. 14 Control flowchart of the proposed combined MPPT method [9]

the polarities of the voltage perturbation (ΔV) and that of the corresponding power change (ΔP) were taken into account and multiplied together. Unfortunately, the results showed better performance for decreasing oscillations amplitude, but the dynamic efficiency is still low. The tracking efficiency showed overshoot values that can reach unjustified hypothetical values up to 400% [10]. Figure 15 shows the flowchart for this method [10].

- Step 1: The tracker senses the module output current $I(k-1)$ and voltage $V(k-1)$ at the $(k-1)$ th step.
 Hint: According to the flowchart, Δc is the voltage step size and $c(k) = V(k)$ and $c(k-1) = V(k-1)$, which are the module measured voltage at the k th step and the preceding step.
- Step 2: The tracker calculates the module power at the $(k-1)$ th step, which is equal to $P(k-1) [= V(k-1) * I(k-1)]$.
- Step 3: The tracker perturbs the voltage to be at the k th step.
- Step 4: The tracker senses the module output current $I(k)$ and voltage $V(k)$ at the (k) th step.
- Step 5: The tracker calculates the module power at the (k) th step, which is equal to $P(k) [= V(k) * I(k)]$.
- Step 6: The tracker calculates the change in module output voltage $\Delta V [= V(k) - V(k-1)]$.
- Step 7: The tracker calculates the change in module output power $\Delta P [= P(k) - P(k-1)]$.
- Step 8: The tracker checks the sign of both ΔV and ΔP .
- Step 8-a: If $dP > 0$ and $dV > 0$, the tracker increases the voltage by decreasing the duty cycle because the type of the DC–DC converter is buck one.

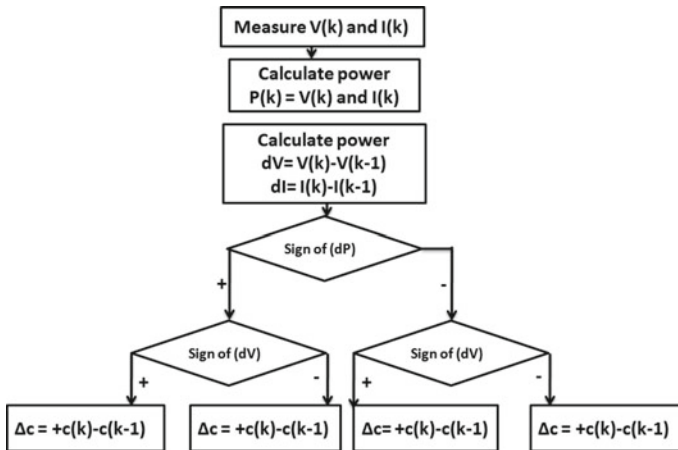


Fig. 15 Flowchart of the proposed method [10]

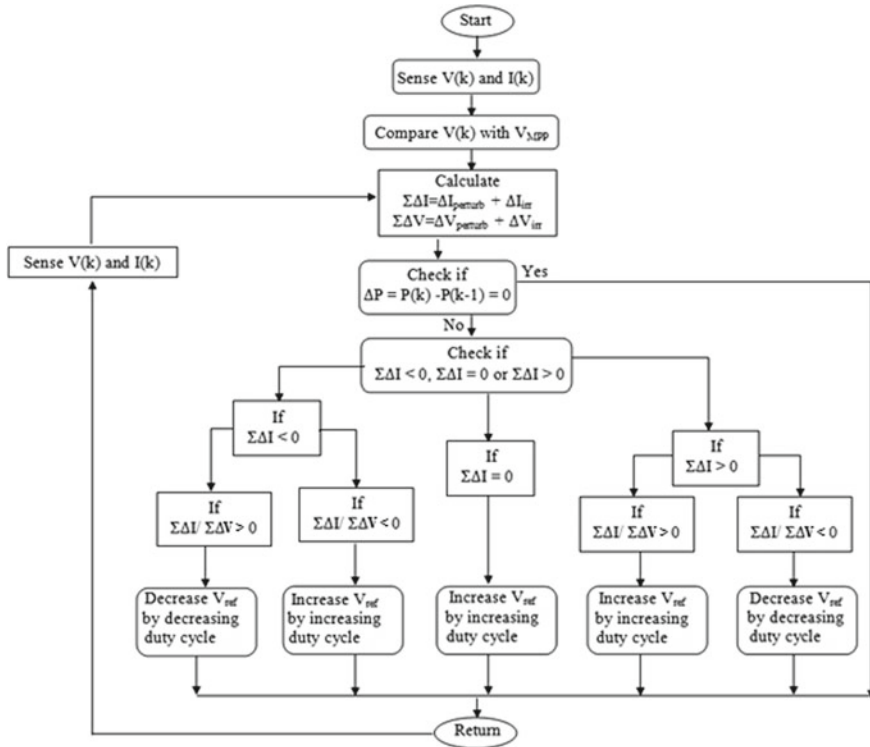


Fig. 16 Flowchart of the modified P&O method proposed in [2]

Step 8-b: If $dP > 0$ and $dV < 0$, the tracker decreases the voltage by increasing the duty cycle.

Step 8-c: If $dP < 0$ and $dV < 0$, the tracker increases the voltage by decreasing the duty cycle.

Step 8-d: If $dP < 0$ and $dV > 0$, the tracker decreases the voltage by increasing the duty cycle.

11 An Improve Perturb-and-Observe-Based MPPT [2]

Abdel-Salam et al. proposed [2] an improved perturb-and-observe method. In comparison with the classical one, the proposed method perturbs the operating voltage and observes the change in module output voltage, current, and power. This method is not in need to detect threshold current parameter to decide on the occurrence of a sudden change in irradiation level or ambient temperature. Moreover, the proposed method tracks the MPP under changes of irradiation level and/or ambient temper-

ature. The authors discuss the performance of the classical P&O in 16 study cases under sudden variation of irradiation level whatever (i) the location of the initial operating point to the right or left of the MPP (ii) the value of the perturbation in irradiation level with large or small step (iii) the direction of the irradiation-level change as increase or decrease. The proposed technique captured the correct MPP in all 16 cases. The proposed technique observes the change in module output voltage ΔV , current ΔI , and power ΔP . The authors use the polarity of ΔI and $\Delta I/\Delta V$ to direct the tracker to the correct MPP whatever there is a change in irradiation level or no. The steady-state efficiency of the proposed technique is equal to 99.48% and its dynamic efficiency is equal to 98.03%. Figure 16 shows the flowchart for this method [2].

- Step 1: Define voltage at maximum power point (V_{MPP}) to the tracker according to the datasheet of the PV module.
- Step 2: The tracker senses the module/array output current $I(k)$ and output voltage $V(k)$ to calculate the tracker power $P(k) (= V(k) * I(k))$ at the k th sampling instance.
- Step 3: The tracker compares the operating voltage $V(k)$ with V_{MPP} to determine where the operating point is located with respect to the MPP.
- Step 4: The tracker perturbs the voltage in the right direction toward the MPP. Hint: The voltage $V(k)$ is compared with V_{MPP} listed in the datasheet in order to perform the first perturbation of the duty cycle in the right direction to sense new values of $V(k + 1)$ and $I(k + 1)$ through steps 3 and 4. These steps are done for the first voltage perturbation step only.
- Step 5: If the net change in power $\Delta P [= P(k + 1) - P(k)]$ is equal to zero, this means that the MPP is captured and the tracker stops.
- Step 6: If the net change in power $\Delta P [= P(k + 1) - P(k)]$ is not equal to zero, this means that the MPP is not captured and the tracker moves to step #7.
- Step 7: The tracker senses the module/array output current $I(k + 1)$ and output voltage $V(k + 1)$ to calculate the tracker power $P(k + 1) (= V(k + 1) * I(k + 1))$ at the $(k + 1)$ th sampling instance.
- Step 8: If there is no sudden change of the irradiation level or ambient temperature, the change of current $\sum \Delta I = \Delta I_{Perturb}$ and the change of voltage $\sum \Delta V = \Delta V_{Perturb}$.
- Step 9: If there is a sudden change of irradiation level or ambient temperature, the net change of current $\sum \Delta I [= \Delta I_{Perturb} + \Delta I_{irr/temp}]$ and the net change of voltage $\sum \Delta V [= \Delta V_{Perturb} + \Delta V_{irr/temp}]$.
- Step 10: The tracker senses the net change in current $\sum \Delta I$ and voltage $\sum \Delta V$ after each perturbation whatever there is a sudden change in irradiation level or ambient temperature or not.
- Step 11: The tracker checks if $\sum \Delta I = 0$, $\sum \Delta I > 0$ or $\sum \Delta I < 0$.
- Step 11.I: If $\sum \Delta I = 0$, the tracker increases the duty cycle to increase the operating voltage toward the MPP.

- Step 11.II: If $\sum \Delta I > 0$, the tracker checks $\sum \Delta I / \sum \Delta V$.
- Step 11.II.a: If $\sum \Delta I > 0$ and $\sum \Delta I / \sum \Delta V > 0$, the tracker increases the duty cycle to increase the operating voltage toward the MPP because the type of the DC–DC converter is boost one.
- Step 11.II.b: If $\sum \Delta I > 0$ and $\sum \Delta I / \sum \Delta V < 0$, the tracker decreases the duty cycle to decrease the operating voltage toward the MPP.
- Step 11.III: If $\sum \Delta I < 0$, the tracker checks $\sum \Delta I / \sum \Delta V$.
- Step 11.III.a: If $\sum \Delta I < 0$ and $\sum \Delta I / \sum \Delta V > 0$, the tracker decreases the duty cycle to decrease the operating voltage toward the MPP.
- Step 11.III.b: If $\sum \Delta I < 0$ and $\sum \Delta I / \sum \Delta V < 0$, the tracker increases the duty cycle to increase the operating voltage toward the MPP.
- Step 12: If the net change in power $\Delta P [= P(k + 1) - P(k)]$ is equal to zero, this means that the MPP is captured and the tracker stops its MPP tracking.
- Step 13: If the net change in power $\Delta P [= P(k + 1) - P(k)]$ is not equal to zero, this means that the MPP is not captured and the tracker returns to step #7.

12 Method Proposed Based on Normalized Power Change [11]

Ahmed et al. proposed a method [11] to enhance the dynamic efficiency of the tracker of the classical P&O method. This method is based on an adaptive perturbation step size (ΔV) in the range 0.5–2% of the open-circuit voltage V_{oc} to decrement the oscillation amplitude. Figure 17 shows the flowchart for this method [11].

- Step 1: The tracker starts by climbing the P – V curve with step size equal to 2% of the V_{oc} until it reaches the vicinity of MPP similar to the classical P&O method.
- Step 2: The operating point oscillates around MPP. The oscillation is detected by a special mechanism [11] and the perturbation size is reduced until it reaches a certain minimum value 0.5% of the open-circuit voltage (V_{oc}).
Hint: Due to the small oscillation, there will be always a difference in power (ΔP) at every consecutive sample. The value of $\Delta P/P$ is kept below a certain threshold limit (Tr_1) as the perturbation size has reached its minimum value.
- Step 3: If $\Delta P/P > Tr_1$, the irradiance experiences a change.
Hint: To determine whether the irradiance follows a slope or a step change, another threshold value (Tr_2) is introduced. If $Tr_1 < \Delta P/P < Tr_2$, the change in the irradiance is considered as gradual. On the other hand, if $\Delta P/P > Tr_2$, the irradiance is considered to change rapidly from one level to another level.

- Step 4: If $\Delta P/P > Tr_2$, the tracker increases the perturbation size to 2% of the $V_{o.c}$ to ensure that the MPP is tracked at a new level of irradiance according to the classical P&O method.
- Step 5: If $Tr_1 < \Delta P/P < Tr_2$, the tracker increases the perturbation size to 1% of the $V_{o.c}$ to ensure that the MPP is tracked at a new gradual change.

It is worthy to mention that the values of Tr_1 and Tr_2 have not been defined [11].

13 Three-Point Weight Comparison Method [12]

This method tried to avoid the oscillation problem of the voltage perturbation around the MPP and the problem of sudden variation of solar irradiation [12]. The classical P&O method compares only two points, which are the present operation point and the subsequent point after voltage perturbation, to observe their changes in power and thus decide whether increase or decrease of the module voltage is requested. In comparison with the classical one, the method of the three-point weight comparison perturbs the module operating voltage and compares the module output power at three points of the P - V curve. Figure 19 shows the flowchart of the three-point weight comparison method. The main issue of this method is that its speed is very low because the number of perturbations per iteration is three from A to B, from B to C, and from C to A. As shown from cases (1) and (2) in Fig. 18, the MPP is tracked and the tracker did not stop but perturb the operating voltage again to complete the iterative procedure making large power loss.

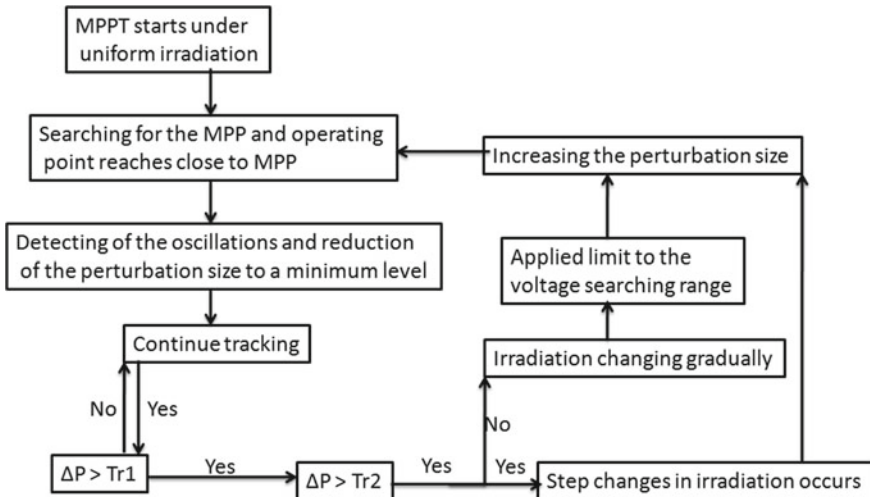


Fig. 17 Flowchart of the modified P&O method proposed in [11]

- Step 1: The tracker senses the module/array output current (I_A) and output voltage (V_A) to calculate the power (P_A) at the operating point A, which is equal to $I_A * V_A$.
- Step 2: The tracker perturbs the voltage from A to B.
- Step 3: The tracker senses the module/array output current (I_B) and output voltage (V_B) to calculate the power $P_B [= I_B * V_B]$ for the operating point B after first perturbation.
- Step 4: The tracker doubly perturbs the voltage in the opposite direction from B to C.
- Step 5: The tracker senses the module/array output current (I_C) and output voltage (V_C) to calculate the power $P_C [= I_C * V_C]$ for the operating point C after double perturbation in the opposite direction.
- Step 6-a: The tracker compares the three points to determine the direction of the next perturbation.
- Step 6-b: If $P_B \geq P_A$ and $P_A > P_C$, the tracker sets the operating point at B by increasing the duty cycle to increase the voltage because of the type of the DC–DC converter is boost one (case (1) in Fig. 18).
- Hint: The voltage step size value is equal to “e” according to the flowchart.

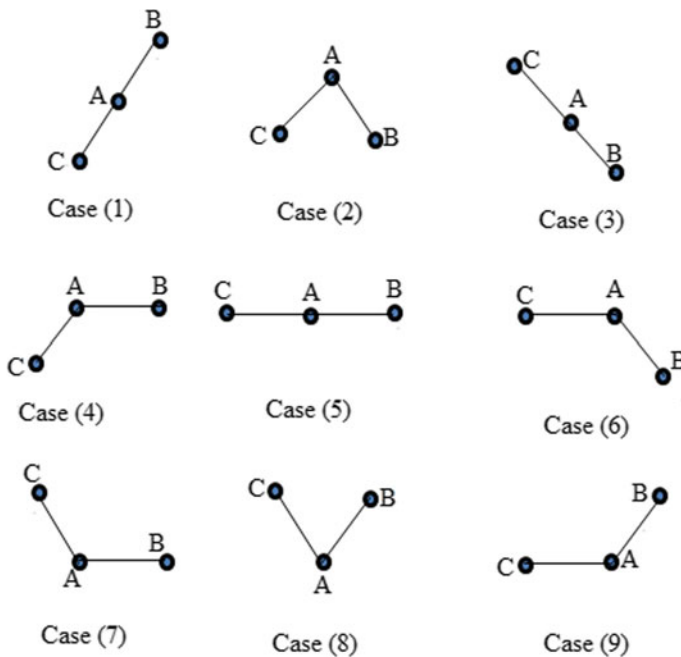


Fig. 18 Possible states of the three perturbation method [12]

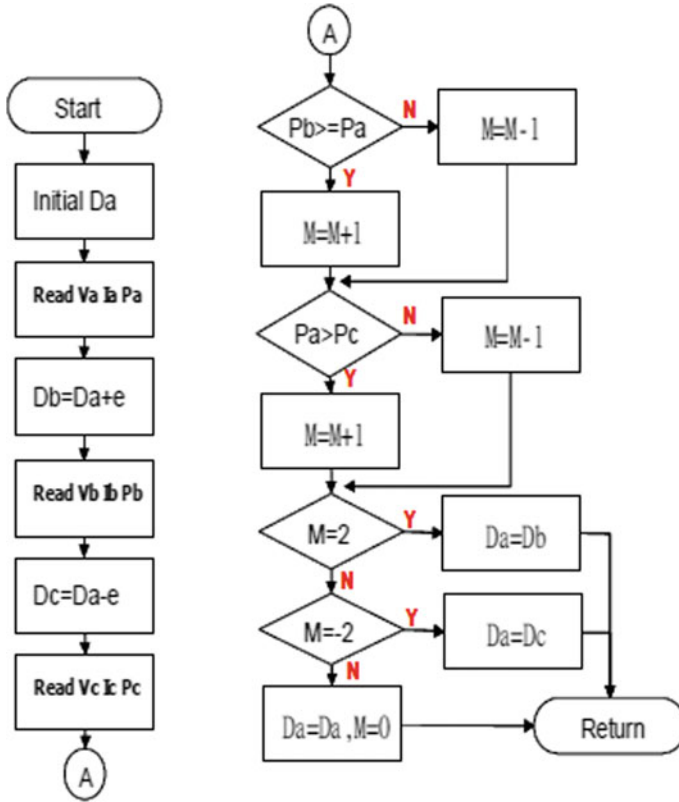


Fig. 19 Algorithm for the three-point weight comparison [12]

- Step 6-c: If $P_B < P_A$ and $P_A < P_C$, the tracker sets the operating point at C by stopping the tracking process because the tracker is already at point C (case (3) in Fig. 18).
- Step 6-d: If $P_B > P_A$ and $P_A < P_C$, the tracker sets the operating point at A by increasing the duty cycle to increase the voltage (cases (4) and (5) in Fig. 18).
- Step 6-e: If $P_B < P_A$ and $P_A > P_C$, the tracker sets the operating point at A by increasing the duty cycle to increase the voltage (case (2) in Fig. 18).
- Step 6-f: If $P_B < P_A$ and $P_A = P_C$, the tracker sets the operating point at A by increasing the duty cycle to increase the voltage (case (6) in Fig. 18).
- Step 6-j: If $P_B = P_A$ and $P_A < P_C$, the tracker sets the operating point at C by stopping the tracking process because the tracker is already at point C (case (7) in Fig. 18).
- Step 6-h: If $P_B > P_A$ and $P_A < P_C$, the tracker sets the operating point at C by stopping the tracking process because the tracker is already at point C (case (8) in Fig. 18).

- Step 6-i: If $P_B > P_A$ and $P_A = P_C$, the tracker sets the operating point at B by increasing the duty cycle to increase the voltage (case (9) in Fig. 18).
- Step 7: The tracker returns back to step 1.

14 Voltage-Hold Perturbation and Observation “VH-P&O” Method [13]

Abdalla et al. proposed [13] a modified method based on the voltage-hold perturbation and observation “VH-P&O” to track correctly the MPP under irradiation changes. Figure 20 shows the flowchart of the VH-P&O method. Actually, this method has large oscillation amplitude the same as the classical one as well as the tracking speed of this method is equal to that of the classical one.

- Step 1: The tracker senses module/array output voltage $V(n-1)$ and current $I(n-1)$ at the $(n-1)$ th step to calculate the power $P(n-1) [= V(n-1) * I(n-1)]$ and the capacitor voltage C_{PV} .
- Step 2: The tracker perturbs the voltage.
- Step 3: The tracker senses module/array output voltage $V(n)$ and current $I(n)$ at the (n) th step to calculate the power $P(n) [= V(n) * I(n)]$.
- Step 4: The tracker calculates the change in power $\Delta P [= P(n) - P(n-1)]$.
- Step 5: The tracker follows the MPP until it oscillates around the MPP.
- Step 6: The change in power due to oscillation is equal to ΔP .
- Step 7: To capture MPP, the tracker sets the operating point at $\Delta P/2$ to overcome the oscillation problem.

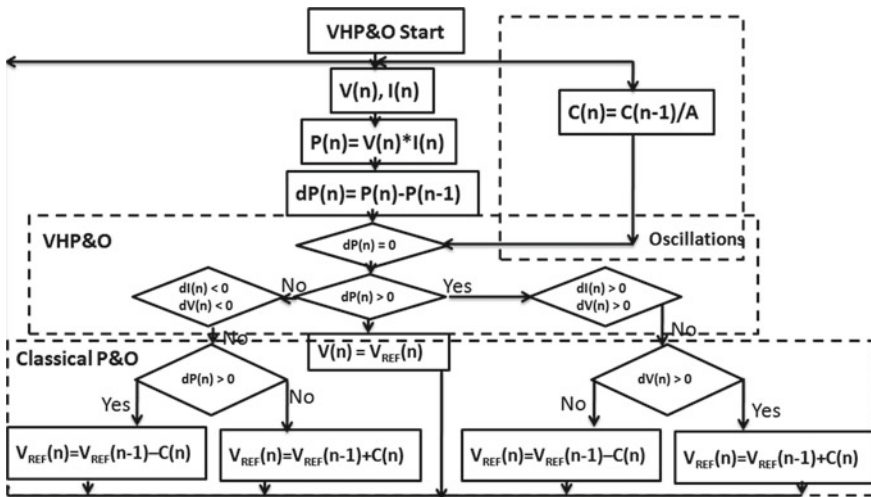


Fig. 20 Proposed VH-P&O MPPT algorithm [13]

- Step 8: If $\Delta P > 0$, $\Delta I > 0$, and $\Delta V > 0$, the tracker holds directly the reference voltage to the capacitor voltage.
- Step 9: If $\Delta P < 0$, $\Delta I > 0$, and $\Delta V > 0$, the tracker decreases the duty cycle to decrease the voltage because the type of DC–DC converter is boost one.
- Step 10: If $\Delta P < 0$, $\Delta I > 0$, and $\Delta V < 0$, the tracker increases the duty cycle to increase the voltage.
- Step 11: If $\Delta P > 0$, $\Delta I > 0$, and $\Delta V > 0$, the tracker increases the duty cycle to increase the voltage.
- Step 12: If $\Delta P > 0$, $\Delta I > 0$, and $\Delta V < 0$, the tracker decreases the duty cycle to decrease the voltage.
- Step 13: If $\Delta P < 0$, $\Delta I < 0$, and $\Delta V < 0$, the tracker holds directly the reference voltage to the capacitor voltage.

15 Curve-Fitting Method [14]

A curve-fitting-based method was proposed [14] to improve the performance of the classical P&O by determining an optimum PV voltage close to that corresponding to maximum power (V_{mpp}) of the datasheet of the PV module/array. Then, the classical P&O method was applied with a small step size until reaching the real MPP. The idea of this method is to predict the P – V curve of a PV module by using mathematical equations or numerical approximations. This attempt to improve the performance of the classical P&O method did not provide satisfactory results where the average efficiency did not exceed 89.2%. Also, the tracking efficiency is very low during high temperatures and low irradiation levels. This is in addition to the fact that this method is not suitable under slope variation of solar irradiation and ambient temperature.

$$a = 5.75 \times 10^{-7} T_{\text{Cell}}^2 - 2.3 \times 10^{-2} T_{\text{Cell}} - 2.08 \times 10^{-3} \quad (2)$$

$$b = -4 \times 10^{-5} T_{\text{Cell}}^2 + 1.17 \times 10^{-3} T_{\text{Cell}} + 0.101 \quad (3)$$

$$c = 7.25 \times 10^{-4} T_{\text{Cell}}^2 - 1.26 \times 10^{-2} T_{\text{Cell}} - 1.9 \quad (4)$$

$$d = -4.08 \times 10^{-3} T_{\text{Cell}}^2 + 2.37 \times 10^{-2} T_{\text{Cell}} + 19.35 \quad (5)$$

$$e = 4.18 \times 10^{-3} T_{\text{Cell}}^2 + 3.4 \times 10^{-2} T_{\text{Cell}} - 12.4 \quad (6)$$

$$P_{\text{PV}} = a V_{\text{PV}}^4 + b V_{\text{PV}}^3 + c V_{\text{PV}}^2 + d V_{\text{PV}} + e \quad (7)$$

At MPP

$$\frac{dP_{\text{PV}}}{dV_{\text{PV}}} = 4a V_{\text{PV}}^3 + 3b V_{\text{PV}}^2 + 2c V_{\text{PV}} + d \quad (8)$$

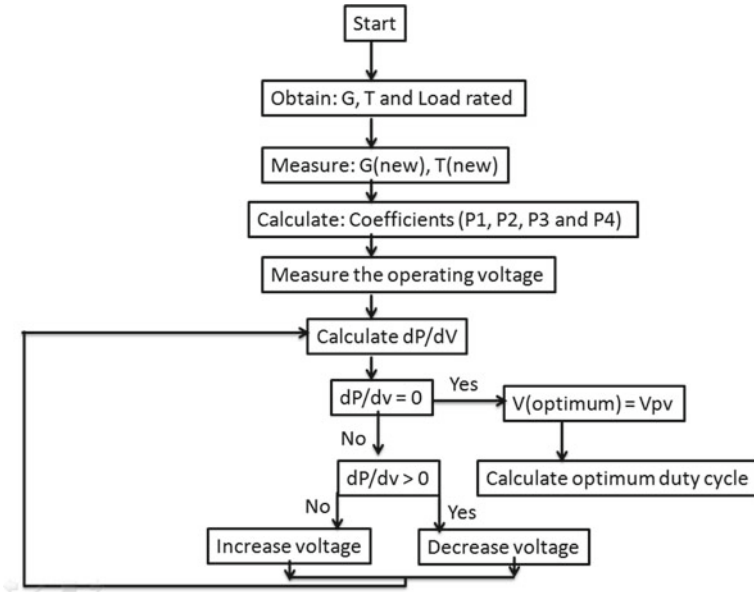


Fig. 21 Flowchart of the curve-fitting method [14]

$$V_{mpp} = \frac{-b \pm \sqrt{b^2 - 3ac}}{3a} \quad (9)$$

- Step 1: Define the module/array specifications at STC to the tracker (Fig. 21).
- Step 2: The tracker senses module/array output current I_{PV} and output voltage V_{PV} as well as the irradiation level and ambient temperature.
- Step 3: The tracker calculates the module/array output power P_{PV} and the cell temperature (T_{cell}).
- Step 4: The tracker calculates the four coefficients (a , b , c , d , and e) by using Eqs. (2–6).
- Step 5: The tracker uses V_{PV} , P_{PV} , and the coefficients calculated in step 4 to construct Eq. (7).
- Step 6: The tracker differentiates Eq. (7) to generate Eq. (8).
- Step 7: The tracker determines V_{mpp} by using Eq. (9).
- Step 8: The tracker checks if the right-hand side of Eq. (8) equals to zero?
- Step 8-a: If it is equal to zero, the tracker stops tracking process.
- Step 8-b: If it is large than zero, the tracker increases the voltage with small step size to capture MPP by increasing the duty cycle as the type of the DC–DC converter is boost one.
- Step 8-c: If it is less than zero, the tracker decreases the voltage with small step size to capture MPP by decreasing the duty cycle.

Step 9: The tracker returns back to step 8.

Step 9-a: If step 8 is achieved, the tracker stops tracking process.

Step 9-b: If step 8 is not achieved, the tracker proceeds back to step 1.

16 Output Power Control-Based Method [15]

Azab proposed [15] an enhanced perturb-and-observe method. This enhanced method is based on defining the value of the maximum power (P_{\max}) according to the datasheet of the PV module, which is the main drawback disadvantage of the method. Figure 22 shows the flowchart for this method. The maximum efficiency of this method is only 95% and the tracking speed is low as outlined in the reported results. Figure 22 shows the flowchart for this method.

Step 1: Define P_{\max} at STC according to the datasheet of the PV module.

Step 2: The tracker senses the module/array output voltage V and current I .

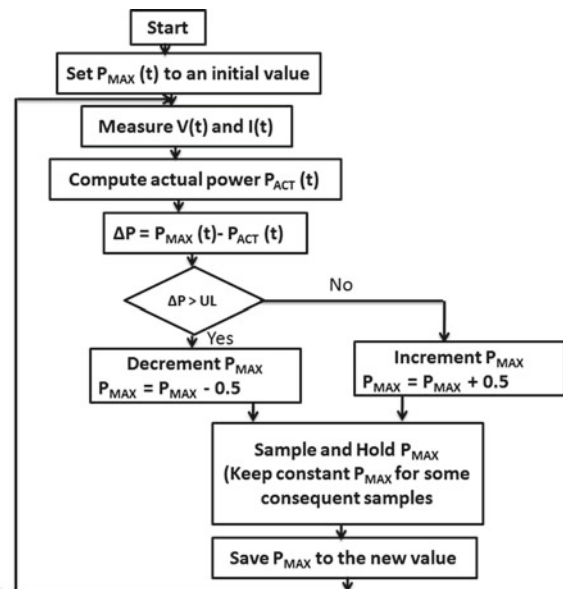
Step 3: The tracker calculates the actual power $P_{\text{actual}} [= I * V]$.

Step 4: The tracker compares P_{\max} with P_{actual} .

Step 4-a: If $[P_{\max} - P_{\text{actual}}]$ equal to zero, the tracker stops tracking because it captured the MPP.

Step 4-b: If $[P_{\max} - P_{\text{actual}}]$ exceeds zero, the tracker increases P_{\max} until $P_{\max} = [P_{\text{actual}} + 0.5]$.

Fig. 22 Flowchart of the proposed method [15]



Step 4-c: If $[P_{\max} - P_{\text{actual}}]$ less than zero, the tracker decreases P_{\max} until $P_{\max} = [P_{\text{actual}} - 0.5]$.

Step 5: Set P_{\max} equals to P_{actual} .

Step 6: Back to step 1.

17 Modified Adaptive Hill Climbing Method [16]

Xiao et al. proposed [16] a modified adaptive hill climbing method. This method is called “MAHC” and based on the following equation:

$$a(K) = M * \frac{|\nabla P|}{a(K-1)} \quad (10)$$

where ΔP is the change in module output power from voltage perturbation steps (k) and $(k + 1)$ and is equal to $P(k + 1) - P(k)$ and M is a constant parameter. The parameter (a) is an online parameter to change the perturbation step size to be suitable for sudden changes in the irradiation level. The value of (M) depends on the PV size and its chosen value has not justified yet. Figure 23 shows the flowchart for this method.

Step 1: Define the values of ε and M to the tracker algorithm

Hint: ε refers to a certain current value defined to the tracker to detect if there is a sudden change in irradiation level or not.

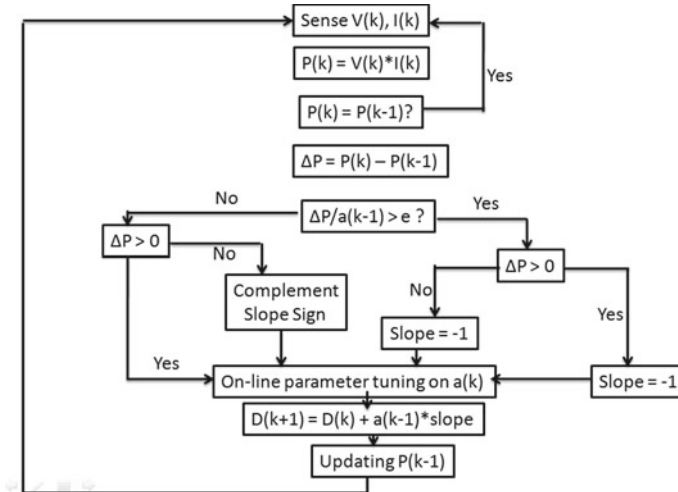


Fig. 23 Flowchart of the method proposed in [16]

- Step 2: The tracker senses the module/array output current $I(k - 1)$ and output voltage $V(k - 1)$ at the $(k - 1)$ th step.
- Step 3: The tracker calculates the output power at $(k - 1)$ th step, which is equal to $P(k - 1) [= V(k - 1) * I(k - 1)]$.
- Step 4: The tracker perturbs the voltage to be at the (k) th step.
- Step 5: The tracker senses the module/array output voltage $V(k)$ and current $I(k)$ at the (k) th step.
- Step 6: The tracker calculates the power at the (k) th step which is equal to $P(k) [= I(k) * V(k)]$.
- Step 7: The tracker calculates the change in power $\Delta P [= P(k) - P(k - 1)]$.
- Step 8: If $\Delta p = 0$ (reaching MPP), the tracker stops perturbation, and if $\Delta p \neq 0$, the tracker continues to next step.
- Step8-a: If $|\Delta P/a(k - 1)| > \varepsilon$, $\Delta P > 0$, and (slope = +1), the tracker increases the voltage with a new step size determined according to Eq. (10).
Hint: Slope dP/dV is the ratio between the change of output power and the change of output voltage. If the slope is less than zero, the tracker will assign -1 to the slope and if the slope exceeds zero, the tracker will assign $+1$ to the slope.
- Step8-b: If $|\Delta P/a(k - 1)| > \varepsilon$, $\Delta P < 0$, and (slope = -1), the tracker decreases the voltage with the new step size according to Eq. (10).
- Step8-c: If $|\Delta P/a(k - 1)| < \varepsilon$, $\Delta P > 0$, and (slope = +1), the tracker increases the voltage with the new step size according to Eq. (10) by increasing the duty cycle as the type of the DC–DC converter is boost one.
- Step8-d: If $|\Delta P/a(k - 1)| < \varepsilon$, $\Delta P < 0$, and (slope = -1), the tracker decreases the voltage with the new step size according to Eq. (10).
- Step 9: The tracker returns to step 1.

18 IP&O Method [17]

Jung et al. proposed [17] an improved perturb-and-observe method, named (IP&O). This method is based on the bandwidth of the module P – V curve. Figure 24 shows the flowchart for this method.

- Step 1: The tracker senses the module/array output current $I(k - 1)$ and output voltage $V(k - 1)$ at the $(k - 1)$ th step.
- Step 2: The tracker calculates the output power at $(k - 1)$ th, which is equal to $P(k - 1) [= V(k - 1) * I(k - 1)]$.
- Step 3: The tracker calculates the maximum power by using $P_{\max} = P(k - 1)/\text{band}$.
Hint: Band is equal to $V_{o,c}$ minus twice the operating voltage $V(k - 1)$.
- Step 4: The tracker compares step #2 with step #3.
- Step 4.1: If step #2 > step #3, the tracker goes to step #4.
- Step 4.2: If step #2 = step #3, the tracker stops.

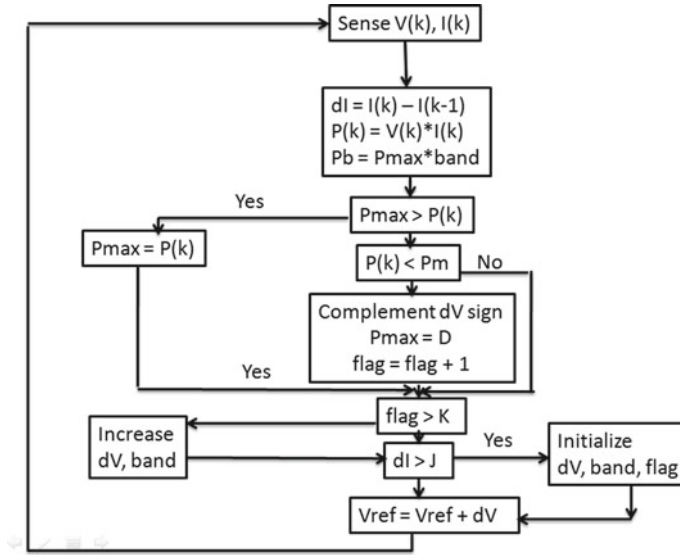


Fig. 24 Flowchart of the method proposed in [17]

Step 4.3: If step #2 < step #3, the tracker decreases the operating voltage by decreasing the duty cycle as the type of the DC–DC converter is boost one.

19 Two-Loop-Based P&O Proposed Method [18]

Chih-Chiang et al. proposed [18] a method based on the classical P&O method. This method includes two loops. The first one is the irradiation loop to be applied under non-uniform conditions. The second loop is the classical P&O loop to be applied under uniform conditions. The switching between the two loops depends on the value of the module output current. Figure 25 shows the flowchart for this method.

Step 1: Define the value of ε to the tracker.

Hint: ε refers to a certain value of current to be defined to the tracker for detecting if there is a sudden change in irradiation level or not.

Step 2: The tracker senses the module/array output current $I(k - 1)$ and output voltage $V(k - 1)$ at the $(k - 1)$ th step.

Step 3: The tracker calculates the output power at the $(k - 1)$ th step, which is equal to $P(k - 1) [= V(k - 1) * I(k - 1)]$.

Step 4: The tracker perturbs the voltage to be at the (k) th step.

Step 5: The tracker senses module/array output voltage $V(k)$ and current $I(k)$ at the (k) th step.

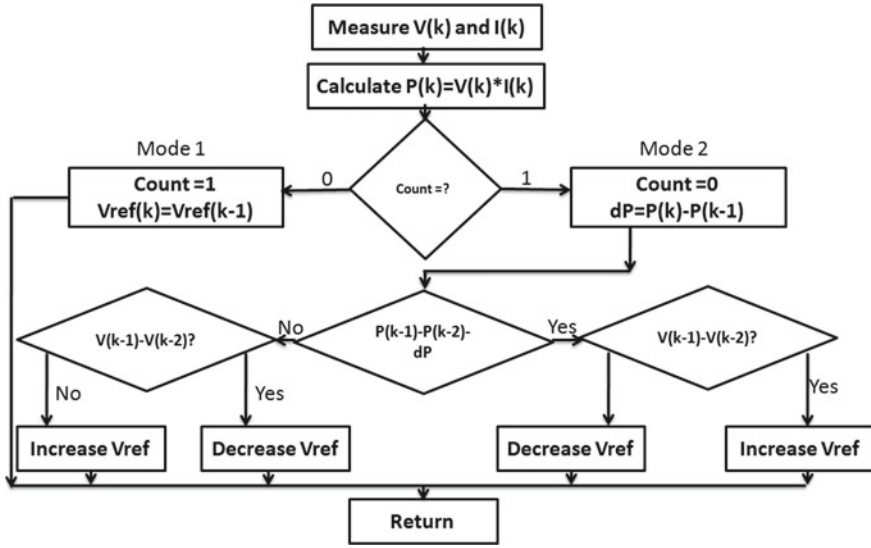


Fig. 25 Flowchart of the method proposed in [18]

- Step 6: The tracker calculates the power at the (k) th step, which is equal to $P(k)$ [$= I(k) * V(k)$].
- Step 7: The tracker calculates the change in current dI [$= I(k) - I(k - 1)$].
- Step 8: The tracker calculates the change in voltage dV [$= V(k) - V(k - 1)$].
- Step 9: The tracker calculates the change in power dP [$= P(k) - P(k - 1)$].
- Step 10: If dI [$= I(k) - I(k - 1)$] $> \varepsilon$, the irradiation level increases and the tracker increases voltage by decreasing the duty cycle as the type of the DC–DC converter is buck one.
- Step 11: If dI [$= I(k) - I(k - 1)$] $< -\varepsilon$, the irradiation level decreases and the tracker decreases voltage by increasing the duty cycle.
- Step 12: If $\text{abs } dI$ [$= I(k) - I(k - 1)$] $< \varepsilon$, the tracker applies the classical P&O method.
- Step 12-a: If dP is positive and the voltage perturbation is positive, the tracker decreases the duty cycle to increase the voltage.
- Step 12-b: If dP is positive and the change in voltage perturbation is negative, the tracker increases the duty cycle to decrease the voltage.
- Step 12-c: If dP is negative and the change in voltage perturbation is positive, the tracker increases the duty cycle to decrease the voltage.
- Step 12-d: If dP is negative and the change in voltage perturbation is negative, the tracker decreases the duty cycle to increase the voltage.
- Step 13: If $dP = 0$ (reaching MPP), the tracker stops tracking, and if $dP \neq 0$, the tracker returns to step 1.

20 Optimized Perturb-and-Observe Method (OP&O) [19]

Femia et al. proposed [19] an optimized P&O technique based on variable step size. This technique tried to solve the problem of oscillation around the MPP which faces the classical one. The tracker step size is adaptive according to the location of the operating point.

21 Open-Circuit Voltage-Based Method [20]

Bennett et al. proposed [20] a modified P&O method based on solving two problems facing the classical one. (i) Trade-off problem between its tracking speed and oscillation amplitude at uniform irradiation level. (ii) Its failure in MPPT under increasing/decreasing irradiation with slope. The complexity of the modified method is very high. At open-circuit condition, the tracker makes the duty cycle equal to zero thus making high power loss in the system.

22 An Optimized P&O Method Based on Combination with Other Method [21]

In 2016, Mohapatra et al. presented [21] a global approximation model for mapping the input–output nonlinear relation of a PV array, where the solar irradiation and ambient temperature are input variables. The current (I_{MPP}) and voltage (V_{MPP}) values corresponding to the MPP were collected at different irradiation levels and ambient temperature values. The collected data was utilized for training and testing a back-propagation neural network (NN) to locate the MPP whatever the values of the irradiation level and ambient temperature. The steady-state and dynamic efficiencies of the proposed technique are equal to 96%.

23 An Adaptive P&O Method [22]

Zakzouk et al. proposed [22] a modified P&O technique depending on a variable perturbation step during sudden variation of ambient temperature, being dependent on ΔP , voltage perturbation ΔV , and $\Delta P/\Delta V$. This is unlike the classical P&O technique, which is dependent on the power change (ΔP) only. More detailed comparison is given in Table 1.

Table 1 Comparison between the proposed method and other modified MPPT algorithms under sudden variation of solar irradiation as regards to the used sensor (s) as well as the steady-state and dynamic efficiency values

References	Sensor (s)	Steady-state efficiency	Dynamic efficiency	
Classical P&O method	V and I	82–85%	82–85%	Values reported in publication [9] referred to the paper
		96%	91%	Values reported in publication [23] referred to the paper
		96.98%	91.90%	Values evaluated by simulation made by the present authors
[4, 5]	V and I	99.60%	99.60%	Values reported in the paper
[6]	V and I	97.50%	95%	Values evaluated by the present authors from paper results
[7]	V and I	98.50%	96.10%	Values evaluated by the present authors from paper results
[8]	V and I	98.15%	96%	Values evaluated by the present authors from paper results
[9]	V and I	97%	95%	Values reported in the paper
[20]	V and I	97.10%	96.33%	Values evaluated by the present authors from paper results
[10]	V and I	Unjustified hypothetical value 400%	Unjustified hypothetical value 400%	Values evaluated by the present authors from paper result
[12]	V and I	97%	92%	Values evaluated by the present authors from paper results
[13]	V and I	91%	91%	Values evaluated by simulation made by the present authors
[14]	V, I, temperature and irradiation	90%	89%	Values evaluated by the present authors from paper results

(continued)

Table 1 (continued)

References	Sensor (s)	Steady-state efficiency	Dynamic efficiency	
[16]	V and I	97.30%	96.30%	Values evaluated by the present authors from paper results
[17]	V and I	–	–	–
[18]	V and I	83.60%	83.60%	Values evaluated by simulation made by the present authors
[19]	V and I	Not available	Not available	–
[22]	V and I	99.80%	99.80%	Values reported in the paper
[2]	V and I	99.48%	98.03%	Values reported in the paper

24 Conclusions

The classical perturb-and-observe method may fail or deviate from tracking the right direction to capture the correct maximum power point (MPP) of a PV module exposed to a suddenly changed solar irradiation or ambient temperature. The classical method fails to capture the MPP when the solar irradiation or ambient temperature follows a ramp with different slopes. This is because the method can't discriminate whether the change in module power is due to its own voltage perturbation or due to the change in the irradiation or ambient temperature level. Numerous approaches for improving, adapting, and optimizing the classical P&O method have been published. However, they differ in many aspects such as tracking speed, tracking accuracy, steady-state efficiency, and dynamic efficiency as well as the number of used sensors, complexity, and cost. This chapter is aimed at reviewing the challenges facing the classical perturb-and-observe method in order to improve it under sudden and ramp variations of irradiation levels and/or ambient temperature.

References

1. Zainuri M, Radzi M, Soh AC et al (2014) Development of adaptive perturb and observe-fuzzy control maximum power point tracking for photovoltaic boost dc-dc converter. *IET Renew Power Gener* 8(2):183–194
2. Abdel-Salam M, EL-Mohandes M, Goda M (2018) An improved perturb-and-observe based MPPT method for PV systems under varying irradiation level. *Solar Energy* 171:547–561
3. Dolara A, Faranda R, Leva S (2009) Energy comparison of seven MPPT techniques for PV systems. *J Electromagn Anal Appl* 1(3):152–162
4. Sera D, Teodorescu R, Kerekes T, Blaabjerg F (2006) Improve MPPT method for rapidly changing environmental conditions. In: *Proceedings of 12th conference on electronics and*

- motion control, Montreal, Quebec, Canada, 2006, pp 1614–1619
5. Sera D, Teodorescu R, Hantschel J, Knoll M (2008) Optimized maximum power point tracker for fast-changing environmental conditions. *IEEE Trans Ind Electron* 55(7):2629–2637
 6. Yafaoui A, Wu B, Cheung R (2007) Implementation of maximum power point tracking algorithm for industrial photovoltaic systems. In: *Proceedings of 2nd conference on Canadian solar buildings*, Calgary, Canada, 10–14 June 2007, pp 1–6
 7. Liu C, Wu B, Cheung R (2004) Advanced algorithm for MPPT control of photovoltaic systems. In: *Proceedings of conference on Canadian solar buildings*, Montreal, Canada, 20–24 August 2004, pp 20–24
 8. Killi M, Samanta S (2015) Modified perturb and observe MPPT algorithm for drift avoidance in photovoltaic systems. *IEEE Trans Ind Electron* 3(2):1–10
 9. Dorofte C, Borup U, Blaabjerg F (2005) A combined two-method MPPT control scheme for grid-connected photovoltaic systems. In: *Proceedings of European conference on power electronics and applications*, Dresden, Germany, September 2005, pp 11–14
 10. Kamala V, Premkumar K, Bisharathu A, Ramaiyer S (2017) A modified perturb & observe MPPT technique to tackle steady state and rapidly varying atmospheric conditions. *Sol Energy* 157:419–426
 11. Ahmed J, Salam Z (2015) An improved perturb and observe (P&O) maximum power point tracking (MPPT) algorithm for higher efficiency. *Appl Energy* 150:97–108
 12. Jiang J, Huang T, Hsiao Y, Chen Ch (2005) Maximum power tracking for photovoltaic power systems. *Tamkang J Sci Eng* 8(2):147–153
 13. Abdalla I, Zhang L, Corda J (2011) Voltage-hold perturbation & observation maximum power point tracking algorithm (VH-P&O MPPT) for improved tracking over the transient atmospheric changes. In: *Proceedings of conference power electronics and applications*, Birmingham, United Kingdom, 30 August 2011, pp 1–10
 14. Khatib T, Mohamed A, Amim N (2010) An improved indirect maximum power point tracking method for standalone photovoltaic systems. In: *Proceedings of conference applications of electrical engineering*, Selangor, Malaysia, 23–25 March 2010, pp 56–62
 15. Azab M (2007) A new maximum power point tracking for photovoltaic systems. *World Acad Sci Eng Technol* 44:571–574
 16. Xiao W, Dunford W (2004) A modified adaptive hill climbing MPPT method for photovoltaic power systems. In: *Proceedings of conference on IEEE 35th annual power electronics specialists*, Aachen, Germany, 20–25 June 2004, pp 1957–1963
 17. Jung Y, So J, Yu G, Choi J (2005) Improved perturbation and observation method (IP&O) of MPPT control for photovoltaic power systems. In: *Proceedings of thirty-first IEEE conference on photovoltaic specialists*, Daejeon, South Korea, 15–17 February 2005, pp 1788–1791
 18. Chih-Chiang H, Jong-Rong L (2001) Fully digital control of distributed photovoltaic power systems. In: *Proceedings of IEEE international symposium on industrial electronics*, Pusan, Korea, June 2001, pp 1–6
 19. Femia N, Petrone G, Spagnuolo G, Vitelli M (2005) Optimization of perturb and observe maximum power point tracking method. *IEEE Trans Power Electron* 20(4):963–973
 20. Bennett T, Zilouchian A, Messenger R (2013) A proposed maximum power point tracking algorithm based on a new testing standard. *Sol Energy* 89:23–41
 21. Mohapatra A, Nayak B, Mohanty K (2016) Performance improvement in MPPT of SPV system using NN controller under fast changing environmental condition. In: *IEEE 6th international conference on power systems (ICPS)*, New Delhi, India, 4–6 March 2016, pp 1–5
 22. Zakzouk N, Elsharty M, Abdelsalam A, Helal A (2015) Improved performance low-cost incremental conductance PV MPPT technique. *IET Renew Power Gener* 10(4):561–574
 23. Genta G, Murtaza A (2014) Robust techniques for the optimal operation of photovoltaic systems, PH. D. thesis, Politecnico University, Torino, Italy, April, 2014

Performance Analysis of Maximum Power Point Tracking (MPPT) for PV Systems Under Real Meteorological Conditions



K. M. Abo-Al-Ez, S. S. Kaddah, S. Diab and El-H. Abdraboh

Abstract In this chapter, the performance of PV systems in terms of maximum power point tracking (MPPT) is studied under the effect of different metrological conditions. Due to the obscurity and lack of credible solar irradiation information, it is important to estimate solar irradiation on horizontal and inclined surfaces by the use of a mathematical model, which considers meteorological data of the location under study. The proposed approach to develop this model is to estimate the global solar radiation on the inclined PV array, then dividing it into its main components. Each of the major metrological conditions affects the PV system performance by affecting a particular component of the total irradiance reaching it. This is thoroughly analyzed in detail in the sections of this chapter, mainly for partial shading conditions, angle of incidence, air mass, and dust. After that, the effect of each of the metrological conditions is modeled associated with a particular component of the global irradiance. Then, an aggregated irradiance model incorporating the effects of all the major metrological conditions is developed to show the reductions in the received irradiance and the generated power. Lastly, this chapter proposes an improved maximum power point tracking (MPPT) algorithm with variable step size, which is suitable for multiple maximum power points occurring during partial shading conditions.

1 Overview

Solar energy is an everlasting energy that can play a major part in fulfilling a considerable share of the global energy demand. African countries such as Egypt and South

K. M. Abo-Al-Ez (✉)

Faculty of Engineering and the Built Environment, Center for Distributed Power and Electronics Systems (CDPES), Cape Peninsula University of Technology (CPUT), Symphony Way, Bellville Campus, Cape Town 7535, South Africa

e-mail: aboalezk@cput.ac.za

S. S. Kaddah · S. Diab · El-H. Abdraboh

Department of Electrical Engineering, Faculty of Engineering, Mansoura University, El-Gomhoria St., Mansoura 35516, Egypt

© Springer Nature Switzerland AG 2020

A. M. Eltamaly and A. Y. Abdelaziz (eds.), *Modern Maximum Power Point Tracking Techniques for Photovoltaic Energy Systems*, Green Energy and Technology, https://doi.org/10.1007/978-3-030-05578-3_7

Africa have shining sun during summer and winter; therefore, the incident radiation must be used for environmental and economic reasons. Photovoltaic (PV) systems are largely employed for sustainable development of small urban communities in the African continent, where access to energy resources of the main power grid is almost impossible. Thus, the typical scenario of the PV system utilization in this context is the smart microgrid model, where these systems are used for domestic purposes such as water pumping and street lightening. The environmental benefits by using PV systems for domestic applications instead of fossil fuel-based systems are notable [1–3]. While the advantages of the PV powered systems make it a favorable option for rural areas, the deviation of its performance is unavoidable. This is due to major metrological factors that seriously reduce the amount of the received irradiance and thus reduce the output power. Those factors are partial shading condition (PSC), dust settlement on the PV array surface, air pollution, relative humidity, angle of incidence, and air mass [4–8]. Stable and reliable operation of smart microgrids involving a considerable penetration level of PV systems is dependent upon finding the maximum power point (MPP) with different metrological conditions. Therefore, PV systems need to be designed properly considering site meteorological characteristics in order to utilize these systems economically and efficiently [9–12].

Some recent research work has addressed the operation of PV systems under different metrological conditions. Each of those metrological factors affects a certain component of the irradiance, which reaches the PV module. The estimation of global irradiance on inclined surfaces from meteorological data of site was presented in [13–27]. The influence of the temperature and the irradiance was considered in the developed mathematical models presented in [28–38]. The objective was to use those models in developing control techniques for PV-islanded and grid-connected operation. The partial shading condition was discussed in some recent research papers [37, 39–55]. It was found that the partial shading factor has the worst effect on the PV system performance, as it creates multiple maximum power points, which in turn causes the malfunction of the conventional maximum power point tracking system [56–58].

Although the models considered the temperature and the irradiance along with the shading effect, other metrological factors were not considered. Other research papers have expanded the modeling process to include more metrological factors as discussed in [36, 59–61]. Those papers found that in actual installation, PV modules operate at a broad extent of angles of incidence (AOI) and air mass (AM) values. Although the accuracy of those models has increased, the dust effect was not considered. Therefore, the dust effect was studied and analyzed in [62, 63], as one of the major factors causing the reduction of the transmittance of the PV system and the reduction of the overall system efficiency. It focused on analyzing the negative effects of dust density decomposition and the types of dust on the irradiance received by PV modules and consequently on the PV performance. However, those models did not incorporate the dust effect with other factors to show their combined effect.

To be able to study the irradiance received by a PV system under variable metrological circumstances, it is essential to estimate the irradiance on inclined PV array through an accurate model and dividing the global irradiance into its main compo-

nents. After that, the effect of each of the metrological conditions is modeled on a particular part of the irradiance, and an aggregated irradiance model that incorporates all the major metrological conditions is developed to assess the reduction in the irradiance value received by a PV module, hence the deviation of the PV system performance.

This chapter is organized as follows; Sect. 2 presents the estimation of the received solar irradiation. Section 3 analyzes the effect of metrological conditions on the PV system performance. This section starts with the PSC and its effect on the PV system operation. Thereafter, Sect. 3 analyzes other affecting conditions mainly the angle of incidence, the air mass, and the dust type. Section 4 presents an aggregated irradiance mathematical model under different metrological factors. Finally, in Sect. 5 an improved maximum power point tracking algorithm is presented.

2 Estimation of the Received Solar Irradiance

To model the different metrological conditions affecting the PV system performance, mainly the performance related to tracking the maximum power produced, an accurate estimation of each part of the global irradiance on the inclined PV array has to be done, and then insert the effect of each metrological factor on a particular component of the global irradiance.

The proposed algorithm shown in Fig. 1 estimates the hourly irradiance on inclined surface for a particular day, knowing only the site meteorological parameters such as latitude (L), sun duration (S/S_0), mean sea level pressure (MSL), water vapor pressure (V), temperature (T), and relative humidity (RH).

The first step is using two different empirical models to estimate the value of the irradiation on horizontal surfaces \bar{H} taking into consideration the effect of the meteorological parameters for the site under study. Then divide the value of \bar{H} into the beam irradiation (\bar{H}_B) and the diffuse irradiation (\bar{H}_D) components. After that, the irradiation on inclined surface (\bar{H}_T), its diffused component (\bar{H}_{DT}), beam component (\bar{H}_{BT}), and reflected component (\bar{H}_{RT}) are estimated on different orientations using isotropic and anisotropic models.

2.1 Estimation of Irradiation on Horizontal Surface

For estimating the irradiation on horizontal surface, the day considered is the day when the solar declination angle (δ) is equal to the angular tilt average of the month. The recommended day for each month is given in Table 1 [15, 17, 18]. There are several empirical models using meteorological parameters at different sites, which can be used for estimating the value of \bar{H} as shown in the following two models:

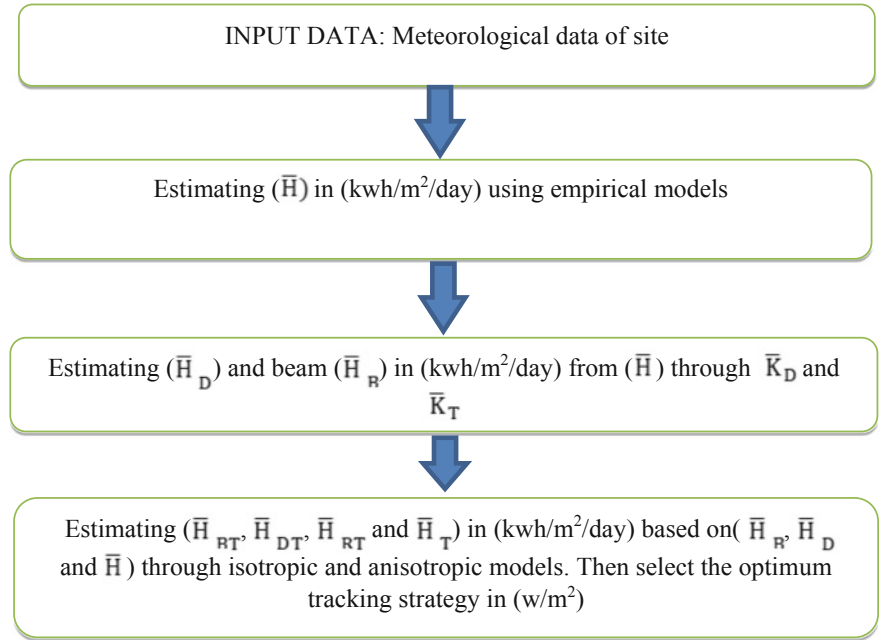


Fig. 1 Proposed algorithm for estimating Geometric relationships \bar{H}_T

Table 1 Average day and corresponding δ each month

Month	Date	Day number in year	δ (degree)
January	17	17	−20.9
February	16	47	−13.0
March	16	75	−2.4
April	15	105	9.4
May	15	135	18.8
June	11	162	23.1
July	17	198	21.2
August	16	228	13.5
September	15	258	2.2
October	15	288	−9.6
November	14	318	−18.9
December	10	344	−23.0

• **Model (1):**

The sunshine duration data based on Angström model [13, 16, 17, 19, 20] are given as:



**Iran Solar
Magazine**

$$\bar{H} = \bar{H}_o \times \{A + B(\bar{S}/\bar{S}_o)\} \quad (1)$$

$$\bar{S}_o = \frac{2}{15} \cos^{-1}(-\tan \phi \tan \delta) \quad (2)$$

where A and B are constants that are 0.295 and 0.423, respectively; ϕ is the latitude, and it is 31.07 (degree) for Al-Arish site in Egypt [13].

• **Model (2):**

The MSL, V , T , and RH were added to the model of Angström as discussed in [15], and it is given as follows:

$$\bar{H} = \bar{H}_o \times \{a + b(\bar{S}/\bar{S}_o) + cT + dV + eR_H + fP\} \quad (3)$$

$$\bar{H}_o = \frac{24 \times 3.6 \bar{H}_{on}}{\pi} \left(\cos \phi \cos \delta \sin \omega_s + \frac{\pi \omega_s}{180} \sin \phi \sin \delta \right) \quad (4)$$

$$\bar{H}_{on} = S_c \left[1 + 0.033 \cos \left(\frac{360n}{365} \right) \right] \quad (5)$$

$$\omega_s = \cos^{-1}(-\tan(\Phi) \times \tan(\delta)) \quad (6)$$

where

$$a = 0.129, b = 0.382,$$

$$c = -0.009, d = -0.001, e = 0, f = 0$$

\bar{H}_o	<i>The monthly average daily irradiation of horizontal surfaces (kwh/m²/day)</i>
\bar{H}_{on}	<i>The corresponding normal component</i>
S_c	<i>Solar constant = 1367 W/m²</i>
n	<i>The day number in the year</i>
ω_s	<i>The sunshine hour angle in degrees</i>

The meteorological data for Al-Arish are given in Table 2 [15].

The value of \bar{H} for Al-Arish city is calculated through the previously explained two models, and the results are compared with the measured values as shown in Fig. 2.

Table 2 Meteorological data for Al-Arish city

Month	\bar{S}	$T(^{\circ}C)$	V (hpa)	MSL (hpa)	R (%)
January	7.6	20.1	11.4	1018.1	74.0
February	7.9	17.8	9.5	1021.0	67.3
March	8.5	19.7	10.6	1015.2	66.7
April	9.5	23.5	11.3	1015.2	59.3
May	11.3	27.0	16.5	1014.2	70.0
June	12.6	29.0	19.0	1012.0	70.0
July	12.0	32.2	23.8	1009.2	70.0
August	11.9	30.5	23.5	1010.2	71.7
September	10.7	29.8	20.8	1012.5	68.7
October	9.50	25.5	19.6	1013.2	73.5
November	8.50	21.1	15.4	1014.9	72.3
December	7.70	19.0	11.6	1018.8	71.0
Mean	9.81	24.6	16.08	1014.54	69.54

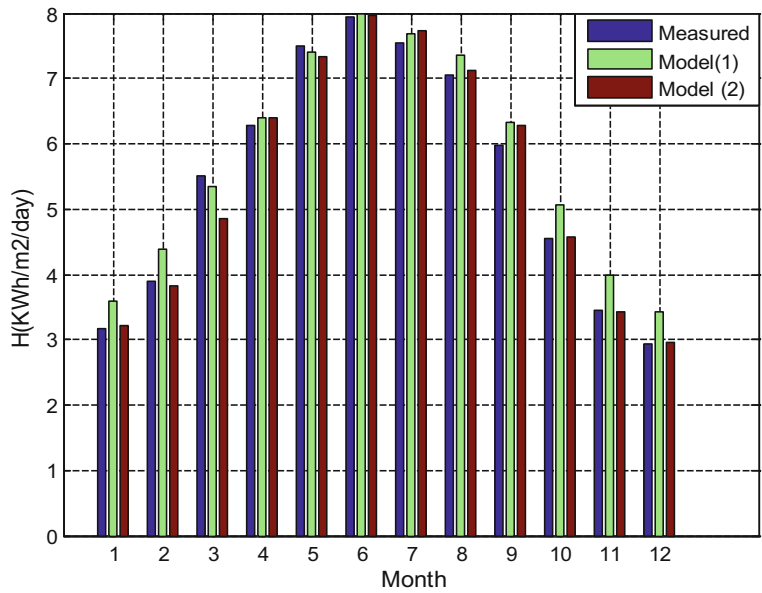


Fig. 2 Comparison between measured and estimated \bar{H}

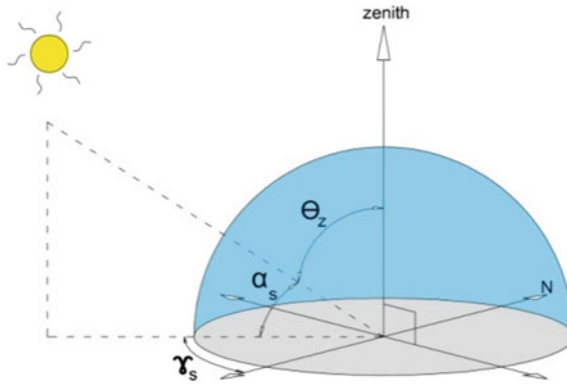


Fig. 3 Geometric relationships between a horizontal and the incoming beam where Δ_z —Zenith angle, angle between the vertical and the line to the sun; α_s —solar altitude angle, complement of the zenith angle; and γ_s —solar azimuth angle, angular displacement from south of the projection of the solar ray on the horizontal plane

The accuracy of the two models is assessed through the mean relative deviation (MRD) between the measured and the estimated values as shown [20]:

$$\text{MRD} = \frac{1}{12} \sum_{i=1}^{12} \frac{\bar{H}_{i,\text{measured}} - \bar{H}_{i,\text{estimated}}}{\bar{H}_{i,\text{measured}}} \times 100 \quad (7)$$

From the results, MRD for model (1) is 7.2864% and MRD for model (2) is 2.4522%. The least MRD is with model (2), so it is more accurate. In addition, it is noted that model (2) permits including several meteorological parameters, which may change under different conditions.

2.2 Estimation of Daily Global Irradiation on Inclined Surface

The geometric relationships between the horizontal and the incoming solar ray, that is, the position of the solar ray relative to that surface, can be described in terms of several angles as shown in Fig. 3 [17].

The geometric relationships between an inclined surface and the incoming solar ray can be described in terms of several angles as shown in Fig. 4 [18].

The irradiance on inclined surface consists of three parts, namely beam or direct, diffused, and reflected components. To be able to estimate \bar{H}_T , the first step is to estimate the \bar{H}_B and \bar{H}_D , since the reflected part equals zero on horizontal surface.

The value of \bar{H}_D and \bar{H}_B can be calculated through the monthly average daily cloudiness index as presented in Eq. (8) [17, 21–23]:

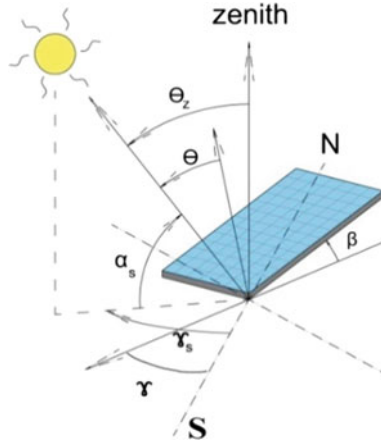


Fig. 4 Geometrical configuration of PV module on inclined surface where γ —surface azimuth angle, $-180^\circ \leq \gamma \leq 180^\circ$; θ —angle of incidence, angle between the solar ray on a surface and the normal to that surface [degree]; and β —the slope, $0^\circ \leq \beta \leq 180^\circ$

$$\vec{H}_D = \vec{H} \times \vec{K}_D \quad (8)$$

The value of \vec{K}_D is estimated by correlating it to the clearness index \vec{K}_T (which is \vec{H}/\vec{H}_o). There are several models that correlate \vec{K}_D to \vec{K}_T each based on data collected from several stations. But all the estimated correlations were found to be almost similar to each other and only depend on the season [17]. Suggested correlation of \vec{K}_D versus \vec{K}_T and sunset hour angle for the tilted angle (ω'_s degree) are estimated according to Erbs as follows [17, 19, 21, 22]:

$$\omega'_s = \min \left(\frac{\cos^{-1}[-\tan(\theta) * \tan(\delta)]}{\cos^{-1}[-\tan(\varphi - \beta) * \tan(\delta)]} \right) \quad (9)$$

For $\omega_s \leq 81.4$ and $0.3 \leq \vec{K}_T \leq 0.8$

$$\vec{K}_D = 1.391 - 3.560\vec{K}_T + 4.189\vec{K}_T^2 - 2.137\vec{K}_T^3 \quad (10)$$

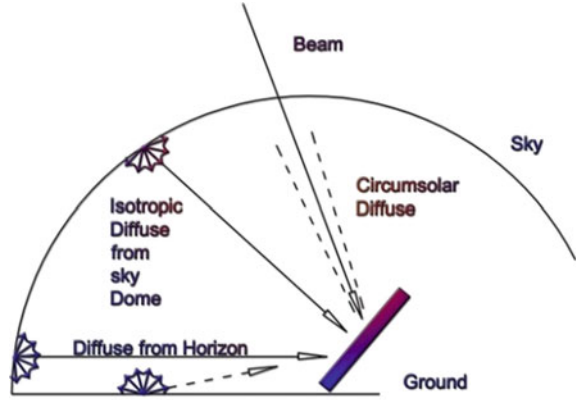
And for $\omega_s > 81.4^\circ$ and $0.3 \leq \vec{K}_T \leq 0.8$

$$\vec{K}_D = 1.311 - 3.022\vec{K}_T + 3.427\vec{K}_T^2 - 1.821\vec{K}_T^3 \quad (11)$$

$$\vec{H}_B = \vec{H} - \vec{H}_D \quad (12)$$

The values of \vec{H}_T and its components are calculated as given in [17–19, 23, 24] as follows:

Fig. 5 Distribution of diffuse irradiation



$$\bar{H}_T = \bar{H}_{BT} + \bar{H}_{RT} + \bar{H}_{DT} \quad (13)$$

$$\bar{H}_{BT} = \bar{H}_B \times \bar{R}_B \quad (14)$$

$$\bar{R}_B = \frac{\cos(\varphi - \beta) \cos \delta \sin \omega'_s + \left(\frac{\pi}{180}\right) \omega'_s \sin(\varphi - \beta) \sin \delta}{\cos \varphi \cos \delta \sin \omega_s + \left(\frac{\pi}{180}\right) \omega_s \sin \varphi \sin \delta} \quad (15)$$

$$\bar{H}_{RT} = \bar{H} \times \bar{R}_R \quad (16)$$

$$\bar{R}_R = \rho \times \frac{1 - \cos \beta}{2} \quad (17)$$

$$\bar{H}_{DT} = \bar{H}_D \times \bar{R}_D \quad (18)$$

where

\bar{R}_B solar ray geometric tilt factor

ρ the solar reflectivity index, and it is assumed to be = 0.2

\bar{R}_D the monthly average daily diffuse geometric tilt factor

Φ the latitude, $-90^\circ \leq \varphi \leq 90^\circ$.

Diffuse irradiation on inclined surface includes three components, namely isotropic ($\bar{H}_{DT,iso}$), circumsolar ($\bar{H}_{DT,cs}$), and horizon ($\bar{H}_{DT,hz}$). Distribution of diffuse irradiation showing its three parts as adapted from Perez et al. is shown in Fig. 5 [17]. There are several models as Lui and Jordan model which estimates ($\bar{H}_{DT,iso}$) only, Hay and Davis model which estimates both ($\bar{H}_{DT,iso}$) and ($\bar{H}_{DT,cs}$), and HDKR model which estimates the three components of diffused irradiance [17, 22, 23]. So, HDKR model will be considered in this study. The formulation for this model is given below.

• **HDKR model formulation:**

$$\bar{H}_{DT} = \bar{H}_{DT,iso} + \bar{H}_{DT,cs} + \bar{H}_{DT,hz} \quad (19)$$

$$\bar{R}_D = \left\{ (1 - A_i) \left(\frac{1 + \cos \beta}{2} \right) \left[1 + f \sin^3 \left(\frac{\beta}{2} \right) \right] + A_i \bar{R}_B \right\} \quad (20)$$

$$f = \sqrt{\frac{\bar{H}_B}{\bar{H}}} \quad (21)$$

$$A_i = \frac{\bar{H}_B}{\bar{H}_0} \quad (22)$$

From Eqs. (18) and (20), the value of \bar{H}_{DT} , given by Eq. (19), becomes as:

$$\bar{H}_{DT} = \bar{H}_D \times \left\{ (1 - A_i) \left(\frac{1 + \cos \beta}{2} \right) \left[1 + f \sin^3 \left(\frac{\beta}{2} \right) \right] + A_i \bar{R}_B \right\} \quad (23)$$

The three models are applied using MATLAB to estimate diffuse and global irradiation on inclined surface, and results are shown in Fig. 6.

From results shown in Fig. 7, the HDKR model estimates all the components of diffuse component and gives the highest value for the irradiation on inclined surface, followed by Hay and Davis model and Liu and Jordan model, respectively.

The MRD of \bar{H}_{DT} estimated by each of Lui and Jordan model and Hay and Davis model from that estimated by HDKR model is 14.2465 and 1.2430%, respectively. The MRD for \bar{H}_T for each of Lui and Jordan model and Hay and Davis model from HDKR model is 3.9313 and 0.3466%, respectively. The monthly average daily global irradiation on inclined surface is estimated based on HDKR model through Eq. (24):

$$\begin{aligned} \bar{H}_T = & (\bar{H}_B + \bar{H}_D A_i) \bar{R}_B + \bar{H}_D (1 - A_i) \left(\frac{1 + \cos \beta}{2} \right) \left[1 + f \sin^3 \left(\frac{\beta}{2} \right) \right] \\ & + \bar{H}_\rho \left(\frac{1 - \cos \beta}{2} \right) \end{aligned} \quad (24)$$

The step following the selection of HDKR model to estimate the monthly average daily global irradiation on inclined surface is to select the optimum tracking strategy, which leads to increase the irradiance received on the PV array surface along all the days of the year for a given site under study. There are several tracking strategies, such as the annual strategy [23], the seasonal strategy [17, 26], and the daily strategy [17, 19, 25, 26].

For a PV module rotated about a horizontal east–west axis with a daily adjustment, the angle of incident is expressed as [17, 19]:

$$\cos \theta = \sin^2 \delta + \cos^2 \delta \cos \omega \quad (25)$$

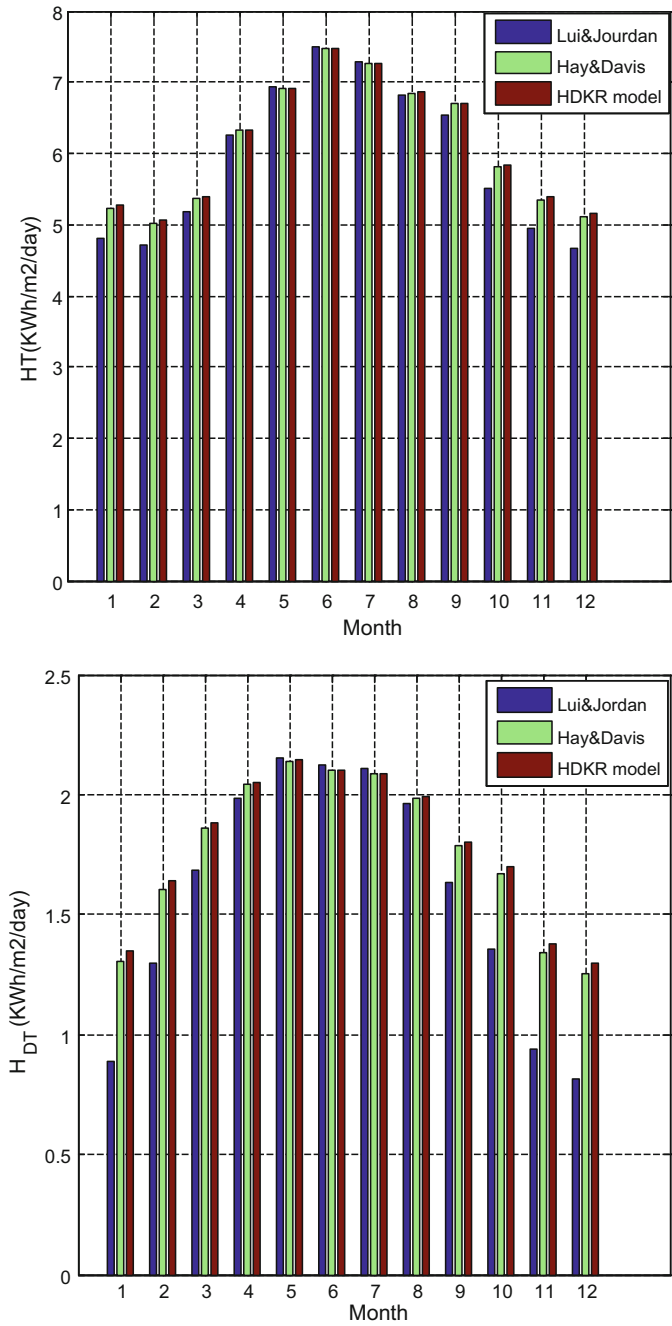


Fig. 6 Estimated \bar{H}_{DT} and \bar{H}_T

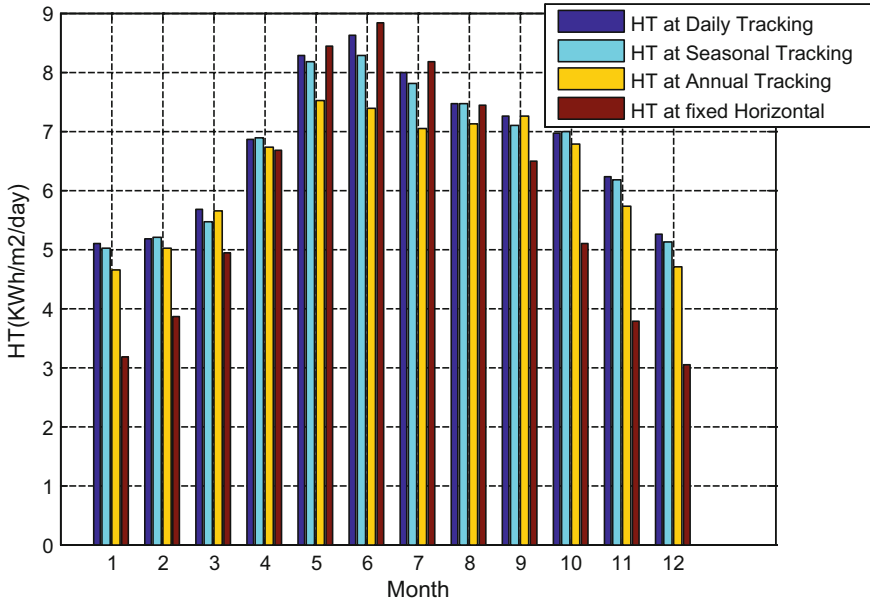


Fig. 7 Estimated (\bar{H}_T) under different tracking strategies

$$\omega = (t - 12) \times 15 \quad (26)$$

$$\beta = |\phi - \delta| \quad (27)$$

$$\gamma = \begin{cases} 0^\circ & \text{if } \phi - \delta > 0 \\ 180^\circ & \text{if } \phi - \delta \leq 0 \end{cases} \quad (28)$$

where ω is the sun hour angle (degree).

The solar irradiation values received on a tilted PV array at different tilt angles are estimated through a developed MATLAB model using Eq. (24). The values of irradiation received on inclined plane \bar{H}_T are estimated when received on different tilt angles. These tilt angles are derived based on different tracking strategies, namely seasonal, daily, and annual. These values of \bar{H}_T are compared with the daily irradiation received on horizontal plane \bar{H} , and results of comparison are shown in Fig. 8.

Relative increase in irradiance received due to different tracking strategies and results are given in Table 3.

From results shown in Fig. 7 and Table 3, the daily optimal tilt angle leads to the maximum values of irradiation received along the months of the year.

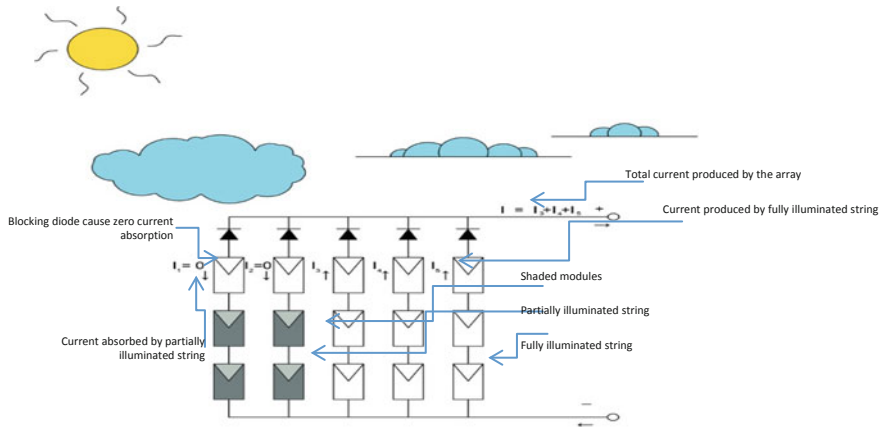


Fig. 8 PV array under partial shading through passing clouds

Table 3 Relative increase in \bar{H}_T from \bar{H}

Tracking strategy	Relative increase %
Annual optimal	16.42
Seasonal optimal	22.68
Daily optimal	24.38

3 Effect of Metrological Conditions on PV System Performance

Metrological conditions cause performance deviation of PV systems and have mutual effect on each other. The main metrological condition affecting the performance of PV systems is the partial shading condition (PSC). Other conditions that of significance are dust settlement on the PV array surface, angle of incidence, and air mass. In this section, the focus is on the PSC, and the effect of other conditions is presented briefly.

3.1 Partial Shading Condition (PSC)

PSC can occur due to shading from tree leaves falling over cells, birds or bird litters on cells, or soft shading due to neighboring buildings or arrays or passing clouds. When PSC occurs, the consequences are as follows:

1. The shaded area passes currents higher than their short-circuit current in the reverse direction as shown in Fig. 9; hence, it operates in consuming mode rather than generating mode unless blocking diodes are inserted [42, 52].

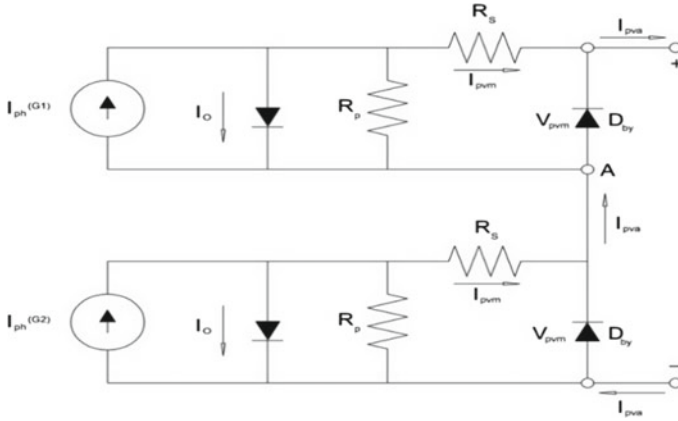


Fig. 9 Equivalent circuit of PV module partially shaded

2. The array partially shaded has several peaks in its P–V characteristic curve, and the traditionally tracking methods will fail to track maximum output power with them [43–48].
3. If excessive reverse bias voltage occurs, due to high shading ratios, the internal diode of the module shown in Fig. 9 offers high resistance creating an open circuit in the entire PV module causing hot spot point, which can damage the diode itself [42].

The irradiance received by the PV module \bar{H}_T is composed of direct or beam H_B , diffuse H_D , and reflected H_R components. Also, the diffuse component is composed of isotropic H_D^{ISO} and circumsolar H_D^{CIR} and horizon H_D^{HZ} components. Nevertheless, the effective shading ratios are applied only to the direct component and circumsolar part of diffuse [49, 53]. The PV module type, which is considered in this study, is Bpsx3150 W module with specifications given in [61].

The irradiance $\bar{H}_{T,sh}$ received by cells, which are shaded by different shading ratios of Sh (referring to the percentage area of the cell, which is shaded), can be calculated from Eq. (29) [45, 48, 49]:

$$\bar{H}_{T,sh} = (\bar{H}_{DT,cs} + \bar{H}_{BT})(1 - S_h) + \bar{H}_{DT,iso} + \bar{H}_{DT,hz} + \bar{H}_{RT} \quad (29)$$

In addition, the value of $\bar{H}_{T,sh}$ at different shading ratios is simulated in Fig. 10. At 17 January in Al-Arish city, the shading effect is studied with different shading ratios. The shading factor F is calculated from Eq. (30) [39, 48, 53], and it can be used to estimate I_{SC} under PSC.

$$F = \frac{\bar{H}_{T,sh}}{\bar{H}_T} = \frac{I_{sc, sh}}{I_{sc}} \quad (30)$$

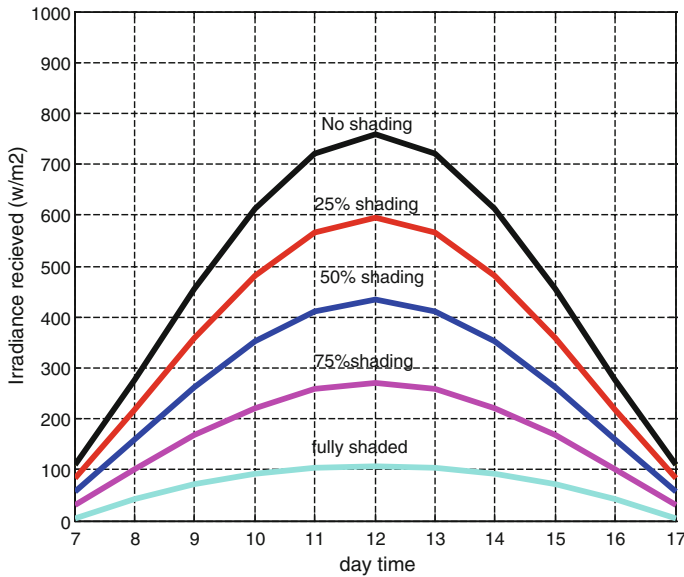


Fig. 10 Irradiance received $\bar{H}_{T,sh}$ in (w/m²) at different shading ratios

As more of the module gets shaded, the system shows multiple maximum power points, making identification of the real one difficult for traditional trackers, and potentially leads to oscillations about MPP or other undesirable behaviors as simulated in Fig. 11.

3.2 Effect of Other Metrological Conditions

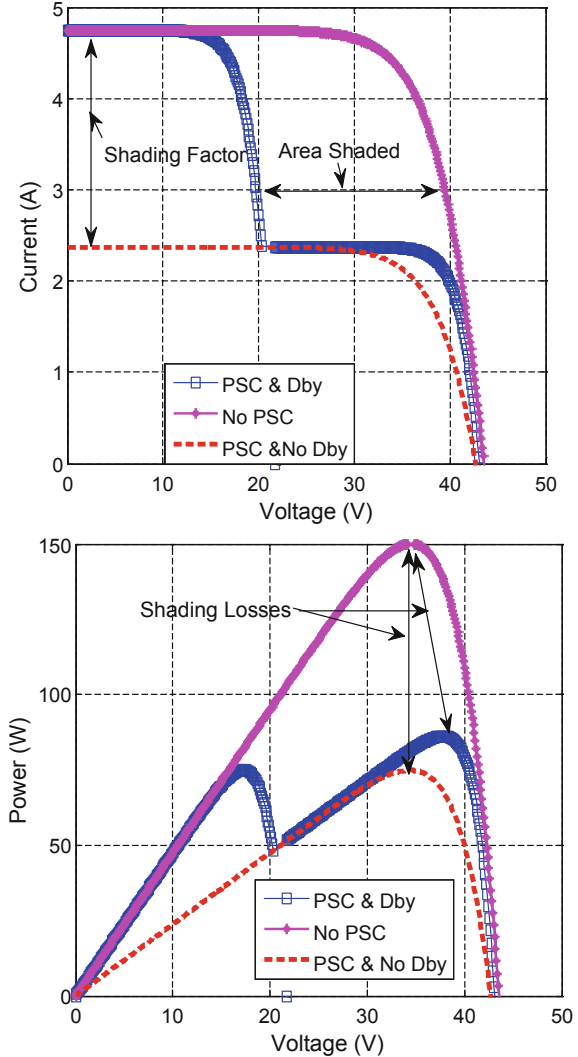
3.2.1 Angle of Incidence (AOI)

The angle of incidence (AOI) is the angle between the incident solar ray on a PV array and the normal to the array. The AOI influences the irradiance value received by a PV module by what so-called the optical effect which accounts for reflectivity losses [4, 5]. The irradiance received by the PV module considering AOI effect, $\bar{I}_T(\text{AOI})$, can be calculated by the following steps as given in [4, 5]:

$$\bar{I}_T(\text{AOI}) = [f_1(\text{AOI}) \times \bar{I}_{BT}] + f_d \times \bar{I}_{DT} \quad (31)$$

A fifth-order regression is used to determine $f_1(\text{AOI})$ which is given as follows [59]:

Fig. 11 I–V and P–V c/cs of PV module under PSC



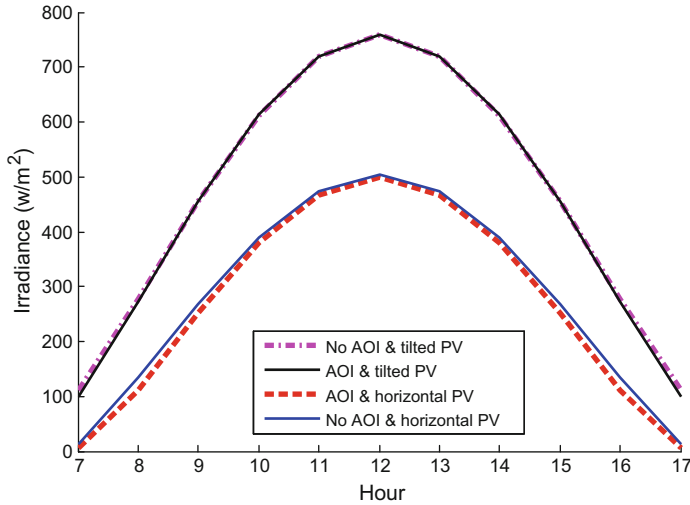
$$f_1(AOI) = b_0 + b_1 + AOI + b_2(AOI)^2 + b_3(AOI)^3 + b_4(AOI)^4 + b_5(AOI)^5 \quad (32)$$

where f_d is the fraction of diffuse irradiance used by module, typically assumed = 1; $b_0, b_1, b_2, b_3, b_4, b_5$ are constants given in Table 4 [4].

For both the day and site under study, the AOI effect on the irradiance received by PV module when it is placed on both horizontal plane and inclined at daily optimal tilt angle plane is simulated and results are shown in Fig. 13 compared to that received irradiance without the AOI effect. From Fig. 12, it can be noted that the AOI effect

Table 4 Polynomial coefficients for AOI

b_0	b_1	b_2	b_3	b_4	b_5
1.0	$-2.438\text{e}-3$	$3.103\text{e}-4$	$-1.246\text{e}-5$	$2.112\text{e}-7$	$-1.359\text{e}-9$

**Fig. 12** Irradiance received by horizontal and tilted PV module with AOI effect

is not obvious for the inclined surface because the AOI result was less than 60° . However, this effect was obvious with larger values of AOI resulted in case of the horizontal surface.

3.2.2 Effect of Air Mass (AM)

Air mass (AM) is relative trajectory index that the solar beam has to travel through the atmosphere before arriving to the land. An $AM = 1$ when the sun is directly overhead at a sea level site (at noon); $AM = 10$ or greater near sunrise and sunset [5, 61]. The irradiance received by the PV module with air mass effect can be calculated by Eq. (33) [5].

$$\bar{I}_T(AM) = \bar{I}_T \times f_2(AM_a) \quad (33)$$

A fourth-order regression is used to determine the air mass function $f_2(AM_a)$. The values of the polynomial coefficients are provided in [61] and expressed as:

$$f_2(AM_a) = a_0 + a_1 \Delta AM_a + a_2 (AM_a)^2 + a_3 (AM_a)^3 + a_4 (AM_a)^4 \quad (34)$$

Table 5 Sandia polynomial coefficients for AM

PV module	a_0	a_1	a_2	a_3	a_4
Bp sx3150	0.9415	0.05272800	−0.009588	0.00067629	−1.8111E−05
Uni-solar US-21	1.0470	0.00082115	−0.025900	0.00317360	0.00011026

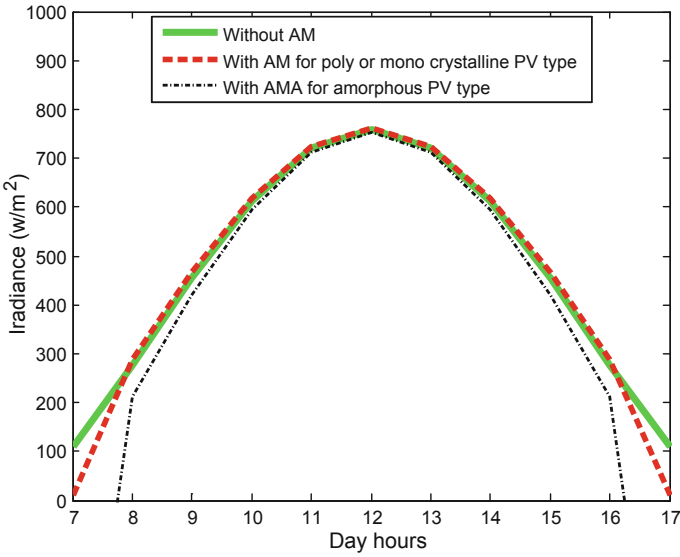


Fig. 13 Irradiance received by different types of PV module with AM effect

where $a_0, a_1, a_2, a_3, a_4, a_5$ are constants based on PV type and given in Table 5 [61].

For the day and site under study, the received irradiance with AM effect for different types of PV arrays along day hours is shown in Fig. 13.

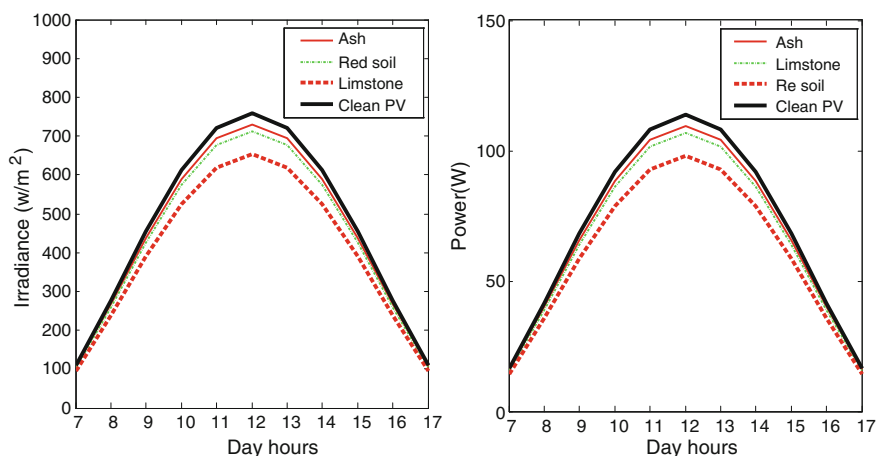
From Fig. 13, the manufacturing material of the PV array is affecting the amount of reduction in the received irradiance when AM effect is considered.

3.2.3 Effect of Dust Type

Different types of dust such as red soil, limestone, and flying ash affect the received irradiance. A reliable and practical relation developed to study the dust-type effect on maximum power extracted P_{\max} from PV systems is given in [63]. P_{\max} is directly proportional to the solar irradiance as explained in [59]. The dust coefficient “Aj” is given in Table 6 [63]. When considering a dust density of 0.63 gm/m² of different dust types, both the irradiance received by PV module and the power output from it are simulated and shown in Fig. 14. The irradiance received by the PV module under dust effect can be calculated as:

Table 6 Coefficient of standard deviation for different dust types

Pollutant	A_j
Ash	0.06 ± 0.024
Limestone	0.10 ± 0.034
Red soil	0.24 ± 0.085

**Fig. 14** Irradiance received and power extracted by clean and dusty surface

$$\bar{I}_T(\text{Dust}_j) = \bar{I}_T(\text{Clean}) \cdot e^{-A_j \Delta M_j} \quad (35)$$

From the simulation results shown in Fig. 14, it is obvious that the red soil dust causes the most severe performance deviation the PV array, and then comes the limestone, and the least effect is caused by ash.

4 Aggregated Irradiance Model Under Different Metrological Conditions

It is essential to combine those effects in an aggregated model that can accurately describe the irradiance received by a PV module for one or more of those factors.

The performance of a PV module shows deviation under different ambient factors discussed in the previous section. It is essential to combine those effects in an aggregated detailed model that can accurately describe the irradiance received by a PV module for one or more of those factors.

Table 7 P_{\max} at noon considering different metrological conditions

Measured values	AOI	Air mass	Dust	PSC	All conditions
$I_{sc}(A)$	3.6038	3.6195	3.4718	2.8301	2.7840
$P_{\max}(w)$	113.7341	114.2304	109.5540	89.2539	87.7972
$PR(\%)$	0	-0.4	3.675	21.5	24.775

The following steps show how the model is derived:

- *Insert the shading effect:*

$$\bar{I}_T(\text{sh}) = (1 - \text{sh})(\bar{I}_{BT} + \bar{I}_{DT,\text{cir}}) + \bar{I}_{DT,\text{iso}} + \bar{I}_{RT} \quad (36)$$

- *Add the AM effect to Eq.(3.36) as follows:*

$$\bar{I}_T(\text{sh}, \text{AOI}) = (1 - \text{sh})(\bar{I}_{BT} \times f_2(\text{AOI}) + \bar{I}_{DT,\text{cir}}) + \bar{I}_{DT,\text{iso}} + \bar{I}_{RT} \quad (37)$$

- *Add the AM effect to Eq. (3.37) as follows:*

$$\bar{I}_T(\text{sh}, \text{AOI}, \text{AMA}) = f_1(\text{AMA})[(1 - \text{sh})(\bar{I}_{BT} \times f_2(\text{AOI}) + \bar{I}_{DT,\text{cir}}) + \bar{I}_{DT,\text{iso}} + \bar{I}_{RT}] \quad (38)$$

- *Add the dust effect to Eq. (3.38) to get the aggregated model:*

$$\bar{I}_T(\text{All}) = [\bar{I}_T(\text{sh}, \text{AOI}, \text{AMA})].e^{-A_j \Delta M_j} \quad (39)$$

In a proposed scenario, consider PV module protected by two bypass diodes that one cell inside it is under PSC of 25%, and also a density of 0.63 gm/m^2 of ash dust is deposited on it. Consider both AM and AOI effects for site and day under study. The simulated irradiance received considering each of these metrological conditions separately with the other conditions deactivated and then with all conditions integrated is shown in Fig. 15. Also, P_{\max} at noon is simulated in Table 7.

Taking the metrological conditions' effect into consideration shows a serious decrease in the value of the irradiance received by the PV system; hence, the produced PV power is severely decreased.

From results in Table 7, it can be noted that there is an important deviation in the performance after considering all the metrological factors. The negative sign noted when considering AM effect means that the power increased.

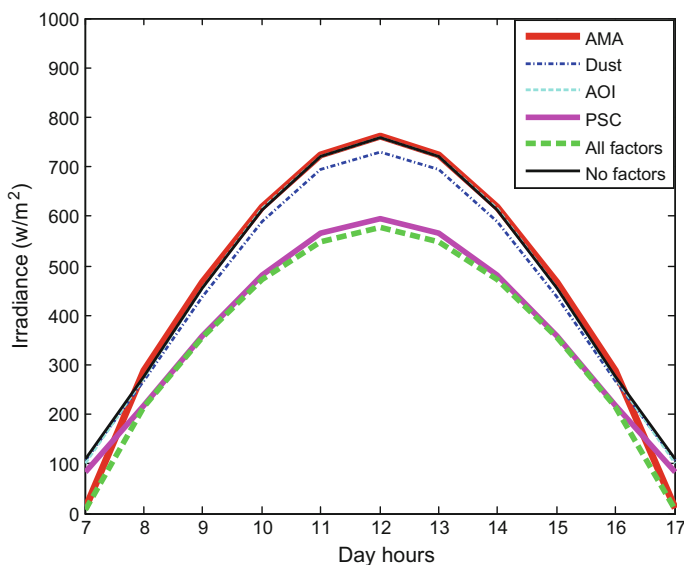


Fig. 15 Irradiance received by PV module under different ambient factors

5 Improved PV Maximum Power Point Tracking

The MPPT systems use controller to implement defined algorithms to extract maximum power from PV system. Among several MPPT algorithms, the most used and famous algorithms are perturb and observe (P&O) and incremental conductance (IC) methods. It was found that the tracking methods depending on P&O algorithms are widely applied due to their speed and simplicity. Also, they can be implemented using cheap digital devices with high tracking efficiency that could reach 93% under normal conditions [64, 65].

The principle of P&O algorithm is to perturb the operating voltage by a defined step size ΔV and observe the power variation ΔP . If it was positive, so the voltage should be perturbed, else the perturbation direction should be altered to the opposite direction [66]. The most important disadvantage in P&O method is that it oscillates around the maximum power point. In addition, it shows erratic behavior when operating under rapid change of irradiance.

Assume that the operating point is perturbed around MPP at the lower irradiance level as shown in Fig. 16. Then, the irradiance increased rapidly to the next higher level, the observed ΔP will be positive, the MPPT is in the right direction, and the operating point will move from point A to B instead of considering that this is happening because of the irradiance increase. If the irradiance continues to increase rapidly, the MPPT will observe positive measured ΔP , when the operating point is perturbed from right to left, will consider that this is happening because of getting closer to the MPP and not because of irradiance increase, and will move to point C

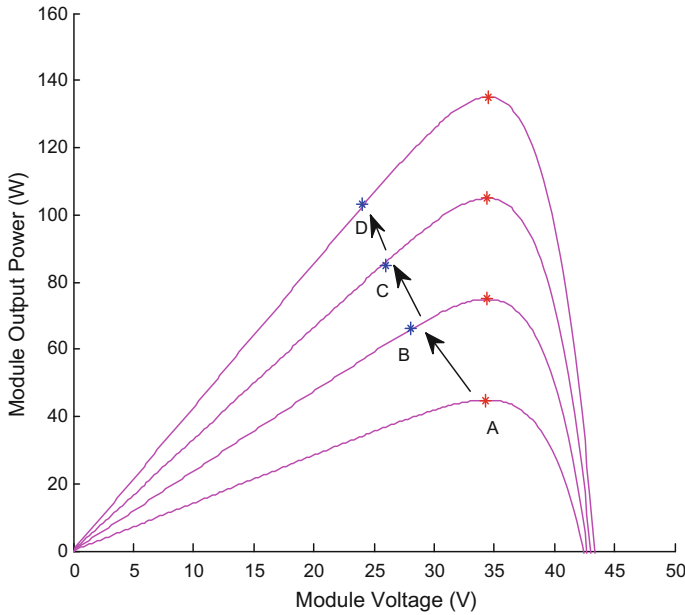


Fig. 16 Erratic behavior of P&O method

and then D, respectively, and this will cause the operating point to continue deviation from actual MPP until the irradiance settles down or changes slowly.

The incremental conductance (IC) algorithm solves the problem of mal-operation of P&O algorithm under rapid irradiance change. It is based on defining the location of the MPP by calculating the slope of the power voltage curve [67].

A scenario of irradiance along day hours of the site under study, which is gradually changing, is shown in Fig. 17, and will be used to study the efficiency of different MPPT algorithms. Both P&O and IC methods are implemented for the scenario of irradiance under study, and the results are shown in Fig. 18.

From Fig. 18, it can be noted that the performance of both methods is the same under the case of gradual change in irradiance. In this work, improvements of the classic P&O algorithm are proposed to overcome the previously mentioned drawbacks. The improvements applied to classic P&O algorithm are listed as follows:

- For the oscillations around MPP, small step size will minimize the oscillation but causes slow MPPT. So, a variable step size will be used instead of a fixed step size and the perturbation of voltage is selected to be proportional to the change in power [64, 68]

$$V_{\text{ref}}^* = V_{\text{ref}} + C * \frac{\Delta P}{\Delta V} \quad (40)$$

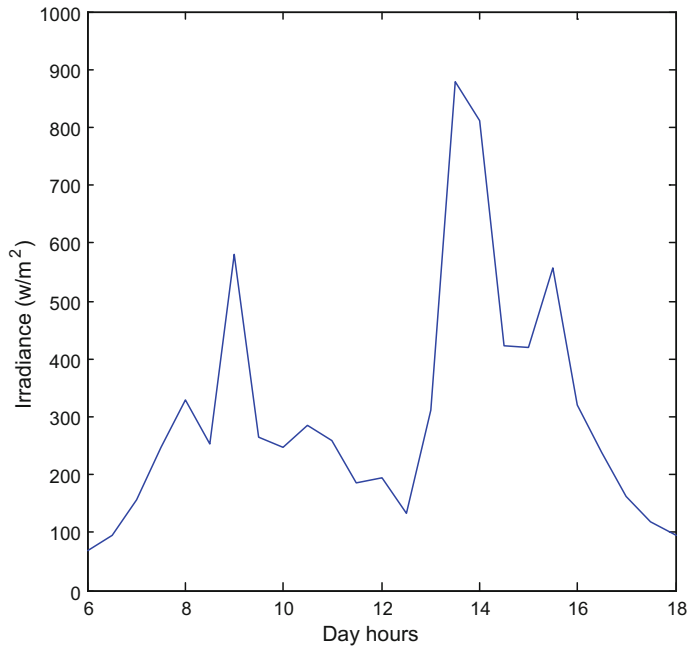


Fig. 17 Gradually changing irradiance in a cloudy day

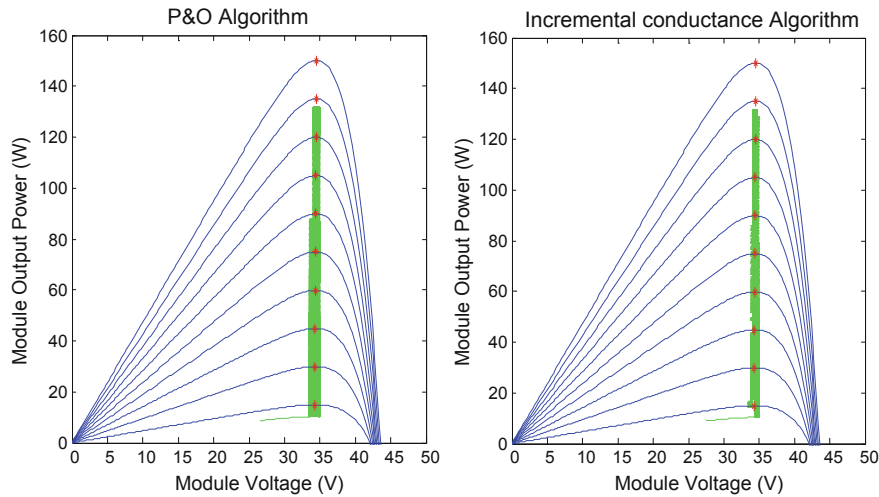


Fig. 18 Simulation of MPP using P&O and IC algorithms

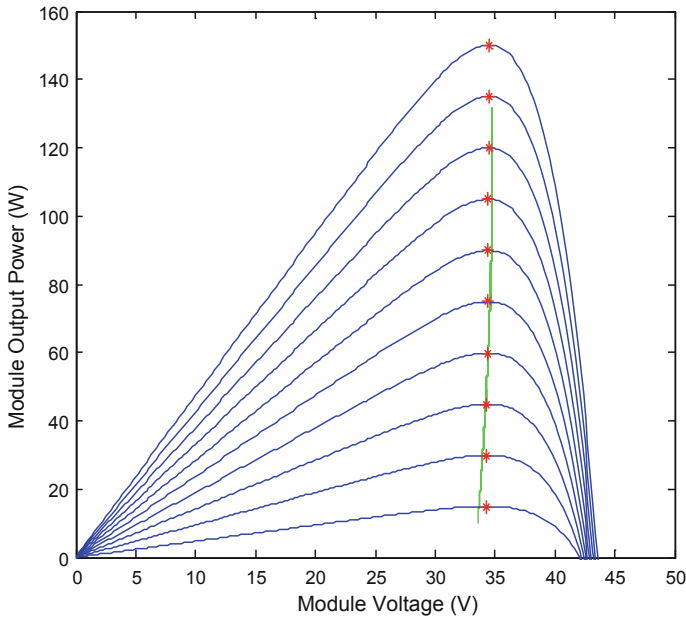


Fig. 19 Algorithm of improved P&O method

where V_{ref} is the reference voltage of the MPP; C is a PV constant that depends on manufacturer.

- In order to increase the tracking speed and to solve the failure of P&O under rapid changes of irradiance, the following improvement is done. Since the open-circuit voltage V_{oc} is affected by variation of irradiance and temperature, the reference voltage is set to a fraction of open-circuit voltage to check periodically the change in the irradiance and compensate for this change, as follows:

$$V_{\text{ref}} = K_{\text{oc}} * V_{\text{oc}} \quad (41)$$

where K_{oc} is the proportionality constant for open-circuit voltage and ranges between 0.71 and 0.78 [38, 65]. The improved algorithm is shown in Fig. 19.

Simulation results for irradiance profile of Fig. 18 with the improved MPPT algorithm are shown in Fig. 20.

From results shown in Fig. 20, it is noted that the oscillations around MPP are almost vanished. Tracking efficiency is the ratio between MPP reached by tracking system and theoretical MPP at the same condition [65]. Figure 21 shows the MPP when implementing both classic and improved P&O algorithms and comparing them with the theoretically calculated MPP. From results shown in Fig. 21, it is noted that the tracking efficiency increased from 88% with classic P&O to 99% with improved P&O under steady-state condition.

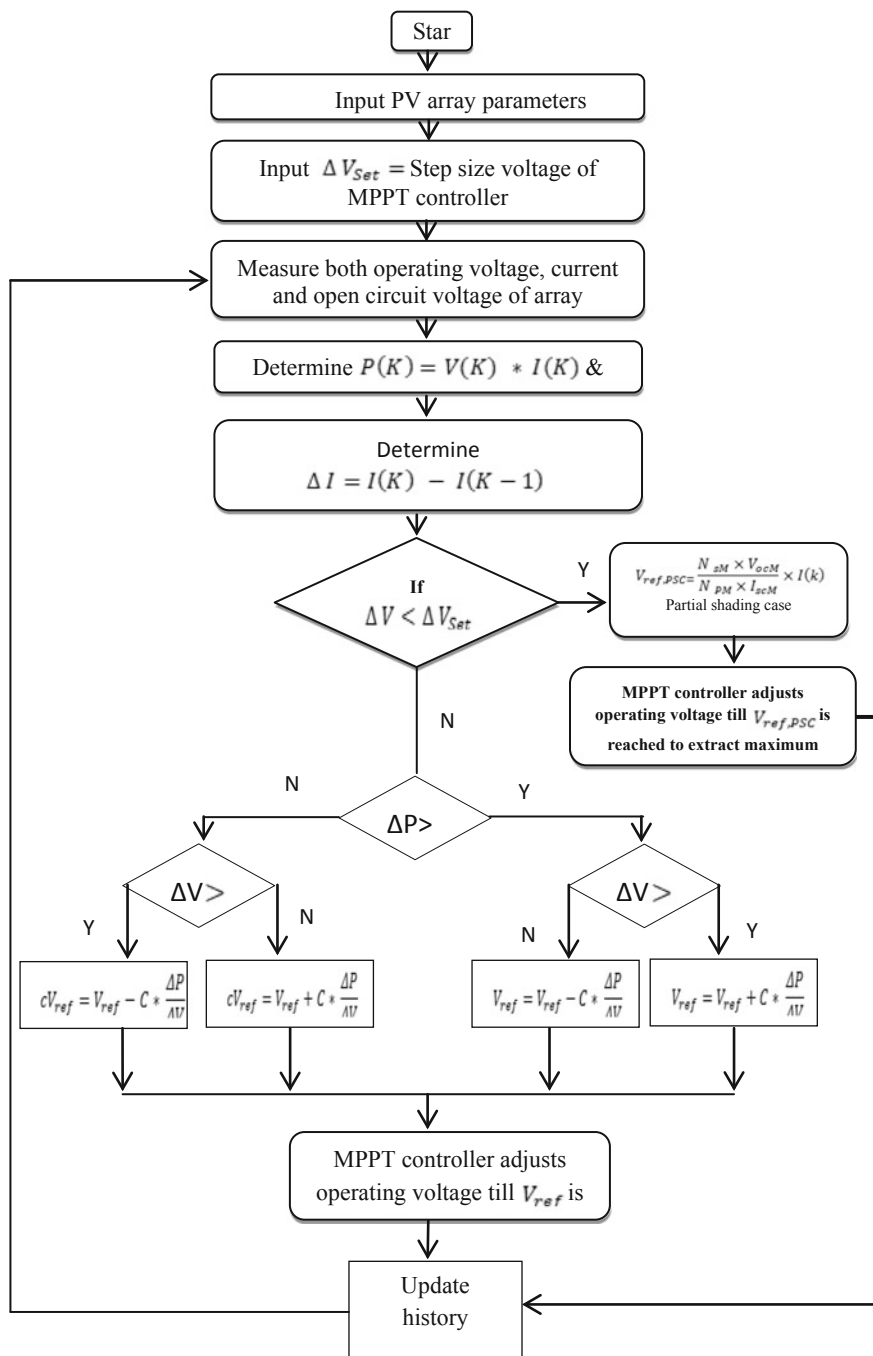
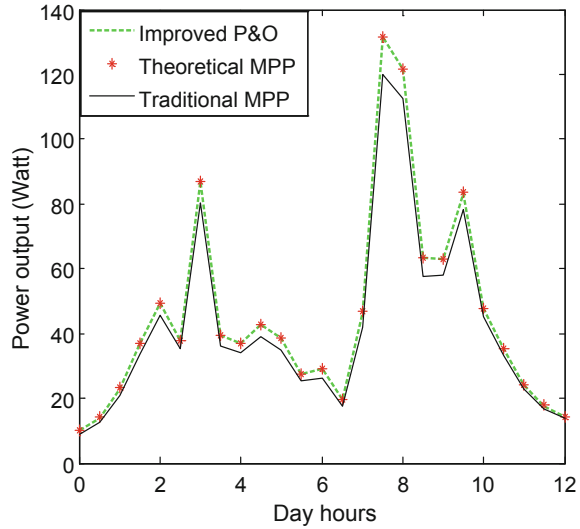


Fig. 20 Simulation of MPP using improved P&O method

Fig. 21 MPP for classic and improved P&O method



The third improvement is essential to solve the MPPT failure under PSC. PSC is mathematically checked through the following models [56, 57]:

$$\Delta V = V(k) - V(k-1) < \Delta V_{\text{SET}} \quad (42)$$

$$I = \frac{I(k) - I(k-1)}{I(k-1)} < \Delta I_{\text{SET}} = \frac{I(k)}{N_P} \quad (43)$$

where k is the sampling number; N_P and N_s are the numbers of parallel and series modules in array, respectively; ΔV_{SET} is the step size of voltage (v).

If the two conditions in Eqs. (42) and (43) are satisfied, the reference voltage of MPP is changed according to the following model:

$$V_{\text{ref}} = V_{\text{PSC}}^* = \frac{N_{\text{SM}} \times V_{\text{ocM}}}{N_{\text{PM}} \times I_{\text{scM}}} \times I(k) \quad (44)$$

where V_{PSC}^* is the reference voltage of the MPP under PSC (v); V_{ocM} is the module open-circuit voltage (v); I_{scM} is the module short-circuit current (A).

Consider one module protected by two diodes under PSC of one cell by 75%, and the c/cs of this module and the simulation of the performance using both the classic and the improved P&O methods are simulated as shown in Fig. 22.

Under uniform illumination, the MPP is $P(n)$. The classic P&O under PSC shifts the operating point to the local MPP at the same maximum power point voltage, V_{ref} , and the resulted MPP is 46.26 (w). Whereas the improved P&O moves the maximum power point voltage to V_{PSC}^* , then the improved algorithm of P&O continues the tracking with variable step size of perturbation till the global MPP is reached at

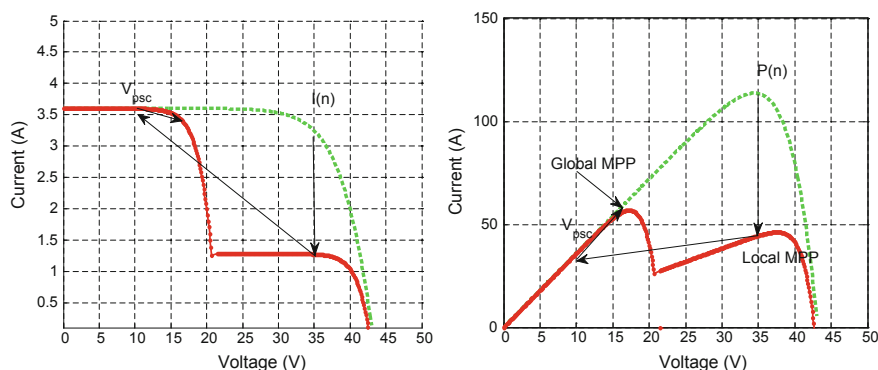


Fig. 22 I-V and P-V c/s for improved P&O MPPT algorithm under PSC

56.86 (w). From Fig. 22, it is evident that the improved P&O increases the tracking efficiency under PSC to be 99.9% where it is 81.35% for classic P&O.

6 Conclusions

This chapter investigated the challenges facing the implementation of widespread stand-alone photovoltaic systems in smart microgrids. The first challenge was developing a proposed algorithm for estimating the irradiance received by an inclined PV module from daily estimations knowing only the meteorological data for the site. The second contribution was developing an aggregated irradiance model considering different metrological factors, to study the irradiance value received under real installation conditions. The third contribution was the development of an improved P&O MPPT algorithm with variable step size to solve the problems of the classic P&O method, which are mainly the oscillations around MPP, the failure of tracking under rapid changes of irradiance, and the mal-operation under PSC.

References

1. Chueco-Fernández F, Bayod-Rújula Á (2010) Power supply for pumping systems in northern Chile: photovoltaics as alternative to grid extension and diesel engines. *Energy* 35(7):2909–2921
2. Chandel S, Nagaraju Naik M, Chandel R (2015) Review of solar photovoltaic water pumping system technology for irrigation and community drinking water supplies. *Renew Sustain Energy Rev* 49:1084–1099
3. Armanuos A, Negm A, Tahan A (2016) Life cycle assessment of diesel fuel and solar pumps in operation stage for rice cultivation in Tanta, Nile Delta, Egypt. *Procedia Technol* 22:478–485
4. <https://www.nrel.gov/docs/fy14osti/60272.pdf>

5. http://energy.sandia.gov/wp-content/gallery/uploads/Semprius_perf_model_final.pdf
6. Seyedmahmoudian M, Mekhilef S, Rahmani R, Yusof R, Renani E (2013) Analytical modeling of partially shaded photovoltaic systems. *Energies* 6(1):128–144
7. Styszko K, Jaszczur M, Teneta J, Hassan Q, Burzyńska P, Marcinek E, Łopian N, Samek L (2019) An analysis of the dust deposition on solar photovoltaic modules. *Environ Scie Pollut Res* 26(9):8393–8401
8. Cano J (2012) Photovoltaic modules. Proquest, Umi Dissertatio
9. Mohammadi A, Mezzai N, Rekioua D, Rekioua T (2014) Impact of shadow on the performances of a domestic photovoltaic pumping system incorporating an MPPT control: a case study in Bejaia, North Algeria. *Energy Convers Manag* 84:20–29
10. Zheng J, Chai Y, Zhu S, Shen X, Li J, Wang X (2013) The dynamic characteristics of photovoltaic generation system under partially shaded conditions. In: 2013 IEEE PES Asia-Pacific power and energy engineering conference (APPEEC), Kowloon, pp 1–4
11. Madziga M, Rahil A, Mansoor R (2018) Comparison between Three off-grid hybrid systems (solar photovoltaic, diesel generator and battery storage system) for electrification for Gwakwani village, South Africa. *Environments* 5(5):57
12. Barrueto Guzmán A, Barraza Vicencio R, Ardila-Rey J, Núñez Ahumada E, González Araya A, Arancibia Moreno G (2018) A cost-effective methodology for sizing solar PV systems for existing irrigation facilities in Chile. *Energies* 11(7):1853
13. El-Sebaai A, Trabea A (2003) Estimation of horizontal diffuse solar radiation in Egypt. *Energy Convers Manag* 44(15):2471–2482
14. El-Sebaai A, Trabea A (2018). Estimation of horizontal diffuse solar radiation in Egypt
15. Trabea A, Shaltout M (2000) Correlation of global solar radiation with meteorological parameters over Egypt. *Renew Energ* 21(2):297–308
16. <https://ojs.cvut.cz/ojs/index.php/ap/article/view/1057>
17. Duffie J, Beckman W (2013) Solar engineering of thermal processes. Wiley, Hoboken
18. Araneo R, Grasselli U, Celozzi S (2014) Assessment of a practical model to estimate the cell temperature of a photovoltaic module. *Int J Energy Environ Eng* 5(1)
19. <https://www.ijert.org/phocadownload/V11I5/IJERTV11I55008.pdf>
20. https://www.researchgate.net/publication/267200948_Solar_house_and_weather_factors_in_Bejaia_city_Algeria
21. Engerer N (2011) Simulating photovoltaic array performance using radiation observations from the Oklahoma Mesonet (Doctoral dissertation, University of Oklahoma)
22. <http://www.ijssrp.org/research-paper-1212/ijssrp-p1255.pdf>
23. Darhmaoui H, Lahjouji D (2013) Latitude based model for Tilt angle optimization for solar collectors in the Mediterranean region. *Energy Procedia* 42:426–435
24. <https://journals.squ.edu.om/index.php/tjer/article/download/113/125>
25. https://www.researchgate.net/publication/261173026_Population_Density_and_Area_weighted_Solar_Irradiation_global_Overview_on_Solar_Resource_Conditions_for_fixed_tilted_1-axis_and_2-axes_PV_Systems
26. <http://www.iwtc.info/wp-content/uploads/2011/07/G103.pdf>
27. Kibirige B (2018) Monthly average daily solar radiation simulation in northern KwaZulu-Natal: a physical approach. *South African J Sci* 114(9/10)
28. El-Saadawi M, Hassan A, Abo-Al-Ez K, Kandil M (2011) A proposed framework for dynamic modelling of photovoltaic systems for DG applications. *Int J Ambient Energy* 32(1):2–17
29. Chin V, Salam Z, Ishaque K (2015) Cell modelling and model parameters estimation techniques for photovoltaic simulator application: a review. *Appl Energy* 154:500–519
30. Chegaar M, Hamzaoui A, Namoda A, Petit P, Aillerie M, Herguth A (2013) Effect of illumination intensity on solar cells parameters. *Energy Procedia* 36:722–729
31. Jena D, Ramana V (2015) Modeling of photovoltaic system for uniform and non-uniform irradiance: a critical review. *Renew Sustain Energy Rev* 52:400–417
32. <http://www.icrepq.com/icrepq'10/619-Hernanz.pdf>
33. <http://www.elctrica.ufpr.br/graduacao/e-books/Principles%20Of%20Semiconductor%20Devices.pdf>

34. Altas IH, Sharaf AM (2007) A photovoltaic array simulation model for Matlab-Simulink GUI environment. In: 2007 international conference on clean electrical power, Capri, pp 341–345
35. Aissou S, Rekioua D, Mezzai N, Rekioua T, Bacha S (2015) Modeling and control of hybrid photovoltaic wind power system with battery storage. *Energy Convers Manag* 89:615–625
36. Guechi A, Chegaar M, Aillerie M (2012) Environmental effects on the performance of nanocrystalline silicon solar cells. *Energy Procedia* 18:1611–1623
37. Dubey S, Sarvaiya J, Seshadri B (2013) Temperature dependent photovoltaic (PV) efficiency and its effect on PV production in the world—a review. *Energy Procedia* 33:311–321
38. Bouraiou A, Hamouda M, Chaker A, Sadok M, Mostefaoui M, Lachtar S (2015) Modeling and simulation of photovoltaic module and array based on one and two diode model using Matlab/Simulink. *Energy Procedia* 74:864–877
39. <http://www.diva-portal.org/smash/get/diva2:754340/FULLTEXT01.pdf>
40. Guerrero J, Muñoz Y, Ibáñez F, Ospino A (2014) Analysis of mismatch and shading effects in a photovoltaic array using different technologies. In: IOP conference series: materials science and engineering, vol 59, p 012007
41. Tian H, Mancilla-David F, Ellis K, Muljadi E, Jenkins P (2012) A cell-to-module-to-array detailed model for photovoltaic panels. *Sol Energy* 86(9):2695–2706
42. <https://archive-ouverte.unige.ch/unige:39174>
43. Shankar G, Mukherjee V (2015) MPP detection of a partially shaded PV array by continuous GA and hybrid PSO. *Ain Shams Eng J* 6(2):471–479
44. <http://www.rroij.com/open-access/global-maximum-power-point-trackingunder-partial-shading-condition-usingsepic-converter.php?aid=43234>
45. Goss B, Cole I, Betts T, Gottschalch R (2014) Irradiance modelling for individual cells of shaded solar photovoltaic arrays. *Sol Energy* 110:410–419
46. Deline C, Dobos A, Janzou S, Meydbray J, Donovan M (2013) A simplified model of uniform shading in large photovoltaic arrays. *Sol Energy* 96:274–282
47. Fialho L, Melicio R, Mendes V, Figueiredo J, Collares-Pereira M (2014) Effect of Shading on series solar modules: simulation and experimental results. *Procedia Technol* 17:295–302
48. Martínez-Moreno F, Muñoz J, Lorenzo E (2010) Experimental model to estimate shading losses on PV arrays. *Sol Energy Mater Sol Cells* 94(12):2298–2303
49. Perpiñán O (2012) Cost of energy and mutual shadows in a two-axis tracking PV system. *Renew Energy* 43:331–342
50. Jang M, Choi J, Ko J, Mun J, Chung D (2010) Control of a novel PV tracking system considering the shadow influence. In: ICCAS 2010, Gyeonggi-do, pp 1229–1234
51. https://link.springer.com/chapter/10.1007%2F978-3-642-34396-4_15
52. Maine T, Bell J (2008) Maximum power extraction from partially shaded PV arrays. In: Prasad D, Morrison G (eds) Proceedings of the 3rd international solar energy society conference, Asia Pacific Region, incorporating the 46th Australian New Zealand Solar Energy Society Conference (ISES-AP-08), 25–28 November, 2008, Australia, NSW, Sydney
53. Drif M, Pérez P, Aguilera J, Aguilar J (2008) A new estimation method of irradiance on a partially shaded PV generator in grid-connected photovoltaic systems. *Renew Energy* 33(9):2048–2056
54. <https://solarprofessional.com/articles/design-installation/q-a-calculating-inter-row-spacing#.XBJ6wtszaiM>
55. Kaddah SS (2006) Genetic algorithm based optimal operation for photovoltaic systems under different fault criteria. In: Power systems conference MEPCON, vol 2, pp 556–561
56. https://link.springer.com/chapter/10.1007/978-1-4471-2467-2_11
57. Li H, Kang K, Chen W, Zeng X (2016) Maximum power point tracking for PV array under partially shaded conditions based on glowworm swarm optimization algorithm. *DESTech Transactions on Computer Science and Engineering, (ICTE)*
58. Ishaque K, Salam Z (2013) A review of maximum power point tracking techniques of PV system for uniform insolation and partial shading condition. *Renew Sustain Energy Rev* 19:475–488
59. Photovoltaic module and array performance characterization methods for all system operating conditions (1996) Washington, DC: United States. Department of Energy. Office of Energy Efficiency and Renewable Energy

60. Knisely B, Janakeeraman SV, Kuitche J, TamizhMani G (2013) Validation of IEC 61853-2 standard (draft): angle of incidence effect on photovoltaic modules. In: 2013 IEEE 39th photovoltaic specialists conference (PVSC), Tampa, FL, pp 0675–0680
61. <https://www.amazon.es/Preliminary-Investigation-Correcting-Variations-Spectrum/dp/1249131634>
62. https://www.irishellas.com/files/Analysis-of-dust-losses-in-photovoltaic-moules_2011.pdf
63. Mostefaoui M, Ziane A, Bouraiou A, Khelifi S (2019) Effect of sand dust accumulation on photovoltaic performance in the Saharan environment: southern Algeria (Adrar). *Environ Sci Pollut Res* 26(1):259–268
64. Abdelilah B, Mouna A, KouiderM'Sirdi N, El Hossain A (2018) Implementation of maximum power point tracking (MPPT) solar charge controller using Arduino. In: IOP Conference Series: Materials Science and Engineering, vol 353, p 012024
65. Kamran M, Mudassar M, Fazal M, Asghar M, Bilal M, Asghar R (2018) Implementation of improved Perturb & Observe MPPT technique with confined search space for standalone photovoltaic system. *J King Saud Univ Eng Sci*
66. Ali A, Sayed M, Mohamed E (2018) Modified efficient perturb and observe maximum power point tracking technique for grid-tied PV system. *Int J Electr Power Energy Syst* 99:192–202
67. Bendib B, Belmili H, Krim F (2015) A survey of the most used MPPT methods: conventional and advanced algorithms applied for photovoltaic systems. *Renew Sustain Energy Rev* 45:637–648
68. Harrag A, Messalti S (2015) Variable step size modified P&O MPPT algorithm using GA-based hybrid offline/online PID controller. *Renew Sustain Energy Rev* 49:1247–1260

ANN and Multiple Linear Regression Based Modelling for Experimental Investigation of Photovoltaic Module Maximum Power Production Under Outdoor Condition of Mountainous Region



Amit Kumar Yadav and Hasmat Malik

Abstract Manufacturer gives photovoltaic (PV) module rating in standard test conditions (STC) which incorporate solar radiation (SR), temperature 1000 W/m^2 and 25°C , respectively. These STC hardly happen in outside conditions; thus, this study presents experimentation analysis of 74 Wp PV module, and maximum power and performance degradation are calculated. Based on experimental data, multiple linear regression (MLR) and artificial neural network (ANN) models are created using different input variables. Mean square error in ANN model is measured by performance plot. It is found that ANN furnishes improved result than MLR. The new correlations of PV maximum power are developed in terms of solar radiation (SR), short-circuit current (I_{sc}) and open-circuit voltage (V_{oc}), which can be used to estimate maximum power of 74 Wp in mountainous regions of India. The performance ratio of 74 Wp multi-crystalline PV module is found to be 70%. The SR varies from 119.8 to 415.6 W/m^2 , and maximum power, I_{sc} and V_{oc} vary from 28.22 to 42.72 W, from 1.78 to 4.90 A and from 20.18 V to 20.96 V, respectively.

Keywords Artificial neural network · Power prediction · Maximum power · Multiple linear regression · Photovoltaic module · Multi-crystalline silicon

A. K. Yadav (✉)

Electrical and Electronics Engineering Department, National Institute of Technology, Sikkim, Ravangla, Barfung Block, South Sikkim 737139, India
e-mail: amit1986.529@rediffmail.com

H. Malik

Department of Instrumentation and Control Engineering, Netaji Subhas University of Technology, Delhi 110078, India
e-mail: hasmat.malik@gmail.com

© Springer Nature Switzerland AG 2020

A. M. Eltamaly and A. Y. Abdelaziz (eds.), *Modern Maximum Power Point Tracking Techniques for Photovoltaic Energy Systems*, Green Energy and Technology, https://doi.org/10.1007/978-3-030-05578-3_8

229

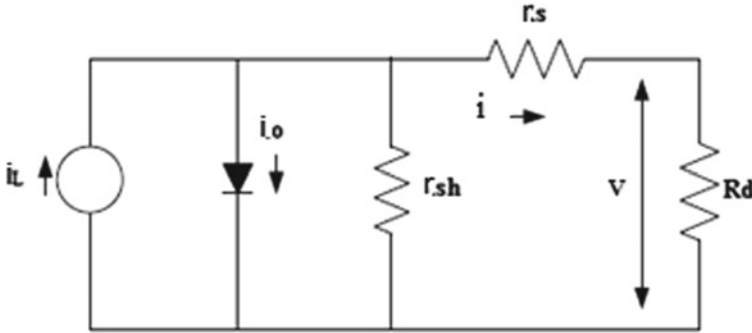


Fig. 1 Solar cell circuit

1 Introduction

Due to environmental concern and decreasing nature of conventional energy sources, renewable energy sources (RESs) have drawn attention worldwide. Among RESs, solar energy has huge potential and is converted into electricity due to photovoltaic effect by photovoltaic (PV) module [1].

PV modules consist of solar cell which follows nonlinear electrical characteristics. It is dependent on cell temperature and solar radiation. The solar cell circuit diagram with one diode is shown in Fig. 1, and its $I - V$ curve is expressed as follows:

$$i = i_L - i_o \left\{ \exp \left(\frac{q}{akT_c} (v + ir_s) \right) - 1 \right\} - \frac{v + ir_s}{r_{sh}} \quad (1)$$

where i_o is reverse saturation current of diode, i_L is photon current, q is electron charge, a is ideality factor, k is Boltzmann constant, T_c is cell temperature, r_{sh} is shunt resistance that has large value and r_s is series resistance that has small value, so it cannot be taken in the analysis.

Solar radiation (SR) and ambient temperature affect PV power which varies for different sites which require modelling of PV cells and modules. Moreover, testing condition of PV module is given under STC which rarely occurs outdoor. Therefore, to predict PV power of outdoor condition becomes an important issue. On this aspect, several authors used ANN to model PV system for different variables' prediction [2–27]. In a study performed by Yadav and Chandel [28], experimental analysis of PV module's electrical characteristics under outdoor conditions for different Indian sites remains a major research gap which is carried out in this study. Based on experimental readings, prediction accuracy of ANN models is evaluated.

2 Proposed Approach

The proposed approach for power production of a PV module under outdoor condition of mountainous region is presented in Fig. 2, which shows the complete procedure for forecasting of PV module power. The proposed approach includes the twelve basic steps to perform the forecasting of PV module power (P_{\max}). These steps are explained in detail as given below:

Step 1: Develop the experimentation setup for the study.

Step 2: After proper development of experimentation, measure the I – V curve, V_{oc} , I_{sc} and SR for further study.

Step 3: Calculate the PV module maximum power (P_{\max}) as per recorded dataset.

Step 4: After the computation of P_{\max} , prepare the dataset for the development of ANNs model.

Step 5: Prepare the training and testing dataset files for further utilization.

Step 6: Design the ANNs models by using training dataset.

Step 7: Train the ANNs models as per set value of hidden layer neurons of each model.

Step 8: Compute the ANNs model's performance measures (i.e. MAPE).

Step 9: Compare the computed MAPE value with standard MAPE value which is $MAPE < 10$

if Yes: go to Step 10

if No: go back at Step 6 (at Step 6, change the model parameters, hidden layer neurons, etc.).

Step 10: Test the model with unknown dataset. Both testing dataset and training datasets are different.

Step 11: After successful testing, predict the P_{\max} .

Step 12: Save the model for future purpose applications.

The detail explanation related to each step of the presented proposed approach has been presented in subsequent sections. In that subsequent sections, the PV module parameters used for the study, experimentation procedure, site location, ANN architecture and performance analysis (energy generated, yield and performance ratio) have been explained in detail which are very useful for the researchers.

3 PV Module Parameters

A 74 Wp Si multi-crystalline PV module is experimented. The measuring instruments are digital multimeter with DC accuracy: $\pm 0.5\% + 3$ digits and AC accuracy: $\pm 1\% + 3$ digits and auto digital lux meter with measuring range varying from 2000 to 50,000 lx which are utilized for measuring I – V . The measurement under STC provided by manufacturer Sova Power is given in Table 1.

Fig. 2 Proposed approach for forecasting of power production (P_{\max}) of a PV module under outdoor conditions

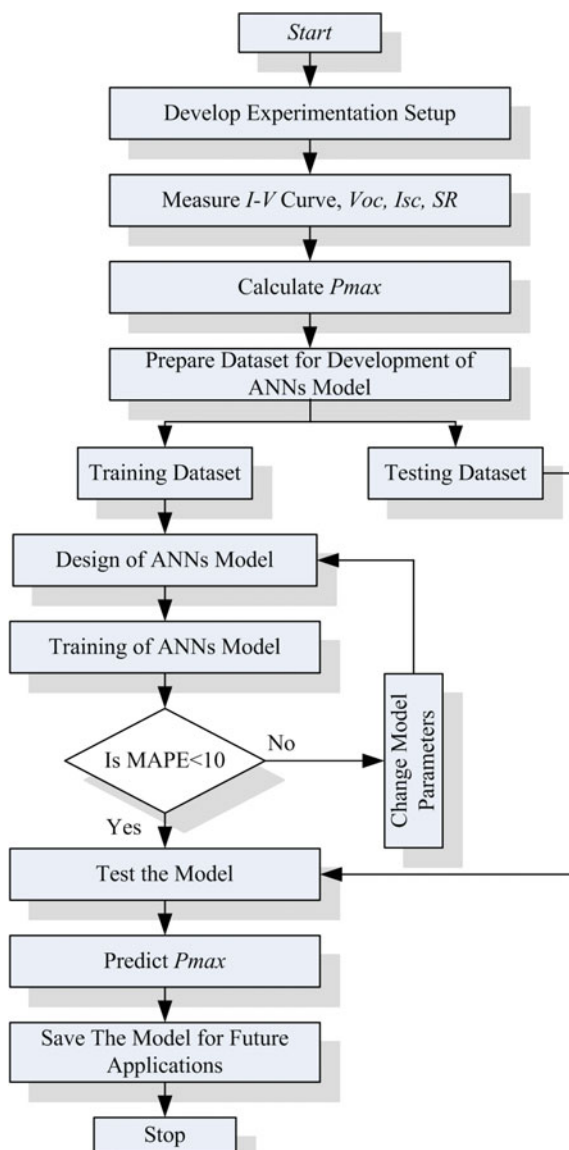
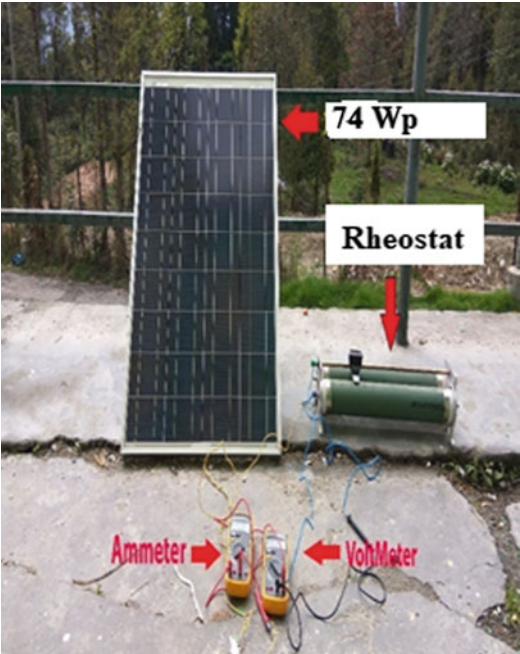


Table 1 74 Wp PV module as per manufacturer data at STC

PV module characteristics	Manufacturer data
Module type	SS 74P
Maximum value of power (P_{\max})	74 W
Voltage at maximum power (V_{mp})	17.86 V
Current at maximum power (I_{mp})	4.19 A
Open-circuit voltage (V_{oc})	21.89 V
Short-circuit current (I_{sc})	4.48 A
Cell efficiency (%)	13.7
Module efficiency (%)	11.9

Fig. 3 Experiment setup



4 Experimentation

I–*V* curve measurement of 74 Wp PV module which is carried out at National Institute of Technology (NIT) Sikkim, India, is shown in Fig. 3, and solar radiation measurement is shown in Fig. 4. The experiments are performed in sunny day at different time periods in the month of April. The lux meter is used to measure solar radiation intensity, and conversion formula $\frac{\text{lumen}}{\text{watt}} = 2.732$ is used for wavelength 420 nm [29].

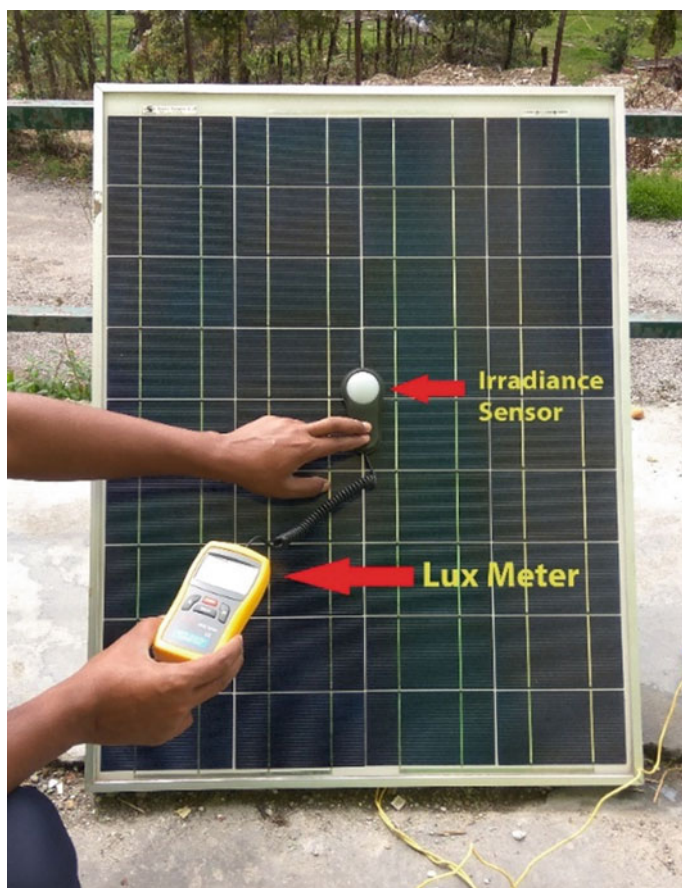


Fig. 4 Lux meter reading

Site Location

NIT Sikkim, India (Latitude: 27.29°N, Longitude: 88.35°E), is located in Ravangla, Barfung Block, South Sikkim (Fig. 5). Ravangla or Rawangla or Ravongla is a small tourist town situated at an elevation of 2133.6 m in South Sikkim district of the Indian state of Sikkim. The average temperature and rainfall are 14.0 °C and 2.43 m length, respectively. Throughout the year, temperatures vary by 11.6 °C. The average solar radiation intensities are of about 4.79 KWh/m²/day approximately. The wind speed of this area is normal mostly above the optimum level (4.1 m/s). But during the months April to July, it gets a favourable wind speed (max 5.88 m/s).

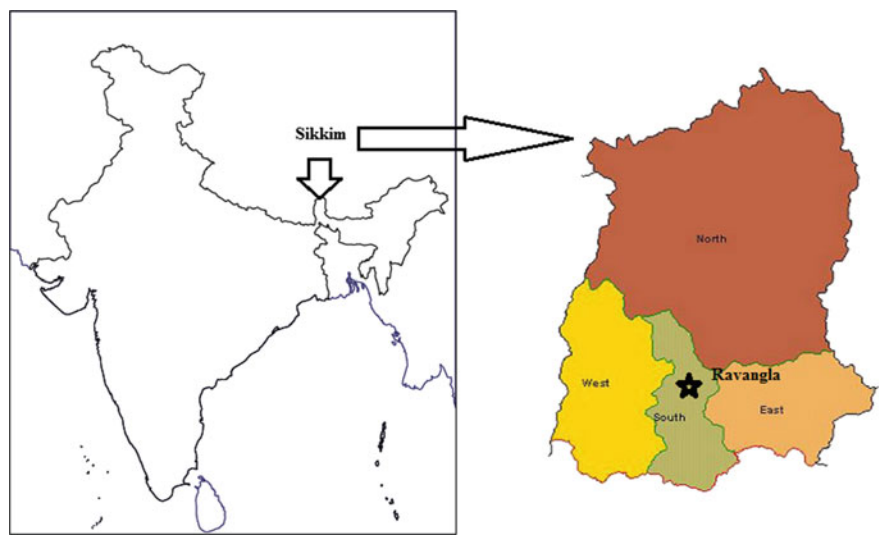


Fig. 5 Location map of Sikkim in India

5 Artificial Neural Network

ANNs are information processing systems, implemented and constructed to model the human brain. ANN performs data clustering, approximation, vector quantization, optimization function, classification and pattern matching. ANN consists of nodes or units or neurons configured in regular architectures and operates in parallel. ANN involves input, hidden and output layers (Fig. 6). Calculation of hidden neurons is given in Refs. [30, 31].

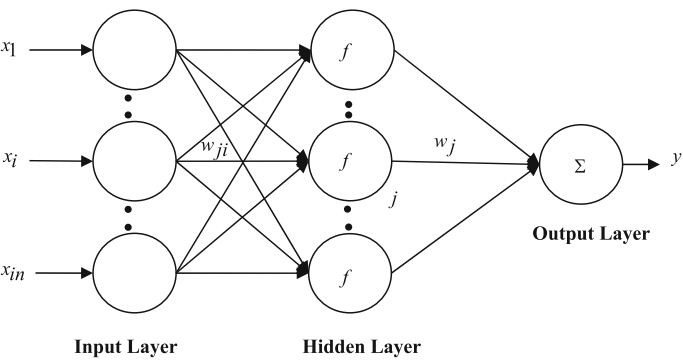


Fig. 6 ANN architecture

6 PV Performance Analysis

The total energy generated daily ($\text{Energy}_{(ac,d)}$) and monthly ($\text{Energy}_{(ac,m)}$) by the PV system [32, 33] is given as follows:

$$\text{Energy}_{(ac,d)} = \sum_{t=1}^{24} E(ac, t) \quad (4)$$

$$\text{Energy}_{(ac,m)} = \sum_{d=1}^n E(ac, d) \quad (5)$$

where n is days in month and $\text{Energy}(ac, t)$ is the instantaneous measured value.

Yield and Performance Ratio

Performance ratio (PR), final yield (Y_F) and reference yield (Y_R) are given by the following equations.

$$Y_F = \frac{E_{ac}}{P_{PV, \text{Rated}}} \quad (6)$$

$$Y_R = \frac{H_t \text{ (kWh/m}^2\text{)}}{G \text{ (kW/m}^2\text{)}} \quad (7)$$

where H_t (kWh/m²) is total in-plane SR and G is reference SR and its value is 1 kW/m²

$$\text{PR} = \frac{Y_F}{Y_R} \quad (8)$$

PR indicates performance loss year-wise.

7 Results and Discussion

The reading for I – V characteristics for 74 Wp PV module under outdoor condition for different time periods on 14 April 2017 is shown in Fig. 7, and maximum power is given in Table 2. ANN models' prediction accuracy is calculated with MAPE given by Lewis [34].

ANN-1, ANN-2 and ANN-3 models are created using MATLAB software (R 2011a), and training algorithm used is Levenberg–Marquardt (LM) algorithm. The input variables for ANN-1, ANN-2 and ANN-3 are SR, V_{oc} and I_{sc} , respectively. The output variable for all ANN models is maximum power. Twelve data points are used for training, and four data points are utilized for testing. ANN-1, ANN-2 and

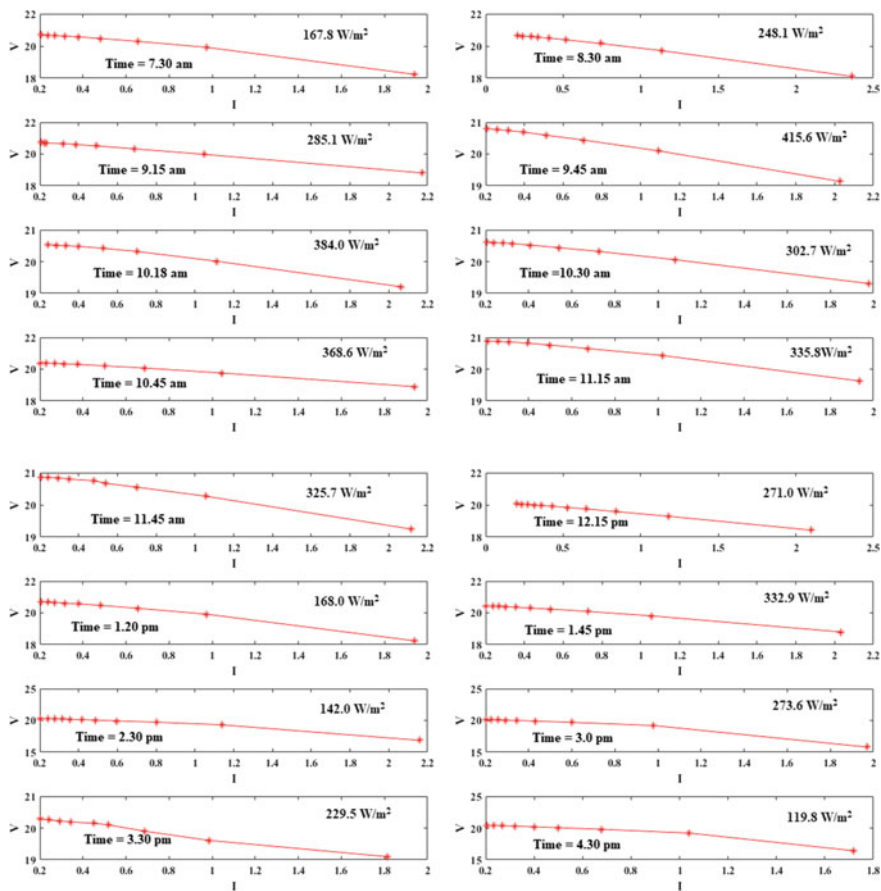


Fig. 7 *I*–*V* characteristics at different time periods and solar radiation

ANN-3 performance plots are shown in Fig. 8, which represents that mean square error is decreasing with increasing epoch number.

The fit plots of ANN-1, ANN-2 and ANN-3 are shown in Fig. 9. The fit plot provides error between output and target. It also provides targets and output value of training and validation for model.

The error histogram plots of ANN-1, ANN-2 and ANN-3 are shown in Fig. 10. The blue, green and red bars represent training, validation and testing, respectively. The histogram plot gives error training, validation and testing, respectively.

The training plots of ANN-1, ANN-2 and ANN-3 are shown in Fig. 11, showing predicted value is close to measured values. $Y = T$ denotes perfect plot; that is, data points lie on a line with slope of 45°. Regression plot presents output and target correlation. For training, R value is close to 1, showing high correlated value.

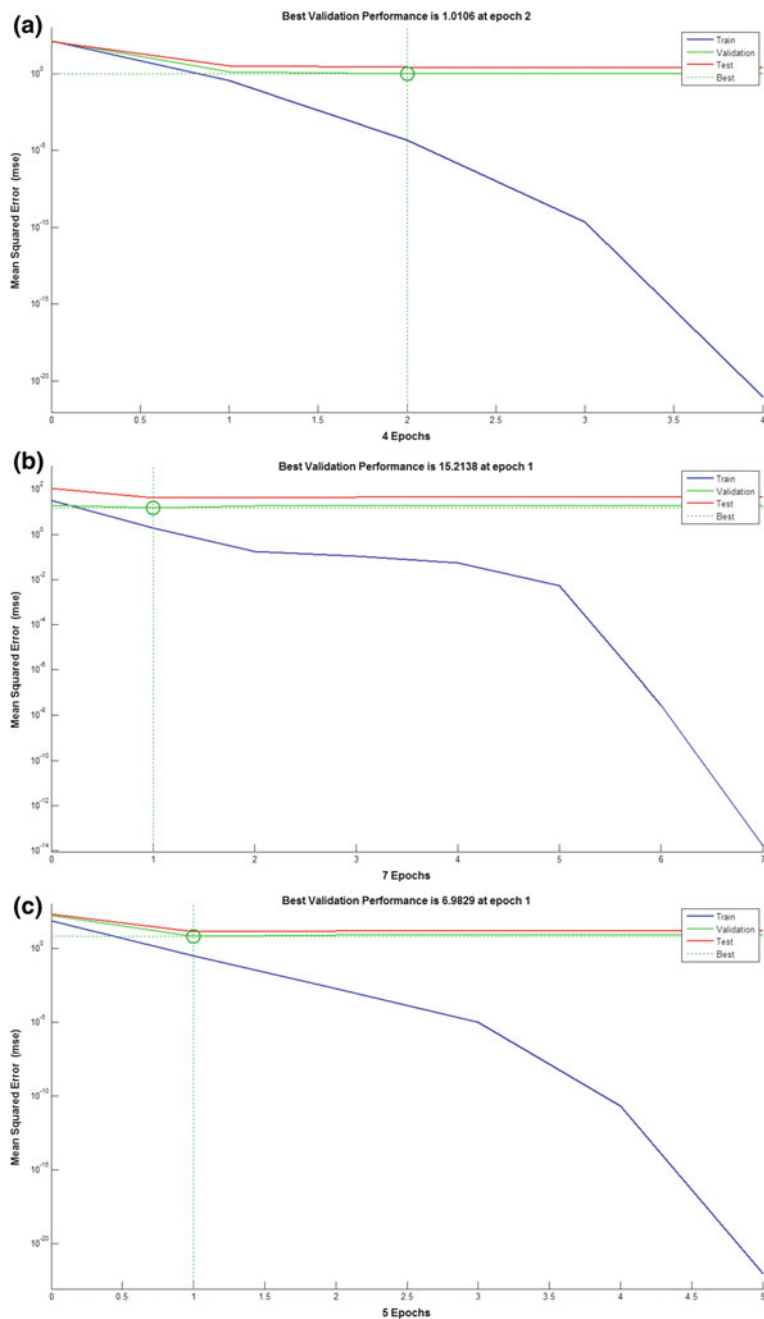


Fig. 8 Performance plot of **a** ANN-1, **b** ANN-2 and **c** ANN-3

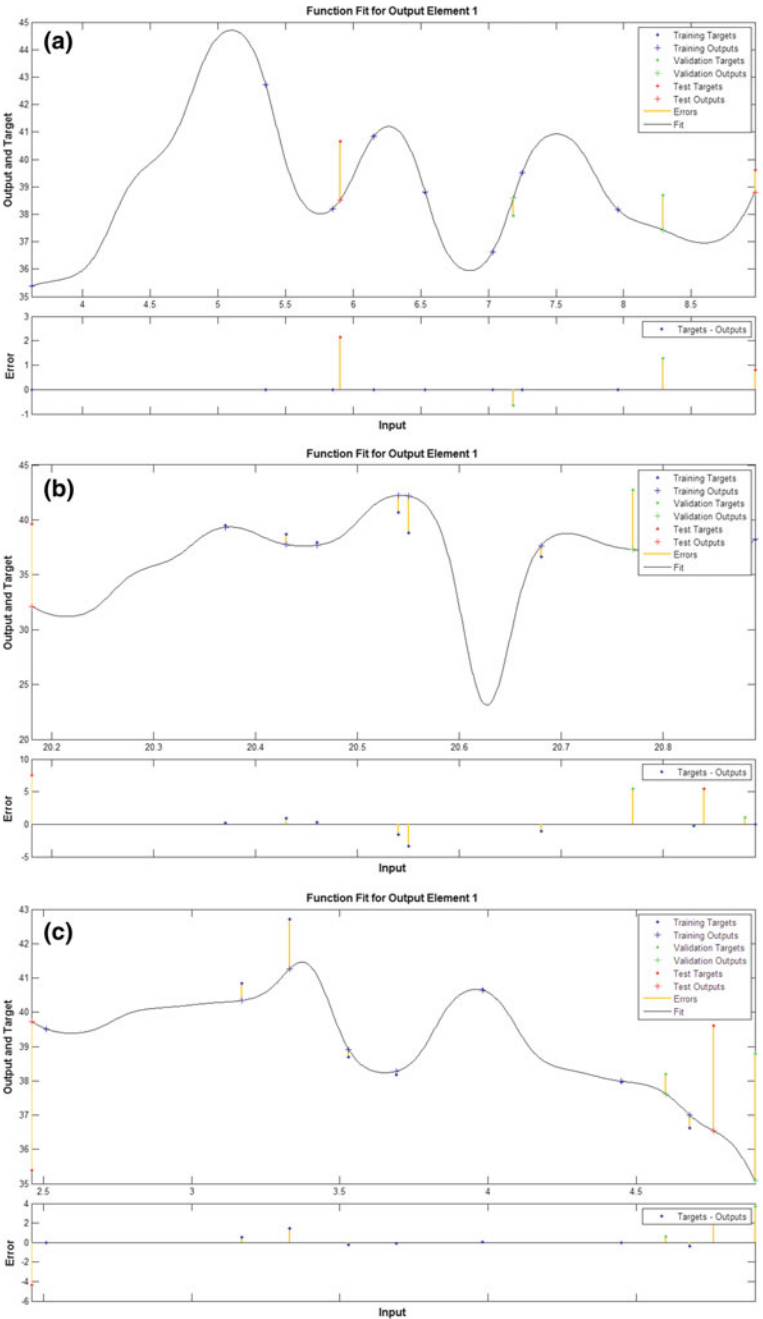


Fig. 9 Fit plot of a ANN-1, b ANN-2 and c ANN-3

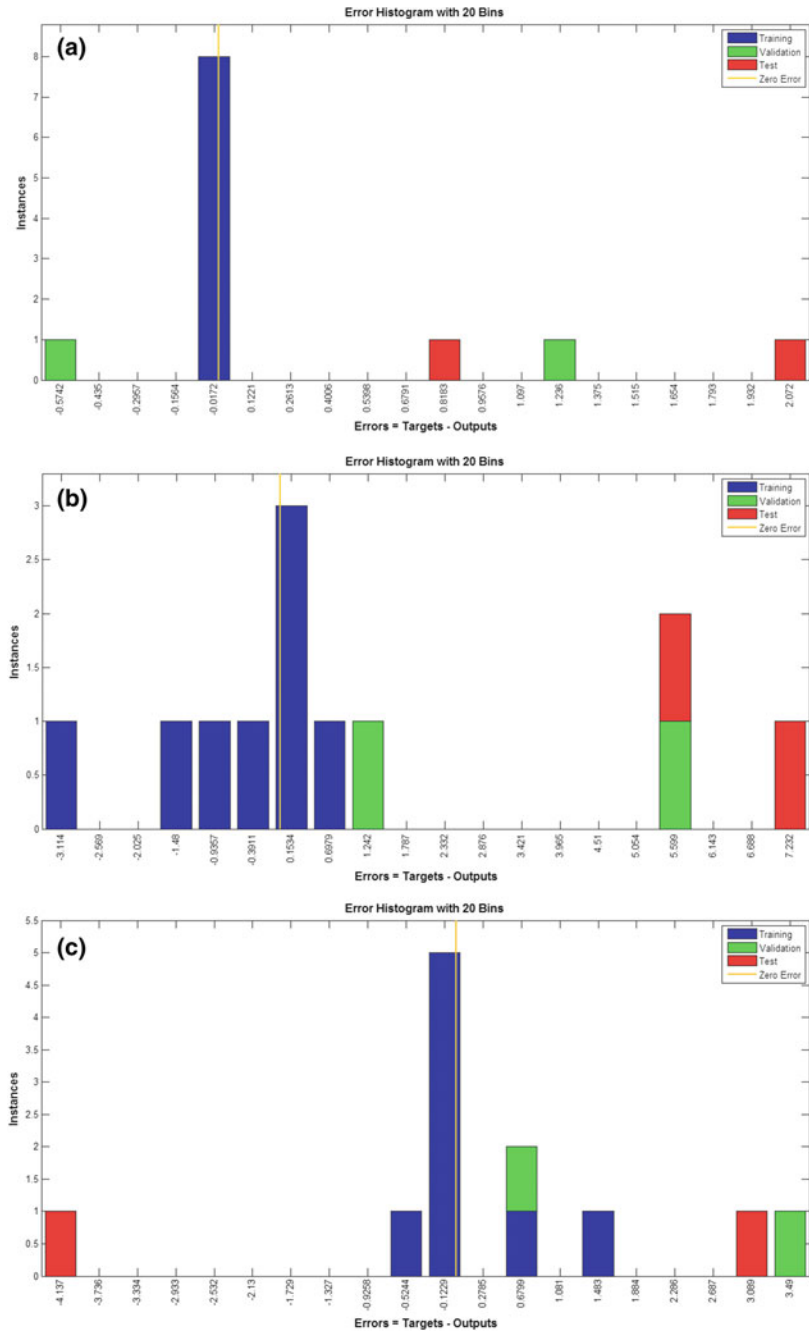


Fig. 10 Error histogram plot of a ANN-1, b ANN-2 and c ANN-3

Table 2 Experimental value of SR and PV modules' electrical parameters

S. No.	Time	SR (W/m ²)	I_{sc} (A)	V_{oc} (V)	P_{max} (W)
1	7:30 AM	167.8	2.46	20.83	35.39
2	8:30 AM	248.1	3.33	20.77	42.72
3	9:15 AM	285.1	3.17	20.84	40.72
4	9:45 AM	415.6	4.9	20.55	39.61
5	10:18 AM	384	4.76	20.18	38.7
6	10:30 AM	302.7	3.69	20.88	38.8
7	10:45 AM	368.6	4.68	20.68	38.18
8	11:15 AM	335.8	4.45	20.46	39.52
9	11:45 AM	325.7	3.98	20.54	36.62
10	12:15 PM	271	3.53	20.43	38.2
11	1:20 PM	168	2.51	20.37	36.42
12	1:45 AM	332.9	4.6	20.89	37.96
13	2:30 PM	142	2.08	20.32	31.15
14	3:00 PM	273.6	4.05	20.96	40.67
15	3:30 PM	229.5	3.17	20.5	33.7
16	4:30 PM	119.8	1.78	20.68	28.22

The maximum MAPE of training and testing data for ANN-1, ANN-2 and ANN-3 models is given in Tables 3 and 4. The MAPE in testing for ANN models with inputs as SR, V_{oc} and I_{sc} is 6.4, 11.3 and 7.9%, respectively, showing SR is the most influencing variable, but for sites where measuring SR is not available, V_{oc} and I_{sc} can be used for prediction of PV maximum power with acceptable accuracy.

Multiple Linear Regression (MLR) Models

In MLR model, output Y is related to input X for each observation as follows:

$$E(Y/X) = \alpha + \beta_1 X_1 + \dots + \beta_p X_p \quad (17)$$

Table 3 Prediction accuracy of training datasets

Models	Input	MAPE (%)	RMSE
ANN-1	SR	1.0	0.8
ANN-2	V_{oc}	5.1	3.3
ANN-3	I_{sc}	3.1	1.9

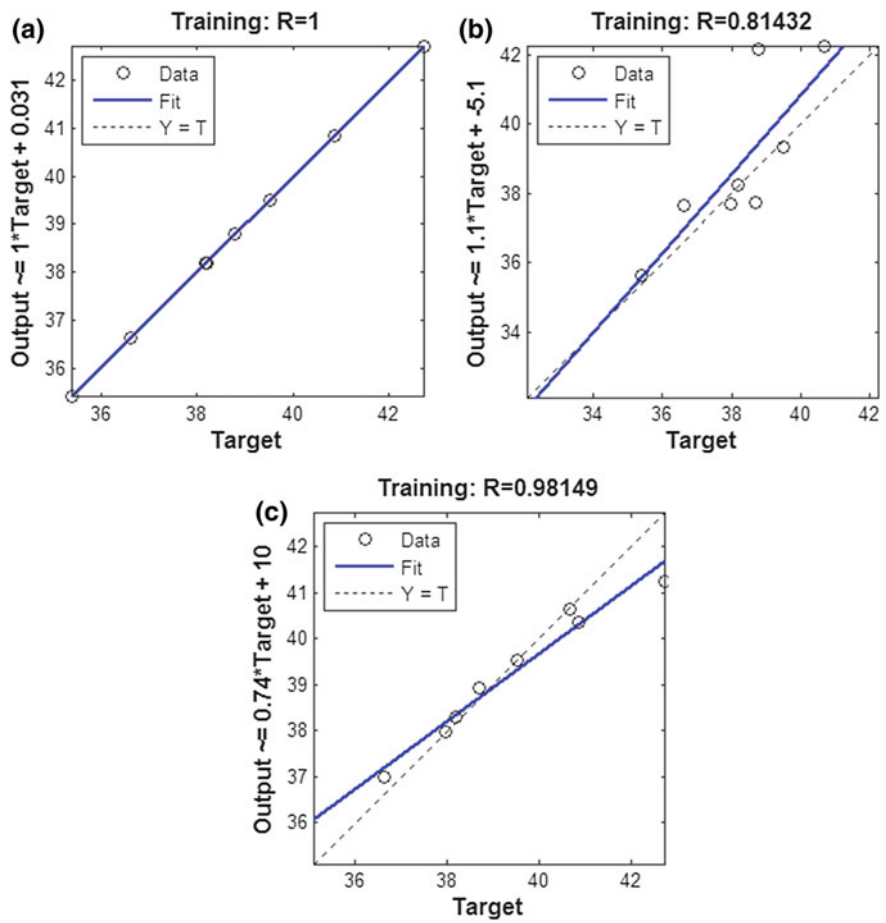


Fig. 11 Training plot of **a** ANN-1, **b** ANN-2 and **c** ANN-3

Table 4 Prediction accuracy of testing datasets

Models	Input	MAPE (%)	RMSE
ANN-1	SR	6.4	4.2
ANN-2	V_{oc}	11.3	4.3
ANN-3	I_{sc}	7.9	3.8

Table 5 MLR models

Models	Correlations	MAPE	Highlights
MLR-1	$PV_{max.power} = -64.2661 + 0.0072SR + 4.5298V_{oc} + 0.7813I_{sc}$	5.4	
MLR-2	$PV_{max.power} = -65.8801 + 0.0103SR + 4.6310V_{oc}$	5.4	High prediction accuracy
MLR-3	$PV_{max.power} = 28.8302 + 0.0049SR + 1.3495I_{sc}$	6.0	
MLR-4	$PV_{max.power} = 29.6470 + 0.0102SR$	6.1	

Table 6 PA

Parameters	Value
$E_{(ac,d)}$	349.1 Wh/day
Y_F	4.7 kWh/kWp
Y_R	6.7 h
PR	70%

where α is intercept and β_j are coefficients or slopes.

Four MLR models (MLR-1, MLR-2, MLR-3 and MLR-4) are developed using least squares approach (Table 5). MLR MAPE value changes from 5.4 to 6.1%, showing high prediction accuracy as per Lewis.

MLR and ANN models of this study are compared with the study performed by Yadav and Chandel [28]; it is found that prediction lies in high accuracy range.

Performance Analysis (PA) of PV Module

Based on experimental readings given in Table 2, performance parameters of 74 Wp Si multi-crystalline PV module are calculated as given in Table 6.

Conclusions

In this paper, three ANNs (ANN-1, ANN-2 and ANN-3) and four new multiple linear regression models (MLR-1, MLR-2, MLR-3 and MLR-4) are proposed to predict maximum power of 74 Wp Si multi-crystalline PV under outdoor condition. The results are obtained by achieving the outdoor measurements of 74 Wp PV module in mountainous region located at a height of 2133.6 m which is characterized by average level of solar irradiance. The input variables to ANN-1, ANN-2 and ANN-3 are SR, V_{oc} and I_{sc} , respectively. MLR-1 correlates PV_{max} as a function of SR, V_{oc} and I_{sc} , MLR-2 correlates PV_{max} as a function of SR and V_{oc} , MLR-3 correlates PV_{max} as a function of SR and I_{sc} , and MLR-4 correlates PV_{max} as a function of SR. The MAPE for ANN-1, ANN-2 and ANN-3 is 6.4, 11.3 and 7.9%, respectively, showing with SR as inputs has least MAPE but using I_{sc} as inputs to ANN model can be used for prediction with high accuracy. The MAPE for MLR-1, MLR-2, MLR-3

and MLR-4 is 5.4, 5.4, 6.0 and 6.1%, respectively. These methods are useful for photovoltaic installation to find out maximum power provided by the systems.

The study has also included the performance analysis of PV module. The total energy generated, final yield, reference yield and performance ratio of 74 Wp multi-crystalline PV module are 349.1808 Wh/day, 4.7187 kWh/kWp, 6.756 h and 70%.

Acknowledgements The authors would like to thanks the reviewers for providing valuable suggestion for the enhancement of the quality of the chapter. The authors would also like to thanks Mr. Manish Kumar technician and Chandan Kumar, Undergraduate 3rd year student, EEE, NIT Sikkim for providing support in doing experiment.

References

1. Eltamaly AM (2018) Performance of MPPT techniques of photovoltaic systems under normal and partial shading conditions. In: *Advances in renewable energies and power technologies*. Elsevier, pp 115–161
2. Bahgat ABG, Helwa NH, Ahamd GE, Shenawy ETE (2004) Estimation of the maximum power and normal operating power of a photovoltaic module by neural networks. *Renewable Energy* 29:443–457
3. Almonacid F, Rus C, Hontoria L, Fuentes M, Nofuentes G (2009) Characterisation of Si-crystalline PV modules by artificial neural networks. *Renewable Energy* 34:941–949
4. Almonacid F, Fernández EF, Rodrigo P, Higuera PJ, Rus-Casas C (2013) Estimating the maximum power of a High Concentrator Photovoltaic (HCPV) module using an Artificial Neural Network. *Energy* 53:165–172
5. Almonacid F, Rus C, Hontoria L, Muñoz FJ (2010) Characterisation of PV CIS module by artificial neural networks. A comparative study with other methods. *Renewable Energy* 35:973–980
6. Sulaiman SI, Rahman TKA, Musirin I (2009) Partial evolutionary ANN for output prediction of a grid-connected photovoltaic system. *Int J Comput Electr Eng* 1(1):40–45
7. Bonanno F, Capizzi G, Graditi G, Napoli C, Tina GM (2012) A radial basis function neural network based approach for the electrical characteristics estimation of a photovoltaic module. *Appl Energy* 97:956–961
8. Mellit A, Pavan AM (2010) Performance prediction of 20 kWp grid-connected photovoltaic plant at Trieste (Italy) using artificial neural network. *Energy Convers Manage* 51:2431–2441
9. Mellit A, Sağlam S, Kalogirou SA (2013) Artificial neural network-based model for estimating the produced power of a photovoltaic module. *Renewable Energy* 60:71–78
10. Brano VL, Giuseppina CG, Falco MD (2014) Artificial neural networks to predict the power output of a PV panel. *Int J Photo Energy* 1:12
11. Piliouguine M, Elizondo D, Mora-López L, Sidrach-de-Cardona M (2015) Modelling photovoltaic modules with neural networks using angle of incidence and clearness index. *Prog Photovoltaics Res Appl* 23:513–523
12. Veerachary M, Yadaiah N (2000) ANN based peak power tracking for PV supplied dc motors. *Solar Energy* 69(4):343–350
13. Graditi G, Ferlito S, Adinolfi G, Tina GM, Ventura C (2014) Performance estimation of a thin-film photovoltaic plant based on an Artificial Neural Network model. In: *The fifth International Renewable Energy Congress IREC*
14. Hiyama T, Kitabayashi K (1997) Neural network based estimation of maximum power generation from PV module using environmental information. *IEEE Trans Energy Convers* 12(3):241–247
15. Fernández EF, Almonacid F, Sarmah N, Rodrigo P, Mallick TK, Pérez-Higuera P (2014) A model based on artificial neuronal network for the prediction of the maximum power of a low concentration photovoltaic module for building integration. *Solar Energy* 100:148–158

16. Askarzadeh A (2014) Voltage prediction of a photovoltaic module using artificial neural networks. *Int Trans Electr Energy Syst* 24(12):1715–1725
17. Saberian A, Hizam H, Radzi MAM, Kadir MZAA, Mirzaei M (2014) Modelling and prediction of photovoltaic power output using artificial neural networks. *Int J Photoenergy* 2014:1–10
18. Niu D, Wei Y, Chen Y (2013) Photovoltaic power prediction based on scene simulation knowledge mining and adaptive neural network. *Math Probl Eng* 2013:1–6
19. Jiang LL, Maskell DL, Patra JC (2012) Chebyshev functional link neural network-based modeling and experimental verification for photovoltaic arrays. In: *The 2012 International Joint Conference on Neural Networks (IJCNN)*, pp 1–8
20. Hussain TN, Sulaiman SI, Musirin I (2013) A hybrid artificial neural network for grid-connected photovoltaic system output prediction. In: *2013 IEEE Symposium on Computers & Informatics (ISCI)*, pp 108–111
21. Sulaiman SI, Muhammad KS, Musirin I, Shaari S (2013) Hybridization of meta-evolutionary programming and artificial neural network for predicting grid-connected photovoltaic system output. In: *2013 IEEE TENCON Spring Conference*, pp 445–449
22. Eltamaly AM, Farh HMH, Othman MF (2018) A novel evaluation index for the photovoltaic maximum power point tracker techniques. *Solar Energy* 174:940–956
23. Ramawan MK, Othman Z, Sulaiman SI, Musirin I, Othman N (2014) A hybrid bat Algorithm Artificial Neural Network for grid-connected photovoltaic system output prediction. In: *2014 IEEE 8th International Power Engineering and Optimization Conference (PEOCO)*, pp 619–623
24. Singh VP, Vijay V, Bhatt MS, Chaturvedi DK (2013) Generalized neural network methodology for short term solar power forecasting. In: *2013 13th International Conference on Environmental and Electrical Engineering*, pp 58–62
25. Singh VK, Vaibhav K, Chaturvedi DK (2012) Solar power forecasting modeling using soft computing approach. In: *2012 Nirma University International Conference on Engineering (NUICONE)*, pp 1–5
26. Huang C, Bensoussan A, Edesess M, Tsui KL (2016) Improvement in artificial neural network-based estimation of grid connected photovoltaic power output. *Renewable Energy* 97:838–848
27. Hosseini SA, Kermani AM, Arabhosseini A (2019) Experimental study of the dew formation effect on the performance of photovoltaic modules. *Renewable Energy* 130:352–359
28. Yadav AK, Chandel SS (2017) Identification of relevant input variables for prediction of 1-minute time step photovoltaic module power using Artificial Neural Network and Multiple Linear Regression Models. *Renew Sustain Energy Rev* 77:955–969
29. <http://www.dfisica.ubi.pt/~hgil/Fotometria/HandBook/ch07.html>
30. Chow SKH, Lee EWM, Li DHW (2012) Short-term prediction of photovoltaic energy generation by intelligent approach. *Energy Build* 55:660–667
31. Frederick M (1996) *Neuroshell 2 Manual*, Ward Systems Group Inc.
32. Ayompe LM, Duffy A, McCormack SJ, Conlon M (2011) Measured performance of a 1.72 kW rooftop grid connected photovoltaic system in Ireland. *Energy Convers Manage* 52:816–825
33. Marion B, Adelsten J, Boyel K, Hayden H, Hammon B, Fletcher T, Canada B, Narang D, Kimber A, Michell L, Rich G, Towsend T, Detride A, Kimbler A (2005) Performance parameters for grid-connected PV system. In: *Proceedings of the 31st IEEE photovoltaic specialist conference, Lake Buena Vista, FL*. pp 1601–1606
34. Lewis CD (1982) *International and business forecasting methods*. Butter-worths, London

Adaptive Fuzzy Logic Controller as MPPT Optimization Technique Applied to Grid-Connected PV Systems



Mohamed M. Refaat, Yousry Atia, M. M. Sayed and Hossam Abdel Fattah

Abstract This chapter presents a complete design of maximum power point tracking control scheme applied to single-phase single-stage and two-stage grid-connected PV systems based on an adaptive fuzzy controller (AFLC). This technique is proposed to enhance the efficiency of a photovoltaic (PV) array and diminish the output power oscillations. The adaptive nature of the proposed controller provides online tuning of fuzzy rules parameters to deal with varying sun radiation and ambient temperature. Ranges of input variables of fuzzy system are defined using genetic algorithm. The adaptive MPPT controller is compared with existing setups, namely the “incremental conductance” (IC) technique and fuzzy logic controller (FLC). The inverter controller is designed in the synchronous frame so that a simplified controller such as PI-controller is implemented. Simulation and experimental results demonstrate the supremacy of the adaptive technique in terms of the speed of tracking and oscillations reduction around the maximum point of power–voltage (P – V) curve.

1 Introduction

Due to the variations in environmental conditions and the stochastic behavior of PV systems, MPPT techniques need to satisfactorily operate at various weather or load conditions. Various MPPT techniques, with different implementation complexity and cost, have been applied to PV systems. Typical techniques include “perturbation and observation” (P&O), incremental conductance, fuzzy system, particle swarm optimization (PSO), and artificial neural networks (ANNs) [1–4]. P&O technique is based on perturbation of PV operating voltage and power to reach the MPP. The disadvantages of this technique are typically the high oscillations generated around the MPP, and the failure to achieve maximum power under rapid changing of envi-

M. M. Refaat · Y. Atia (✉)

Photovoltaic Cells Department, Electronics Research Institute, Cairo, Egypt
e-mail: yousry_atia@yahoo.com

M. M. Sayed · H. A. Fattah

Electrical Power and Machines Department, Faculty of Engineering, Cairo University, Giza, Egypt

© Springer Nature Switzerland AG 2020

247

A. M. Eltamaly and A. Y. Abdelaziz (eds.), *Modern Maximum Power Point Tracking Techniques for Photovoltaic Energy Systems*, Green Energy and Technology, https://doi.org/10.1007/978-3-030-05578-3_9

ronmental conditions [1, 2]. IC technique provides a solution for the systems exposed to rapid variation in solar radiation but is also plagued by high oscillations around the maximum power point (MPP) [1, 3].

FLC attempts to overcome these problems. Microcontrollers have made using FLC popular for MPPT over the last decade [5–7]. As mentioned in [8, 9], fuzzy logic controllers have the advantages of working with imprecise inputs, not needing an accurate mathematical model, and handling nonlinearity. However, the design of a FLC requires the selection of the size of the rule base, the shape and parameters of the membership functions, and the rule inference mechanism. Increasing the number of rules to improve the performance corresponds to a substantial increase in memory requirements and the program execution time. That is known in the fuzzy literatures as the rule explosion phenomenon. Further, the conventional MPPT FLC lacks the ability of self-tuning.

The authors in [10] propose a MPPT using fuzzy set theory to improve energy conversion efficiency. Fuzzy algorithm based on 25 linguistic rules describing the operator's control strategy is applied to control step-up converter for MPPT. FLC based on coarse and fine mode is incorporated in order to reduce not only the time required to track the MPP but also the fluctuation of power. The suggested algorithm increases the memory requirement and does not have the ability of self-tuning. In [11], a proper MPPT control of photovoltaic array using fuzzy control is developed to obtain maximum power from photovoltaic array. The fuzzy system uses small number of rules. Therefore, this control method is easy to implement to real system. Although the fuzzy system needs a small memory, it lacks the ability of self-tuning. In [12] proposed method of maximum power point tracking using adaptive fuzzy logic control for grid-connected PV system is introduced. It has a good performance and it can also change fuzzy parameters for improving control system. However, this method defines the ranges of error variable at which the scaling factors and the peak of the membership functions change. This method needs high knowledge of the system and is suitable for a certain environmental conditions. Also, it does not ensure the stability and needs large memory size.

In this chapter, AFLC is developed to reach the maximum point of power–voltage curve, to avoid oscillations around the MPP, to increase the speed of tracking, and to cope with rapid variation in ambient weather conditions [13]. In addition, it decreases the number of rules, hence decreases the memory requirements and program execution time. The derivative of PV array power with respect to PV voltage is used to tune the parameters in the consequent part of the rules. Estimated parameters are obtained using Lyapunov theory and variable structure, which ensure the stability and increase robustness.

2 Design of MPPT Controller

PV systems can be connected to the grid using two setups: single-stage and two-stage arrangements as shown in Figs. 1 and 2, respectively. In single-stage configuration,

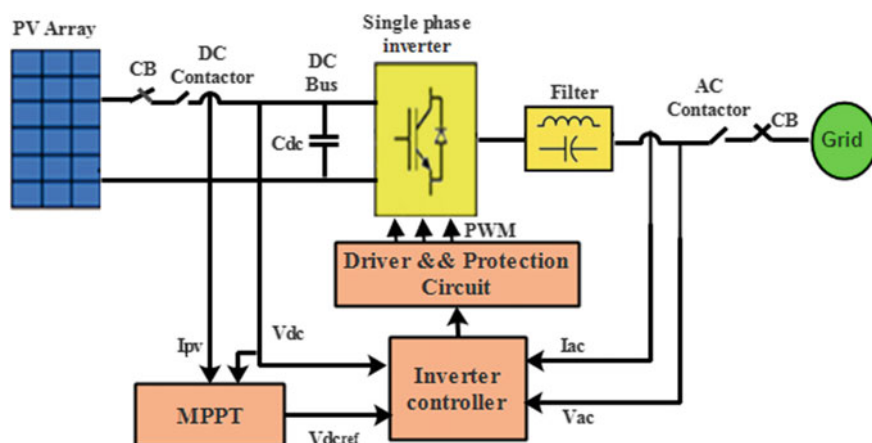


Fig. 1 Proposed single-stage system

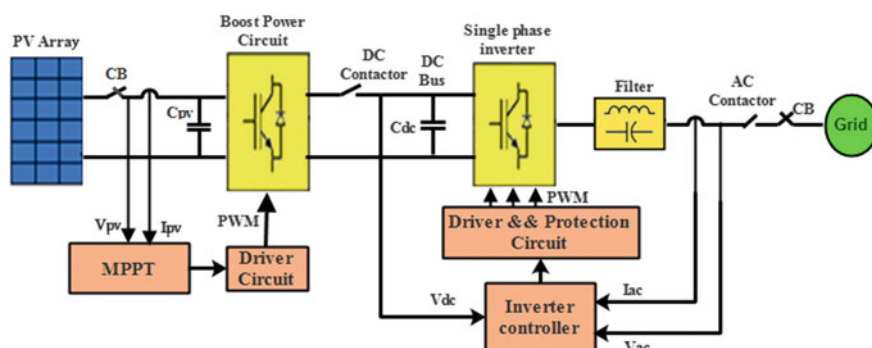


Fig. 2 Proposed two-stage system

PV array is connected to the grid through DC–AC converter, which is responsible for MPPT and power control. In two-stage configuration, the PV system is connected to the grid through two stages: a DC–DC converter (boost converter) for raising or reducing the PV voltage and for performing MPPT and a DC–AC converter for controlling the output active and reactive power and for synchronizing with the power grid. In general, the grid-tied mode controller comprises two parts: PV side generator controller (MPPT) and inverter-side controller.

This chapter focuses on the design of MPPT controller in single-stage and two-stage systems. To design a dynamic MPPT controller, it is necessary to determine the maximum step size and the minimum sampling rate between every perturbation. In this chapter, a simplified design guideline is selected to determine both parameters in two-stage and single-stage grid-connected systems [14, 15].

2.1 Step Size and Perturbation Period Calculation

Two-Stage System

As specified previously, MPPT controllers are applied to the boost converter to extract the maximum PV array power. In grid-connected PV systems, the impact of single-phase voltage source inverter is neglected as it operates at constant DC-link Voltage. In addition, the bandwidth of the DC-link voltage control loop must be higher than the bandwidth of PV side controller. In this section, the minimum settling time of the boost converter is determined and is compared with the settling time of the DC-link voltage control loop of the inverter. The maximum of both is selected as the minimum perturbation period of the MPPT controller.

A small signal transient analysis model has been developed to investigate the effects of step size (\tilde{d}) and the perturbation time (\tilde{t}) on the system dynamics. A simplified circuit for the system is shown in Fig. 3. In this analysis, the shunt resistance (R_{sh}) is neglected. Moreover, the PV array can be modeled using an equivalent resistance (R_{eq}) and voltage source (v_{eq}) and are obtained by Eqs. (1) and (2), respectively [16].

$$R_{eq} = -\left[\frac{\partial i_{pv}}{\partial v_{pv}}\right]^{-1} = \frac{N_s n v_t \exp\left(-\left(\frac{v_{pv} + i_{pv} \frac{N_s}{N_p} R_s}{N_s n v_t}\right)\right) + i_0 \frac{N_s}{N_p} R_s}{N_p i_o} \quad (1)$$

$$V_{eq} = V_{pv} + R_{eq} i_{pv} \quad (2)$$

The inputs of the system are v_{eq} , DC-link voltage (v_{dc}) and duty cycle (d); and the outputs are the PV array voltage (v_{pv}) and PV current (i_{pv}). The linear model of the system is given as follows [17]:

$$\begin{bmatrix} \dot{\tilde{v}_{pv}} \\ \dot{\tilde{i}} \end{bmatrix} = \begin{bmatrix} \frac{-1}{c_{pv} R_{eq}} & \frac{-1}{c_{pv}} \\ \frac{1}{L} & \frac{-r_L}{L} \end{bmatrix} \begin{bmatrix} \tilde{v}_{pv} \\ \tilde{i}_L \end{bmatrix} + \begin{bmatrix} 0 \\ \frac{v_{c_{dc}}}{L} \end{bmatrix} \begin{bmatrix} \tilde{d} \end{bmatrix}$$

$$\begin{bmatrix} \tilde{v}_{pv} \end{bmatrix} = \begin{bmatrix} 1 & 0 \end{bmatrix} \begin{bmatrix} \tilde{v}_{pv} \\ \tilde{i}_L \end{bmatrix} \quad (3)$$

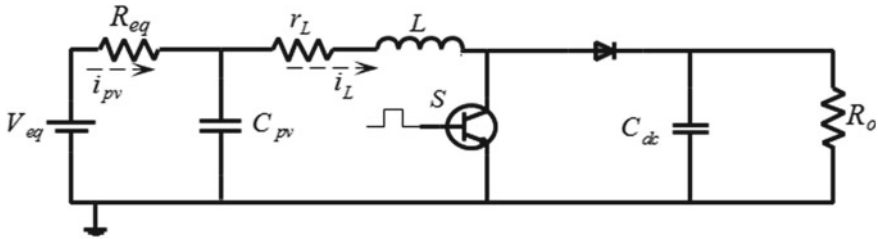


Fig. 3 Equivalent circuit of two-stage system

The system transfer function is deduced as:

$$H(s) = \frac{\tilde{v}_{pv}}{\tilde{d}} = \frac{-\frac{v_{c_{dc}}}{LC_{pv}}}{s^2 + \frac{(r_L c_{pv} + \frac{L}{R_{eq}})}{LC_{pv}}s + \frac{(\frac{r_L}{R_{eq}} + 1)}{LC_{pv}}} \quad (4)$$

From the model in (4), the system natural frequency and damping ratio are

$$\omega_n = \sqrt{\frac{r_L + R_{eq}}{LC_1 R_{eq}}} \quad (5)$$

$$\xi = \frac{1}{2} \frac{r_L R_{eq} c_1 + L}{\sqrt{LC_1 r_L R_{eq} + LC_1 R_{eq}^2}} \quad (6)$$

\tilde{t} can be considered equivalent to the 2% settling time for the power transient signal. Therefore, the minimum \tilde{t} can be calculated as:

$$\tilde{t} \geq \frac{4}{\xi \omega_n} = \frac{8LC_1 R_{eq}}{r_L R_{eq} c_1 + L} \quad (7)$$

The time domain equation of the system is provided in Eq. (8). The higher-order terms can be neglected, and Eq. (8) is simplified to Eq. (9).

$$\tilde{v}_{pv} = -\frac{v_{c_2}}{\left(\frac{r_L}{R_{eq}} + 1\right)} \left[1 - \frac{e^{-\xi \omega_n t}}{\sqrt{1 - \xi^2}} \sin(\omega_d t + \theta) \right] \tilde{d} \quad (8)$$

$$\tilde{v}_{pv} = -\frac{v_{c_{dc}}}{\left(\frac{r_L}{R_{eq}} + 1\right)} \tilde{d} \quad (9)$$

From Eq. (9), the step size of the controller should be selected higher than the peak of noise in the measured signal.

Single-Stage System

In single-stage systems, the maximum perturbation frequency must be lower than the bandwidth of outer loop in single-phase inverter controller. In addition, the step size of the controller is selected higher than the peak of noise in the measured signal.

3 Fuzzy Logic Controller (FLC) as MPPT Technique

FLC has been broadly used for industrial applications since an accurate mathematical model is not required, and that it has the flexibility of handling nonlinearities. The structure of FLC is composed of four parts: the fuzzifier, the knowledge base, the inference engine, and the defuzzifier as depicted in Fig. 4 [8].

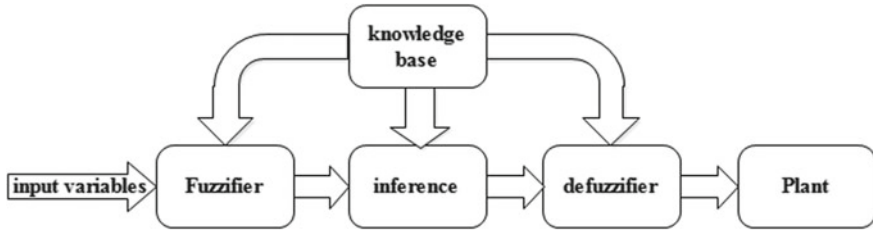


Fig. 4 Structure of FLC

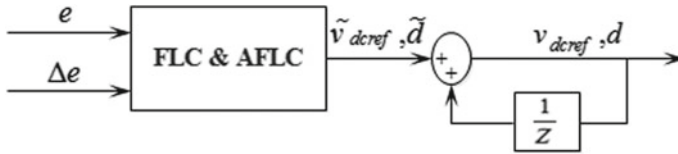
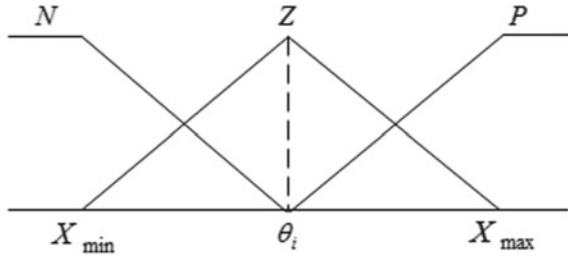


Fig. 5 Structure of MPPT controller-based FLC and AFLC

Fig. 6 Inputs and output membership functions



MPPT-based FLC has two inputs error (e) and change of error (Δe); one output is the change in duty cycle (\tilde{d}) in two-stage system or the change in DC-link voltage (\tilde{v}_{dcref}) in single-stage system. The output of the fuzzy logic controller is then integrated to generate the control signal (d or v_{dcref}) as shown in Fig. 5. e and Δe at the k th sampled time are defined as follows:

$$e(k) = \frac{\Delta p_{pv}}{\Delta v_{pv}} = \frac{p_{pv}(k) - p_{pv}(k-1)}{v_{pv}(k) - v_{pv}(k-1)}$$

$$\Delta e = e(k) - e(k-1) \quad (10)$$

Each of the input and output fuzzy variable is assigned three linguistic values negative (N), zero (Z), and positive (P). Each linguistic value is represented by triangle membership function as shown in Fig. 6. The values X_{max} and X_{min} represent the maximum and minimum variation of the input and output signals. These values are selected based on the simulation information or an optimization technique. Let $X_{max} = -X_{min}$ and the range of each fuzzy variable is normalized between -1 and $+1$ by introducing a scaling factor ($k = 1/X_{max}$) to represent the actual signal.

In this work, the range of the inputs is selected through studying the relation between $(e, \Delta e)$ and v_{pv} at various environmental conditions. Then, using an optimization technique, genetic algorithm (GA) is selected; the optimum scaling factors are obtained.

GA algorithm is predicated on principles of natural evolution and survival of the fittest. It begins by shaping decision variables and the objective function. Then, it considers multiple candidate solutions (populations) to the problem and proceeds by moving this population of solutions toward a global optimum [18]. Thus, as population evolves, the optimum solution is achieved. GA encompasses a main generational process cycle. Within this cycle, GA begins by haphazardly generating an initial population and this population is exposed to genetic operators. The general flow diagram of process cycle is given in Fig. 7. This algorithm recurrent till stopping criterion is achieved.

MATLAB provides an optimization toolbox that includes a GA-based solver. To use the optimization application, the following data is used:

- The selected cost function is:

$$\text{obj}(e) = \int e^2 dt \quad (11)$$

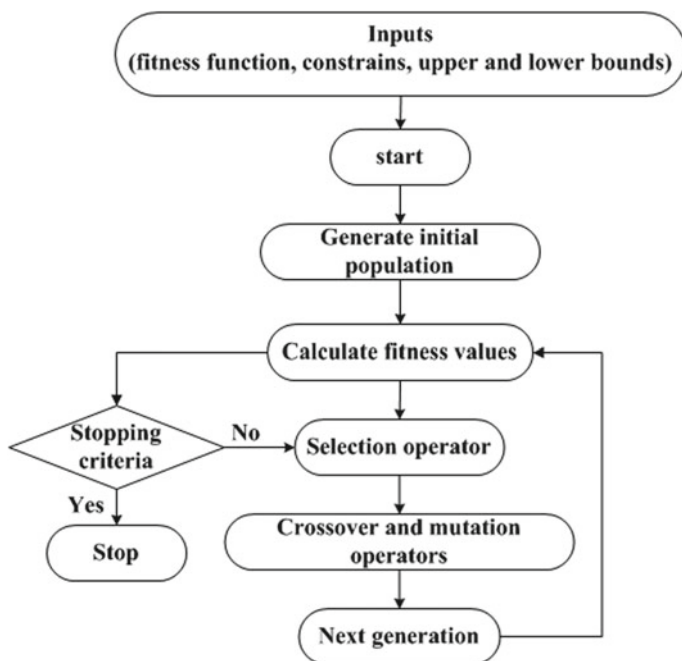


Fig. 7 Flow chart of genetic algorithm

Table 1 Fuzzy rules of two-stage system

e	Δe		
	N	Z	P
N	P	P	Z
Z	P	Z	N
P	Z	N	N

Table 2 Rules of FLC

e	Δe		
	N	Z	P
N	N	N	Z
Z	N	Z	P
P	Z	P	P

- Upper and lower bounds are determined through studying the response of input variables at different environmental conditions.

A symmetrical fuzzy rule set is used to describe the fuzzy controller, as described in Tables 1 and 2. Using the center of gravity defuzzification method, the appropriate crisp control is then generated. Let θ_i represents the centroids of the i th membership function of the output variable. Thus, for h rules, the output of the fuzzy system is calculated as follows:

$$\tilde{d}, \tilde{v}_{dc} = \frac{\sum_1^h \omega_i \theta_i}{\sum_1^h \omega_i} = \underline{\theta}^T \underline{\tau} \quad (12)$$

where $\tau_i = \frac{\omega_i}{\sum_1^h \omega_i}$ and the strength of the i th rule is ω_i . It is calculated based on interpreting the “AND” conjunction as a product of the membership values corresponding to the measured values of e and Δe .

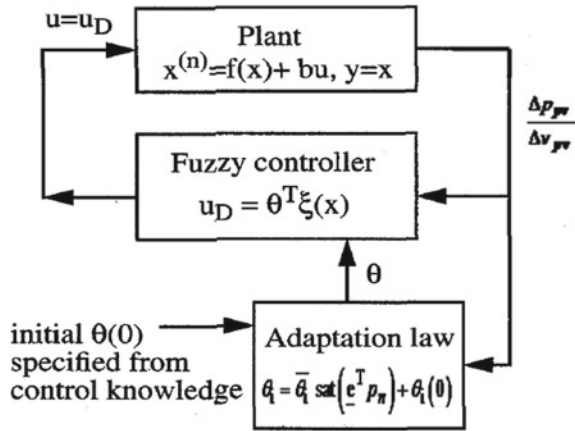
4 Adaptive Fuzzy Control (AFLC) as MPPT Technique

In this part, a computationally efficient algorithm is suggested to tune θ_i online such that the regulator will have an improved performance. The suggested algorithm based on AFLC and its structure is shown in Fig. 8. The proposed MPPT technique reduces the rule base size, decreases the required memory, and has a good performance in the training phase as it makes use of the initial rule base defined for the fuzzy logic controller [19, 20].

θ_i can be estimated as follows [20]:

Consider the nonlinear system (3) is represented by:

Fig. 8 The basic structure of AFLC [20]



$$\ddot{x} = f(x) + bu \quad (13)$$

$$y = x \quad (14)$$

where x the state-variable vector, u is the control signal. We can choose the control u to cancel the nonlinearity and design the controller based on linear control theory (e.g., pole placement) the control law is:

$$u^* = \frac{1}{b} [-f(x) + \ddot{y}_m + \underline{k}^T \underline{e}] \quad (15)$$

If the tracking error is

$$e = y_m - x, \quad \dot{e} = \dot{y}_m - \dot{x}, \quad \ddot{e} = \ddot{y}_m - \ddot{x} \quad (16)$$

The tracking error state vector, \underline{e} , can be selected as

$$\underline{e} = [e \ \dot{e}]^T \quad (17)$$

and the design vector, \underline{k} , is given by

$$\underline{k}^T = [k_2 \ k_1]$$

Substituting u^* for u from (15) to (13) leads to

$$\ddot{x} = \ddot{y}_m + \underline{k}^T \underline{e} \quad (18)$$

Noting the above definition of the tracking error (\underline{e}) is possible to rewrite as

$$\ddot{e} + \underline{k}^T \underline{e} = \ddot{e} + k_1 \dot{e} + k_2 e = 0 \quad (19)$$

The characteristic equation of error model (19) is given by:

$$\ddot{s} + k_1 \dot{s} + k_2 = 0 \quad (20)$$

The design parameters k_1, \dots, k_n are selected such that the roots of (20) are on the left-hand side of the S-plane to ensure the stability.

If the model suffers a considerable uncertainty or input disturbance and noisy measurements, the controller performance degrades significantly. Here, we assume $f(x)$ and b are unknown and the ideal controller (15) cannot be implemented. However, we have the fuzzy IF-THEN rules in Tables 1 and 2 that describe behavior of the controller. Therefore, a reasonable idea is to replace u^* by fuzzy system; i.e., it is possible to write

$$u^* \approx \underline{\theta}^{*T} \underline{\tau}(x) \quad (21)$$

where $\underline{\theta}^*$ is the vector of the centroids of the membership functions assigned to u^* and $\underline{\tau}(x)$ is the vector of fuzzy basis functions.

The control law in (21) is implemented based on an estimate $\underline{\theta}$ of the true value of $\underline{\theta}^*$. Hence, the control law can be written as:

$$u = u_c(\underline{\theta}, \underline{x}) = \underline{\theta}^T \underline{\tau}(x) \quad (22)$$

Substituting $u_c(\underline{\theta}, \underline{x})$ in (13) leads to

$$\ddot{x} = f(\underline{x}) + bu_c(\underline{\theta}, \underline{x}) \quad (23)$$

Adding and subtracting bu^* to (23) result in

$$\ddot{x} = f(\underline{x}) + bu^* + b(u_c(\underline{\theta}, \underline{x}) - u^*) \quad (24)$$

Similar to the derivation of (19), it is possible to show that the error model corresponding to the closed-loop system is

$$\ddot{e} = -\underline{k}^T \underline{e} + b(u^* - u_c(\underline{\theta}, \underline{x})) \quad (25)$$

Equation (25) can be put on the vector form by choosing

$$\begin{aligned} \dot{e}_1 &= \dot{e} = e_2, \\ \dot{e}_2 &= \ddot{e} = -\underline{k}^T \underline{e} + b(u^* - u_c(\underline{\theta}, \underline{x})) \end{aligned} \quad (26)$$

So, the state space model takes the form

$$\dot{\underline{e}} = \Lambda_c \underline{e} + b_c (u^* - u_c(\underline{\theta}, \underline{x})) \quad (27)$$

where

$$\Lambda_c = \begin{bmatrix} 0 & 1 \\ -k_2 & -k_1 \end{bmatrix}, \quad b_c = \begin{bmatrix} 0 \\ b \end{bmatrix}$$

The design parameters k_1, \dots, k_n are selected such that the eigenvalues of Λ_c are located in a pre-specified region of the left-hand side of the S-plane.

The adaptation law of $\underline{\theta}$ is typically based on the second method of Lyapunov to ensure the stability of the adaptive system. To illustrate that, consider the following Lyapunov function:

$$V = \frac{1}{2} \underline{e}^T P \underline{e} + \frac{b}{2} \underline{\varphi}^T \Gamma^{-1} \underline{\varphi} \quad (28)$$

where P and Γ are positive definite matrices and $\underline{\varphi} = \underline{\theta}^* - \underline{\theta}$ is the estimation error. The calculation of P and Γ are shown below. The designer normally picks up the matrix Γ as a diagonal matrix that determines the adaptation rate as shown below. The time derivative of V is

$$\dot{V} = \frac{1}{2} (\underline{e}^T P \dot{\underline{e}} + \dot{\underline{e}}^T P \underline{e}) + b \underline{\varphi}^T \Gamma^{-1} \dot{\underline{\varphi}} \quad (29)$$

Substituting for \underline{e} from Eq. (27) in Eq. (29) leads to

$$\dot{V} = \frac{1}{2} \underline{e}^T (P \Lambda_c + \Lambda_c^T P) \underline{e} + \underline{\varphi}^T \tau(\underline{x}) b_c^T P \underline{e} + b_c \underline{\varphi}^T \Gamma^{-1} \dot{\underline{\varphi}} \quad (30)$$

The closed-loop system in (27) is stable if \dot{V} is negative semi-definite. Since Λ_c has stable eigenvalues, it is true that P is the solution of the algebraic Lyapunov equation

$$P \Lambda_c + \Lambda_c^T P = -Q \quad (31)$$

where Q is a positive semi-definite matrix that is arbitrarily chosen by the designer. Select the adaptation law as

$$\dot{\underline{\varphi}} = -\frac{1}{b} b_c^T P \underline{e} \Gamma \tau(\underline{x}) \quad (32)$$

Hence, Eq. (30) is possible to rewrite as

$$\dot{V} = -\frac{1}{2} \underline{e}^T Q \underline{e} \quad (33)$$

Equation (33) clearly shows that the closed-loop system (27) is stable if the adaptation law (32) is employed. To implement (33) and calculate $\underline{\theta}$, it is assumed that the variation of $\underline{\theta}^*$ is much slower than that of $\underline{\theta}$; i.e., $\underline{\theta}^*$ is locally constant. The estimate of $\underline{\theta}$ is given by

$$\dot{\underline{\theta}} = \frac{1}{b} \underline{b}_c^T P \underline{e} \Gamma \tau(\underline{x}) \quad (34)$$

The designer chooses the adaptation gain Γ as a diagonal matrix with the i th diagonal element γ_i . Because of the special structure of the vector, the product $\underline{b}_c^T P$ is equivalent to $b p_2$ where p_2 is the 2th row of P and the adaptation law in (34) is simplified to

$$\dot{\theta}_i = \gamma_i \underline{e}^T p_n \tau_i(\underline{x}) \quad (35)$$

The adaptation law (35) suffers some drawbacks since it adopts a pure integrator. Techniques such as the projection algorithm and sigma modification have been used to improve the estimator performance. In [21], the variable structure algorithm is used to implement the estimator since it leads to a robust performance and an efficient numerical implementation. Hence, the estimator is implemented as

$$\theta_i = \overline{\theta}_i \text{sat}(\underline{e}^T p_n) + \theta_i(0) \quad (36)$$

where $\overline{\theta}_i$ is a constant set by the designer to specify the possible variation of θ_i around initial value $\theta_i(0)$.

The proposed MPPT controller can be summarized as follows [17]:

Step 1: Define the inputs scaling factors ($k_{\Delta e}$, k_e) and output scaling factor ($k_{\tilde{v}_{\text{def}}}$ or $k_{\tilde{d}}$) as described in Sect. 3.

Step 2: Specify perturbation period as presented in Sect. 2.

Step 3: Define fuzzy rules as given in Tables 1 and 2.

Step 4: Specify k_1 and k_2 .

Step 5: Use the simulation to tune p_2 .

Step 6: Verify that Lyapunov equation is satisfied:

$$P \Lambda_c + \Lambda_c^T P < 0 \quad (37)$$

Step 7: Use the adaptation law in (41) to estimate the centroids of the output membership functions.

Step 8: Calculate the step size as described in Eq. (17).

Step 9: The output of MPPT controller is given by.

$$u(k) = u(k-1) + \tilde{u}(k) \quad (38)$$

where u represent d or v_{dref} .

5 Inverter-Side Controller Design

Grid-connected PV systems must achieve the general requirement of distributed generators connected to power systems. These requirements typically include synchronization, voltage regulation, and lower THD in the injected current [21]. This section addresses a complete design of the control unit applied to a single-phase H-bridge grid-connected inverter in synchronous reference (DQ) frame [17, 22–24]. The dynamic of the AC-side variables in DQ-frame is given as follows [17]:

$$\begin{aligned}\frac{di_{gd}}{dt} &= L_s \omega_o i_{gq} - r_s i_{gd} + v_{td} - v_{gd} \\ \frac{di_{gq}}{dt} &= -L_s \omega_o i_{gd} - r_s i_{gq} + v_{tq} - v_{gq}\end{aligned}\quad (39)$$

where $\begin{pmatrix} v_{td} \\ v_{tq} \end{pmatrix} = \begin{pmatrix} m_d v_{dc} \\ m_q v_{dc} \end{pmatrix}$

Figure 9 shows the structure of the inverter-side controller. It consists of four loops: pulse width modulation (PWM), phase-locked loop (PLL), current control loop, and DC-link voltage loop [17].

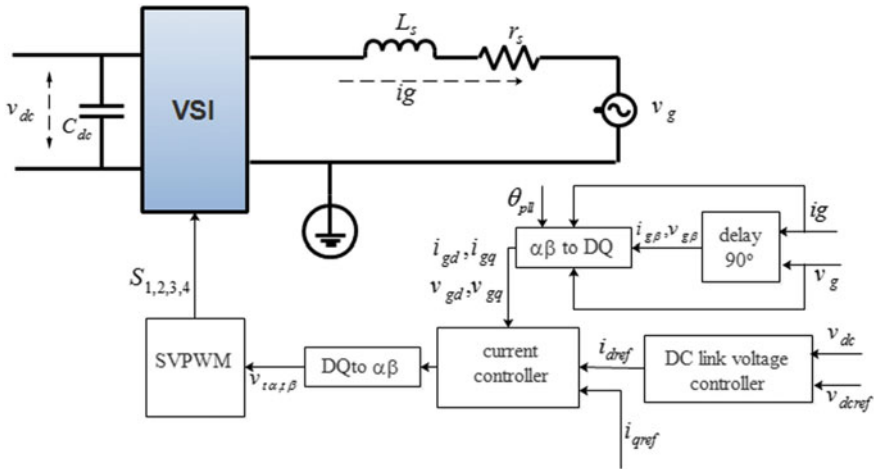


Fig. 9 Proposed inverter-side controller

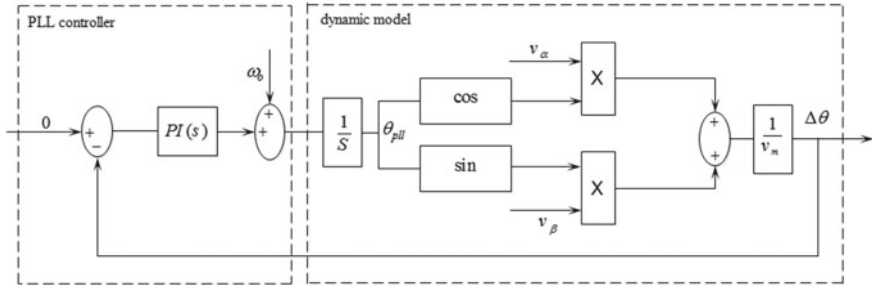


Fig. 10 Schematic diagram of $\alpha\beta$ PLL method

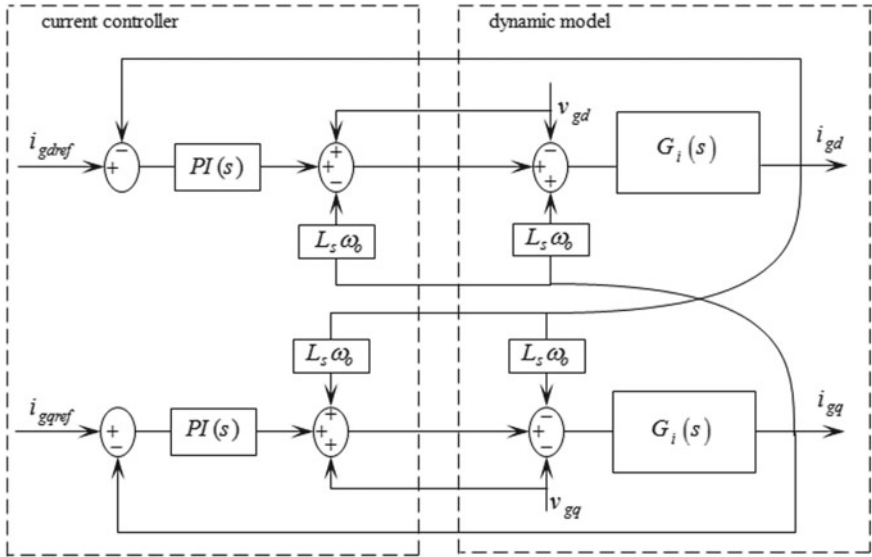


Fig. 11 Block diagram of current control loop

5.1 Grid Synchronization

The grid angle detection at the point of common coupling (PCC) must be assessed to synchronize with the utility grid. In this way, a PLL algorithm is prescribed to have exact and quick grid angle detection [25, 26].

The selected PLL technique in this work is the stationary reference frame phase-locked loop ($\alpha\beta$ PLL) as shown in Fig. 10. Parameters of PLL controller are [17]:

$$k_{iL} = \frac{\omega_{npll}^2}{v_m} \quad (40)$$

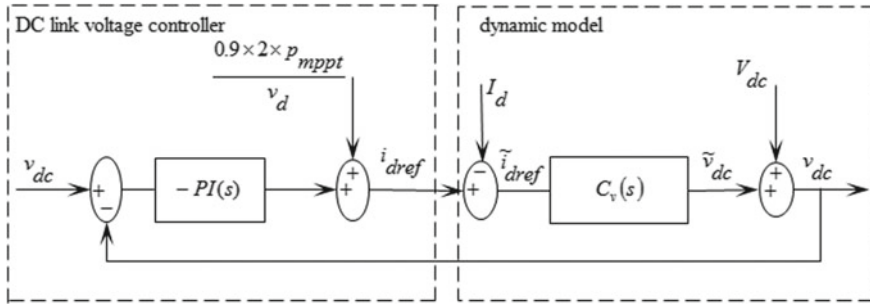


Fig. 12 Control block diagram of DC-link loop

$$k_{pL} = \frac{2\xi_{pll}\omega_{npll}}{v_m} \quad (41)$$

where ω_{npll} and ξ_{pll} are the selected natural frequency and damping ratio of the PLL loop.

5.2 Current Controller Design

The objective of current regulator is to track the reference signals (i_{gdref} and i_{gqref}) with acceptable dynamic response. Current control loop is shown in Fig. 11. It shows that the d - and q -axes control loops are identical. Thus, both compensators can also be identical. The parameters of PI-controller are designed as follows [17]:

$$k_{pi} = \omega_{ii} L_s \quad (42)$$

$$k_{ii} = \frac{k_{pi} R_s}{L_s} \quad (43)$$

where the bandwidth (ω_{ii}) of the closed-loop system is considerably smaller, for example, ten times, than the switching frequency. L_s and R_s are the inductance and the resistance of inverter output filter.

5.3 DC-Link Voltage Controller Design

DC-link voltage regulation is essential to maintain the power balance between the input power (p_{dc}), from PV array or DC-to-DC converters, and the output AC power to the utility (p_i). In Fig. 12, the negative sign is included in the controller to compensate the negative sign of the DC-link model. The parameters of PI-controller are [17]:

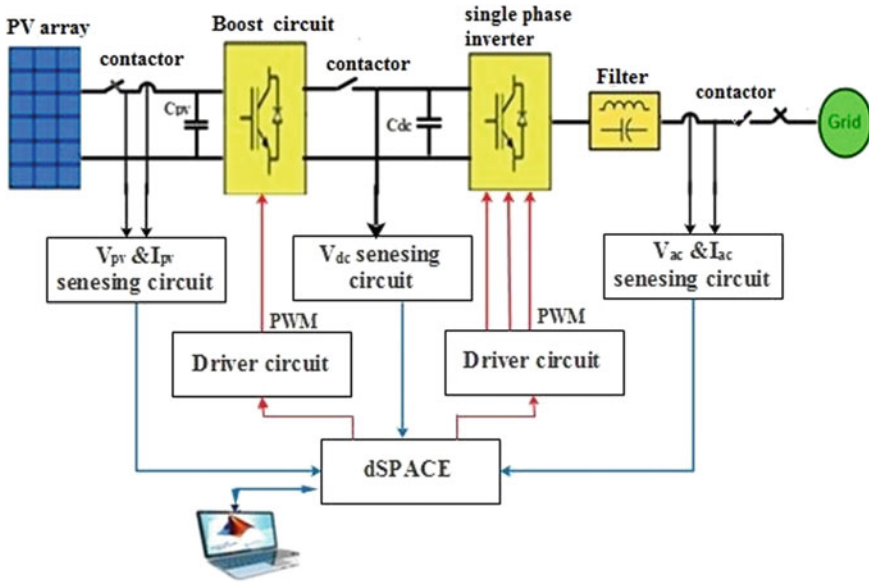


Fig. 13 Schematic circuit of two-stage single-phase grid-connected PV system

$$k_{iv} = \frac{\omega_g^2}{k_{sys} \sqrt{(1 - T_c T_z \omega_g^2)^2 + (T_c + T_z)^2 \omega_g^2}} \quad (44)$$

$$k_{pv} = T_c k_{iv} \quad (45)$$

where $k_{sys} = \frac{2r_s i_{gdo} + V_{gdo}}{2C_{dc} V_{dco}}$, $T_z = \frac{L_s i_{gdo}}{2r_s i_{gdo} + V_{gdo}}$, $T_c = \frac{1 - \omega_g T_z}{\omega_g + T_z \omega_g^2}$ and ω_g the selected gain crossover frequency.

6 Simulation and Experimental Results

6.1 Two-Stage System

In this study, 1.81 kW PV array is interfaced with single-phase grid-connected VSI through a boost converter. The boost converter is designed to operate in the continuous conduction mode. PV array comprises four TSM-295 PC14 modules connected in series as one string. The parameters of the system are given in Table 3. The parameters of the inverter side controller are given in Table 4. The systems are intended for evaluation purposes in a laboratory environment at Electronics Research Institute (ERI) as shown in Figs. 13 and 14. The main components of the system are given in Table 5.

Table 3 System parameters

C_{pv}	2200 μ F
C_{dc}	3300 μ F
L	5 mH
r_L	0.1 Ω
L_s	5 mH
R_s	0.1 Ω
v_g	220 V

Table 4 inverter-side controller parameters

k_{pl}	k_{il}	k_{pi}	k_{ii}	k_{pv}	k_{iv}
2.57	2730.3 s^{-1}	30	620 s^{-1}	0.36	21.2 s^{-1}

Table 5 Components of the system

Item	Part
PV array	1
Voltage source inverter	2
Boost converter	3
Inverter output filter (5 mH)	4
Inductor of the boost converter	5
Current and voltage transducers circuit	6
dSPACE MicroLabBox	7
Miniature circuit breaker (MCB)	8
Grid (AC) Contactor and PV (DC) contactor	9
Inverter interfacing board	10
Power supply	11
Oscilloscope	12

Table 6 Designed parameters of MPPT controller (two-stage system)

FLC, AFLC				IC	
k_e	$k_{\Delta e}$	$k_{\tilde{d}}$	\tilde{t}	\tilde{t}	\tilde{d}
0.375	0.126	0.02	0.5 s	0.5 s	0.01

Figures 15 and 16 show the response of R_{eq} and \tilde{t} at various irradiance levels and module temperatures. The figures show that \tilde{t} increases with decreasing v_{pv} and solar insulation and with increasing the module temperature. Therefore, these conditions should be considered in the design of \tilde{t} . The figures also show that the maximum settling time of boost converter at different environmental conditions is smaller than the settling time of DC-link voltage loop (0.2 s); hence, \tilde{t} should be selected higher than 0.2 s.

The range of input variables for FLC and AFLC are selected based on Figs. 17 and 18. The initial rules for AFLC are given in Table 7. It is depicted that the absolute

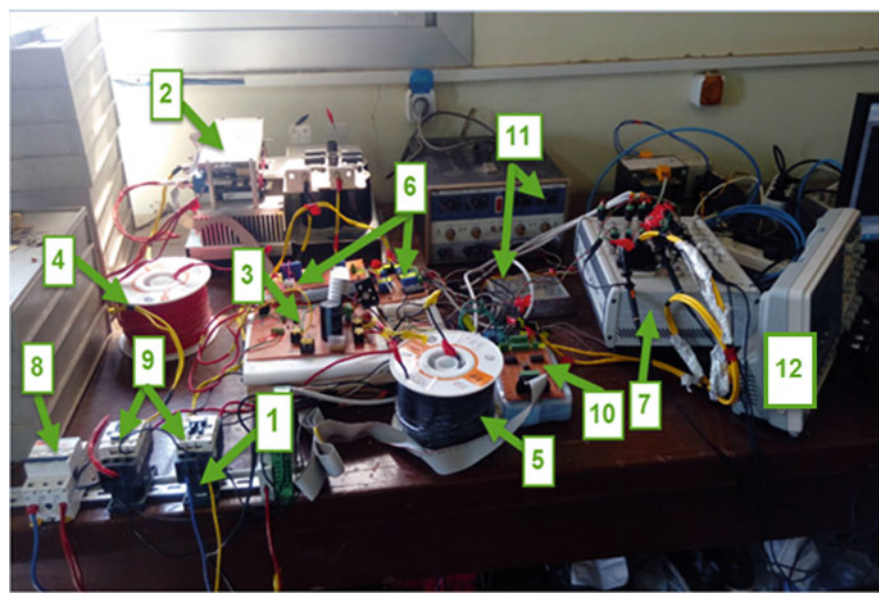


Fig. 14 General view of the experimental bench

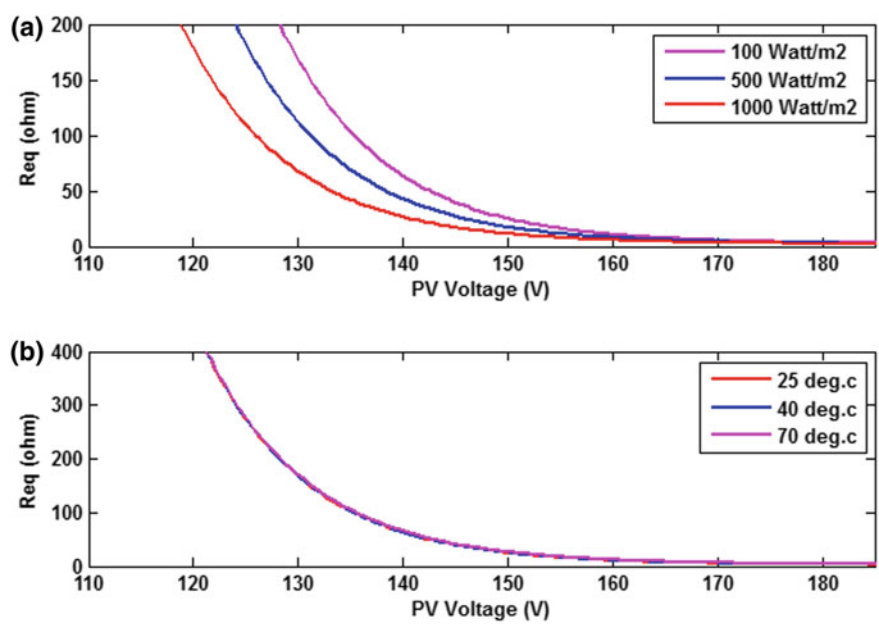


Fig. 15 Relation between R_{eq} and v_{pv} in two-stage system **a** at different irradiance levels and module temperature 25 °C **b** at different module temperatures and irradiance

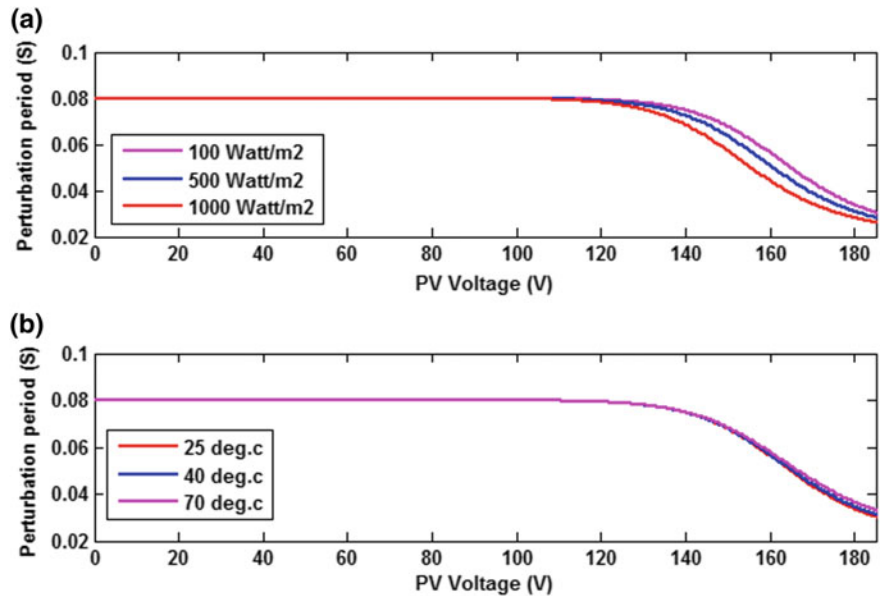


Fig. 16 Relation between \tilde{i} and v_{pv} in two-stage system **a** at different irradiance levels and module temperature 25 °C **b** at different module temperatures and irradiance 100 W/m²

Table 7 Initial rules of the AFLC (two-stage system)

e	Δe		
	N	Z	P
N	0.5	0.5	0
Z	0.5	0	−0.5
P	0	−0.5	−0.5

values of e and Δe increase with increasing solar radiation and module temperature. Based on these figures, the upper and lower bands for genetic toolbox in MATLAB are defined. The optimum scaling factors of the inputs are presented in Fig. 19. The selected parameters of IC, FLC and AFLC are provided in Table 6.

For experimental evaluation, the system is subject to the following sequence of events: The MPPT algorithm is inactive until i_{pv} (at duty cycle = 0.5) is about 1 A, then the MPPT algorithm is activated at point “start.” This permits the algorithms to be tested in similar conditions. Solar radiation and module temperature are measured at this condition. Solar radiation and module temperature are 800 W/m² and 60 °C.

Figures 20, 21, 22, 23, 24, 25, 26, and 27 show the simulation and experimental results of the adaptive MPPT controller, FLC, and IC technique at irradiance 800 W/m² and module temperature 60 °C. Figure 22 shows the movement of the operating point on power–voltage curve of the PV array. It shows that the operating point moves from right-hand side of MPP and settles at the MPP. The results show

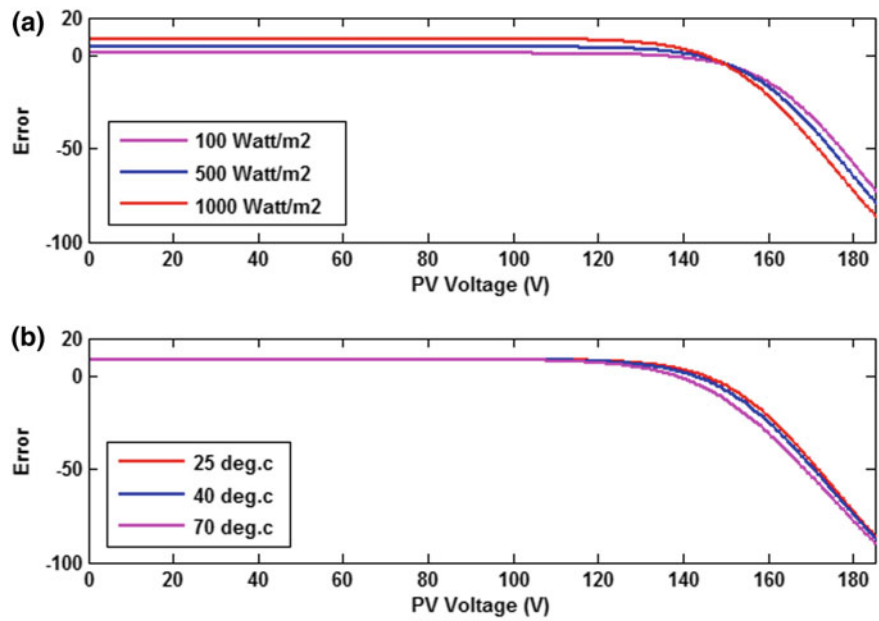


Fig. 17 e is plotted against v_{pv} in two-stage system **a** at different irradiance levels and module temperature 25 °C **b** at different module temperatures and irradiance 1000 W

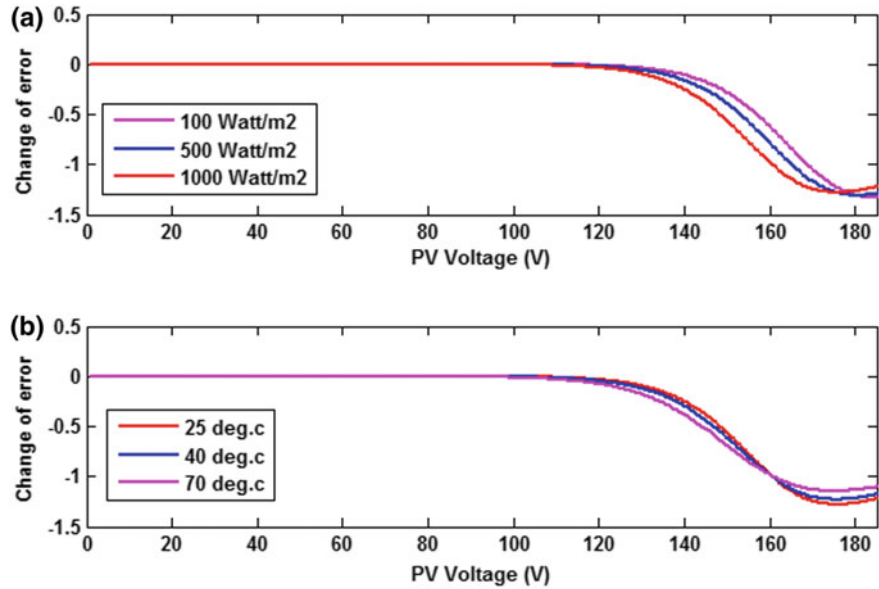


Fig. 18 Δe is plotted against v_{pv} in two-stage system **a** at different irradiance levels and module temperature 25 °C **b** at different module temperatures and irradiance 1000 W/m²

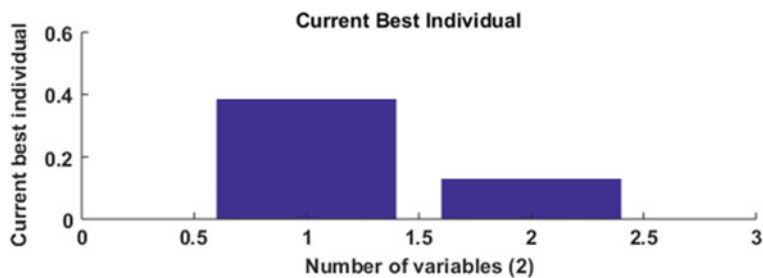


Fig. 19 Selected k_e and $k_{\Delta e}$ in two-stage system using genetic toolbox

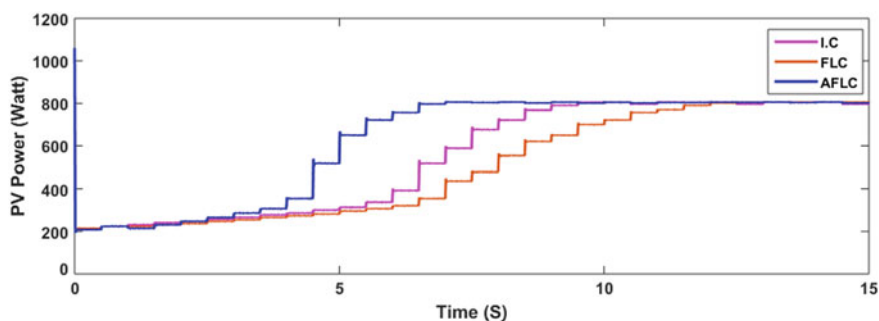


Fig. 20 Simulation results: p_{pv} using AFLC, FLC, and IC at irradiance 800 W/m^2 and module temperature 60°C in two-stage system

that the IC algorithm shows low oscillations at the MPP, but the tracking speed is decreased. On the other hand, the adaptive technique provides high tracking speed with acceptable oscillations at the MPP. The performance of AFLC is compared with FLC using the same number of rules and scaling factors. Non-adaptive fuzzy controller presents high oscillations in extracted PV power and voltage and slow response compared to the adaptive technique. Figure 28 shows the injected current to the grid.

To test the performance of proposed technique at different conditions, we depend on the simulation results as we cannot control the environmental conditions. Figures 20, 21, 22, 23, 24, 25, 26, and 27 show that experimental and simulation results are the same. Hence, we can predict that the simulation and experimental results at other conditions are also the same.

Figures 29, 30, 31, and 32 show the simulation results of the adaptive MPPT controller, FLC, and IC technique at different irradiance levels and different module temperatures. Simulation results show that the proposed MPPT technique has the superiority in tracking speed and reduction of output oscillations as anticipated.

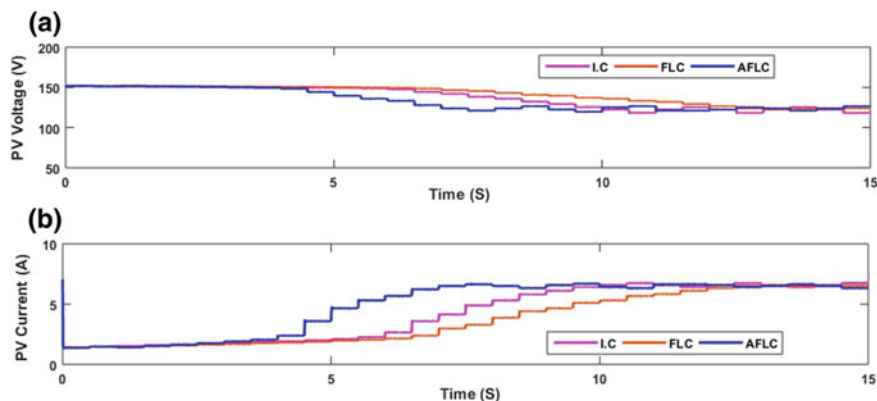


Fig. 21 Simulation results: **a** v_{pv} **b** i_{pv} , at irradiance 800 W/m^2 and module temperature 60°C in two-stage system

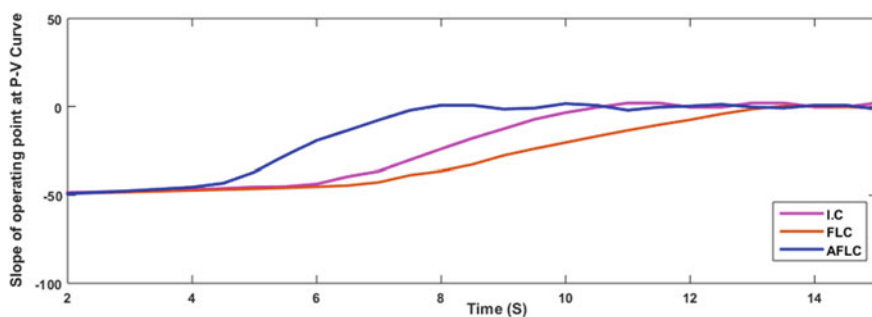


Fig. 22 Simulation results: slope of operating point on P - V curve at irradiance 800 W/m^2 and module temperature 60°C in two-stage system

6.2 Single-Stage System

The selected system consists of 12 PV modules connected in series as one string, and the parameters of the proposed system are in Table 3. The systems are intended for evaluation purposes in a laboratory environment at ERI. Figure 33 shows the schematic diagram of single-stage single-phase grid-connected system. In this test, the boost converter in Fig. 14 is omitted (Fig. 34).

The range of input variables for FLC and AFLC are selected based on Figs. 35 and 36, and the optimum scaling factors are selected using genetic algorithm as shown in Fig. 37. The parameters of MPPT techniques are given in Table 8 and the initial rules for AFLC are given in Table 9.

For experimental evaluation, the system is subject to the following sequence of events: The MPPT algorithm is inactive until v_{dc} is regulated at 460 V and selects the condition at which i_{pv} at this operating point is about 2 A. At point “start,” the MPPT

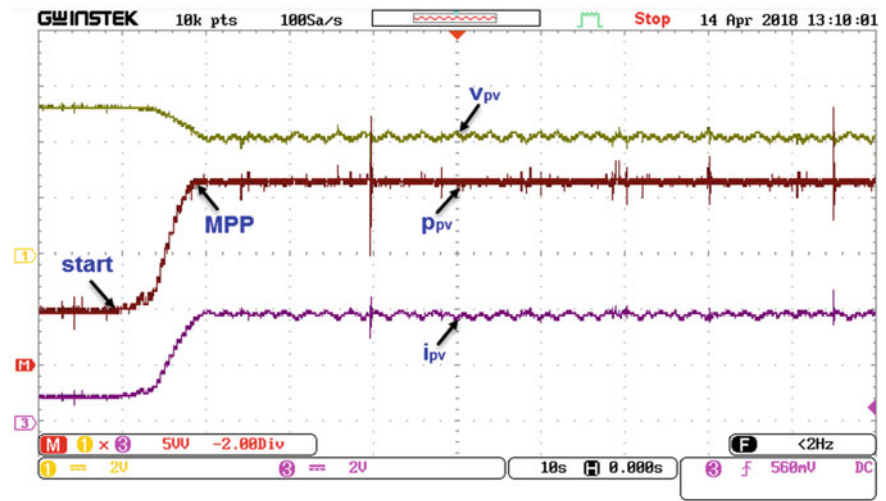


Fig. 23 Experimental results: **a** v_{pv} **b** i_{pv} , and p_{pv} using IC at irradiance 800 W/m^2 and module temperature 60°C in two-stage system. Scale: 60 V/div , 3 A/div , 200 W/div

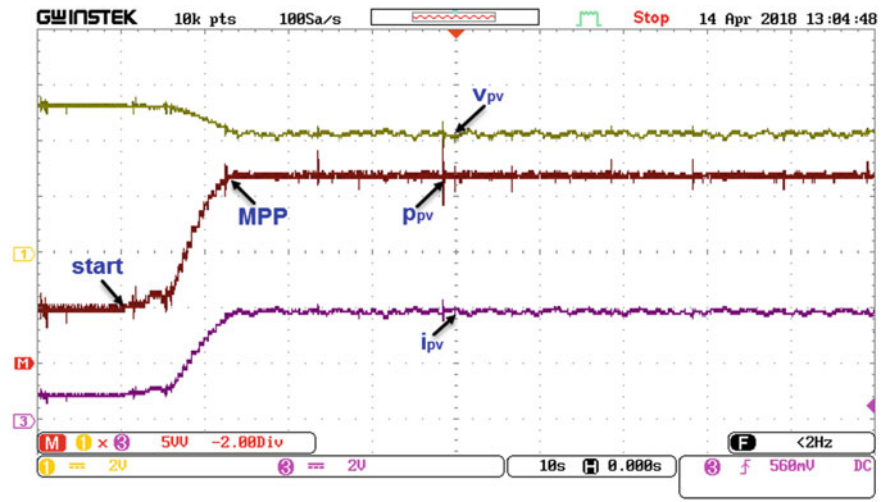


Fig. 24 Experimental results: **a** v_{pv} **b** i_{pv} , and p_{pv} power using FLC at irradiance 800 W/m^2 and module temperature 60°C in two-stage system. Scale: 60 V/div , 3 A/div , 200 W/div

Table 8 Designed parameters for single-stage system

FLC, AFLC				IC	
k_e	$k_{\Delta e}$	$k_{\tilde{v}}$	\tilde{t}	\tilde{t}	\tilde{v}
0.57046	0.11581	6	0.5 s	0.5 s	3

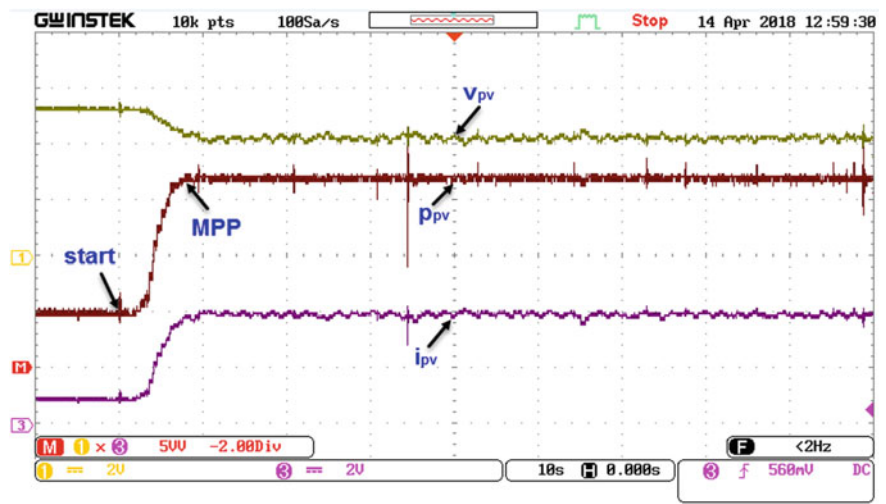


Fig. 25 Experimental results: v_{pv} , i_{pv} , and p_{pv} using AFLC at irradiance 800 W/m^2 and module temperature 60°C in two-stage system. Scale: 60 V/div , 3 A/div , 200 W/div

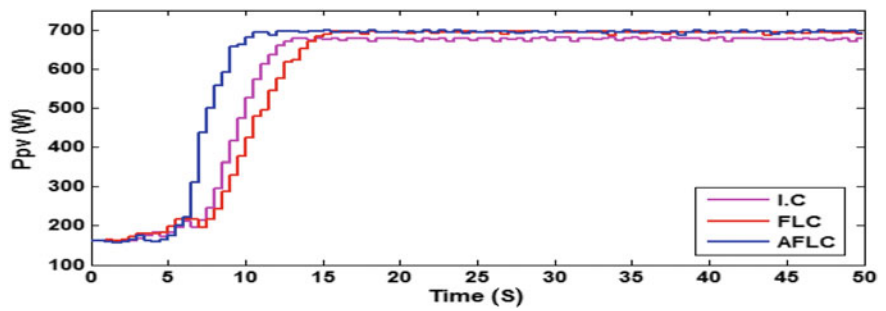


Fig. 26 Experimental results: comparison between the extracted PV powers at irradiance 800 W/m^2 and module temperature 60°C in two-stage system

Table 9 Initial rules of the AFLC (single-stage system)

e	Δe		
	N	Z	P
N	-1	-1	0
Z	-1	0	1
P	0	1	1

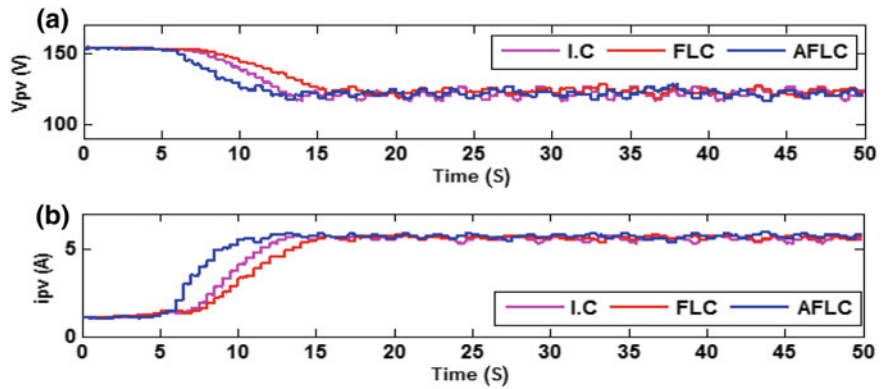


Fig. 27 Experimental results: **a** v_{pv} **b** i_{pv} , at irradiance 800 W/m^2 and module temperature 60°C in two-stage system

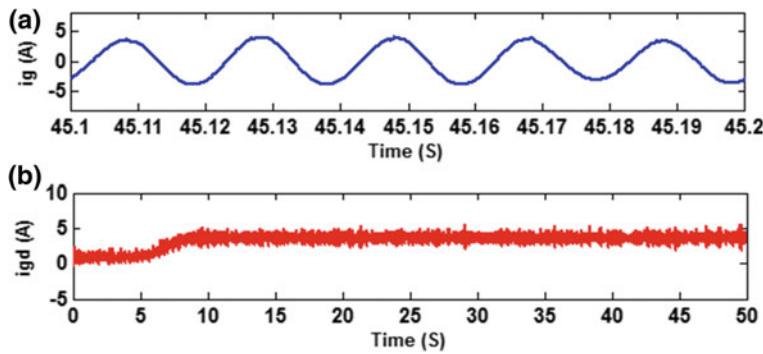


Fig. 28 Experimental results: i_g and i_{gd} at unity power factor in two-stage system

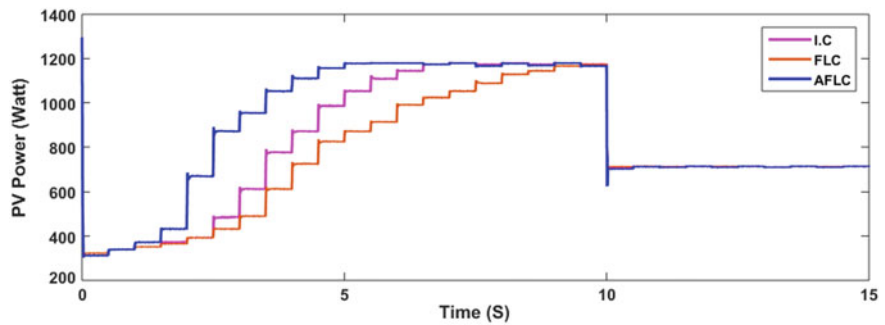


Fig. 29 Simulation results: p_{pv} using AFLC, FLC, and IC at different irradiance levels (1000 W/m^2 until 10 s, and 600 W/m^2 from 10 to 15 s) in two-stage system

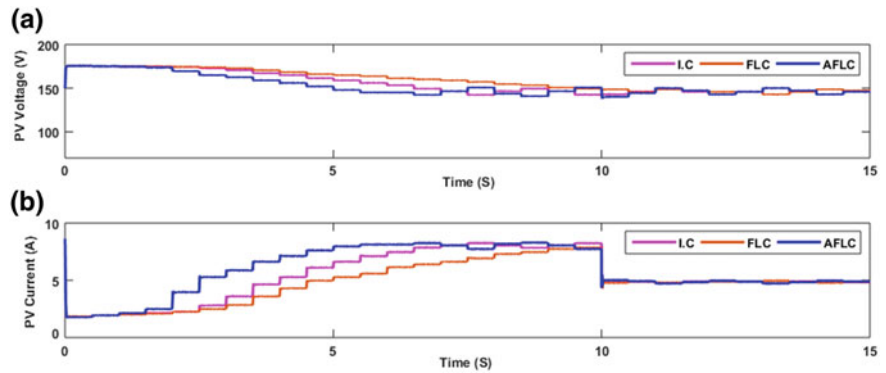


Fig. 30 Simulation results: **a** v_{pv} **b** i_{pv} , at different irradiance levels (1000 W/m^2 until 10 s, and 600 W/m^2 from 10 to 15 s) in two-stage system

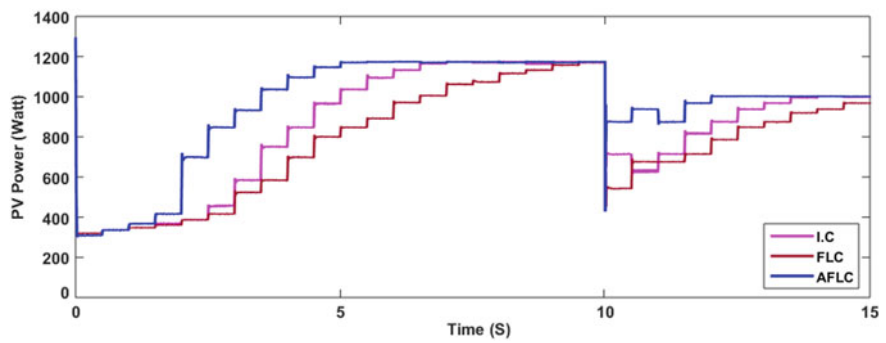


Fig. 31 Simulation results: p_{pv} using AFLC, FLC, and IC at different module temperatures (25°C until 10 s, and 60°C from 10 to 15 s) in two-stage system

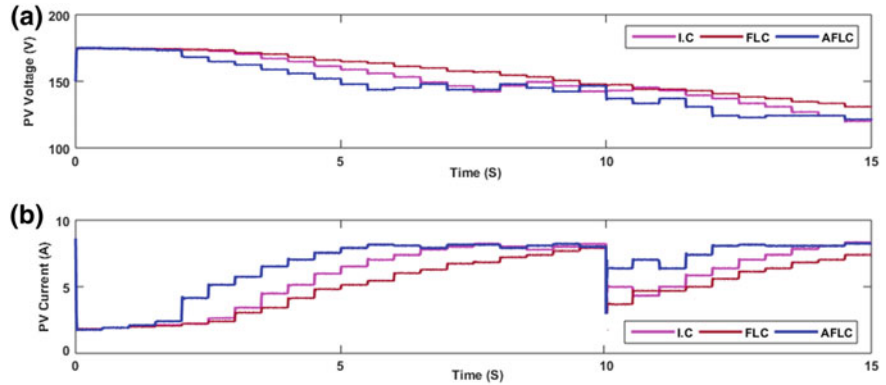


Fig. 32 Simulation results: **a** v_{pv} **b** i_{pv} , at different module temperatures (25°C until 10 s, and 60°C from 10 to 15 s) in two-stage system

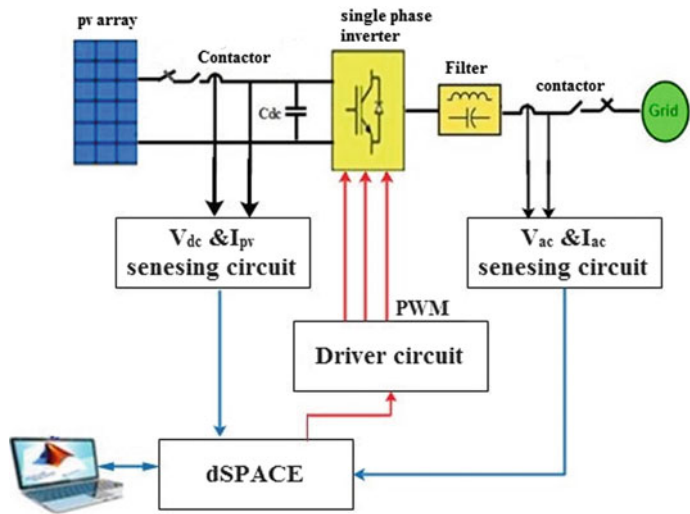


Fig. 33 Schematic circuit of single-stage single-phase grid-connected PV system

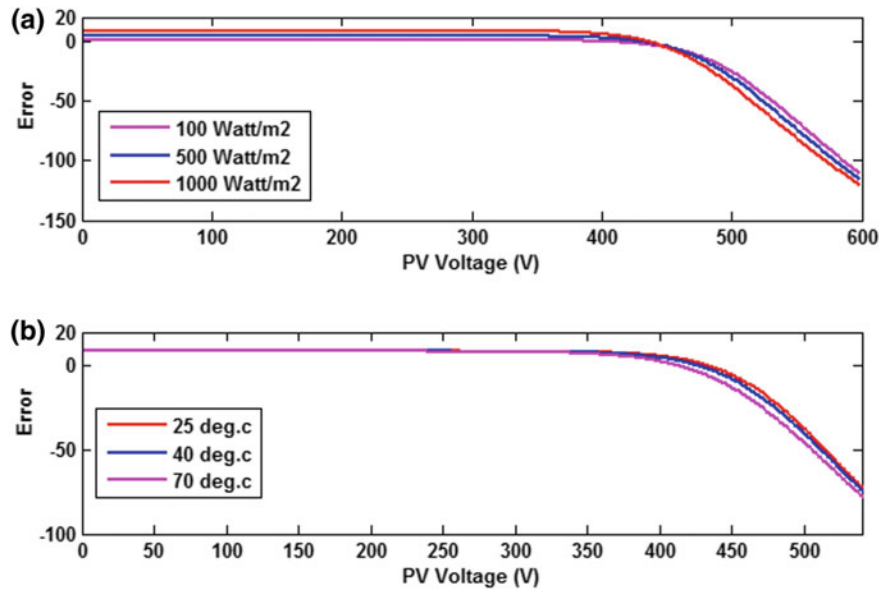


Fig. 34 e is plotted against v_{pv} in single-stage system **a** at different irradiance levels and module temperature 25 °C **b** at different module temperatures and irradiance 1000 W/m²

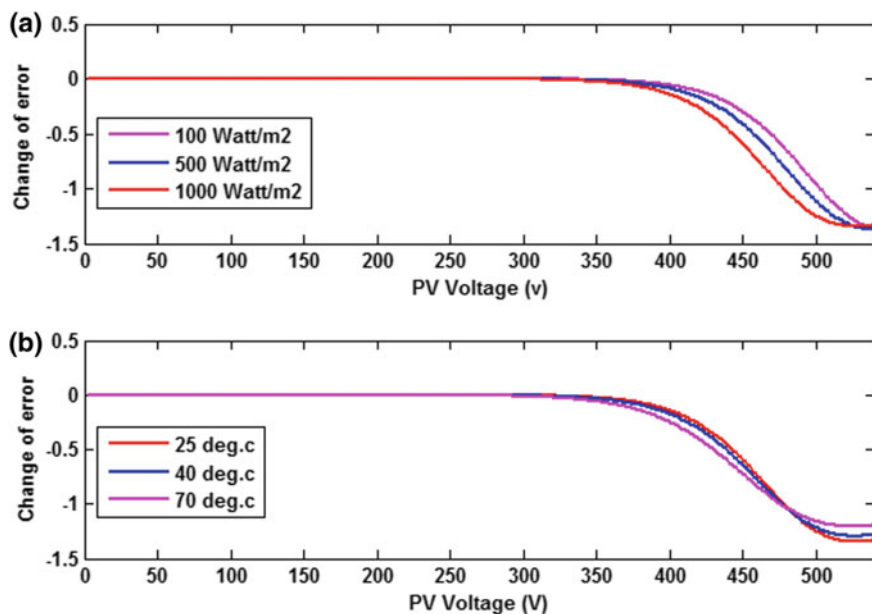


Fig. 35 Δe is plotted against v_{pv} in single-stage system **a** at different irradiance levels and module temperature 25 °C **b** at different module temperatures and irradiance 1000 W/m²

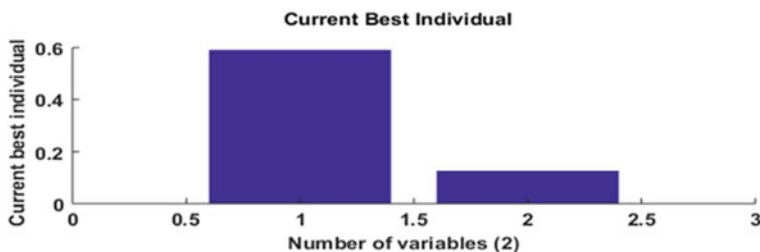


Fig. 36 Selected k_e and $k_{\Delta e}$ in single-stage system using genetic toolbox

algorithm is activated. This permits the algorithms to be tested in similar conditions (not the same). Solar radiation and module temperature are measured at this condition using. Solar radiation and module temperature are 800 W/m² and 60 °C.

Figures 37, 38, 39, 40, 41, 42, 43, and 44 show the simulation and the experimental results of the adaptive MPPT controller, FLC, and IC technique at irradiance 800 W/m² and module temperature 60 °C. Figure 25 shows the movement of the operating point on power–voltage curve of the PV array. It shows that the operating point moves from right-hand side of MPP and settles at the MPP. The results verify that the adaptive MPPT algorithm reaches the MPP faster than IC and FLC with acceptable dynamic response. Figure 45 shows i_g and i_{gd} when MPPT algorithm is activated.

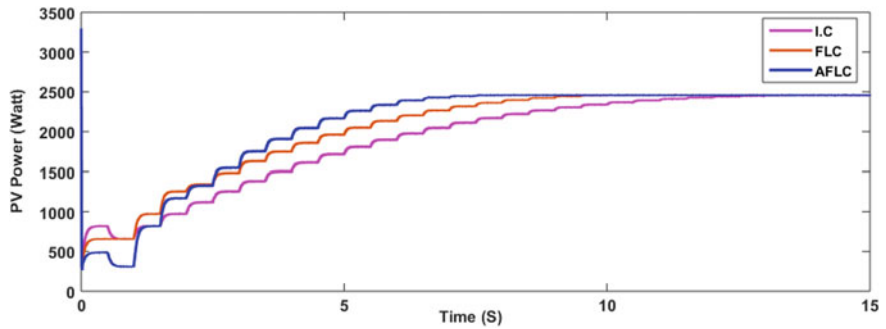


Fig. 37 Simulation results: p_{pv} using AFLC, FLC, and IC at irradiance 800 W/m^2 and module temperature 60°C in single-stage system

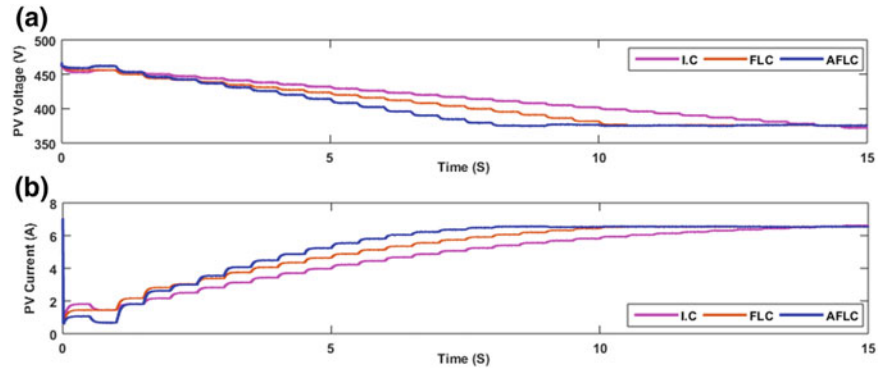


Fig. 38 Simulation results: **a** v_{pv} **b** i_{pv} , at irradiance 800 W/m^2 and module temperature 60°C in single-stage system

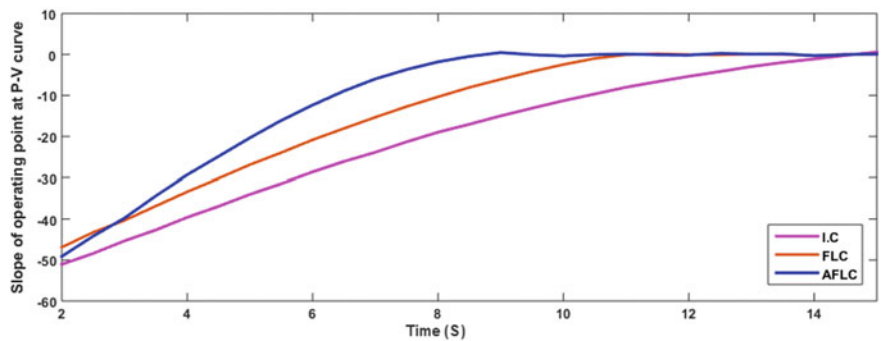


Fig. 39 Simulation results: slope of operating point on P - V curve at irradiance 800 W/m^2 and module temperature 60°C in single-stage system

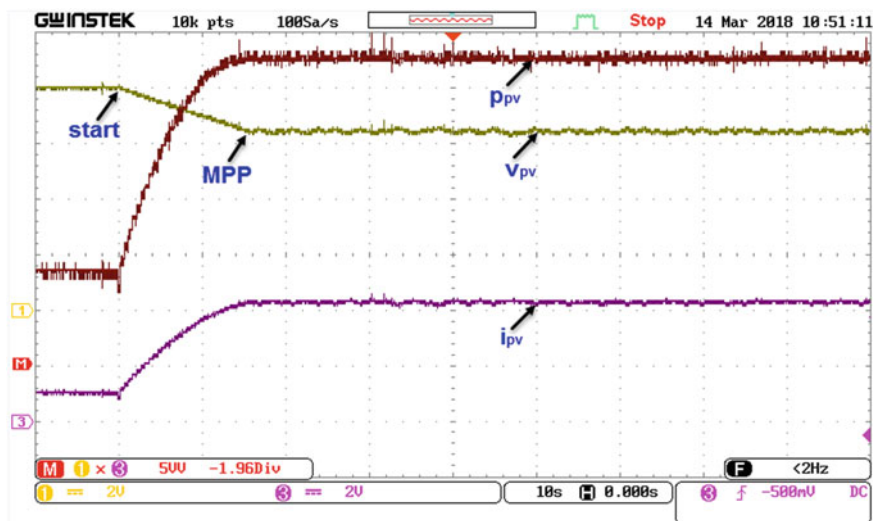


Fig. 40 Experimental results: **a** v_{pv} **b** i_{pv} , and p_{pv} using IC in single-stage system. Scale: 120 V/div, 3 A/div, 380 W/div

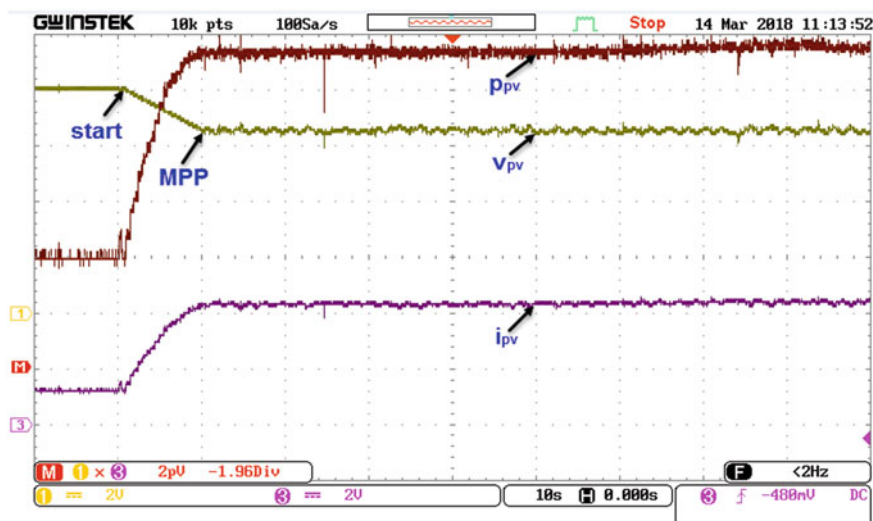


Fig. 41 Experimental results: **a** v_{pv} **b** i_{pv} , and p_{pv} using FLC in single-stage system. Scale: 120 V/div, 3 A/div, 380 W/div

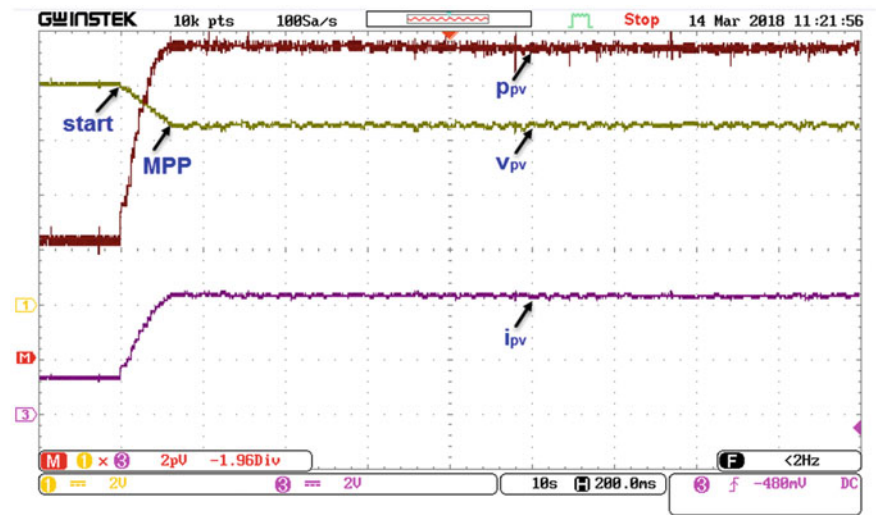


Fig. 42 Experimental results: **a** v_{pv} **b** i_{pv} , and p_{pv} using AFLC in single-stage system. Scale: 120 V/div, 3 A/div, 380 W/div

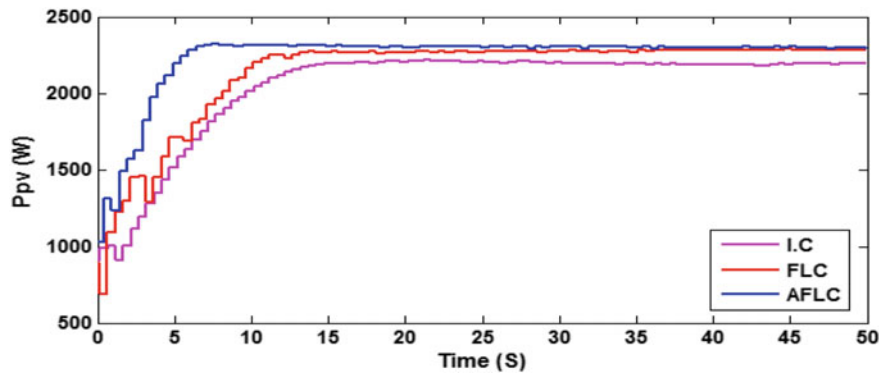


Fig. 43 Experimental results: comparison between the extracted PV powers using IC, FLC, and AFLC in the single-stage system at irradiance 800 W/m² and module temperature 60 °C in single-stage system

As mentioned before, the performance of proposed technique is tested at different conditions using simulation results. Figures 46, 47, 48, and 49 show the simulation results of the adaptive MPPT controller, FLC, and IC technique at different irradiance levels and different module temperatures. Simulation results show that the proposed MPPT technique has the superiority in tracking speed and reduction of output oscillations as anticipated.

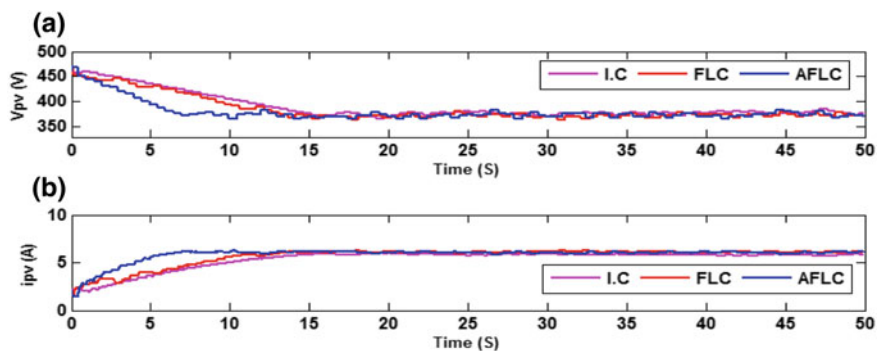


Fig. 44 Experimental results: **a** v_{pv} **b** i_{pv} , at irradiance 800 W/m^2 and module temperature 60°C in single-stage system

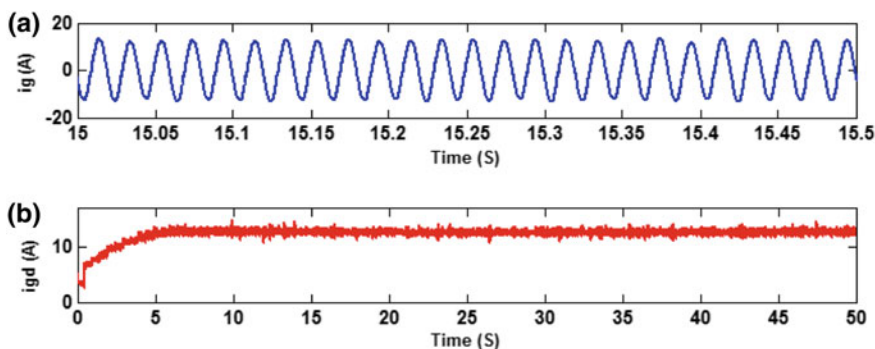


Fig. 45 Experimental results: i_g and i_{gd} at unity power factor in single-stage system

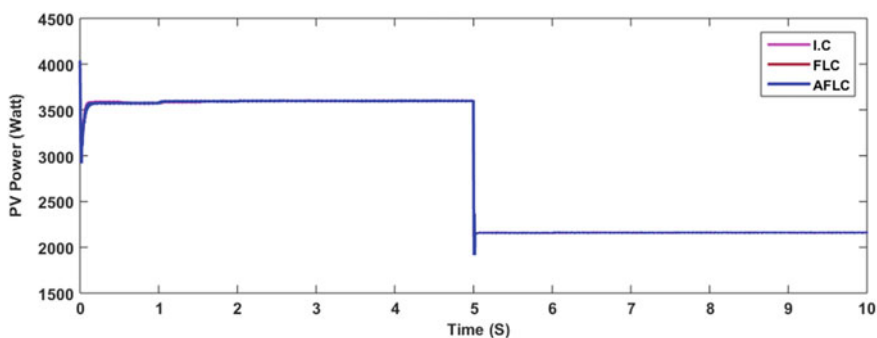


Fig. 46 p_{pv} using AFLC, FLC, and IC at different irradiance levels (1000 W/m^2 until 5 s, and 600 W/m^2 from 5 to 10 s)

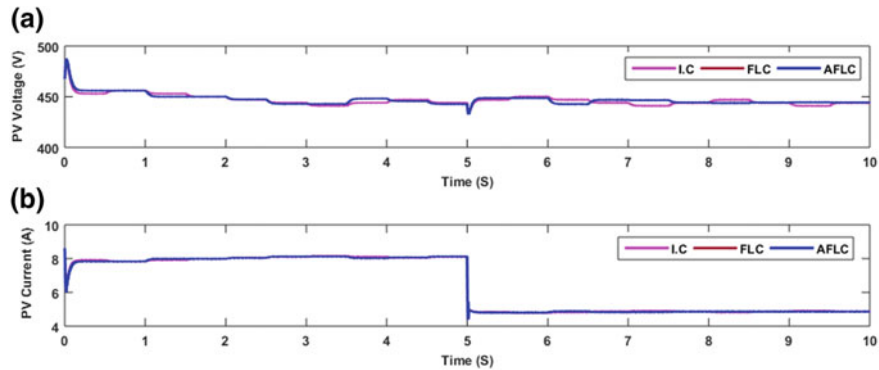


Fig. 47 **a** v_{pv} **b** i_{pv} , at different irradiance levels (1000 W/m^2 until 5 s, and 600 W/m^2 from 5 to 10 s) in single-stage system

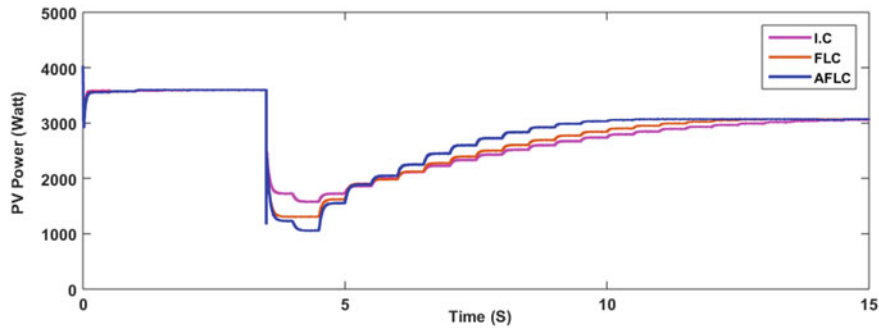


Fig. 48 p_{pv} using AFLC, FLC, and IC at different module temperatures (25°C until 3.5 s, and 60°C from 3.5 to 15 s) in single-stage system

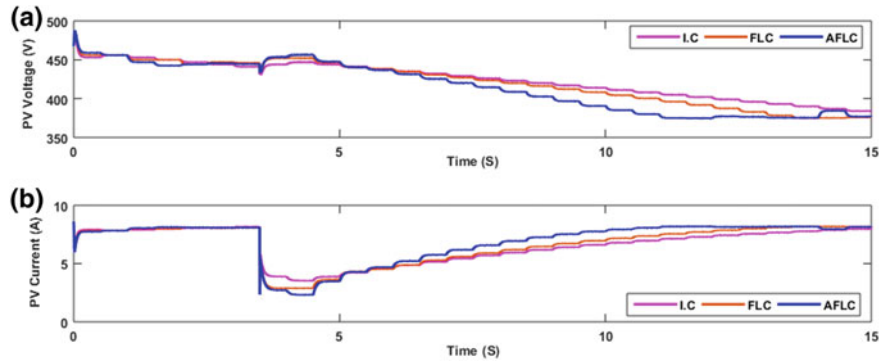


Fig. 49 **a** v_{pv} **b** i_{pv} , at different module temperatures (25°C until 3.5 s, and 60°C from 3.5 to 15 s) in single-stage system

7 Conclusion

In this chapter, AFLC as MPPT optimization technique applied to two-stage and single-stage configurations are presented. Moreover, it presents a simplified method to select the minimum step size and the minimum perturbation period for MPPT controller applied to grid-connected PV systems. It also introduces method to select the range of input variables of fuzzy system based on genetic algorithm.

The performance of AFLC was examined at different environmental conditions and was compared with FLC and fixed step IC in single-stage and two-stage systems. The simulation and experimental results showed that AFLC reached the MPP faster with low oscillations; hence, the efficiency is increased, the fluctuation in power decreases, and the output power quality of the system increases in single-stage and two-stage systems. They also demonstrated that FLC as MPPT technique needed an increase in the number of rules to improve the performance corresponds to a substantial increase in memory requirements and the program execution time. Further, MPPT-based FLC lacked the ability of self-tuning. The adaptive MPPT technique diminished the impact of input disturbances. Moreover, it was more robust and has a good performance in the training phase. The proposed MPPT technique reduced the rule base size and decreases the required memory and decreases the execution time.

The control of the grid-tied single-phase inverter in DQ-frame is designed. The experimental results show that the high quality of the current injected into the grid.

References

1. Subudhi B, Pradhan R (2013) A comparative study on maximum power point tracking techniques for photovoltaic power system. *IEEE Trans Sustain Energy* 4(1):89–98
2. Femia N, Petrone G, Spagnuolo G, Vitelli M (2005) Optimization of perturb and observe maximum power point tracking method. *IEEE Trans Power Electron* 20(4):963–973
3. Hussein KH, Mota I, Hoshino T, Osakada M (1995) Maximum photovoltaic power tracking: an algorithm for rapidly changing atmospheric conditions. *IET* 142(11):59–64
4. Elobaid LM, Abdelsalam AK, Zakzouk EE (2015) Artificial neural network-based photovoltaic maximum power point tracking techniques: a survey. *IET Renew Power Gener* 9(8):1043–1063
5. Mathew A, Selvakumar AI (2006) New MPPT for PV arrays using fuzzy controller in close cooperation with fuzzy cognitive network. *IEEE Trans Energy Convers* 21(3):793–803
6. Chiu C-S (2010) T-S fuzzy maximum power point tracking control of solar power generation systems. *IEEE Trans Energy Convers* 25(4):1123–1132
7. Senjyu T, Uezato K (1994) Maximum power point tracker using fuzzy control for photovoltaic arrays. In: *Proceedings of IEEE international conference on industrial technology*, pp 143–147
8. Kosko B (1997) *Fuzzy engineering*. Prentice Hall International, New Jersey, CA
9. Elshafei L, El-Metwally KA, Shaltout AA (2005) A variable-structure adaptive fuzzy-logic stabilizer for single and multi-machine power systems. *Control Eng Pract* 13:413–423
10. Won C-Y, Kim D-H, Kim S-C, Kim W-S, Kim H-S (1994) A new maximum power point tracker of photovoltaic arrays using fuzzy controller. In: *Proceedings of 25th annual IEEE power electronics specialists conference*, pp 396–403
11. Simoes MG, Franceschetti NN, Friedhofer M (1998) A fuzzy logic based photovoltaic peak power tracking control. In: *Proceedings of IEEE international symposium on industrial electronics*, pp 300–305

12. Patcharaprakiti N, Premrudeepreechacharn S (2002) Maximum power point tracking using adaptive fuzzy logic control for grid-connected photovoltaic system. In: IEEE power engineering society winter meeting, pp 372–377
13. Refaat MM, Atia Y, Sayed MM, Abdel Fattah HA (2017) Maximum power point tracking of photovoltaic system using adaptive fuzzy controller. In: Proceedings of the 5th international conference on advanced control circuits and systems (ACCS'017), Alexandria, Egypt
14. Ahmed A (2010) Power conditioning for small scale hybrid PV-wind generation system. Doctor of Philosophy's thesis. School of Engineering and Computing Sciences, 2010, Durham University, UK
15. Femia N, Petrone G, Spagnuolo G, Vitelli M (2013) Power electronics and control techniques for maximum energy harvesting in Photovoltaic systems. CRC Press, Boca Raton
16. Villalva MG, Ruppert EF, Filho ER (2009) Analysis and simulation of the P&O MPPT algorithm using a linearized PV array model. In: Proceedings of the 10th Brazilian, 2009, Bonito-Mato Grosso do Sul, Brazil
17. Refaat MM (2018) Maximum power point tracking for grid connected PV systems. Master of Science's thesis, 2018, Faculty of Engineering, Cairo university, Egypt
18. Deb SG (2012) Optimal sizing of a stand-alone solar-wind-battery-DG/biomass hybrid power system to meet the load demand of a typical village at Sagar Island using genetic algorithm. MSc thesis, 2012, Faculty of engineering and Technology, Jadavpur University, Kolkata, Indian
19. Hsu L, Costa R (1994) Analysis and design of I/O based variable structure adaptive control. IEEE Trans Autom Control 39(1)
20. Elshafei AL (2000) Adaptive fuzzy control of nonlinear systems via a variable-structure algorithm. In: IEEE international symposium on intelligent control, Vancouver, Canada
21. IEEE Application Guide for IEEE Std 1547™ (2003) IEEE standard for interconnecting distributed resources with electric power systems. The published standard is available from the IEEE Std 1547-2003 web page. (IEEE standard for interconnecting distributed resources with electric power systems, IEEE Std 1547-2003, pp 0_1–16)
22. Yazdani A, Iravani R (2010) Voltage sourced converters in power system. Wiley, London
23. Silva SM, Lopes BM, Filho BJ, Campana RP (2004) Performance evaluation of PLL algorithms for single phase grid-connected systems. In: Proceedings of the IEEE industry applications conference, Seattle, WA, USA
24. Yongheng Y, Blaabjerg F (2012) Synchronization in single-phase grid-connected photovoltaic systems under grid faults. In: Proceedings of the 3rd international symposium on power electronics for distributed generation systems (PEDG), Aalborg, Denmark
25. Crowhurst B, El-Saadany EF, El-Chaar L, Lamont LA (2010) Single-phase grid-tie inverter control using DQ transform for active and reactive load power compensation. In: Proceedings of the international conference on power and energy (PECon), 29 November–1 December 2010, Kuala Lumpur, Malaysia
26. Guo XQ, Wu WY, Gu HR (2001) Phase locked loop and synchronization methods for grid interfaced converters: a review. Przegląd Elektrotechniczny (Electr Rev) 87(4):182–187

Performance Improvement of Perturb and Observe Maximum Power Point Tracking Technique for Solar PV Applications



Ihechiluru Fortune Anya, Chitta Saha, Hafiz Ahmed, M. N. Huda
and Sujan Rajbhandari

Abstract The renewable energy market has increased significantly over the last decade, and the solar photovoltaic (PV) power generation is becoming important in many countries globally with a particular interest in the field of distributed electric power generation. A regular and accurate examination and evaluation of the photovoltaic system performance and efficiency are very essential in the sense that they provide vital information of the system's quality evaluation for the users, installers, as well as the manufacturers. The maximum power point of a solar panel varies with the irradiation and temperature and the control algorithms are commonly used for the maximization of the power extraction from PV arrays known as maximum power point tracking (MPPT) algorithms. Perturb and Observe (P&O) algorithm is one of the popular techniques frequently used due to its easy implementation and low cost. The MPPT technique is mainly used for obtaining the maximum power from the solar PV module and conversion circuit to the load and improving the power quality of PV power generation for grid connection. Perturb and Observe maximum power point tracking (MPPT) is extensively used in charge controllers for extracting maximum power from photovoltaic (PV) module irrespective of irradiance, temperature and load variation. The standard P&O MPPT technique has drawbacks bordering on fast convergence time to a maximum power point, poor system response to fast-changing irradiance and steady-state oscillation with a fixed step size. This chapter discusses the detailed operation and implementation of an improved P&O algorithm technique to resolve the various challenges of the standard P&O algorithm. This technique segments the operational region of the PV array into four operating sectors based on the sector location from the maximum power point (MPP), step size modifications are implemented. Furthermore, the critical comparison is made between the new P&O method and the standard P&O method. Finally, the hardware implementation

I. F. Anya (✉) · C. Saha · M. N. Huda · S. Rajbhandari

School of Computing, Electronics and Mathematics, Coventry University, Priory Street, Coventry CV1 5FB, UK

e-mail: anyai@uni.coventry.ac.uk

H. Ahmed

School of Mechanical, Aerospace and Automotive Engineering, Coventry University, Priory Street, Coventry CV1 5FB, UK

© Springer Nature Switzerland AG 2020

A. M. Eltamaly and A. Y. Abdelaziz (eds.), *Modern Maximum Power Point Tracking Techniques for Photovoltaic Energy Systems*, Green Energy and Technology, https://doi.org/10.1007/978-3-030-05578-3_10

283

of both MPPT algorithms is discussed in order to evaluate their performance and efficiency. The measured results show that the average efficiency of the proposed system is 96.89% which is more than 4% higher than the standard system.

Nomenclature

N_{pr}	Parallel connected strings
I	Solar PV output current
I_{sc}	Short circuit current (A)
V_{pv}	Output voltage of solar PV
MPPT	Maximum power point tracking
InCond.	Incremental conductance
P&O	Perturb and observe
q	Electron charge
FCIC	Fast-changing irradiance condition
UIC	Uniform irradiance condition
STC	Standard test conditions
N_{se}	Series connected strings
I_{PH}	Light-generated current
I_D	Diode saturation current
V_{oc}	Open circuit voltage (V)
A	Diode ideality factor
R_s	Series resistance
R_{sh}	Shunt resistance
G	Average solar irradiation
K	Boltzmann's constant
T	Cell temperature
BC	Boost converter

1 Introduction

The global investment in the solar power market has increased ten folds over the last decade, and the applications of the photovoltaic (PV) system are becoming important in many countries globally due to the decline in the cost of solar PV modules. However, the performance/efficiency of the PV still is one of the major challenges for researchers and usually depends on the PV module conversion efficiency and the installed site atmospheric condition. The performance is mostly influenced by both external and internal factors such as radiation, wind, electrical losses, structural features, pollution, visual losses, ageing, temperature and shading [1–4]. Solar PV demonstrate a nonlinear behaviour and possess a specific position on its characteristic PV curve where the cell extracts maximum power and functions at maximum

efficiency. Figure 1 shows a typical current–voltage (I–V) and power–voltage (P–V) characteristic curve of a solar PV.

The maximum power point tracking (MPPT) system is applied to facilitate the delivery of maximum power during the solar PV operation. It tracks the maximum power variations created by the variations in the atmospheric conditions and other contributing factors. The MPPT system is essentially a power electronic device introduced between the load and generating source (the solar PV array). The power electronics circuits are operated together with the control algorithm of the MPPT to achieve the extraction of maximum power. Presently, there are several MPPT techniques to extract MPP under uniform irradiance condition (UIC), fast-changing irradiance condition (FCIC) and partial shading condition (PSC). The maximum power generation of the solar PV system changes with variations in atmospheric condition, and this influences the electrical characteristics of the load. As a result, the internal impedance of the solar PV system is hardly matched to the impedance of the load. The main purpose of the MPPT is to match the impedance of the solar PV system to the impedance of the load by modifying the converter's duty cycle. Therefore, the MPP can be located notwithstanding the unpredictability of the solar PV characteristic curve [5–7]. There are several MPPT techniques that have been studied to track solar PV MPP. Significant research has been carried out over the last decade to extract maximum power from the solar PV system using different algorithm; For example, Eltamaly et al. in [32] compiled a comprehensive review of the most common and efficient MPPT techniques. This has been used to draw a comparative analysis with the proposed system. Authors in [8–10] presented various MPPT techniques covering different necessities according to cost, simplicity, the speed of convergence, tracking efficiency, sensor requirements, operation at steady state and hardware implementation. The performance of some MPPT techniques supersedes some others for similar operating conditions. Also, Karami et al. and

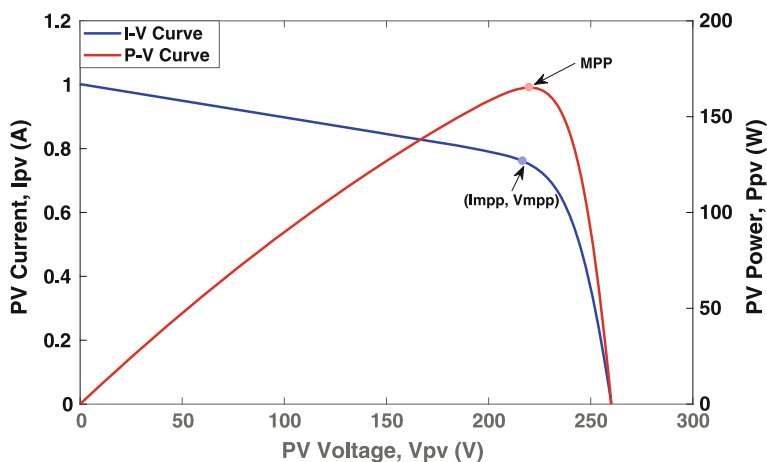


Fig. 1 I–V and P–V characteristic curves

Ezinwanne et al. in [11, 12] analysed and conducted a review of energy performance and cost comparison of MPPT techniques, and they found that the hybrid MPPT which is a combination of MPPT techniques is more beneficial compared to a single MPPT technique. This would mitigate noise from the extracted power in the event of low irradiance conditions and PSC. The tracking efficiency, dynamic response and steady-state operation of the system are critical areas to be taken into account for a successful MPPT control design when assessing the performance of the modified MPPT system. The MPP needs to be tracked rapidly under UIC, FCIC and PSC. The system tracking efficiency is crucial to assess the success of the MPPT process as it measures the ratio of actual power extracted from the solar PV to the expected theoretical power expected for a particular period. Equation (1) is implemented to evaluate the tracking efficiency of the solar PV system [31];

$$\eta = \frac{1}{s} \sum_i^s \frac{P_{\text{real},i}}{P_{\text{max},i}} \quad (1)$$

where P_{real} is the i th sample of the power measured during solar PV MPPT implementation, P_{max} is the i th sample of the true power expected from the solar PV under given atmospheric conditions and s being the complete number of samples. A faster tracking speed leads to a lower loss in the solar PV system. Once the MPP has been achieved, the MPPT control algorithm needs to maintain constant operation at this point for the required period. However, this is practically unachievable due to the nature of the perturbation of MPPT algorithms. Nonetheless, the steady-state error has to be to the barest minimum [13].

According to the MPPT algorithm classification, there are direct and indirect MPPT techniques. P&O and IC are known as a direct method, and they can be implemented using the system information at a particular period to achieve the MPP [14–18]. The indirect methods (fuzzy logic control, fractional short circuit current, fractional open circuit voltage, etc.) rely on the parameters of the system [19, 20]. The Perturb and Observe (P&O) method is the most ubiquitous when compared with other methods as a result of its simple operation and low-cost implementation due to the low number of sensors required. Some MPPT methods such as self-oscillation (SO) method, extremum seeking (ES) control, incremental conductance (IC) are derived from P&O technique with variations in the implementation of perturbation or the variable observed. The first P&O MPPT implementation dates back to the 1970s when it was employed for aerospace applications. It has evolved overtime and is presently popular for MPPT. The P&O MPPT technique exists in two configurations; the duty cycle perturbation where the converter operates in open loop after each perturbation and reference voltage perturbation where the converter is equipped with a feedback voltage loop [34]. The P&O MPPT is dependent on the step size. The standard P&O MPPT implements a specific step size. So with the application of a large specific step size, MPP is achieved fast but high steady-state oscillations occur. With the application of a small specific step size, it takes longer time to achieve MPP causing power loss and low steady-state oscillations. Also, with FCIC, the standard P&O

MPPT underperforms with respect to tracking the MPP. Studies have been carried out drawing comparisons between perturbation of voltage and the duty cycle. It has been deduced that with a high rate of voltage perturbation, the system may have poor stability but possesses a faster dynamic response and in comparison, duty cycle displays better stability with poor performance under FCIC [21, 22]. Ahmed et al. proposed a modified P&O MPPT algorithm to decrease the steady-state error and to prevent the loss of direction during tracking. Their technique is further verified with experimental results and the measured results show a 1.1% improvement in tracking efficiency on the standard P&O MPPT for slow irradiance change and 12% for FCIC. However, the system response was almost similar to the standard P&O MPPT showing no improvement [27]. Ahmed and Salam proposed an improved P&O MPPT algorithm that implements a special control mechanism to change the perturbation size around MPP to reduce the steady-state oscillation. It delivers a 2% improvement in tracking efficiency in comparison with the standard P&O MPPT. However, the system requires long computational time that impacts the response of the controller. Therefore, impeding it from improving the efficiency any further [23]. In [24], a modified P&O control algorithm has been implemented for a hybrid PV and wind system. The MPPT algorithm tracks power for both generating sources, however, the tracking loop experiences large noise and the system has a significant steady-state error which does not aid efficient system operation. In [25], an improved version of P&O MPPT with a checking algorithm has been proposed. It drastically reduces the dynamic response of the system, and however, there is a spike before the power settles at MPP. Also, the perturbation of the duty cycle was high resulting in poor performance under FCIC. Ghassami et al. present a modified P&O MPPT algorithm to improve the system operation under FCIC. It implements the I-V characteristic curve to distinguish the shifting point of operation from the environmental change. The response of the standard P&O MPPT under FCIC is considerably improved on however, high steady-state oscillations exist which creates power loss to counter power loss prevented from an improved response time [26].

The evolution of the perturbation process has given rise to another MPPT approach known as particle swarm optimization (PSO). PSO utilizes low-cost digital controllers and performs well under extreme test conditions [34]. Authors in [35] have demonstrated a hybrid implementation of PSO to track the MPP when the PV module is influenced by partial shading. This implementation combines fuzzy logic control with PSO to properly track the global maximum power point in the system. Fuzzy logic control (FLC) is another recent MPPT technique which does not need any technical knowledge for the PV system, and it is known to perform efficiently for fast-changing test conditions. Artificial neural network(ANN) technique is an intelligent MPPT approach to resolve nonlinear PV characteristic curve. These recent MPPT approaches have their benefits and drawbacks. The P&O has an easy construction and implementation; however, it experiences oscillations during steady-state operation. The IC is better responsive to FCIC than the conventional P&O, it is also accurate. However, this accuracy depends on the size of the increments. In comparison with the recent approaches, PSO has a larger optimization potential that can be achieved in a less complex fashion. However, it can experience partial optimism that could

influence its speed and direction control. FLC is a robust, rapid MPPT approach that yields better stability during various conditions. However, it is expensive, highly complex and its efficiency is reliant on the accuracy of the rules. The ANN approach can be in various forms. It displays fast tracking speed and yields better stability during various conditions. It is also expensive, highly complex and needs a broad and extensive information about the solar PV parameters.

In this chapter, an improved efficient variable step P&O algorithm is proposed to improve system dynamic response, decrease the steady-state oscillations and improve the system behaviour during FCIC. This method involves the segmentation of the PV array characteristic curve into different operating segments. As a result of this segmentation, the system is subject to step size modifications based on the segment location from MPP. If the operating point is far from the MPP, large step voltage size is employed for the perturbation of reference voltage to improve the system response, and on the other hand, small step voltage size is employed with the operating point near the MPP. This algorithm presents a fast and stable MPPT technique, which tracks the MPP at various atmospheric conditions with a low number of sensors. The proposed system is simulated on the MATLAB/Simulink environment, and the simulated results are verified with experimental results using the laboratory scale solar emulator system.

2 System Configurations

The solar PV system has the PV cell as its basic constituent. PV cells are connected in series and/or parallel into what is called a PV module, and PV modules are wired in series and/or parallel to build a PV Array. The I - V relationship is as given by [28];

$$I = N_{pr} I_{PH} - N_{pr} I_D \left[\exp \left(\frac{q \{ V_{pv} + I R_s \}}{N_{sc} K A T} \right) - 1 \right] - \frac{V_{pv} + I R_s}{R_{sh}} \quad (2)$$

where the parameters are described under the nomenclature. The irradiance, G and temperature, T influence the light-generated current, I_{PH} .

$$V_{out} = \frac{V_{pv}}{1 - D} \quad (3)$$

In [28], the interrelation of subsidiary parameters to the parameters in Eq. (2) has been fully expressed. See Table 1 for solar PV output characteristics for the standard test conditions (STC). The STC of a photovoltaic module is a test performed at irradiation of 1000 W/m^2 , a temperature of 25°C and an air mass of 1.5 (which is the equivalent for Europe) in order to have a uniform test condition of the PV modules thereby making it possible in conducting uniform comparison with PV modules made by different manufacturers. Figures 2 and 3 demonstrate the solar I - V and P - V characteristic with the variation of irradiation and temperature. As stated, the

Table 1 Solar PV module characteristics

Maximum power	165 W
Voltage at maximum power	220 V
Current at maximum power	0.75 A
Open circuit voltage	260 V
Short circuit current	1 A

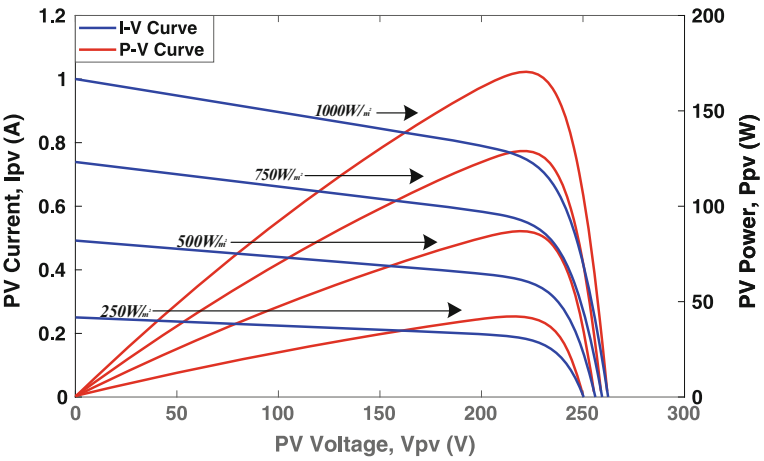


Fig. 2 Solar I – V and P – V characteristic curves for irradiation variation at 25 °C

DC/DC converter (boost converter) serves as an interface between the solar PV and the load. It steps up the voltage, V_{pv} from the solar PV to an output, according to Eq. (3) based on the duty cycle, D which is set to 0 for an open switch and 1 for a closed switch.

3 P&O MPPT Algorithms

The definition of the standard P&O MPPT algorithm clearly indicates that the output power variation at the peak point of the P–V characteristic curve would be zero ($\Delta P_{pv} = 0$). The algorithm functions by performing perturbation (rising and declining) at the voltage of the solar PV and evaluates the resulting power $P_{(n)}$ to the initial power before perturbation $P_{(n-1)}$. During the observation, if there is an increase in the solar PV power ($\Delta P_{pv} > 0$) after perturbation, the process of perturbation should continue in the same direction else transposed to the reverse. The process of perturbation is performed recurrently until MPP is achieved at ($\Delta P_{pv} = 0$). The standard P&O algorithm can be implemented where a reference voltage, V_{ref} is essentially the tool for perturbation. The V_{ref} is compared with V_{pv} and an error signal is achieved. This is fed to a proportional integral (PI) controller which appropriately determines

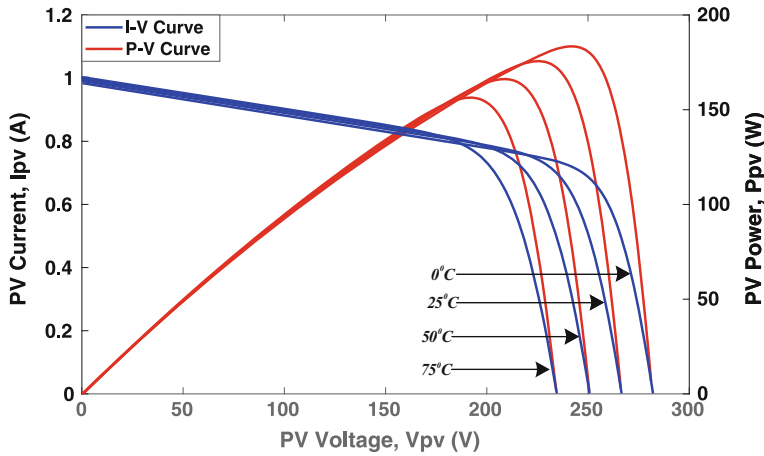


Fig. 3 Solar I – V and P – V characteristic curves for temperature variation at 1000 W/m^2

the proportional gain, (K_p) and integral gain, (K_i) to deliver a desired response. Once the PV output power is fed to the boost converter, PI controller functions by regulating the duty cycle. Also, the duty cycle can be the perturbation tool, and the power can be observed and computed at every pulse width modulation (PWM) cycle [29].

The step size determines the amplitude of steady-state oscillations at the MPP, and the standard P&O algorithm is typically implemented using a fixed step size. For a small step size, there is a trade-off as the steady-state oscillations are at the barest minimum, but the dynamic response of the system to achieve MPP is slow and a longer time is taken to achieve MPP. Alternatively, a large step size increases the response of the system to achieve MPP and less time is taken to achieve MPP. However, there is a considerable increase in the steady-state oscillation [21, 22].

The proposed P&O algorithm splits the P – V characteristic curve operational region into four segments as exhibited in Fig. 4. This permits the implementation of variable step size depending on the distance between the operating point and the MPP. With a long distance from the MPP (segments 1 and 4), a large step size is implemented to decrease the response time and cause less time to be taken to achieve MPP. With a close distance to the MPP (segments 2 and 3), a small step size is implemented to lessen the steady-state oscillations at the MPP. Figure 5 illustrates the flow diagram for the proposed P&O algorithm. This approach eliminates the high steady-state oscillation accompanied with a large step size, and it mitigates the poor response of the system which creates a longer period to track the MPP due to a small step size. It is also an efficient tracking during FCIC.

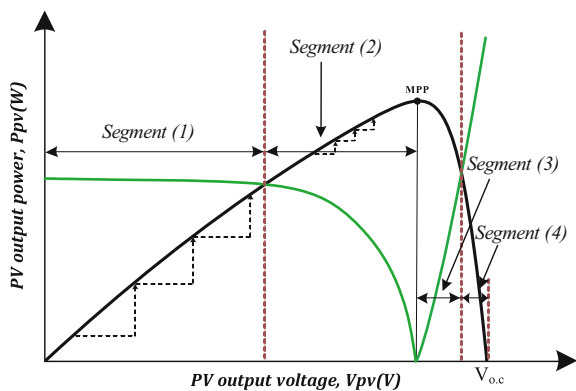


Fig. 4 Proposed P&O MPPT concept

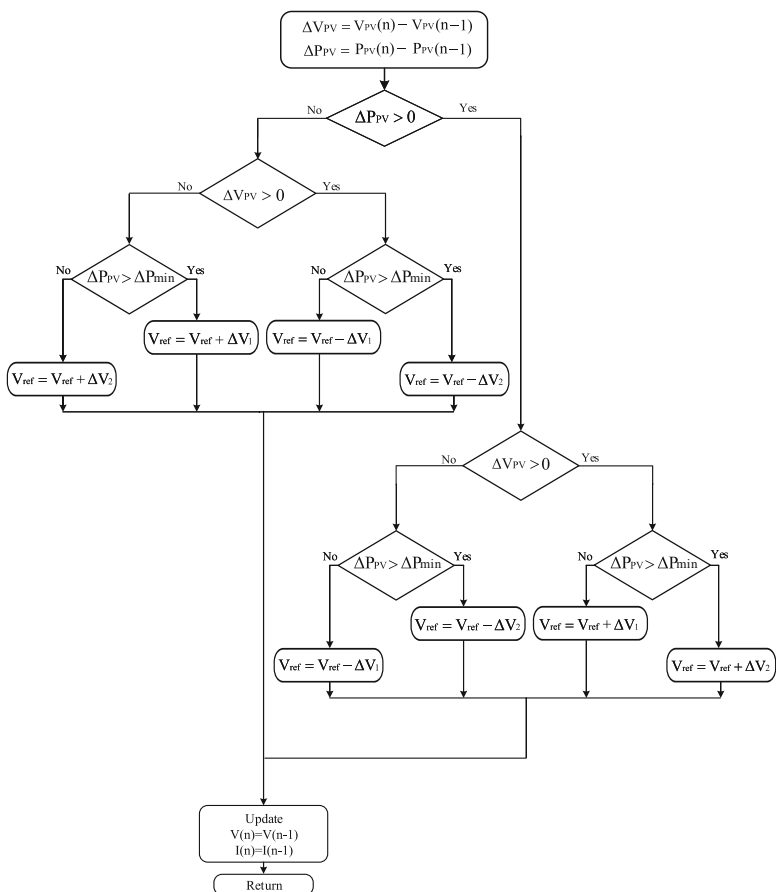


Fig. 5 Flow diagram of the proposed P&O MPPT algorithm

4 Simulation and Experiment

A stand-alone solar PV system of the proposed system is simulated in the MATLAB/Simulink environment to evaluate the performance. This comprises of a boost converter placed in between solar PV array and resistance to serve as a load. A MOSFET gate signal controls the converter with a switching frequency of 10 kHz. 100 μf capacitor and 3 mH inductor rating were used for filtering. The large step size of 0.01 and small step size of 0.0001 have been implemented for the P&O procedure. For stable operation, these parameters have been achieved from the evaluation of the boost converter topology based on the system power specifications.

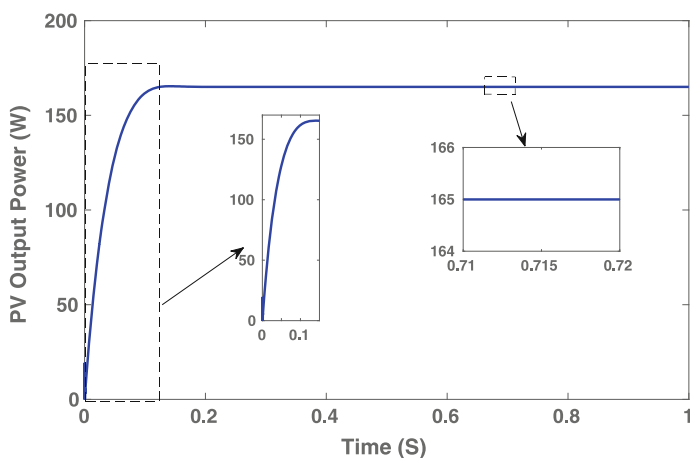


Fig. 6 Output power for small step size standard P&O system

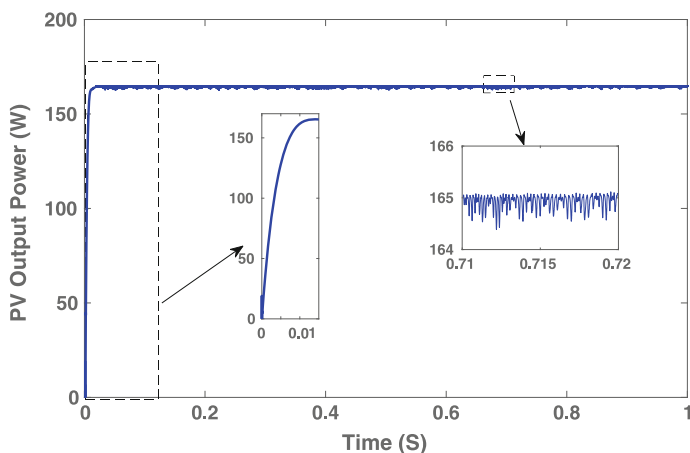


Fig. 7 Output power for large step size standard P&O system

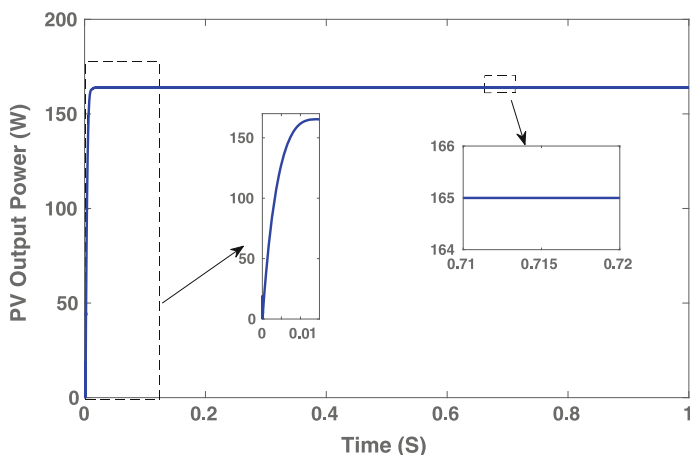


Fig. 8 Output power for proposed P&O system

To verify the performance of the proposed system over the standard system, a rigorous profile of extreme atmospheric conditions were considered. Firstly, tests were performed based on the standard and proposed P&O MPPT under STC for UIC.

Further tests were performed on step changing irradiance and FCIC under the standard temperature of 25 °C. The step changing irradiance profile is illustrated in Fig. 9, and the FCIC is as illustrated in Fig. 13 [30, 31]. The tests were carried out for 1 s duration. Figure 6 illustrates the solar PV output power for a small step size under UIC. The results display no oscillations at the MPP. However, the system MPP tracking performance is poor as it takes 100 ms to achieve MPP. Figure 7 illustrates the solar PV output power for a large step size under UIC. From the zoomed areas, it displays improved MPP tracking performance with a response time under 10 ms to achieve MPP. However, large steady-state oscillations exist around the MPP with a peak difference of 1 W which eventually influences the solar PV output power. Figure 8 illustrates the solar PV output power for the proposed system under UIC. It is evident from the zoomed areas that the proposed system improves the time to reach MPP and minimizes the steady-state oscillations. Thus, bringing together the benefits of small and large step size systems and improving on their shortcomings.

The results of the test performed under the step changing irradiance profile on the small step size and large step size standard and the proposed P&O MPPT systems are illustrated in Figs. 10, 11 and 12. The small step size system takes a longer time to achieve MPP for the different irradiances. For 250 W/m², it takes 30 ms to settle at an MPP of 44.64 W. To get to 750 W/m², it takes 90 ms to settle at MPP. To get to 1000 W/m², it takes 100 ms to settle at MPP. In the same way, the large step size system has a better tracking ability and achieves MPP in less time.

However, it displays high steady-state oscillations with a peak difference of 1 W. The proposed system as illustrated in Fig. 12 improves the time to track MPP and

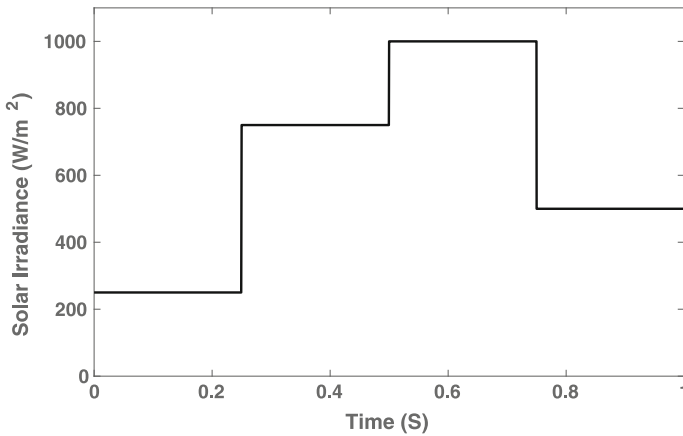


Fig. 9 Step changing irradiance profile [30]

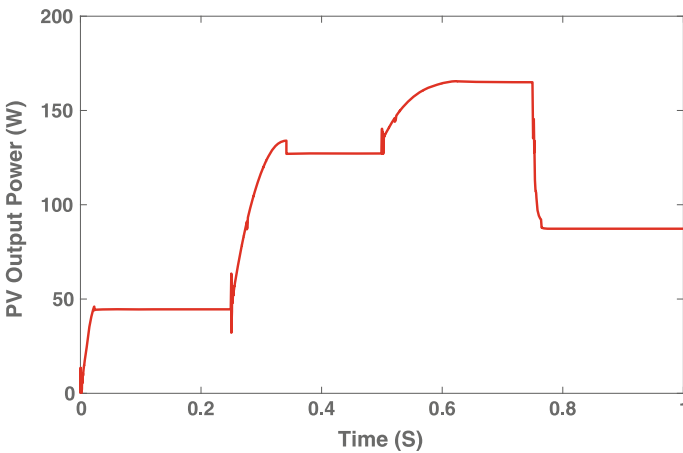


Fig. 10 Output power for small step size standard P&O system under step changing Irradiance

minimizes the steady-state oscillations. It clearly combines the advantages of small and large step size systems and prevents the disadvantages attached to them.

Figure 14 illustrates the comparison between the theoretical results of solar PV output power standard P&O and proposed P&O MPPT techniques. It clearly indicates that the proposed system performs better than the standard one. The standard system performs poorly for decreasing solar irradiance when the solar irradiance drop is steep. This is typical as the standard system loses direction when tracking MPP for FCIC. This poor performance is corrected with the proposed system (Fig. 13).

Figure 15 illustrates the tracking efficiency of the standard and the proposed P&O system for the solar irradiance profile in Fig. 13 and this is calculated using Eq. (1). From the result in Fig. 15, the proposed system is more efficient. The average

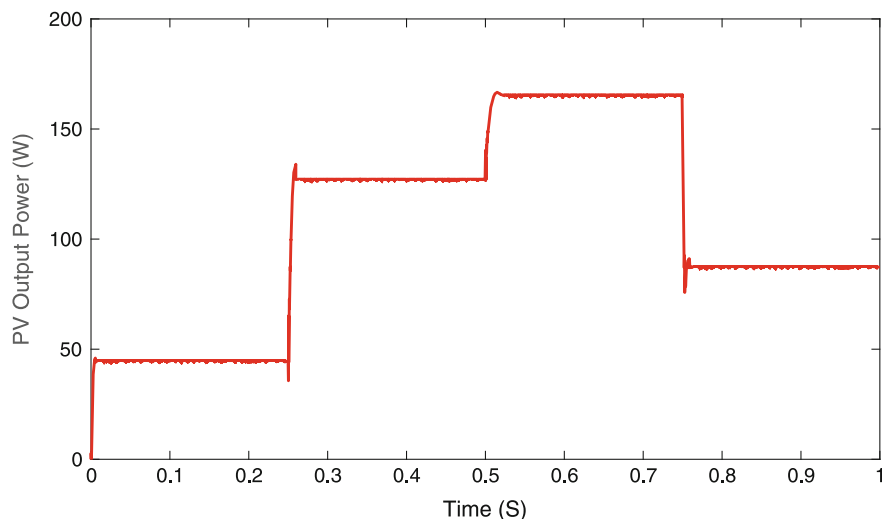


Fig. 11 Output power for large step size standard P&O system under step changing irradiance

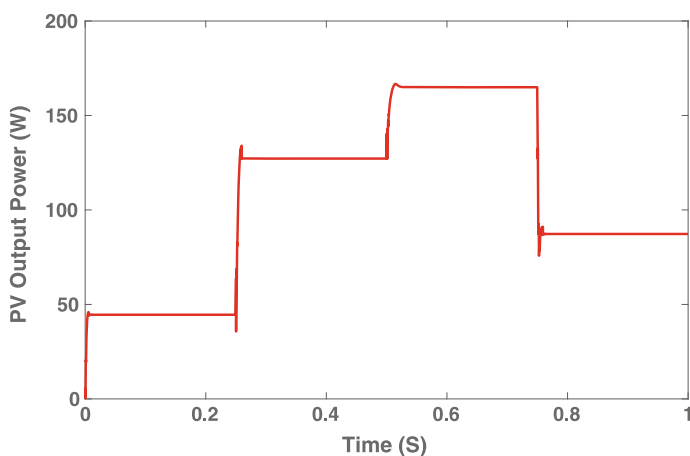


Fig. 12 Output power for proposed P&O system under step changing irradiance

efficiency for the standard system is 92.55% and that of the proposed system is 96.89%. There is, therefore, an improvement of over 4% (Table 2).

The performance of the standard P&O MPPT algorithm and the proposed P&O MPPT algorithm was experimentally evaluated. Figure 16 shows the system set-up for the experimental implementation of the solar PV system. The test bench comprises of a digitally controlled HV solar MPPT DC-DC converter using texas instrument C2000 piccolo microcontroller unit (MCU), current and voltage sensors, PV power supply unit, digital oscilloscope, resistive load and a computer for MPPT

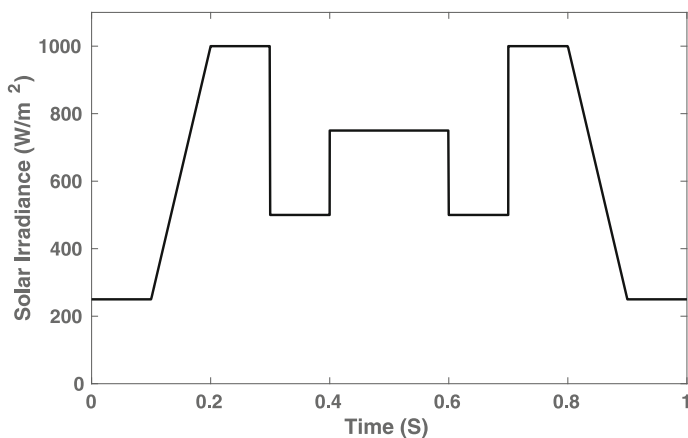


Fig. 13 Fast-changing irradiance profile [31]

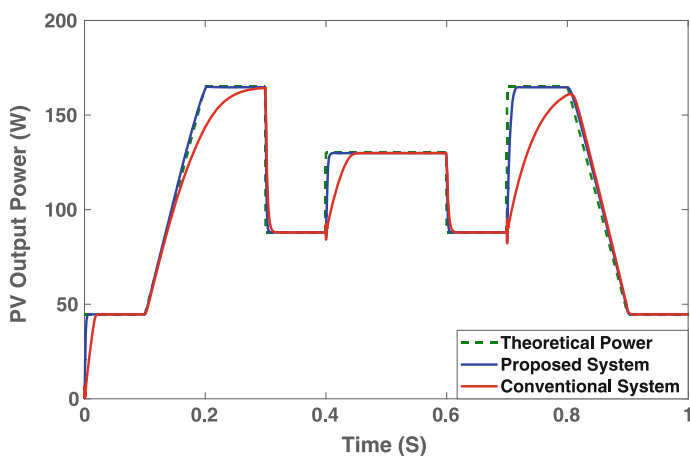


Fig. 14 Solar PV output power under step changing irradiance

implementation. For the duration of UIC, the PV power supply unit provides uniform irradiance at a set percentage equivalent to 1000 W/m^2 . The PV panel output voltage and current are measured and then the measured values are used to compute the required power by the MPPT algorithm. V_{pv} is applied to the boost controller of the MCU; the hardware is regulated by the MCU by implementing four PWM outputs and three feedback signals. The feedback signals implement the control loops of the voltage and current for the boost controller. The PV panel provides an output voltage of 220 V with an output current of 0.75 A , and the boost controller produces an output voltage of approximately 403 V . The switch PWM signals minimize the ripple in the PV panel current. The MPPT algorithm is responsible for determining a set reference V_{pv_ref} for the V_{pv} by implementing a control system to regulate V_{pv} .

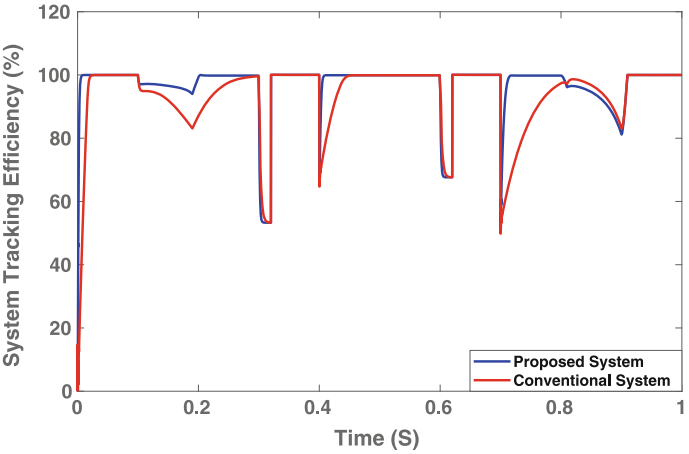


Fig. 15 Solar PV tracking efficiency

Table 2 Comparative analysis of P&O MPPT techniques

Evaluated parameters	Proposed method	[33]	[15]	[14]	[27]
Set-up	Stand-alone PV	Stand-alone PV	Stand-alone PV	Stand-alone PV	Stand-alone PV
Converter	Boost	Buck-boost	Boost	Boost	Buck-boost
Tracking method	Variable step size based on engendered curve	Fixed step size	Variable step size	Confined search space	Adaptive step size
Application	UIC and FCIC	Ramp profile	Step profile	UIC and FCIC	FCIC
Simulation or experiment	Both	Simulation	Simulation	Both	Both
Conclusions	Improved efficiency for UIC and FCIC	Poor performance at low irradiance	Steady-state oscillation reduced but displays poor initial response	Reduced response time, improved steady-state operation	Improved steady-state operation and efficiency for FCIC

when it goes over or under the V_{pv_ref} . The resistive load is connected to the output of the boost converter and draws a current of 0.41 A. Another test is also performed on step changing irradiance and the results are as illustrated in Figs. 17, 18 and 19.

In Figs. 17 and 18, the results for the hardware implemented PV system can be seen under UIC. This shows that the P&O gets to the appropriate MPP which is 165 W. The proposed P&O system has a tracking ability that is better than that of the standard P&O system as the standard P&O system takes 0.5 s to achieve MPP

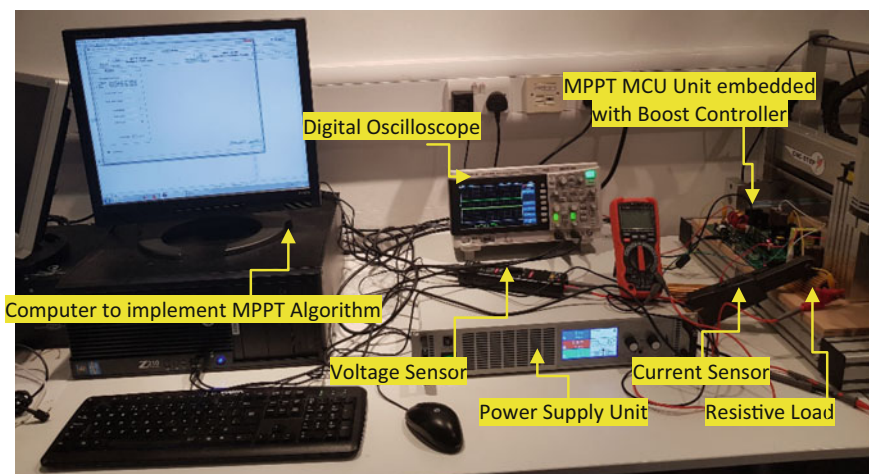


Fig. 16 MPPT hardware implementation set-up

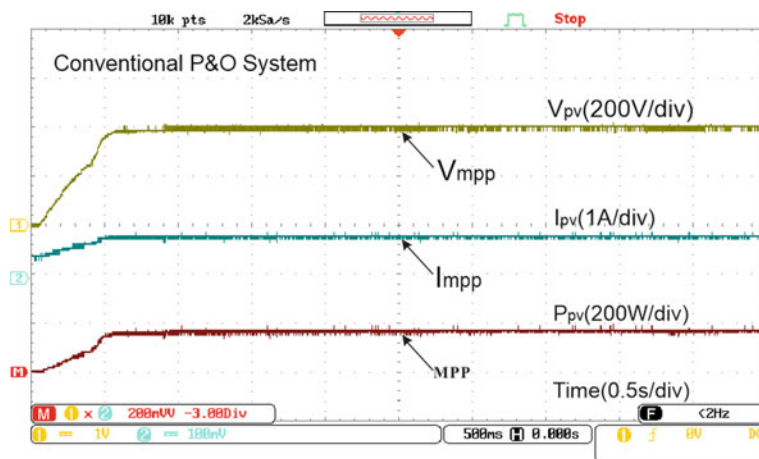


Fig. 17 Measured waveforms (V_{pv} , I_{pv} , P_{pv}) versus time for standard P&O MPPT under UIC

as against 0.02 s by the proposed P&O system. Figure 19 illustrates the tracking ability of the proposed P&O system under step changing irradiance. This has been achieved by varying the irradiance from 1000 to 500 W/m² to 1000 W/m². From the results, the system performs properly as it tracks the MPP of 88 W at 500 W/m² and is capable of regaining the original MPP of 165 W at 1000 W/m².

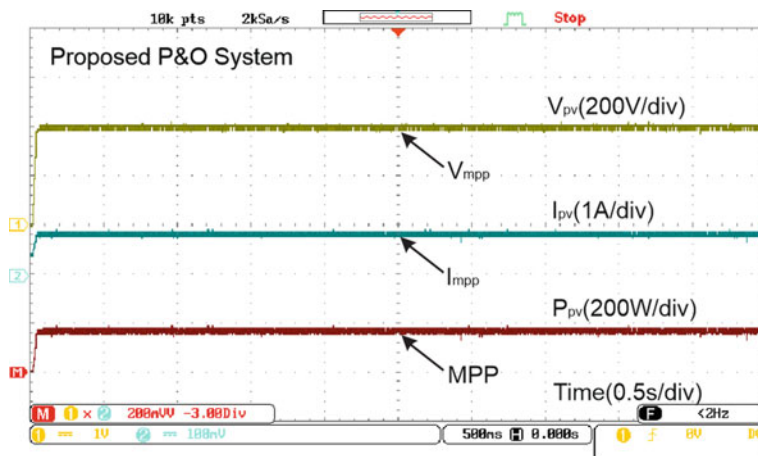


Fig. 18 Measured waveforms (V_{pv} , I_{pv} , P_{pv}) versus time for proposed P&O MPPT under UIC

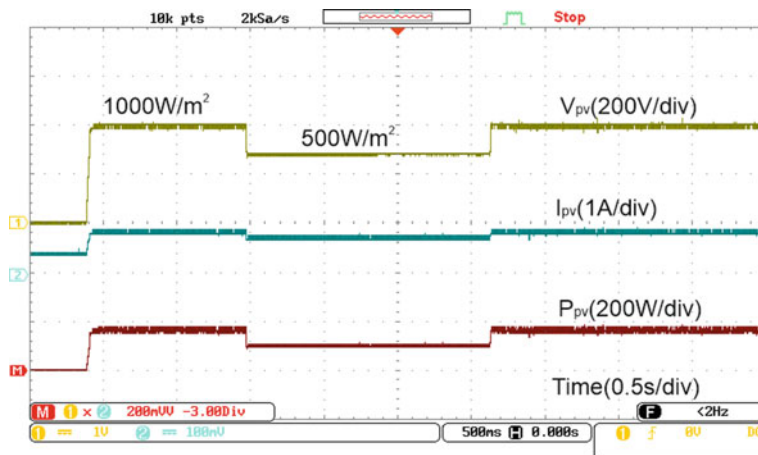


Fig. 19 Measured waveforms (V_{pv} , I_{pv} , P_{pv}) versus time for proposed P&O MPPT under step changing irradiance

5 Conclusions

In this chapter, an improved P&O algorithm has been presented that enhances the MPPT dynamic response, MPPT performance and decreases the steady-state oscillations at the MPP of a solar PV system and improves its behaviour during certain atmospheric conditions. This system splits the P–V characteristic curve into segments and carries out a multi-segment variable size control system of variation of the voltage step size. The proposed algorithm is simulated on MATLAB/Simulink and experimented with a laboratory scale solar development system. The tracking efficiency

of the proposed system, as well as its performance, are evaluated with the standard P&O system. The simulation and measured results show a significant improvement on the dynamic response as well as the steady-state oscillations. Ultimately, this technique improves the overall system efficiency compared to the standard system under various atmospheric conditions.

References

1. United Nations Environment Programme [Ed.] Frankfurt School of Finance and Management and Bloomberg New Energy (2006) Global trends in renewable energy investment, p 84
2. Said SAM, Hassan G, Walwil HM, Al-Aqeeli N (2018) The effect of environmental factors and dust accumulation on photovoltaic modules and dust-accumulation mitigation strategies. *Renew Sustain Energy Rev* 82:743–760
3. Verma S, Verma HK (2013) Modeling & analysis of standalone photovoltaic system, no 2, pp 259–265
4. Sulaiman SA, Singh AK, Mokhtar MMM, Bou-Rabee MA (2014) Influence of dirt accumulation on performance of PV panels. *Energy Procedia* 50:50–56
5. Enrique JM, Andújar JM, Bohó Rquez MA (2009) A reliable, fast and low cost maximum power point tracker for photovoltaic applications. *Sol Energy* 84:79–89
6. Liu L, Meng X, Liu C (2015) A review of maximum power point tracking methods of PV power system at uniform and partial shading. *Renew Sustain Energy Rev* 53:1500–1507
7. Belhachat F, Larbes C (2018) Review of global maximum power point tracking techniques of photovoltaic system under partial shading conditions in renewable and sustainable energy R. *Renew Sustain Energy Rev* 92:513–553
8. Verma D, Nema S, Shandilya AM, Dash SK (2015) Maximum power point tracking (MPPT) techniques: recapitulation in solar photovoltaic systems. *Renew Sustain Energy Rev* 54:1018–1034
9. Ram JP, Babu TS, Rajasekar N (2017) A comprehensive review on solar PV maximum power point tracking techniques. *Renew Sustain Energy Rev* 67:826–847
10. Ramli MAM, Twaha S, Ishaque K, Al-Turki YA (2017) A review on maximum power point tracking for photovoltaic systems with and without shading conditions. *Renew Sustain Energy Rev* 67:144–159
11. Karami N, Moubayed N, Outbib R (2017) General review and classification of different MPPT techniques. *Renew Sustain Energy Rev* 68(2015):1–18
12. Ezinwanne O, Zhongwen F, Zhijun L (2017) Energy performance and cost comparison of MPPT techniques for photovoltaics and other applications. *Energy Procedia* 107:297–303
13. Islam H et al (2018) Performance evaluation of maximum power point tracking approaches and photovoltaic systems. *Energies* 11(2):365
14. Kamran M, Mudassar M, Rayyan Fazal M, Usman Asghar M, Bilal M, Asghar R (2018) Implementation of improved Perturb & Observe MPPT technique with confined search space for standalone photovoltaic system
15. John R, Mohammed SS, Zachariah R (2018) Variable step size Perturb and observe MPPT algorithm for standalone solar photovoltaic system. In: *Proceedings 2017 IEEE international conference intelligent techniques control optimization and signal process (INCOS 2017)*, pp 1–6
16. Piegari L et al (2015) Optimized adaptive perturb and observe maximum power point tracking control for photovoltaic generation. *Energies* 8(5):3418–3436
17. Loukriz A, Haddadi M, Messalti S (2016) Simulation and experimental design of a new advanced variable step size incremental conductance MPPT algorithm for PV systems. *ISA Trans* 62:30–38

18. Soon Tey K, Mekhilef S (2014) Modified incremental conductance MPPT algorithm to mitigate inaccurate responses under fast-changing solar irradiation level. *Sol Energy* 101:333–342
19. Bendib B, Belmili H, Krim F (2015) A survey of the most used MPPT methods: and advanced algorithms applied for photovoltaic systems. *Renew Sustain Energy Rev* 45:637–648
20. Kabalci E (2017) Maximum power point tracking (MPPT) algorithms for photovoltaic systems. Springer, Cham, pp 205–234
21. Kivimäki J, Kolesnik S, Sitbon M, Suntio T, Kuperman A (2017) Revisited perturbation frequency design guideline for direct fixed-step maximum power point tracking algorithms. *IEEE Trans Ind Electron* 64(6):4601–4609
22. Elgendy MA, Atkinson DJ, Zahawi B (2016) Experimental investigation of the incremental conductance maximum power point tracking algorithm at high perturbation rates. *IET Renew Power Gener* 10(2):133–139
23. Ahmed J, Salam Z (2015) An improved perturb and observe (P&O) maximum power point tracking (MPPT) algorithm for higher efficiency. *Appl Energy* 150:97–108
24. Kumar K, Prabhu KR, Ramesh Babu N. Design and analysis of modified single P&O MPPT control algorithm for a standalone hybrid solar and wind energy conversion system. *Gazi Univ J Sci* 30(4):296–312
25. Alik R, Jusoh A (2017) Modified perturb and observe (P&O) with checking algorithm under various solar irradiation. *Sol Energy* 148:128–139
26. Akbar Ghassami A, Mohammad Sadeghzadeh S, Soleimani A (2013) A high performance maximum power point tracker for PV systems. *Int J Electr Power Energy Syst* 53:237–243
27. Ahmed J, Ahmed J, Member S, Salam Z (2016) A modified P&O maximum power point tracking method with reduced steady state oscillation and improved tracking efficiency. *IEEE Trans Sustain Energy* 30(29(January)):1–10
28. Abdullahi N, Saha C, Jinks R (2017) Modelling and performance analysis of a silicon PV module, vol 033501, pp 1–11
29. Tan CW, Green TC, Hernandez-Aramburo CA (2008) Analysis of perturb and observe maximum power point tracking algorithm for photovoltaic applications. In: 2008 IEEE 2nd international power energy conference, no PECon 08, pp 237–242
30. Abdourraziq MA, Ouassaid M, Maaroufi M, Abdourraziq S (2013) Modified P&O MPPT technique for photovoltaic systems. In: IEEE, pp 20–23
31. Belkaid A, Colak I, Isik O (2016) Photovoltaic maximum power point tracking under fast varying of solar radiation
32. Eltamaly AM, Farh HMH, Othman MF (2018) A novel evaluation index for the photovoltaic maximum power point tracker techniques. *Sol. Energy* 174:940–956
33. Ishaque K, Salam Z, Lauss G (2014) The performance of perturb and observe and incremental conductance maximum power point tracking method under dynamic weather conditions. *Appl Energy* 119:228–236
34. Femia N, Petrone G, Spagnuolo G, Vitelli M (2013) Power electronics and control techniques for maximum energy harvesting in photovoltaic systems, USA, FL. CRC, Boca Raton
35. Farh HMH, Eltamaly AM, Othman MF (2018) Hybrid PSO-FLC for dynamic global peak extraction of the partially shaded photovoltaic system

An Efficient MPPT and Reliable Protection Scheme for PV-Integrated Microgrid Under Partial Shading and Array Faults



Murli Manohar, Ebha Koley and Subhojit Ghosh

Abstract The manifested merits associated with solar energy including high sustainability, zero greenhouse gas emission and economic operation have encouraged wide penetration of photovoltaic (PV) systems in the microgrid, during the last few decades. However, the intermittency caused due to the fluctuating nature of solar irradiance demands an efficient maximum power point tracking (MPPT) algorithm for PV-integrated microgrids. The scenarios related to partial shading and faults in PV array impact the voltage–current behaviour resulting in the failure of conventional MPPT techniques in accurately estimating the operating point. The incorrect estimation by MPPT techniques quite often affects the operation of overcurrent protection modules. In this regard, this chapter presents an accurate sine cosine optimization (SCA)-based MPPT algorithm which will search the global operating point irrespective of the condition (i.e. in the event of partial shading or array faults), while avoiding undesired activation of the protection system. Besides this, a reliable protection scheme is proposed to detect and classify the faults in the distribution line under dual operating modes of microgrid (i.e. grid-connected and islanding). The instantaneous voltage–current signals recorded at the relaying bus are preprocessed through discrete wavelet transform (DWT) to obtain the discriminatory attributes, which are further utilized by the hybrid framework of artificial neural network (ANN) and SCA to perform the intended protection tasks under both modes of microgrid operation. The performance of the proposed MPPT technique and protection scheme has been analysed against a wide range of operating scenarios with real-time validation on OPAL-RT digital simulation platform.

Keywords Maximum power point tracking (MPPT) · Sine cosine algorithm (SCA) · Microgrid protection · Real-time validation

M. Manohar · E. Koley · S. Ghosh (✉)

Department of Electrical Engineering, National Institute of Technology, Raipur, Chhattisgarh, India

e-mail: sghosh.ele@nitrr.ac.in

© Springer Nature Switzerland AG 2020

A. M. Eltamaly and A. Y. Abdelaziz (eds.), *Modern Maximum Power Point Tracking Techniques for Photovoltaic Energy Systems*, Green Energy and Technology, https://doi.org/10.1007/978-3-030-05578-3_11

303

Acronyms

ANN	Artificial neural network
BPNN	Backpropagation neural network
DER	Distributed energy resources
GMPP	Global maximum power point
LMPP	Local maximum power point
MSE	Mean square error
MPP	Maximum power point
MPPT	Maximum power point tracking
PCC	Point of common coupling
PLL	Phase-locked loop
PV	Photovoltaic
PVDG	Photovoltaic distributed generator
SCA	Sine cosine algorithm
SDG	Synchronous distributed generator
VSC	Voltage source converter

Symbols

D	Dimension of objective function
$F(x)$	Objective function
X	Population
N	Number of population
$iter_{max}$	Number of iterations
$X_{k,iter}$	Position of k th solution
r_1, r_2, r_3	Random numbers
ε	Error constant
V_o, I_o	Array output voltage and current
d	Duty ratio of DC–DC converter
$\varnothing_{jk}(t)$	Mother wavelet function
$y_{low}[k]$	Output of low-pass filter
x	Set of input samples
y	Set of features
T	Training dataset
e_i	Difference between actual and estimated value
R_f	Fault resistance
L_f	Fault location
θ_f	Fault inception angle
G	PV irradiance
S1, S2, S3, S4	Sections of microgrid
L1, L2, L3, L4 and L5	Loads of microgrid system

1 Introduction

The rising power demand and the increased emphasis on the reduction of fossil fuels have motivated the search for an alternative source of energy. In this regard, the adoption of distributed energy resources for providing reliable power supply at the distribution level has introduced the concept of microgrid [1]. Over the last few decades, photovoltaic (PV) power generation has gained widespread attention as compared to other distributed energy resources in microgrids, due to its ease of integration and sustainability of solar energy [2].

A primary challenge towards the reliable and efficient operation of any photovoltaic-integrated microgrid system relates to the requirement of extracting maximum power from the PV source irrespective of the operating condition. The highly nonlinear nature of the I – V characteristics and its high sensitivity on irradiance level and ambient temperature makes the task of maximum power point tracking (MPPT) quite challenging [3]. A large number of MPPT techniques have been proposed in literature based on the algorithm employed, converter topology and applications [4–10]. Majority of the reported MPPT works have been designed and validated for standalone systems. Some of the recently proposed techniques in this context include Monod equation-based tracking algorithm [4], power increment-based technique [5], Bat algorithm-based scheme [6], global maximum power tracking algorithm [7], Cuckoo search-based maximum power point (MPP) method [8], limited search space-based global MPPT [9], fuzzy logic-based tracking approach [10, 11], MPPT algorithm based on artificial vision [12] and an improved perturb and observe method [13]. Further, some of the MPPT algorithms have been developed for grid-connected PV systems [14–16]. Most of the conventional MPPT techniques are designed to operate only during uniform irradiance variation as determined using past data. However, the variation in PV irradiance level is highly stochastic and does not remain uniform throughout the day. Quite often, due to the occurrence of partial shading, multiple peaks are obtained in the P – V curve, which are known as local MPPs. So, to determine the global MPP among them is a challenge. In this regard, various MPPT algorithms have been developed for PV systems with an objective to track global MPP during partial shading condition [5, 6, 8, 17–20]. However, the majority of existing MPPT algorithms have been devised for standalone systems only and not extended for application in PV-integrated microgrids.

The limited works reported for MPPT in microgrids [21, 22] have not concentrated on the influence of distribution line faults, on MPP operation, and the effect it would have on the protection scheme. Further, the impact of array faults on the MPPT needs to be investigated during both islanding and grid-connected mode of operation of the microgrid. In this regard, the present work is motivated by the need to develop a reliable MPPT technique, which is insensitive to partial shading, array faults, and distribution line disturbances, and further make the protection scheme of the microgrid immune to the operation of MPPT. The immunity would disallow any change in the operation of PV (due to partial shading or array faults), to affect the operation of the protection scheme, thus preventing any maloperation of relay.

In the absence of such immunity, there is high probability that the relay threshold setting may be satisfied for faults/disturbances in DC (PV source) side without any fault on the distribution end, thus leading to relay maloperation. Physical phenomena which might result in such faults/disturbance include strong wind, stormy weather and any improper connection between two points in the array that can initiate an arc. Similar maloperation can also happen, when a fault on the distribution line may not actuate the protection algorithm because of sudden reduction in the irradiance level. In this regard, a MPPT algorithm has been proposed which is able to track the global MPP during diverse operating and fault scenarios of the PV array as well as during disturbances in distribution lines of the PV-integrated microgrid.

Further, the MPPT algorithm has been integrated with a ANN-based protection scheme intended to perform the tasks of fault detection/classification and section identification in both operating modes of the microgrid. Both the MPPT and protection tasks have been formulated as an optimization problem and solved using sine cosine algorithm (SCA). The sine cosine optimization algorithm is a population-based heuristic algorithm, which initiates with random parameterization and moves towards the best solution using a trigonometric path [23]. For the protection algorithm, the DWT-derived attributes from the raw voltage and current signals are fed to the ANN modules for training to perform the necessary input–output mapping. The use of SCA helps to obtain the ANN architecture with optimal weight and bias parameters.

The contributions of the proposed work are outlined below:

- (1) The tracking of MPP in the PV-integrated microgrids has been achieved using sine cosine algorithm. The proposed MPPT technique takes care of variations in solar irradiance levels and change in the operating point of PV source due to partial shading and array faults.
- (2) A protection algorithm for PV-integrated microgrid based on the combined framework of SCA and ANN is proposed to perform fault detection/classification and section identification. The protection scheme is integrated with the SCA-based MPPT algorithm, which allows preventing possible maloperation of the relays under varying PV operation and distribution line scenarios.
- (3) The proposed scheme has been extensively validated under different scenarios involving partial shading and array faults, as well as different symmetrical and unsymmetrical fault scenarios. Further, to validate the effectiveness of the proposed scheme under practical settings, real-time simulations have been carried out on the OPAL-RT digital simulation platform.

The chapter is organized as follows. In the next section, the microgrid system under study is described with the MPPT control and array faults. Sections 3 and 4 describe the development of SCA-based MPPT algorithm and the hybrid SCA-ANN-based protection scheme, respectively. The performance evaluation of the proposed MPPT and protection scheme with real-time time validation is summarized in Sect. 5 followed by the conclusion in Sect. 6.

2 Modelling and Simulation of PV-Integrated Microgrid

The microgrid system considered in the present study has been represented by a single line diagram in Fig. 1. The system operates at 34.5 kV, 60 Hz, with two sources, i.e. synchronous (SDG) and inverter-interfaced (PVDG) DERs connected at buses B3 and B4, respectively [24]. The line is divided into four sections, namely (S1, S2) and (S3, S4) spread over the length of 20 km with L1, L2, L3, L4 and L5 representing loads. The power conditioning unit for interfacing PV array with the AC grid includes a DC–DC boost converter equipped with SCA-based maximum power point tracking (MPPT) algorithm, voltage source converter (VSC) with converter control unit, and phase-locked loop (PLL) for synchronization.

The PVDG unit connected to bus B4 of the microgrid contains four shunt-connected PV arrays as shown in Fig. 2. The power output of each array is fed to the DC–DC converter and based on the voltage and current output of the array, and the duty cycle of each converter is controlled by the proposed SCA-based MPPT controller to track the maximum power point. The PV arrays are formed by the interconnection of modules in series–parallel arrangement as shown in Fig. 3. The configuration of each array is composed of three parallel strings with four modules in each string. In order to ensure the protection of PV array, a bypass diode is connected across each module and blocking diode in each parallel string. During partial shading, the bypass diode conducts to isolate the partially shaded module and hence avoids the effect of undesirable hot spots. The task of blocking diode is to prevent the back-feed current flow between the parallel connected strings [25]. In order to analyse the performance of proposed SCA-based MPPT algorithm under different operating conditions of the PV array, various types of array fault scenarios including the line–line fault between the parallel string, line–line fault within the same string, line–ground and partial shading have been simulated (discussed later in Table 2) as marked for representation with the symbols #1, #2, #3, #4, respectively, in Fig. 3.

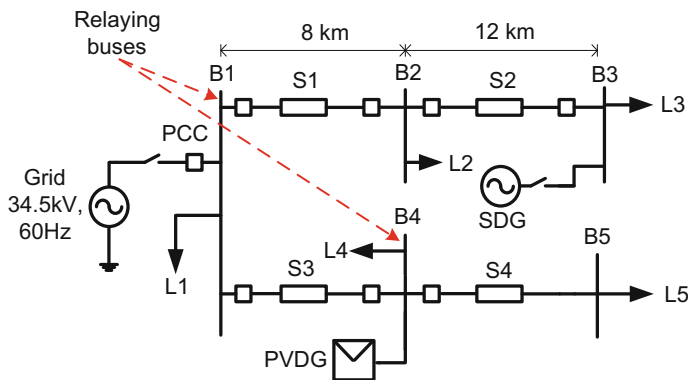


Fig. 1 Single line diagram of PV-integrated microgrid under study

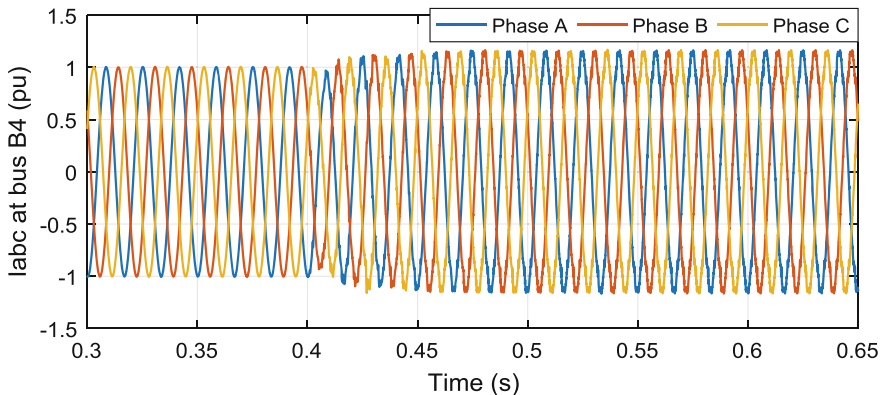


Fig. 4 Three-phase instantaneous current recorded at bus B4 due to the line–line fault in the PV array at $t = 0.4$ s

To analyse the effect of a fault in the PV array on the current profile in the distribution line and hence on the possible maloperation of overcurrent relay, a line-to-line fault in PV array has been simulated during the islanded mode and the corresponding three-phase line current in bus B4 (Fig. 1) has been depicted in Fig. 4. It can be observed that there is a substantial increase in the line current similar to symmetrical fault after the initiation of array fault. The threshold-based overcurrent relay dependent only on the magnitude of line current will not be able to differentiate between array fault and symmetrical fault, thereby providing tripping signal for both the cases.

3 Proposed SCA-Based MPPT Scheme

3.1 Sine Cosine Optimization Algorithm

Sine cosine algorithm (SCA) is a recently proposed evolutionary optimization technique [23], which aims at maximizing the probability of obtaining globally optimal solution for the optimization problem at hand. This is achieved by initializing the algorithm with a set of random possible solutions and iteratively oscillates them around the best solution using trigonometric functions. The algorithm has been found to be quite effective in solving complex nonlinear multimodal functions. For the present problem of tracking MPP, SCA is used to solve the objective function framed by quantifying the power derived from the PV source. Similarly for the pro-

tection task, the objective function corresponds to the deviation between the power system state (healthy or faulty) and the output of the ANN trained to perform the tasks of fault detection/classification and section identification. The optimizing variables considered for the MPPT and protection-based optimization problems are duty ratio and ANN architecture parameters, respectively. The initialized random variables for both the problems are iteratively modified using sine and cosine functions until a convergence criterion is achieved [23].

Similar to most of the existing population-based heuristic optimization techniques, the overall task of minimizing the objective function in SCA is broadly composed of two stages, i.e. exploration and exploitation. During the exploration stage, the possible solutions are perturbed randomly along different directions with the aim of locating regions with low value of objective function. In the exploitation stage, relatively reduced perturbations with lesser randomness are imparted to the solutions to move them closer to the globally optimal solution in the search space.

For solving the D -dimensional objective function $F(x)$ with $X = [x_1, x_2, \dots, x_D]$, assuming the SCA is initialized with population size $= N$ for iter_{\max} number of iterations, the k th solution ($k \leq N$) in the first iteration is represented as:

$$X_k = [x_1^k, x_2^k, \dots, x_D^k] \quad (1)$$

Iteratively, the solutions are updated as

$$X_{k,\text{iter}+1} = X_{k,\text{iter}} + r_1 \times \sin(r_2) \times |r_3 P_{k,\text{iter}} - X_{k,\text{iter}}| \quad (2)$$

$$X_{k,\text{iter}+1} = X_{k,\text{iter}} + r_1 \times \cos(r_2) \times |r_3 P_{k,\text{iter}} - X_{k,\text{iter}}| \quad (3)$$

where $X_{k,\text{iter}}$ represents the current position of k th solution at iteration $= \text{iter}$ and $X_{k,\text{iter}+1}$ is the updated solution. The parameters r_1, r_2, r_3 are random numbers, and $P_{k,\text{iter}}$ is the most optimal solution obtained till iter iteration.

The above equations can be combined by using a random number r_4 as:

$$X_{k,\text{iter}+1} = \begin{cases} X_{k,\text{iter}} + r_1 \times \sin(r_2) \times |r_3 P_{k,\text{iter}} - X_{k,\text{iter}}| & r_4 < 0.5 \\ X_{k,\text{iter}} + r_1 \times \cos(r_2) \times |r_3 P_{k,\text{iter}} - X_{k,\text{iter}}| & r_4 \geq 0.5 \end{cases} \quad (4)$$

The parameters r_1, r_2, r_3 and r_4 are responsible for carrying out the search for the global solution in N -dimensional space. The parameter r_1 decides the movement of the solutions in a particular direction; that is, it regulates the extent of exploration and exploitation. For maintaining a proper balance between exploration and exploitation, r_1 is adopted to assume large values in the initial iterations, followed by reducing it as:

$$r_1 = a - \text{iter} \frac{a}{\text{itermax}} \quad (5)$$

where a is a constant. During the initial iterations, the possible solutions move randomly in different directions. The initial movement relates to the wider exploration of the search space with increased distance among the solutions. However, in the later iterations, when some optimal directions towards the global solution are identified, the information is exploited for convergence towards the globally best position in the search space. Following the selection of search direction, the perturbation towards or away from the optimal solution is decided based on the control parameter r_2 ($0 < r_2 < 2\pi$). The influence of the destination point $P_{k,\text{iter}}$ on the distance from the present solution is incorporated in terms of r_3 by taking $r_3 > 1$ for emphasizing the effect and $r_3 < 1$ for deemphasizing the effect.

3.2 Proposed MPPT Algorithm

The application of SCA for solving the MPPT problem has been depicted in the form of a flow chart in Fig. 5. The objective function solved by SCA for achieving MPPT is given as:

$$\max_d f(d) = V_o \times I_o \quad (6)$$

where d is the duty ratio for switching the DC–DC converter and I_o is the array current. With the PV array output voltage defined as V_{array} , V_o is given as:

$$V_o = \frac{V_{\text{array}}}{1 - d} \quad (7)$$

For an initially generated population of duty ratios with $0 < d < 1$, the algorithm is executed by updating the initial duty ratios using (4). The power extracted from the PV array for the corresponding duty ratio is compared with the power obtained in the previous iteration for determining the optimality of d . The iterative process of updating the duty ratio is carried out till no significant improvement in the power extracted from the optimal solution is observed for some successive iterations.

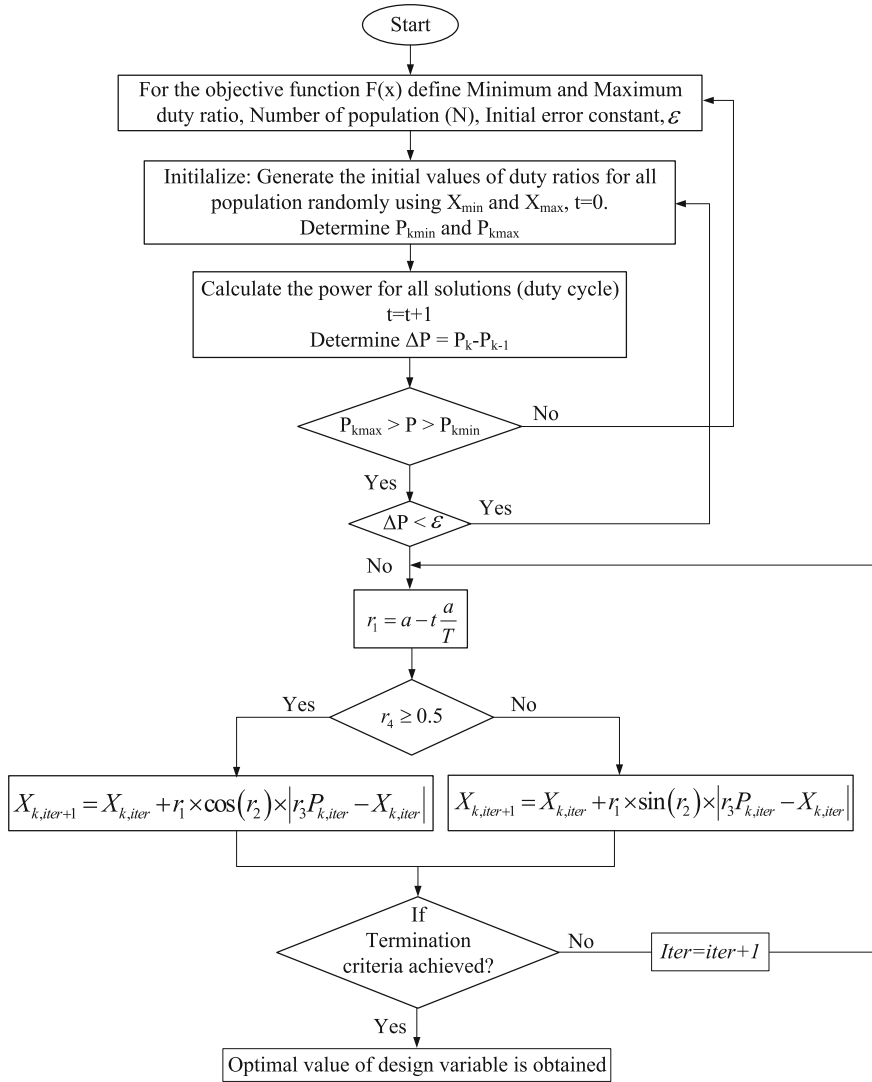


Fig. 5 Flow chart of sine cosine optimization-based MPPT algorithm

4 Development of Proposed Protection Scheme

The reliable operation of a microgrid demands a fast and reliable protection technique to detect/classify faults and identify the faulty section for early restoration of power supply. In this regard, a protection scheme based on combined framework of wavelet transform, SCA, and ANN has been proposed in this chapter for both grid-connected and islanded operation.

4.1 Feature Extraction

Wavelet transform is a widely used tool to analyse and register the pattern obtained post-occurrence of any disturbance or fault in the power system. It splits the signal into various scales corresponding to different frequency patterns through translation (shift in time) and dilation (compression in time) of mother wavelet [26]. The mother wavelet can be represented by the following relation:

$$\varnothing_{jk}(t) = 2^{-j/2} \phi(2^{-j}t - k) \quad (8)$$

where $k, j \in Z$ (integers).

Analysis of a signal is carried out by wavelets using multi-resolution technique at different resolution and frequencies. The decomposition of an sampled input signal $x(n)$ carried out through low-pass Butterworth filtering is governed by the following equation:

$$y_{\text{low}}[k] = \sum x[n] \cdot h[2k - n] \quad (9)$$

where $y_{\text{low}}[k]$ is the output of low-pass filter $h[n]$ obtained after down sampling by 2. In the present work, a total of 12 signals including B1 and B4 bus voltage, current in sections S1, S2, S3 and S4 for all the three phases A, B and C have been considered for the feature extraction process. The feature variables consisting of the standard deviation of approximate coefficients of signals obtained using DWT are represented as:

$$y = [sV_{a1}, sV_{b1}, sV_{c1}, sV_{a2}, sV_{b2}, sV_{c2}, sI_{a1}, sI_{b1}, sI_{c1}, sI_{a2}, sI_{b2}, sI_{c2}] \quad (10)$$

The training dataset containing of x input samples and y feature variables has been formulated as:

$$T = \{(x_i, y_j), \quad i = 1, 2, \dots, N; \quad j = 1, 2, \dots, 12\} \quad (11)$$

In order to demonstrate the distinct behaviour of derived features, the standard deviation of approximate wavelet coefficients derived from the current signal obtained at bus B1 through the simulation of AG fault against variation in PV irradiance level (100–1000 W/m²), fault location (1–16 km), fault resistance (0–100 Ω) under grid-connected and islanded mode is depicted in Fig. 6a, b, respectively. Pre-processing and feature extraction are followed by the development of SCA-ANN-based classification module for performing fault detection/classification and section identification separately for both modes of microgrid operation.

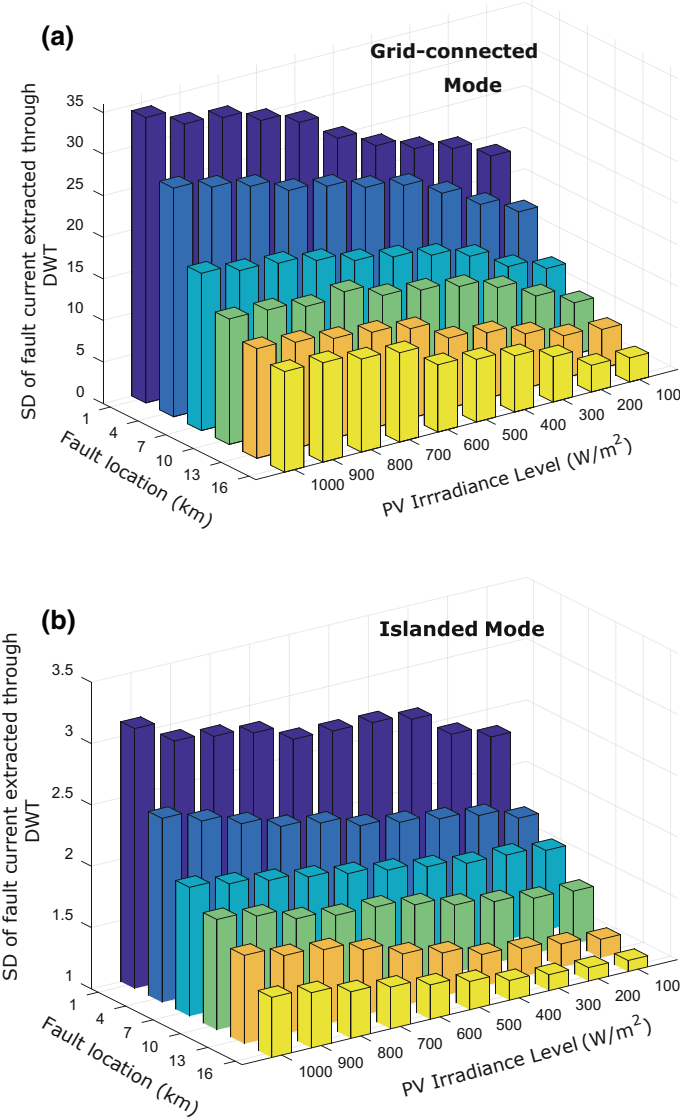


Fig. 6 Standard deviation of fault current at bus B1 (AG fault) extracted through DWT with variation in PV irradiance level and fault location during **a** grid-connected mode and **b** islanded mode

4.2 Development of Hybrid SCA-ANN Algorithm for Fault Detection/Classification and Section Identification

The present subsection discusses the development of the proposed SCA-ANN protection algorithm for performing the tasks of fault detection/classification and section identification. The intended tasks have been framed as a classification problem and solved using feedforward ANNs. For this, the microgrid under study has been simulated for wide scenarios involving variation in both PV operating and distribution line fault parameters.

Owing to the limitation of local convergence to suboptimal solution in the conventional gradient-based back-propagation algorithm for training feedforward ANNs, SCA has been adopted for deriving the optimal architecture and parameters (weights and biases) of ANN modules. For this, the objective function has been framed using the mean square error (MSE) between the ANN and actual output as

$$f(x) = \frac{\sum_{i=1}^n e_i^2}{n} \quad (12)$$

where e_i represents the deviation between ANN and simulated model output for the i th training data and the optimizing vector X comprises the biases of individual neurons and the weights connecting the different neurons in the ANN architecture. The SCA has been used to solve (12) by initializing with a set of random combination of weights and biases. For each combination, the ANN is simulated for a particular operating state of the microgrid. The various states simulated during the training phase of the ANN consist of varying irradiance (100–1000 W/m²), different types of array faults, varying distribution line fault parameters (fault resistance, inception angle and location) under dual operating modes (Islanded and grid-connected) modes of the microgrid. The various permutation and combination of the PV operating and fault parameters together with some healthy scenarios constitute the training and testing dataset of the ANN. The deviation between the simulated output of the ANN and the actual system output is calculated for all the training samples. Using SCA, the initial weight and bias values are updated till convergence, with the aim of reducing $f(x)$ in (12).

The overall process of deriving the features representing the operation of the power system and further using them to train the ANN and hence iteratively derive the optimal ANN structure using SCA has been described in Fig. 7 [27]. The details of the optimal architecture obtained using SCA for ANN-1 to ANN-4 modules are described in Fig. 8. For all the neurons, tangent sigmoid activation function has been used. Post-convergence of SCA, the trained ANN, describes the most optimal mapping between the extracted features for different cases with the corresponding state (faulty/healthy) and further the fault type and section (if applicable).

The proposed protection scheme comprises of different ANN modules dedicated to perform specific tasks. Modules ANN-1 and ANN-3 have been assigned to perform fault detection/classification task under grid-connected and islanded mode, respec-

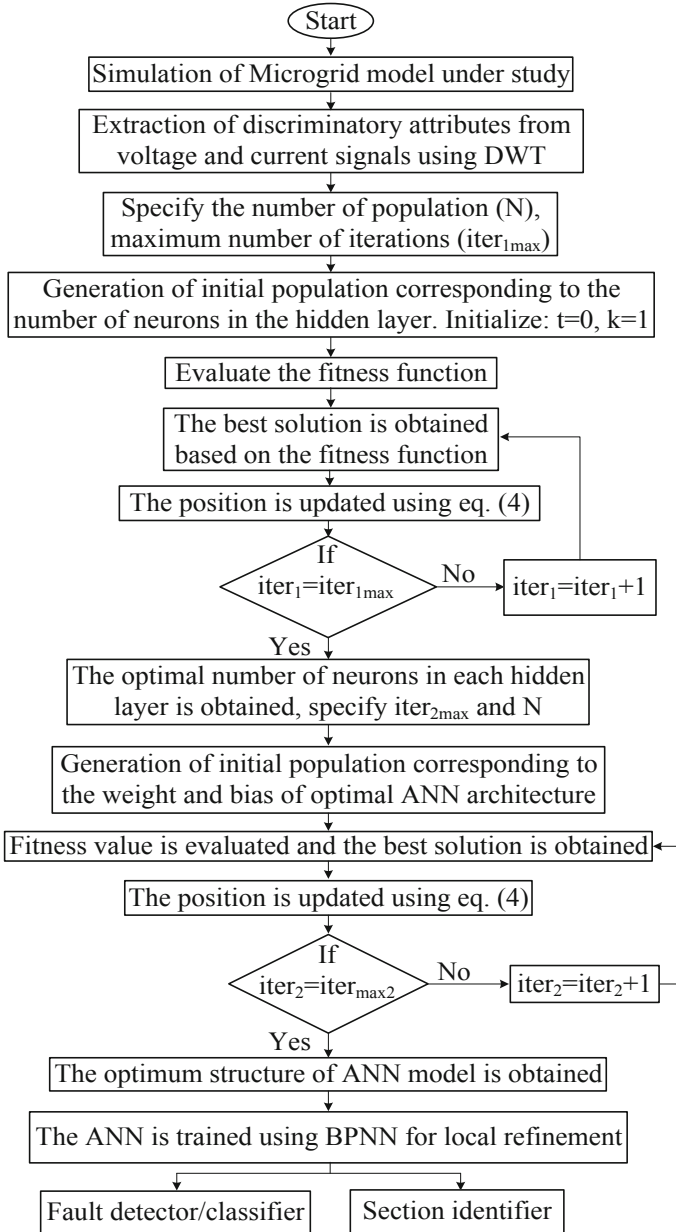


Fig. 7 Flow chart of SCA-ANN-based protection algorithm

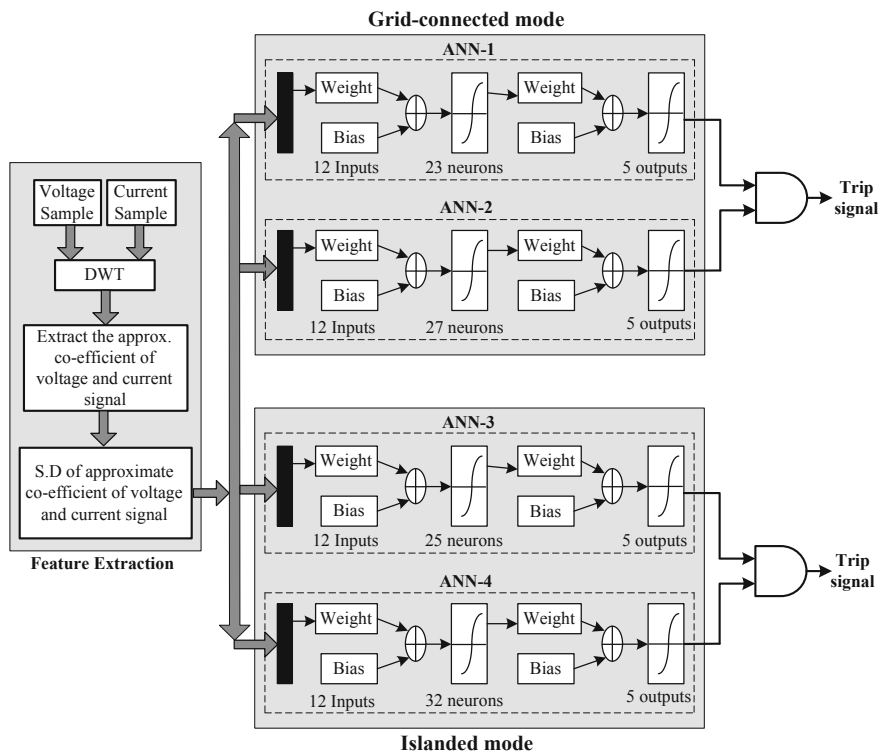


Fig. 8 Proposed protection scheme based on DWT and SCA-ANN

tively. The section identification task to determine the faulty section is performed by the modules, ANN-2 and ANN-4, respectively, for the grid-connected and islanded mode. The fault detection/classification module provides an output regarding the state of the distribution line (faulty or healthy) and occurrence of array fault (if any). For all the modules, a total of twelve neurons in the input layer representing the input attribute derived using DWT are selected. The total number of neurons in the output layer is five for each module. For ANN-1 and ANN-3, the 5-bit output represents the state of the line (first four bit corresponding to fault in phases A, B, C, G and the last bit for external PV array fault). For ANN-2 and ANN-4, first four bit represents the faulty section in the distribution line and the last bit represents the occurrence of external fault. Based on the output of fault detector/classifier and section identifier, regarding the fault type and faulty section, respectively, relaying decision is made to generate trip signal to respective breaker for isolation of the faulty feeder.

5 Performance Evaluation

The effectiveness of the proposed SCA-based MPPT and microgrid protection scheme has been examined in this section, in terms of achieving the twin objectives of maximum power extraction from the PV source and providing protection to the distribution line against symmetrical and unsymmetrical faults. The MPPT technique has been validated against wide variation in the irradiance levels, different types of array faults and faults in the distribution system. Similarly, the protection scheme for the PV-integrated microgrid has been validated with regard to its response against faults in both islanded and grid-connected mode and also under disturbances (irradiance variation and array faults) in the PV operation. The validation allows examining the immunity of the MPPT scheme to variation in the operating scenario of the distribution line and also of the protection scheme on the variation in the PV operation.

5.1 Validation of SCA-Based Proposed MPPT Scheme

As mentioned earlier, the SCA-based MPPT scheme discussed in Sect. 3 aims at extracting maximum power from the PV source under varying irradiance resulting from weather intermittency and array faults. For the different cases simulated for validating the scheme, MPPT is being achieved while the microgrid is in operation. The performance of the proposed SCA-based MPPT technique in tracking the global maximum power point (GMPP) has been described in the following subsections.

5.1.1 Partial Shading

Partial shading conditions are characterized by non-uniform distribution of PV irradiance level across the modules of the array. In such cases, multiple peaks are obtained on the power–voltage curve of the array. Tracking the GMPP among the multiple peaks is the main challenge for any MPPT scheme. In this regard, to examine the effectiveness of the proposed SCA-based MPPT technique against different partial shading profiles, seven patterns involving variation in irradiance levels across the modules have been generated. The power–voltage characteristics of the array, depicting the GMPP for each pattern, are shown in Fig. 9. The first pattern contains single peak, as it has been simulated considering uniform irradiance of 1000 W/m^2 across the modules, whereas other patterns contain three local maximum power point (LMPP) and one GMPP.

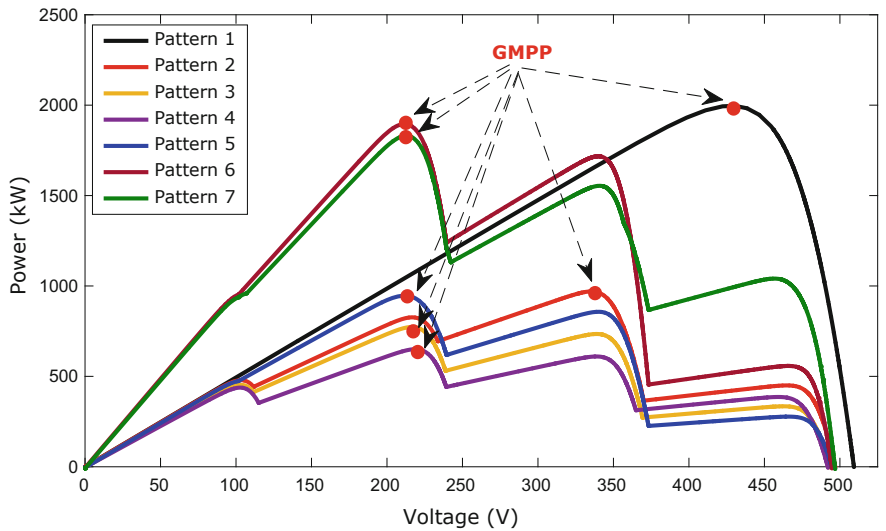


Fig. 9 Power–voltage curve of PV array for the patterns 1–7

Pattern	Irradiance levels (kW/m ²)				Position of GMPP peak	Power at GMPP (kW)	Tracking efficiency (%)
	G1	G2	G3	G4			
Pattern-1	1	1	1	1	1st	2100.05	100.00
Pattern-2	1	0.8	0.6	0.2	3rd	1028.73	99.84
Pattern-3	0.95	0.75	0.65	0.25	2nd	821.5	99.57
Pattern-4	0.925	0.625	0.375	0.175	2nd	692.71	99.89
Pattern-5	1	0.525	0.95	0.125	1st	1008.06	99.50
Pattern-6	1	0.525	0.95	0.125	1st	2016.12	98.70
Pattern-7	1	0.525	0.95	0.125	2nd	1950.4	99.98
Overall tracking efficiency (%)							99.64

The performance of the proposed MPPT scheme has been analysed in terms of the tracking efficiency (%) [28], which is defined as the ability of a MPPT technique in extracting maximum power from the available power of the array. The obtained results are summarized in Table 1. The overall average tracking efficiency of 99.64% shows the efficacy of proposed scheme against different partial shading conditions.

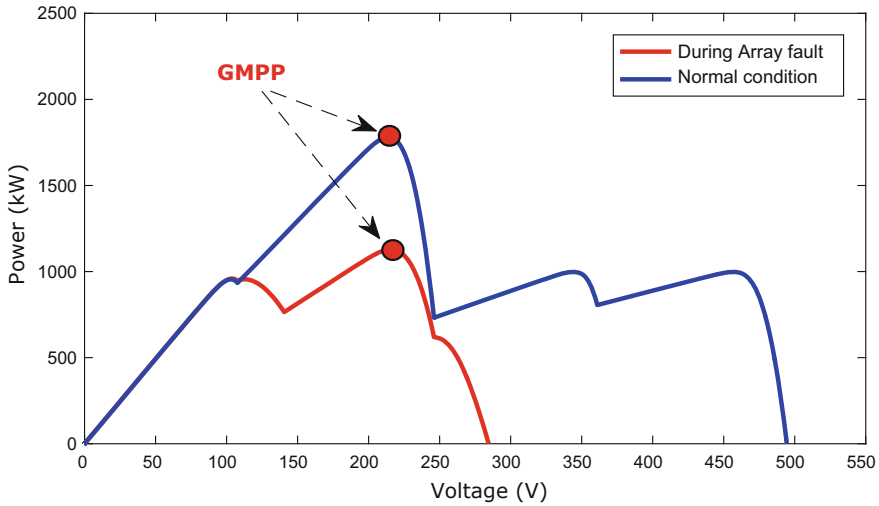


Fig. 10 Power–voltage curves under normal and line–line fault in PV array

5.1.2 PV Array Faults

During faults in the PV array, the MPPT schemes aim at optimizing the output power. This causes a significant reduction in the array current, thus leading to maloperation of overcurrent relays due to underreach. In the course of tracking the MPP, the operating array voltage is reduced (Fig. 10) to increase the power [2]. Hence, it is required to test the performance of the proposed MPPT scheme with regard to PV array faults. The occurrence of faults in the PV array may contain some resistance due to the poor contact between the fault points. In this regard, the performance of the proposed SCA-based MPPT scheme has been substantiated against the PV array faults including line–line and line–ground with wide variation in fault parameters (fault resistance and location). The high degree of tracking efficiencies (%) obtained by the proposed MPPT technique against each type of array fault simulated at specified locations (Fig. 3) as summarized in Table 2 confirms the effectiveness of the scheme in tracking the global MPP without misguiding the protection devices.

5.2 Validation of SCA-ANN-Based Protection Scheme

The pattern of data (both training and testing) generated by simulating the micro-grid system under different operating scenarios involving PV array faults (line–line and line–ground) and all the 11 types of fault (symmetrical and unsymmetrical) in distribution line for both the operating modes are summarized in Table 3. The no-fault cases include PV irradiance variation, partial shading and load variation.

Table 2 Performance of proposed scheme under faults in PV array

Type of array fault	Fault parameters		Performance of proposed scheme		
	Fault location	Fault resistance (Ω)	Power at GMPP (kW)	Tracking efficiency (%)	Fault detector output
Line–line	Between points P1 and P2	1	856.98	99.35	PV fault
	Between points P1 and P4	5	936.56	99.12	PV fault
	Between points P3 and P4	10	1194.62	98.86	PV fault
	Between points P2 and P3	15	1056.39	99.65	PV fault
Line–ground	Between points P1 and ground	5	1253.29	98.87	PV fault
	Between points P5 and ground	10	1345.69	99.34	PV fault
Low irradiance			No-fault

A total number of 19,450 cases were generated, comprising of 19,000 distribution line faults and 250 PV array faults in each operating mode of the microgrid. From the data generated, 70% of the cases have been used to train the respective ANN module and the rest 30% is utilized for the testing purpose.

The performance of the proposed SCA-ANN-based scheme has been evaluated by analysing the effectiveness of fault detector/classifier and section identifier in accurately detecting/identifying the fault type and faulty zone under each mode of microgrid operation. The detailed result analysis of each protection module has been discussed in the subsequent subsections.

5.2.1 Fault Detection/Classification

To examine the appropriateness of the proposed SCA-ANN-based scheme in accurately performing the tasks of fault detection/classification, the performance of the modules ANN-1 and ANN-3 (detailed in Sect. 4.2) has been analysed in this subsection. The fault-wise performance of proposed fault detector/classifier modules under different operating scenarios is detailed in Table 4, in which an overall accuracy

Table 3 Pattern of data generation

Parameters	Specification	Mode of operation		Total number of cases
		Grid-connected	Islanded	
Distribution line				
Fault types	AG, BG, CG, AB, AC, BC, ABG, ACG, BCG, ABC, ABCG	11	11	38,200
Fault section pairs	(S1, S2), (S3, S4)	2	2	
Fault resistance, R_f (in Ω)	1, 50, 100	3	3	
Irradiance range, G (W/m ²)	100–1000	19	19	
Inception angle, θ_f (in $^{\circ}$)	0, 90	2	2	
Fault location, L_f (in km)	1–20 km (in steps of 2 km)	10	10	
No-fault cases	Load variation (5–40%) and PV irradiance variation	100	100	
PV array				
Fault types	Line–line, line–ground	250	250	700
Partial shading conditions	20–50%	100	100	

of 99.37 and 98.79% has been obtained, respectively, for the grid-connected and islanded mode operation of the microgrid.

The reliability assessment of the proposed SCA-ANN-based fault detector and classifier has been performed in terms of the following statistical indices:

- (i) **Dependability:** It quantifies the possibility of misdetection of fault and is accounted as the percentage of the total number of correctly predicted fault cases to the total number of actual fault cases.
- (ii) **Security:** It is related to the possibility of generating false alarms and is expressed as the percentage of the total number of no-fault cases correctly predicted to the total number of actual no-fault cases.

The higher degree of dependability and security shown in Table 5 validates the effectiveness of the proposed fault detector/classifier in providing protection against wide variation in operating conditions during both grid-connected and islanded mode.

Table 4 Performance of the proposed SCA-ANN-based fault detector/classifier

Type of fault	No. of test cases	Grid-connected mode (ANN-1)		Islanded mode (ANN-3)	
		Misdetetection	Accuracy (%)	Misdetetection	Accuracy (%)
AG	958	0	100.00	1	99.90
BG	958	3	99.69	5	99.48
CG	958	4	99.58	3	99.69
AB	228	1	99.56	6	97.37
AC	228	5	97.81	5	97.81
BC	228	1	99.56	2	99.12
ABG	958	3	99.69	7	99.27
ACG	958	5	99.48	6	99.37
BCG	958	0	100.00	7	99.27
ABC	228	1	99.56	3	98.68
ABCG	958	4	99.58	0	100.00
PV fault	75	2	97.33	3	96.00
No-fault	60	0	100.00	1	98.33
Overall Accuracy (%)		99.37		98.79	

Table 5 Performance indices of proposed fault detector/classifier

Mode of operation	Fault case		No-fault cases		Performance indices	
	Actual	Predicted	Actual	Predicted	Dependability (%)	Security (%)
Grid-connected	7693	7664	60	60	99.62	100
Islanded		7645		59	99.37	98.33

5.2.2 Section Identification

The performance of section identification modules (ANN-2 and ANN-4) has been analysed in this section. The section-wise classification accuracy (%) of each module has been summarized in Table 6. It can be observed that the proposed SCA-ANN-based section identifier is efficiently contributing to providing the intended protection to microgrid by achieving an accuracy of 99.65 and 99.38%, respectively, for grid-connected and islanded mode.

Table 6 Section-wise performance of section identification modules

Performance of section identifier					
Sections	No. of actual test cases	Mode of operation			
		Grid-connected (ANN-2)		Islanded (ANN-4)	
		No. of correctly predicted cases	Accuracy (%)	No. of correctly predicted cases	Accuracy (%)
S1	1538	1538	100.00	1537	99.93
S2	2308	2304	99.83	2305	99.87
S3	1538	1536	99.87	1535	99.80
S4	2308	2305	99.87	2307	99.96
Ext	75	74	98.67	73	97.33
Overall accuracy		99.65%		99.38%	

5.3 Real-Time Validation

The analysis required for the validation of a MPPT and protection scheme for microgrid system involves complex computations, which might be difficult to implement on a digital platform. Hence, to test the feasibility of the proposed SCA-based MPPT and SCA-ANN-based protection scheme for real-time settings, the microgrid system shown in Fig. 1 has been implemented on OPAL-RT (OP5600) platform and the performance has been analysed. The OPAL-RT digital simulation platform facilitates the interfacing of microgrid system modelled in MATLAB/Simulink environment to the RT-LAB software, which enables faster execution through parallel computing to obtain precise results. The interaction of the proposed protection algorithm with the OPAL-RT digital simulation platform has been demonstrated in Fig. 11. The time-domain voltage and current signals recorded at the relaying buses are extracted through the input–output channels of OPAL-RT. The signals are processed through discrete wavelet transform (DWT) to obtain the input features which are further used as input to the SCA-ANN-based protection module for making the final relaying decision. The experimental set-up demonstrating the interface of microgrid system with the OPAL-RT hardware is depicted in Fig. 12. To validate the response of proposed scheme, an ACG fault has been simulated at $t = 4.5$ s in section S3 during islanded mode, with the parameters, $S = 650 \text{ W/m}^2$, $R_f = 1 \text{ }\Omega$ and $L_f = 3 \text{ km}$. The pre- and post-fault voltage and current recorded at bus B1 are shown in Figs. 13 and 14, respectively. The appropriateness of the proposed scheme in providing the intended protection to the microgrid even under low irradiance level has been substantiated by the generation of trip signal post 11 ms of the fault inception as depicted in Fig. 15.

The response of the proposed scheme has been analysed against wide variation in operating scenarios under dual operating modes (grid-connected and islanded) of PV-fed microgrid. As observed from the real-time results, the proposed SCA-

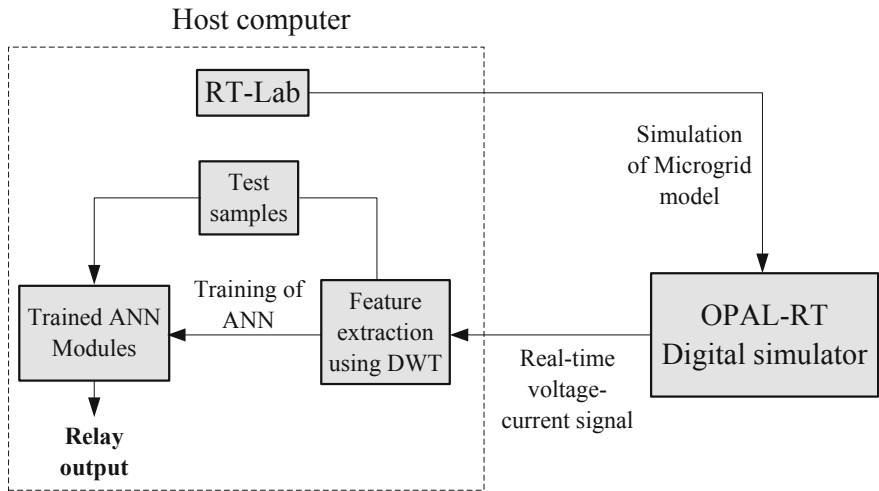


Fig. 11 Block diagram representing the implementation of proposed scheme on OPAL-RT platform

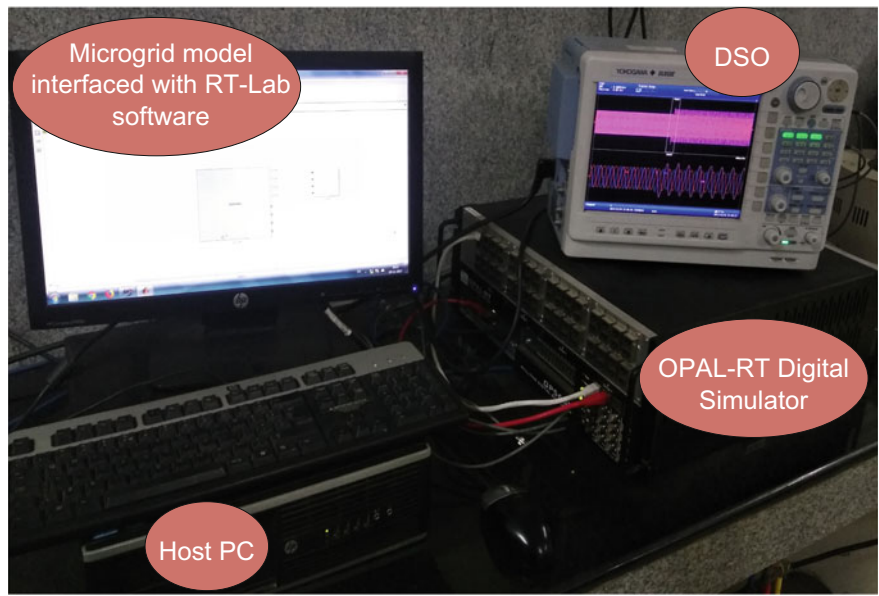


Fig. 12 Experimental set-up of OPAL-RT

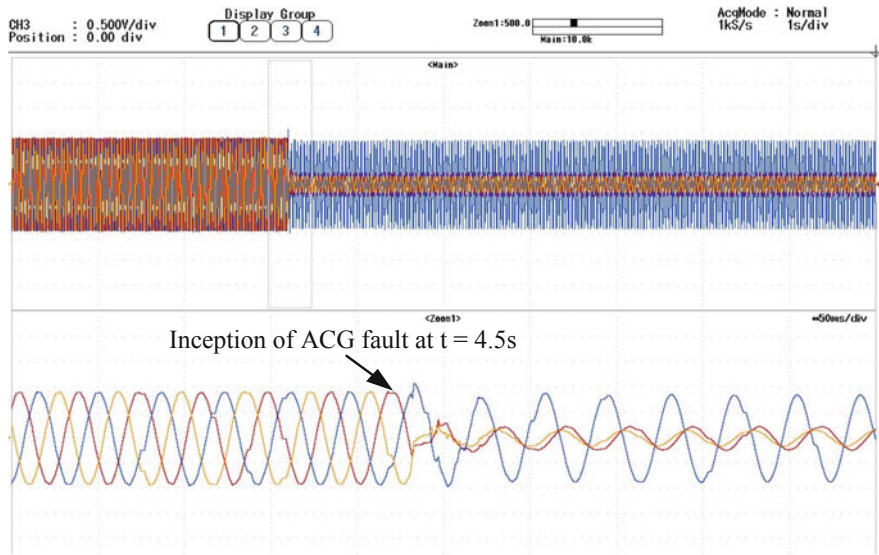


Fig. 13 Three-phase voltage at bus B1 during an ACG fault at $t = 4.5$ s

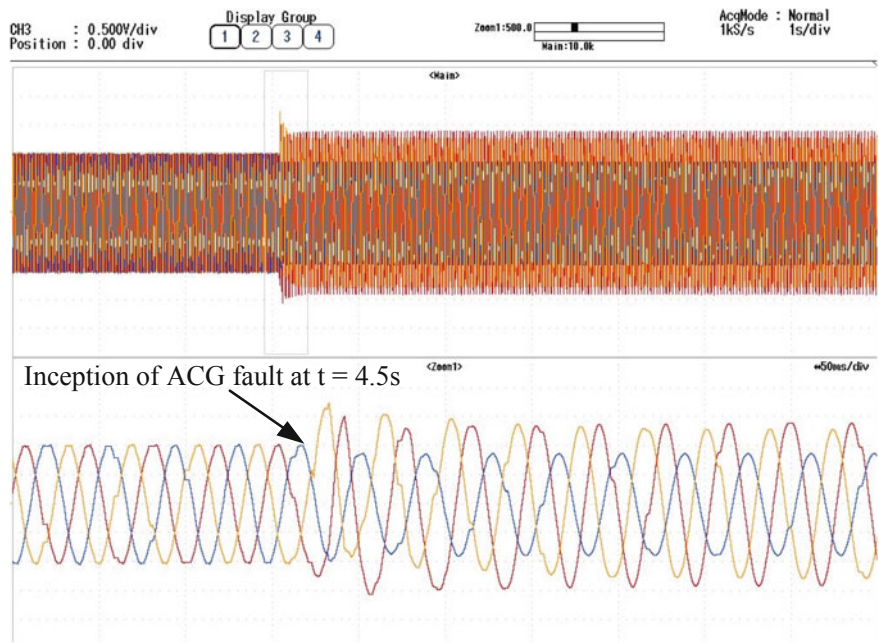


Fig. 14 Three-phase current at bus B1 during an ACG fault at $t = 4.5$ s

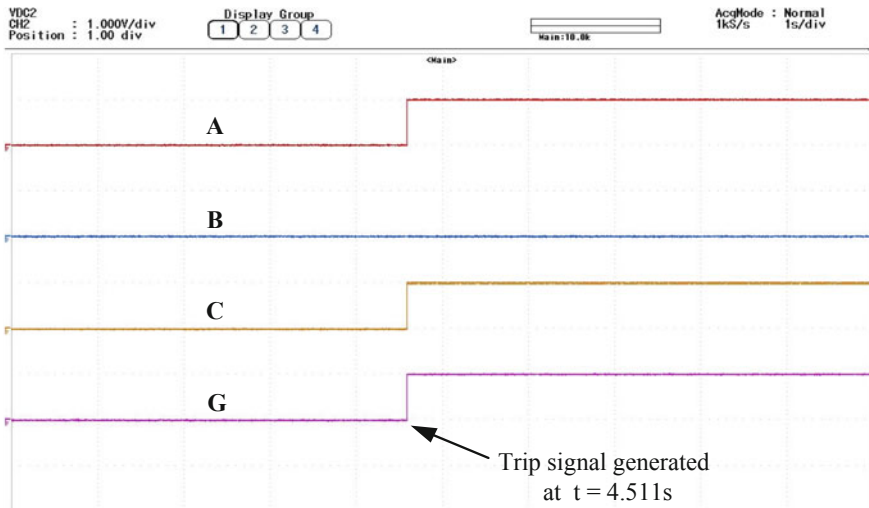


Fig. 15 Trip signal generated by the relay at $t = 4.511$ s

ANN-based scheme is found to generate the trip signal within 1 cycle (16.67 ms) of the fault inception, which confirms the suitability of the scheme for practical field applications.

6 Conclusions

The rising power demand and the stress on the use of sustainable energy resource with low carbon emission have given a fillip to the use of PV-integrated microgrids. However, the highly stochastic nature of PV operation resulting from varying irradiance levels, partial shading and faults in PV array poses a great challenge for the existing MPPT schemes to track the global MPP for PV-fed microgrids. Also, the MPPT algorithm influences the protection schemes and quite often misguides the relaying operation leading to its maloperation (underreach and overreach). In this regard, a SCA-based MPPT and a SCA-ANN-based protection scheme have been proposed to meet the dual objectives of tracking the maximum power under partial shading and array faults as well as providing intended protection to the PV-integrated microgrid against faults in PV array and distribution lines (symmetrical and unsymmetrical faults) under both modes of microgrid operation. The proposed MPPT and protection scheme has been validated against diverse operating conditions of both the PV and distribution system. The obtained result confirms the efficacy of the developed scheme in meeting the dual objectives. To examine the performance of the proposed scheme for practical settings, it has also been substantiated by performing real-time simulation on OPAL-RT platform.

References

1. Xu X, Mitra J, Wang T, Mu L (2016) An evaluation strategy for microgrid reliability considering the effects of protection system. *IEEE Trans Power Deliv* 31(5):1989–1997
2. Zhao Y, De Palma J-F, Mosesian J, Lyons R, Lehman B (2013) Line–line fault analysis and protection challenges in solar photovoltaic arrays. *IEEE Trans Industr Electron* 60(9):3784–3795
3. Rezk H, Eltamaly AM (2015) A comprehensive comparison of different MPPT techniques for photovoltaic systems. *Sol Energy* 112:1–11
4. Camilo JC, Guedes T, Fernandes DA, Melo JD, Costa FF, Sguarezi Filho AJ (2019) A maximum power point tracking for photovoltaic systems based on Monod equation. *Renew Energy* 130:428–438
5. Li X, Wen H, Chu G, Hu Y, Jiang L (2018) A novel power-increment based GMPPT algorithm for PV arrays under partial shading conditions. *Sol Energy* 169:353–361
6. Kaced K, Larbes C, Ramzan N, Bounabi M, elabadine Dahmane Z (2017) Bat algorithm based maximum power point tracking for photovoltaic system under partial shading conditions. *Sol Energy* 158:490–503
7. Labar H, Kelaiaia MS (2018) Real time partial shading detection and global maximum power point tracking applied to outdoor PV panel boost converter. *Energy Convers Manag* 171:1246–1254
8. Ahmed J, Salam Z (2014) A Maximum Power Point Tracking (MPPT) for PV system using Cuckoo Search with partial shading capability. *Appl Energy* 119:118–130
9. Ashouri-Zadeh A, Toulabi M, Dobakhshari AS, Taghipour-Broujeni S, Ranjbar AM (2018) A novel technique to extract the maximum power of photovoltaic array in partial shading conditions. *Int J Electr Power Energy Syst* 101:500–512
10. Al-Majidi SD, Abbod MF, Al-Raweshidy HS (2018) A novel maximum power point tracking technique based on fuzzy logic for photovoltaic systems. *Int J Hydrogen Energy* 43(31):14158–14171
11. Farh HMH, Eltamaly AM, Othman MF (2018) Hybrid PSO-FLC for dynamic global peak extraction of the partially shaded photovoltaic system. *PLoS ONE* 13(11):e0206171
12. Martin AD, Vazquez JR, Cano JM (2018) MPPT in PV systems under partial shading conditions using artificial vision. *Electr Power Syst Res* 162:89–98
13. Abdel-Salam M, El-Mohandes M-T, Goda M (2018) An improved perturb-and-observe based MPPT method for PV systems under varying irradiation levels. *Sol Energy* 171:547–561
14. El Aamri F, Maker H, Sera D, Spataru SV, Guerrero JM, Mouhsen A (2018) A direct maximum power point tracking method for single-phase grid-connected PV inverters. *IEEE Trans Power Electron* 33(10):8961–8971
15. Aouchiche N, Aitcheikh MS, Becherif M, Ebrahim MA (2018) AI-based global MPPT for partial shaded grid connected PV plant via MFO approach. *Sol Energy* 171:593–603
16. Suo C, Zhang W, Wu G, Gui J, Zhao L, Ma C (2015) Modelling and simulation of MPPT algorithm for PV grid-connected system. *Integr Ferroelectr* 162:18–23
17. Ramaprabha R, Balaji M, Mathur BL (2012) Maximum power point tracking of partially shaded solar PV system using modified Fibonacci search method with fuzzy controller. *Int J Electr Power Energy Syst* 43(1):754–765
18. Akrami M, Pourhossein K (2018) A novel reconfiguration procedure to extract maximum power from partially-shaded photovoltaic arrays. *Sol Energy* 173:110–119
19. Eltamaly AM, Farh HMH, Othman MF (2018) A novel evaluation index for the photovoltaic maximum power point tracker techniques. *Sol Energy* 174:940–956
20. Eltamaly AM, Farh HMH (2019) Dynamic global maximum power point tracking of the PV systems under variant partial shading using hybrid GWO-FLC. *Sol Energy* 177:306–316
21. Abdelsalam AK, Massoud AM, Ahmed S, Enjeti PN (2011) High-performance adaptive perturb and observe MPPT technique for photovoltaic-based microgrids. *IEEE Trans Power Electron* 26(4):1010–1021

22. Alajmi BN, Ahmed KH, Finney SJ, Williams BW (2013) A maximum power point tracking technique for partially shaded photovoltaic systems in microgrids. *IEEE Trans Industr Electron* 60(4):1596–1606
23. Mirjalili S (2016) SCA: a sine cosine algorithm for solving optimization problems. *Knowl-Based Syst* 96:120–133
24. Hooshyar A, El-Saadany EF, Sanaye-Pasand M (2016) Fault type classification in microgrids including photovoltaic DGs. *IEEE Trans Smart Grid* 7(5):2218–2229
25. Bansal R (2017) *Handbook of distributed generation*. Springer International Publishing, Switzerland
26. Valsan SP, Swarup KS (2009) Wavelet transform based digital protection for transmission lines. *Int J Electr Power Energy Syst* 31(7–8):379–388
27. Shukla SK, Koley E, Ghosh S (2018) A hybrid wavelet–APSO–ANN-based protection scheme for six-phase transmission line with real-time validation. *Neural Comput Appl* 1–15
28. Kumar N, Hussain I, Singh B, Panigrahi BK (2017) Peak power detection of PS solar PV panel by using WPSCO. *IET Renew Power Gener* 11(4):480–489

Artificial Bee Colony-Based GMPPT for Non-homogeneous Operating Conditions in a Bifacial CPVT System



Cihan Demircan, Ali Keçebaş and Hilmi Cenk Bayrakçı

Abstract Photovoltaic (PV) modules directly convert the solar energy into electricity with electrical efficiency in 10–20%. The rest of the incident solar radiation reflects from front surface and converts into thermal energy which leads to an increase in the PV module temperature. Thus, PV module efficiency decreases. PV power production can be increased with utilize of thermal energy or cooling of PV module. Photovoltaic–thermal (PV/T) technologies provide both electricity and thermal energy. PV/T absorbs thermal energy from PV module which may lead to decrease the PV module temperature. Thus, its electrical efficiency is higher with respect to PV systems. However, PV/T collectors suffer for high capital costs. To improve their profitability, many concentrating PV (CPV) have been developed to increase the incident solar radiation on the PV surface, simultaneously reducing PV material for unit receiver area. Both electricity and thermal energy from the sun more effectively is used with this mechanism called concentrating photovoltaic–thermal (CPVT) technology. This chapter focuses on artificial bee colony (ABC)-based global maximum power point tracking (GMPPT) for PV string structures in a bifacial CPVT system. This power conditioning unit is applied to bifacial CPVT system for efficient utilization of solar energy under four different non-homogeneous solar radiation and module temperature operating conditions.

C. Demircan (✉)

Department of Energy Systems Engineering, Graduate School of Natural and Applied Sciences, Süleyman Demirel University, 32260 Isparta, Turkey
e-mail: cihandemircan48@gmail.com

A. Keçebaş

Department of Energy Systems Engineering, Technology Faculty, Muğla Sıtkı Koçman University, 48000 Muğla, Turkey

H. C. Bayrakçı

Department of Mechatronics Engineering, Technology Faculty, Isparta University of Applied Sciences, 32260 Isparta, Turkey

© Springer Nature Switzerland AG 2020

A. M. Eltamaly and A. Y. Abdelaziz (eds.), *Modern Maximum Power Point Tracking Techniques for Photovoltaic Energy Systems*, Green Energy and Technology, https://doi.org/10.1007/978-3-030-05578-3_12

1 Introduction

Renewable energy resources (RESs) are energy types that are not consumed, are environmentally friendly, and have intermittent energy. The limited nature of energy and the increasing energy demands every day have increased the importance of efficiently using energy that can be produced from energy resources. For continuity of electrical energy, it is necessary to ensure energy demands can be met by diversifying energy resources. RESs are superior as they can be easily integrated into the power grid and can supply energy requirements for rural areas distant from the power grid. With the fall in initial investment costs in recent years, interest in solar energy as RES has increased from both society and industry, institutions, and organizations.

Photovoltaic (PV) cells are a popular issue of solar energy because they do not have a moving part in electricity generation, they do not harm the environment, they can be easily integrated into buildings, and they can reach thousands of MW power from a few Watts. In other words, PV module prices are decreasing each year thanks to the increase in the installed capacity of PV in the world.

The fact that solar energy is intermittent and variable and that PV performance depends on solar radiation, ambient temperature, and wind speed increases the importance of using output power effectively in PV modules. In other words, studies are carried out to increase the module efficiency in PV modules. Two important environmental parameters affecting the performance of PV modules are solar radiation and module temperature. In recent years, concentrating systems have been developed to increase the radiation coming to the PV module surface, and active and passive cooling systems are carried out in order to reduce the temperature of the module.

In the concentrating PV (CPV) technology, the amount of solar radiation coming to the PV surface is increased. In this way, an extensive solar radiation is reflected onto the PV module from a curved reflective mirror with wide area. However, the increase in solar radiation in CPV systems causes the temperature of the PV modules to increase. Therefore, PV modules can be permanently damaged at extreme temperatures. To prevent this, PV cells are actively or passively cooled. For active cooling a fluid and a channel through which it flows are used. Thus, both electricity and thermal energy are produced from solar energy. Such systems are called as concentrating PVT (CPVT).

In CPVT systems, solar radiation at each point on the groove (cylindrical, triangular, etc.) has the same value. On the one hand, the fluid cools the PV modules, respectively, while the fluid flows along the groove, but, on the other hand, its temperature increases as the fluid flows along the groove. Thus, the fluid temperature increases. Due to the increase in temperature as the fluid reaches the end of the groove, the cooling amount of the PV modules at the end is reduced. The temperature of a PV module is higher than the previous one. The fluid reaches the maximum temperature at the end of the groove. Therefore, non-homogeneous temperature distribution occurs in PV modules. In addition, there are differences in the current and voltage values of the PV modules.

In PV systems, in cases where the distribution of temperature and solar radiation is not homogeneous, as mentioned above, mismatches occur in the current–voltage–power curves. The occurrence of these mismatches causes a loss of power. PV power regulation units are becoming more important in order to minimize the loss of mismatch.

The performance of PV modules varies according to material properties and environmental conditions (temperature, solar radiation, etc.). Power regulation units are used to make the PV modules more efficient in the production of power mismatches, to use them in the most efficient way, and to ensure the highest level of power transfer to the output load. Power regulation equipment is DC/DC converters. The converter provides the connection between the PV modules and the load. Maximum power point tracking (MPPT) algorithms are the ones that provide the most efficient power to the load. The MPPT devices that monitor the output power of the PV transmit the highest power by controlling duty cycles of the DC/DC converters. The focus is on maximum power point (MPP) tracking (MPPT) systems ensuring effective use of electrical energy from concentrator photovoltaic–thermal systems (CPVT) using electrical and thermal energy from solar energy. Rezk and Eltamaly [1] compared and assessed MPPT algorithms based on perturb and observe (P&O), incremental conductance (INC), hill climbing (HC), and fuzzy logic (FLC) for photovoltaic systems. Their results showed that FLC-MPPT algorithms were superior to the other algorithms. In other their studies, authors reviewed and discussed of evaluation index of MPPT algorithms [2]. Algarin et al. [3] compared FLC-based MPPT and P&O MPPT structures for a 65 W PV module. The results demonstrated the superiority of the FLC-based MPPT in terms of settling time, power loss, and oscillations at the operating point. Tang et al. [4] combined a traditional FLC algorithm with fractional order (FO) structure and improved MPPT performance. They compared the proposed FO-FLC structure with classic FLC and FO-INC algorithms and proved the proposed structure was better than others. Boukenoi et al. [5] investigated P&O, INC, HC, and FLC-MPPT structures experimentally. For an efficient MPPT power regulation unit, studies were completed on the Takagi–Sugeno fuzzy model by Ounnas et al. [6]. Yilmaz et al. [7] completed studies on FLC-MPPT for a battery charge control unit for PV. Zainal et al. [8] recommended an FLC-based constant voltage (CV) MPPT system structure for a cooling-integrated PV system.

Based on environmental and working conditions, the current–voltage values at the MPP display differences. Therefore, the tracking power gains great importance. Due to environmental conditions like buildings, trees, and dust, partial shading reduces the PV power output [9, 10]. In circumstances with partial shading, more than one MPP forms. These are defined as local and global MPP. To produce maximum levels of power from solar energy, the DC–DC converter should work at the global MPP. As a result, it becomes even more important that MPPT algorithms track power in partial shading conditions. Traditional MPPT techniques provide superior performance with uniform radiation distribution. However, in non-uniform partial shading situations, tracking power at the global point is unsuccessful as more than one MPP forms [11, 12]. Hence, research is performed about intelligent global MPPT techniques tracking power at the global point. The use of GMPPT algorithms from among artificial

intelligence optimization algorithms developed in engineering has come to the fore in recent years. For these, both experimental and simulation studies are performed to improve the working performance of PV systems, and thus, solar energy is used more efficiently and effectively. Rezk et al. [13] compared different meta-heuristic-based GMPPT algorithms under partial shading. Benyoucef et al. [14] tested the artificial bee colony (ABC) algorithm for the MPPT technique with simulation and experimental studies under different shading conditions. The results obtained were compared with particle swarm optimization (PSO) algorithm. Seyedmahmoudian et al. [15] combined differential evolution (DE) and PSO algorithms for a PV system and completed both simulation and hardware applications with the hybrid algorithm structure. Sundareswaran et al. [16] completed both simulation and experimental studies with the ABC algorithm to increase PV power output under partial shading conditions. They compared the ABC-MPPT power regulation unit with classic PSO and enhanced P&O MPPT techniques. Javed et al. [17] applied a generalized pattern research (GPR) algorithm to a partial shading PV system and compared with traditional P&O and PSO algorithms. Kumar and Rao [18] tested the whale optimization algorithm for different PV system connections and partial shading conditions and compared with the grey wolf optimization (GWO) algorithm and PSO algorithm. Kaced et al. [19] presented both simulation and experimental applications of the bat algorithm for partial shading conditions. Ram and Rajasekar [20] completed both simulation and experimental work on the flower pollination algorithm (FPA) for GMPPT power regulation. Similarly, the Lider PSO algorithm was applied by Ram and Rajasekar [21] and compared with the P&O and traditional PSO algorithm. Rezk and Fathy [22] assessed six different shading conditions in learning-teaching optimization algorithm-based MPPT studies. The artificial fish swarm algorithm was applied to a GMPPT unit by Mao et al. [23]. Wu et al. [24] applied the chicken swarm optimization method to a PV-MPPT system. PSO and GWO based hybrid FLC-MPPT studies presented in [25, 26]. Finally, ABC and hill climbing-based hybrid single sensor MPPT study published in [27].

In this chapter, the electrical performance of the standard and bifacial CPVT systems were investigated under four different circumstances. In the bifacial CPVT system, mismatch losses in current and voltage as temperature along with solar radiation are not homogeneous and more than one peak point forms in a series-connected PV strings. As a result, this study applied the ABC algorithm to track the global peak point of the MPPT unit for effective and efficient use of solar energy in a CPVT system. A study of the proposed bifacial CPVT system is not found in the literature. However, there are studies about standard CPVT systems. Bernardo et al. [28] performed application and simulation of a parabolic-trough-triangular design CPVT system for three different locations. They were concluded that the CPVT system produced 3.6–4.4 times more electricity for three different places than the conventional PV system. Calise and Vanoli [29] designed and simulated a CPVT with triple groove using zero-dimensional energy balances. The effect of triple groove length and fluid channel diameter on temperature distribution and thermal and electrical performance of CPVT system were investigated. It has been observed that the length of the groove and the diameter of the fluid channel increase the CPVT operating

temperature, thus decreasing both thermal and electrical efficiency. Similarly, Calise et al. [30] modeled the same CPVT system with finite volumes method. They investigated the temperature distributions, electrical and thermal efficiency of the CPVT system at 10 and 20 m lengths, and the exergy efficiency of the system according to different fluid flow rates. As the length of the CPVT system increased, the fluid output temperature increased, and therefore, the electrical and exergy efficiencies decreased slightly. It was seen that the fluid output temperatures decreased rapidly between 85 and 110 °C at the rate of 0.1 kg/h, and the thermal and electrical efficiency increased rapidly. Calise et al. [31] presented the energy and environmental performance simulation of a CPVT system for a desiccant-based air handling unit. According to the results, CPVT system provided approximately 60% of the thermal energy requirement. The energy saving was found to vary between 81 and 89% according to the water heating requirement. Finally, Manokar et al. [32] investigated the performance of a water-cooled CPVT system. They examined the change in PV cell temperature relative to the solar radiation for the standard PVT and triangular CPVT.

2 System, Modeling, and Optimization

In this section, the standard and proposed bifacial CPVT systems are described. In addition, necessary information about the mathematical modeling of PV modules for the CPVT systems, the MPPT power conditioning units playing an important role in PV systems, the optimization process of the ABC algorithm, and some case study applications are presented.

2.1 *Parabolic-Trough Bifacial CPVT System*

A schematic diagram for the parabolic-trough CPVT system is given in Fig. 1. As seen in this figure, this system consists of a parabolic-trough concentrator, a hollow triangular prismatic groove, a duct through which the fluid flows in the groove, and PV modules joined on the groove. It is contemplated that the mirror is used along the concentrator. The triangular groove is placed in the focus of the concentrator. One surface of the triangle groove is positioned perpendicular to the sunbeam, while the other two surfaces face the concentrator. The PV module series are mounted on two surfaces that are opposite with the reflector. A fluid duct is inserted into the hollow triangular prismatic groove to cool the PV modules and thereby increasing the electrical efficiency. The PV modules are cooled by any type of cooling fluid flowing through this fluid duct. Therefore, the temperature of the fluid exiting the CPVT system is increased. This fluid temperature can be used in thermal energy applications, e.g., space heating. Thus, in CPVT system thermal energy is used along with electrical energy. Additionally, the upper surface of the triangular section

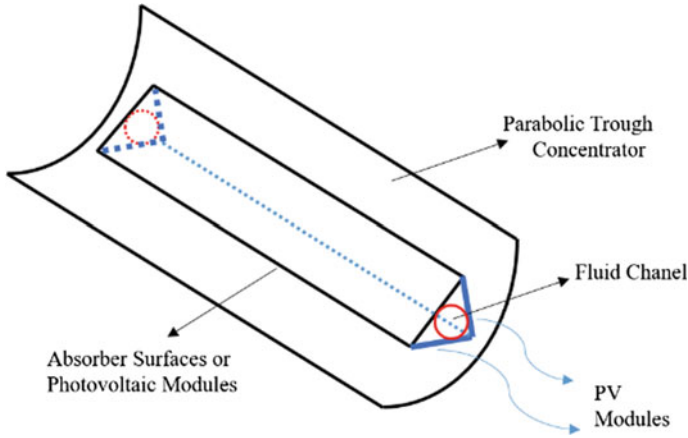


Fig. 1 General schematic diagram of the CPVT system

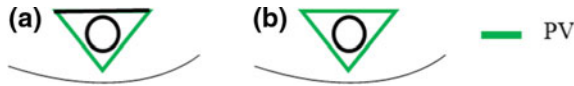


Fig. 2 Design differences of CPVT systems: **a** the standard CPVT system, and **b** the bifacial CPVT system

is the cooling surface in standard CPVT systems, while in the proposed bifacial CPVT system a PV module string is designed in this surface. This means that all surfaces of the triangular prismatic groove are covered with three PV module strings. Its schematic diagram is shown in Fig. 2. As seen in the figure, while the standard CPVT system uses two PV module strings on only two surface of the groove (Fig. 2a), the bifacial CPVT system uses three PV module strings on all surfaces of the groove (Fig. 2b).

While the amount of radiation on the PV module surfaces is almost the same on both surfaces of the standard CPVT system, in the bifacial CPVT system it is nearly the same for the two PV module strings facing the parabolic-trough concentrator; however, it is different for the sun-facing surface of the groove. In other words, while the two PV module strings in both systems use direct radiation, the PV module string on the sun-facing surface in the bifacial CPVT system uses total radiation. When examined in terms of temperature, the cooling degrees of the PV modules will be different as the different fluid temperature occurs in each node along triangular prismatic groove; however, mismatch occurs due to non-homogeneous temperature circumstances in PV modules in both systems. In addition, due to connections of the PV modules and their strings, the behavior under non-homogeneous working conditions can be investigated using current, voltage, and power graphs.

A diagram associated with non-homogeneous working conditions due to radiation and temperature naturally occurring in the standard and bifacial CPVT systems is

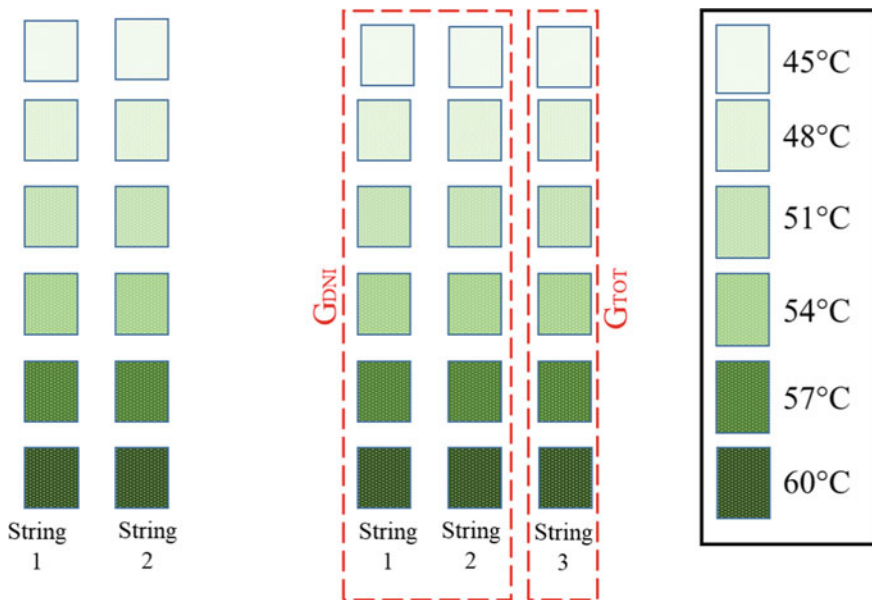


Fig. 3 Non-homogeneous operating conditions of the CPVT system with two and three strings

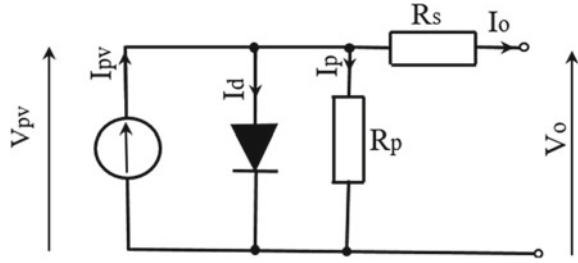
presented in Fig. 3. Here, total radiation and direct beam radiation are taken as 1000 and 800 W/m², respectively. The concentration rate of the CPVT system is chosen as 2.5. As the fluid heats up with each step, it is assumed that the temperatures of the PV modules will increase from 45 to 57 °C. Based on these assumptions, some case studies and assessments are performed.

2.2 Mathematical Modeling of PV

Modeling is required to investigate the dynamic behavior of PV modules under certain conditions. The single diode model [33–38], double diode model [39, 40], and transistor models [41] have been developed to model the nonlinear dynamic behavior of PV modules. The most commonly used model in the literature is the single diode model. The single diode model based on four parameters considers series resistance, while the five-parameter-based model considers series resistance along with parallel resistance values. The equivalent circuit based on five parameters for PV modules is shown in Fig. 4. In this chapter, the single diode model with five parameters is used. The correlations between current and voltage for the four- and five-parameter-based models of a PV module are given in Eqs. (1) and (2).

$$I_o = I_{pv} - I_d \left(e^{\frac{q(V_o + R_s I_o)}{nkT}} - 1 \right) \quad (1)$$

Fig. 4 Five-parameter PV equivalent circuit



$$I_o = I_{pv} - I_d \left(e^{\frac{q(V_o + R_s I_o)}{nkT}} - 1 \right) - \frac{V_o + R_s I_o}{R_p} \quad (2)$$

where I_o , I_{pv} , and I_d donate the load, PV, and diode currents, respectively; q is electron charge, n is diode ideality factor, k is the Boltzmann constant, and R_s and R_p are series and parallel resistance values.

In short-circuit current and open-circuit operation conditions [33],

$$I_{sc} = I_o - I_d \left[e^{\frac{q I_{sc} R_s}{nkT}} - 1 \right] - \frac{I_{sc} R_s}{R_p} \quad (3)$$

$$0 = I_o - I_d \left[e^{\frac{q V_{oc}}{nkT}} - 1 \right] - \frac{V_{oc}}{R_p} \quad (4)$$

where I_{sc} and V_{oc} represent short-circuit current and open-circuit voltage, respectively.

According to PV module temperature, I_{sc} and V_{oc} values estimated as the following,

$$I_{sc,T} = I_{sc} (1 + \lambda (T_{pv} - 25)) \quad (5)$$

$$V_{oc,T} = V_{oc} (1 + \beta (T_{pv} - 25)) \quad (6)$$

where λ , β , and T_{pv} shows that current–temperature coefficient, voltage–temperature coefficient, and PV module temperature.

The parameters for the PV modules used in this chapter are given in Table 1. Their mathematical modeling is performed in the MATLAB/SIMULINK program [42] using the PV module parameters for the five-parameter equivalent circuit. With the aid of the modeled PV module, five modules are connected as series to obtain a PV module string.

Table 1 Datasheet values of the TPS105S-5W PV module [43]

Parameter	Value	Parameter	Value
I_{sc} (A)	0.32	V_{oc} (V)	21.5
I_{mp} (A)	0.29	V_{mp} (V)	17.5
λ (%/K)	0.05	β (%/K)	-0.32
Sizes (cm)	19.3×23.3	Weight (kg)	0.54

2.3 DC–DC Converter

The power conditioning units in PV systems consist of the MPPT units and DC–DC converter. Maximum power point tracking (MPPT) units that monitor the output power of the PV transmit the highest power by controlling duty cycles of the DC/DC converters. Therefore, MPPT algorithms control the duty cycle ratio (D). Controlled linked to the current and voltage values at the maximum power point, this parameter varies between 0 and 1. The pulse width modulation (PWM) is set according to this value. The value when the switching element for the PWM signal is closed (signal = 1) (ton) represents the ratio of the switching time rate to the duty cycle ratio. For switching elements, generally metal oxide semiconductor field effect transistors (MOSFET) and isolated gate bipolar transistors (IGBT) are used. According to the D value calculated by the MPPT algorithm, the PWM signal is produced. This signal reaches the MOSFET or IGBT and ensures control of the DC–DC converter. These parameters are updated according to the current and voltage input–output values, and thus, maximum power tracking occurs.

2.4 Artificial Bee Colony Algorithm

Investigation of processes involving intelligent behavior present in nature has encouraged researchers to develop new optimization methods. Karaboğa [44] developed the artificial bee colony (ABC) algorithm modeling the food search behavior of bees. For the sake of simplicity, the model based on the developed ABC algorithm includes some assumptions. The first of these is that the number of employed bees is equal to the total number of food sources. The number of employed bees is accepted as being equal to the number of onlooker bees. The bee assigned to a source with nectar consumed transforms into a scout. The food source locations represent the possible solutions to the optimization problems, and the nectar amounts in the food sources are equivalent to the quality (fit) of the solutions related to that source. While the ABC optimization algorithm attempts to find the location of the source with most nectar it attempts to find points providing the minimum or maximum of a problem in solution space.

Onlooker bees waiting in the hive watch dances indicating rich sources and choose a source linked to the dance frequency which is proportional to the quality of the food.

The basic steps of the ABC algorithm are as follows [45]:

Step 1: production of initial food source regions.

REPEAT

Step 2: sending employed bees to the food source regions.

Step 3: calculation of probability values according to information coming from employed bees using probabilistic selection.

Step 4: see Eq. (9).

Step 5: abandoning consumed sources and producing scouts

UNTIL (cycle number = maximum cycle number).

If we consider search space as food sources found around the hive, production of the initial food source region is based on the algorithm producing random food source locations equivalent to solutions in search space. The random location production process occurs by producing random values between the upper and lower limits for each parameter, as follows:

$$x_{ij} = x_j^{\min} + r \text{ and } (0, 1) \left(x_j^{\max} - x_j^{\min} \right) \begin{cases} i = 1, \dots, SN \\ j = 1, \dots, SD \end{cases} \quad (7)$$

Calculation of quality,

$$\text{fitness}_i \begin{cases} \frac{1}{1+f_i}, & f_i \geq 0 \\ 1 + \text{abs}(f_i), & f_i < 0 \end{cases} \quad (8)$$

The ratio of a source's fit value to the sum of fit values of all the sources refers to the probability of that source's chance of being selected relative to the other sources, as expressed below:

$$p_i = \frac{\text{fitness}_i}{\sum_{j=1}^{SN} \text{fitness}_j} \quad (9)$$

At the end of each cycle, counters check whether the solution development occurs after all employed bees and onlooker bees have completed search processes. Whether a bee has used a source or not, in other words whether the nectar has been consumed or not, is known by the solution abandonment counters. If the solution abandonment counter for a source is above a certain threshold value, this source must be left by the employed bee as it is consumed and the bee must begin to search for another solution. This means the employed bee associated with the consumed solution must become a scout. After becoming a scout, this bee begins the random solution search process. The threshold value used to determine whether a source is consumed is an important control parameter in the ABC algorithm and is called the "limit." In

the basic ABC algorithm, only one explorer bee is allowed to search in each cycle. Detailed information about the ABC algorithm may be found in the related references [46, 47].

The colony size, colony cycle number, and limit values of the ABC algorithm were chosen as 10, 10, and 100 in this study. An Intel Processor i7-6700HQ CPU 2.60 GHz, 16 GB RAM 64 bit ASUS computer was used.

3 Case Studies for CPVT Systems

PV strings of CPVT system are investigated and compared with four different case studies in order to effect of concentrating in CPVT system. Standard and proposed CPVT systems are considered with and without concentrating. Firstly, first case focus on standard test conditions (STC) (1000 W/m^2 , 25°C) operating conditions of PV strings. On the other hand, other case different (non-homogeneous) temperature distribution of CPVT strings is investigated for effect of temperature increasing due to fluid. In the other two different cases, concentrating of CPVT system and their PV string connections are taken into account. Details of four different case studies are presented below.

Case 1: Consider operation under STC for PV strings belonging to standard and proposed CPVT systems.

Case 2: Consider operation under non-homogeneous working conditions shown in Fig. 13.3 with 1000 W/m^2 solar radiation for PV strings belonging to standard and proposed CPVT systems.

Case 3: Consider operation under non-homogeneous circumstances shown in Fig. 3 along with total and direct beam solar radiation values of 1000 and 800 W/m^2 for PV series belonging to standard and proposed CPVT systems. Serial connection between the PV strings is considered.

Case 4: Consider operation under non-homogeneous circumstances shown in Fig. 3 along with total and direct solar radiation values of 1000 and 800 W/m^2 for PV series belonging to standard and proposed CPVT systems. Parallel connection between the PV strings is considered.

In order to evaluate four different cases, CPVT system is modeled as an algorithm developed on MATLAB/SIMULINK program. Modeled system is shown in Fig. 5. As can be seen in this figure, a boost converter and inverter connect to PV system. The I_{pv} and V_{pv} values are tracked when runned MPP operation on CPVT system. Duty cycle of the boost converter is optimized in order to be operated MPP of inverter or load. Its value is selected between 0.3 and 0.9 in optimization process. Thus, ABC-based GMPPT application is implemented.

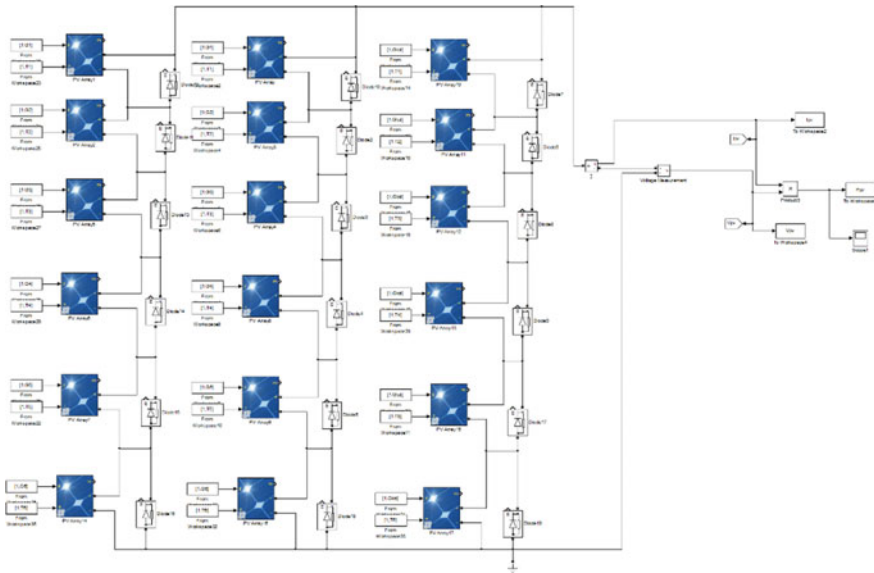


Fig. 5 ABC-GMPPT application of proposed CPVT system using MATLAB/SIMULINK

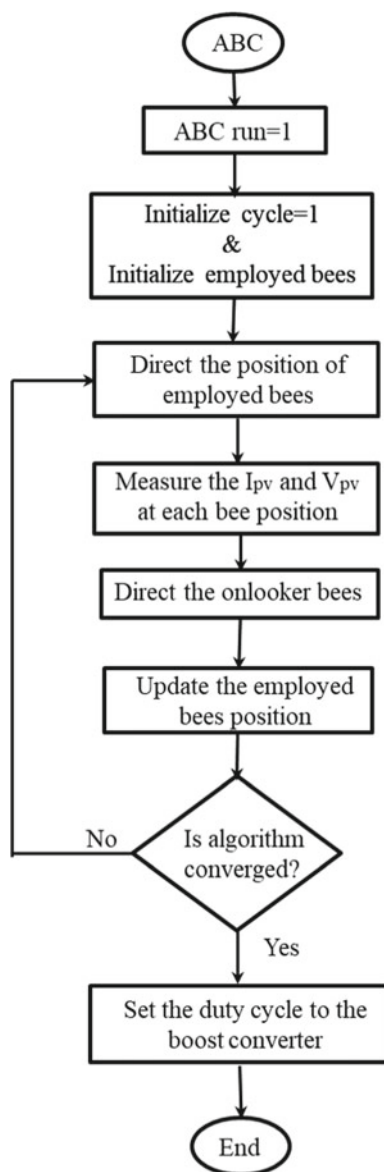
Flowchart of ABC-based GMPPT power conditioning unit is given in Fig. 6. As shown in Fig. 6, the I_{pv} and V_{pv} values are measured in each bee position after the initialize. Changing objective function (P_{pv}) is observed at each a D value. According to this change, boost converter is operated at MPP in optimum D value and then tracking of maximum power is done.

4 Results and Discussion

In this study, electrical performance of PV strings belonging to the standard and proposed CPVT systems was investigated under different working conditions. The performance of the MPPT power conditioning unit was investigated according to peak points formed in situations where the strings are connected in series or in parallel. Under different conditions, the duty cycle is maximized with the ABC algorithm to transfer the load to power at maximum value.

The PV modules were modeled in the MATLAB/SIMULINK program to investigate the performance of PV strings belonging to the CPVT system. The single diode model was used for PV mathematical modeling. Additionally, to reduce losses due to partial shading of the PV strings under any conditions, bypass diodes are added. The electrical power produced by the CPVT system is transferred to inverter using a DC–DC boost. A 5 mH inductor with 100 μ F input capacitor is used.

Fig. 6 Flowchart of ABC-GMPPT applications



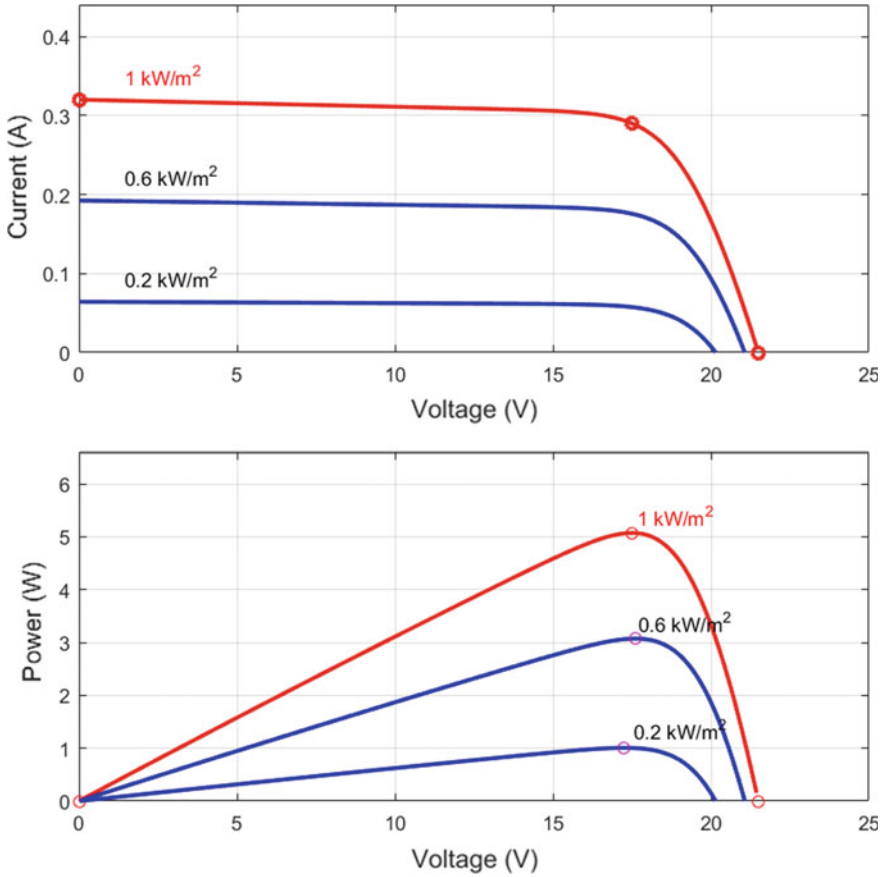


Fig. 7 I–V and P–V graphics PV module for 25 °C module temperature and different solar radiation

The datasheet values for a TPS105S-5 W PV module are presented in Table 1. According to the datasheet values, the results under standard test conditions (STC) (1000 W/m^2 , 25°C) and obtained with different radiation conditions are shown in Fig. 7 (red line). As seen in the figure, when module voltage is 17.5 V, the maximum value of output power (5.07 W) is reached and then falls. Due to the nonlinear behavior of the PV modules, output power falls rapidly as open-circuit voltage is approached. Additionally, PV power works close to maximum power in the interval from 17.2 to 17.7 V. For different module temperatures at 1000 W/m^2 , the I–V and P–V curves for the PV module are given in Fig. 8. The increase in module temperature increases the I_{sc} value by a very small amount and reduces V_{oc} voltage by a larger proportion. As a result, the PV module power reduces. This indicates a nonlinear situation is present.

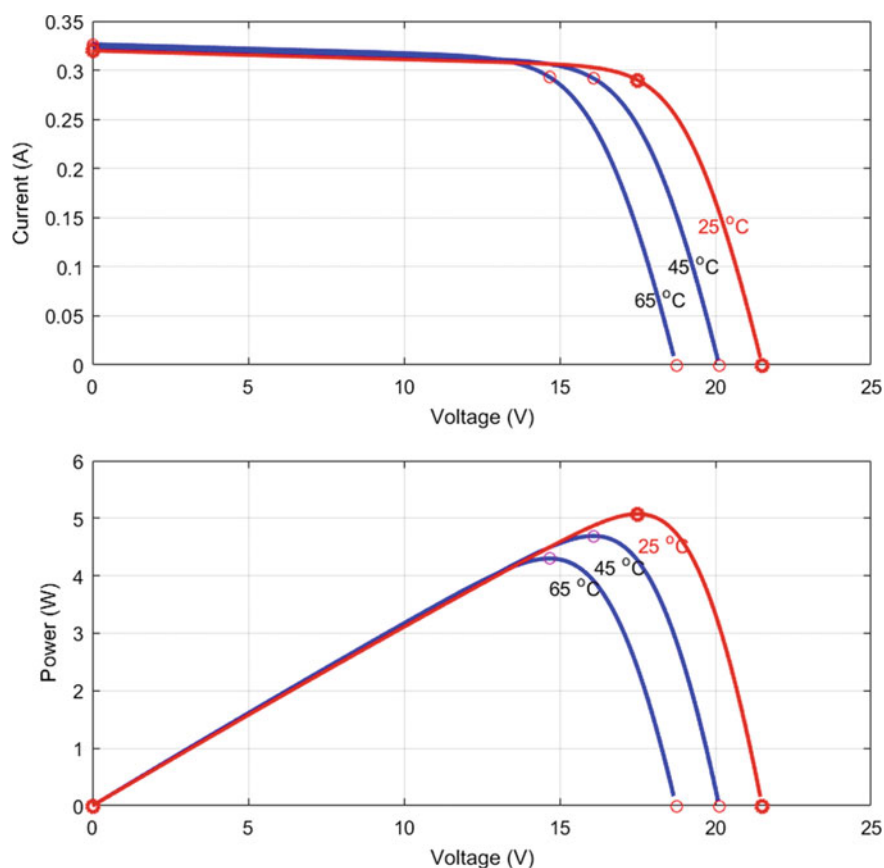


Fig. 8 I–V and P–V graphics PV module for 1000 W/m² solar radiation and different module temperature

Variation of the PV module output power according to environmental conditions is variable due to the nonlinear situation of the current and voltage values which increases the importance of maximizing the output power value obtained from the PV module. As a result, there is a need for power conditioning units.

Four different case studies were examined for the standard and proposed CPVT system. In Case 1, the performance of the PV strings was investigated under STC. The current, voltage, and power variations for this case are presented in Fig. 9. As seen in the figure, the maximum power that can be obtained from a standard system is 60.91 W, while it is 91.37 W for the proposed CPVT system. If both systems are operated at the MPP with nearly 105 V, the proposed system produces 50% more electrical energy compared to the standard system.

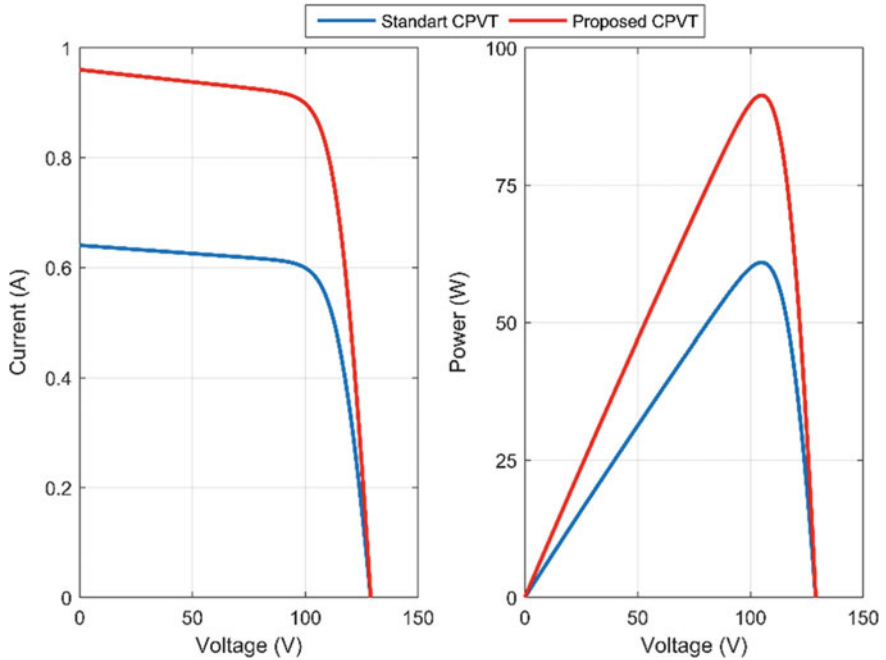


Fig. 9 PV performance changing for Case 1

Table 2 Performances of the CPVT system for different case studies

Cases	CPVT	I_{mp} (A)	V_{mp} (V)	P_{mp} (W)	I_{sc} (A)	V_{oc} (V)
Case 1	Standard	0.5801	105	60.9105	0.64	127.7
	Proposed	0.8702	105	91.371	0.96	127.7
Case 2	Standard	0.5904	92.32	54.505728	0.649	116.5
	Proposed	0.8742	93.59	81.816378	0.9735	116.5
Case 3	Standard	0.5728	179.6	102.87488	0.6452	240.3
	Proposed	0.564	177.1	99.8844	0.6452	357.7
		0.3029	303.5	91.93015		
Case 4	Standard	1.15	89.79	103.2585	1.292	120.1
	Proposed	1.451	89.79	130.28529	1.617	120

When non-homogeneous temperature distributions due to thermal energy are considered for the CPVT system (Case 2), the power for the standard and proposed systems fall to 54.51 and 81.82 W. Operation at the maximum power point brings voltage to 92.32 V. The variation graphs for this case are shown in Fig. 10. As seen in the figure, temperature increase reduces the open-circuit voltage value from 127.6 V (Case 1) to 116.5 V. The detailed values for these cases are given in Table 2. Other parameters may be investigated on this table.

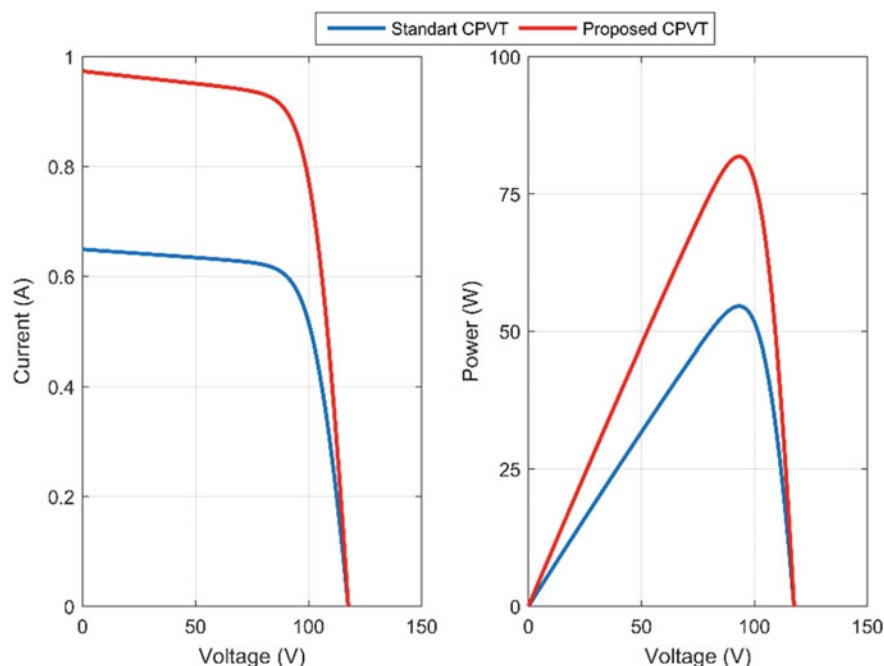


Fig. 10 PV performance changing for Case 2

When the concentrated and direct beam radiation values are considered along with non-homogeneous temperature distributions due to thermal energy in the CPVT system, only the non-homogeneous temperature case is present in the standard system. However, the non-homogeneous case due to both temperature and radiation is present in the proposed system. As a result, the connection types for the PV strings in the system are assessed. The serial connections (Case 3) and parallel connection (Case 4) are considered for the PV strings. Variations obtained from both types are shown in Figs. 11 and 12. As seen in the figures, more than one peak forms in the proposed CPVT system due to the differences in PV current due to radiation in the serial-linked system. At the same time, the maximum power that can be produced by the proposed system is a little lower than from the standard system. In other words, the power values at the MPP for the standard and proposed CPVT systems are 102.87 and 99.88 W. The voltage and power values at the local peak point are nearly 303.5 V and 91.93 W. It can be understood that operation of the MPPT unit at the global peak point becomes very important to increase power production and efficiency. In the parallel-linked systems (Case 4, Fig. 12), there is a single peak point. At the same time, the power gain is nearly 30% higher compared to the serial-linked system.

Above, assessment of the four cases is presented. For assessment of the situation where global peak point tracking can be completed for the MPPT power conditioning

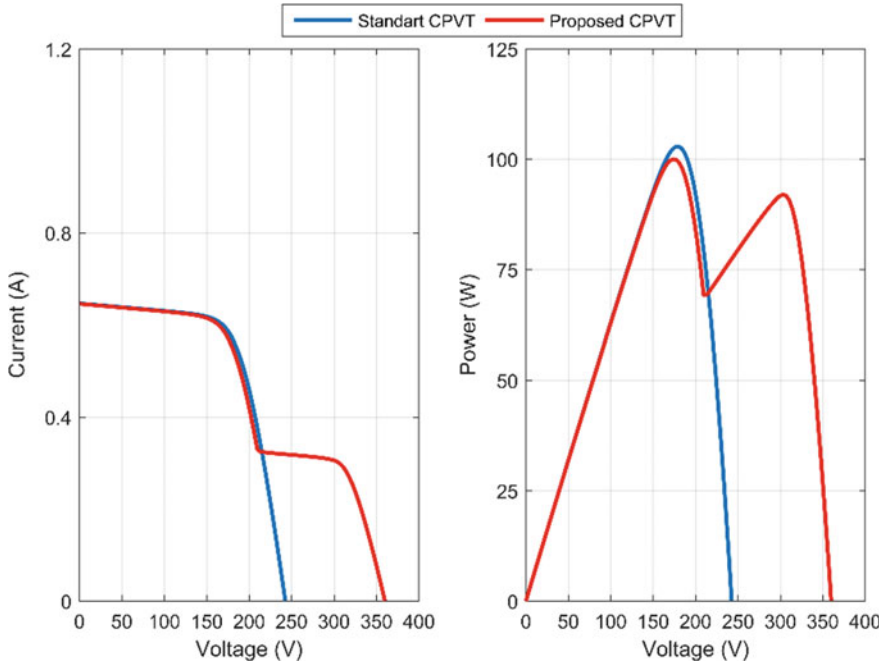


Fig. 11 PV performance changing for Case 3

unit in the CPVT system, the working conditions for the proposed CPVT system in Case 3 and Case 4 were considered.

The ABC-based GMPPT application results completed in this study are given in Fig. 13. As mentioned previously, the performance of the ABC-GMPPT power conditioning unit was assessed under working conditions in Case 3 and Case 4. As observed in the figure, there are fluctuations due to the transitional circumstances in the time period from 0 to 0.125 s. After 0.125 s, the system operates close to maximum power, but occasional 1–2 W power reductions occur. As understood from Figs. 11 and 13, the system (Case 3) V_{mp} values are in close regions and thus power production and load transfer occur at the global peak point (nearly 100 W). As shown in Fig. 13, parallel linking of the PV strings in the system both reduces the effect of mismatch due to non-homogeneous radiation and temperatures and increases power production. Finally, the parallel connections of PV strings increase the power production. If more than one peak point occurs due to any circumstance, the ABC algorithm-based GMPPT techniques unit will ensure power is transferred to load at the maximum level. In this way, the use of solar energy may be completed more efficiently and effectively.

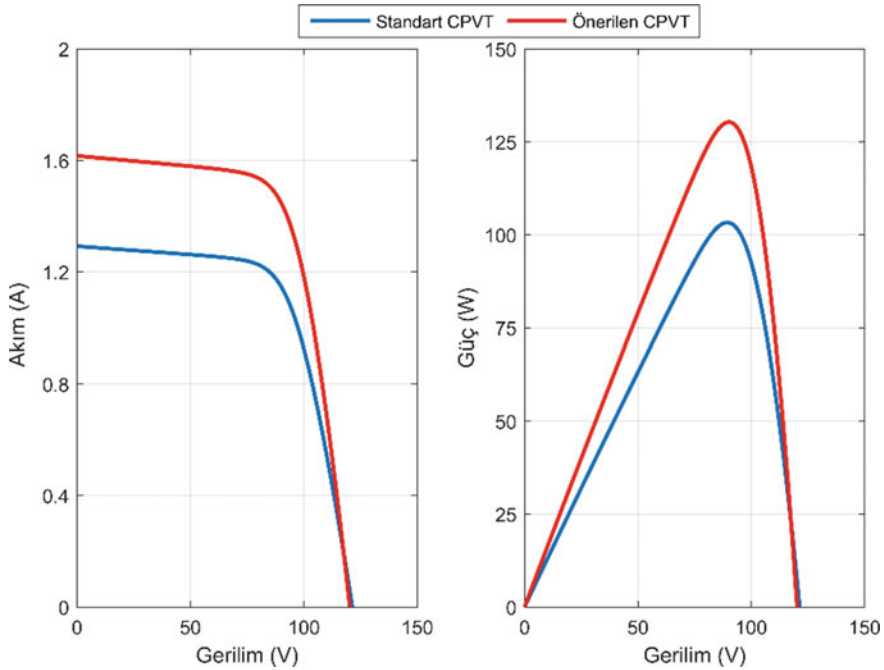


Fig. 12 PV performance changing for Case 4

5 Conclusions

It is very important to consider the effect of system and environmental conditions on PV performance when planning photovoltaic systems. In this study, standard and bifacial (proposed) CPVT systems had performance variation investigated considering four different working conditions. The MPPT power conditioning units used between the PV systems and load performed global point power tracking using the artificial bee colony. The results obtained show that more than one peak point forms under non-homogeneous radiation and temperature conditions if the proposed CPVT system has PV strings connected in series and less power production occurs compared to parallel-linked PV strings. Under these conditions, the designed ABC-GMPPT techniques unit transfers to the load at the maximum power point and thus effective and efficient use of solar energy occurs.

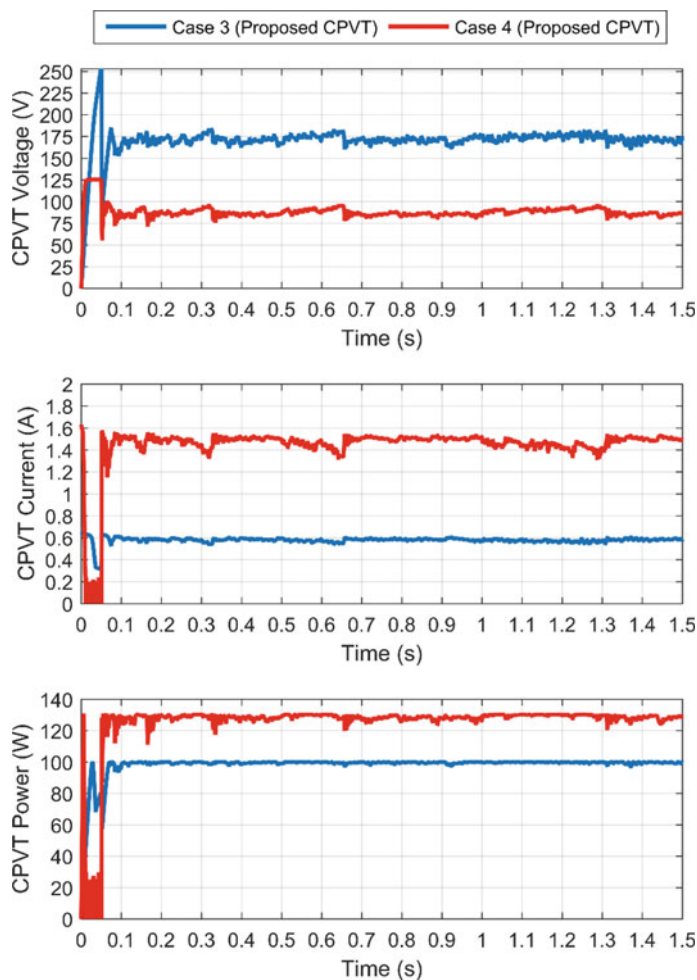


Fig. 13 ABC-GMPPT application results for proposed CPVT system in different case studies

References

1. Rezk H, Eltamaly AM (2015) A comprehensive comparison of different MPPT techniques for photovoltaic systems. *Sol Energy* 112:1–11. <https://doi.org/10.1016/j.solener.2014.11.010>
2. Eltamaly AM, Farh HMH, Othman MF (2018) A novel evaluation index for the photovoltaic maximum power point tracker techniques. *Sol Energy* 174:940–956. <https://doi.org/10.1016/j.solener.2018.09.060>
3. Algarín CR, Giraldo JT, Álvarez OR (2017) Fuzzy Logic Based MPPT Controller for a PV System. *Energies* 10:2036. <https://doi.org/10.3390/en10122036>
4. Tang S, Sun Y, Chen Y, Zhao Y, Yang Y, Szeto W (2017) An enhanced MPPT method combining fractional-order and fuzzy logic control. *IEEE J Photovoltaics* 7:640–650. <https://doi.org/10.1109/JPHOTOV.2017.2649600>

5. Boukenoui R, Ghanes M, Barbot JP, Bradai R, Mellit A, Salhi H (2017) Experimental assessment of maximum power point tracking methods for photovoltaic systems. *Energy* 132:324–340. <https://doi.org/10.1016/j.energy.2017.05.087>
6. Ounnas D, Ramdani M, Chenikher S, Bouktir T (2017) An efficient maximum power point tracking controller for photovoltaic systems Using Takagi-Sugeno fuzzy models. *Arabian J Sci Eng* 42:4971–4982. <https://doi.org/10.1007/s13369-017-2532-0>
7. Yilmaz U, Kircay A, Borekci S (2018) PV system fuzzy logic MPPT method and PI control as a charge controller. *Renew Sustain Energy Rev* 81:994–1001. <https://doi.org/10.1016/j.rser.2017.08.048>
8. Zainal NA, Yusoff AR, Apen A (2019) Integrated cooling systems and maximum power point tracking of fuzzy logic controller for improving photovoltaic performances. *Measurement* 131:100–108. <https://doi.org/10.1016/j.measurement.2018.08.056>
9. Eke R, Demircan C (2015) Shading effect on the energy rating of two identical PV systems on a building façade. *Sol Energy* 122:48–57. <https://doi.org/10.1016/j.solener.2015.08.022>
10. Koutroulis E, Blaabjerg F (2017) Overview of maximum power point techniques for photovoltaic energy production systems. In: Blaabjerg F, Ionel DM (eds) *Renewable energy devices and systems with simulations in MATLAB and ANSYS*. CRC Press, Taylor and Francis, pp 91–130
11. Ji Y-H, Jung D-Y, Won C-Y, Lee B-K, Kim J-W (2009) Maximum power point tracking method for PV array under partially shaded condition. In: *Proceedings of IEEE energy conversion congress and exposition*. pp 307–312
12. Ramli MAM, Twaha S, Ishaque K, Al-Turki YA (2017) A review on maximum power point tracking for photovoltaic systems with and without shading conditions. *Renew Sustain Energy Rev* 67:144–159. <https://doi.org/10.1016/j.rser.2016.09.013>
13. Rezk H, Fathy A, Abdelaziz AY (2017) A comparison of different global MPPT techniques based on meta-heuristic algorithms for photovoltaic system subjected to partial shading conditions. *Renew Sustain Energy Rev* 74:377–386. <https://doi.org/10.1016/j.rser.2017.02.051>
14. Benyoucef AS, Chouder A, Kara K, Silvestre S, Ait Sahed O (2015) Artificial bee colony based algorithm for maximum power point tracking (MPPT) for PV systems operating under partial shaded conditions. *Applied Soft Comput* 32:38–48. <https://dx.doi.org/10.1016/j.asoc.2015.03.047>
15. Seyedmahmoudian M, Rahmani R, Mekhilef S, Oo AMT, Stojchevski A, Soon TK, Ghandhari AS (2015) Simulation and hardware implementation of new maximum power point tracking technique for partially shaded PV system using hybrid DEPSO method. *IEEE Trans Sustain Energy* 6:850–862. <https://doi.org/10.1109/TSTE.2015.2413359>
16. Sundareswaran K, Sankar P, Nayak PSR, Simon SP, Palani S (2015) Enhanced energy output from a PV system under partial shaded conditions through Artificial Bee Colony. *IEEE Trans Sustain Energy* 6:198–209. <https://doi.org/10.1109/TSTE.2014.2363521>
17. Javed MY, Murtaza AF, Ling Q, Qamar S, Gulzar MM (2016) A novel MPPT design using generalized pattern search for partial shading. *Energy Build* 133:59–69. <https://doi.org/10.1016/j.enbuild.2016.09.054>
18. Kumar CHS, Rao RS (2016) A novel global MPP tracking of photovoltaic system based on whale optimization algorithm. *Int J Renew Energy Dev* 5:225–232. <https://doi.org/10.14710/ijred.5.3.225-232>
19. Kaced K, Larbes C, Ramzan N, Bounabi M, Dahmane ZE (2017) Bat algorithm based maximum power point tracking for photovoltaic system under partial shading conditions. *Sol Energy* 158:490–503. <https://doi.org/10.1016/j.solener.2017.09.063>
20. Ram JP, Rajasekar N (2017) A new global maximum power point tracking technique for solar photovoltaic (PV) system under partial shading conditions (PSC). *Energy* 118:512–525. <https://doi.org/10.1016/j.energy.2016.10.084>
21. Ram JP, Rajasekar N (2017) A new robust, mutated and fast tracking LPSO method for solar PV maximum power point tracking under partial shaded conditions. *Appl Energy* 201:45–59. <https://doi.org/10.1016/j.apenergy.2017.05.102>

22. Rezk H, Fathy A (2017) Simulation of global MPPT based on teaching–learning-based optimization technique for partially shaded PV system. *Electr Eng* 99:847–859. <https://doi.org/10.1007/s00202-016-0449-3>
23. Mao M, Duan Q, Duan P, Hu B (2018) Comprehensive improvement of artificial fish swarm algorithm for global MPPT in PV system under partial shading conditions. *Trans Inst Meas Control* 40:2178–2199. <https://doi.org/10.1177/0142331217697374>
24. Wu Z, Yu D, Kang X (2018) Application of improved chicken swarm optimization for MPPT in photovoltaic system. *Optimal Control Appl Methods* 39:1029–1042. <https://doi.org/10.1002/oca.2394>
25. Farh HMH, Eltamaly AM, Othman MF (2018) Hybrid PSO-FLC for dynamic global peak extraction of the partially shaded photovoltaic system. *PLoS ONE* 13(11):e0206171. <https://doi.org/10.1371/journal.pone.0206171>
26. Eltamaly AM, Farh HMH (2019) Dynamic global maximum power point tracking of the PV systems under variant partial shading using hybrid GWO-FLC, *Solar Energy* 177:306–316. <https://doi.org/10.1016/j.solener.2018.11.028>
27. Goud JS, Kalpana R, Singh B, Kumar S (2018) Maximum power point tracking technique using artificial bee colony and hill climbing algorithms during mismatch insolation conditions on PV array. *IET Renew Power Gener* 12:1915–1922. <https://doi.org/10.1049/iet-rpg.2018.5116>
28. Bernardo LR, Perers B, Hakansson H, Karlsson B (2011) Performance evaluation of low concentrating photovoltaic/thermal systems: a case study from Sweden. *Sol Energy* 85:1499–1510. <https://doi.org/10.1016/j.solener.2011.04.006>
29. Calise F, Vanoli L (2012) Parabolic trough photovoltaic/thermal collectors: design and simulation model. *Energies* 5:4186–4208. <https://doi.org/10.3390/en5104186>
30. Calise F, Palombo A, Vanoli L (2012) A finite-volume model of a parabolic trough photovoltaic/thermal collector: energetic and exergetic analyses. *Energy* 46:283–294. <https://doi.org/10.1016/j.energy.2012.08.021>
31. Calise F, Dentice d'Accadia M, Roselli C, Sasso M, Tarielli F (2014) Desiccant-based AHU interacting with a CPVT collector: simulation of energy and environmental performance. *Sol Energy* 103:574–594. <https://doi.org/10.1016/j.solener.2013.11.001>
32. Manokar AM, Winston DP, Vimala M (2016) Performance analysis of parabolic trough concentrating photovoltaic thermal system. *Procedia Technol* 24:485–491. <https://doi.org/10.1016/j.protcy.2016.05.083>
33. De Soto W, Klein SA, Beckman WA (2006) Improvement and validation of a model for photovoltaic array performance. *Sol Energy* 80:78–88. <https://doi.org/10.1016/j.solener.2005.06.010>
34. Villalva MG, Gazoli JR, Filho ER (2009) Comprehensive approach to modelling and simulation of photovoltaic arrays. *IEEE Trans Power Electron* 24:1198–1208. <https://doi.org/10.1109/TPEL.2009.2013862>
35. Lo Brano V, Ciulla G (2013) An efficient analytical approach for obtaining a five parameters model of photovoltaic modules using only reference data. *Appl Energy* 111:894–903. <https://doi.org/10.1016/j.apenergy.2013.06.046>
36. Shongwe S, Hanif M (2015) Comparative analysis of different single-diode PV modelling methods. *IEEE J Photovoltaics* 5:938–946. <https://doi.org/10.1109/JPHOTOV.2015.2395137>
37. Yıldırım N, Tacer E (2016) Identification of photovoltaic cell single diode discrete model parameters based on datasheet values. *Sol Energy* 127:175–183. <https://doi.org/10.1016/j.solener.2016.01.024>
38. Senturk A, Eke R (2017) A new method to simulate photovoltaic performance of crystalline silicon photovoltaic modules based on based on datasheet values. *Renew Energy* 103:58–69. <https://doi.org/10.1016/j.renene.2016.11.025>
39. Barth N, Jovanovic R, Ahzi S, Khaleel MA (2016) PV panel single and double diode models: optimization of the parameters and temperature dependence. *Sol Energy Mater Sol Cells* 148:87–98. <https://doi.org/10.1016/j.solmat.2015.09.003>
40. Elbaset AA, Ali H, El Sattar MA (2016) New seven parameters model for amorphous silicon and thin film PV modules based on solar irradiance. *Sol Energy* 138:26–35. <https://doi.org/10.1016/j.solener.2016.08.056>

41. Zegaoui A, Aillerie M, Petit P, Charles JP (2016) Universal transistor-based hardware simulator for real time simulation of photovoltaic generators. *Sol Energy* 134:193–201. <https://doi.org/10.1016/j.solener.2016.05.005>
42. Mathwork, Matlab <https://www.mathworks.com/>. (Access: 11.08.2018)
43. Topray Solar www.topraysolar.com. (Access: 11.08.2018)
44. Karaboga D (2005) An ideal based on honey bee swarm for numerical optimization. Technical Report—TR06 Erciyes University, Engineering Faculty, Computer Engineering Department, Kayseri, Turkey
45. Karaboga D, Akay B (2009) A comparative study of artificial bee colony algorithm. *Appl Math Comput* 214:108–132. <https://doi.org/10.1016/j.amc.2009.03.090>
46. Özkaraca O, Keçebaş P, Demircan C, Keçebaş A (2017) Thermodynamic optimization of a geothermal-based organic rankine cycle system using an artificial bee colony algorithm. *Energies* 10:1691. <https://doi.org/10.3390/en10111691>
47. Özkaraca O, Keçebaş A, Demircan C (2018) Comparative thermodynamic evaluation of a geothermal power plant by using the advanced exergy and artificial bee colony methods. *Energy* 156:169–180. <https://doi.org/10.1016/j.energy.2018.05.095>

MPPT of PV System Under Partial Shading Conditions Based on Hybrid Whale Optimization-Simulated Annealing Algorithm (WOSA)



Ahmed A. Zaki Diab

Abstract In this chapter, a hybrid optimization algorithm of whale optimization algorithm with simulated annealing (WOSA) has been proposed for tracking the global maximum power point (MPP) for photovoltaic (PV) system under partial shading condition (PSC). The main target of this chapter is to discuss the performance of the PV system under partial shading. Also, the chapter introduces a novel hybrid optimization algorithm to enhance the overall performance of the PV system under different conditions of operation. MATLAB/Simulink package has been used to evaluate the proposed algorithm. The results demonstrate that, the hybrid WOSA has a good efficiency of tracking with acceptable convergence speed.

Keywords Partially shaded PV system · Hybrid optimization technique · Whale optimization-simulated annealing algorithm (WOSA)

1 Introduction

The power generation efficiency of the PV system is significantly low. Moreover, the power generated is largely dependent on intermittent weather conditions and therefore these sources show low reliability [1, 2]. As the photovoltaic unit has nonlinear characteristics, it makes the output power significantly affected by changes in solar radiation, ambient temperature, and the load [3–5]. The efficiency of the PV solar system can be increased by tracking the point of maximum power point (MPP); therefore, MPP tracking for the PV system under normal and transient condition is an important point for researchers in order to obtain the best operation and reduce the cost of the generated units from such a system [6–8]. Bypass diodes can be connected in shunt with the modules. In this case, these diodes have no effect in the normal operating condition, but when the modules are subjected to shadow effect, the current is transferred through the forward biased diodes instead of the modules. As a

A. A. Z. Diab (✉)

Electrical Engineering Department, Faculty of Engineering, Minia University, Minia, Egypt
e-mail: a.diab@mu.edu.eg

© Springer Nature Switzerland AG 2020

A. M. Eltamaly and A. Y. Abdelaziz (eds.), *Modern Maximum Power Point Tracking Techniques for Photovoltaic Energy Systems*, Green Energy and Technology, https://doi.org/10.1007/978-3-030-05578-3_13

355

result, the P – V characteristics a partially shaded PV module will have various local peaks, but only one global peak. Since the global maximum point is rather tracking, traditional methods for tracking MPP are less efficient under PSC. The classical techniques for MPP tracking, such as incremental conductance (INC), incremental resistance (INR), hill climbing, perturb and observe, fuzzy logic, and neural network have not the flexibility to differentiate between the global and local points of the peak power, which in turn leads to a reduction in the tracking system efficiency [3–7]. In the last years, various modern techniques, which rely mainly on optimization techniques, were explored for catching the MPP [8–16]. The major objective for all these techniques is to raise the efficiency of the PV generating system when operating under PSC [8]. A number of optimization techniques such as genetic [9], PSO [10], ant colony optimization [11], and cuckoo search [12] optimization algorithms are applied for MPPT in the PV systems under PSC. Furthermore, different metaheuristic optimization techniques are tested and compared for MPPT of the PV systems under different PSC in [13]. In [14, 15], the artificial bee colony (ABC) technique is presented and evaluated based on the simulation and experimental tests. Reference [16] introduced a hybrid differential evolution and PSO (DEPSO) for catching the MPP in the PV system with experimental tests. In [17], a comparison between the gray wolf optimization (GWO) and PSO techniques-based tracker is introduced. In [18], FPA for MPPT is simulated and tests with hardware configuration. Other techniques have been applied for MPPT in the PV systems under PSC such as learning-teaching optimization algorithm [19], the artificial fish swarm algorithm [20], and the chicken swarm optimization technique [21]. Other techniques have been presented and analyzed [8]. Moreover, in [22, 23], a number of optimization algorithms which applied for tracking the MPP under various patterns of shadow have been comprehensively analyzed. The comparison results show that slap swarm optimization technique and flower pollination algorithm and hybrid particle swarm optimization-gravitational search algorithm (PSOGSA) have the best performance rather than other techniques such as PSO with respect to the convergence speed and tracking efficiency. However, a novel dynamic global MPP tracker based on hybrid GWO-FLC of the PV systems under partial shading has been presented in [24]. Also, a hybrid PSO-FLC algorithm had been proposed to deal with the problem of MPPT of the partially shaded photovoltaic system in [25]. The presented results show that the hybrid GWO-FLC and hybrid PSO-FLC algorithm deal effectively with the problem of MPP of the partially shaded photovoltaic system.

With the increased installations of the PV energy systems, effective algorithms for MPPT have to be developed for enhancing the efficiency of conversion of the PV plants under PSC. In the present chapter, a solution for tracking the PV system's MPP when partially shaded, based on the application of WOSA hybrid optimization algorithm, is introduced. The target from applying the optimization algorithm is to access the global MPP, which can be generated from the PV system, not the local ones. The performance of the MPP system has been assessed using MATLAB/Simulink simulation package. The main contributions of this chapter can be written as follows:

- MPPT of PV system under partial shading based on a novel hybrid WOSA algorithm is presented.
- The purpose of hybridization between the two algorithms of WOA and SA is to improve the tracking performance and efficiency of PV systems.
- The proposed algorithm is validated using simulation tests of a considered PV system under different shading patterns. In this chapter, the evaluation of the proposed hybrid WOSA algorithm based on six different shading conditions has been presented.
- The results of the applied hybrid optimization technique are compared with those obtained by only WOA and SA algorithms to prove the effectiveness and superiority of the proposed methodology.

2 PV System Under PSC

Figure 1 shows the design of PV system configuration which used in the chapter to evaluate the different optimization techniques. The system configuration has (8S1P configuration) comprises of 8 panels in one string. Each module has 72 series connected multi-crystalline silicon cells with maximum power of 51 W. The total extracted power from the model at standard conditions is 400 Wp (i.e., 8×51 W) [26]. Table 1 illustrates random patterns for telling the effect of PSC. In the tested module, it is assumed that each two connected panels are exposed under the same irradiance. The performance of the PV module under uniform irradiance of 1 kW/m² and under different five random patterns has been displayed in Fig. 2. The figure shows the power versus voltage and current versus voltage curves. From the figure, with varying the PSC conditions, the characteristics of the PV modules are reformed. As example, under uniform irradiance the maximum extracted power from the PV system is 404.9 W and the *P–V* curve has one MPP. But under the third pattern, the

Table 1 Different partial shading patterns for tests cases W/m² and the maximum power point under each case

	Irradiance	MPP		Irradiance	MPP
Uniform irradiance	1000	404.9 W	PSC pattern #3	1000	199.4 W
	1000			800	
	1000			600	
	1000			400	
PSC pattern #1	1000	197.6 W	PSC pattern #4	1000	342.5 W
	1000			1000	
	400			800	
	400			800	
PSC pattern #2	400	261.3 W			
	800				
	1000				
	1000				

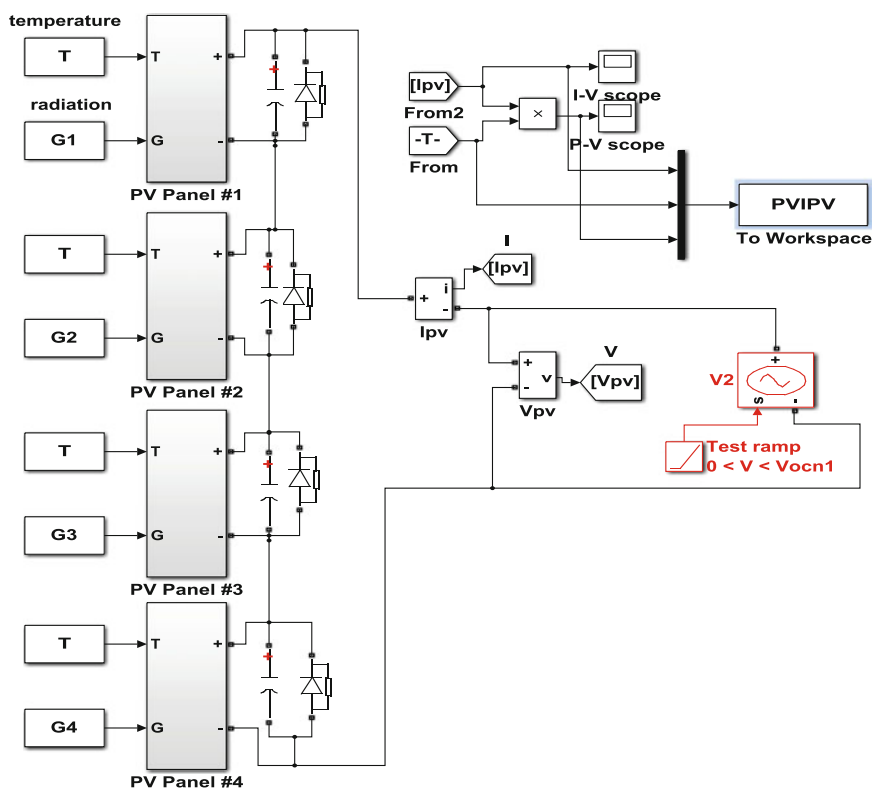


Fig. 1 Simulink model for PV system (each two series modules have the same irradiance)

maximum power is 199.4 W, and it is located at the second peak from three peaks in the P – V curve. Furthermore, the MP for the different pattern was given in Table 1.

3 Whale Optimization Algorithm (WOA)

Application of the metaheuristics algorithms for solving the optimization problems to reach and determine the global optima without mathematical derivation and with simple, flexible mechanism is considered one of the aspects of recent research. The whale optimization algorithm (WOA) has been built on the whale hunting technique. This pursuing procedure is called bubble net feeding strategy. Humpback whales want to chase little fishes near the surface by making bubble net around the prey rises along a circle path as shown in Fig. 3. The mathematical formulation of this phenomenon can be written as [27–29]:

$$D = \left| \vec{C} \cdot \vec{X}^*(t) - \vec{X}(t) \right| \quad (1)$$

$$X(t+1) = \vec{X}^*(t) - \vec{A} \cdot \vec{D} \quad (2)$$

where t is the iteration, \vec{A} and \vec{D} are the coefficient vectors, \vec{X}^* indicates the vector of the best solution, \vec{X} indicates the position vector, $||$ indicates the absolute value, and \cdot indicates an element-by-element multiplication. The position vector of best solution \vec{X}^* is updated when a better solution is found.

$$\vec{A} = 2\vec{a} \cdot \vec{r} - \vec{a} \quad (3)$$

$$\vec{C} = 2 \cdot \vec{r} \quad (4)$$

where \vec{a} in Eqs. (3) and (4) is linearly diminished from 2 to 0 through the number of iteration (in investigation and exploitation stages) and \vec{r} is an arbitrary vector in the range of $[0, 1]$. This parameter is random to achieve the balanced between exploitation and investigation stages.

A. Bubble-net assaulting strategy (exploitation stage):

Two approaches are utilized to figure the air bubble net conduct of humpback whales as below:

I. Shrinking circling system:

Equation (3) has explained this approach. The fluctuation scope of A is additionally diminished by a . As such, A will be random in the interval $[-a, a]$, where a is diminished from 2 to 0 throughout iterations. \vec{A} is in $[-1, 1]$, the new position of

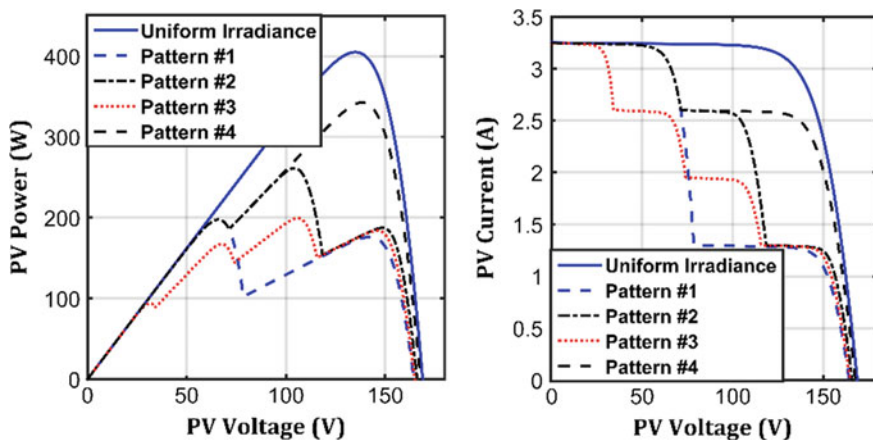


Fig. 2 Characteristics of PV system under different patterns of irradiance

a search operator has been estimated between the first position of the agent and the position of the present best agent. Figure 3a displays the probable positions from (X, Y) in the direction of (X^*, Y^*) which can be accomplished by $0 \leq A \leq 1$ in a 2D space.

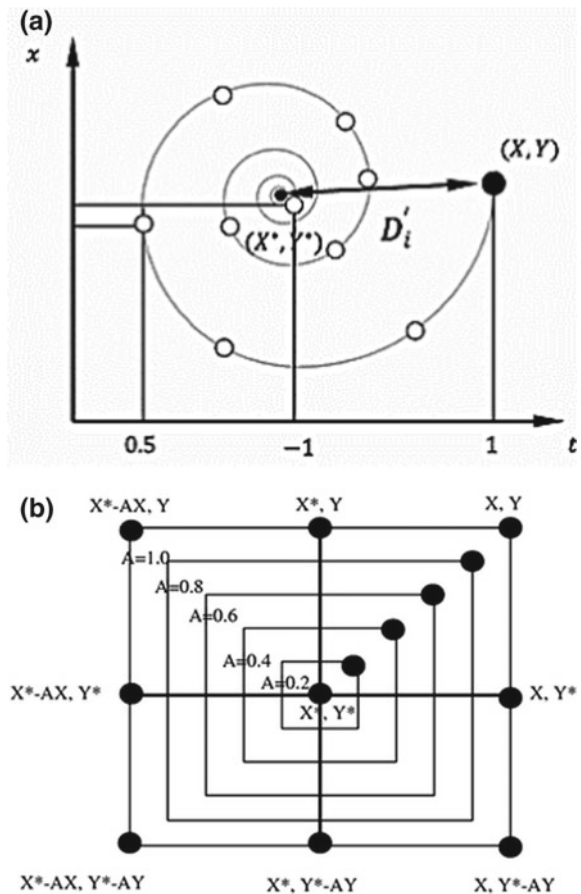
II. Spiral updating position:

This approach shown in Fig. 3b depends on determining the distance between the whale located at (X, Y) and prey located at (X^*, Y^*) . Equation (5) represents the spiral path between the position of whale (current position) and prey (best solution).

$$\vec{X}(t+1) = \vec{D}' \cdot e^{bl} \cdot \cos(2\pi l) + \vec{X}^*(t) \quad (5)$$

where $\vec{D}' = \vec{X}^*(t) - \vec{X}(t)$ demonstrates the separation of the i th whale to the prey (best solution), b is a constant for characterizing the state of the logarithmic spiral

Fig. 3 **a** Bubble net search spiral updating position mechanism, **b** bubble net search shrinking encircling mechanism [27, 28]



and in this work its value is taken equal to 1 and l is a random number in between $[-1, 1]$ and varied at each iteration. Whales swim around the prey inside shrinking circle and along a spiral form. There is a probability of half to select one of two approaches as shown:

$$\vec{X}(t+1) = \begin{cases} \vec{X}^*(t) - \vec{A} \cdot \vec{D} & \text{if } p < 0.5 \\ \vec{D}' \cdot e^{bl} \cdot \cos(2\pi l) + \vec{X}^*(t) & \text{if } p \geq 0.5 \end{cases} \quad (6)$$

where p is an arbitrary number in the range between $[0, 1]$. It is generated using a random function and is varied at each iteration.

B. Scan for prey (investigation stage)

whales pursue randomly as per the position of each other. Thus, \vec{A} is utilized with the random values more than 1 or under -1 to make search agent to move far from a reference whale. The position of search agent has been updated in the investigation stage as per an arbitrarily picked search agent rather than the best pursuit agent exposed in this way. This scheme and $|\vec{A}| > 1$ highlight investigation and tolerate the WOA calculation to perform a global pursuit. The mathematical expression can be written as follows:

$$D = |\vec{C} \cdot \vec{X}_{\text{rand}} - \vec{X}| \quad (7)$$

$$\vec{X}(t+1) = \vec{X}_{\text{rand}} - \vec{A} \cdot \vec{D} \quad (8)$$

The flowchart of WOA technique is depicted in Fig. 4. Moreover, the pseudocode of WOA can be expressed as the following:

```

Initialize whales positions
Find the current best position  $X^*$ 
while (termination criterion does not meet)
  for each whale position
    Update a, A, C, l, and p
    If  $p < 0.5$ 
      If  $|\vec{A}| < 1$ 
        Update position according to Eq. (2)
      else if  $|\vec{A}| > 1$ 
        Select position  $x$  randomly
        Update position according to Eq. (8)
      end
    else if  $p > 0.5$ 
      update position spirally using Eq. (5)
    end
  end
  Adjust position inside search space boundaries

```

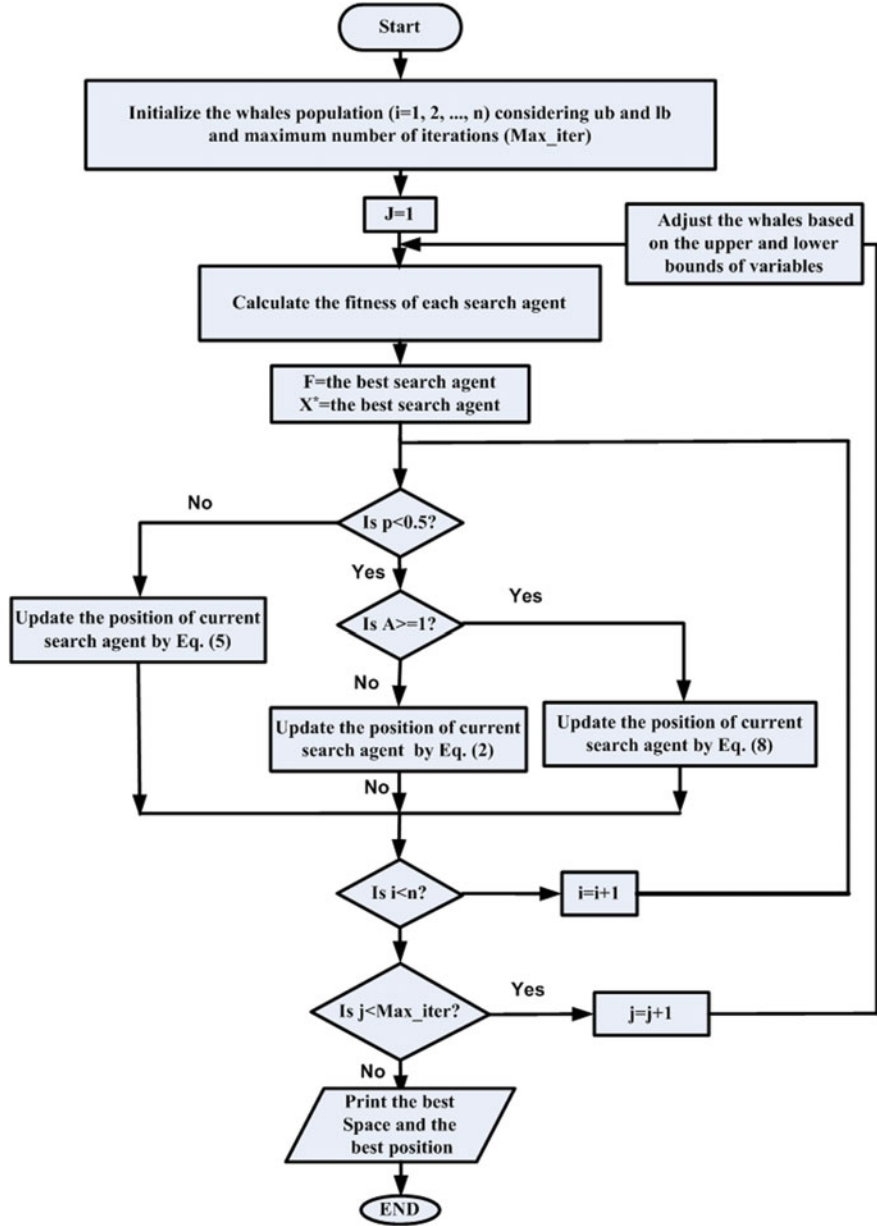


Fig. 4 Flowchart of WOA technique, where X_i is the duty cycle and the fitness is the PV power

```

Update the current best position  $X^*$ 
end
return  $X^*$ 
end procedure

```

4 Simulated Annealing

Simulated annealing (SA) is one of the metaheuristic optimization techniques. It is presented first time by Kirkpatrick et al. [30]. Moreover, SA can avoid the problem of selecting a local optimal solution based on a certain probability. As general, a random initial solution has been generated to start the algorithm. After that, at each iteration, the solution will be generated based on evaluation of a fitness function and a well-defined neighborhood mathematical structure [30–32]. The global optimum solution is reached based on selecting the neighbor which is fitter than the old point. However, the worst one will be taken into consideration with a certain probability $P = e^{-\theta/T}$ to avoid the local optimum solution. Where θ equals the difference between the fitness of best solution and the trail solution. Furthermore, T is a variable parameter with iterations (called the temperature) [30–32]. The flowchart of the SA algorithm has been shown in Fig. 5. The basic SA algorithm is as follows:

```

Sol = Generate Initial Random Solution ()
T = initial temperature (T_0)
WHILE termination conditions not met
sol1 = Pick_At_Random (of the neighborhood N(s))
Evaluation of a fitness function
IF fitness (sol1) > fitness (sol)
sol = sol1
ELSE
Accept sol1 as new solution with probability  $p(T, sol1, sol)$ 
ENDIF
Update (T)
ENDWHILE
Output the Best Solution

```

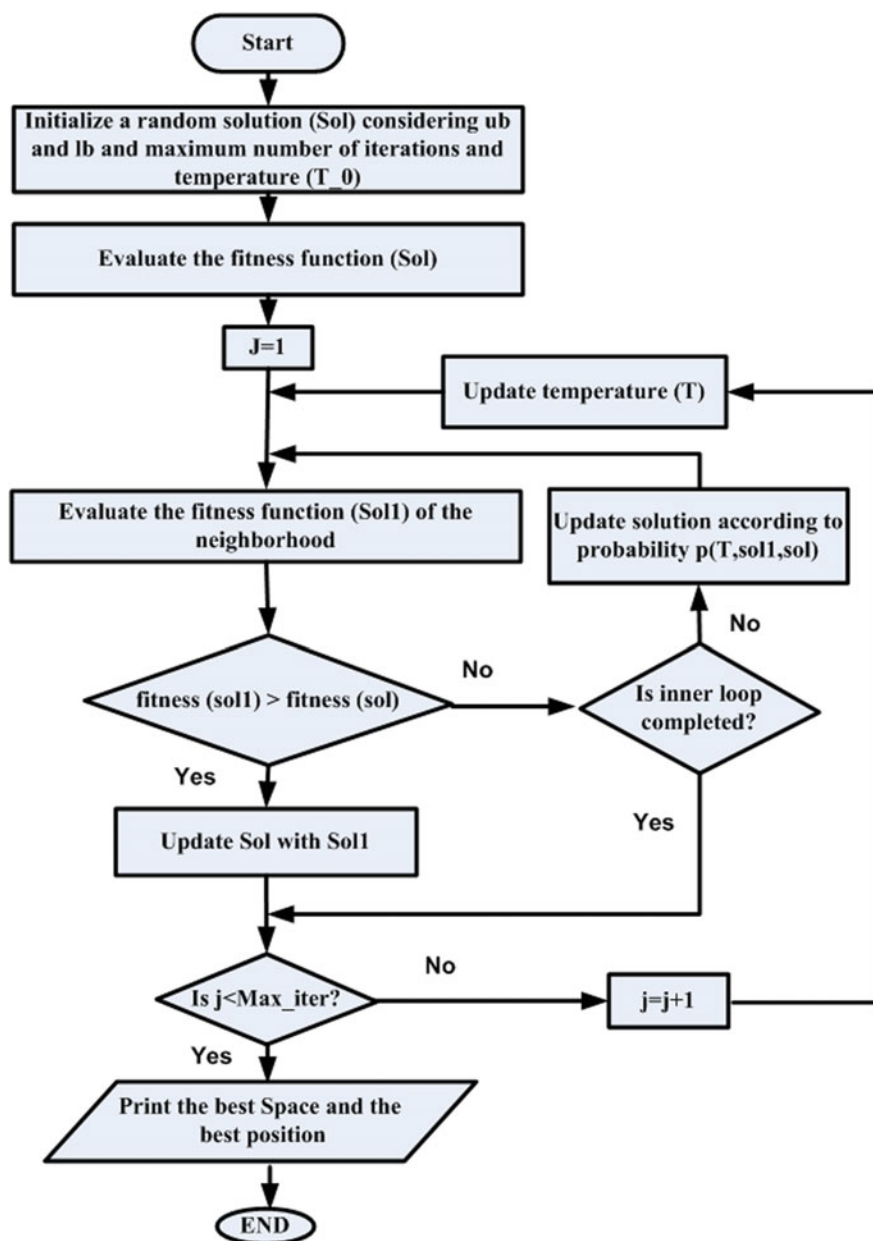



Fig. 5 Flowchart of SA algorithm

5 Hybrid WOSA

The search process in metaheuristic optimization has two phases of exploration and exploitation [33]. This process differs from algorithm to other based on the algorithm nature. The balance between exploitation to determine the local optimum and exploration to effectively determine the global solution is very effective in the performance of any optimization technique. So, the optimization techniques must randomly explore the global solution in the search space. Then, the second phase of exploitation to search for the optimized solution around the promising area(s) of the search space is activated. Exploitation concerns to the local search ability in the region space around the determined solution by the exploration phase. The proposed hybrid WOSA is to find this suitable balance between the two phases. The results show also the WOA fails for solving a few optimization problems.

In literature, two main types of hybridization models from the different optimization techniques have been reported. The first one is called low-level teamwork hybrid (LTH). In the LTH hybrid model, one optimization technique is embedded to aid for searching the global optimal solution from the neighbors. The second model of hybridization models is called high-level relay hybrid (HRH). In HRH model, one algorithm is applied after applying the second algorithm and finding the optimal solution. Here in this work, the SA algorithm is used to enhance the best solution of the WOA technique. The flowchart of the In HRH model for WOSA optimization technique has been shown in Fig. 6.

6 Results and Discussions

The evaluation of the proposed WOSA technique is done based on MATLAB/Simulink package. The MPP trackers have been tested under different condition of operation. In each case of study, the tracking efficiency and convergence speed have been visualized and compared against the WOA and SA algorithms. Figure 7 shows the Simulink model of the overall PV system with MPP tracker. The PV system consists of PV module, DC/DC boost converter (switching frequency of 30 kHz). The input inductance is 1 mH and output capacitor is 47 μ F with 60 Ω resistive loads. The using of the optimization algorithm aims to generate the duty cycle for DC/DC converter for extracting the maximum power from the PV module.

Case 1 The first case of study is under uniform irradiance and normal temperature as 1000 W/m² and 25 °C, respectively. The performance of the hybrid WOSA optimization algorithm was compared with the performance of SA and WOA techniques. The results of this case to evaluate the three optimization techniques have been shown in Fig. 8. The figure shows the WOSA has the better performance rather than the two other algorithms. The time simulation results of the PV system have been shown in Fig. 9. From the results, it is clearly shown that the hybrid WOSA algorithm can track the MPP faster than the WOA technique while the SA technique is failed to

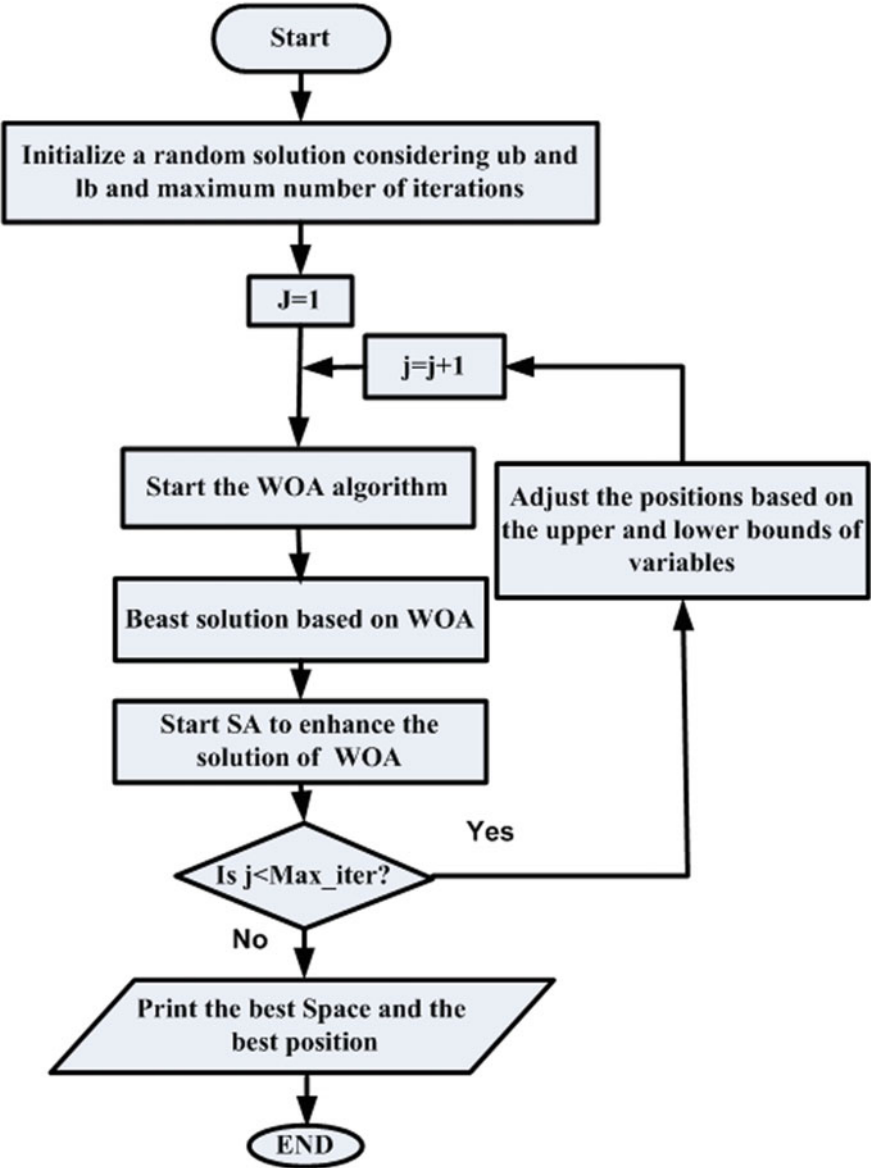


Fig. 6 Flowchart of the In HRH model for WOSA optimization technique

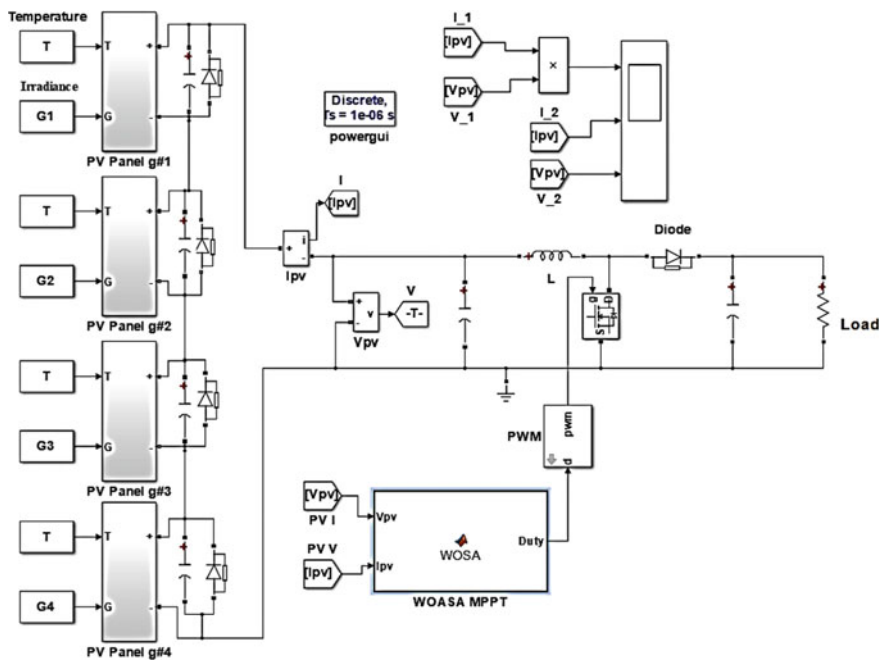


Fig. 7 Simulink model of the overall PV system with optimized MPP tracker

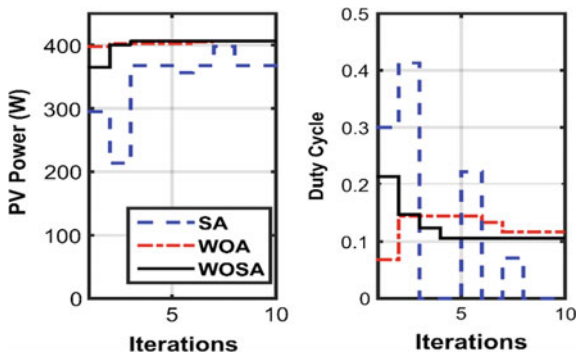


Fig. 8 Convergence curve and duty cycle versus iterations system for WOA, SA, and WOSA techniques under uniform irradiance

catch the MPP. The proposed technique can reach the MPP at 3 iterations while the WOA algorithm reaches at 7 iterations.

Case 2 The first pattern of partial shading has been studied in this case of study. The convergence curves of the PV system for the three algorithms have been shown in Figs. 10 and 11. The figures demonstrate that the WOSA has the best convergence curve with acceptable convergence speed of 7 iterations. While the WOA cannot catch

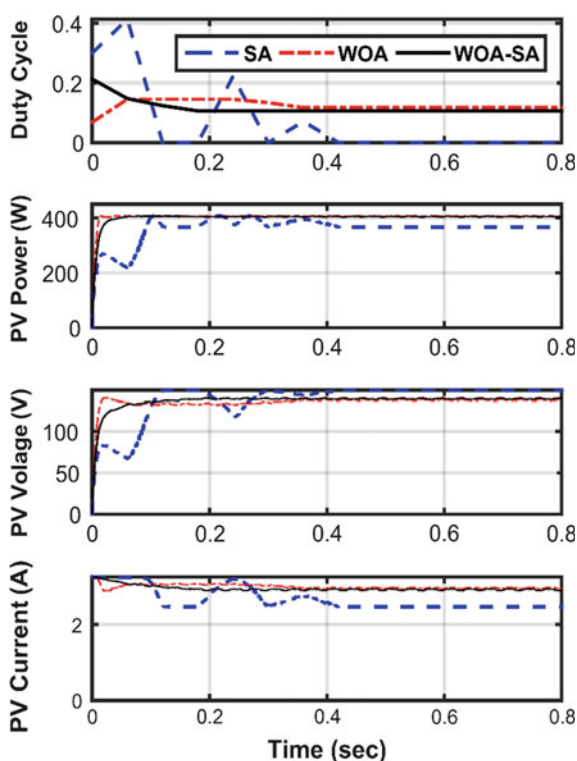


Fig. 9 Detailed simulation results for the performance of PV system under uniform irradiance shading pattern; WOA, SA, and WOSA-based trackers

the MPP, the SA algorithm can determine the MPP at 8 iterations. The efficiency of tracking of the hybrid algorithm is better than in the case of WOA or SA techniques. The simulation validation of the PV system with the three trackers has been shown in Fig. 10. The figure shows the superiority of the PV system with the hybrid WOSA-based tracker.

Case 3 In this case of study, the second pattern has been assumed in simulation tests. The power of the PV system under this case of study has three peaks and the second peak is the global MPP. Figure 12 shows the convergence curves and the duty cycle via iteration for the three presented algorithms. Again, the WOSA base tracker has the best performance with 5 iterations of convergence characteristics. Moreover, the dynamic simulation of the PV system with the three algorithms has been shown in Fig. 13.

Case 4 For more validating of the hybrid WOSA algorithm, the third shading pattern has been assumed in this case of study. Figures 14 and 15 show the convergence performance of the three algorithms and the time simulation of the PV system under the third shading pattern. The results prove the superiority of the hybrid WOSA

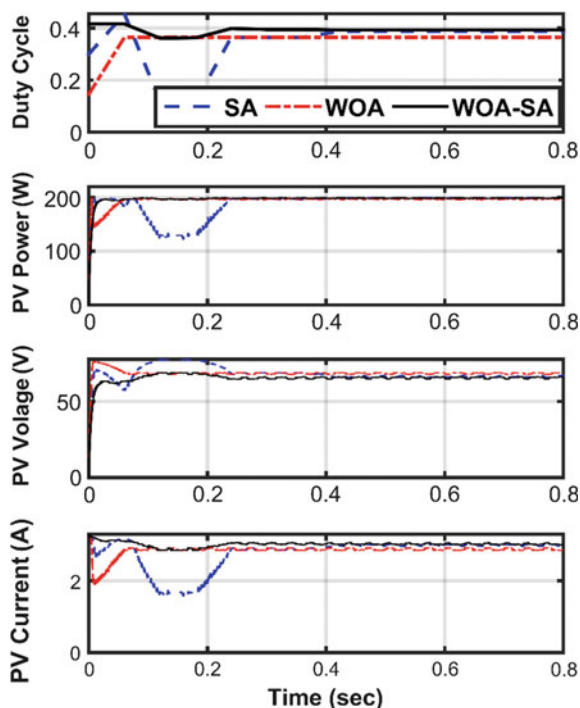


Fig. 10 Detailed simulation results for the performance of PV system under first shading pattern; WOA, SA and WOSA-based trackers

optimization algorithm for tracking the global MPP. The results show that the hybrid WOSA technique reaches the MPP faster than the other two algorithms.

The fourth pattern is selected in this case of study. In this case of study, the P - V curve has two peaks. Moreover, the MPP is the second peak point. The results of such tested case have been shown in Figs. 16 and 17. The figures show that the hybrid WOSA-based tracker has the best performance rather than the WOA while the SA-based tracker is failed to determine the MPP.

The output power of the PV system with WOA, SA, and WOSA algorithms under different PSC has been displayed in Figs. 18 and 19. From these figures, the presented hybrid WOSA-based tracker caught the global MPP with acceptable tracking efficiency for all cases of PSC. In most of the cases, The SA-based tracker cannot catch the global MPP. As a general conclusion, the convergence speed of WOSA-based tracker is better than that with WOA. The results validate that the hybridization of the two algorithms WOA and SA improves the system performance under all different cases of study.

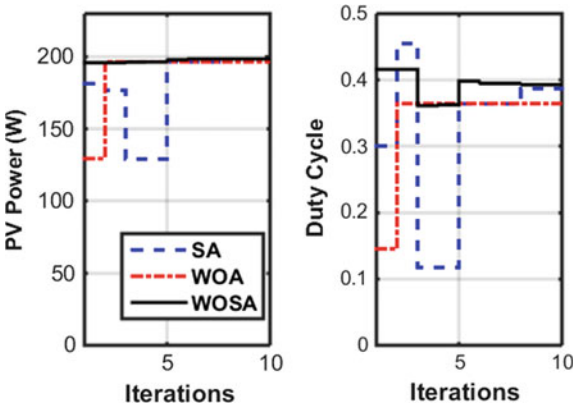


Fig. 11 Convergence curve of the PV system for WOA, SA, and WOSA techniques under first partial shading patterns

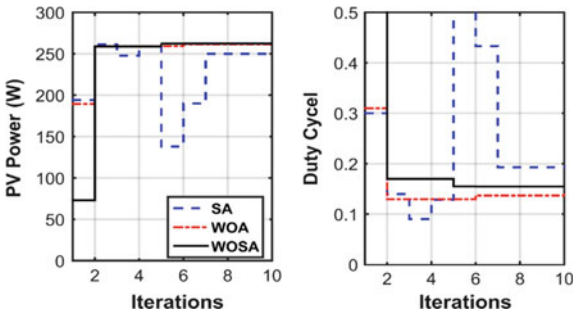


Fig. 12 Convergence curve of the PV system with WOA, SA, and WOSA techniques under second partial shading patterns

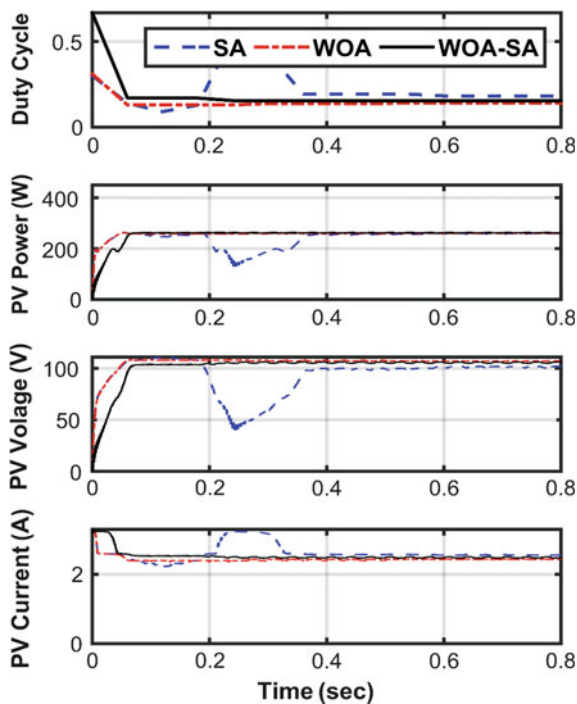


Fig. 13 Detailed simulation results for the performance of PV system under second shading pattern; WOA, SA, and WOSA-based trackers

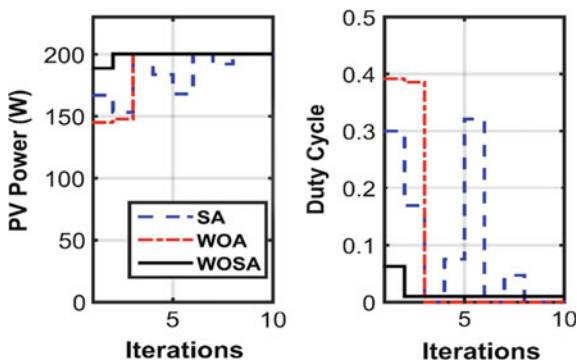


Fig. 14 Convergence curve and duty cycle versus iterations for WOA, SA, and WOSA techniques under third partial shading patterns

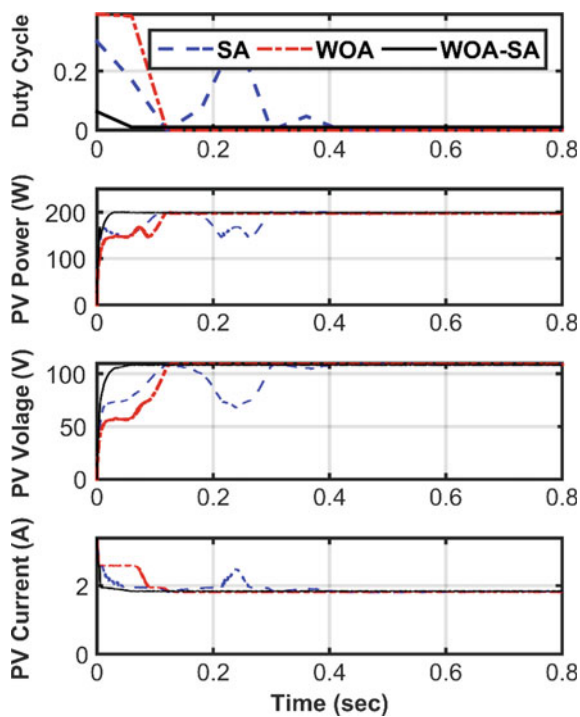


Fig. 15 Detailed simulation results for the performance of PV system under third shading pattern; WOA, SA, and WOSA-based trackers

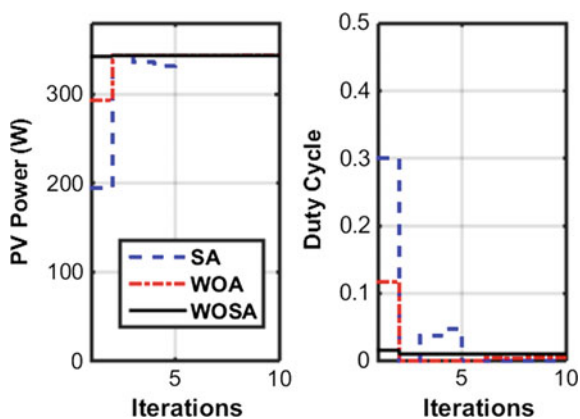


Fig. 16 Convergence curve and duty cycle versus iterations for WOA, SA, and WOSA techniques under fourth partial shading patterns

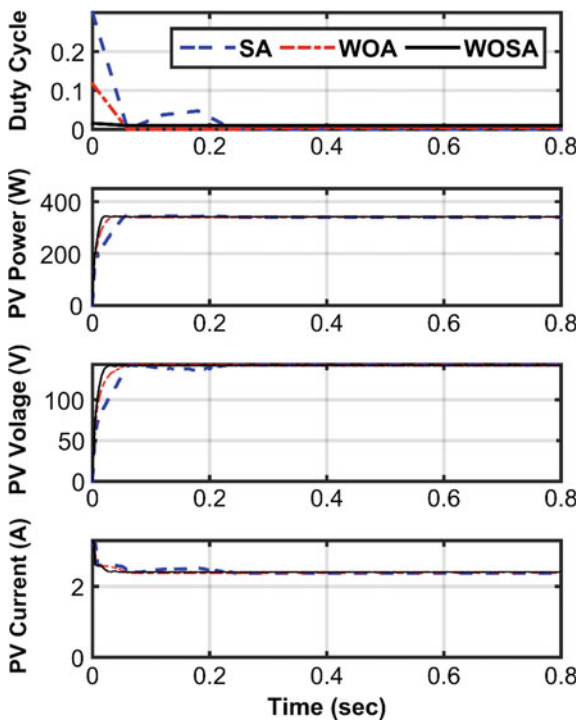


Fig. 17 Detailed simulation results for the performance of PV system under fourth shading pattern; WOA, SA, and WOSA-based trackers

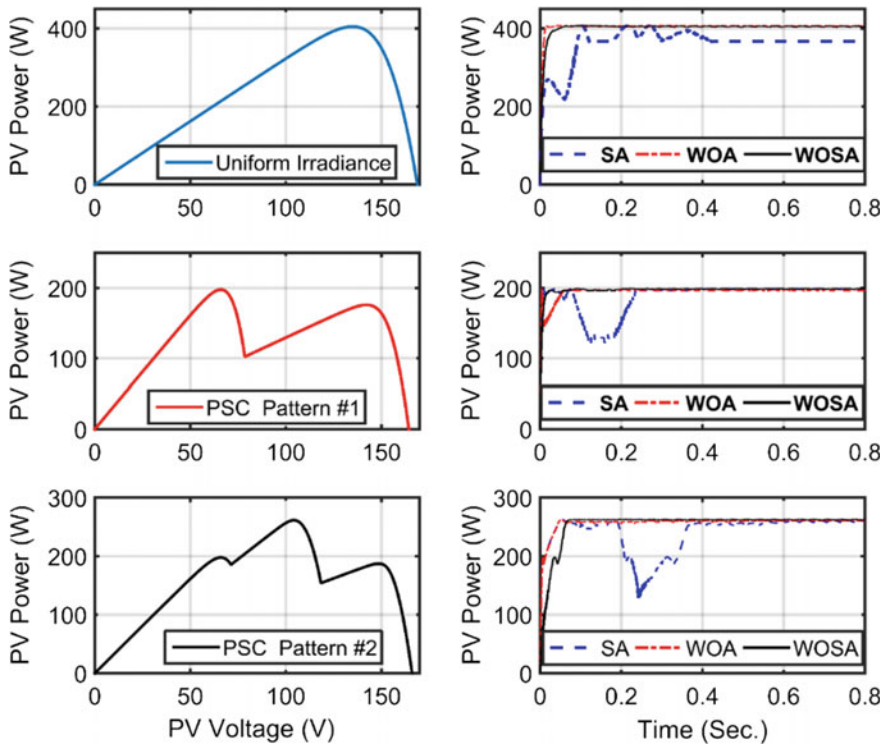


Fig. 18 P - V curve and the output power of PV system for WOA, SA, and WOSA algorithms under uniform patterns, first and second patterns

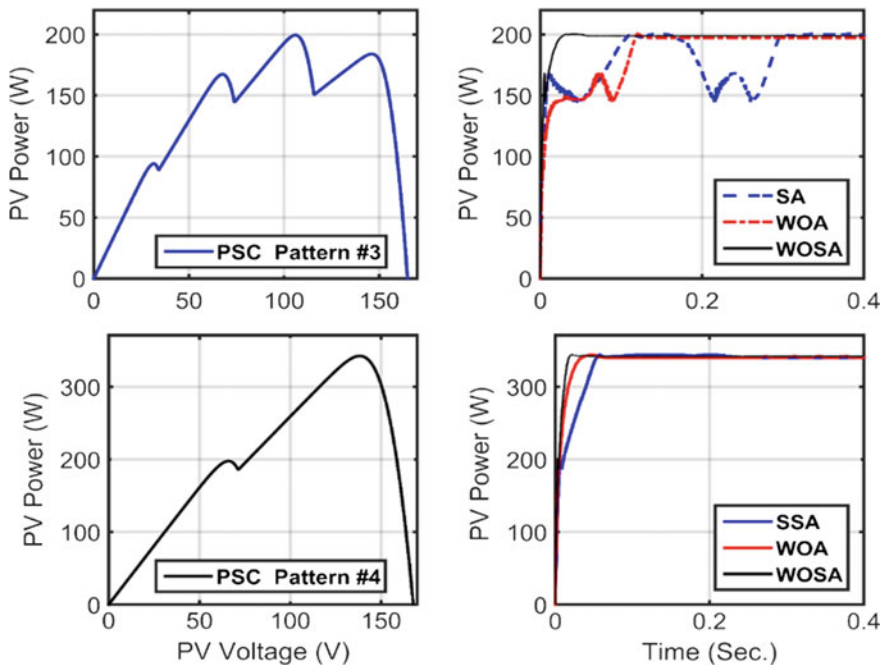


Fig. 19 P – V curve and the output power of the PV system for WOA, SA, and WOSA algorithms under third and fourth patterns

7 Conclusion

In this chapter, a hybrid WOSA technique is introduced for improving the efficiency of PV system under partially shading. The presented algorithm has been applied to track the global MPP from the multiple local peaks in $P-V$ curve. A comprehensive evaluation of the presented hybrid tracker has been carried out using MATLAB/Simulink package. The results of the hybrid WOSA algorithm have been compared with the results of WOA and SA techniques. The simulation results demonstrate that the overall performance of the PV system with WOSA technique is better than the other two techniques. Moreover, the performance of the WOSA is faster than the other algorithms in terms of convergence speed. Future research should further develop and confirm these algorithms with more cases of study and different configurations of PV systems. Moreover, experimental validation of the application of recent optimization techniques should be carried in the future work. Furthermore, in future research, more research is needed to apply and test recent and hybrid optimization techniques with intelligent control methods such as fuzzy logic and neural networks for improving the performance of PV systems under partial shading conditions.

References

1. Berrera M, Dolara A, Leva S, Experimental test of seven widely adopted MPPT algorithms. In: IEEE Bucharest power tech conference, June 28th—July 2nd, Bucharest, Romania, 2009. <https://doi.org/10.1109/ptc.2009.5282010>
2. Sreekanth S, Raglend IJ (2012) A comparative and analytical study of various incremental algorithms applied in solar cell. In: International conference on computing, electronics and electrical technologies [ICCEET], Kumaracoil, India, 21–22 March, pp 452–456. <https://doi.org/10.1109/icceet.2012.6203876>
3. Rezk H, Eltamaly AM (2015) A comprehensive comparison of different MPPT techniques for photovoltaic systems. *Solar Energy* 112:1–11. <https://doi.org/10.1016/j.solener.2014.11.010>
4. Fangrui L, Shanxu D, Fei L, Bangyin L, Yong K (2008) A variable step size INC MPPT method for PV systems. *IEEE Trans Ind Electron* 55(7):2622–2628. <https://doi.org/10.1109/TIE.2008.920550>
5. Emad MA, Masahito S (2010) Modified adaptive variable step-size MPPT based-on single current sensor. In: TENCON 2010—IEEE region 10 conference, Fukuoka, Japan, 21–24 Nov 2010, pp 1235–1240. <https://doi.org/10.1109/TENCON.2010.5686360>
6. Xiao W, Dunford WG (2004) A modified adaptive hill climbing MPPT method for photovoltaic power systems. In: 35th annual IEEE power electronics specialist conference, Aachen, Germany, vol 3, pp 1957–1963. <https://doi.org/10.1109/pesc.2004.1355417>
7. Tey KS, Mekhilef S, Yang H, Chuang M (2014) A differential evolution based MPPT method for photovoltaic modules under partial shading conditions. *Int J Photoenergy* 2014:1–10. <https://doi.org/10.1155/2014/945906>
8. Eltamaly AM, Farh HMH, and Othman MF (2018) A novel evaluation index for the photovoltaic maximum power point tracker techniques. *Solar Energy* 174:940–956. <https://doi.org/10.1016/j.solener.2018.09.060>
9. Daraban S, Petreus D, Morel C (2013) A novel global MPPT based on genetic algorithms for photovoltaic systems under the influence of partial shading. In: IECON 2013–39th annual conference of the IEEE, Vienna, Austria, 1013 Nov 2013, pp 1490–1495. <https://doi.org/10.1109/iecon.2013.6699353>

10. Phimmason V, Kondo Y, Kamejima T, Miyatake M Evaluation of extracted energy from PV with PSO-based MPPT against various types of solar irradiation changes. In: IEEE international conference on electrical machines and systems, Korea, pp 487–492, 2010
11. Jiang L, Maskell D, Patra J (2013) A novel ant colony optimization based maximum power point tracking for photovoltaic systems under partially shaded conditions. *Energy Build* 58:227–236. <https://doi.org/10.1016/j.enbuild.2012.12.001>
12. Ahmed J, Salam Z (2014) A maximum power point tracking (MPPT) for PV system using Cuckoo search with partial shading capability. *Appl Energy* 119:118–130. <https://doi.org/10.1016/j.apenergy.2013.12.062>
13. Rezk H, Fathy A, Abdelaziz AY (2017) A comparison of different global MPPT techniques based on meta-heuristic algorithms for photovoltaic system subjected to partial shading conditions. *Renew Sustain Energy Rev* 74:377–386. <https://doi.org/10.1016/j.rser.2017.02.051>
14. Benyoucef AS, Chouder A, Kara K, Silvestre S, Ait Sahed O (2015) Artificial bee colony based algorithm for maximum power point tracking (MPPT) for PV systems operating under partial shaded conditions. *Appl Soft Comput* 32:38–48. <http://dx.doi.org/10.1016/j.asoc.2015.03.047>
15. Sundareswaran K, Sankar P, Nayak PSR, Simon SP, Palani S (2015) Enhanced energy output from a PV system under partial shaded conditions through artificial bee colony. *IEEE Trans Sustain Energy* 6:198–209. <https://doi.org/10.1109/TSTE.2014.2363521>
16. Seyedmahmoudian M, Rahmani R, Mekhilef S, Oo AMT, Stojchevski A, Soon TK, Ghandhari AS (2015) Simulation and hardware implementation of new maximum power point tracking technique for partially shaded PV system using hybrid DEPSO method. *IEEE Trans Sustain Energy* 6:850–862. <https://doi.org/10.1109/TSTE.2015.2413359>
17. Kumar CHS, Rao RS (2016) A novel global MPP tracking of photovoltaic system based on whale optimization algorithm, *Int J Renew Energy Dev* 5:225–232. <https://doi.org/10.14710/ijred.5.3.225-232>
18. Ram JP, Rajasekar N (2017) A new global maximum power point tracking technique for solar photovoltaic (PV) system under partial shading conditions (PSC). *Energy* 118:512–525. <https://doi.org/10.1016/j.energy.2016.10.084>
19. Rezk H, Fathy A (2017) Simulation of global MPPT based on teaching–learning-based optimization technique for partially shaded PV system. *Electr Eng* 99:847–859. <https://doi.org/10.1007/s00202-016-0449-3>
20. Mao M, Duan Q, Duan P, Hu B (2018) Comprehensive improvement of artificial fish swarm algorithm for global MPPT in PV system under partial shading conditions. *Trans Inst Meas Control* 40:2178–2199. <https://doi.org/10.1177/0142331217697374>
21. Wu Z, Yu D, Kang X (2018) Application of improved chicken swarm optimization for MPPT in photovoltaic system. *Optimal Control Appl Methods* 39:1029–1042. <https://doi.org/10.1002/oca.2394>
22. Zaki Diab AA, Rezk H (2017) Global MPPT based on flower pollination and differential evolution algorithms to mitigate partial shading in building integrated PV system. *Solar Energy*, 157:171–186. <https://doi.org/10.1016/j.solener.2017.08.024>
23. Mohamed MA, Zaki Diab AA, Rezk H (2019) Partial shading mitigation of PV systems via different meta-heuristic techniques. *Renew Energy* 130:1159–1175. <https://doi.org/10.1016/j.renene.2018.08.077>
24. Farh HMH, Eltamaly AM, Othman MF (2018) Hybrid PSO-FLC for dynamic global peak extraction of the partially shaded photovoltaic system. *PloS ONE* 13(11):e0206171. <https://doi.org/10.1371/journal.pone.0206171>
25. Eltamaly AM, Farh HMH (2019) Dynamic global maximum power point tracking of the PV systems under variant partial shading using hybrid GWO-FLC. *Solar Energy* 177:306–316. <https://doi.org/10.1016/j.solener.2018.11.028>
26. LA361K51S -Multi-crystalline photovoltaic module datasheet
27. Mirjalili S, Lewis A (2016) The whale optimization algorithm. *Adv Eng Softw* 95:51–67. <https://doi.org/10.1016/j.advengsoft.2016.01.008>
28. Aljarah I, Faris H, Mirjalili S (2018) Optimizing connection weights in neural networks using the whale optimization algorithm. *Soft Comput* 22(1). <https://doi.org/10.1007/s00500-016-2442-1>

29. Kumar, CHS, Rao RS (2016) A novel global MPP tracking of photovoltaic system based on whale optimization algorithm. *Int J Renew Energy Dev* 5(3):225–232. <http://dx.doi.org/10.14710/ijred.5.3.225-232>
30. Kirkpatrick S, Gelatt CD, Vecchi MP (1983) Optimization by simulated annealing. *Science* 220(4598):671–680. <https://doi.org/10.1126/science.220.4598.671>
31. E. Nery Chaves, J. Henrique Reis, E. A. Alves Coelho, L. C. Gomes de Freitas, J. B. Vieira Junior and L. C. Freitas (2016) Simulated annealing—MPPT in partially shaded PV systems. *IEEE Latin Am Trans* 14(1):235–241. <https://doi.org/10.1109/tla.2016.7430084>
32. Wang F, Zhu T, He X, Fan Y, Zhuo F, Yi H (2017) Application of enhanced simulated annealing GMPPT algorithm for different PV systems in mismatch. In: 2017 19th European conference on power electronics and applications (EPE'17 ECCE Europe), Warsaw, Poland, pp P.1–P.5. <https://doi.org/10.23919/epe17ecceurope.2017.8099026>
33. Mafarja MM, Mirjalili S (2017) Hybrid whale optimization algorithm with simulated annealing for feature selection. *Neurocomputing*, 260:302–312. <https://doi.org/10.1016/j.neucom.2017.04.053>

MPPT-Based Particle Swarm and Cuckoo Search Algorithms for PV Systems



Farag K. Abo-Elyousr, Alaaeldin M. Abdelshafy and Almoataz Y. Abdelaziz

Abstract The increased penetration of photovoltaics (PVs) within power system on both islanded and grid-tied inverters encourages researchers to develop several maximum power point tracking (MPPT) algorithms. The main target of this chapter is to enable PV systems to participate effectively in power systems by harvesting the possible PV maximum power from a solar panel. Two evolutionary algorithms for MPPT were developed and compared, namely particle swarm optimization (PSO) algorithm and the recent cuckoo search (CS). The proposed controllers employ DC/DC boost converter to harvest the maximum power available from the PV resource. System programming and modeling is done using MATLAB/SIMULINK software. The obtained results are compared with the mature perturb and observe (P&O) algorithm under several operating conditions such as irradiance, temperature, and partial shading. The developed controllers require only the PV voltage and current, which makes them economically cost and attractive in the PV transient and steady-state operating conditions.

Keywords Photovoltaics · Maximum power point tracking · Particle swarm optimization · Cuckoo search · Partial shading

F. K. Abo-Elyousr (✉) · A. M. Abdelshafy
Electrical Engineering Department, Faculty of Engineering, Assiut University, Assiut 71516, Egypt
e-mail: farag@aun.edu.eg

A. M. Abdelshafy
e-mail: eng_allaeldeen_2007@yahoo.com

A. Y. Abdelaziz
Faculty of Engineering and Technology, Future University in Egypt, New Cairo, Egypt
e-mail: almoataz.abdelaziz@fue.edu.eg

© Springer Nature Switzerland AG 2020

A. M. Eltamaly and A. Y. Abdelaziz (eds.), *Modern Maximum Power Point Tracking Techniques for Photovoltaic Energy Systems*, Green Energy and Technology, https://doi.org/10.1007/978-3-030-05578-3_14

Acronyms

DERs	Distributed energy resources
PVs	Photovoltaics
MPP	Maximum power point
GMPP	Global MPP
MPPT	Maximum power point tracking
EA	Evolutionary algorithm
P&O	Perturb & observe method
CS	Cuckoo search
PSO	Particle swarm optimization
PWM	Pulse width modulation
DC/DC	DC to DC conversion

Symbols

D	Duty cycle
D_{\min}	Minimum duty cycle
D_{\max}	Maximum duty cycle
f_s	Switching frequency
L	Inductance
N_p	Number of series modules of the solar array
N_s	Number of parallel models of the solar array
V_{mp}	Solar array voltage at MPP
I_{mp}	Solar array current at MPP
P_{mp}	Maximum power that could be drawn from the PV framework configuration
R_L	Equivalent load resistance
V_{oc}	Module open-circuit voltage
I_{dc}	Inductor current
I_{sc}	Module short-circuit current
i_{pv}	Instantaneous PV current
CD	Current position of a particle duty cycle
v	Particle velocity
V_{\min}	Minimum allowed Voltage
V_{dc}	DC-link capacitor voltage
C_{dc}	DC-link capacitor

1 Introduction

Recently, cumulative demand of energy has pushed many governments all over the world to consider modern distributed energy resources (DERs) as one of their priorities to address energy production [1]. Photovoltaic (PV) energy is considered a leading energy resource among DERs. It reaches about 320 GW from the world energy production in 2016 [2]. PVs are not harmful to the environment and save crude oil energy production considerably. In recent years, PVs are used in many applications such as electric transportation, water desalination systems, and road lighting [3, 4]. A considerable amount of research was done in [5] to upgrade PV performance in terms of high efficiency in small-scale water pumping systems. Besides, it decreases the overall greenhouse gas production whenever connected to an electric network system. PVs come among the priority alternatives for islanded, rural, and remote areas systems [6].

The energy yielded from the PVs is markedly influenced by the external weather [7, 8]. Partial shading lends itself as a substantial weather condition to vary power-voltage (P-V) characteristics of the PV frameworks [9, 10]. Thence, PVs show multiple power peaks if they confront multiple partial shading conditions. However, there exists one global MPPT due to the bypass diode [11]. Normally, a DC/DC converter is utilized to decrease the partial shading impacts and extract the MPPT of the PV arrays [12, 13]; thence, several MPPT techniques have been reported in the literature. In [14], the incremental conductance method is conducted experimentally, in which the system reaches the MPPT within 3 s. Conventional MPPT methods such as incremental resistance, perturb and observe, hill climbing, neural network, and fuzzy were reported in [11, 15–21].

Although conventional methods are used satisfactorily to solve MPPT issues, they showed some limitations regarding partial shading, in which there exist multiple peaks within the PV arrays P-V curve [20]. Alternatively, several evolutionary algorithms (EA) have been considered to find global maximum power point (MPP) for PV arrays. The utilized EA algorithms include: genetic algorithm [20, 22], particle swarm optimization (PSO) [23, 24], ant colony [25], mine blast optimization [26], teaching-learning-based technique [26, 27], and gray wolf algorithm [21]. Although the above EAs work satisfactorily regarding MPPT, there is still a need to develop modern EAs. Recently, cuckoo search (CS) has been utilized in [28] to solve load frequency issues, and it shows very satisfactorily results compared to genetic algorithm and particle swarm optimization. This encourages the authors to develop a modern EA based on CS algorithm to solve MPPT issues.

This chapter suggests a recent optimizer based on CS technique to solve MPPT issues. Besides, another algorithm based on PSO is developed with an objective to verify the effectiveness of both optimizers against different conditions. The obtained results are compared to the well-known P&O method.

2 System Description

The schematic diagram is shown in Fig. 1. Each module is investigated by considering Tata Power Solar Systems TP250MBZ as an example. Also, the module has 60 series cells with 249 W theoretical maximum power. The framework comprises four PV modules connected in series. The behavior of the PV module is expressively impinged by, namely, temperature, irradiance, and partial shading conditions. In the subsequent sections, each online optimizer will be trialed for different temperature, irradiance, and partial shading conditions.

2.1 Impact of Module Irradiance

Each individual module is subjective to change the MPP by the received solar irradiance as shown in Fig. 2, in which the module I_{sc} is highly affected by solar irradiance. Consequently, the MPP varies significantly by solar irradiance variation.

2.2 Impact of Module Temperature

The array type, current-voltage (I-V), and P-V characteristics of each module are given in Fig. 3. The module open-circuit voltage (V_{oc}) is significantly invoked by

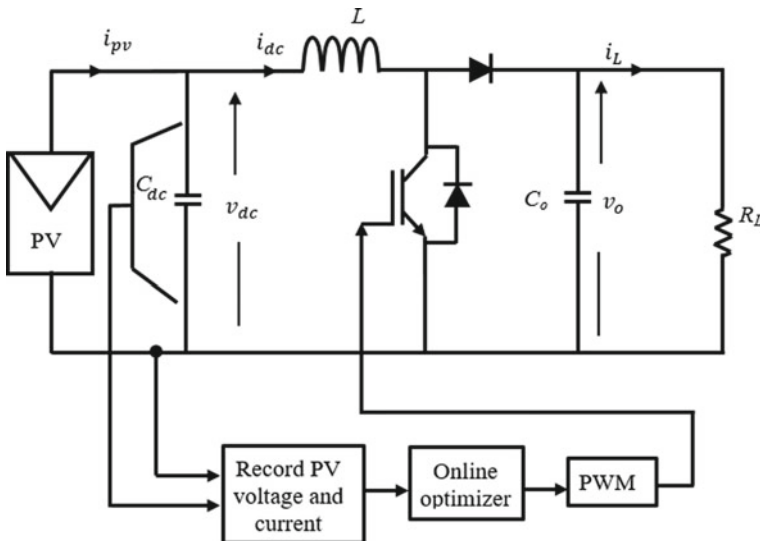


Fig. 1 Structure of the PV framework module

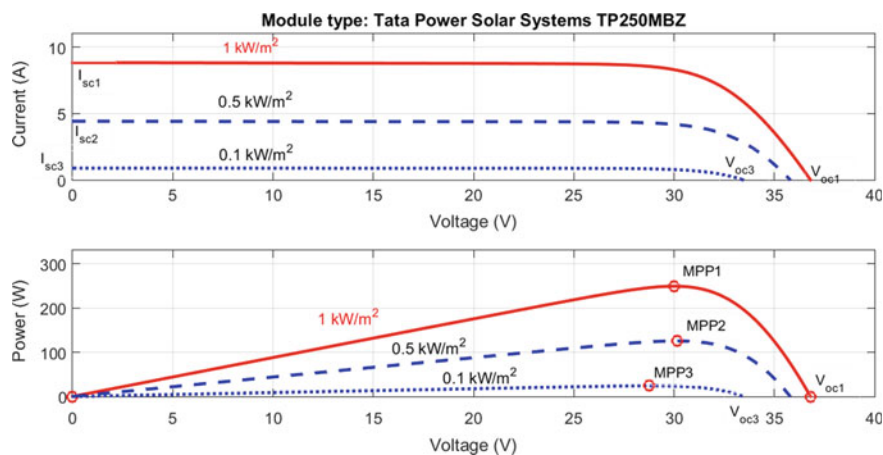


Fig. 2 Properties of the PV module for 25 °C with different, **a** I-V curve, **b** P-V curve

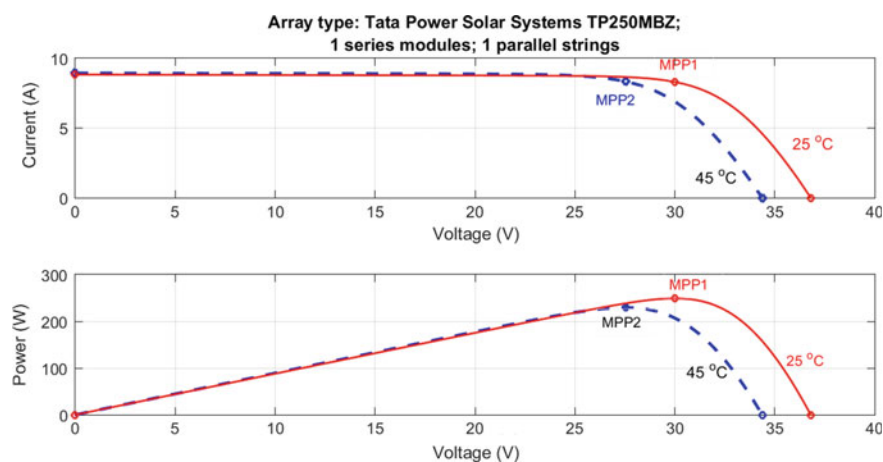


Fig. 3 Properties of the PV module with different temperatures for irradiance of 1000 W/m², **a** I-V curve, **b** P-V curve

temperature. Consequently, the MPP moves to the left and down with the increase in module temperature with the changes in the PV module temperature.

2.3 Impact of Partial Sharing

The connection diagram of the PV framework is shown in Fig. 4. In addition to clouds movements, the shadows movements of buildings cause partial shading problems. This behavior sequentially results in multiple peaks in the I-V and P-V curves of

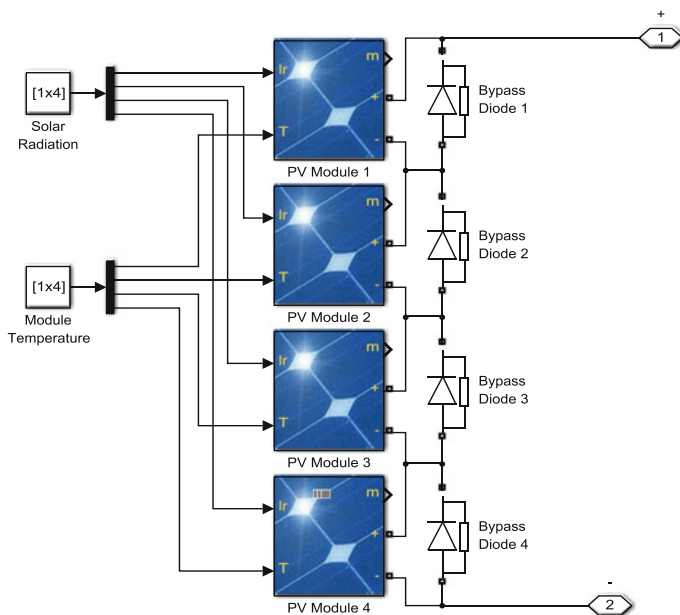


Fig. 4 MATLAB/Simulink PV framework connection

PV arrays configuration. As shown in Fig. 5, two irradiance patterns are shown: (a) The four modules have identical irradiance (1000 W/m^2); (b) the PV modules have isolations: 1000, 300, 600, and 500 W/m^2 , respectively. In addition to multiple peaks, the global MPP (GMPP) moves to the left and down. An effective optimizer should not be trapped in local MPP, in which the PV power may be less the GMPP. Thence, tracking the GMPP is imperative action. In the following, each of the developed online optimizers' applicability will be checked to distinguish GMPP.

3 System Design

The power drawn the PV module is handled by the online developed optimizers to obtain the maximum available power with the accessible irradiance.

3.1 Selection of the PV Array

The PV array is to be chosen according to maximum load requirements. The array maximum power is calculated according to (1), in which N_p and N_s are the parallel and series modules, respectively, I_{mp} is whole PV framework configuration current

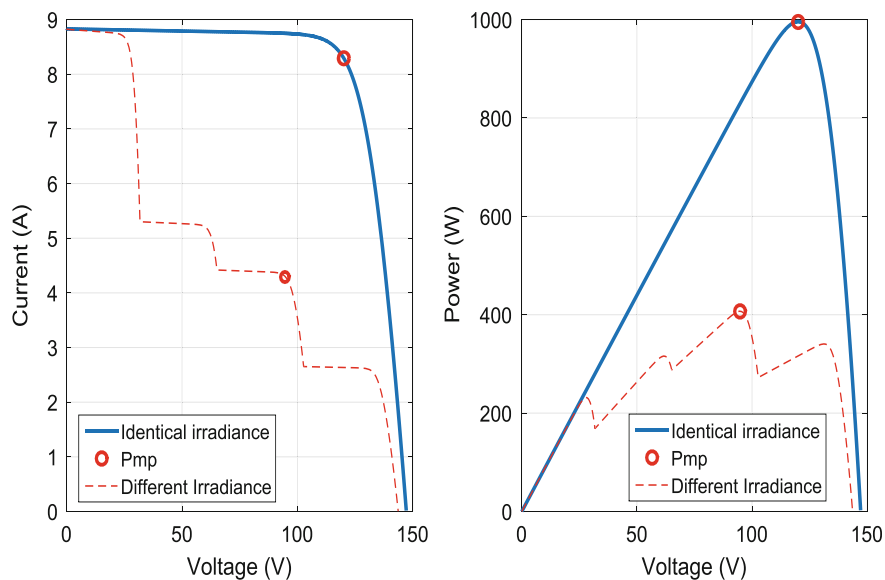


Fig. 5 Properties of the PV curves with different irradiances

Table 1 Specifications of one solar module

Item	Value	Unit
V_{oc}	36.8	V
I_{sc}	8.8	A
V_{mp}	30	V
I_{mp}	8.3	A
Module peak power	249	W
N_s	4	—
N_p	1	—

at the MPP, and V_{mp} is the whole PV framework configuration voltage. The PV specifications for one module are given in Table 1.

$$\begin{aligned}
 P_{mp} &= (N_p \times I_{mp}) \times (N_s \times V_{mp}) \\
 &= (1 \times 8.3) \times (4 \times 30) = 996
 \end{aligned} \tag{1}$$

3.2 Design of DC-Link Capacitor

Normally, capacitors are designed to meet energy demands during transient times such as rapid changes in irradiation and load. The next generic equation given in (2)

is employed to design DC-link capacitor, which is connected in parallel with the PV array as shown in Fig. 1.

$$\frac{1}{2}C_{dc}\left[V_{dc}^2 - V_{min}^2\right] = P_{mp} \times \Delta t \quad (2)$$

where V_{dc} is the DC-link or PV voltage, V_{min} is the minimum PV allowed voltage, and Δt is the transient time. The switching frequency (f_s) of the system is 50 kHz. Using V_{dc} to equal the PV array framework voltage at MPP (120 V), V_{min} equals half the PV array voltage at MPP (60 V), and Δt equals three times the switching period results in C_{dc} of about 10 μ F.

3.3 Design of Output Filter Capacitor

For DC/DC boost converters, the output voltage V_o is regulated at specific value. For design procedures, this value is assumed twice the PV array framework voltage at MPP (240 V). The filter output capacitor (C_o) provides the load energy during fall of irradiance or heavy partial shading. Thence, a time of 1 ms is assumed for Δt . Using the same generic equation given in (2) with V_{min} of 120 V and P_{mp} of 996 W results in a value for C_o of at least 0.23 mF [5].

3.4 Design of Equivalent Load Resistance

Neglecting PV and boost converter losses, the capacity of the output power is equivalent to the input power (996 W), which results in equivalent load resistance of about 58 Ω according to (3).

$$R_L = \frac{V_o^2}{P_{mp}} = \frac{240^2}{996} = 58\Omega \quad (3)$$

3.5 Design of Boost Converter Inductance

To design the boost converter inductance, the maximum and minimum duty cycles are determined first as in (4) and (5), respectively.

$$D_{min} = \frac{V_o - V_{dc,max}}{V_o} = \frac{240 - 120}{240} = 0.5 \quad (4)$$

$$D_{min} = \frac{V_o - V_{dc,min}}{V_o} = \frac{240 - 60}{240} = 0.75 \quad (5)$$

To guarantee the PV array current in the continuous conduction mode, the minimum duty cycle and the $V_{dc,max}$ are utilized [29]. Thence, the inductance value is given in (6).

$$L = \frac{V_{mp} \times D_{min}}{\Delta I_{dc} \times f_s} = \frac{120 \times 0.5}{1 \times 50,000} = 1.2 \text{ mH} \quad (6)$$

4 Problem Description

The study in this chapter brings together two recent online EAs optimizers and the P&O method to harvest and track the MPP from a solar array. The duty cycle of the DC/DC boost converter is updated through the operation of the online developed optimizers.

4.1 Overview of Particle Swarm Optimization

PSO was developed in an analogy to animal swarms behavior to find a global objective function solution, in which each animal is considered a particle [4, 30]. In this optimizer, the velocity of the swarm is utilized to adjust the current position (CD) of a particle as in (7) and (8), respectively, in which ω_o is the inertia weight, r_1 , r_2 , c_1 , and c_2 are decided randomly between 0 and 1, G_{best} is a global best for the solution, and P_{best} is called the personal best.

$$v_i^{k+1} = \omega_o v_i^k + c_1 r_1 (G_{best} - CD_i^k) + c_2 r_2 (P_{best} - CD_i^k) \quad (7)$$

$$CD_i^{k+1} = CD_i^k + v_i^{k+1} \quad (8)$$

The online operation of the PSO is depicted in Fig. 6, in which the duty cycle (D) is initialized randomly and stored in a predefined matrix size. The online PSO optimizer sends the estimated global best duty cycle (G_{best}) to the PWM box. The optimizer operates as long as the load needs power.

4.2 Overview of Online Cuckoo Search Optimizer

Cuckoo search was inspired in a previously reported study by X. Yang in 2010 to find an optimization function solution by imitating cuckoo reproduction parasitism [28, 31]. CS employs Levy flights to update duty cycles values as in (9) and (10) in terms of the gamma-function(γ), respectively [32, 33], with all unknown parameters' values which are given in the appendices.

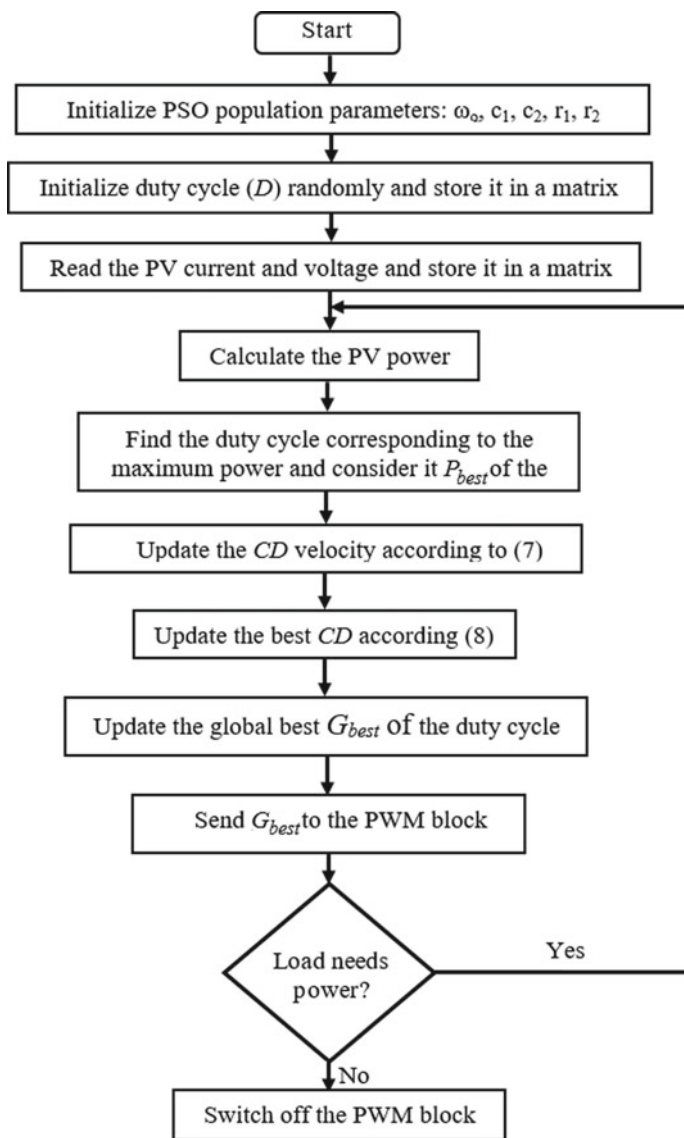


Fig. 6 Flowchart of online PSO-based optimizer

$$\delta = \left[\frac{\gamma(1 + \beta) \times \sin \pi \times \left(\frac{\beta}{2}\right)}{\gamma\left(\frac{1+\beta}{2}\right) \times \beta \times 2^{\frac{\beta-1}{2}}} \right]^{\frac{1}{\beta}} \quad (9)$$

$$CD_i^{k+1} = CD_i^k + \alpha \times G_{\text{best}} \times \frac{|u|}{|v|^{\frac{1}{\beta}}} \quad (10)$$

The functions u and v are uniformly distributed matrices with a zero mean value and standard deviations of 1 and δ , respectively. The online operation of the CS optimizer is depicted in Fig. 7, in which the duty cycle (D) is initialized randomly and stored in a predefined matrix size also. The online CS optimizer excludes the worst solutions and exchanges them by new nests. Each is considered a solution. Thence, the CS sends the estimated global best duty cycle to the PWM box. Also, the optimizer operates as long as the load needs power.

4.3 Overview of Perturb and Observe Method

The operation of the P&O method is implemented in Fig. 8 [34, 35]. The basic principle of this method depends on the PV power signal. The accuracy of this method depends on the selection of the duty cycle perturbation (C), which will be added or subtracted to update the DC/DC converter switch duty cycle.

5 Simulated Results

In order to investigate the applicability and efficacy of the developed online optimizers, a MATLAB/Simulink 2015a model was implemented. The online optimizers are called instantaneously within the execution procedures of the DC/DC boost converter to assess the required duty cycle. Several irradiance and temperature patterns are considered to trial the efficacy of the online optimizers to find a GMPP.

5.1 Identical Temperature and Irradiance

In this scenario, the four modules have the same temperature (25 °C) and irradiance (1000 W/m²). Figures 9 and 10 show the PV array performances. It is clear that the developed online EA algorithms give satisfactory results compared with P&O method. The performance under P&O method suffers from large ripples in the PV voltage and current profiles. This behavior emerges from the P&O nature, as it always oscillates around the MPP by a small increment. At the end of 1 s simulation, the

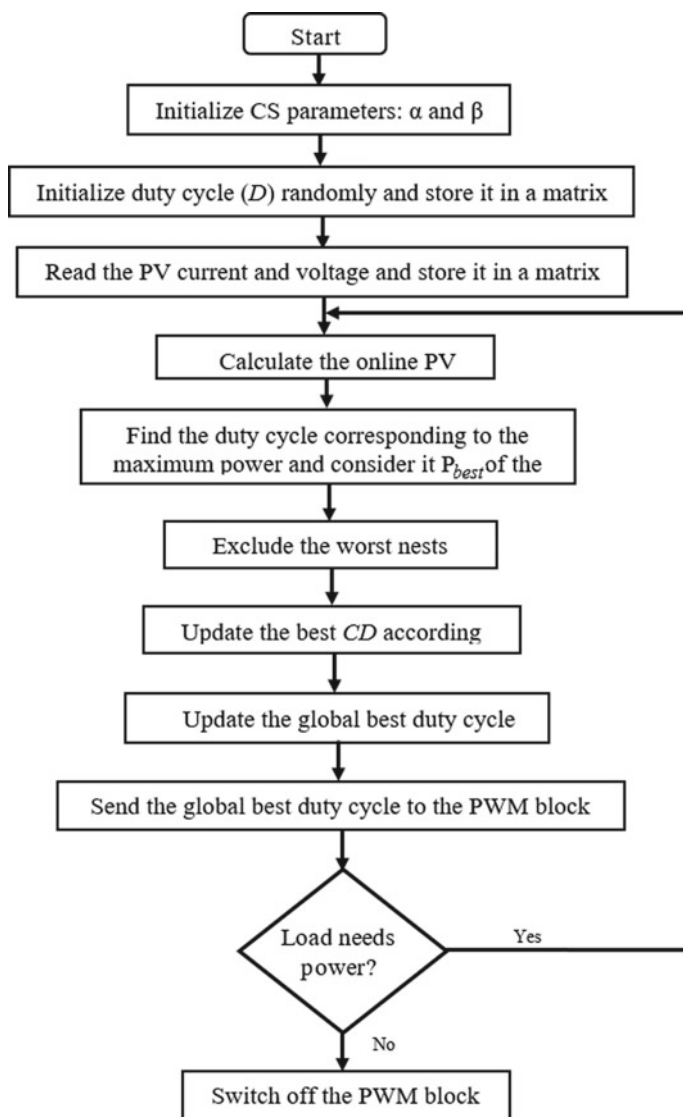


Fig. 7 Flowchart of online CS-based optimizer

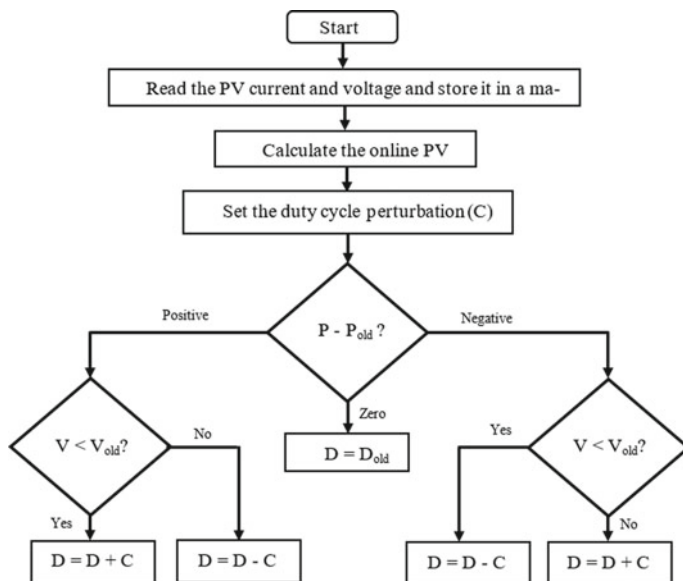


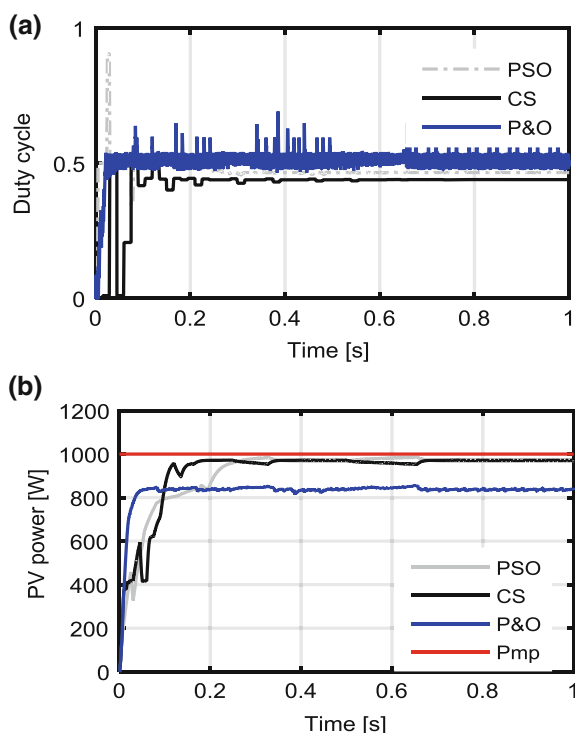
Fig. 8 Flowchart of P&O method

developed algorithms record 96.75, 97.15, and 83.76% accuracy for PSO, CS, and P&O, respectively, to track the MPP. Thus, the MPPT problem was solved.

5.2 Impact of Irradiance

In order to investigate the stability performance of the developed algorithms against transient conditions, one of the four modules irradiance is changed suddenly to 500 W/m^2 . Such situation could happen with the movement of clouds. Consequently, the MPP moves from the solid curve to the dashed one as shown in Fig. 11, which corresponds to 996 and 741 W for both curves, respectively. The system performances are given in Figs. 12 and 13. It is clear that the P&O method suffers from large ripples in the duty cycle performance due to irradiance sudden changes. The online EAs gave satisfactory results with PSO records the closest MPP to the standard value. Thence, the efficacy of the developed online optimizers to solve the MPPT issues was affirmed.

Fig. 9 PV Performance under uniform irradiance, **a** duty cycle, **b** PV power



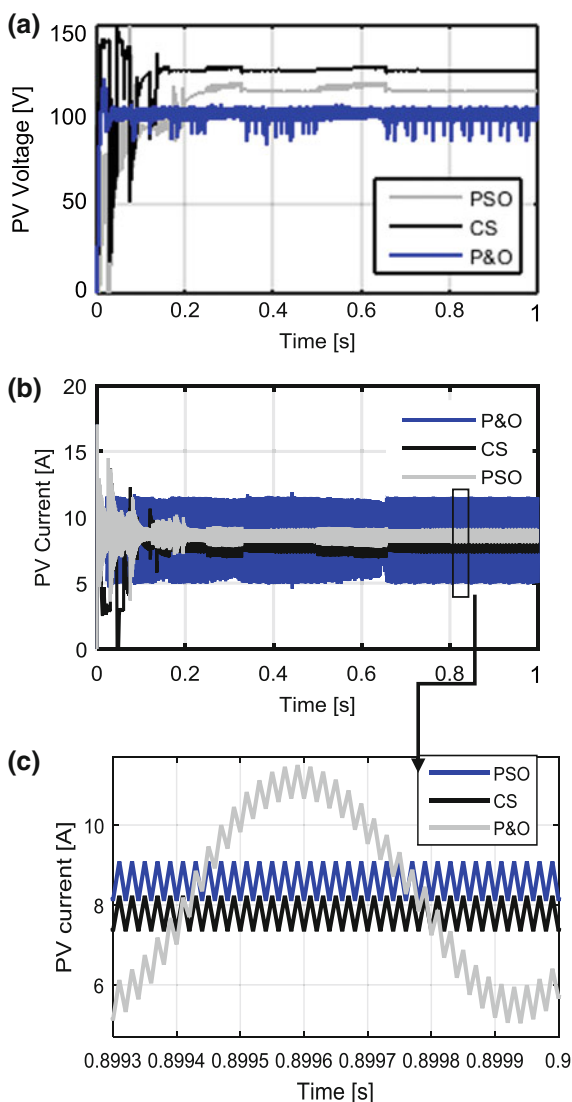
5.3 Impact of Temperature

In this scenario, one arbitrary PV module temperature is increased to 45 °C at 0.6 s. The corresponding PV curves are shown in Fig. 14. The MPP was slightly moved left and decreased to 976 W. Such behavior could happen if insolation and shadow scattered in an uneven manner among individual modules due to building. Besides, it occurs if one module receives negative current for any unusual reason. The PV framework performances are given in Fig. 15. It is clear that the developed online EAs gave very satisfactorily results. They record around 97% efficiency for both algorithms. Thus, the problem of solving MPPT was confirmed.

5.4 Impact of Partial Shading

In this scenario, the performance of the developed online optimizers will be checked against several local MPPT options. Because there are several local MPPs, the optimizer has to look for GMPP to track. The PV modules have the same operating temperature (25 °C). Arbitrarily, the operating conditions with PV irradiance pat-

Fig. 10 PV current and voltage under uniform irradiance, **a** PV voltage, **b** PV current, **c** maximized current image



terns of Fig. 5 are chosen with GMPP of 407 W. Some of the system performances are given in Fig. 16a. As expected, the P&O method fails to find a global MPP to track. It was entrapped and oscillates around the first local MPP from the left on the P-V curve as shown in Fig. 16b. Besides, the CS outperforms the PSO in getting higher efficiency. It records 99.31% compared to 99.28% for PSO.

Another irradiance pattern was arbitrary chosen as 800, 600, 500, and 1000, respectively, which corresponds to a PV behavior as shown in Fig. 17. Both CS and PSO algorithms showed high efficiency of about 99.4 at steady state. Still, the

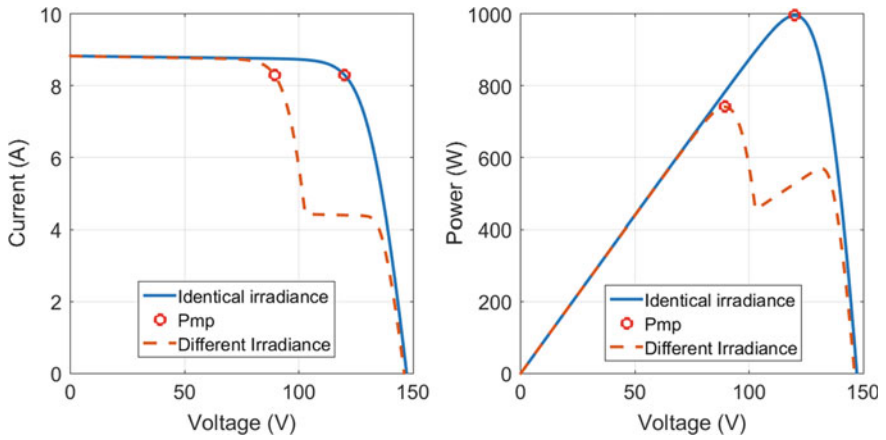
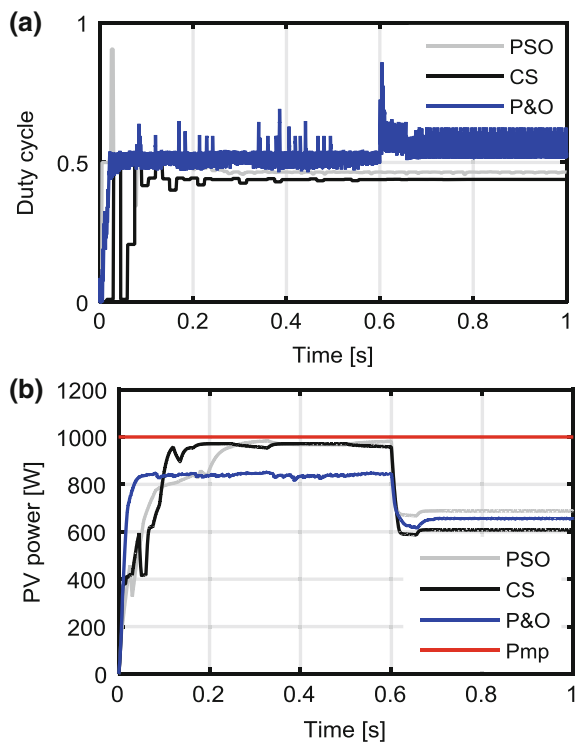


Fig. 11 PV curves for scenario 2

Fig. 12 PV performance for scenario 2, **a** duty cycle, **b** PV power



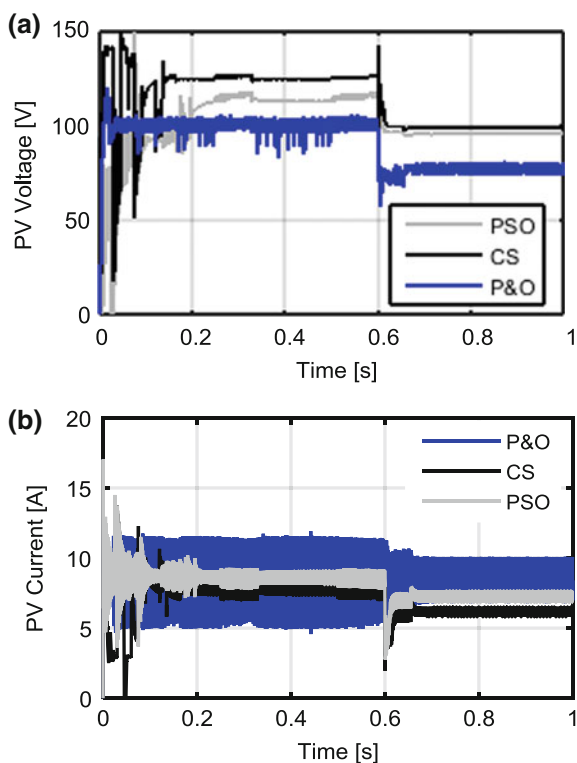


Fig. 13 PV current and voltage performance for scenario 2, **a** PV voltage, **b** PV current

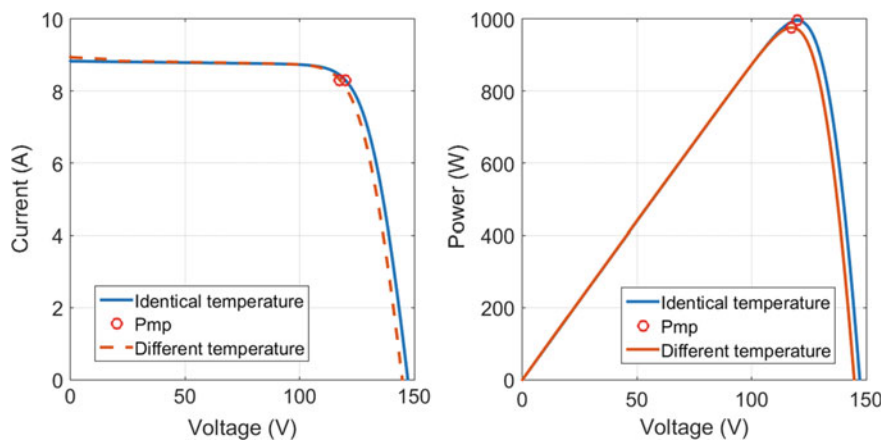
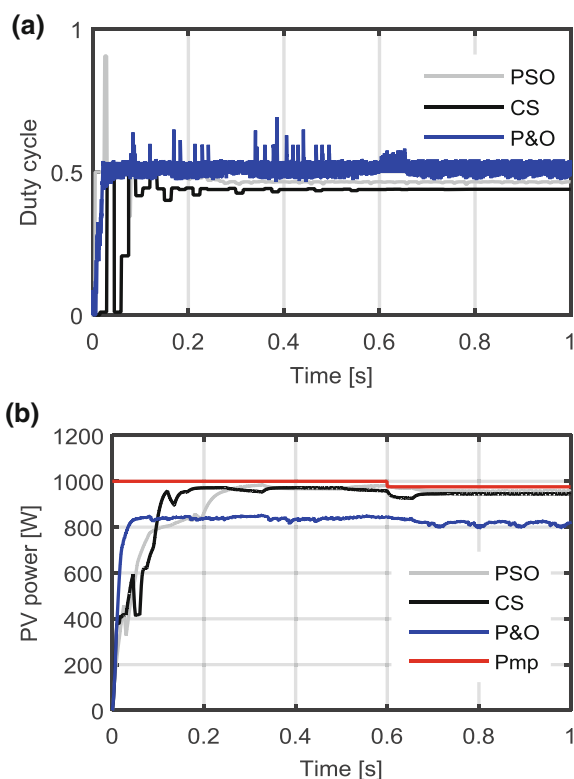


Fig. 14 PV curves for scenario 3

Fig. 15 PV performances for scenario 3, **a** duty cycle, **b** PV power

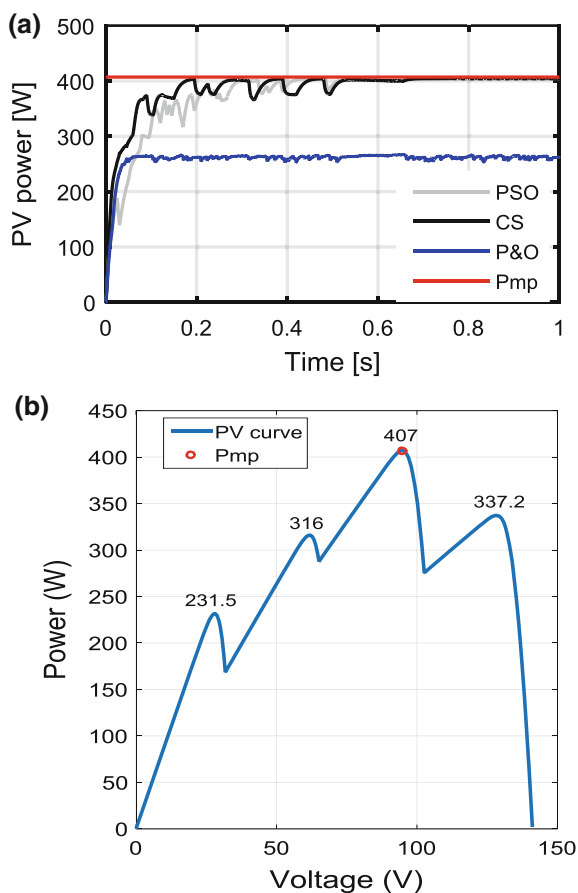


P&O was trapped near the second peak. It is obvious that the developed online EA algorithms show better performance. CS algorithm shows faster performance in finding the GMPP.

6 Discussions

PSO and CS showed satisfactory performance under identical temperature and irradiance conditions with about 0.18 and 0.22 s settling times for each correspondingly as in Fig. 9b. Under partial shading, there is only one GMPP and several local MPPs, depending on the number of modules. CS algorithm demonstrated a good exploration performance to catch the GMPP; however, both algorithms showed exploitation behavior at steady state to hold operation around the GMPP. Besides, both algorithms illustrated satisfactory behavior with respect to transient behavior without oscillation at steady-state long-term operating conditions. However, in a clear manner, P&O could not track the GMPP under partial shading conditions. Thus, the ability of the developed PSO and CS algorithms was proved in tracking a global

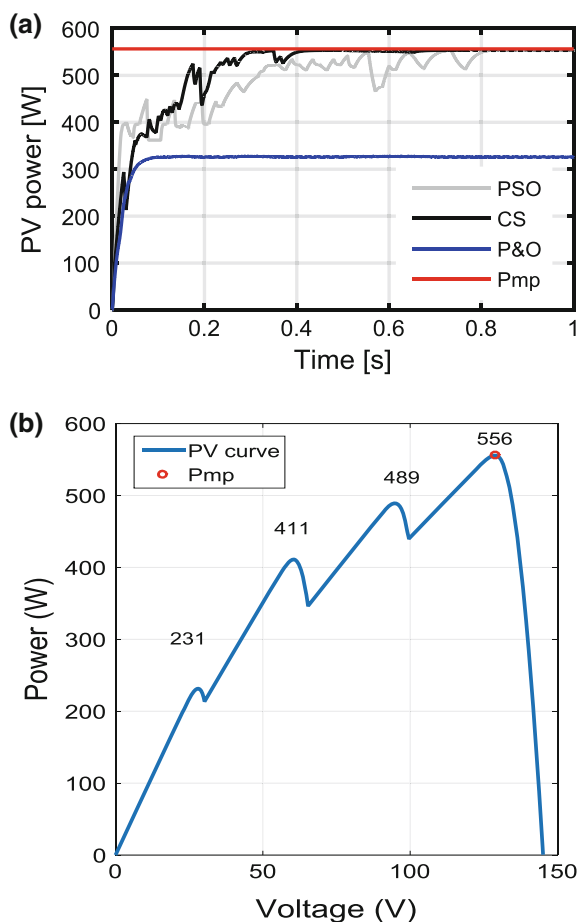
Fig. 16 PV performances under the first partial shading pattern conditions, **a** PV power, **b** local and global MPP



maximum power point under partial shading with different irradiance patterns. From the above reported simulation results, the following notices can be drawn:

- All algorithms show better performance to solve MPPT problem as in Figs. 9 and 10, respectively.
- CS outperforms the other algorithms to find a GMPP under partial conditions as in Fig. 16.
- PSO outperforms the other algorithms under transient operations to find the GMPP. This comes back to the nature of the PSO algorithm as in Figs. 13 and 15, respectively, which has a high exploitation property as reported by the second author in [4].
- P&O method fails to find a global MPPT, as it is always trapped and oscillates around the first local MPPT.

Fig. 17 PV performances under the second partial shading pattern conditions, **a** PV power, **b** local and global MPP



7 Conclusions

In this chapter, two online EAs are trialed and compared to solve MPPT problem under different operating conditions. Both algorithms show high applicability to remedy partial shading problem and find a global maximum power point among several local power points. Based on the simulated results, the following conclusions can be drawn: (1) The PSO outperforms CS to remedy transient conditions. (2) CS outperforms PSO to find a global maximum power point with higher efficiency. The results reveal the superiority of both algorithms to solve MPPT problem. For future works, both algorithms can be combined together to get the benefits of the PSO exploitation characteristics and CS exploration property.

Appendix

1. PSO parameters: $\omega_0 = 0.4$, $c_1 = 1.2$, $c_2 = 2$, r_1 and r_2 are randomly chosen during each execution; size of duty cycle matrix is 4 by 1
2. CS parameters: $\alpha = 0.8$, $\beta = 1.5$, size of duty cycle matrix is 4 by 1
3. P&O: the P&O increment in duty cycle (C) is 0.001.

References

1. Abo-Elyousr FK (2016) Load frequency controller design for two area interconnected power system with DFIG based wind turbine via ant colony algorithm. In: Middle east power system conference (MEPCON'16), IEEE conference, Cairo, Egypt, pp 253–260
2. Al-Shetwi AQ, Sujod MZ (2018) Grid-connected photovoltaic power plants: a review of the recent integration requirements in modern grid codes. *Int J Energy Res* 42:1849–1865
3. Mohammed MA, Eltamaly AM, Farh HM, Alolah AI (2015) Energy management and renewable energy integration in smart grid system. *IEEE Int Conf Smart Grid Eng* 1:1–6 (SEGE, Oshawa, Canada)
4. Abdelshafy AM, Hassan H, Jurasz J (2018) Optimal design of a grid-connected desalination plant by renewable energy resources using a hybrid PSO-GWO approach. *Energy Conv Manag* 173:331–347
5. Singh B, Sharma U, Kumar S (2018) Standalone photovoltaic water pumping system using induction motor drive with reduced sensors. *IEEE Trans On Ind Appl* 54:3645–3655
6. Abo-Elyousr FK, Elnozahy A (2018) Bi-objective economic feasibility of hybrid micro-grid systems with multiple fuel options for islanded areas in Egypt. *Renew Energy* 128:37–56
7. Berrera M, Dolara A, Faranda R, Leva S (2009) Experimental test of seven widely-adopted MPPT algorithms. In: IEEE powertech conference, IEEE conference, Bucharest, Romania, pp 1–8
8. Faranda R, Leva S (2008) Energy comparison of MPPT techniques for PV systems. *WSEAS Trans Power Systems* 3:446–455
9. Rezk H, Eltamaly AM (2015) A comprehensive comparison of different MPPT techniques for photovoltaic systems. *Solar Energy* 112:1–11
10. Ahmed EM, Shoyama M (2011) Variable step size maximum power point tracker using a single variable for stand-alone battery storage PV systems. *J Power Electron* 11:218–227
11. Ramily MA, Twaha S, Ishaque K, Al-Turki YA (2017) A review on maximum power point tracking for photovoltaic systems with and without shading condition. *Renew Sust Energy Rev* 67:144–159
12. Abo-Elyousr FK, Abdelaziz AY (2018) Optimal PI microcontroller-based realization for technical trends of single-stage single-phase grid-tied PV. *Eng Sci Technol Int J (JESTECH)*. 21:945–956. <https://doi.org/10.1016/j.jestech.2018.07.007>
13. Hussaine L, Olias E, Quitero J, Barrado A (2014) Power control for grid connected application based on the phase shifting inverter output voltage with respect to the grid voltage. *Electr Power Energy Syst* 52:250–260
14. Abu-Zaher M, Atia Y, Abo-Elyousr FK, El-Zohri EH (2018) Implementation of MPPT algorithm for single-stage grid-connected photovoltaic system using incremental conductance method. *J Rene Energy Sust Devel (RES D)* 4:57–64
15. Ahmed J, Salam Z (2015) An improved perturb and observe (P&O) maximum power point tracking (MPPT) algorithm for higher efficiency. *Appl Energy* 150:97–108
16. Xiao W, Dunford WG (2004) A modified adaptive hill climbing MPPT method for photovoltaic power systems. In: IEEE power elect specia conference, IEEE conference, Ashen, Germany, vol 3, pp 1957–1963

17. Tey KS, Mekhilef S, Yang HT, Chuang MK (2014) A differential evolution based MPPT method for photovoltaic modules under partial shading conditions. *Int J Photoenergy* 1:1–10
18. Koutroulis E, Blaabjerg F (2012) A new technique for tracking the global maximum power point of PV arrays operating under partial shading-condition. *IEEE J Photovoltaics* 2:184–190
19. Chen Y, Jhang Y, Liang R (2016) A fuzzy-logic based auto-scaling variable step-size MPPT method for PV systems. *Solar Energy* 126:53–63
20. Shaiek Y, Smida MB, Sakly MB, Mimouni MF (2013) Comparison between conventional methods and GA approach for maximum power point tracking of shaded solar PV generators. *Sol Energy* 90:107–122
21. Eltamaly AM, Farh HM, Othman MF (2018) A novel evaluation index for the photovoltaic maximum power point tracker techniques. *Solar Energy* 174:940–956
22. Daraban S, Petreus D, Morel C (2014) A novel MPPT (maximum power point tracking) algorithm based on a modified genetic algorithm specialized on tracking the global maximum power point in photovoltaic systems affected by partial shading. *Energy* 74:374–388
23. Ishaque K, Salam Z, Shamsudin A, Amjad M (2012) A direct control based maximum power point tracking method for photovoltaic system under partial shading condition using particle swarm optimization algorithm. *Appl Energy* 99:414–422
24. Babu TS, Rajasekar N, Sangeetha K (2015) Modified particle swarm optimization technique based maximum power point tracking for uniform and under partial shading condition. *Appl Soft Comput* 34:613–621
25. Jiang LL, Maskell DL, Parta JC (2013) A novel ant colony optimization-based maximum power point tracking for photovoltaic systems under partially shaded conditions. *Energy Build* 58:227–236
26. Fathy AA, Rezk H (2016) A novel methodology for simulating maximum power point trackers using mine blast optimization and teaching learning based optimization algorithms for partially shaded photovoltaic systems. *J Rene Sust Energy* 8:23503–23511
27. Rezk H, Fathy A (2017) Simulation of global MPPT based on teaching-learning-based optimization technique for partially shaded PV systems. *Electr Eng* 99:847–859
28. Abdelaziz AY, Ali ES (2016) Load frequency controller design via artificial cuckoo search algorithm. *Elect Power Comp Syst* 44:90–98
29. Mohan N, Undeland T, Robbins W (2009) *Power electronics: converters, applications, applications*, 2nd edn. Wiley, India, pp 172–178
30. Sharaf AM, Mavalizah H, Ahmadi A, Shayanfar H, Gandoman FH, Homaee H (2018) *Application of new fast, efficient self adjusting PSO search algorithm in new power systems*, 1st edn. Elsevier Publisher, Book chapter 3, New York, USA
31. Yang X (2010) *Engineering optimization: an introduction with metaheuristic applications*, 1st edn. Wiley Publisher, New Jersey, USA, pp 242–244
32. Gandami AH, Yang XS, Alavi AH (2013) Cuckoo search algorithm: a meta heuristic approach to solve structural optimization problems. *Eng Comp* 29:17–35
33. Bindu A, Radi M (2013) Economic load dispatch using cuckoo search algorithm. *Int J Eng Res Appl* 3:498–502
34. Bendib B, Kri F, BelmiliH, Almi MF, Bolouma S (2014) An intelligent MPPT approach based on neural-network voltage estimator and fuzzy controller, applied to a stand-alone PV system. In: *IEEE 23rd International Symposium on Industrial Elect (ISIE)*, Istanbul, Turkey, pp 404–409
35. Youssef AM, Abo-Elyousr FK (2017) Fuzzy logic speed control for three-phase induction motors by photovoltaic system with a robust MPPT. *J Electr Eng* 17:1–15

A New Hybrid Moth Flame Optimizer-Perturb and Observe Method for Maximum Power Point Tracking in Photovoltaic Energy System



Saber Arabi Nowdeh, Mohammad Jafar Hadidian Moghaddam,
Shohreh Nasri, Almoataz Y. Abdelaziz, Mahmood Ghanbari and Iraj Faraji

Abstract In this chapter, a new hybrid moth flame optimizer-perturb and observe method that is called HMFOPO is used to solve the MPPT problem for PV energy system in order to provide an optimal response due to achieving the maximum PV module power. In the proposed scheme, by using the MFO optimization method, the photovoltaic curve is investigated and then the P&O method is implemented by starting from the position of the best moth of the MFO algorithm. Therefore, a combination of MFO and P&O methods joins the derived intelligence from MFO with the fast convergence of P&O to form a proper method with high speed, accuracy, and efficiency due to solving MPPT problem. By using the HMFOPO method, search variables are considered as voltage and the objective function including the power of the PV system is optimized by evaluating the power-voltage curve that should be sampled online. In this study, by considering the conditions of rapid changes and PSC, the efficiency of the PV module is investigated. There are also different scenarios to verify the performance of the proposed method under standard situations, rapid change conditions, and partial shade exploitation. The capability of HMFOPO in different scenarios such as standard condition and various patterns of partial shading from different perspectives such as the efficiency and convergence speed are

S. Arabi Nowdeh (✉)
Golestan Technical and Vocational Training Center, Gorgan, Iran
e-mail: saber.arabi17@gmail.com

M. J. H. Moghaddam
College of Engineering and Science, Victoria University, Melbourne, Australia

S. Nasri
Department of Electrical Engineering, Islamic Azad University, Najafabad Branch, Najafabad Isfahan, Iran

A. Y. Abdelaziz
Electric Power and Machine Department, Faculty of Engineering, Ain Shams University, Cairo, Egypt

M. Ghanbari
Department of Electrical Engineering, Gorgan Branch, Islamic Azad University, Gorgan, Iran

I. Faraji
Department of Electrical Engineering, Islamic Azad University, Khalkhal Branch, Khalkhal, Iran

© Springer Nature Switzerland AG 2020

401

A. M. Eltamaly and A. Y. Abdelaziz (eds.), *Modern Maximum Power Point Tracking Techniques for Photovoltaic Energy Systems*, Green Energy and Technology, https://doi.org/10.1007/978-3-030-05578-3_15

investigated, and the results are compared with the obtained results from P&O and MFO methods. The simulation results show that the proposed hybrid method benefits higher speed and convergence efficiency in solving the MPPT problem and reaching the GMPP and extracts more power from the PV system.

Keywords Maximum power point tracking · Photovoltaic energy system · Partial shading · Hybrid moth flame optimizer-perturb and observe

1 Introduction

In comparison with traditional non-renewable sources like fossil fuels, the renewable energy source (RES) technologies such as photovoltaic (PV) systems are sophisticated, inexpensive, and widespread. Some applications of PVs include water pumping, power supply of residential premises, battery charging, and to name but a few. Employing semiconductors in PV arrays, solar energy is easily converted to electricity. Thanks to the considerable benefits of PV systems from economic and environmental points of view, the demand for PV systems is exponentially growing. Nonetheless, the application of PV systems has encountered limitations due to the two major reasons: the installation cost is high and the efficiency is low in case of changes in the weather conditions. Consequently, an interesting approach, named maximum power point tracking (MPPT), has been proposed and widely used to efficiently use a given PV system [1, 2]. Yet, since PVs suffer from low-efficiency problems, for which a solution must be provided. The MPPT method has to be utilized to increase the efficiency of PVs in different weather condition. In fact, tracking the maximum power point ensures the efficiency improvement of PV systems. To this end, a controller is used in PV systems to adjust the duty cycle of the load. Moreover, some factors impact the operation of PVs and prevent the system to operate at the maximum power point, among which are the changes in solar radiation, temperature, and load size. Additionally, when a PV system is under partial shading conditions (PSC), it is difficult or impossible to operate at the MPP. The changes in solar radiation affect the current greater than the voltage such that the reduction of radiation results in current reduction, and finally, the output power is decreased [3]. Furthermore, the temperature has an adverse effect on the voltage of PV system such that when the ambient temperature increases the voltage is decreased, which finally leads to output power reduction. Under partial shading conditions, the output power curve of PV arrays witnesses several maxima. Hence, a novel algorithm should be introduced to ensure the system is operating on its maximum power point even when the conditions change [3, 4].

A significant amount of research has been conducted by scholars to improve the operation of PV systems. For instance, introducing novel techniques and algorithms to reach the MPP is one of these approaches. To this end, a great number of literature have focused on such methods. Two commonly used methods for MPPT include perturbation and observation (P&O) [5] and hill-climbing (H&C) [6] because a fewer

number of sensors are needed in these techniques, as a result the implementation and operation of such methods is easy and simple. The fundamental rule of P&O and H&C is to produce perturbation on the voltage signal and observe the output power. If the output power is increased, the perturbation is maintained in the same direction; otherwise the next perturbation is reversed. Regarding the point that the H&C method also makes an effort to regulate the PV voltage to track the maximum voltage point, the fundamental rule of H&C algorithm is identical to that of P&O method. The major disadvantage of these two methods is that the algorithm is subjected to tracking errors if the operational point changes fast and also the algorithm is not capable to track the MPP. In [7], the incremental conductance (IncCond) algorithm is presented to track the maximum power point of a PV system. This algorithm makes a comparison between the incremental and momentary conductance of PV cells and supplies the load with PV's output energy. The fundamental rule of this approach is the zero-derivative of power per voltage or current. The main demerit of IncCond method is that it needs control circuitry. Using the ripple correlation control (RCC) method [8] along with a convertor results in noticeable ripples in the employed control strategy when trying to control the MPPT. When solar radiation is high, it provides a satisfactory performance. However, under low radiation level, the efficiency of tracking process shows a significant decrease. Short-circuit current (SSC) [9] and open-circuit voltage (OCV) [10] are used to determine the current and voltage of the maximum power point. To this end, the load of the PV array is disconnected from the system. Therefore, since the load had to be removed periodically these methods are not considered as appropriate approaches to find the MPP, even though they are cost-effective and can be easily implemented. Notwithstanding this, due to the facility of use, SSC and OCV methods may be utilized in a hybrid approach.

Artificial intelligence (AI) methods [11] as substitute techniques for traditional methods are used in many different engineering areas to solve convoluted problems. To use artificial neural networks (ANNs) for the MPP problem, it is essential to determine the weights (W_i) of synapses regarding the correlation among the inputs and outputs of the PV system. As a result, the PV cell or array should be investigated for a roughly long period of time to provide a specific pattern between the inputs and outputs of the ANN. However, once the ANN's structure is determined and it is trained in a cumbersome manner, it would be easy to accurately reach the MPPT and not much effort is required with respect to the PV variables. Even so, carrying out a frequent training process needs new set of data. This is somehow time-consuming and quite a significant amount of data sets must be provided for training the ANN. Another method that is widely used for MPPT is fuzzy logic (FL), which is mostly employed for partial shading conditions. Although ANN and FC provide satisfactory results, they suffer from the complexity and burdensome of computations needed to implement these methods [12]. During the past years, some new researches have been carried out in the realm of solving the MPPT problem in the PV systems. Besides that, the effects of PSC on the MPPT problem were investigated. It was concluded that it is a challenging task to accurately track the maximum power point using the conventional techniques under PSCs. So some novel MPPT methods and algorithms, most of which inspired by the nature are applied to solve the MPPT problem. Two most common

methods of this category to name are particle swarm optimization (PSO) method [13] and genetic algorithm (GA) [14]. These two optimization approaches are easy to implement using a cost-effective digital controller. Additionally, since the global peak power point is successfully maintained even under partial shading, PSO and GA are promising methods in this regard. Recently, many studies have been conducted on MPPT problem solution, but there is still a need for powerful methods in this area to achieve high efficiency of MPP tracking.

The major objective of this chapter is to access the global maximum power point (GMPP) of the PV system through improving the tracking efficiency and reducing or even eliminating the output power oscillations of the PV array under PSCs. In recent years, a novel nature-inspired meta-heuristic algorithm known as moth-flame optimization (MFO) algorithm was introduced by Mirjalili [15]. MFO imitates the swirling (spiral) movement of moths surrounding a candlelight. Based on the obtained results and rapid convergence feature of the MFO algorithm compared with similar methods, it is proved that MFO provides high optimization accuracy and required low computational burden [16–19]. Moreover, a fewer number of variables and operators are required in MFO compared to similar evolutionary techniques and this has led to the widespread application of this method for MTTP problems. In this chapter, MFO is combined with P&O and a novel hybrid method known as HMFOPPO is implemented to solve the optimization problems under PSCs and find the MPP for the PV system.

The chapter is organized as follows. The model of PV system is described in Sect. 2. Section 3 illustrates various PV system patterns both under standard conditions and partial shading conditions. Furthermore, the proposed HMFOPPO method for MPPT is introduced and explained in Sect. 4. Finally, the simulation results and conclusions are presented in Sects. 5 and 6, respectively.

2 Modeling of PV Energy System

Various models have been adopted in the literature for PV modules up to this date. Single-diode model [12–14] is one of the rampant and simple models in this regard, where a paralleled current source, a diode, and a resistor are employed. Figure 1 shows the equivalent circuit of a solar cell. Single-diode model was adopted in this study to simulate the considered PV system because the proposed model is efficient and compromises between simplicity and accuracy.

The output current of the PV cell is expressed as follows [12–14]:

$$\begin{aligned}
 I_{PV} &= I_{PH} - I_D - \frac{V_{PV} + R_s I_{PV}}{R_{sh}} \\
 &= I_{PH} - I_{PH} \left[\exp \left(\frac{V_{PV} + R_s I_{PV}}{V_{ta}} \right) - 1 \right] - \frac{V_{PV} + R_s I_{PV}}{R_{sh}} \quad (1)
 \end{aligned}$$

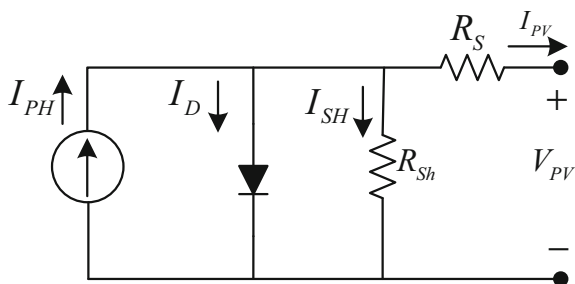


Fig. 1 Single-diode model of a PV cell

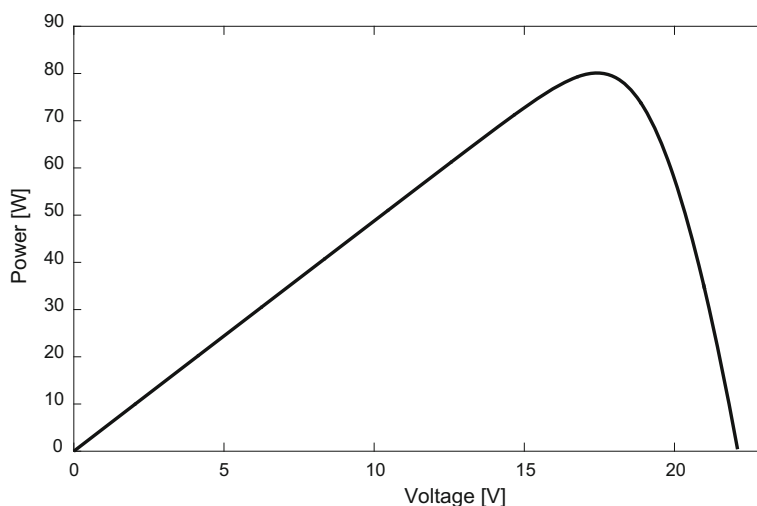


Fig. 2 P-V characteristics curve for a PV cell

where $V_t = \frac{kT}{q}$. Two remaining unknown parameters, i.e. R_s and R_p in Eq. (1), are obtained by matching the maximum calculated power from the model with the peak power of MPP (maximum power point) datasheet [12–14].

The P-V and I-V characteristic curves for a given PV system, both nonlinear, are illustrated in Figs. 2 and 3, respectively. When there is no shading conditions and the PV are exposed to standard test condition (radiation of 1 kW/m^2 and temperature of 25°C), only one peak point is seen in the P-V curve. Nevertheless, several peak points are available on the curve under PSCs.

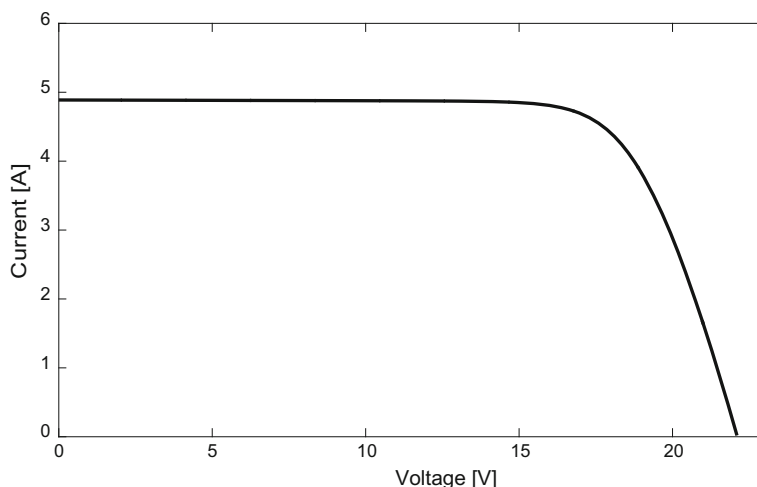


Fig. 3 I-V characteristics curve for a PV cell

3 PV System in Partial Shading Condition

The ambient temperature and solar radiation intensity are two major factors affecting the output voltage and current of a PV system. The former parameter has a sensible impact on the voltage, while the latter impacts the current. In fact, the output voltage and current determine the maximum power point [12–14]. More radiation in the solar system generates more power and vice versa. In accordance with Figs. 2 and 3, i.e. the P-V and I-V curves, it is clear that there is merely one optimal point where the maximum amount of power is provided to the PV system. In large-scale PV arrays, there are series-parallel structures of PV modules, each of which consist a string of PV cells in series. Due to various parameters like shading, clouds, and weak solar radiation, a number of modules show poor performance. The phenomenon where an array lacks enough solar radiation or is somehow deprived of solar radiation is known as partial shading condition (PSC) [12–14]. The largest point among these peak points is known as the global maximum power points (GMPP). The other maxima are called local maximum power points (LMPP). The amplitude and position of LMPPs are dependent on the structure of PV modules and the shading patterns [13].

It is incumbent to utilize intelligent optimization techniques to reach the GMPP under PSCs. The reason behind this fact is that the conventional MPPT methods cannot provide the convergence to the GMPP. Table 1 lists the required technical variables and parameters used in the PV array of this survey.

In this study, three patterns for PV modules configurations have been considered as data of Table 2 and Fig. 4. In pattern 1, the solar radiation of each cell is equal to 1 kW/m^2 named standard test condition (STC) and also in patterns 2 and 3, different partial shading conditions are considered (Fig. 5).

Table 1 Parameters of the single PV cell (BP SX 80) [20]

Parameter	Value
Maximum power	80 W
Open-circuit rated voltage (V_{ocn})	22.1 V
The voltage of maximum power point (V_{mp})	17.6 V
Short-circuit rated current (I_{scn})	4.8 A
Current of maximum power point (I_{mp})	4.6 A
Temperature coefficient	$-0.080\text{ V}/^{\circ}\text{C}$

Table 2 solar data of PV modules configuration in different pattern [20]

Pattern	Solar Irradiance (kW/m^2)			
SP1	1	1	1	1
SP2	1	0.5	1	1
SP3	1	0.7	0.1	1

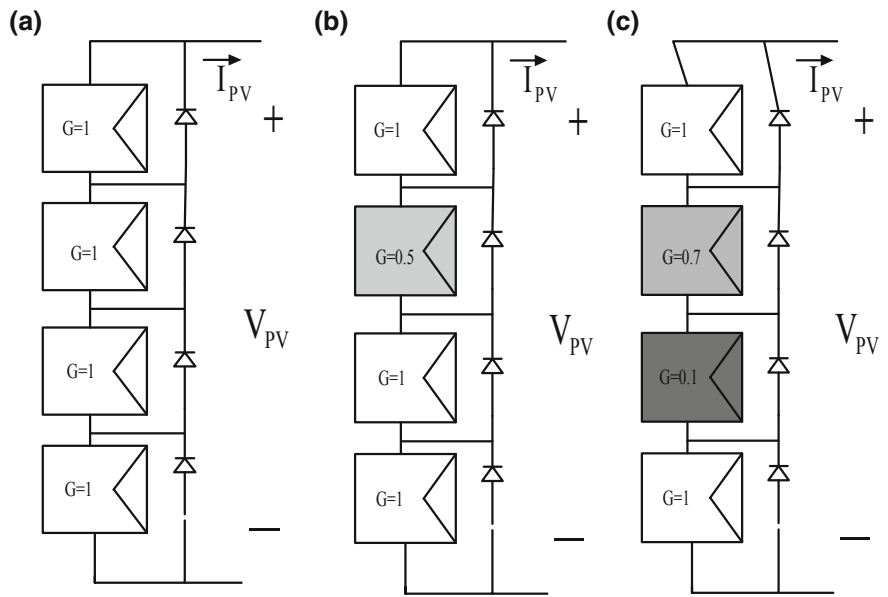


Fig. 4 PV modules configuration in different pattern, **a** pattern 1 (STC), **b** pattern 2 and pattern 3

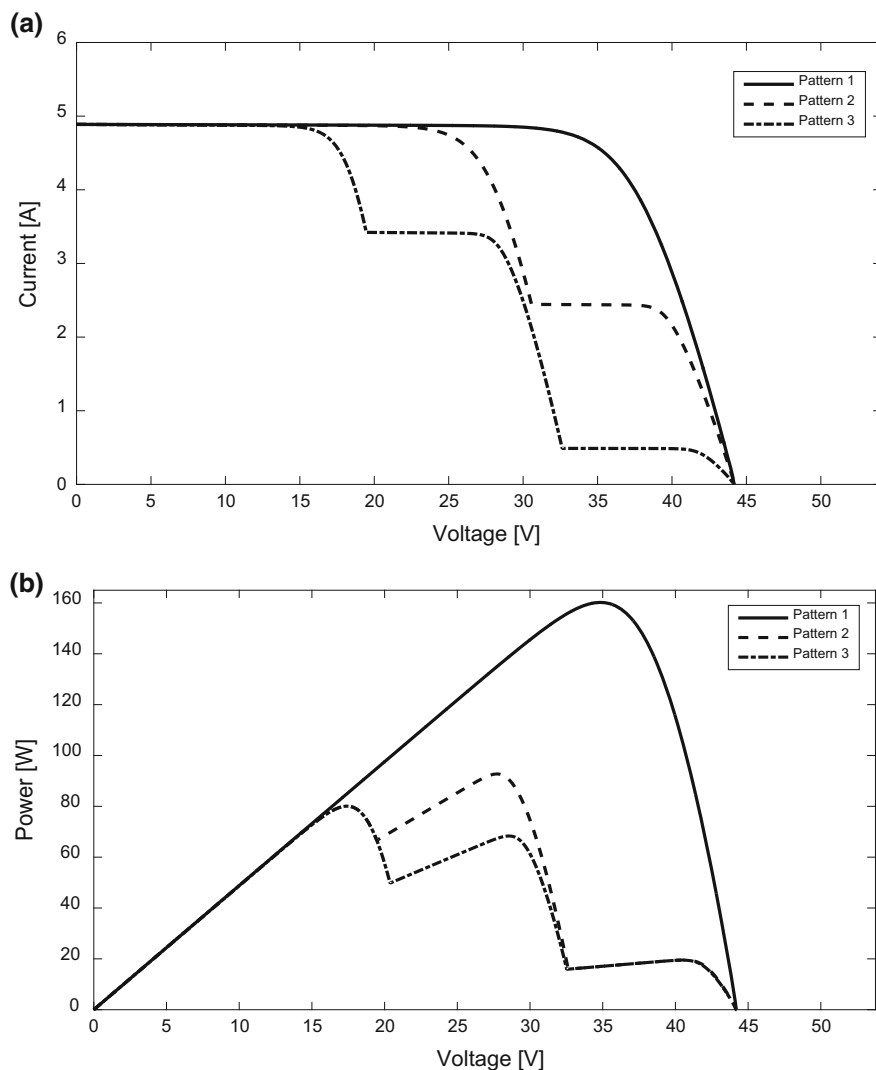


Fig. 5 Characteristics curve of PV modules under different patterns, **a** I-V curve and **b** P-V curve

4 Proposed Method

The understudy PV system, shown in Fig. 6, is comprised of several PV modules, a DC/DC boost converter, and a load. After the calculation of voltage and current and multiplying them, the output power of the PV system is provided to apply to the MPPT algorithm. Then, duty cycle d is established using the algorithm and the DC/DC boost converter is enabled. The value of d as a decision variable in the

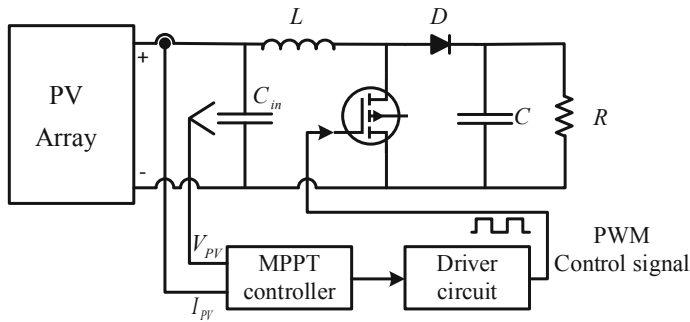


Fig. 6 A general block diagram of the MPPT algorithm

algorithm determines the PV output power known as the fitness value [12–14, 20]. One inference from this fact is that the determined optimal d by the MPPT algorithm gives the maximum extractable power from the PV system.

In this study, P&O, MFO, and the proposed HMFOPO method are utilized to solve the MPPT problem.

4.1 Moth-Flame Optimizer

Moths employ a mechanism named transverse orientation for routing. In this method, a moth flies by maintaining a constant angle with respect to the Moon, and this is a very efficient mechanism for flying in a direct path for long distances. MFO algorithm is an inspiration of this behavior. In the proposed algorithm, it is assumed that the moths are candidate solutions and the moths' positions are variables of the problem. Therefore, by changing their position vectors, moths can fly in 1D to 3D or even higher dimension spaces [15, 18, 19].

In MFO algorithm, a set of moths are represented in a matrix form as follows [15, 18, 19].

$$M = \begin{bmatrix} m_{1,1} & m_{1,2} & \cdots & m_{1,d} \\ m_{2,1} & m_{2,2} & \cdots & m_{2,d} \\ \vdots & \vdots & \vdots & \vdots \\ \vdots & \vdots & \vdots & \vdots \\ m_{n,1} & m_{n,1} & \cdots & m_{n,d} \end{bmatrix} \quad (2)$$

where n is the number of moths, and d denotes the number of variables.

For all moths, the values of fitness function are taken into account as [15, 18, 19]:

$$OM = \begin{bmatrix} OM_1 \\ OM_2 \\ \vdots \\ \vdots \\ OM_n \end{bmatrix} \quad (3)$$

A matrix similar to moth matrix is considered for flames [15, 18, 19]:

$$F = \begin{bmatrix} F_{1,1} & F_{1,2} & \cdots & \cdots & F_{1,d} \\ F_{2,1} & F_{2,2} & \cdots & \cdots & F_{2,d} \\ \vdots & \vdots & \vdots & \vdots & \vdots \\ \vdots & \vdots & \vdots & \vdots & \vdots \\ F_{n,1} & m_{n,1} & \cdots & \cdots & F_{n,d} \end{bmatrix} \quad (4)$$

For all flames, the values of fitness function are assumed as [15, 18, 19]:

$$OF = \begin{bmatrix} OF_1 \\ OF_2 \\ \vdots \\ \vdots \\ OF_n \end{bmatrix} \quad (5)$$

Moths and flames both are solutions of the problem. The difference between them is the way they are updated at each iteration. Moths are the real search factors, which move around the search space. However, flames are the best positions of moths obtained so far. MFO algorithm approximates the global optimum of optimization problems, which is defined as follows [15, 18, 19].

$$MFO = (I, P, T) \quad (6)$$

In the above equation, I is a function generated by an initial population of moths and their corresponding fitness values. Function P , as the main function, moves the moths in the search space. Function T provides the correct value if the termination criteria is met; otherwise, it brings the incorrect value [15]. I , P , and T define the general framework of the MFO algorithm. Function I generates the initial solutions and calculates the values of fitness function. Any random distribution can be used for this function. After initialization, function P is repeatedly executed until function T brings the correct value. Function P is the main function and moves the moths in the search space. To mathematically model this behavior, the position of each moth with respect to the flame is updated using the following equation [15, 18, 19].

$$M = S(M_i, F_j) \quad (7)$$

In the above equation, M_i is the i -th moth, F_j represents the j -th flame, and S is the spiral function.

A spiral-logarithmic algorithm is utilized in this algorithm as the main updating mechanism. However, any type of spiral function subject to the following constraints can be employed for this objective:

- The start point of the spiral must begin from the moth.
- The end point of the spiral must be the moth's position.
- The amplitude oscillation of the spiral must not exceed the search space.

Considering these three points, a spiral-logarithmic function for the mechanism of MFO algorithm is defined as follows [15].

$$S(M_i, F_j) = D_i \cdot e^{bt} \cdot \cos(2\pi t) + F_j \quad (8)$$

In the above equation, D_i is the distance of the i -th moth from the j -th flame, b is a constant to define the spiral-logarithmic shape, and t denotes a random number in the range of $[-1, 1]$.

D_i is calculated as [15]:

$$D_i = |F_j - M_i| \quad (9)$$

4.2 P&O Method

The P&O method is based on the comparison of the output voltage and power changes of the PV system. Thereby, first, the current and voltage of the modules should be sampled to calculate the voltage and power variations. In this method, the parameter X represents the reference signal. If X is the voltage ($X = V$), the task is to move this parameter's value to V_{MPP} . Consequently, the instantaneous voltage moves toward V_{MPP} so as to the output power matches the MPP. To this end, a constant but small perturbation is imposed to the PV cell's voltage. To vary the operating point, a sequence of perturbations is imposed by $C = \Delta V$, when a given perturbation is applied, the changes of power in the output (ΔP) are measured and if it has a positive value the power point is moving toward the MPP; otherwise, it moves away from the MPP. For the former and latter cases, positive and negative voltage perturbations are imposed, respectively. Once the MPP is reached, the procedure will be terminated [5].

4.3 HMFOPO Method

In the proposed method, by using the MFO optimization method, the photovoltaic curve is investigated and then the P&O method is implemented by starting from the position of the best moth of the MFO algorithm. Therefore, the combination of MFO and P&O methods joins the derived intelligence from MFO with the fast convergence of P&O to form a proper method with high speed, accuracy, and efficiency due to solving MPPT problem. By using the HMFOPO method, search variables are considered as voltage and the objective function including the power of the PV system is optimized by evaluating the P-V curve that should be sampled online.

The main objective of MFO algorithm in the MPPT controller is to find an operating point corresponding to the maximum output power from the PV module. Hence, the objective function is in the form of maximizing the PV power, where the MFO algorithm must move along the maximization of the objective function. In the proposed approach, the optimization variable is the voltage of PV, and the control variable is the duty cycle of the DC/DC converter. The optimization problem is defined as follows:

$$\begin{cases} \max f(V_{pv}, I_{pv}) = \max\{P_{pv}\} \\ 0 < V_{pv} < V_{oc} \end{cases} \quad (10)$$

In other words, the terminal voltage should be constrained between the open-circuit voltage and zero voltage values, and the converter switching must be performed such that the maximum power is extracted in the output. Identical to all population-based optimization algorithms, first, a number of initial operating points should be defined as the initial population to start the search process in the default range. It is worth mentioning that the optimization procedure and its results are independent of the initial population. Therefore, these initial values are random values where they can adopt any value.

Another critical factor in optimization programs is the number of search particles, in short n_{pop} , which is selected between 6 and 10 by trial and error. A fewer number of particles results in non-convergence of the algorithm to the global MPP; on the other hand, a more number of populations decelerates the algorithm and wastes time. After assessing the initial population and when the fitness function corresponding to each of the particles is specified, new particles should be produced according to the older ones. Each optimization algorithm has its own exclusive updating method.

The following steps are taken for implementation of MFO method:

Step (1) The number of moths is selected equal to 8, and *pop* matrix is defined as a linear distribution between the minimum and maximum values as the initial values for the duty cycle of the converter.

To determine the fitness of moths, the amount of generated power by the PV system is measured at each of those values. The produced power is calculated by multiplying V_{pv} and I_{pv} , and the corresponding fitness vector (the power value of the PV array) is defined.

Step (2) With regard to the value of the produced power corresponding to each of duty cycle values, pop and fitness vectors are sorted in an ascending manner:

$Fitness_sort = sort(fitness)$: The sorted fitness vector from minimum to maximum.
 $pop_sort = pop(Index: fitness_sort)$: The population sorted vector corresponding to the sorted fitness.

Step (3) If it is the algorithm's first iteration, the following step is implemented:

In the first iteration, $dist$ vector ($D_i = |F_j - M_i|$) is defined and calculated as the distance of a moth from sorted moths: $dist = |pop_sort - pop|$

Using the $dist$ vector and sorted vector pop_sort , new population is established:

$$pop_{new} = r_1 \times dist \times e^{k-m} + r_2 \times pop_sort$$

In the above equation, r_1 and r_2 are two random numbers. Also, k is a random number in the range $[-1, 1]$, and m is the mitigating factor of the algorithm. With the increase in the number of algorithm iterations, m decreases the first term and increases the second term (pop_sort).

Step (4) There are three decision vectors from iterations two or higher:

- New population vector, pop_2 ;
- Population vector in the previous iteration, pop_old ;
- Vector pop_sort .

The new vector is formed using these three vectors. For this end, all three vectors are put in a vector and then sorted based on the fitness of each moth. Then, one-third of the population is taken and the rest is eliminated. Thereby, the moths with the higher fitness values are maintained and those with less fitness values are removed from the competition.

Consequently, in the algorithm output, the best duty cycle of the converter is determined optimally corresponding to the maximum PV power. Next, the optimal duty cycle ($d_{optimal}$) of the initial value of the duty cycle is applied through P&O method.

The implementation steps of P&O method for solving the MPPT problem are summarized in the below.

- The P&O method starts with the determined $d_{optimal}$ in the MFO method as the initial value of the converter's duty cycle.
- After the modification of the converter's duty cycle, a disturbance is applied to the operating voltage of PV. If the output power of the PV module is increased, the duty cycle is also varied along with it; otherwise, it is varied in the inverse direction.
- The previous step is repeated until the GMPP is reached.
- At each 0.1 s, the output power of the PV module is measured and if the power change in the output power samples is greater than 1% of the rated output power of the PV, algorithm is carried out again from the start point.

The flowchart of the proposed method is illustrated in Fig. 7.

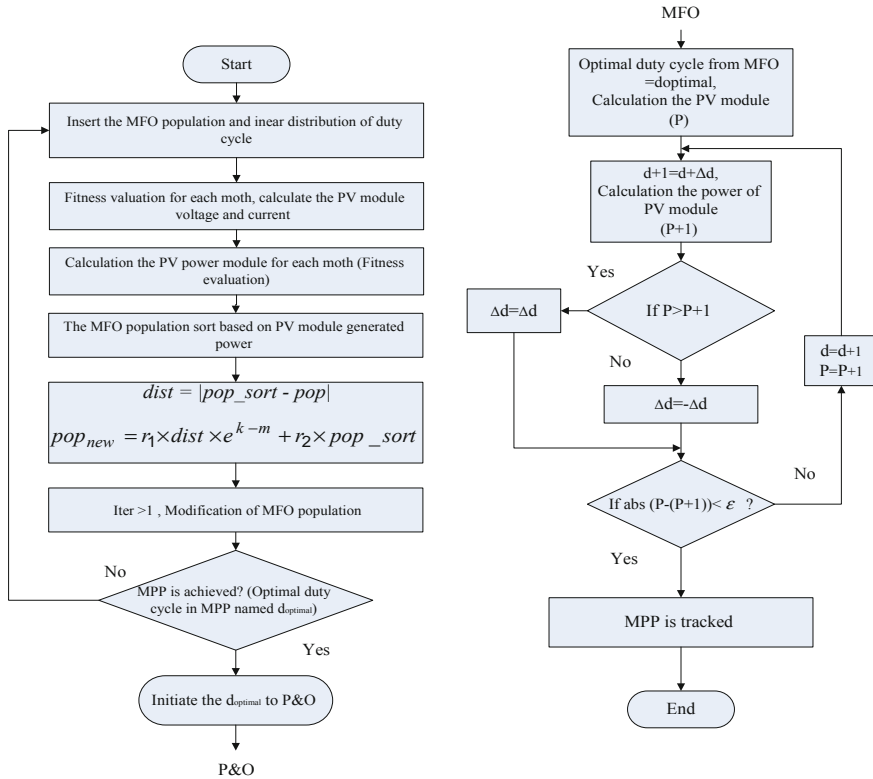


Fig. 7 Flow chart of hybrid proposed algorithm

5 Simulation Results and Discussion

The obtained simulation results for the MPPT of the under-study PV system, both for standard and various PSCs, are described using the HMFOP method. To prove the superiority and efficiency of the HMFOP method, other competent methods like P&O and MFO are also tested. The comparison between these three methods is carried out in terms of the convergence speed, extracted output power, and the GMPP tracking efficiency. These tests were performed under standard and partial shading conditions. The simulation time was assumed 20 s, where 10 s is allotted to the standard condition and other 10 s is assigned to the partial shading condition. The simulations were carried out in MATLAB/SIMULINK software. Also the values of components of the DC/DC converter are presented in Table 3.

Table 3 Values of components of the DC/DC converter [21]

Components	Values
Load resistor (RL)	1 Ω
Inductor (L)	300 μ H
Input capacitor (Cin)	100 μ F
Output capacitor (Cout)	990 μ F
MOSFet’s switching frequency (fs)	100 kHz

5.1 Simulation Results Under Different Patterns

The simulation results under standard (pattern 1) and shading (patterns 2 and 3) conditions are given in Figs. 8 and 9. The initial duty cycle for the P&O method is assumed 0.55 s. The P&O method is trapped in the local maxima and fails to extract the maximum power from the PV system under both standard and shading conditions. On the other hand, the MFO algorithm succeeds in reaching the MPP although with a minor error with respect to the GMPP.

According to the obtained results from the proposed HMFOPO method, it is observed that in solving the problem, in addition to extracting higher power, it reaches the GMPP with a higher convergence speed. Therefore, one can infer that the combination of P&O and MFO methods, known as HMFOPO hybrid method, provides a method with higher speed and convergence accuracy in solving the MPPT problem to each the GMPP.

5.2 Comparison of Results

P&O, MFO, and HMFOPO methods were compared in terms of the convergence speed, maximum extracted power, and the GMPP tracking efficiency, and the results are reported in Tables 4, 5 and 6. The efficiency is calculated as the ratio of the photovoltaic output power to its peak power. The obtained results prove that the convergence speed of the proposed HMFOPO algorithm to the global MPP is remarkably high in comparison with P&O and MFO methods. Therefore, the required time to reach the GMPP is the least in the proposed method. Also, these results show the superiority of the HMFOPO method in terms of GMPP tracking efficiency in comparison with the P&O and MFO methods. The maximum power values for patterns 1, 2, and 3 are 160 W, 120.1, and 92.73 W, respectively. According to Table 4, the P&O method extracted 155.50, 96.57, and 90.62 W output powers for patterns 1, 2, and 3, respectively. The maximum power for the pattern 1 is obtained as 157.35 W by MFO, and the HMFOPO algorithm is converged to 159.72 W. In the pattern 2, it is converged to 118.98 W using MFO and in HMFOPO is converged to 119.47 W. In the pattern 3, it is converged from 90.75 W using MFO and in HMFOPO is converged from 91.95 W. The results show that the HMFOPO is extracted more

Fig. 8 Tracking curve of MPP for different methods under patterns 1–2

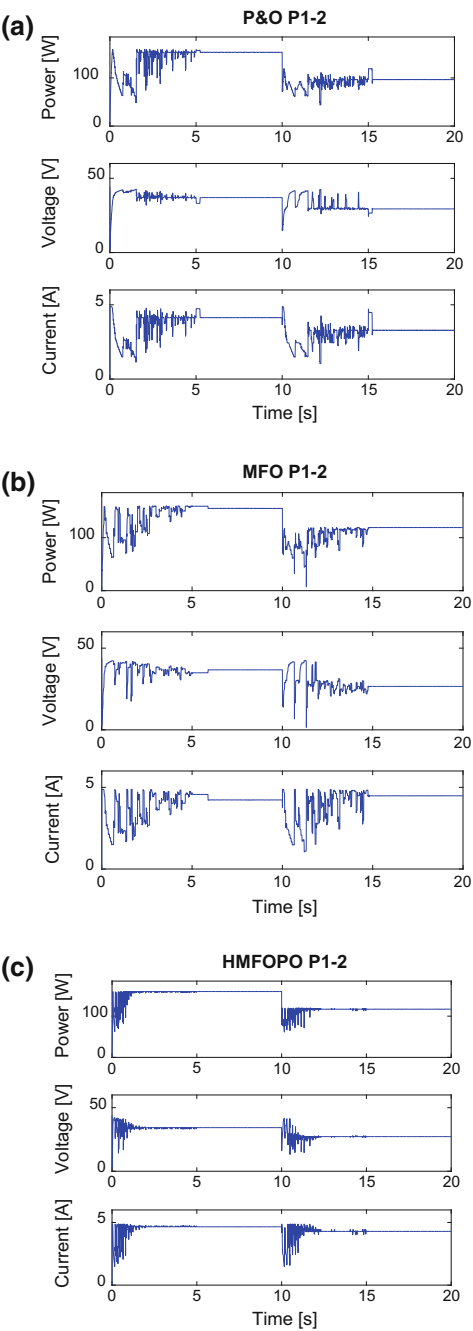


Fig. 9 Tracking curve of MPP for different methods under patterns 1–3

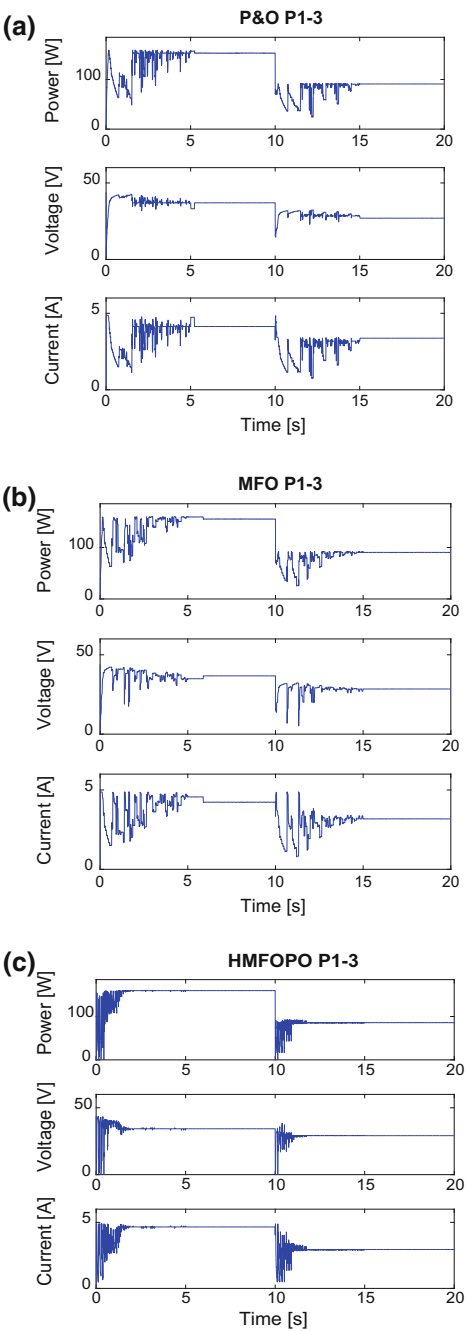


Table 4 Performance comparison of MPPT methods in terms of maximum extracted power

MPPT algorithm	Pattern 1	Pattern 2	Pattern 3
Maximum power	160	120.1	92.73
P&O	155.50	96.57	90.62
MFO	157.35	118.98	90.75
HMFOPO	159.72	119.47	91.95

Table 5 Performance comparison of MPPT methods in terms of tracking efficiency

PMPPT Algorithm	Pattern 1	Pattern 2	Pattern 3
P&O	97.18	80.40	97.72
MFO	98.34	99.06	97.86
HMFOPO	99.82	99.47	99.15

Table 6 Performance comparison of MPPT methods in terms of convergence speed

MPPT Algorithm	Pattern 1	Pattern 2	Pattern 3
P&O	5.22	5.28	4.98
MFO	5.79	4.77	4.66
HMFOPO	1.67	2.30	1.81

power than P&O and MFO. Based on Tables 5 and 6, the HMFOPO method benefits higher convergence speed and convergence efficiency. The tracking efficiency of P&O, MFO, and HMFOPO methods for pattern 1 is 97.18, 98.34, and 99.82%, respectively. The values for pattern 2 are 80.40, 99.06, and 99.47%, respectively. Additionally, these values for pattern 3 are 97.72, 97.86, and 99.15%, respectively, where obtained results prove the superiority of the proposed method in solving the MPPT problem with high convergence speed.

6 Conclusion

To solve the maximum power point tracking problem for a photovoltaic system under both standard and partial shading conditions, this chapter introduced a novel hybrid method, known as HMFOPO. The proposed method is superior to P&O and MFO methods in terms of convergence speed, the GMPP tracking efficiency, and extraction of power. HMFOPO reaches the GMPP with a low number of iterations. Comparison of the MFO, PO, and HMFOPO results verified the superiority of the proposed hybrid method with less computational error, more tracking efficiency, and more convergence speed in achieving global MPP.

References

1. Ramli MA, Twaha S, Ishaque K, Al-Turki YA (2017) A review on maximum power point tracking for photovoltaic systems with and without shading conditions. *Renew Sustain Energy Rev* 67:144–159
2. Kabalci E (2017) Maximum power point tracking (MPPT) algorithms for photovoltaic systems. In *Energy Harvesting and Energy Efficiency*. Springer, Cham, pp 205–234
3. Sefa I, Altin N, Ozdemir S (2017) Maximum power point tracking algorithms for partial shaded PV systems. In *Energy Harvesting and Energy Efficiency*. Springer, Cham, pp 261–292
4. Belhachat F, Larbes C (2018) A review of global maximum power point tracking techniques of photovoltaic system under partial shading conditions. *Renew Sustain Energy Rev* 92:513–553
5. Linus RM, Damodharan P (2015) Maximum power point tracking method using a modified perturb and observe algorithm for grid connected wind energy conversion systems. *IET Renew Power Gener* 9(6):682–689
6. Alajmi BN, Ahmed KH, Finney SJ, Williams BW (2011) Fuzzy-logic-control approach of a modified hill-climbing method for maximum power point in microgrid standalone photovoltaic system. *IEEE Trans Power Electron* 26(4):1022–1030
7. Elgendy MA, Zahawi B, Atkinson DJ (2013) Assessment of the incremental conductance maximum power point tracking algorithm. *IEEE Trans Sustain Energy* 4(1):108–117
8. Casadei D, Grandi G, Rossi C (2006) Single-phase single-stage photovoltaic generation system based on a ripple correlation control maximum power point tracking. *IEEE Trans Energy Convers* 21(2):562–568
9. Husain MA, Tariq A, Hameed S, Arif MSB, Jain A (2017) Comparative assessment of maximum power point tracking procedures for photovoltaic systems. *Green Energy Environ* 2(1):5–17
10. Montecucco A, Knox AR (2015) Maximum power point tracking converter based on the open-circuit voltage method for thermoelectric generators. *IEEE Trans Power Electron* 30(2):828–839
11. Punitha K, Devaraj D, Sakthivel S (2013) Artificial neural network based modified incremental conductance algorithm for maximum power point tracking in photovoltaic system under partial shading conditions. *Energy* 62:330–340
12. Algazar MM, El-Halim HA, Salem MEEK (2012) Maximum power point tracking using fuzzy logic control. *Int J Electr Power Energy Syst* 39(1):21–28
13. Sundareswaran K, Palani S (2015) Application of a combined particle swarm optimization and perturb and observe method for MPPT in PV systems under partial shading conditions. *Renew Energy* 75:308–317
14. Daraban S, Petreus D, Morel C (2014) A novel MPPT (maximum power point tracking) algorithm based on a modified genetic algorithm specialized on tracking the global maximum power point in photovoltaic systems affected by partial shading. *Energy* 74:374–388
15. Mirjalili S (2015) Moth-flame optimization algorithm: a novel nature-inspired heuristic paradigm. *Knowl-Based Syst* 89:228–249
16. Mei RNS, Sulaiman MH, Mustaffa Z, Daniyal H (2017) Optimal reactive power dispatch solution by loss minimization using moth-flame optimization technique. *Appl Soft Comput* 59:210–222
17. Trivedi IN, Jangir P, Parmar SA, Jangir N (2016) Optimal power flow with voltage stability improvement and loss reduction in power system using moth-flame Optimizer. *Neural Comput Appl* 30:1–16
18. Buch H, Trivedi IN, Jangir P (2017) Moth flame optimization to solve optimal power flow with non-parametric statistical evaluation validation. *Cogent Eng* 4(1):1286731
19. Li C, Li S, Liu Y (2016) A least squares support vector machine model optimized by moth-flame optimization algorithm for annual power load forecasting. *Appl Intell* 45(4):1166–1178

20. soufyane Benyoucef A, Chouder A, Kara K, Silvestre S (2015) Artificial bee colony based algorithm for maximum power point tracking (MPPT) for PV systems operating under partial shaded conditions. *Appl Soft Comput* 32:38–48
21. Kheldoun A, Bradai R, Boukenoui R, Mellit A (2016) A new Golden Section method-based maximum power point tracking algorithm for photovoltaic systems. *Energy Convers Manag* 111:125–136

A New Hybrid Method Based on Gray Wolf Optimizer-Crow Search Algorithm for Maximum Power Point Tracking of Photovoltaic Energy System



Faraji Davoodkhani, S. Arabi Nowdeh, Almoataz Y. Abdelaziz, Saeedeh Mansoori, Sh. Nasri and Mohammad Alijani

Abstract In this study, a new hybrid method as gray wolf optimizer (GWO)-crow search algorithm (CSA) (hGWO-CSA) is proposed for solving the MPPT problem in PV energy system. In the proposed method, at first the GWO is applied for MPPT solution and then the optimal duty cycle determined by GWO is considered as the initial value to CSA method. In the hybrid method, the advantages of each method are combined that it is a method with high convergence accuracy and speed and is not trapped in local optimal and quickly achieves to global optimal. The proposed method performance is analyzed in MPPT solution under standard and partial shading condition (PSC), in solar and temperature variations and also considering various types of DC/DC converters. To verify the validity of the hGWO-CSA, the results are compared with GWO and CSA methods. The results show the superiority of the hGWO-CSA in achieving the GMPP with higher convergence speed and less transient oscillations in different condition and in comparison with GWO and CSA methods. Also, the results show that the PV system with the buck-boost converter has better performance due to the wider operation area in terms of extracted power and tracking efficiency than the other DC/DC converters.

F. Davoodkhani

Department of Electrical Engineering, Islamic Azad University, Khalkhal Branch, Khalkhal, Iran

S. Arabi Nowdeh (✉)

Golestan Technical and Vocational Training Center, Gorgan, Iran

e-mail: saber.arabi17@mail.com

A. Y. Abdelaziz

Electric Power and Machine Department, Faculty of Engineering, Ain Shams University, Cairo, Egypt

S. Mansoori

Department of Electrical and Computer Engineering, University of Mohaghegh Ardabili, Ardabil, Iran

Sh. Nasri

Department of Electrical Engineering, Islamic Azad University, Najafabad Branch, Najafabad Isfahan, Iran

M. Alijani

Department of Electrical Engineering, University of Hadaf, Sari, Iran

© Springer Nature Switzerland AG 2020

A. M. Eltamaly and A. Y. Abdelaziz (eds.), *Modern Maximum Power Point Tracking Techniques for Photovoltaic Energy Systems*, Green Energy and Technology, https://doi.org/10.1007/978-3-030-05578-3_16

Keywords Maximum power point tracking · Photovoltaic energy system · Partial shading · Hybrid gray wolf optimizer-crow search algorithm

1 Introduction

Photovoltaic (PV) energy is considered as one of the most promising renewable energy sources. The PV cell is considered to be as an essential part of the photovoltaic system. In this system, PV radiation energy is converted into electricity by photovoltaic effects [1, 2]. Receiving the maximum power point (MPP) from photovoltaic systems has a very important role due to increasing the efficiency. This can be done by connecting a controller to the MPP due to regulating the work cycle for the load. On the other hand, due to changing the output characteristic of photovoltaic systems under various factors such as radiation and temperature variations, changing the load size and partial shaded conditions (PSC), these systems work at the MPP rarely [2, 3]. The output characteristic of the PV cells has multiple maximums when they are under PSC [4]. Therefore, in the operation of photovoltaic cells, an algorithm that guarantees MPP should be used when the operational point changes. Additionally, DC/DC converters are widely used in PV systems as a mediate between PV panel and load, where it is possible to track the MPP. By changing the duty cycle, the load impedance seen by the source is varied and at the MPP it is matched with the source, so the maximum power is transferred. For maximum power extraction, the load has to be matched with the current and voltage of the PV panel. The converter design should be such that it is connected directly to the PV panel and it is expected to follow the MPP.

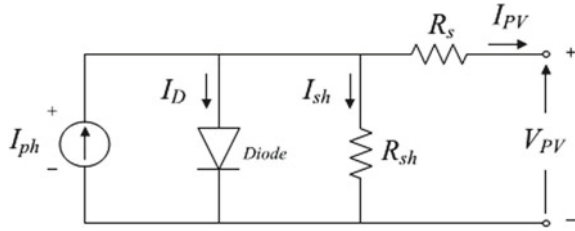
A lot of work has been done to improve the performance of photovoltaic (PV) systems through the development of new algorithms in order to access to maximum power point tracking (MPPT). Perturb and observe method (P&O) [5] and hill-climbing method (H&C) [6] are widely used for MPPT due to this fact that they require a smaller number of sensors, and therefore, their implementation is simple. The incremental conductance (INC) algorithm [7] that compares incremental and momentary conductance of PV can track the MPP of a photovoltaic system and deliver a high photovoltaic energy to the load. Ripple correlation control (RCC) [8] with the help of the converter due to controlling MPPT causes the ripple in the control strategy. This method works very well in a high sunlight, but tracking efficiency decreases in some conditions such as the low radiation. By removing the load of the photovoltaic array, the current and voltage in the MPP of the photovoltaic system can be determined by short-circuit current (SCC) [9] and open-circuit voltage (OCV) methods [10]. However, the implementation simplicity of these algorithms causes that they can be used as parts of a new combination technique. Artificial intelligence (AI) techniques are used as alternative methods instead of the conventional techniques [11]. These techniques have been used to solve complex practical problems in various fields. The fuzzy logic method has also been successfully used to track the maximum general power in photovoltaic systems under PSC. These methods have promising

results, but they have big disadvantages like computational complexity [12]. Due to the disadvantages of conventional MPPT algorithms, several random algorithms, and artificial intelligence methods have been developed. These new MPPT algorithms, inspired by the nature and biology structure, have been developed to maximize the output power arising from the photovoltaic array. These methods are particle swarm optimization (PSO) [13] and genetic algorithm (GA) [14]. PSO and GA optimization methods are easy to calculate and can be easily implemented on a low-cost digital controller. Also, these methods are very successful due to obtaining the global peak under PSC. In [15], gray wolf optimizer (GWO) is developed to solve the MPPT problem considering DC/DC boost converter. The PSO method and its modified version [16] have been used for global MPP (GMPP) tracking considering the buck-boost converter, and suitable results have been obtained. Cuckoo search algorithm (CSA) [17] is used for MPPT in PV systems with a buck converter and under PSC. Also, MPPT by using golden section optimization (GSO) algorithm considering the buck converter is implemented in [18]. In [19], MPPT is done using genetic algorithm (GA) in PV systems, where a boost converter is utilized. Artificial bee colony (ABC) optimization method is used in [20] for improving MPPT in PV system under PSC considering a boost converter. In [21], simulated annealing (SA) algorithm considering DC/DC boost converter, in [22] bat algorithm using buck-boost converter, is applied for MPPT solution of PV modules under partial shading conditions.

In addition, one of the important problems in solving the MPPT problem is utilizing an appropriate DC/DC converter. Since a suitable DC/DC converter plays a crucial role in achieving the maximum power of a given PV system, the impacts of buck, boost, and buck-boost converters on problem solution of PVs MPPT have to be accurately investigated. Hence, although selecting a desired DC/DC converter for implementing MPPT system and the performance evaluation of various types of DC/DC converters are considerably effective on optimal operation of the PV system considering their operational and non-operational regions, they have not yet been clearly studied and compared. Therefore, the performance evaluation of DC/DC converters on problem solution of PVs MPPT is essential. The buck converter may not track the MPP under high temperature (low voltage) and high radiation (high current) since these environmental conditions established the MPP on the non-operational region. Also, the boost converter is not capable of MPP tracking under low temperature (high voltage) and low irradiation (low current). The buck-boost, or any similar static characteristic converters, are able to find the MPP independently on the environmental conditions, thus, this converters family are more appropriate to be employed as MPPT, mainly in a situation which the environmental conditions range widely.

There are many literature works that discuss and compare the performance of each of the MPPT methods. However, the reviews of these researches are not yet updated and do not cover all MPPT methods under uniform radiation conditions and PSC has not been properly evaluated on PVs MPPT in view of convergence speed and efficiency. In this chapter, a new hybrid method as gray wolf optimizer (GWO)-crow search algorithm (CSA) (hGWO-CSA) is proposed for solving the MPPT problem

Fig. 1 Single diode model of a PV cell [13]



in PV energy system. The GWO is presented based on hunting behavior of gray wolves [15] and recently the CSA is presented in [23], and this algorithm is based on the hiding of the crows extra food and call for food hiding place at the needed time. Moreover, the effects of various types of DC/DC converters such as buck, boost, and buck-boost in MPPT problem solution are accurately studied in view of convergence speed, accuracy, and efficiency considering different partial shading conditions. So, to verify the validity of the proposed hGWO-CSA method, the obtained results are compared with the GWO and CSA method. In Sect. 2, modeling of PV energy system is presented, also PV module characteristics are described in Sect. 2, too. The MPPT proposed method is presented in Sect. 3. In Sect. 4, the simulation results are presented and in Sect. 5, the results are concluded.

2 Modeling of PV Energy System

Figure 1 shows the single diode model of a PV cell. Based on Fig. 1, the amount of generated electrical energy by the PV system is represented by current I_{ph} which is proportional to the solar radiation. The series and shunt resistors denote the internal resistance and leakage current, respectively [13].

The mathematical equation of the PV cell is expressed as [13]:

$$I_{PV} = I_{ph} - I_D - \frac{V_D}{R_{Sh}} \quad (1)$$

The characteristics of a diode can be presented as follows [13]:

$$I_D = I_0 [e^{V_D/V_T A} - 1] \quad (2)$$

The voltage of the diode is also written as [13]:

$$V_D = (V_{PV} + I_{PV} R_S) \quad (3)$$

Photocurrent I_{ph} is defined as (4) [13].

Table 1 Data of the single PV cell (KC200GT) [3]

Parameter	Value
Maximum power (W)	200.143 W
Open-circuit rated voltage (V)	32.9 V
The voltage of maximum power point (V)	26.3 V
Short-circuit rated current (A)	8.21 A
Current of maximum power point (A)	7.61 A
Voltage temperature coefficient (V/K)	−0.123
Current temperature coefficient (A/K)	0.0032
Series cells number	54
Parallel cells number	1

$$I_{Ph} = (I_{SC} + K_1(T - T_{Ref}))\lambda$$

(4)

In the above equations, I_0 is the saturation current of the cell, V_T denotes the thermal voltage of the PV modules, which is equal to kT/q . Also, q is the electrical charge (1.6×10^{-19} C), k represents Boltzmann constant (1.38×10^{-23} J/°K), T is the p-n joint temperature in °K, A shows the ideality factors of the diode and depends on the technology of the PV, I_{SC} shows the short-circuit current of the cell under standard test conditions (STC) (1000 W/m^2 at the temperature of $25\text{ }^\circ\text{C}$), K_1 is the short-circuit current coefficient of the cell, T_{ref} is the reference temperature of the cell, and λ is the solar radiation in W/m^2 [13]. In this study, the data of KC200GT PV module [3] under STC (1000 W/m^2 solar radiation and $25\text{ }^\circ\text{C}$ temperature) are listed in Table 1.

In PV systems, the output power depends on the solar radiation and the ambient temperature. These two factors determine the maximum power point (MPP). In general, the temperature affects the output voltage of the PV system, while solar radiation has an impact on the output current. In other words, the more the PV cell is exposed to the solar radiation, the more current is generated at the output, and vice versa.

3 Proposed Method

The employed MPPT system includes PV modules, a DC/DC boost converter, and a load. The system is shown in Fig. 2. The PV voltage and current are calculated, and the PV power is obtained via multiplying the voltage by current and then is applied to the MPPT algorithm. Using the MPPT algorithm, a duty cycle, d is generated, and DC/DC boost converter is activated (the parameters of DC/DC converter is taken [13]). The amount of duty cycle (d) is considered as a decision-making variable in the MPPT algorithm, and its corresponding output power is assumed as the fitness value. Accordingly, the objective of the MPPT algorithm is to determine the optimal

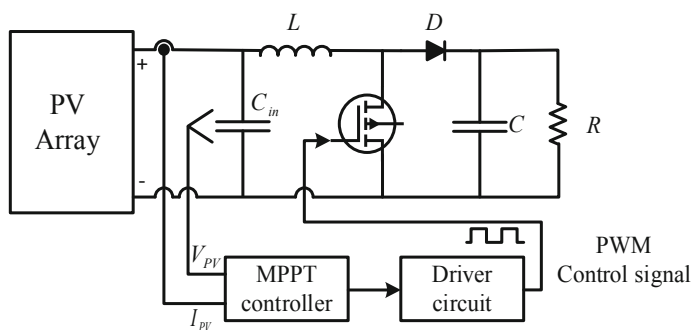


Fig. 2 General block diagram of the MPPT algorithm

duty cycle with the aim of extracting the highest power from the PV system based on the MPPT method.

In this study, the proposed hGWO-CSA method is utilized to solve the MPPT problem considering the boost converter. The hGWO-CSA is implemented based on GWO and CSA combination. In the proposed hybrid method, the advantages of each method are combined that it is a method with high convergence accuracy and speed and is not trapped in local optimal value and quickly achieves to the global optimal solution. In hGWO-CSA method, first, GWO method is used for solving the MPPT problem through which the optimization variable, i.e., the duty cycle of the DC/DC converter is optimally determined. Then, the determined duty cycle by GWO as the initial value is applied to the CSA algorithm, and the CSA is employed to solve the MPPT problem. Each method is described below.

3.1 Gray Wolf Optimizer (GWO) Algorithm

One of the population-based intelligent and evolutionary algorithms is the gray wolf optimizer (GWO) algorithm which was first announced by Mir-Jalali in 2014 [15]. In this algorithm, the performance and behavior of gray wolves for hunting are simulated. The parameters such as α , β , δ , and ω represent the leaders of the group so that α directs the group as the leader and has important decisions about hunting, resting place, and so on. The second group of leadership belongs to β . In addition to being able to help α due to having a good decision, β members are also the best substitutes for the α wolves when they are old or dead. ω but is at the bottom of this group. They are the last wolves that are allowed to eat. The other group members that are not α , β , and ω are called δ . The principles of GWO function are as follows [15]:

- Investigating, pursuing, and following the hunt
- Pursuing, sieging, and harassing the hunt until it stops
- Attacking to the hunt.

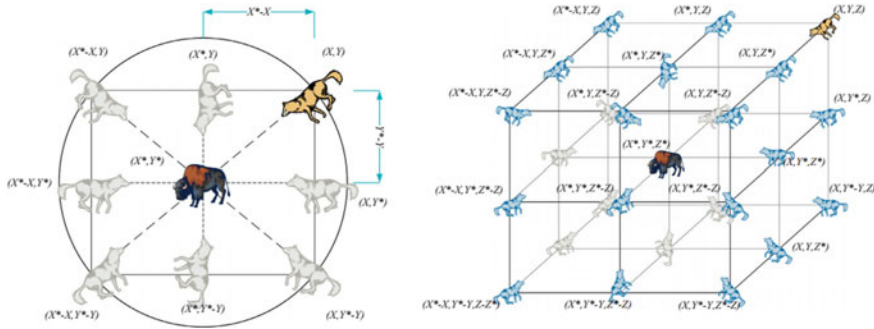


Fig. 3 2D and 3D position vectors and their possible next locations [15]

In the simulation of the GWO, α is considered as a top answer. After that, the next two responses after α are considered β and δ . Finally, the rest answers are regarded ω . Modeling a suitable situation that gray wolves encircle their hunt during hunting are shown as follows:

$$\vec{D} = \left| \vec{C} \cdot \vec{X}_P(t) - \vec{X}_P(t) \right| \quad (5)$$

$$\vec{X}(t+1) = \vec{X}_P(t) - \vec{A} \cdot \vec{D} \quad (6)$$

where t represents the repetition, \vec{A} , \vec{C} , and \vec{X}_P indicate the coefficients vectors, the position of the bait, and the gray wolf, respectively.

The coefficients vector is obtained from the following equation:

$$\vec{A} = 2\vec{a} \cdot \vec{r}_1 - \vec{a} \quad (7)$$

$$\vec{C} = 2\vec{r}_2 \quad (8)$$

where vectors of random numbers at a distance are shown by \vec{r}_1 and \vec{r}_2 that are selected from $[0, 1]$ area and vector \vec{a} decreases from 0 to 2 during repetitions. The 2D and 3D position vectors and their possible next locations in GWO are illustrated in Fig. 3.

To implement the MPPT based on GWO, the duty cycle, D , is defined as a gray wolf. Hence, Eq. (9) can be modified as:

$$D_i(k+1) = D_i(k) - A \cdot D \quad (9)$$

Consequently, the objective function of the GWO algorithm is formulated.

$$P(d_i^k) > P(d_i^{k-1}) \quad (10)$$

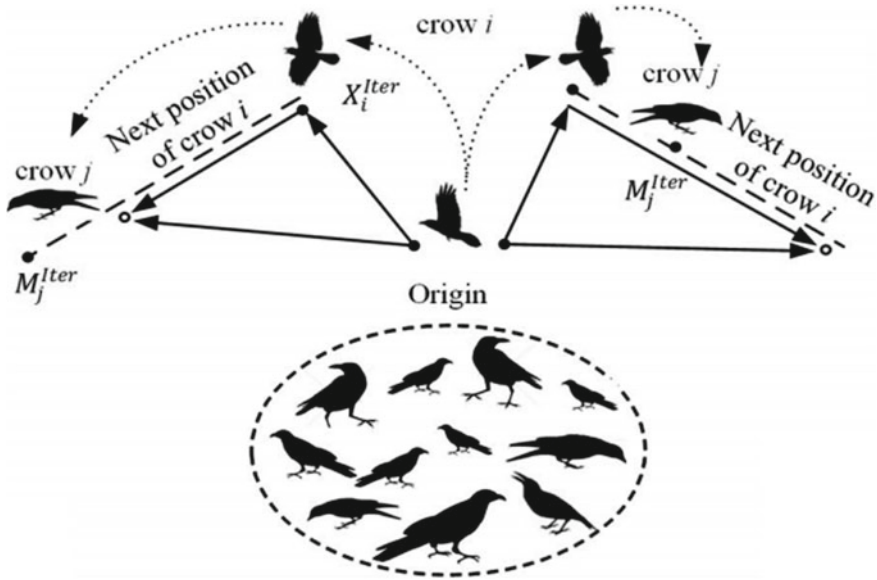


Fig. 4 Structure of CSA [24]

where P shows the power, d is the duty factor, i is the current number of gray wolves, and k is the number of iterations.

3.2 Crow Search Algorithm (CSA)

The novel meta-heuristic crow search algorithm was first introduced by Asgarzadeh (2016) by inspiration from social to smart behavior crows [23]. Meta-heuristic crow search algorithm (CSA) was developed based on smart behavior of crows especially when following and finding food caches of other crows. Principles of this algorithm include the following items [23, 24]:

- Crows live in groups.
- Crows remember positions of their sanctuary.
- Crows track each other to thieve.
- Crows protect their stores against probable thievery.

Structure of CSA is illustrated in Fig. 4. The algorithm procedure is as follows: Similar to other population-based algorithms, it is assumed that there are a number of N crows in the d -dimension search space. Every crow i in the search space is defined by a vector. These vectors are expressed as:

$$x^{i,it} = [x_1^{i,it}, x_2^{i,it}, \dots, x_d^{i,it}] \quad (11)$$

In the above definition: $i = 1, 2, \dots, N$ and $it = 1, 2, \dots, it_{\max}$ where it_{\max} is the maximum number of iterations. Also, every crow has a memory in which it memorizes the best experience of sanctuary position (duty cycle of DC/DC converter). At each iteration, the position of crow i 's sanctuary is presented by $m^{i,it}$. The position is the best place observed by crow i so far and is described by

$$m^{i,it} = [m_1^{i,it}, m_2^{i,it}, \dots, m_d^{i,it}] \quad (12)$$

Crows move in this space and search for better food supplies (sanctuaries). Updating steps for crow positions are performed as below.

Step 1: A crow is randomly selected among the population (a random integer between 1 and N , for example, j). Crow i attempts to track crow j to find its sanctuary (m^j). In this case, according to awareness of crow j about being tracked by crow i , two modes may occur. To simulate these modes, a random number with a uniform distribution between 0 and 1 is generated. If this value is greater than a parameter called awareness probability (AP), then go to Step 2, otherwise go to Step 3.

Step 2: In this mode, crow j is not aware of being tracked by crow i . Therefore, crow i reached crow j 's sanctuary based on the following equation:

$$x^{i,it+1} = x^{i,it} + r_i \times fl \times (m^{i,it} - x^{i,it}) \quad (13)$$

where $x^{i,it+1}$ is crow i 's position at iteration $t + 1$, $x^{i,it}$ is crow i 's position at iteration t , $m^{i,it}$ is memorized position of crow j at iteration t , r_i is a random number with uniform distribution in the range $[0, 1]$, and fl is named flight length.

Small values of fl are results of local search (neighborhood of $x^{i,it}$), and big values are the results of global search (away from $x^{i,it}$). If fl value is chosen less than 1, then the next position of crow i will be along the distance line between $x^{i,it}$ and $m^{i,it}$. If fl value is more than 1, then the next position of crow i is a line that may cross $m^{i,it}$.

Step 3: Crow j knows that crow i is tracking him, so in order to protect his store from crow j with a random movement goes to another place in the environment (search space) and this way crow j is deceived. This is expressed as follows in the summary:

$$x^{i,it+1} = \begin{cases} x^{i,it} + r_i \times fl \times (m^{i,it} - x^{i,it}) & \text{if } r_i \geq AP \\ \text{a random position,} & \text{otherwise} \end{cases} \quad (14)$$

Step 4: After updating the position of crow i , his memory is also updated as:

$$m^{i,it+1} = \begin{cases} x^{i,it+1}, & \text{if } F(x^{i,it+1}) < F(m^{i,it}) \\ m^{i,it}, & \text{otherwise} \end{cases} \quad (15)$$

where $F(\cdot)$ is the value of the objective function (PV power).

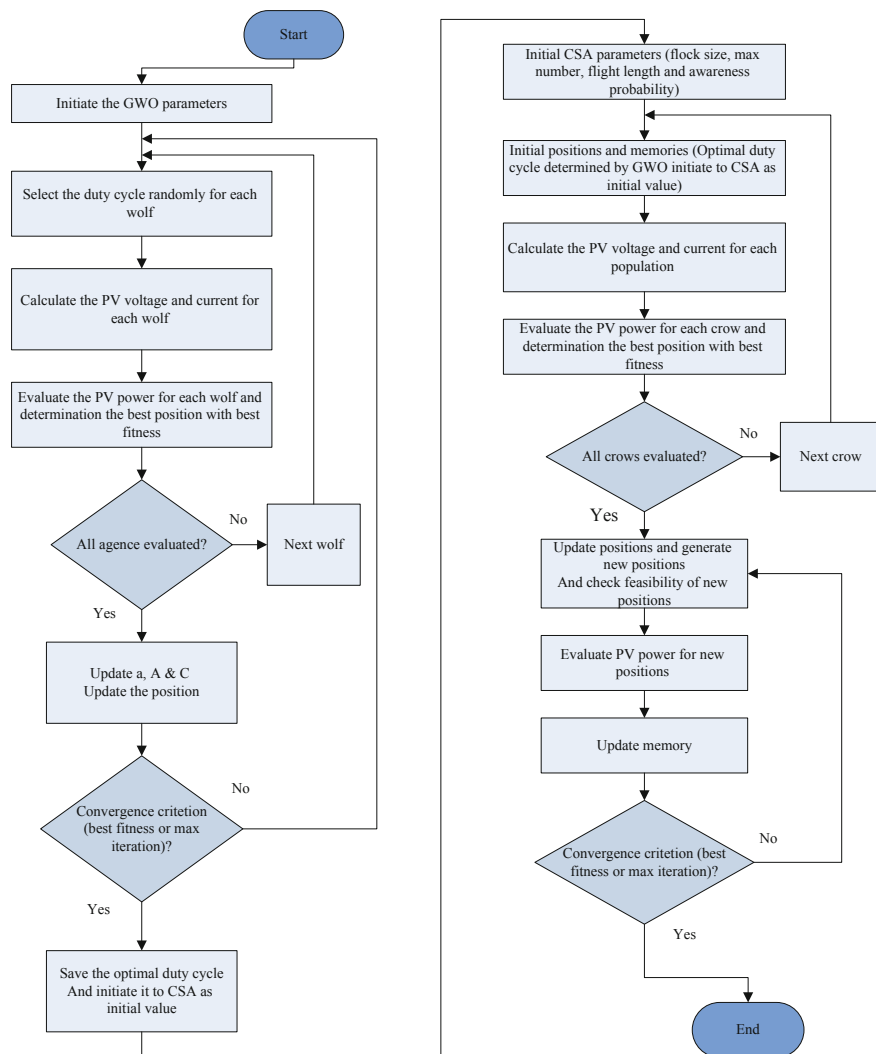


Fig. 5 Flow chart of hybrid proposed algorithm

In CSA, all crows generate new positions and update their memories. These steps continue until the maximum number of iteration it_{max} is reached. Finally, the best solution for memories is selected as the optimized solution by the CSA algorithm.

Flow chart of hybrid proposed algorithm in MPPT solution is illustrated in Fig. 5.

The combined method makes it possible for the presented method to be faster and not optimal locally. GWO's approach to larger scale optimization problems may not be able to achieve rapid convergence and is trapped locally. The proposed method is presented to overcome some of the challenges faced by the optimization method in

terms of increasing problem dimensions and also to achieve faster convergence. The objective is to ensure appropriate coverage of the search space related to the range of optimization variables, as well as to achieve optimal global convergence.

4 Simulation Results

In this section, the MPPT simulation results of the PV system under the standard, different partial shading conditions and also solar and temperature variations using the proposed hGWO-CSA method are presented. Also, to verify the proposed method, the MPPT problem is solved using GWO and CSA methods and the results are compared and analyzed. The simulations are developed in MATLAB/Simulink environment to achieve the GMPP.

4.1 Simulation Results Under STC

In this section, the performance of the proposed method for solving the MPPT problem under STC ($G = 1000 \text{ W/m}^2$, $T = 25 \text{ }^\circ\text{C}$) is described. To assess the capability of the proposed method, the MPPT problem is carried out with both of GWO and CSA methods and then the results are compared. Figure 6 shows the current, voltage, and power of the PV module along with the converter's duty cycle. As seen, the hGWO-CSA method presents lower oscillations and higher convergence speed to reach the GMPP than other methods. One can easily observe that the combination of GWO and CSA lead to the hGWO-CSA method which boosts the performance of each of these methods such that the GMPP is reached at a smaller settling time.

The hGWO-CSA method converges to the MPP, and the voltage and current of the PV module are maintained with no oscillations. The time response of hGWO-CSA for obtaining the steady-state operating point is around 0.01 s, and the corresponding times for GWO and CSA methods are about 0.016 and 0.039 s, respectively. Therefore, the proposed method provides a higher convergence speed. The steady-state value of the PV power for all methods is equal to 198.9 W.

4.2 Simulation Results Under Variable Solar Radiation Conditions

In this section, the effects of solar radiation changes on solving the MPPT problem are evaluated using the proposed method. In this case, the temperature is assumed to be constant equal to $T = 25 \text{ }^\circ\text{C}$. The time step for the solar radiation changes is considered 0.2 s as such that the initial radiation is 400 W/m^2 and it is reached

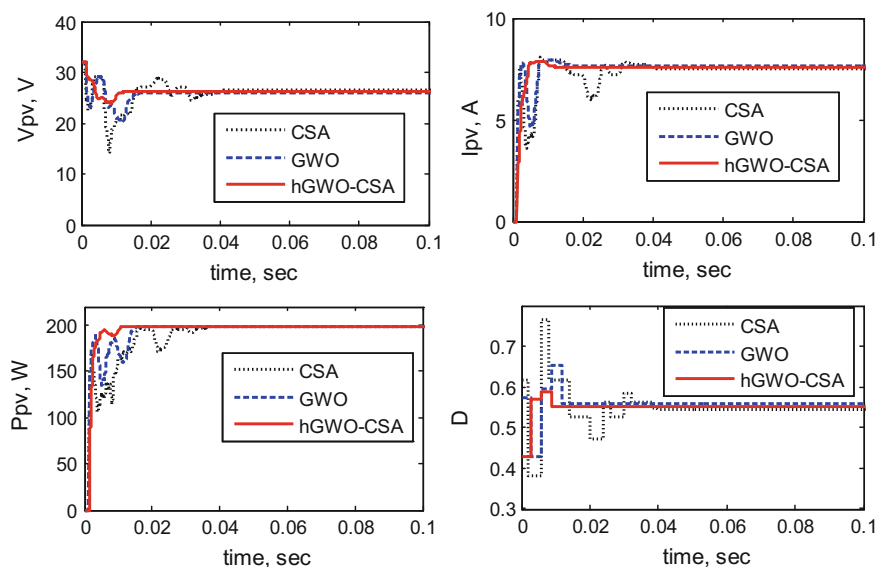


Fig. 6 Tracking curves of the PV module using GWO, CSA, and hGWO-CSA methods under STC

800 W/m² during 0.2–0.4 s, and finally, its value if 1000 W/m² during the time span of 0.4–0.6 s. The obtained results from solving the MPPT problem using different mentioned methods under variable solar radiations are depicted in Fig. 7. According to Fig. 7, the performance of the hGWO-CSA method is significantly superior to other methods in terms of convergence speed and accuracy to reach the maximum power of the PV system, where minor transient oscillations are observed in hGWO-CSA method. In addition, the increase in the radiation reduces the voltage and increases the current of the PV system. As a result, the output power of the PV module is increased. Therefore, the proposed method has better capabilities under variable solar radiations in comparison with other methods.

4.3 Simulation Results Under Variable Temperature Conditions

In this section, the effects of temperature changes on the response of the MPPT problem using the proposed method are investigated. In this case, the solar radiation value is assumed equal to 1000 W/m². The time step for temperature changes is 0.2 s, and the temperature values are selected in a stepwise manner, respectively, equal to 25, 50, and 70 °C. The obtained results from solving the MPPT problem using different methods under variable temperature conditions are shown in Fig. 8. The performance of the hGWO-CSA method compared to other methods is illustrated. Based on the

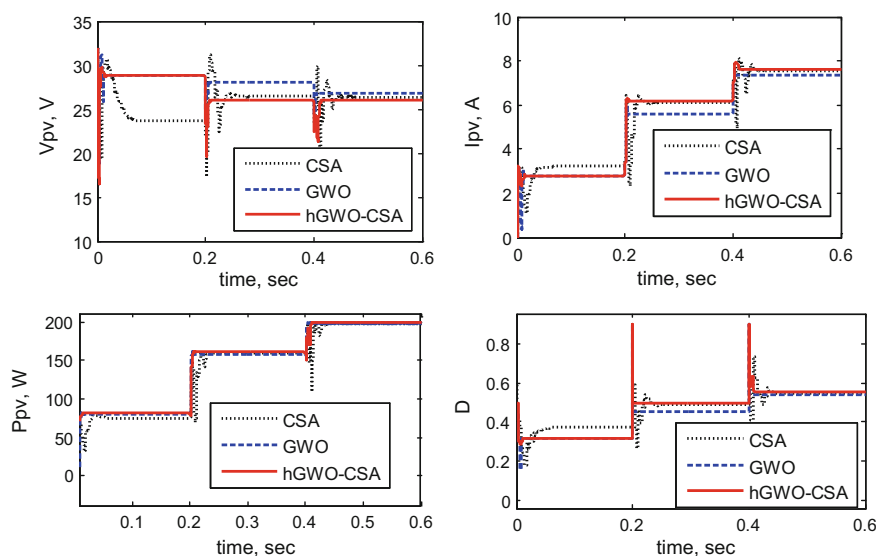


Fig. 7 Tracking curves of the PV module using GWO, CSA, and hGWO-CSA methods under variable solar radiation conditions

results, one can conclude that the increase in the temperature leads to the voltage reduction and as a result output power reduction of the PV module. Additionally, it is observed from the results that the hGWO-CSA method presents lower transient oscillations and higher convergence speed in solving the MPPT problem than other mentioned methods.

4.4 Simulation Results for Shading Pattern 1

In this section, the performance of the proposed method under partial shading conditions (PSCs) is studied. In this case, two PV modules are connected in series to each other. First, the PV modules operate under STC. Next, during 0.2 s, the PSC is applied and the solar radiation for one of the modules is reduced from 1000 to 800 W/m², where under STC and PSC the peak power is 400 W and 340 W, respectively. The simulation results of the PV system using GWO, CSA, and hGWO-CSA methods are shown in Fig. 9. At time $t = 0.2$ s, one of the modules receives solar radiation of 800 W/m², and this causes the PV array to suffer from PSC. In this case, the P–V characteristics curve presents two peak points, and the GMPP is 340 W. The results show that hGWO-CSA algorithm rapidly converges to the desired voltage, and this leads to the MPP of 339.5 W under PSC considering the switching losses.

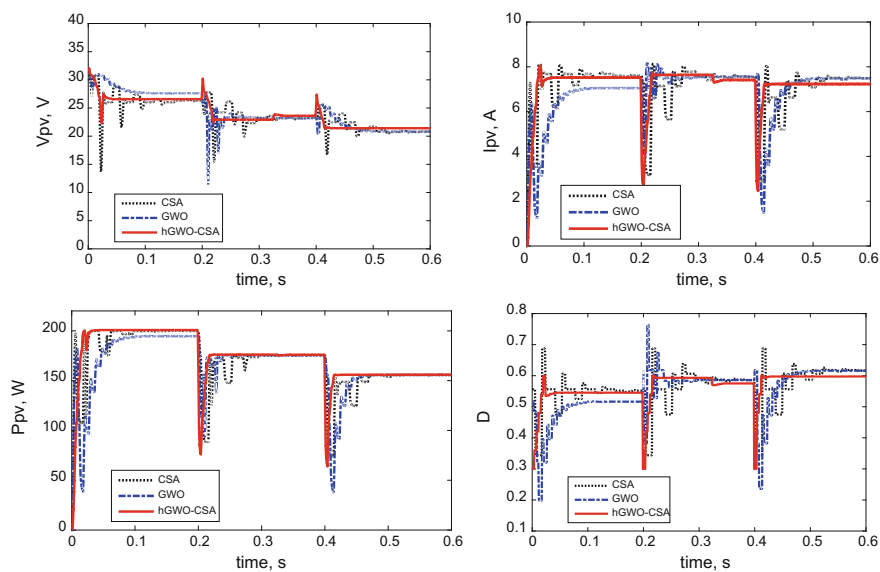


Fig. 8 Tracking curves of the PV module using GWO, CSA, and hGWO-CSA methods under variable temperature conditions

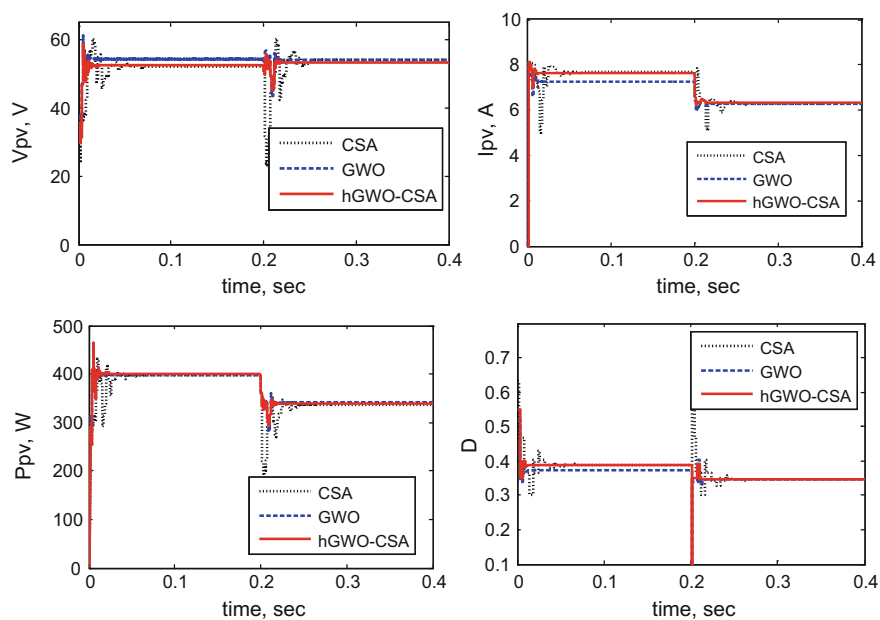


Fig. 9 Tracking curves of the PV module using GWO, CSA, and hGWO-CSA methods under shading pattern 1

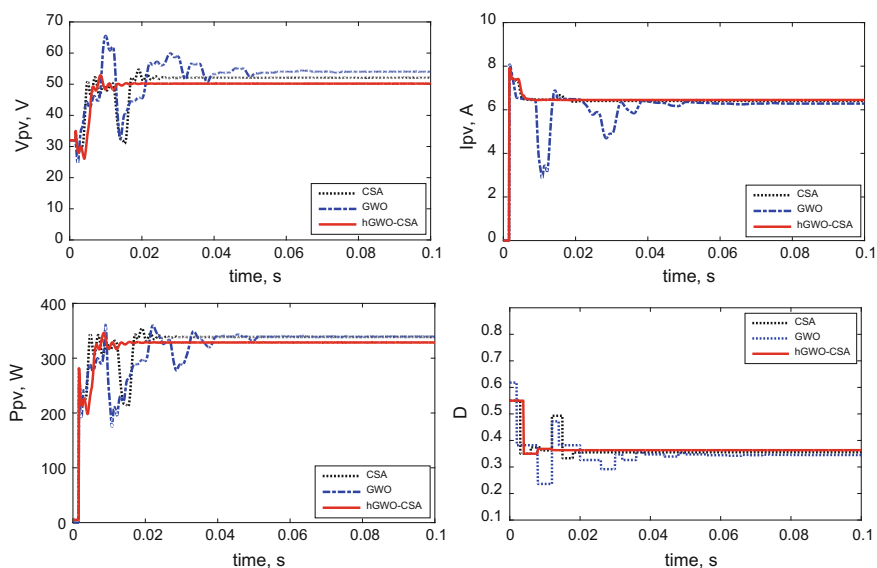


Fig. 10 Tracking curves of the PV module using GWO, CSA, and hGWO-CSA methods under shading pattern 2

Under such conditions, all algorithms have reached the maximum power points. The noticeable difference among these methods is the convergence speed to reach the MPP. The performance of hGWO-CSA method dominates the other methods.

4.5 Simulation Results Under Shading Pattern 2

In this section, two PV modules are connected in series. The shading conditions are considered as follows. One of the PV modules receives solar radiation of 800 W/m^2 and the other one 1000 W/m^2 . The temperature is assumed to be constant equal to 25°C . The obtained results from the simulations for shading pattern 2 are shown in Fig. 10. As seen, the hGWO-CSA-based MPPT is not trapped in the local maximum power point (LMPP) of the P–V curve, but accurately converges to the global MPP (GMPP). As observed from the obtained response, the hGWO-CSA method presents lower power oscillations and rapidly converges to the steady-state condition. In the proposed method, the convergence time is 0.02 s. The corresponding values for GWO and CSA methods are 0.034 s and 0.043 s, respectively. Therefore, similar to other performed simulations, the hGWO-CSA method provides better results compared to GWO and CSA methods under shading pattern 2, and this proves the superiority and efficiency of the proposed method.

4.6 Simulation Results Using Different Converters

The effect of utilizing different DC/DC converters in solving the MPPT problem using hGWO-CSA method and considering shading pattern 2 is studied in this section. In the base mode, the boost converter is considered for simulation. In this section, the performance of the proposed method taking into account the buck and buck-boost converters is also investigated. The power curve of the PV system is shown in Fig. 11. As can be seen, the convergence rate of the MPPT problem equipped with the buck-boost converter is more than the PV system equipped to other converters. Also, the amount of power extracted using the buck-boost converter is more than the

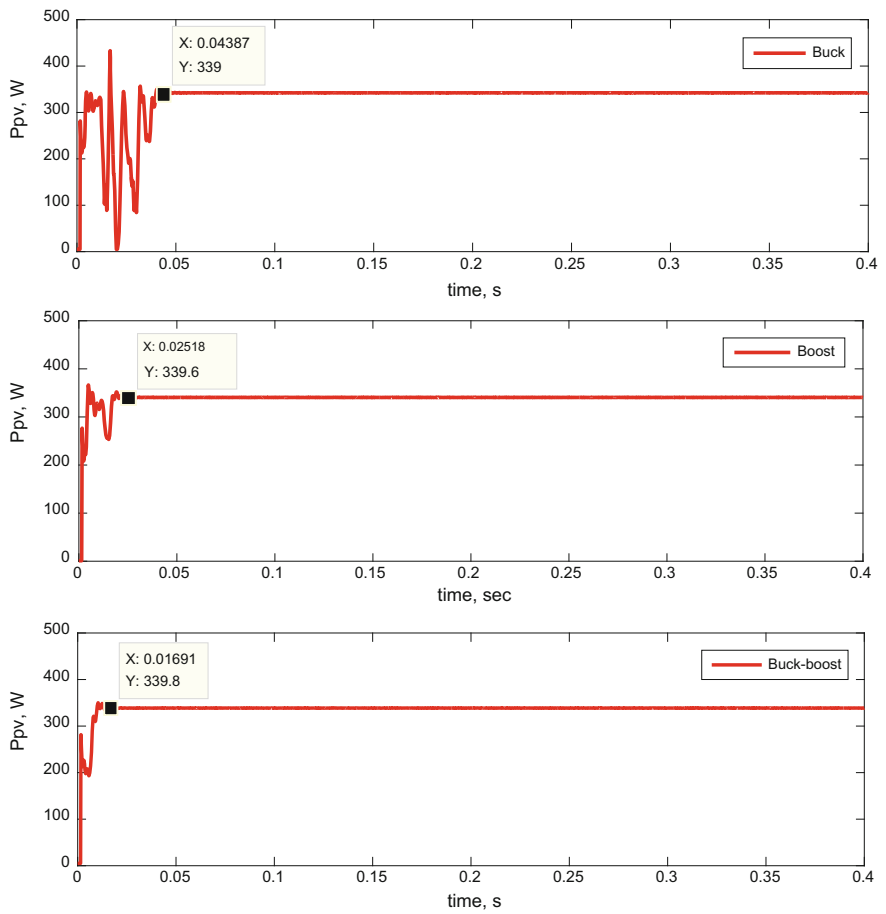


Fig. 11 Tracking curves of the PV module using GWO, CSA, and hGWO-CSA methods under shading condition 2 using different converters

other converters, due to the wider operation range of the buck-boost converter than the other converters.

5 Conclusion

In this chapter, a new method named hybrid gray wolf optimizer-crow search algorithm (hGWO-CSA) is proposed to solve the MPPT problem in PV energy system. In the proposed method, at first the GWO is applied for MPPT solution and then the optimal duty cycle determined by GWO is considered as the initial value to the CSA method. The duty cycle of the converter is considered as the optimization variable, and the output power of the PV system with respect to the determined duty cycle is optimally obtained through the hGWO-CSA method. The superiority of the hGWO-CSA under standard, solar and temperature variations and also in different partial shading patterns is investigated. Also the effects of various types of DC/DC converters are evaluated in MPPT solution. The performance of the hGWO-CSA method is compared with the GWO and CSA method. The obtained results showed that the superiority of the hGWO-CSA in achieving the GMPP with higher convergence speed and less transient oscillations in different conditions and in comparison with GWO and CSA methods. Also, the results showed that the PV system with the buck-boost converter has higher convergence speed and more extracted PV power due to wider operation range than the other DC/DC converters in GMPP finding.

References

1. Subudhi Bidyadhar, Pradhan Raseswari (2013) A comparative study on maximum power point tracking techniques for photovoltaic power systems. *IEEE Trans Sustain Energy* 4(1):89–98
2. Verma D, Nema S, Shandilya AM, Dash SK (2016) Maximum power point tracking (MPPT) techniques: recapitulation in solar photovoltaic systems. *Renew Sustain Energy Rev* 54:1018–1034
3. Kheldoun A, Bradai R, Boukenoui R, Mellit A (2016) A new golden section method-based maximum power point tracking algorithm for photovoltaic systems. *Energy Convers Manag* 111:125–136
4. Liu L, Meng X, Liu C (2016) A review of maximum power point tracking methods of PV power system at uniform and partial shading. *Renew Sustain Energy Rev* 53:1500–1507
5. Elgendy MA, Zahawi B, Atkinson DJ (2012) Assessment of perturb and observe MPPT algorithm implementation techniques for PV pumping applications. *IEEE Trans Sustain Energy* 3(1):21–33
6. Alajmi BN, Ahmed KH, Finney SJ, Williams BW (2011) Fuzzy-logic-control approach of a modified hill-climbing method for maximum power point in microgrid standalone photovoltaic system. *IEEE Trans Power Electron* 26(4):1022–1030
7. Elgendy MA, Zahawi B, Atkinson DJ (2013) Assessment of the incremental conductance maximum power point tracking algorithm. *IEEE Trans Sustain Energy* 4(1):108–117
8. Casadei D, Grandi G, Rossi C (2006) Single-phase single-stage photovoltaic generation system based on a ripple correlation control maximum power point tracking. *IEEE Trans Energy Convers* 21(2):562–568

9. Husain MA, Tariq A, Hameed S, Arif MSB, Jain A (2017) Comparative assessment of maximum power point tracking procedures for photovoltaic systems. *Green Energy Environ* 2(1):5–17
10. Montecucco A, Knox AR (2015) Maximum power point tracking converter based on the open-circuit voltage method for thermoelectric generators. *IEEE Trans Power Electron* 30(2):828–839
11. Punitha K, Devaraj D, Sakthivel S (2013) Artificial neural network based modified incremental conductance algorithm for maximum power point tracking in photovoltaic system under partial shading conditions. *Energy* 62:330–340
12. Algazar MM, El-Halim HA, Salem MEEK (2012) Maximum power point tracking using fuzzy logic control. *Int J Electr Power Energy Syst* 39(1):21–28
13. Sundareswaran K, Palani S (2015) Application of a combined particle swarm optimization and perturb and observe method for MPPT in PV systems under partial shading conditions. *Renew Energy* 75:308–317
14. Daraban S, Petreus D, Morel C (2014) A novel MPPT (maximum power point tracking) algorithm based on a modified genetic algorithm specialized on tracking the global maximum power point in photovoltaic systems affected by partial shading. *Energy* 74:374–388
15. Mohanty S, Subudhi B, Ray PK (2016) A new MPPT design using grey wolf optimization technique for photovoltaic system under partial shading conditions. *IEEE Trans Sustain Energy* 7(1):181–188
16. Ishaque K, Salam Z, Amjad M, Mekhilef S (2012) An improved particle swarm optimization (PSO)-based MPPT for PV with reduced steady-state oscillation. *IEEE Trans Power Electron* 27(8):3627–3638
17. Ahmed J, Salam Z (2013, May) A soft computing MPPT for PV system based on Cuckoo Search algorithm. In: 2013 fourth international conference on power engineering, energy and electrical drives (POWERENG). IEEE, pp 558–562
18. Kheldoun A, Bradai R, Boukenoui R, Mellit A (2016) A new golden section method-based maximum power point tracking algorithm for photovoltaic systems. *Energy Convers Manag* 111:125–136
19. Harrag A, Messalti S (2015) Variable step size modified P&O MPPT algorithm using GA-based hybrid offline/online PID controller. *Renew Sustain Energy Rev* 49:1247–1260
20. Soufyane Benyoucef A, Chouder A, Kara K, Silvestre S (2015) Artificial bee colony based algorithm for maximum power point tracking (MPPT) for PV systems operating under partial shaded conditions. *Appl Soft Comput* 32:38–48
21. Lyden S, Haque ME (2016) A simulated annealing global maximum power point tracking approach for PV modules under partial shading conditions. *IEEE Trans Power Electron* 31(6):4171–4181
22. Kaced K, Larbes C, Ramzan N, Bounabi M, Elabadine Dahmane Z (2017) Bat algorithm based maximum power point tracking for photovoltaic system under partial shading conditions. *Sol Energy* 158:490–503
23. Askarzadeh A (2016) A novel metaheuristic method for solving constrained engineering optimization problems: crow search algorithm. *Comput Struct* 169:1–12
24. Papari B, Edrington CS, Vu TV, Diaz-Franco F (2017, June). A heuristic method for optimal energy management of DC microgrid. In: 2017 IEEE second international conference on DC microgrids (ICDCM). IEEE, pp 337–343

Dynamic Modeling Analysis of Direct-Coupled Photovoltaic Power Systems



Ahmed A. S. Mohamed

Abstract Photovoltaic (PV) cells utilization is getting more attention due to the depletion of the world's natural resources and the increased progress in power electronics and semiconductor technologies. The first step to analyze and study a PV power system is to develop a model that is capable of providing an accurate prediction for the system's performance at different operating conditions. The availability of precise models for PV systems in hand allows the designers, operators, and researchers to predict, optimize, and evaluate the behavior of the system under different dynamics amid the development, which is very helpful for design and control purpose. Additionally, these models help to investigate the interaction between the PV system and other connected networks. Therefore, this chapter presents a general mathematical dynamic modeling technique for direct-coupled PV power systems. The nonlinear mathematical formulas for each component in the system are derived, and the connection among the different components is addressed. The modeling approach is applied to two different direct-coupled PV systems: grid-connected and stand-alone system. The accuracy of the developed models was verified based on the simulation and experimental data. The results demonstrate the ability of the proposed models for predicting the system performance under different environmental and operating conditions.

1 Introduction

Growing concerns for the depletion of the world's natural resources and our future energy supply has increased the need and development of solar power. The most critical advancement in the development of solar technology has been the photo-

A. A. S. Mohamed (✉)

Transportation and Hydrogen Systems Center, National Renewable Energy Laboratory (NREL), Golden, CO, USA

e-mail: Ahmed.Mohamed@nrel.gov

Electrical Power and Machines Department, Faculty of Engineering, Zagazig University, Zagazig, Egypt

© Springer Nature Switzerland AG 2020

A. M. Eltamaly and A. Y. Abdelaziz (eds.), *Modern Maximum Power Point Tracking Techniques for Photovoltaic Energy Systems*, Green Energy and Technology, https://doi.org/10.1007/978-3-030-05578-3_17

439

voltaics (PV). PV power system is a solar energy system that uses semiconductors to directly convert solar radiation into electricity. PV systems are composed of a large number of cells arranged in the formation on a metal frame, which is known as a PV module. When exposed to sunlight, these cells produce a small direct current of electricity, and when used in masse will generate a large amount of electrical power with no moving parts, noise, or emissions [1]. The amount of electricity generated is dependent on several factors, such as the size and arrangement of the PV system, the PV module array, and the efficiency of the electrical components used to convert solar energy into electricity. In general, the PV systems can be categorized based on the connectivity with the power grid, into a grid-connected (utility interactive) or stand-alone (off-grid) system [2]. For each category, the system can be coupled with the load or the grid either directly or indirectly. The indirect-coupled PV system, the DC energy from the PV generator, is regulated and converted to AC to either supply AC loads or feed an AC bus. In direct-coupled PV systems, which are the main focus of this chapter, the PV generator is connected to a DC component (either a load in stand-alone systems or a common bus in grid-connected systems) through a DC–DC converter. Direct-coupled grid-connected PV configurations are commonly used in the DC microgrids structure, in which all the resources and loads are integrated through a common DC bus [3], as indicated in Fig. 1. In this case, the PV system is operating in unidirectional mode to generate the maximum amount of energy and through it in the common bus. The direct-coupled stand-alone PV structures appear in situations, in which the supplied loads are DC, such as DC motors in solar pumping applications [4]. The direct-coupled PV configurations contain a DC–DC converter that is responsible for regulating the array voltage to the appropriate level of the DC element. Additionally, the same converter is in charge of extracting the maximum power from the PV panel regardless of the environmental and load conditions to provide maximum power point tracking (MPPT) capability. The derivation of the dynamic models for the PV panel, DC–DC converter with MPPT and DC element are presented in this work in detail. The dynamic models are utilized to simulate and predict the entire PV systems' performance under different dynamics, such as variation in the weather conditions. Furthermore, they are used to evaluate the tracking performance of the MPPT under different irradiance and temperature conditions. Then, the developed dynamic models are linearized to state the small-signal models for both the grid-connected and stand-alone PV systems. These small-signal models are utilized to predict the effect of the small variation in the solar irradiance, cell temperature, and the duty cycle of the DC–DC converter due to the control and MPPT actions, and to state design criteria for MPPT algorithm's parameters. The developed dynamic and small-signal models are implemented in MATLAB environment and verified by means of the simulation and experimental data.

2 Direct-Coupled Grid-Connected PV Power System

Considering the DC microgrid configuration in Fig. 1, the PV power system under study consists of a PV array connected to a DC bus through a unidirectional DC–DC converter, as shown in Fig. 2. The DC–DC converter is chosen to be a Cuk type to allow both step-up and step-down voltage capability. Additionally, it has a capacitive isolation capability, which protects against switch failure. Moreover, the input current of the Cuk converter is continuous and almost ripple-free output current, which is important for efficient system operation.

The DC bus is coupled to the power grid through a bidirectional three-phase grid-tie converter. This converter is taking charge of managing the power flow between

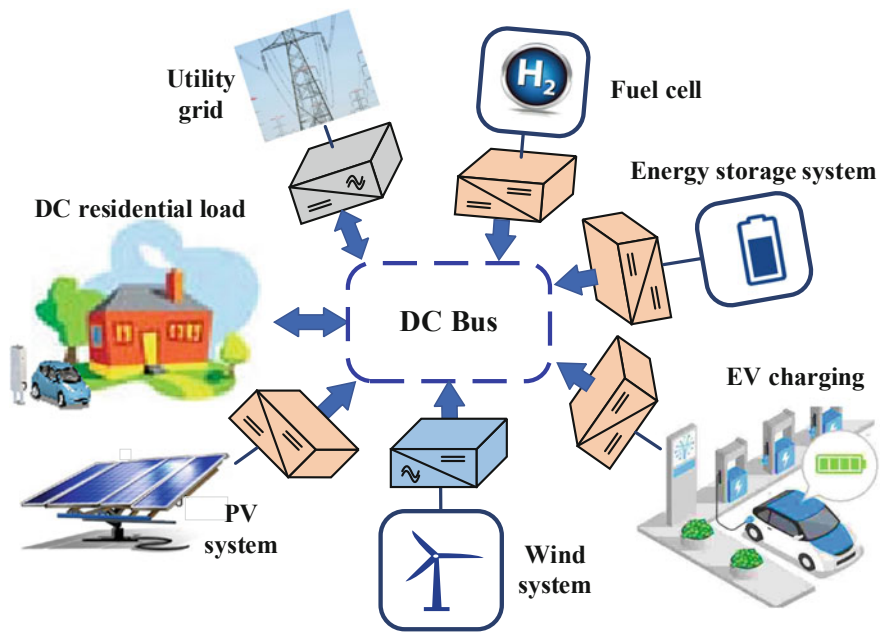
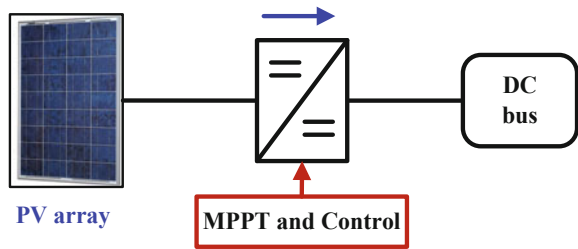


Fig. 1 Block diagram of a DC microgrid configuration

Fig. 2 Block diagram of direct-coupled grid-connected PV power system



the DC microgrid and the utility grid, in addition to regulating the DC bus voltage to a certain level.

3 Nonlinear Dynamic Model of Grid-Connected PV Power System

The details of the nonlinear dynamic equations for the direct-coupled grid-connected PV power system are presented in this section. The model formulas are derived based on the electric circuit model of each component in the system. The individual equivalent circuits are lumped together in one circuit that represents the entire PV power system, as shown in Fig. 3. The system contains a PV array, DC–DC Cuk converter, and DC bus. The PV panel is represented by the single-diode (four parameters) model equivalent circuit. The Cuk converter is modeled by its ideal passive components with neglecting the resistive losses. Since the DC bus voltage is kept fixed by the grid-tie converter, the DC bus is denoted in the model by a fixed DC source (V_{dc}) with a series resistance (R_{dc}) that emulates its resistive losses. The details for the dynamic equations of each component are presented in the following sections.

3.1 PV Panel Dynamic Model

Two advanced equivalent circuit PV models are proposed in the literature: single-diode and double-diode model. The double-diode model features high accuracy since it considers the carriers' recombination. The first diode accounts for carriers diffusing across the P–N junction and recombining in the bulk or at surfaces. The second diode is sometimes attributed to carrier recombination by traps within the depletion region or recombination at an un-passivated cell edge. This model is rarely used due to its complexity, high computational cost, and inability to be parameterized based solely on data sheet information [5]. Single-diode model is the most commonly used in PV systems' studies, because it offers a reasonable

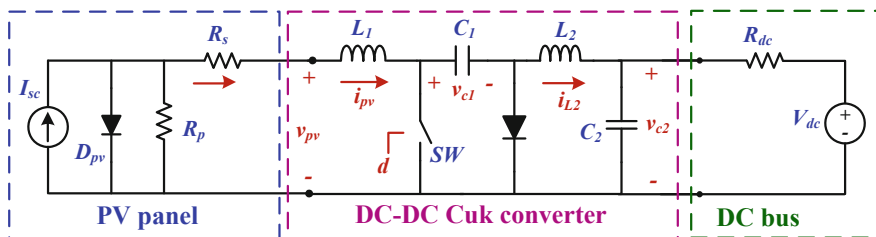


Fig. 3 Equivalent circuit of the direct-coupled grid-connected PV power system under consideration

trade-off between simplicity and accuracy. Also, it has the possibility to be parameterized based on the provided information in the manufacture's datasheet [6]. A comparative analysis between the performances of the single- and double-diode models has been conducted in [7]. The single-diode model shows an average absolute error = 0.0085 and root-mean-square (RMS) error = 1.67%. By using the two-diode model, it introduced some singular solutions. After solving the issue by adding more complexity to the analysis, it gave an average absolute error = 0.0080 and RMS error = 1.35%. Both the errors are slightly reduced compared with the one-diode model results. Also, the study showed that the reverse saturation current of the second diode is indeed extremely close to zero, whereas other parameters are comparable to their counterparts in the one-diode model. It was concluded that the one-diode model is good enough to represent the whole I - V characteristic accurately. Therefore, in this work, the PV panel is modeled based on the single-diode equivalent circuit model, as shown in Fig. 3 and its I - V characteristic is presented in Eq. (1).

$$i_{pv} = I_{sc} - I_r \left(e^{\frac{v_{pv} + i_{pv} R_s}{n V_T}} - 1 \right) - \left(\frac{v_{pv} + i_{pv} R_s}{R_p} \right); V_T = \frac{kT}{q} \quad (1)$$

where i_{pv} and v_{pv} are the PV output current and voltage, respectively, I_{sc} is the photon (short circuit) current, q is the charge of electron (C), k is Boltzmann constant ($\text{kg m}^2/\text{s}^2\text{K}$), T is cell temperature (K), n is the diode ideality factor, R_s is the series resistance, R_p is the parallel resistance, and I_r is reverse saturation current.

The series resistance (R_s) stands for the lumped resistive losses in the current path through the semiconductor material, the metal grid, contacts, and current collecting bus. The parallel resistance (R_p) represents the losses associated with a small leakage of current through a resistive path in parallel with the intrinsic device. These are due to crystal damage and impurities in and near the junction. Considering R_p allows the model to provide a logic behavior under the impact of shading on a string of cells connected in series. The effect of R_p on the PV array performance is less conspicuous compared to the series resistance, but it will become noticeable when a large number of PV modules are connected in parallel for a larger system. The recombination in the depletion region of PV cells provides non-ohmic current paths in parallel with the intrinsic PV cell. This is represented by a single diode with unknown diode ideality factor (n) [8]. This factor (n) ranges from 1 to 2, where 1 ideality factor means ideal diode behavior.

For the purposes of performing small-signal analysis, it is easier to express the PV panel output voltage in terms of its current. By rearranging Eq. (1), a second formula for the PV panel I - V characteristic is obtained, as indicated in Eq. (2).

$$v_{pv} = n V_T \ln \left[\frac{I_r + I_{sc} - i_{pv} - \left(\frac{v_{pv} + i_{pv} R_s}{R_p} \right)}{I_r} \right] - i_{pv} R_s \quad (2)$$

By applying the open-circuit conditions on the PV panel ($v_{pv} = V_{oc}$ and $i_{pv} = 0$), an expression for reverse saturation current in terms of the panel parameters can be obtained, as in Eq. (3).

$$I_r = \frac{(R_p I_{sc} + V_{oc})}{\left[R_p \left(e^{\frac{V_{oc}}{nV_T}} - 1 \right) \right]} \quad (3)$$

where V_{oc} is the open-circuit voltage of the PV module.

By inserting Eq. (3) into Eq. (2), a third accurate formula for the I–V characteristic of PV panel is given in Eq. (4).

$$v_{pv} = nV_T \ln \left[1 + \left(e^{\frac{V_{oc}}{nV_T}} - 1 \right) \left(\frac{R_p (I_{sc} - i_{pv}) + i_{pv} R_s + v_{pv}}{R_p I_{sc} - V_{oc}} \right) \right] - i_{pv} R_s \quad (4)$$

This equation can be simplified under the assumption of $\left(e^{\frac{-V_{oc}}{nV_T}} \ll 1 \right)$, as given in Eq. (5).

$$v_{pv} = V_{oc} + nV_T \ln \left[\frac{R_p I_{sc} - i_{pv} (R_p - R_s) + v_{pv}}{R_p I_{sc} - V_{oc}} \right] - i_{pv} R_s \quad (5)$$

3.2 DC–DC Converter with DC Bus Model

DC–DC Cuk converter is selected in this work to boost up the PV panel voltage to the DC link voltage level. Additionally, it is controlled to track the maximum power of the PV panel regardless of the irradiance and temperature variation. The circuit diagram of Cuk converter is shown in Fig. 3. It consists of an input inductor (L_1) and capacitor (C_1), power electronic switch (SW) [metal–oxide–semiconductor field-effect transistor (MOSFET) or insulated-gate bipolar transistor (IGBT)], which is controlled by the duty cycle (d), power semiconductor diode (D_c), and output filter capacitor (C_2), and inductor (L_2) to smooth the output voltage and current. Under the assumption that the inductor current is always positive, when the switch SW is ON, the diode is OFF and the capacitor C_1 is discharged by the inductor L_2 current. When the switch is OFF, the diode conducts the current of the inductors L_1 and L_2 whereas capacitor C_1 is charged by the inductor L_1 current. The Cuk converter offers several advantages, such as providing capacitive isolation, which protects against switch failure, continuous input current, and almost ripple-free output current, which is important for efficient systems. The passive components (L_1 , L_2 , C_1 , and C_2) are designed based on the switching frequency, and the output voltage and current ripple [8].

Following the state-space representation theory, the dynamic performance of the Cuk converter and DC bus is represented by four nonlinear ordinary differential equa-

tions (ODEs) that describe the inductors' current ($i_{L1} = i_{pv}$ and i_{L2}) and capacitors' voltage (v_{C1} and v_{C2}). The final set of nonlinear ODEs are stated in Eq. (6).

$$\begin{aligned} p i_{pv} &= \frac{1}{L_1} [v_{pv} - (1 - d)v_{C1}] \\ p v_{C1} &= \frac{1}{C_1} [d i_{L2} + (1 - d)i_{pv}] \\ p i_{L2} &= \frac{1}{L_2} (-d v_{C1} - v_{C2}) \\ p v_{C2} &= \frac{1}{C_2} \left(i_{L2} - \frac{v_{C2}}{R_{dc}} + \frac{V_{dc}}{R_{dc}} \right) \end{aligned} \quad (6)$$

where the symbol p represents the differential operator ($\frac{d}{dt}$).

Equations (4) and (6) represent the nonlinear state-space dynamic model for the entire direct-coupled grid-connected PV power system. These equations are implemented and analyzed in MATLAB environment to simulate the PV system performance. Equation (6) is solved by means of the numerical integration technique (Runge–Kutta) and Eq. (4) is solved by the iterative technique (Newton–Raphson).

4 Small-Signal Analysis of Grid-Connected PV Power System

For proper converter control system design, it is necessary to model the system dynamic behavior. In particular, it is required to determine how the variations in the converter duty cycle affect the PV power and voltage. Unfortunately, understanding converter dynamic behavior is hampered by the nonlinear time-varying nature of the switching and pulse-width modulation process. These difficulties can be overcome through the use of waveform averaging and small-signal modeling techniques [9]. The dynamic model that is presented in the previous section is linearized to state the small-signal model for the PV power system.

4.1 PV Panel Small-Signal Model

The main function of MPPT in a PV system is to keep the PV panel working at the maximum power point (MPP) regardless of the irradiance level and temperature. Therefore, in the PV systems that contain MPPT, it is fair enough to assume that the system is always generating the maximum power and the operating point matches the MPP [10, 11]. When the PV panel is operating at MPP, the variation of the operating point around the MPP due to the fast control action (5–20 kHz) can be linearized using the small-signal analysis. This analysis can be performed by assuming small

variations in the different dynamics that the PV panel is usually subjected to. The disturbance in PV panel output is mainly due to the variation of temperature, radiation, and load conditions. Thus, the small variation in the PV output voltage (\hat{v}_{pv}) will be affected by the small variation in PV current (\hat{i}_{pv}), radiation level (\hat{g}), and cell temperature (\hat{t}) [12]. If these conditions slightly change around the operating point, it can be written as:

$$\begin{aligned} G &= G_Q + \hat{g} \\ T &= T_Q + \hat{t} \\ i_{pv} &= I_{pv_Q} + \hat{i}_{pv} \end{aligned}$$

where G , T , and i_{pv} are the dynamic irradiance level, temperature, and PV current, respectively, G_Q , T_Q and I_{pv_Q} are the average of these variables at the quiescent point (Q), and \hat{g} , \hat{t} and \hat{i}_{pv} are their small variations. Thus, the small-signal representation of the PV voltage at any operating point (e.g. MPP) is described in Eq. (7).

$$\hat{v}_{pv} = K_{iv}\hat{i}_{pv} + K_{gv}\hat{g} + K_{tv}\hat{t} \quad (7)$$

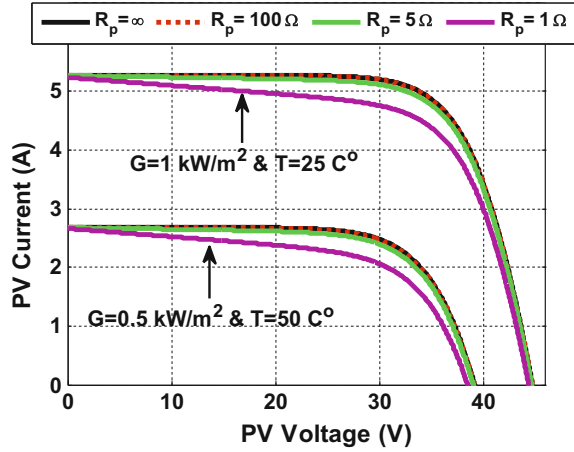
where K_{iv} is the variation of the PV voltage with respect to the variation of PV current, which represents the slope of I–V characteristic at the operating point; K_{gv} is the variation of the PV voltage with respect to the variation of the irradiance level; and K_{tv} is the variation of the PV voltage with respect to the variation of the cell temperature.

These small-signal coefficients (K_{iv} , K_{gv} , and K_{tv}) can be evaluated using an explicit PV voltage equation as a function of current, radiation, and temperature. Small approximation needs to be applied to Eq. (5) to put it in an explicit form. This form can be obtained by neglecting the shunt resistance effect in Eq. (5) by assuming very large resistance ($R_p \approx \infty$). In [13], the effect of R_p on the MPPT control performance is studied for a certain PV module. It shows that at high values of R_p ($\geq 601.34 \Omega$), its effect is negligible. Based on this study, we conduct a study for the effect of R_p on the I–V characteristics of the used PV module (BP 4175T PV array) in this work at different climatic conditions, as depicted in Fig. 4. It can be noticed that for high values of R_p ($\geq 100 \Omega$) its impact on the slope at MPP is negligible, even at different climatic conditions. Therefore, its effect on the small-signal analysis will be unnoticeable. The estimated R_p for the used PV module in this work is 2.8 k Ω , as will be demonstrated later, which is much larger than 100 Ω [13].

By applying this approximation on Eq. (5), an explicit PV model that is appropriate for the small-signal analysis is obtained in Eq. (8).

$$v_{pv} = V_{oc} + nV_T \ln \left[1 - \frac{i_{pv}}{I_{sc}} \right] - i_{pv}R_s \quad (8)$$

Fig. 4 Effect of R_p on I–V characteristics of PV module at different climatic conditions



where V_{oc} , I_{sc} , and V_T are function of the cell temperature and irradiance level as described in Eqs. (9), (10), and (11), respectively.

$$V_{oc}(T, G) = V_{oc0} [1 + \beta(T - T_0)] + V_{T0} \ln\left(\frac{G}{G_0}\right) \quad (9)$$

$$I_{sc}(T, G) = I_{sc0} \left(\frac{G}{G_0}\right) [1 + \alpha(T - T_0)] \quad (10)$$

$$V_T(T) = V_{T0} \left(\frac{T}{T_0}\right) \quad (11)$$

By differentiating Eq. (8) with respect to the PV current, an expression for the coefficient K_{iv} at the Q-point is obtained in Eq. (12).

$$K_{ivQ} = \left. \frac{dv_{pv}}{di_{pv}} \right|_Q = - \frac{nV_{TQ} \left(1 - e^{-\frac{V_{ocQ}}{nV_{TQ}}}\right)}{\left[I_{scQ} - I_{pvQ} \left(1 - e^{-\frac{V_{ocQ}}{nV_{TQ}}}\right) \right]} \quad (12)$$

where the subscript (Q) denotes the variables at the operating point (Q-point).

For the radiation coefficient K_{gv} , Eq. (8) is differentiated with respect to the radiation level (G), as given in Eq. (13).

$$K_{gvQ} = \left. \frac{dv_{pv}}{dG} \right|_Q = \left. \frac{dv_{oc}}{dG} \right|_Q + nV_{TQ} \left. \frac{d}{dG} \left[\ln \left(1 - \frac{i_{pv}}{I_{sc}} \right) \right] \right|_Q - R_s \cdot \left. \frac{di_{pv}}{dG} \right|_Q \quad (13)$$

Using Eqs. (9), (10), and (11), with the assumption of, $\left. \frac{dv_{pv}}{dG} \right|_Q \approx \left. \frac{di_{sc}}{dG} \right|_Q$ at MPP, the final formula for the radiation coefficient at Q-point is given in Eq. (14). Similarly, the temperature coefficient at Q-point, K_{tv} , is presented in Eq. (15).

$$K_{gv_Q} = \left. \frac{dv_{pv}}{dG} \right|_Q = \frac{V_{T_o}}{G_Q} - \left(\frac{I_{sc_o}}{G_o} \right) \left[1 + \alpha(T_Q - T_o) \right] \left(\frac{nV_{T_Q}}{I_{sc_Q}} - R_s \right) \quad (14)$$

$$K_{tv_Q} = \left. \frac{dv_{pv}}{dT} \right|_Q = \beta V_{oc_o} - \left(\frac{\alpha G_Q I_{sc_o}}{G_o} \right) \left(R_s + \frac{nV_{T_Q}}{I_{sc_Q}} \right) + \frac{nk}{q} \ln \left(1 - \frac{I_{pv_Q}}{I_{sc_Q}} \right) \quad (15)$$

where the subscript (*o*) distinguishes the variables at standard test conditions (STC), which are available in the PV module manufacture's datasheet.

4.2 DC–DC Converter and DC Bus Small-Signal Model

The DC–DC converter and DC bus are modeled based on the state-space averaging technique in [14]. Each variable in Eq. (6) is replaced by the superposition of the average value and the variations; $f = F_Q + \hat{f}$ where $f = \{i_{pv}, v_{pv}, v_{C1}, i_{L2}, v_{C2}, D\}$ F_Q is the average value of the variable f at the Q-point and \hat{f} is the variation of f around the Q-point. For example, $i_{pv} = I_{pv_Q} + \hat{i}_{pv}$. In this analysis, the DC components and the second-order small variation terms are neglected. Thus, final small-signal representation of the DC–DC Cuk converter with the DC bus is given in Eq. (16).

$$\begin{aligned} p\hat{i}_{pv} &= \frac{1}{L_1} \left[\hat{v}_{pv} - (D_Q - 1)\hat{v}_{C1} + V_{C1_Q}\hat{d} \right] \\ p\hat{v}_{C1} &= \frac{1}{C_1} \left[D_Q\hat{i}_{L2} + (1 - D_Q)\hat{i}_{pv} + (I_{L2_Q} - I_{pv_Q})\hat{d} \right] \\ p\hat{i}_{L2} &= \frac{1}{L_2} \left(-D_Q\hat{v}_{C1} - \hat{v}_{C2} - V_{C1_Q}\hat{d} \right) \\ p\hat{v}_{C2} &= \frac{1}{C_2} \left(\hat{i}_{L2} - \frac{\hat{v}_{C2}}{R_{dc}} \right) \end{aligned} \quad (16)$$

By mixing the PV array in Eqs. (7), (12), (14), and (15), with the Cuk converter and the DC bus models in Eq. (16), the final small-signal model for grid-connected PV system is obtained. Based on these equations, the state-space representation for the system is given Eq. (17).

$$\dot{\mathbf{x}} = \mathbf{A} \mathbf{x} + \mathbf{B} \mathbf{u}; \quad \mathbf{y} = \mathbf{C} \mathbf{x} + \mathbf{D} \mathbf{u} \quad (17)$$

where $\mathbf{x} = [\hat{i}_{pv} \ \hat{v}_{C1} \ \hat{i}_{L2} \ \hat{v}_{C2}]^T$; $\mathbf{u} = [\hat{d} \ \hat{g} \ \hat{t}]^T$; and $\mathbf{y} = [\hat{i}_{pv} \ \hat{v}_{pv}]^T$.

$$\mathbf{A} = \begin{bmatrix} \frac{K_{iv}}{L_1} & \frac{D_Q-1}{L_1} & 0 & 0 \\ \frac{1-D_Q}{C_1} & 0 & \frac{D_Q}{C_1} & 0 \\ 0 & \frac{-D_Q}{L_2} & 0 & \frac{-1}{L_2} \\ 0 & 0 & \frac{1}{C_2} & \frac{-1}{R_{dc}C_2} \end{bmatrix}; \quad \mathbf{B} = \begin{bmatrix} \frac{V_{C1Q}}{L_1} & \frac{K_{gv}}{L_1} & \frac{K_{iv}}{L_1} \\ \frac{I_{L2Q}-I_{pvQ}}{C_1} & 0 & 0 \\ \frac{-V_{C1Q}}{L_2} & 0 & 0 \\ 0 & 0 & 0 \end{bmatrix}$$

$$\mathbf{C} = \begin{bmatrix} 1 & 0 & 0 & 0 & 0 \\ K_{iv} & 0 & 0 & 0 & 0 \end{bmatrix}; \quad \mathbf{D} = \begin{bmatrix} 0 & 0 & 0 \\ 0 & K_{gv} & K_{iv} \end{bmatrix}$$

4.3 Small-Signal Perturbation Analysis

The maximum power point tracker in PV system is responsible for adjusting the duty cycle of the DC–DC converter to force the operating point to match the MPP. Therefore, the main effect of the controller on MPPT is applying a small variation of duty cycle. By considering fixed temperature and irradiance level, the effect of the small variation of duty cycle on the PV output (voltage, current, and power) at steady state can be investigated by following the state-space averaging technique in [14]. By considering the variation in duty cycle only as an input in Eq. (17), the state-space model can be rewritten as in Eq. (18).

$$\dot{\mathbf{x}} = \mathbf{A} \mathbf{x} + \mathbf{B} \hat{d} \quad (18)$$

$$\text{where } \mathbf{A} = \begin{bmatrix} \frac{K_{iv}}{L_1} & \frac{D_Q-1}{L_1} & 0 & 0 \\ \frac{1-D_Q}{C_1} & 0 & \frac{D_Q}{C_1} & 0 \\ 0 & \frac{-D_Q}{L_2} & 0 & \frac{-1}{L_2} \\ 0 & 0 & \frac{1}{C_2} & \frac{-1}{R_{dc}C_2} \end{bmatrix}; \quad \mathbf{B} = \begin{bmatrix} \frac{V_{C1Q}}{L_1} \\ \frac{I_{L2Q}-I_{pvQ}}{C_1} \\ \frac{-V_{C1Q}}{L_2} \\ 0 \end{bmatrix}$$

By applying the averaging technique in the model in Eq. (18), the average small variation in state-space variables can be evaluated as in Eq. (19).

$$\mathbf{x} = -\mathbf{A}^{-1} \mathbf{B} \hat{d} \quad (19)$$

By solving Eq. (19), the average small variation of the PV current $\langle \hat{i}_{pv} \rangle$ with respect to the perturbation in the duty cycle is stated in Eq. (20).

$$\langle \hat{i}_{pv} \rangle = I_f \langle \hat{d} \rangle \quad (20)$$

$$I_f = -\frac{D_Q V_{C1Q} + R_{dc} (1-D_Q) (I_{pvQ} - I_{L2Q})}{K_{iv} D_Q^2 - R_{dc} (1-D_Q)^2}$$

where D_Q , V_{C1Q} , I_{L2Q} and I_{pvQ} are the steady-state values of the duty cycle, capacitor (C_1) voltage, inductor (L_2) current, and PV current at the MPP, respectively.

The average PV voltage perturbation is obtained by combining Eqs. (7) and (20), as in Eq. (21).

$$\langle \hat{v}_{pv} \rangle = K_{iv} I_f \langle \hat{d} \rangle \quad (21)$$

By applying the small-signal concept and neglecting the second-order variation terms, the PV power small variation $\langle \hat{p}_{pv} \rangle$ is deduced in Eq. (22) [11].

$$\langle \hat{p}_{pv} \rangle = \langle \hat{v}_{pv} \rangle I_{pvQ} + V_{pvQ} \langle \hat{i}_{pv} \rangle \quad (22)$$

Thus, the perturbation in the PV power with respect to the perturbation in the duty cycle is obtained by inserting Eqs. (20) and (21) into Eq. (22), as given in Eq. (23).

$$\langle \hat{p}_{pv} \rangle = (K_{iv} I_{pvQ} + V_{pvQ}) I_f \langle \hat{d} \rangle \quad (23)$$

Equations (20), (21), and (23) represent the key design formula that can be used to choose the proper perturbation size in perturb and observe (P&O) MPPT algorithm. Equation (21) is useful when the control is based on the voltage observation, while Eq. (20) is used when the current observation is considered.

5 Direct-Coupled PV Pumping Power System

Stand-alone PV systems are ideal for remote rural areas where other power sources are either impractical or unavailable [15]. Among the different applications of off-grid PV systems is the PV pumping system (PVPS). This system is widely used in domestic and livestock water supplies and small-scale irrigation systems, especially those employed for water and energy conservation such as low-head drip irrigation systems [16]. Typically, PVPS consists of PV array, drive system, and storage element, which can be a battery bank or/and a water tank. The drive system is composed of a motor pump set and a power-conditioning component to extract the maximum power from the PV panel and drive the motor. The most commonly utilized motor in stand-alone battery-less PVPS is the permanent magnet (PM) DC motor, since it can perform well even under low irradiance level and it is simple in control [4].

In PM DC motor-based PVPS, one or more DC–DC converters are required between the PV panel and the motor for control and drive purposes. Four different system topologies can be found in the literature: (1) direct coupled: the PV panel is directly connected to the motor pump set [17], (2) using MPPT converter: a DC–DC converter is introduced between the PV panel and the motor to perform MPPT [18], (3) using driver converter: in this case, the DC–DC converter is used for motor control [19], and (4) using MPPT and driver converter: two DC–DC converters are used for MPPT and motor drive [20].

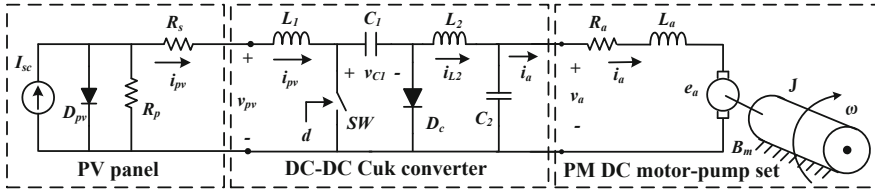


Fig. 5 Equivalent circuit of the direct-coupled PV pumping system under consideration

The PVPS under consideration consists of a PV array connected to a PM DC motor coupled with a positive displacement (PD) hydraulic pump through a DC–DC Cuk converter, as shown in Fig. 5. The mathematical nonlinear and small-signal models for the PVPS are derived similar to the presented analysis for the grid-connected configuration.

5.1 Nonlinear Dynamic Model

In the case of PVPS, the dynamic model for the PV panel is the same as that was presented in Eqs. (1)–(5). The dynamic performance of the Cuk converter and the PM DC motor is represented by the set of nonlinear ordinary differential equations (ODEs) in Eq. (24).

$$\begin{aligned}
 p i_{pv} &= \frac{1}{L_1} (v_{pv} - (1-d)v_{C1}) \\
 p v_{C1} &= \frac{1}{C_1} ((d)i_{L2} + (1-d)i_{pv}) \\
 p i_{L2} &= \frac{1}{L_2} (-(d)v_{C1} - v_a) \\
 p v_a &= \frac{1}{C_2} (i_{L2} - i_a) \\
 p \omega &= \frac{1}{J} (K_T i_a - T_p - B_m \omega) \\
 p i_a &= \frac{1}{L_a} (v_a - R_a i_a - K_E \omega)
 \end{aligned} \tag{24}$$

Equations (4) and (24) represent the nonlinear state-space dynamic model for the entire PVPS. The first four formulas in Eq. (24) represent the Cuk converter supplied from the PV panel. It consists of four passive elements (L_1 , L_2 , C_1 , and C_2), semiconductor diode (D_c), and switch (SW) which is controlled by the duty cycle (d). The last two formulas in Eq. (24) represent the PM DC motor coupled with PD pump (constant torque load), where ω is the motor speed (rad/s), K_E is the *emf* constant (V s/rad), K_T is the torque constant (N m/A), T_p is the load torque (N m),

J is the inertia constant (kg m^2), and B_m is the viscous friction coefficient (N m s). The system dynamic is analyzed by solving Eq. (24) by means of numerical integration technique (Runge–Kutta) and Eq. (4) by iterative technique (Newton–Raphson).

5.2 Small-Signal Model

The small-signal model of the PV panel was presented in Eqs. (7)–(15). The converter and motor dynamics are modeled based on the state-space averaging technique in [14]. Each variable in Eq. (24) is represented by the superposition of the average value and the variation as; $f = F_Q + \hat{f}$ where $f = \{i_{pv}, v_{pv}, v_{C1}, i_{L2}, v_a, \omega, i_a, D\}$ F_Q is the average value of the variable f at the Q-point and \hat{f} is the variation of f around the Q-point.

By mixing the PV array, the Cuk converter and the DC motor models and neglecting the second-order small variations terms, the final small-signal model in state-space representation for the entire PVPS is described in Eq. (25).

$$\dot{\mathbf{x}} = \mathbf{A} \mathbf{x} + \mathbf{B} \mathbf{u}; \quad \mathbf{y} = \mathbf{C} \mathbf{x} + \mathbf{D} \mathbf{u} \quad (25)$$

where $\mathbf{x} = [\hat{i}_{pv} \ \hat{v}_{C1} \ \hat{i}_{L2} \ \hat{v}_a \ \hat{\omega} \ \hat{i}_a]^T$; $\mathbf{u} = [\hat{d} \ \hat{g} \ \hat{t}]^T$; and $\mathbf{y} = [\hat{i}_{pv} \ \hat{v}_{pv}]^T$.

$$\mathbf{A} = \begin{bmatrix} \frac{K_{iv}}{L_1} \frac{D_Q - 1}{L_1} & 0 & 0 & 0 & 0 & 0 \\ \frac{1 - D_Q}{C_1} & 0 & \frac{D_Q}{C_1} & 0 & 0 & 0 \\ 0 & \frac{-D_Q}{L_2} & 0 & \frac{-1}{L_2} & 0 & 0 \\ 0 & 0 & \frac{1}{C_2} & 0 & 0 & \frac{-1}{C_2} \\ 0 & 0 & 0 & 0 & \frac{-B_m}{J} & \frac{K_T}{J} \\ 0 & 0 & 0 & \frac{1}{L_a} & \frac{-K_E}{L_a} & \frac{-R_a}{L_a} \end{bmatrix}; \quad \mathbf{B} = \begin{bmatrix} \frac{V_{C1Q}}{L_1} \frac{K_{gv}}{L_1} \frac{K_{iv}}{L_1} \\ \frac{I_{L2Q} - I_{pvQ}}{C_1} & 0 & 0 \\ \frac{-V_{C1Q}}{L_2} & 0 & 0 \\ 0 & 0 & 0 \\ 0 & 0 & 0 \\ 0 & 0 & 0 \end{bmatrix}$$

$$\mathbf{C} = \begin{bmatrix} 1 & 0 & 0 & 0 & 0 & 0 \\ K_{iv} & 0 & 0 & 0 & 0 & 0 \end{bmatrix}; \quad \mathbf{D} = \begin{bmatrix} 0 & 0 & 0 \\ 0 & K_{gv} & K_{tv} \end{bmatrix}$$

5.3 Small-Signal Perturbation Analysis

Based on the small-signal model presented before, using Eq. (19) and the following the state-space averaging technique [14], the steady-state PV current perturbation with respect to the duty-cycle perturbation is described in Eq. (26).

$$\langle \hat{i}_{pv} \rangle = I_f \langle \hat{d} \rangle \quad (26)$$

$$I_f = - \frac{D_Q B_m V_{C1Q} + (1 - D_Q)(K_T K_e + B_m R_a)(I_{pvQ} - I_{L2Q})}{K_{pv} D_Q^2 B_m - (1 - D_Q)^2 (K_T K_e + B_m R_a)}$$

where D_Q , V_{C1Q} , I_{L2Q} , and I_{pvQ} are the steady-state values of the duty cycle, capacitor (C_1) voltage, inductor (L_2) current, and PV current at the MPP, respectively.

The average PV voltage and power perturbation for PVPS are the same as those presented in Eqs. (21) and (23), respectively. Equations (21), (23), and (26) represent the key design formulas that can be used to choose the proper perturbation size in the MPPT algorithm for direct-coupled PVPSs.

6 PV Panel Parameters' Estimation

In order to analyze and solve the developed dynamic models, the equivalent circuit parameters of the PV modules need to be estimated. The single-diode model has four parameters that need to be estimated to match with the practical I–V characteristics [5]. These parameters are the series resistance (R_s), parallel resistance (R_p), diode ideality factor (n), and reverse saturation current (I_r). In this work, two different parameter estimation techniques are used and compared to extract the PV module parameters. The first one is based on mathematical equations and the measurements of the I–V characteristic's slope at open-circuit voltage and short-circuit current [13]. The second technique is performed by using GA optimization procedure. The details of these methodologies and results are discussed in this section.

6.1 Analytical Parameter Estimation

This methodology is mainly based on measuring the slope of the I–V characteristic of the PV module (given in the datasheet) and some analytical formulas. The first parameter (I_r) is estimated at STC by neglecting the parallel resistance effect in Eq. (3), as given in Eq. (27). Since I_r is a temperature-dependent parameter, its value at a given temperature (T) is updated using Eq. (28) [1].

$$I_{r_o} = \frac{I_{sc_o}}{(e^{V_{oc_o}/nV_T} - 1)} \quad (27)$$

$$I_{r|T} = I_{r|T_o} \cdot \left(\frac{T}{T_o}\right)^{\frac{3}{n}} \cdot e^{\frac{-E_g}{n} (V_T - V_{T_o})} \quad (28)$$

where E_g is the band gap energy; it is the energy that an electron must acquire to jump across the forbidden band to the conduction band, and it is equal to 1.12 eV for silicon.

Until this point, the diode ideality factor is unknown and must be estimated. Ideal diode ($n = 1$) is assumed in this stage until a more accurate value is estimated later by trial and error. The series resistance of the PV module has a large impact on the slope

of the I–V curves near the open-circuit voltage. Hence, the value of R_s is calculated by evaluating the slope $\left(\frac{dV}{dI}\right)$ of the I–V curve at V_{oc} , as indicated in Eq. (29) [22].

$$R_s = -\frac{dV}{dI}\bigg|_{V_{oc}} - \left(\frac{nV_T}{I_r e^{\left(\frac{V_{oc}}{nV_T}\right)}} \right) \quad (29)$$

The parallel resistance of the PV module has a large impact on the slope of the I–V curves near the short-circuit current. Thus, the value of R_p is calculated by evaluating the slope $\left(\frac{dV}{dI}\right)$ of the I–V curve published on the datasheet at I_{sc} and substituting in Eq. (30) [22]. The last parameter is the diode ideality factor, which is estimated by trial and error, such that its value attains the best match with the I–V curves on the datasheet.

$$R_p = \frac{-\left(\frac{dV}{dI}\bigg|_{I_{sc}} + R_s\right)}{1 + \frac{I_r}{nV_T} \cdot \left(\frac{dV}{dI}\bigg|_{I_{sc}} + R_s\right) \cdot e^{\left(\frac{R_s I_{sc}}{nV_T}\right)}} \quad (30)$$

6.2 GA-Based Parameters' Estimation

GA is a stochastic search algorithm that emulates biological evolutionary theories to solve optimization problems [23]. It enables parallel search from a population of points. Based on the literature, GA shows massive success in estimating the system parameters in many different applications due to the following reasons [24, 25]:

- It enables parallel search from a population of points. Therefore, it has the ability to avoid being trapped in a local optimal solution, unlike traditional methods, which search from a single point.
- It supports probabilistic selection rules, not deterministic ones.
- It behaves well in the case of noisy or stochastic objective function.
- It does not require explicit definitions.
- It is very efficient in the case of cheap cost function (which is our case).

Therefore, GA has been used in this study to extract the best combination of the parameters, such that the error between the measured (from the datasheet) and the simulated I–V characteristics is minimum. The settings of the GA are presented in Table 1. The upper and lower boundaries are selected to cover a wide range for each variable. These ranges are identified based on the physical representation for each variable and using the analytical formulas presented in the previous section. A large number of populations and generations are considered to guarantee finding the optimum solution. Several runs were carried out to confirm the consistency of the final results.

Table 1 Settings for GA parameters' estimation

Parameter		Value
Bounds	Variable	$\left[R_s \ R_p \ n \ I_r \right]$
	Lower	$[0.00001, 1000, 1, 1 \times 10^{-10}]$
	Upper	$[0.01, 1 \times 10^{30}, 2, 1 \times 10^{-3}]$
Populations		200
Mutation		Uniform 80%
Crossover		0.8
Generations		100

Table 2 BP 4175T PV module specifications at STC

Electrical characteristic	Value
Open-circuit voltage (V_{oc})	43.6 V
Short-circuit current (I_{sc})	5.45 A
Voltage at maximum power ($V_{mp@STC}$)	35.4 V
Current at maximum power ($I_{mp@STC}$)	4.94 A
Maximum power ($P_{max@STC}$)	175 W
Temperature coefficient of I_{sc}	$(0.065 \pm 0.015)\%/^{\circ}\text{C}$
Temperature coefficient of V_{oc}	$-(0.5 \pm 0.05)\%/^{\circ}\text{C}$
Module efficiency	14%

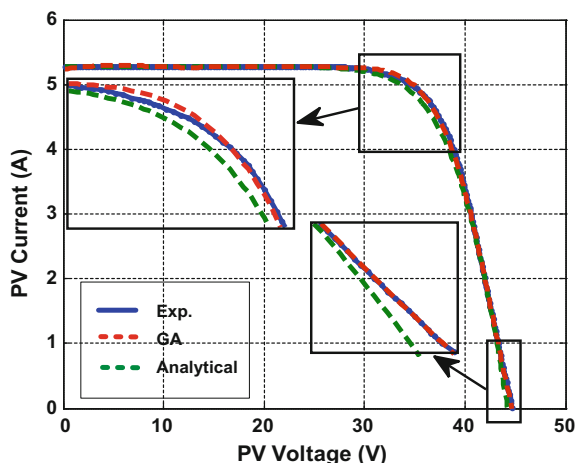
6.3 Parameters' Estimation Results

The two techniques of parameters' estimation are utilized to extract the parameters of the commercial BP 4175T PV module [26]. The electrical characteristics and specifications of this module at STC [$G_o = 000 \text{ W/m}^2$ at the air mass (A.M) = 1.5 and $T_o = 25^{\circ}\text{C}$] are given in Table 2.

The two techniques are implemented in MATLAB environment and applied for BP 4175T PV module. The final extracted parameters from each technique are presented and compared in Table 3. Moreover, the I–V characteristic of PV module is plotted at STC using the parameters estimated by each technique and compared with the measured I–V characteristic in Fig. 6. It can be observed that GA technique shows the most accurate results. GA-based parameters give 4.77% of current error, while the analytical technique presents 6.45%. The parameters that show the least error (GA-based) are considered in this work to model the performance of the PV module.

Table 3 Extracted parameters of BP 4175T PV module

Method	R_s (Ω)	R_p (Ω)	n	I_r (A)	Current error (%)
Analytical	0.0068	1000.8	1.6	$1.45 * 10^{-6}$	6.45
GA	0.00657	$2.8 * 10^3$	1.51	$7.0685 * 10^{-7}$	4.77

Fig. 6 Comparison between I–V characteristic for BP 4175T PV module at STC from measurement and simulated using GA- and analytical based parameters

6.4 Model Verification Based on Experimental Tests

The system described in Figs. 3 and 5 is implemented, simulated, and tested under fast variations of climatic conditions. The simulation results are obtained by solving the developed dynamic models for both systems and comparing their results with the experimental data from laboratory-scale prototypes. The experimental test setup is shown in Fig. 7. It consists of a commercial BP 4175T PV array connected to the DC element (DC bus in grid-connected system and DC motor pump in PVPS) through a DC–DC Cuk converter and its control. The PV array was emulated by XR375-15.9 Programmable DC MAGNA power supply. The conventional P&O MPPT algorithm was implemented using DSpace 1104 microcontroller board. The DC–DC converter is built using HGTG30N60C3D IGBT power switch and FFPF15S60S power diode. The commercial SKHI 22A H4 R gate driver was considered to drive the IGBT. Hall Effect LEM voltage and current sensors are utilized to measure the PV voltage and current. The DC bus was emulated using a DC supply in parallel with resistive load. The motor pump set was emulated using motor generator set. A PM DC motor was coupled to a DC generator with a resistive load connected to the generator output terminals. Adjusting the resistive load changes the load on the PM DC motor. The nominal values for the chosen system's components are given in Table 4. The converter switching frequency is 10 kHz, and the perturbation rate is 50 variations/sec.

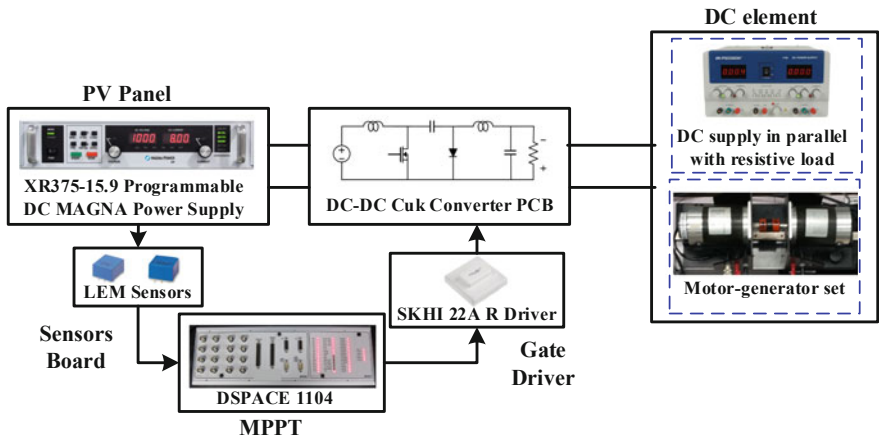


Fig. 7 Experimental setup of direct-coupled PV power systems

Table 4 Specifications of hardware components of the DC–DC converter and PM DC motor

Component	Model/rating
Power IGBT	HGTG30N60C3D, 600 V, 63 A
Power diode	FFPF15S60S, 600 V, 15 A
Gate driver	Hybrid Dual SKHI 22 A/B H4 (R)
Current sensor	LA25-NP 713194
Voltage sensor	LV25-P 712100
Motor poles	2
Motor speed	4000 rpm
Motor power	250 W
Motor voltage	42 V
Motor current	8.4 A

7 Grid-Connected PV System Results

The direct-coupled grid-connected PV system with P&O MPPT algorithm was tested, and the results are compared with the developed model results, as depicted in Figs. 8 and 9. The figures show the PV power, current, and voltage profiles under the fluctuation of environmental conditions. Figure 8 illustrates the system performance under the fast variation of irradiance level. As it can be noticed, very good agreement is noticed between the experimental tests and the simulated data using the developed models. Moreover, the system dynamics under the fast variation of the temperature are described in Fig. 9. Good correlation can be observed between the simulated and measured values.

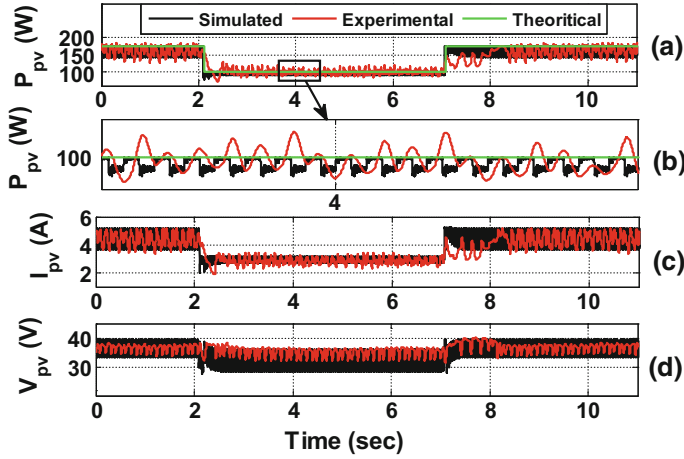


Fig. 8 Experimental and simulation results of PV grid-connected system with P&O algorithm under variation of irradiance level, **a** PV power, **b** PV power zoomed, **c** PV current, and **d** PV voltage

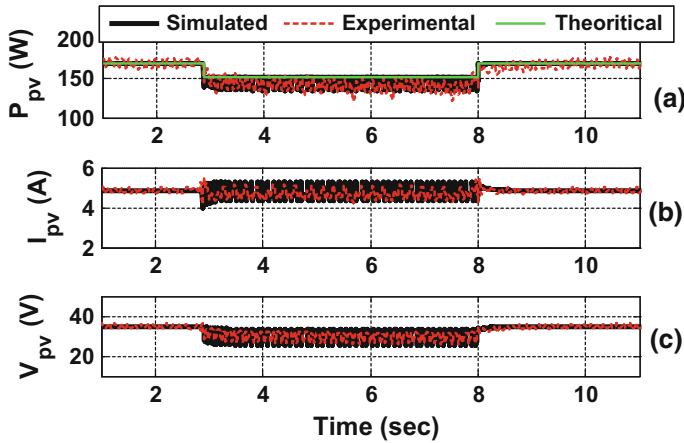


Fig. 9 Experimental and simulation results of PV grid-connected system with P&O algorithm under variation of temperature, **a** PV power, **b** PV current, and **c** PV voltage

8 Stand-Alone PV Pumping System Results

The direct-coupled PVPS with P&O MPPT algorithm was tested, and the results are compared with the outcomes from the developed model, as presented in Figs. 10 and 11. The figures show the motor performance under the fast variation of irradiance level. Figure 10 illustrates the motor power (P_m), voltage (V_m), and current (I_m) profiles. Figure 11 shows the motor speed (N_m) and torque (T_m) profiles. As it

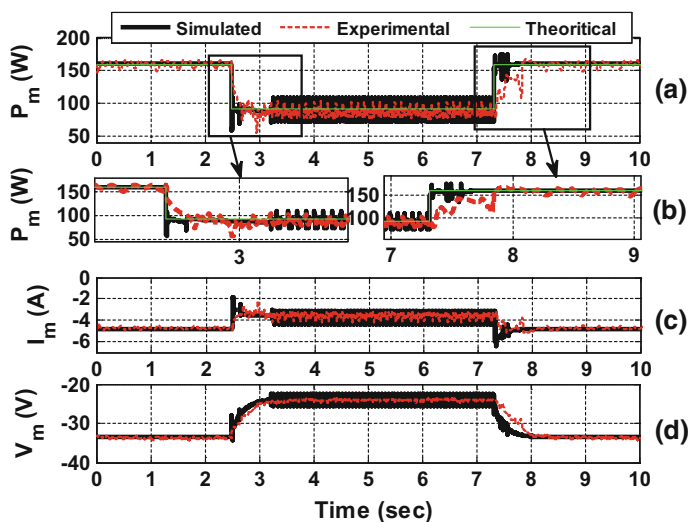


Fig. 10 Experimental and simulated PVPS performance with P&O algorithm under variation of irradiance level, **a** motor power, **b** motor power zoomed, **c** motor current, and **d** voltage

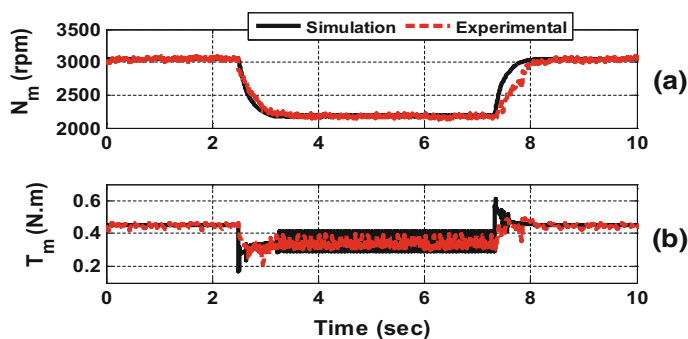


Fig. 11 Experimental and simulated PVPS performance with P&O algorithm under variation of irradiance, **a** motor speed and **b** motor torque

can be observed, a very good correlation is noticed between the measured data and the data from the developed models. The results demonstrate the accuracy of the developed models and their capability to predict the system performance under different dynamics.

9 Conclusions

In this chapter, a general approach for modeling the direct-coupled PV power systems was presented. Detailed nonlinear dynamic models for two PV systems are addressed: grid-connected system and stand-alone PV pumping system. The combination of nonlinear and ordinary differential equations (ODEs) was developed to represent the entire PV systems' dynamics, including a PV generator, DC–DC converter, and DC element (DC bus in case of grid-connected system and PM DC pump in case of PVPS). Moreover, the dynamic models were linearized to develop small-signal models for the same systems. The small-signal models were utilized to investigate the effect of duty-cycle perturbation on the performance of the PV generator in terms of power, current, and voltage. The final design formulas for MPPT algorithm parameters are derived, which can be utilized to decide the perturbation size in the MPPT algorithm. Two different parameters' estimation techniques, analytical and using GA, were utilized to accurately estimate the PV generator parameters. The developed models were implemented and analyzed in MATLAB environment. The accuracy of the proposed models was verified based on the simulation data and experimental tests.

References

1. Masters GM (2013) Renewable and efficient electric power systems, 2nd edn. Wiley, Hoboken, New Jersey
2. Balfour J (2011) Introduction to photovoltaic system design, 1st edn. Jones & Bartlett Learning, Burlington, MA
3. Dragičević T, Lu X, Vasquez JC, Guerrero JM (2016) DC microgrids—part II: a review of power architectures, applications, and standardization issues. *IEEE Trans Power Electron* 31(5):3528–3549
4. Mohamed AAS, Metwally H, Farahat M (2011) Optimal design of solar water pumping systems. Master of Science in Electrical Engineering, Zagazig University, Egypt
5. Mahmoud Y, El-Saadany EF (2015) A photovoltaic model with reduced computational time. *IEEE Trans Industr Electron* 62(6):3534–3544
6. Mahmoud YA, Xiao W, Zeineldin HH (2013) A parameterization approach for enhancing PV model accuracy. *IEEE Trans Ind Electron* 60(12):5708–5716
7. Lim LHI, Ye Z, Ye J, Yang D, Du H (2015) A linear identification of diode models from single #x2013; characteristics of PV panels. *IEEE Trans Industr Electron* 62(7):4181–4193
8. Farahat MA, Metwally HMB, Abd-Elfatah Mohamed A (2012) Optimal choice and design of different topologies of DC–DC converter used in PV systems, at different climatic conditions in Egypt. *Renew Energy* 43:393–402
9. Middlebrook R, Cuk S (1976) A general unified approach to modelling switching-converter power stages. *IEEE Power Electron Spec Conf* 1976:18–34
10. Piegari L, Rizzo R (2010) Adaptive perturb and observe algorithm for photovoltaic maximum power point tracking. *IET Renew Power Gener* 4(4):317–328
11. Ahmed A, Ran L, Moon S, Park J-H (2013) A fast PV power tracking control algorithm with reduced power mode. *IEEE Trans Energy Convers* 28(3):565–575
12. Mohamed AAS, Berzoy A, Mohammed OA (2017) Design and hardware implementation of FL-MPPT control of PV systems based on GA and small-signal analysis. *IEEE Trans Sustain Energy* 8(1):279–290

13. Li X, Li Y, Seem JE, Lei P (2016) Detection of internal resistance change for photovoltaic arrays using extremum-seeking control MPPT signals. *IEEE Trans Control Syst Technol* 24(1):325–333
14. Middlebrook R, Cuk S (1976) A general unified approach to modelling switching-converter power stages. In: 1976 IEEE Power Electronics Specialists Conference, pp 18–34
15. Rezkallah M, Hamadi A, Chandra A, Singh B (2015) Real-time HIL implementation of sliding mode control for standalone system based on PV array without using dumpload. *IEEE Trans Sustain Energy* 6(4):1389–1398
16. Mapurunga Caracas JV, De Carvalho Farias G, Moreira Teixeira LF, De Souza Ribeiro LA (2014) Implementation of a high-efficiency, high-lifetime, and low-cost converter for an autonomous photovoltaic water pumping system. *IEEE Trans Ind Appl* 50(1):631–641
17. Elgendy MA, Zahawi B, Atkinson DJ (2012) Assessment of perturb and observe MPPT algorithm implementation techniques for PV pumping applications. *IEEE Trans Sustain Energy* 3(1):21–33
18. Chandel SS, Nagaraju Naik M, Chandel R (2015) Review of solar photovoltaic water pumping system technology for irrigation and community drinking water supplies. *Renew Sustain Energy Rev* 49:1084–1099
19. Mohamed AAS, Berzoy A, Mohammed O (2014) Optimized-fuzzy MPPT controller using GA for stand-alone photovoltaic water pumping system. In: IECON 2014—40th Annual Conference of the IEEE Industrial Electronics Society, pp 2213–2218
20. Daoud A, Midoun A (2010) Maximum power point tracking techniques for solar water pumping systems. *Revue des Energies Renouvelables* 13(3):497–507
21. Mahmoud YA, Xiao W, Zeineldin HH (2013) A parameterization approach for enhancing PV model accuracy. *IEEE Trans Industr Electron* 60(12):5708–5716
22. Mohamed A, Metwally H, Farahat M (2012) Photovoltaic water pumping systems. LAP LAMBERT Academic Publishing
23. Simon D (2013) Evolutionary optimization algorithms, 1st edn. Wiley, Hoboken, New Jersey
24. Fazzolari M, Alcalá R, Nojima Y, Ishibuchi H, Herrera F (2013) A review of the application of multiobjective evolutionary fuzzy systems: current status and further directions. *IEEE Trans Fuzzy Syst* 21(1):45–65
25. Ramadan AA, Faheem MT, Amer AF, Sallam SA (2004) New genetic-based design of a Pi-like fuzzy logic speed controller for an induction motor. In: Second IEEE international conference on computational cybernetics, 2004. ICCC 2004, pp 25–32
26. bp 4175t pv module datasheet—Google Search, 20 Oct 2015 (Online). Available https://www.google.com/?gws_rd=ssl#q=bp+4175t+pv+module+datasheet. Accessed 20 Oct 2015

Status Monitoring and Performance Investigation of a 5.1 kW Rooftop Grid-Tie Photovoltaic Energy System in Egypt



Ahmad H. Besheer, Mohamed A. Eldreny, Hassan Rashad
and Ahmed Bahgat

Abstract Although, the existence of many solar projects in Egypt in previous years, it is evident that the lack of long-term monitoring for operational behavior and reliability investigation of such systems in Egypt may impede the successful implementation of the recent Egyptian plan for diversifying its energy source. This chapter presents a comprehensive status investigation and performance analysis of a photovoltaic energy system installed at the Faculty of Engineering—Cairo University. An integrated monitoring scheme is included using a proposed monitoring scheme that provides increased flexibility if it is compared to traditional schemes that need particular data logging system and special hardware design. The system with a total capacity of 5.1 *kwp* feeds the utility via grid-tie inverter who plays an essential role in monitoring the health of the system. An additional in-plane solar radiation and temperature sensors for recording the climatic conditions on the spot of PVES are erected and configured data are monitored, collected, and analyzed following the international standards of IEC 61724. The influence of dynamic fluctuations in solar radiation is taken into account by analyzing the data of three typical operating days of sunny, average cloudy, and cloudy conditions. The collected data help in conceiving the status and the health of each system's component. The impact of the newly installed PV system on the electrical network is also initially investigated at the inverter level. A comparison of the system performance under study with other monitored PV systems reflects good matching and large potential of the newly installed system in the subsequent years.

A. H. Besheer (✉)

Environmental Studies and Research Institute, University of Sadat City, Sadat City, Egypt
e-mail: ahmed.tawfeek@esri.usc.edu.eg

M. A. Eldreny · H. Rashad · A. Bahgat

Electrical Power and Machines Department, Faculty of Engineering, Cairo University, Giza, Egypt

© Springer Nature Switzerland AG 2020

463

A. M. Eltamaly and A. Y. Abdelaziz (eds.), *Modern Maximum Power Point Tracking Techniques for Photovoltaic Energy Systems*, Green Energy and Technology, https://doi.org/10.1007/978-3-030-05578-3_18

1 Introduction

Recent years have witnessed an increased interest in installing and operating PV energy systems either for regions deprived of electricity or to support and diversify the power sources fed to the grid. This led to more technical research that facilitates the control and the integration of such system within the existing electrical network; see, for instance, [1–3]. Egypt has average solar insolation of over 2000 kWh/m² which is double the energy produced from the sun in a square meter in Germany. This means that installing a solar plant in Egypt would result in higher power production rate if it is compared with other places around the world. Egypt's energy supply mix is heavily reliant on unsustainable energy resources having a composition of around 88% fossil fuels while the remaining 12% are mainly hydropower from the Aswan High Dam. The country's energy mix has not really earned the title of the mix as it is solely focused on conventional power sources despite the abundance of other resources such as solar and wind [4]. In February 2008, the Egyptian Supreme Council of Energy has put his ambitious directive to satisfy 20% of the generated electricity by renewable energy by 2020. This was followed by approving the Egyptian Solar Plan in July 2012 that targets to install 3500 MW by 2027 [5]. To be in-line with these directives that will certainly lead to drastically change in the Egyptian power system and the energy market, the research team in the automatic control group in Electrical Power and Machines Department, Cairo University, Egypt took actions to stimulate the new power system environment and to understand the operational behavior of the two basic renewable energy-based generation systems. A research project has been funded by STDF—Egypt in late 2015—to install two photovoltaic energy systems to work in two separate modes— grid-connected and stand-alone—in Automatic Control Laboratory in the Library Building at Faculty of Engineering, Cairo University. This project aims to promote research in the area of PV energy system (PVES) monitoring, operation, and control with special consideration to the grid integration. The gained experience during the project stages in the design, installation, and operational monitoring allows showing the benefits of this technology and evaluating its impact on both utility and autonomous scale.

In general, the behavioral evaluation studies of such systems [6–12] are deemed to be the best method to comprehend the performance and to determine the behavior of PV systems in real climatic circumstances. In most cases, these evaluation studies could result in setting the prospect of these energy-producing systems in a region [6] and may assist in maintaining, operating, and designing novel PV power system as well [7]. In [8], the real behavior of two PV generation stations connected to the grid located in northern Italy that utilize asymmetrical panel technologies is tested. The paper initially assessed the real performance of these stations and the effects of changing environmental conditions and the variation of panel behavior as well as electrical parts on its operational performance. In [9], the same direction is assumed where comparison of the performance for two grid-tie PVESs erected in the same region is performed. The suitable choice of system's sections and parts such as PV modules, converters, and wiring system are emphasized. In [10], a very small photovoltaic

system that is integrated with the low-voltage distribution panel of an Irish building is analyzed. The results give premeditation of system performance that assists in estimating the economic and environmental impacts on such energy systems.

Although most of the above-mentioned studies are carried out for small-scale PV systems, the work in [13] tested and checked the operational behavior of relatively large-scale PV energy system (3 MW) in India. The results determined the fluctuation in the PV system output under different daily environmental situations. Performance analysis of 3.6 kW grid-connected photovoltaic generation unit in Egypt is studied in [14]. This work only gives some preliminary performance indices for the proposed PV system and did not use adequate performance indicators following the IEC 61724 standard [15].

Back surface temperature, front surface soiling, cells' mismatch, and losses are reported in several papers [16–18] to have a direct influence on PVES operational performance. The losses mechanism for any PVES can be split to capture losses which are mainly due to the attenuation of the incoming solar radiation and system losses which are mainly due to wiring and inverter losses. The calculations done in this chapter are mainly based on three essential parameters on understanding the behavior and characterizing the performance of the installed PVES under Egypt climatic and environmental conditions. The base parameters used are the array, reference, and the final yield. These parameters are calculated according to the data collected for the energy produced by the PV generator, the energy output of the inverter, and the energy injected into the grid. The capture and the system losses are computed and hence the performance ratios are produced. Other numerical calculations are also performed that enable us to determine the efficiencies of each system component and to judge the health of the system. The chapter also stresses the importance of the monitoring scheme to investigate the operational status of each component in the PV system. From the collected data, the voltage rise and fluctuations at the inverter level are found to be within the permissible standard limits. In general, the work in this chapter provides a technical description of grid-tie and the off-grid PV systems and an initial evaluation for the performance of the grid-tie PV system for the period of 6 months. The key advantages of this work are two folded. The first one is monitoring the status of a residential scale low-voltage grid-tie-based photovoltaic generation system in order to ensure the health of the system and to improve its components in case of failure. Hence enhance its utilization factor and its annual yield. The second one is evaluating the system operational performance which may serve as a useful data for the low-scale PV projects on the upcoming years in Egypt.

2 System Description

The complete hardware setup for this project in both systems includes PV arrays—grid-tie inverter—stand-alone inverter—charge controller—battery pack—PLC—RTU—local loads—switches—measuring transducers and smart energy meters. These units are assembled in a control panel as shown in Fig. 1, except

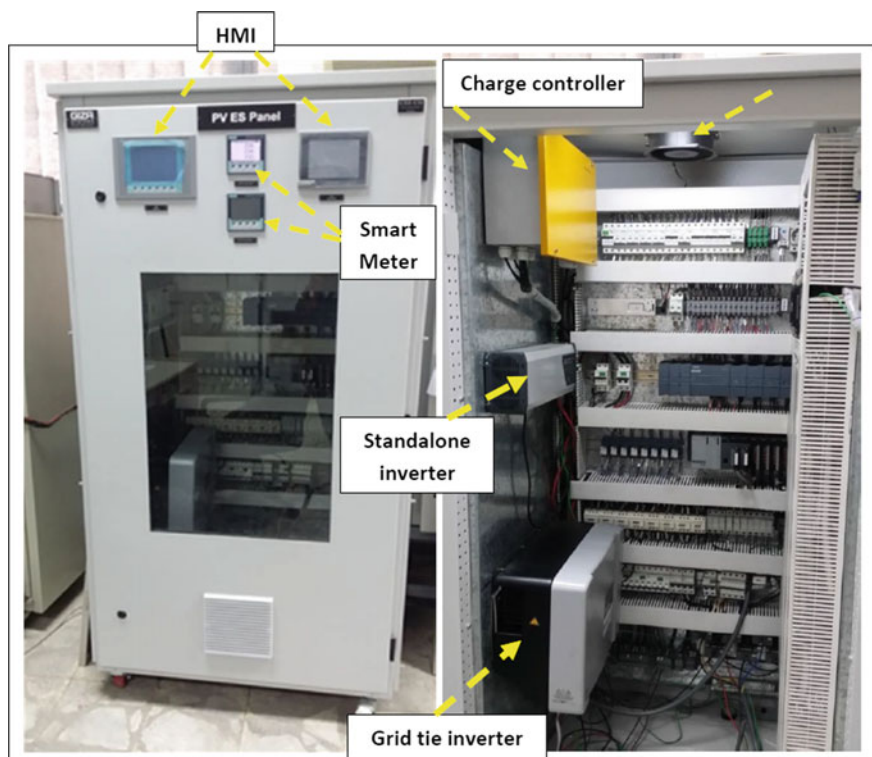


Fig. 1 Control panel for two PVES



Fig. 2 Grid-tie PV arrays

the PV arrays in Figs. 2 and 3 which are mounted on the roof top of the library building. Local loads and the battery pack are placed inside the Automatic Control Laboratory.

The grid-tie PV string consists of twenty poly-crystalline modules of type SUNTECH [19] that are covering a total area of 32.5 m^2 . Each module comprises



Fig. 3 Stand-alone PV arrays

Table 1 Featured parameters of the PV array and module

PV module		PV array	
Parameter	Value	Parameter 6635	Value
Rated max. power (P_{max})	255 W	Rated Max. power (P_{max})	5200 W
Number of solar cells	60	Number of modules in array	20
Area		Total PV area	35.5 m ²
Open-circuit voltage (V_{oc})	37.6 V	Array open-circuit voltage	752 V
Short-circuit current (I_{sc})	8.76 A	Array short-circuit current	8.76 A
Voltage at P_{max} (V_{mp})	30.8 V	Array voltage at P_{max} (V_{mp})	616 V
Current at P_{max} (I_{mp})	8.25 A	Array current at P_{max} (I_{mp})	8.25 A

60 solar cells connected in series. The output power of each used module is 255 Wp and the modules are connected in series to yield 752 DC output voltage. Both the PV array and the PV module featured parameters for this system are summarized in Table 1. A three-phase inverter of type KOSTAL/PICKO 4.2 [20] as shown in Fig. 4a, with input DC minimum and maximum voltages of 180–950 V and output three-phase AC voltage of 380 V, is connected to the PV array which will ensure complying with the 50 Hz low-voltage board in the laboratory. The maximum power of PV inverter is 4.2 kWp. The tilt angle of the modules is 30° facing south according to the orientation of the library building which located at latitude of 30°4′58″ and longitude of 31°16′58″. This location receives 1985 kWh/m² as a total sum of global radiation per annum and has an annual average temperature of 23.5 °C. The total capacity of the system is 5.1 kW with a maximum injected current from the inverter to be 9 A and output voltage range from 184 to 253 VAC with frequency 50 Hz. The three-phase Kostal-PIKO 4.2 inverter is used to feed a synchronized AC energy directly into the low-voltage distribution board of the Automatic Control Laboratory which is connected to the grid via 11 kV/380 V transformer with fixed tap changing steps. The inverter has a rated maximum efficiency of 96% and maximum AC power of 4200 W [20].

The single-line diagram of the grid-tie PVES is shown in Fig. 5. It shows smart meters used for metering and monitoring the following parameters:

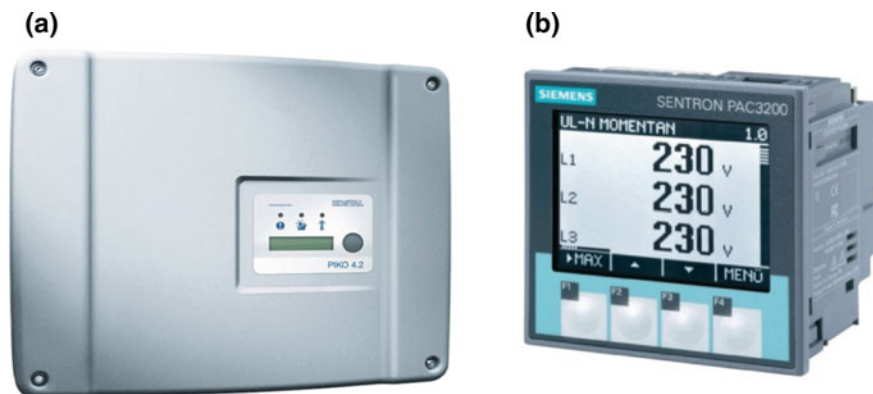


Fig. 4 **a** KOSTAL-PIKO 4.2 grid-tie inverter and **b** SIEMENS, SENTRON PAC3200 Smart energy meter

Voltage—phase to phase, phase to neutral/current/power/power factor/THD per phase/frequency/three-phase average voltage and currently, the details for these meters are presented in the next section. The system is also protected against overloading and short circuit using DC miniature breakers of rating 10 A.

3 Monitoring Schemes Description

The last 15 years have witnessed a regular increase in the statistical average performance ratio of a novel PV installation especially in moderate climates. This improvement is mainly due to increase relying on advanced monitoring schemes and the continuous analysis of the collected data. A search about the word “monitoring” for PV systems in the IEEEExplore database reflects more than 1000 articles in the period from 2010 to 2016 (see for instance [21]). The main purposes of a monitoring scheme are to follow up on the energy yield, to assess the PV system performance, and to timely identify design flaws or malfunction [22].

A separate monitoring scheme for the proposed grid-tie PVES is fully designed to provide useful information about various system operational aspects and the future procedures to refine and enhance their performance. This monitoring scheme is designed to be very flexible, practical, and reliable for real-time monitoring of the developed PV system. It is very cheap in cost if it is compared to the traditional solutions that require dedicated data logging unit and specialized hardware. In the following section, details about this monitoring scheme are presented.

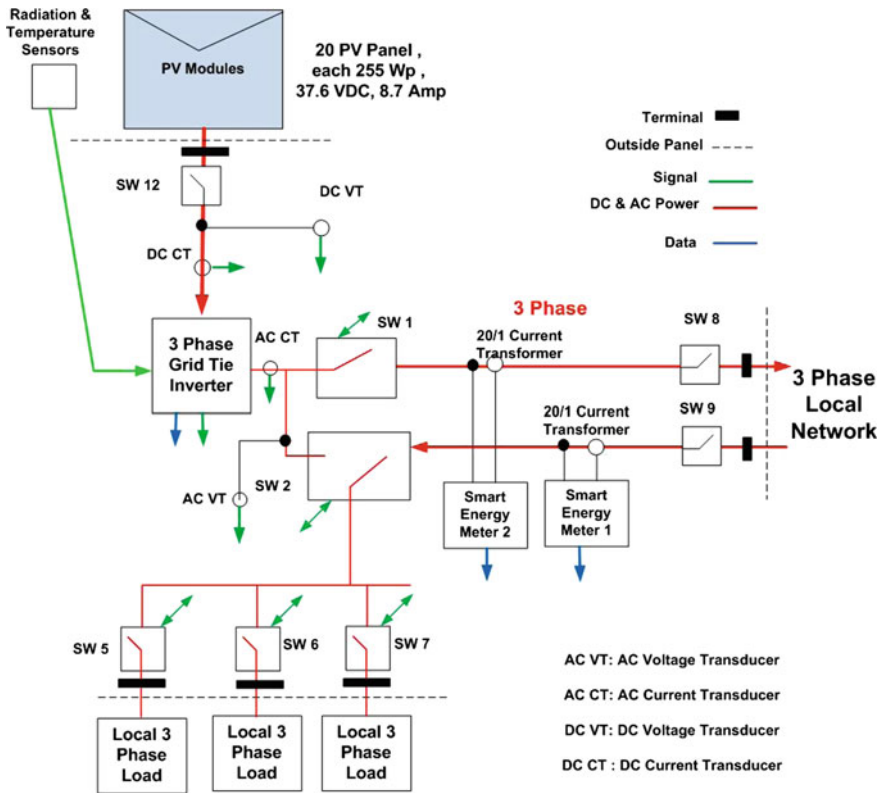


Fig. 5 Single-line diagram of grid-tie PVES

3.1 Monitoring Scheme for the Grid-Tie PVES

The designed monitoring scheme for the first PV system is basically depending on the grid-tie inverter of type KOSTAL version PIKO 4.2. As shown in Fig. 6, the proposed monitoring scheme gets avail from the effective and intrinsic monitoring functions and capabilities of the inverters and their Internet connectivity that enable wide range measurements for the operational parameters of the system. The inverter successfully collects—every 10 min—various kinds of PV measurement data such as PV system production and the climatic ambient conditions and stores it for further processing. The sampling period, the averaging period, and the type of collected data depends mainly on the type of the inverter and its configuration [23]. A PC is connected to the inverter via Ethernet communication cable to download the data for analysis. Dedicated inverter software is used to facilitate communication between the inverter and the PC. The operational range for the inverter DC input voltage is 180 V minimally and 950 V maximally with an MPPT add-on feature, the maximum power of PV inverter is 4.2 kWp and it has one string that can provide the DC link.

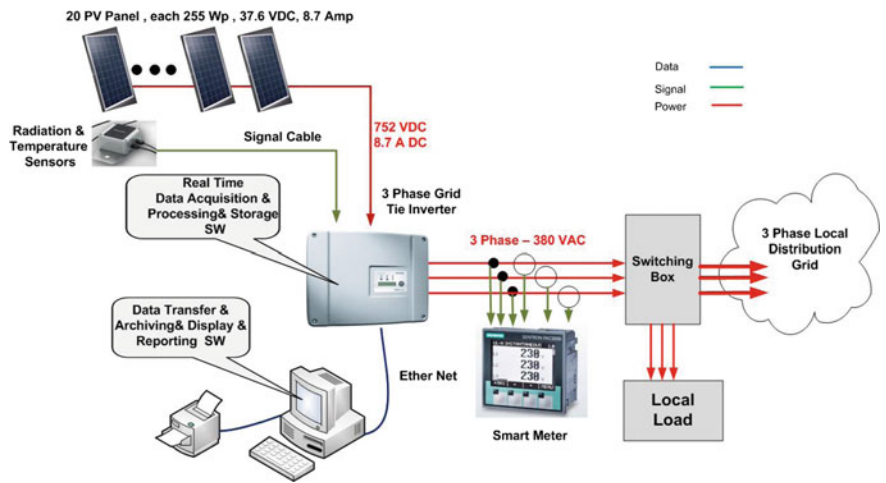


Fig. 6 Monitoring scheme for grid-tie PVES

Table 2 Monitored parameters

Parameter	Unit
Total in-plane radiation	W/m ²
Ambient temperature	°C
PV module surface temperature	°C
DC voltage × 2	V
DC current × 2	A
DC power × 2	kW
AC voltage per each phase	V
AC power per each phase	kW
AC current per each phase	A
Total AC power	kW
PV energy supply	kW h
Energy supply from utility grid	kW h

The system is also equipped with a smart energy metering facility of type SIEMENS, SENTRON PAC3200 [24], that enables metering and monitoring various variables in the proposed PV system. Figure 4b shows the smart energy meter used in this system and Table 2 shows the main monitored parameters for this system.

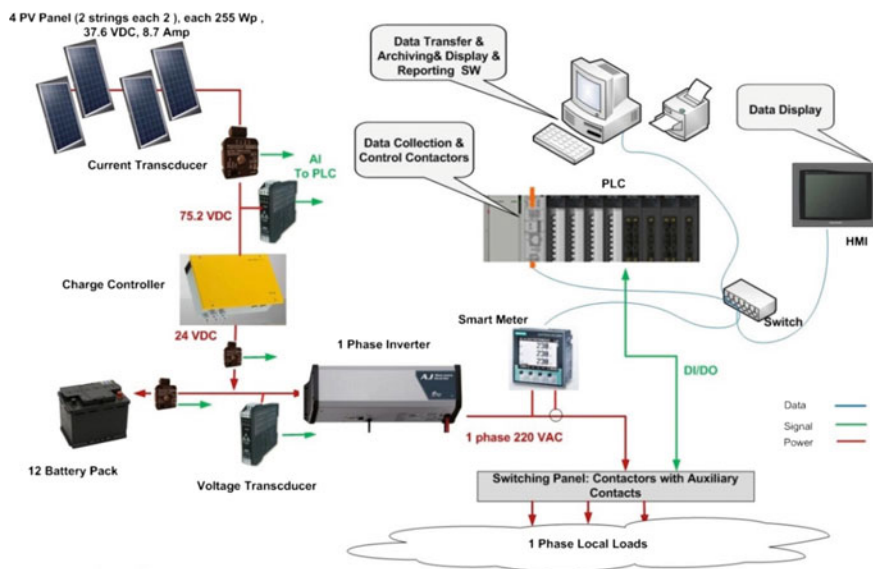


Fig. 7 Monitoring scheme for autonomous PVES

3.2 Monitoring Scheme for the Autonomous PVES

Unlike the monitoring scheme of the grid-tie PV system that mainly depends on the inverter capabilities and features to monitor the status of the system, the designed monitoring scheme for the autonomous PV system is basically depending on voltage and current sensors. As shown in Fig. 7, the proposed monitoring scheme gets data from the PLC that displayed on HMI so it connect to sensors that enable wide range measurements for the operational parameters of the system DC voltage and DC current of PV array, DC voltage and DC current of batteries and AC output voltage and AC output current. The maximum DC input voltage of isolated inverter is 45 V, and maximum power of inverter is 1300 VA. This inverter feeds single-phase loads. The system is also equipped with the same smart energy metering facility of type SIEMENS, SENTRON PAC3200.

4 Status Monitoring

In this section, the operational behavior and the health of the erected grid-tie PV system are completely expressed by presenting sample data for sunny, average cloudy, and heavy cloudy days over the studied period. The grid-tie PVES has been put into operation since June 2016 and the metrological data at the PV site such as the monthly average daily in-plane radiation, ambient, and cell temperatures are calculated for the

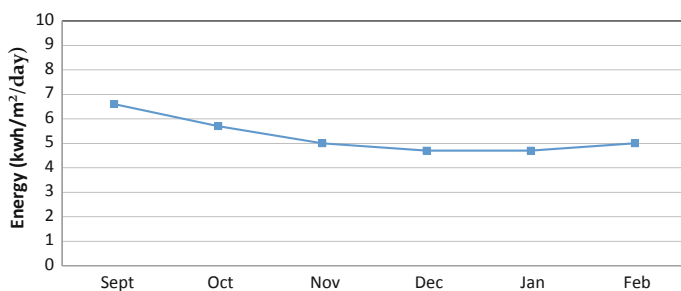


Fig. 8 Monthly average daily in-plane insolation ($I_{i,m}$)

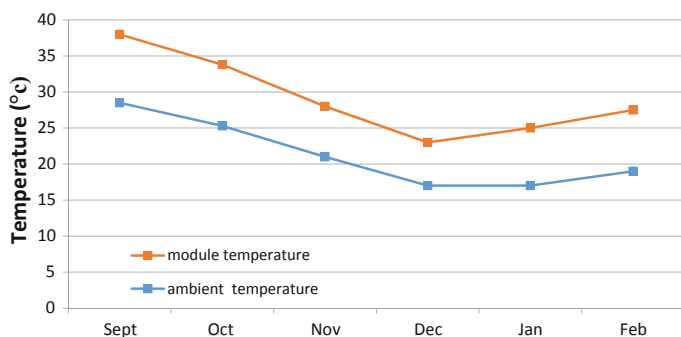


Fig. 9 Monthly average daily ambient ($T_{A,m}$) and module temperatures ($T_{b,m}$)

period of the study and presented in Figs. 8 and 9. Figure 8 represents the monthly average daily global in-plane insolation ($I_{i,m}$) and the Fig. 9 represents monthly average daily ambient ($T_{A,m}$) and module temperatures ($T_{b,m}$).

The monitoring scheme collects and stores totally more than 15 variables. Status investigations for the whole PVES of as well as the main components are represented in Figs. 10, 11, 12, and 13. The PV array status for different daily climatic conditions is shown in Fig. 10a–f over the studied period. Figures 11 and 12 represent the inverter behavior subjected to PV array inputs as depicted in Fig. 10. Figure 13 depicts the overall daily energy output injected to the grid by the PVES along over the studied period.

4.1 Status Monitoring for PV Array

The following points are noticed from Fig. 10a–f:

- (1) The PV array output DC current and voltage show the same nature and trend despite the big fluctuations in the climatic conditions for the chosen days from heavily cloudy to average cloudy to sunny days.

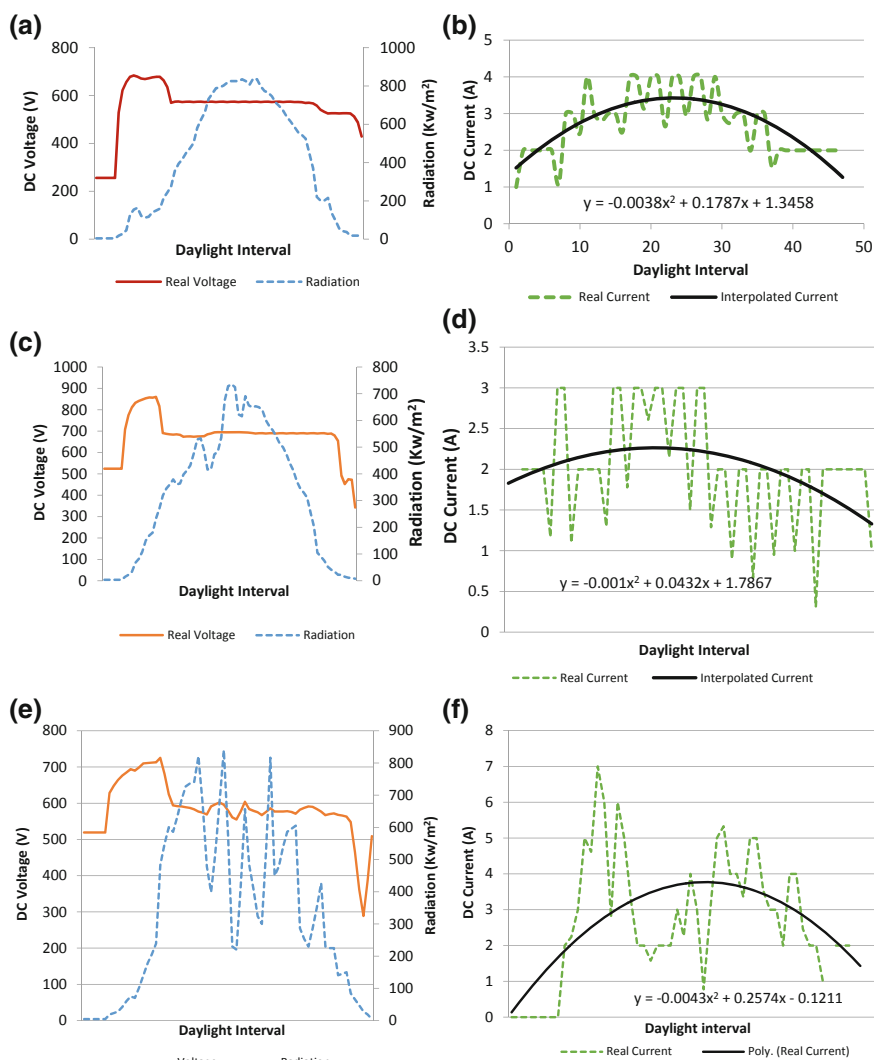


Fig. 10 PV system status monitoring, time versus DC voltage with radiation, and daylight DC current for **a, b** Sunny day, **c, d** average cloudy day, and **e, f** heavily cloudy day

- (2) The maximum DC output voltage for an average cloudy day occurred at 27/10/16; this day represents a higher rate of change of the radiation among the other presented days.
- (3) The amplitude of fluctuations in the output DC current increase with the increasing the degree of variability in the atmospheric conditions (in-plane irradiance) from sunny to heavily cloudy days.

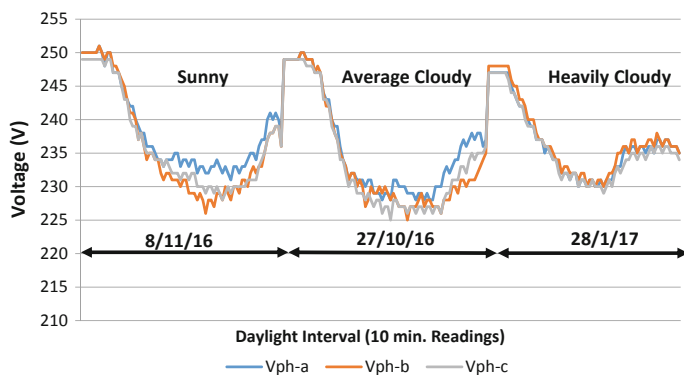


Fig. 11 Three-phase voltage magnitudes at the inverter output

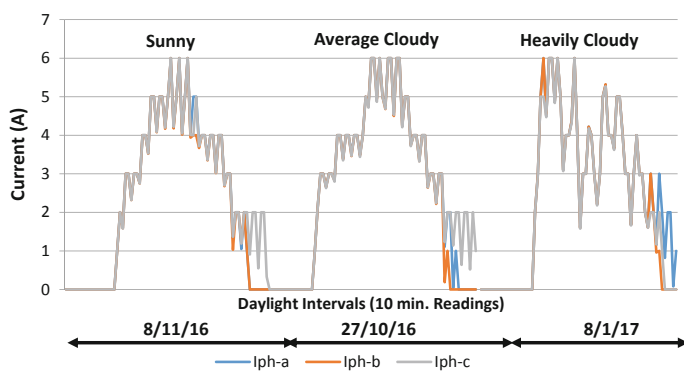


Fig. 12 Three-phase current magnitudes at the inverter output

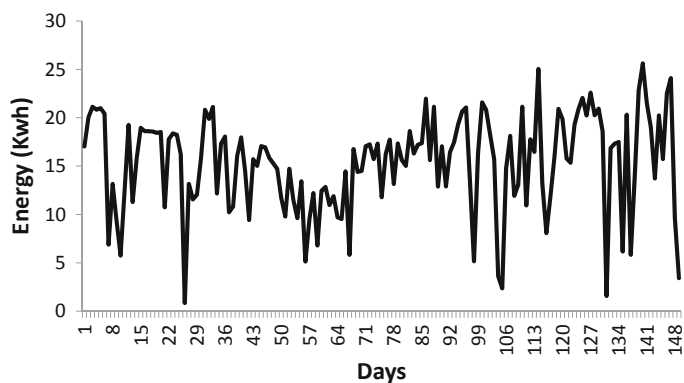


Fig. 13 Daily distribution of the PVES output energy over the period of study

4.2 PV Inverter Status Monitoring

Three- phase current and voltage magnitudes at the output of the inverter are drawn in Figs. 11 and 12. The voltage magnitude is approximately constant during the period of campus peak load demand (8 am–4 pm) while the output voltage of the inverter shows higher values at the period of light or no load (night and early morning). At this period of day, the tap changer of the transformer that feeds the L.V. distribution board (grid) tied with the PV system is set to be high. In general, it is noticed that the voltage magnitude in each phase along with the period of study is within the inverter output voltage constraints range (180–253 v) as per inverter user manual [20]. The three- phase current values at the output of the inverter are strongly related to the solar radiation variations. The inverter current values reach its daily peak with daily peak radiation values at most of the days (clear sunny and average cloudy days). The variations in the current values increase with increasing fluctuation in the solar radiation (heavily cloudy day). These rapid fluctuations—if it exceeds the standard limits—may impact the level of voltage and lead to voltage flicker especially in a high cloudy transients days [25].

4.3 The Whole Grid-Tie PV System Status Monitoring

In addition to Fig. 13 that reflects the daily distribution of the overall energy produced by the PVES during the period of the study, the health of the implemented PV system is completely investigated via comparing the total net benefit from the system in terms of DC power yield from the PV array and the injected AC power yield from the inverter to the local network with the energizing input to the system in terms of total in-plane insolation on a daily basis. Figure 14 shows time versus AC power, DC power, and solar radiation. This figure expresses complete conformity between the daily solar radiation, DC power, and AC power injected from the inverter to the L.V distribution network. This is completely true under any variation of the climatic conditions ranged from clear sunny day to average cloudy and heavily cloudy day. The AC power variations are very high with increasing cloud transients. This power fluctuation may yield large voltage fluctuation that may lead to significant line losses.

One of the PV system interconnection requirements with L.V distribution network imposed by regulatory standards is called voltage quality standard. This criterion is usually tested by checking the operating service voltage range from the PV system to be within certain limit. According to the Egyptian codes [26], the operational voltage range of a solar plant at the point of common coupling with the grid should be (0.85 pu–1.1 pu) for unlimited time period of operation. This range can also be increased to (1.1 pu–1.15 pu) for only 30 min of operation. In our case, this standard is investigated via calculating the variations in the monitored three- phase voltage magnitudes. The average and the maximum per unit values of voltage variation for

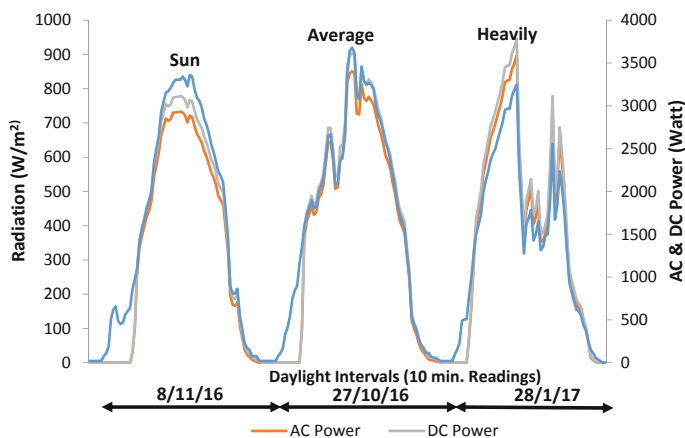


Fig. 14 AC power, DC power, and solar radiation as function of time

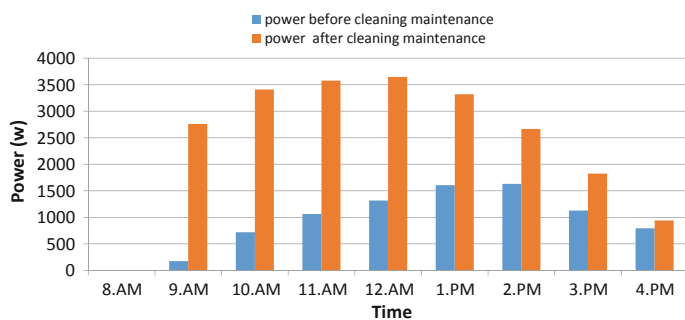


Fig. 15 One-day PV DC terminal output power before and after cleaning maintenance

the three phases voltages a , b , c are (1.076, 1.071, 1.069) and (1.14, 1.14, 1.13), respectively, which are within the specified voltage variation range in [26].

From the whole collected data of the nine months, we noticed that these data reflect two categories of the results. The measured variables show a large variation in its value between the first three months after installation and the next six months afterward. The variation was due to the high rate of dust accumulation at Giza, Egypt—where the system erected—at this period of the year and rarely cleaning maintenance rate for the PV panels. Moreover, the PVES is installed very close to a highly crowded and heavy traffic main road. A comparison between PV DC terminal output power before and after cleaning maintenance shown in Fig. 15 reflects approximately 50% loss in the panel efficiency along over the day due to dust accumulation on the front surface of the PV array.

5 Performance Indices

The results of *subtask 2*, “Analytical PV System Assessment” of the collaborative work within the International Energy Agency’s Photovoltaic power System program IEA PVPS task 13 on the performance and reliability of Photovoltaic systems [27] identified different performance relationships that cover the whole energy conversion chain for grid-tie PVES that may help in determining design errors and common operational faults. It showed that the performance relationships for such systems can be checked in different operational levels. System level and array level constitute the main levels to check the overall efficiency and the thermal behavior of the system. One of the most important indices to be determined in this context what is called performance ratio. The European commission (JRC/ISPR) [28] set a definition for the performance ratio of the PV plant which will be used in this chapter. It includes the capture (the array) losses and the system losses, and it enables evaluating the overall behavior of the PV plant as well as comparing various PV system qualities in different geographical locations. It is also helpful in identifying the need for detailed inspection of the PV system to avoid common problems such as soiling and defective components that need to be replaced. In this chapter, because the system is still in its initial operation phase and historical annual data are still not available (only six months of operation), some of the performance relationship will only be presented here as initial indicators for system behavior and as a characterization for the health of the operation. All the calculated performance indices in this chapter are referred to the IEC standard 61724 [15].

5.1 Results and Interpretation

The monthly output energy of the PV array (E_a) and the total injected energy into the grid from the PV system (E_{inj}) are shown in Fig. 16.

As it can be reflected from Fig. 16, the PVES produces a total 3145.05 kWh of energy but provides 2918.66 kWh of energy to the grid during the period of study. The difference between the energy production and the energy injected to the grid is ranged between 25 and 75 kWh and it represents the energy losses in the system. The lower energy production in this period was in month of December with 437.37 kWh of energy and the maximum energy production was 597.9 kWh in the month of October.

Remark 1 • The number of working days for the system in October is more than the same number in other months by one day so the total monthly array/injected energy in October is slightly more than its value in September although higher input radiation in September.

Figure 17 represents the monthly average system yields (array, reference, and final yield). These performance indices can be calculated according to (1–9).

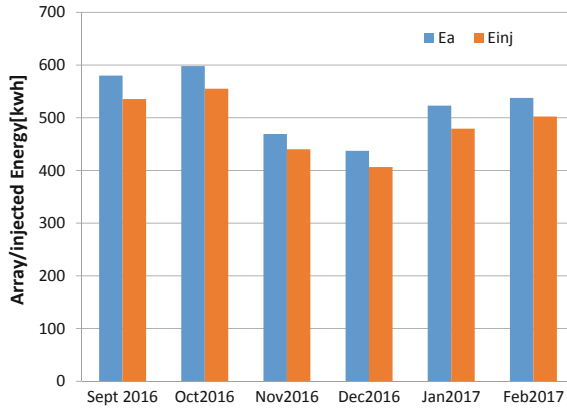


Fig. 16 PV array energy E_a and energy injected to the grid E_{inj}

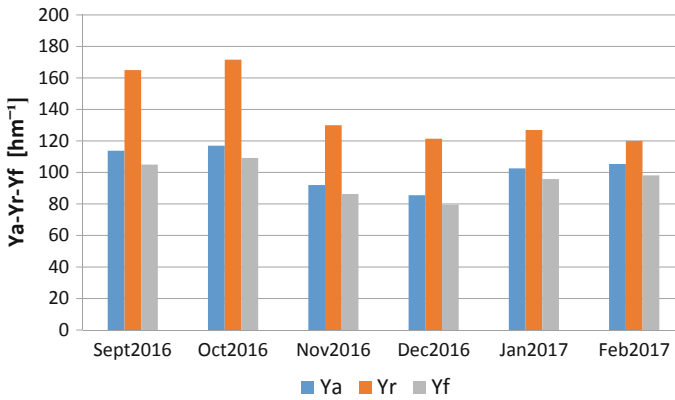


Fig. 17 Variation of array yields Y_a , reference yield Y_r , and final yield Y_f

For the daily and monthly array yield

$$E_{DC,d} = \tau_T \times \sum_{\text{day}} V_{DC,\tau_T} * I_{DC,\tau_T} \quad (1)$$

where τ_T represents the sampling interval in hours over the daylight interval of the day (in our case it is 1/6), \sum_{day} denotes the summation over the day and $E_{DC,d}$ represents daily total DC output energy (kWh).

$$\bar{E}_{DC,d} = \frac{1}{n} \sum_{d=1}^n E_{DC,d} \quad (2)$$

where $\overline{E}_{DC,d}$ represents monthly average daily DC output energy (kWh), $E_{DC,d}$ represents daily total DC output energy (kWh), and n is the number of working days per month (range from 24 days to 27 days).

$$Y_{a,d} = \frac{\overline{E}_{DC,d}}{P_0} \quad (3)$$

where P_0 is the rating capacity of the PV system

$$Y_{a,m} = Y_{a,d} * n \quad (4)$$

For the daily and monthly final yield

$$E_{AC,d} = \tau_T \times \sum_{\text{day}} P_{AC,\tau_T} \quad (5)$$

$$\overline{E}_{AC,d} = \frac{1}{n} \sum_{d=1}^n E_{AC,d} \quad (6)$$

where $\overline{E}_{AC,d}$ represents monthly average daily AC output energy (kWh) and $E_{AC,d}$ represents daily total AC output energy (kWh).

$$Y_{f,d} = \frac{\overline{E}_{AC,d}}{P_0} \quad (7)$$

$$Y_{f,m} = Y_{f,d} * n \quad (8)$$

For the monthly reference yield

$$Y_{r,m} = \frac{I_{i,m}}{G_r} \quad (9)$$

where $I_{i,m}$ is in-plane solar insolation (kWh/m²) and G_r is 1 kW/m².

The array and the final yields are the highest in months of September and October because these months reflect the maximum reference yield (the average inclined solar radiation was seen in Fig. 10) which leads to increasing the energy production and the energy injected to the grid (see Fig. 15). The capture and the system losses are calculated from Eqs. (10)–(11) and compared to the final yield as shown in Fig. 18 to characterize the performance of the PVES.

$$L_{C,m} = Y_{r,m} - Y_{a,m} \quad (10)$$

$$L_{S,m} = Y_{a,m} - Y_{f,m} \quad (11)$$

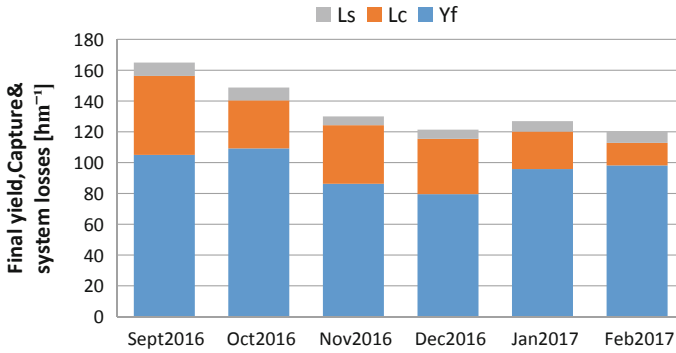


Fig. 18 Comparison between final yield, capture, and system losses

According to the IEC 61724 [15], the best way to characterize the performance of the PV system is to calculate its performance ratio that characterize the impact of the overall losses on the system's rated yield. During real operating conditions, The PR describes how close a PV system performs in an ideal manner. The monthly average daily PR can be calculated using (12)–(13).

$$PR_d = \frac{Y_{f,d}}{Y_{r,d}} \quad (12)$$

where PR_d is the daily PR

$$\overline{PR}_m = \frac{1}{n} \sum_{d=1}^n PR_d \quad (13)$$

where \overline{PR}_m is the monthly average daily PR.

We noticed that in this type of energy system, the losses is directly related to the final yield and as the final yield started to increase as in the month of September, the total system losses start to increase with special attention to the system losses in months of October and September. These two months exhibit more system losses due to the influence of the ambient temperature on the system's cabling and the inverter temperature. The capture losses are also the highest in the month of September due to the unstable weather conditions in Cairo in this month over the other studied months.

Figure 19 shows the monthly performance ratio for the PVES along with the studied period. The minimum PR of the system 0.63 was achieved in the month of September due to the increase in the overall system losses (see Fig. 17) while the maximum PR 0.82 was achieved in the month of February due to the improvement of both the capture losses and the inverter efficiency (see Fig. 19). The results are shown in Fig. 19 reflect good matching with other similar PVES in other world places. The calculated performance ratio of the new grid-tie PVES seems to be comparable with its value in the moderate climate such as Germany [29].

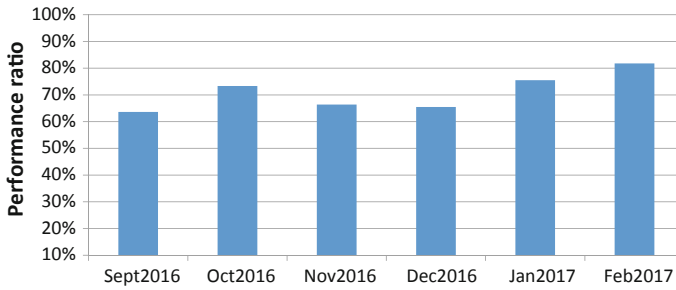
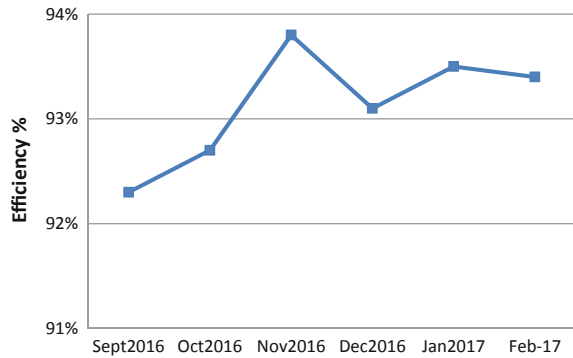


Fig. 19 Monthly performance ratio for the PVES along over the studied period

Fig. 20 Monthly average efficiency of PIKO inverter based on daily average value



5.2 More Performance Indicators

The IEC 61724 states other performance parameters to characterize the overall behavior of the PVES. In this section, the inverter's and system's efficiencies as well as the capacity factor are calculated to complement the operational behavior characteristics and evaluate the performance of the installed PVES under Egypt climatic conditions

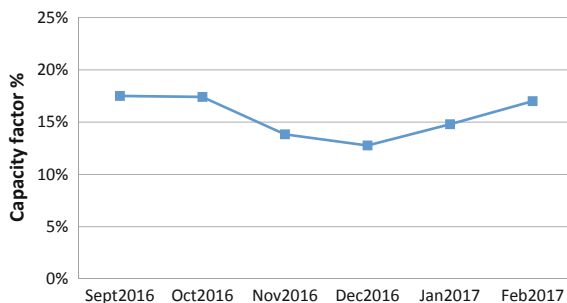
Inverter Efficiency

The monthly inverter efficiency is the ratio of the monthly total AC output energy to the monthly total DC input energy and it can be calculated from (14). Figure 20 shows the variation of this efficiency over the period of study.

$$\eta_{inv,m} = \frac{\sum_{d=1}^n E_{AC,d}}{\sum_{d=1}^n E_{DC,d}} \quad (14)$$

Under the real environmental operating conditions of Cairo over the studied period, the maximum inverter efficiency is found to be 93.8% and it takes place in November because the system losses (cabling + inverter) is minimal while the lowest value is 92.3% happened in September due to higher ambient temperature which affect the performance of the inverter.

Fig. 21 Average capacity factor per month



Remark 2 (a) Despite the reduction recorded on the surrounding temperature (ambient) from November to December, the maximum efficiency of the inverter was achieved in November.

(b) This is explained by noticing that the back surface temperature of the PV modules is approximately the same in both months of November and December so there is no tangible drop in cell temperature, hence, the output DC power/energy—from it—is approximately the same, however the reference yield (Fig. 17) or the radiation of November is higher than its counterpart in December (Fig. 10). This makes the final yield in November slightly higher than the December (Fig. 17); hence, there is an increase in maximum efficiency of the inverter in November.

Capacity Factor

The monthly capacity factor (CF) is defined as the ratio of actual annual/monthly energy injected to the grid by the PV system (E_{inj}) to the total installed capacity of the PV system multiplied by a number of hours per year/month [30, 31].

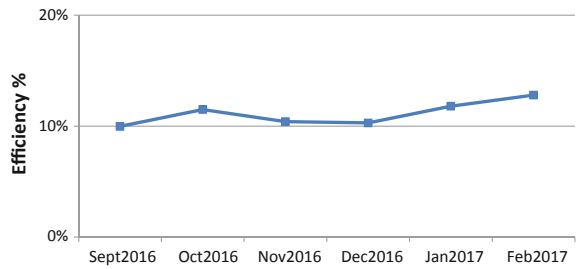
$$CF_m = \frac{\sum_{d=1}^n E_{AC,d}}{P_0 * 24 * n} \quad (15)$$

It relates the actual injected output of the PV plant to the theoretical maximum output of the plant that would be generated if it operated for 24 h per day for a year. Figure 21 reflects that the average capacity factor of the system per month is 15.55%; the highest value of the capacity factor is 17.5% in October due to the increasing energy production and the energy injected to the grid (see Fig. 15). The lowest final yield of the PV system in December leads to 12.76% CF which is the lowest during the period of study.

System Efficiency

The overall efficiency of the whole PV system including every component can be calculated from the total input radiation incident on the PV array area and the total output energy injected to the grid. Both values are readily available from the attached monitoring scheme and the overall system efficiency is calculated using (16).

Fig. 22 Average system efficiency per day for each month



$$\eta_{s,m} = \left(\frac{\sum_{d=1}^n E_{AC,d}}{\sum_{d=1}^n I_d * A} \right) \times 100\% \tag{16}$$

Figure 22 shows the average system efficiency is 11% and the highest value is 12.8% which is achieved at the month of February due to better performance ratio in this month which generally reflects low overall losses and better utilization of solar irradiance and improvement in system component efficiency (see Fig. 20).

Remark 3 (a) The results of the PV grid-tie system in Egypt seem to be comparable with other similar installed systems in different countries all over the world. The following table shows a comparison results for three essential indices (system efficiency, inverter efficiency, and performance ratio)

Country	η Inverter (%)	η PV system (%)	PR	Reference
Egypt	92–94	10–12.8	0.63–0.82	Present study
Italy	90–91	3.7	0.66	[32]
Spain	89.5	13.7	0.69	[33]
Brazil	91	3.7	0.5–0.81	[34]
Ireland	87	7.5–10	0.6–0.62	[35]

(b) The behavior of the system in the first period (6 months) is acceptable and the effect of the losses on the system rated output matches with similar systems in Italy, Ireland, and Spain.

6 Conclusions

The lack of reliable monitoring schemes for PV projects may lead to system failure and will certainly hinder the wide-spread use of such systems. This chapter represents a fully designed 5.1 kW rooftop grid-tie PV energy system along with a complete status monitoring scheme. The system has been put into operation since June 2016

and it was subjected to cleaning routine since September 2016. The operational status of the system is totally investigated via the inverter-based data acquisition system. The monitoring scheme yields a big data file that represents status variations every 10 min for 19 parameters along over the daylight interval for the studied period. The data of three typical operating days (Sunny—average cloudy—heavily cloudy) are extracted and analyzed to check the health of each part of the system and to characterize the status and the system operational behavior under various atmospheric conditions. Moreover, the impact of the newly installed PV system on the network is initially investigated at the inverter level. The voltage rise and fluctuations at the low-voltage distribution board at which the PV system is connected found to be within the permissible limits of the Egyptian code for grid-connected solar energy plants.

Based on the monitored variables and the collected data for the grid-tie PVES, the total DC energy yield from the system during the period is 3145.05 kWh, while the equivalent energy fed to the grid is 2918.66 kWh, and these figures reflect performance ratio that ranges from 0.82 to 0.63. The average system, inverter, and array efficiencies are found to be 11, 93.1 and 14.4%, respectively. The average capacity factor per month is found to be 15.55%. The distribution of the capacity factor during the period of study reflects that increasing this factor will directly lead to increase the net energy injected from the system to the grid. The following concluding remarks from the status monitoring of the PVES can be described as follows:

- (a) The integrated nature of the whole system (the PV panels, inverter, cabling, and other accessories) leads to special performance characteristics that tend to be different than the nature of each component in the system separately.
- (b) For the inverter, we noticed that the characteristics of the inverter under Egypt climatic conditions can be described according to the following two points:
 - In a relatively hot month like September, an increase in the ambient temperature leads to a reduction in the inverter efficiency and vice versa.
 - In a relatively modest months like October and November, This is not true because of the very small reduction in module temperature (approximately constant) and small increase in the final yield.
- (c) For the PV panels, we noticed that the performance of the panels under Egypt climatic conditions is matching the standard performance of PV where the changing of the temperature and the radiation affect heavily the performance of the PV panels.
- (d) For the whole PVES, the captured losses affect directly the performance ratio of the overall system which indicates the importance of routine cleaning for the PV panels in a weather like Egypt

In future, more investigation on system impact on the LV side of the electric network in terms of power quality indices such as voltage quality (voltage flicker, voltage unbalance, and voltage sag/swell) and harmonics (THD) will be performed based on the proposed monitoring scheme (inverter and smart meter).

References

1. Chen L, Mei S (2015) An integrated control and protection system for photovoltaic microgrids. *CSEE J Power Energy Syst* 1(1)
2. Besheer AH, Atawi I (2016) The effect of modeling types characterization for PV power source on maximum power point tracking. *IEEJ Trans Electr Electron Eng* 11(S1)
3. Besheer AH, Adly M (2013) A meta-heuristics search algorithm as a solution for energy transfer maximization in stand alone photovoltaic systems. *Elsevier Int J Electr Power Energy Syst* 51:243–254
4. Contemporary issues of the Egyptian energy sector. Egyptian Center for Economics and Social Rights
5. Renewable Energy Annual Report, 2016, New and Renewable Energy Authority
6. Adaramola MS, Vagnes ET (2015) Preliminary assessment of a small-scale rooftop PV-grid tied in Norwegian climatic conditions. *Energy Convers Manag* 90:458–465
7. Shiva Kumar B, Sudhakar K (2015) Performance evaluation of 10 MW grid connected solar photovoltaic power plant in India. *Energy Reports* 1:184–192
8. Micheli D, Alessandrini S, Radu R, Casula I (2014) Analysis of the outdoor performance and efficiency of two grid connected photovoltaic systems in northern Italy. *Energy Convers Manag* 80:436–445
9. Díez-Mediavilla M, Alonso-Tristán C, Rodríguez-Amigo MC, García-Calderón T, Dieste Velasco MI (2012) Performance analysis of PV plants: optimization for improving profitability. *Energy Convers Manag* 54:17–23
10. Ayompe LM, Duffy A, McCormack SJ, Conlon MC (2011) Measured performance of a 1.72 kW rooftop grid connected photovoltaic system in Ireland. *Energy Convers Manag* 52:816–825
11. Mpholo M, Nchaba T, Monese M (2015) Yield and performance analysis of the first grid connected solar farm at Moshoeshoe I International Airport Lesotho. *Renew Energy* 81:845–852
12. Kumar KA, Sundareswaran K, Venkateswaram PR (2014) Performance study on a grid connected 20 kWp solar photovoltaic installation in an industry in Tiruchirappalli (India). *Energy Sustain Dev* 23:294–304
13. Padmavathi K, Daniel SA (2013) Performance analysis of a 3 MWp grid connected solar photovoltaic power plant in India. *Energy Sustain Dev* 17:615–625
14. Elhodeiby SA, Metwally MH, Farahat AM (2011) Performance analysis of 3.6 kW rooftop grid connected photovoltaic system in Egypt. In: *International Conference on Energy Systems and Technologies (ICEST 2011)*, Cairo, pp 151–157
15. IEC standard 61724. <https://webstore.iec.ch/publication/33622>
16. Monto M, Rohit P (2010) Impact of dust on solar photovoltaic (PV) performance: research status. *Challenges and Recommendations* 14:3124–3131. <https://doi.org/10.1016/j.rser.2010.07.065>
17. Mejia F, Kleissl J, Bosch JL (2014) Impact of The effect of dust on solar photovoltaic systems. *Energy Procedia* 49:2370–2376
18. Karki IB (2015) Effect of temperature on the I-V characteristics of a polycrystalline solar cell. *J Nepal Phys Soc* 3(1)
19. Suntech polycrystalline PV panel 255w data sheet. www.suntech-power.com
20. <http://www.kostal-solar-electric.com/en-GB/Standalone/MediaDispositionViewer.aspx?medid=b9958eaff2404c27bd263895471c042f>
21. Firth SK, Lomas KJ, Rees SJ (2010) A simple model of PV system performance and its use in fault detection. *Sol Energy* 84:624–635
22. Kymakis E, Kalykakis S, Papazoglou TM (2009) Performance analysis of a grid connected PV Park on the island of Crete. *Energy Conv Manage* 50(3):433–438
23. Bayrak G, Cebec M (2013) Monitoring a grid connected PV power generation system with labview. In: *International Conference on Renewable Energy Research and Applications Madrid, Spain, 20–23 October 2013, ICRERA 2013*
24. SIEMENS, SENTRON PAC3200 manual. https://cache.industry.siemens.com/dl/files/150/26504150/att_906558/v1/A5E01168664B-04_EN-US_122016_2016122213163

25. Chidurala A (2016) High penetration of PV systems in low voltage distribution networks: investigation of power quality challenges and mitigation. PhD thesis, the university of queen land, Australia
26. Solar Energy Plants Grid Connection Code, March 2017. <http://egyptera.org/ar/code%20w%20dalil.aspx>
27. Woyte A, Richter M, Moser D, Mau S, Reich N, Jahn U (2013) Monitoring of photovoltaic systems: good practice and systematic analysis. In: 28th European PV Solar energy conference and exhibition, October, France
28. The European commission (JRC/Ispira). <https://ec.europa.eu/jrc/en/about/jrc-site/ispra>
29. Jahn Ulrike, Nasse Wolfgang (2004) Operational performance of grid connected PV systems on buildings in Germany. *Prog Photovolt: Res Appl* 12:441–448. <https://doi.org/10.1002/pip.550>
30. Cherfa F, Hadj Araba A, Oussaidb R, Abdeladima K, Bouchakoura S (2015) Performance analysis of the mini-grid connected photovoltaic system at Algiers. *Energy Procedia* 83:226–236
31. Kymakis Emmanuel, Kalykakis Sofoklis, Papazoglou Thales M (2009) Performance analysis of a grid connected photovoltaic park on the island of Crete. *Energy Convers Manag* 50:433–438
32. Dunlop EW (1997) Electrical characterization and analysis of operating conditions of amorphous silicon building integrated photovoltaic modules. In: 14th European PV solar energy conference 1997, Barcelona, Spain, p 203741
33. Miguel AD, Bilbao J, Cazorro JRS (2002) Performance analysis of a grid-connected PV system in rural site in the Northwest of Spain. In: World Renewable Energy Congress VII 2002, Cologne, Germany
34. Ruther R, Dacoregio MM (2000) Performance assessment of a 2 kWp grid-connected, building integrated, amorphous silicon photovoltaic installation in Brazil. *Prog Photovoltaics Res Appl* 8:257–266
35. Mondol JD, Yohanis Yigzaw, Smyth Mervyn, Norton Brian (2006) Long-term performance analysis of a grid connected photovoltaic system in Northern Ireland. *Energy Convers Manag* 47:2925–2947